SUPERNOVA POLARIZATION SPECTRA CALCULATED USING THE SOBOLEV-H METHOD

By

DAVID JOHN JEFFERY, M.SC.

A Thesis
Submitted to the School of Graduate Studies
in Partial Fulfilment of the Requirements
for the Degree
Doctor of Philosophy

McMaster University

SUPERNOVA POLARIZATION SPECTRA

DOCTOR OF PHILOSOPHY (1988)
(Physics)

McMASTER UNIVERSITY
Hamilton, Ontario

TITLE: Supernova Polarization Spectra
Calculated Using the Sobolev-H Method

AUTHOR: David John Jeffery, B.Sc. (McMaster University)
M.Sc. (McMaster University)

SUPERVISOR: Professor P. G. Sutherland

NUMBER OF PAGES: xi, 354

ABSTRACT

In order to analyze supernova spectropolarimetry a radiative transfer technique is required that can treat polarization and introduces polarizing effects. To do this a modified Sobolev method, here called the Sobolev-H method, was developed for axisymmetric atmospheres with large velocity gradients. The method uses the Stokes parameters to treat the radiation field. It incorporates Hamilton's phase-matrix for resonance scattering by atomic transitions (1947), and thus allows for the polarizing effect of resonance scattering.

The interest in supernova spectropolarimetry is to determine whether supernovae are spherically symmetric or not; the net radiation flux from a spherically symmetric supernovae would not be polarized. A computer program written using the Sobolev-H method calculates the P-Cygni line profiles emerging from homologously expanding atmospheres. A parameter survey of axisymmetric prolate and oblate models has been performed using this program. The survey demonstrates that there is considerable polarization structure associated with the P-Cygni lines. The emission and absorption polarization features have their position angle of polarization shifted from each other by 90° for both prolate and oblate models.

An analysis of the March 6–7 polarization data for Supernova 1987a has been performed. Provided the polarization of 1987a's flux arises from oblate shape asymmetry, the analysis indicates a 50 % asymmetry ($\xi_{obl} \doteq .5$). A similar asymmetry would be required if 1987a were prolate. Since the polarization data indicates that an intrinsic continuum polarization exists, a method here called the discretized continuous opacity or DCO method has been devised in order to calculate continuum polarization. Calculations with the DCO method show that good qualitative agreement with the observed continuum polarization may be achievable.

ACKNOWLEDGEMENTS

I thank my supervisor Dr. Peter Sutherland who has been my teacher and guide through six long years of graduate studies. I also thank Dr. Ralph Pudritz for much encouragement and advice in the last year of those six.

The members of the Theory Group and Department of Physics, past and present, have provided a place and time of fellowship and scholarship for my studies. They are all remembered with gratitude. I especially recall my friends—who all finished their degrees before I finished mine—Graham Glen, Mike Coombes, Walter Stephan, Sikander Azam, and Kailash Ambwani.

I also thank McMaster University and the Natural Sciences and Engineering Research Council of Canada. These institutions, filling the antique rôle of scholar's patron, have provided financial support.

For my parents

Jean and Jack Jeffery

In the Sky We've Sought

New thought increases thought,
On the signs requiring tilted head,
For in the sky they're sought.

The gods these signs wrought,
For the foretelling of each man's thread,
Apportioning his lot.

Magi this lore taught,
The Heaven is like a book where God is read,
New thought increases thought.

An orb on a circle sped,
Perpetual perfect dazzling dot,
Knowingly Plato said.

Long dark ages fought,
While stars Ptolemaic dances lead,
Where in the sky they're sought.

Copernicus was fraught
Of scorn until expiring, nearly dead,
Revealed his thought:

The sun moves not,
The earth and planets around it tread.
New thought increases thought.

Since that said
Ever accumulating new thought,
New fact and theory wed.

Far vistas caught,
And the lens on radiations has fed,
Where in the sky they're sought.

It's a long time to bed,
And all this labour this conclusion got:
The last word's not been read.

The reading, a refreshment brought,
The thinking delays the bed,
New thought increases thought,
For in the sky we've sought.

McMaster University
14 July 1987

TABLE OF CONTENTS

LIST OF FIGURES

Figure

LIST OF TABLES

Table

Introduction

Supernova explosions are usually considered as spherically symmetric events. They are strongly assumed to arise from stars, and stars are quite spherically symmetric. There is little observational data that is inconsistent with a spherically symmetric explosion. Computationally, spherical symmetry is overwhelmingly the most tractable assumption, and so nearly all theoretical supernova calculations assume spherical symmetry. However, there are some reasons to suspect that there could be asymmetric supernovae. Supernova or core collapse computations that include asymmetric effects such as rotation (Müller and Hillebrandt 1981; Hillebrandt 1982; Bodenheimer and Woosley 1983), rotation and magnetic fields (LeBlanc and Wilson 1970; Symbalisty 1984; Symbalisty 1985), and Rayleigh-Taylor instabilities (Chevalier and Klein 1978; Livio *et al.* 1980) do show significant asymmetry in the resulting structures. Some of the variability in the observations of some classes of supernova may owe to asymmetry.

Since the exploding supernova matter cannot be resolved, a direct observation of asymmetry is not possible. However, an asymmetry may manifest itself in the polarization of the observed supernova flux. Supernovae have scattering atmospheres. Scattering by either electrons or resonance transitions is a polarizing process; thus the flux emitted by supernova should be polarized. Since only net flux can be measured, only the net polarization can be measured. A source that is circularly symmetric about the line of sight must by symmetry have zero net polarization no matter how polarized its resolved surface brightness may be. Thus polarized supernova radiation would show that some sort of asymmetry exists.

Unfortunately, the interstellar medium can also polarize radiation on its passage from supernova to Earth. This interstellar polarization (*ISP*) must be subtracted from the observed polarization to obtain the intrinsic supernova polarization. The *ISP* value may not be easy to determine. The *ISP* component from the Galaxy may be determined by observing stars near to the line of sight to the supernova. The component due to the parent galaxy of the supernova may be determined from observing starlight from the region surrounding the supernova; such a determination would often be very approximate. Thus the *ISP* value to subtract will often not be a well known quantity.

Since the ISP can be several percent, it could be considerably larger than the intrinsic polarization. Thus a simple detection of polarization in supernova flux will not by itself yield even qualitative information about the supernova. Fortunately, the ISP is not strongly dependent on wavelength (Serkowski *et al.* 1975), and should not vary on the time scales of supernova evolution. Thus strong wavelength or time variation would be the marks of intrinsic polarization.

After having a means of detecting intrinsic supernova polarization, the question of interpretation is opened. The inevitable procedure in studying astrophysical spectra is to construct a plausible, though perhaps highly simplified, model of an observed object including physical effects that give rise to the features observed. From the model synthetic features are calculated and then the model parameters are varied until a fit to the data is achieved. If the assumed physical model was realistic, then the fitted parameters provide information about the observed object. For supernova polarization the first works on interpretation by model calculation are by Shapiro and Sutherland (1982), and McCall (1984, 1985).

Shapiro and Sutherland considered ellipsoidal atmospheres emitting radiation with a continuum polarization. They calculated the intrinsic supernova polarization to be expected for a range of their model parameters. They hoped that an accurate determination of the ISP, or that the wavelength or time variation of continuum polarization would permit intrinsic supernova polarization to be detected. This intrinsic polarization could then be compared to their calculated polarizations to determine the supernova parameters.

McCall, to obviate to some degree the ISP difficulty, considered the polarization features that would be associated with the P-Cygni line profiles. These profiles are prominent features in the supernova spectra. They extend over wavelength intervals over which the ISP polarization varies slowly. Since the P-Cygni lines owe at least in part to resonance scattering, there should be polarization features correlated with the flux features. McCall considered a simple model consisting of an ellipsoidal scattering atmosphere surrounding an ellipsoidal continuum emitting core. He obtained expressions relating polarization values directly to an asymmetry parameter. McCall's model was very simple; at most qualitative information can be extracted from it even assuming the ISP is accurately known.

These pioneering works on supernova polarization inspired the development of the line polarization calculating technique and line polarization calculations presented in this thesis. The physical model used for the calculations was largely derived from the works of Branch (Branch 1980; Branch *et al.* 1981, 1982, 1983, 1985). However, following Shapiro and Sutherland, and McCall ellipsoidal atmospheres were considered. Other sorts of asymmetry could have been considered. The radiative transfer technique, the Sobolev method, used by Branch had to be modified to treat polarized radiation and to introduce polarizing effects into the scattering process. The modification required the use of Hamilton's phase-matrix for polarizing resonance scattering (Hamilton 1947). To recognize the use of this phase-matrix the modified Sobolev method has been called the Sobolev-H method.

The application of the analysis technique presented in this thesis requires spectropolarimetric data. Before 1987 only two reports of supernova spectropolarimetry existed (McCall *et al.* 1984; McCall 1985). The discovery on 1987 Feb. 24 of a supernova (Supernova 1987a; henceforth SN 1987a) in the nearby galaxy the Larger Magellanic Cloud has provided a remarkable opportunity for spectropolarimetry. Early reports or analyses of spectropolarimetry have been made by Walsh *et al.* (1987), Magalhaes and Velloso (1987), Schwarz and Mundt (1987), Jeffery (1987), Schwarz (1987), and Cropper *et al.* (1987). The spectropolarimetric observations are of great potential value in understanding SN 1987a and other supernovae as well. It is hoped that in the future that spectropolarimetry will be performed on all well observed supernovae.

The outline of this thesis is as follows. Chapter 1 provides an introduction to supernovae, gives a brief review of SN 1987a, and presents the case for asymmetric supernovae. Chapter 2 provides a derivation of the Sobolev and Sobolev-H methods. A discussion of physical validity, and application to supernovae of these methods is given. Chapter 3 reviews the Shapiro and Sutherland, and McCall supernova polarization calculations. Chapter 4 presents the polarization profiles and their analysis for a parameter survey model of atmospheres. Chapter 5 presents an analysis of early spectropolarimetry of SN 1987a. The Conclusion and four appendices appear at the end of the thesis.

Chapter 1

Supernovae, Supernova 1987a, and Asymmetric Supernovae

a) Supernovae

Supernovae are the catastrophic explosions of stars. Their luminosity at maximum is greater than the net luminosity of some galaxies. The kinetic energy of the exploding matter is of order 10^{51} erg which is roughly the energy radiated by a Sun-type star in a 10 billion year lifetime. Gaining an understanding of the physics of these tremendous outbursts is a considerable challenge. In addition to learning about the nature of the explosion itself there are a host of related interests. The expanding, cooling supernova matter (a supernova remnant or SNR) and its interaction with the interstellar matter (ISM) is a long-lived object for radio, X-ray, and optical astronomy. Supernovae, through their remnants, are thought to contribute strongly to the universal abundances of carbon and all heavier elements; thus they are very important to the chemical evolution of the galaxies, not to mention of life. The energy they release may determine the dynamics and heating of the interstellar medium. The remnants from one of the classes of supernova (type II) are predicted to include the exotic compact objects neutron stars and pulsars. The neutrino flux predicted (and confirmed by observation of SN 1987a) for type II supernovae should provide insight not only into supernovae, but into neutrino physics. The great optical luminosity of supernovae makes them useful as distant indicators; they may eventually help to determine accurately Hubble's constant, the distance scale of the universe.

The history of the study of supernovae began in the 1920's and 1930's when it was recognized that novae in spiral nebulae would have to have been very bright if the spiral nebulae were extra-galactic star systems (for a historical review see Trimble 1982). Historically, a nova is a new and temporary star; the name nova comes from latin for new. Novae have been observed and reported throughout astronomical history. Most historical novae, now called classical novae, are theoretically understood to be the thermonuclear explosion of a surface layer of hydrogen accreted onto a white dwarf from a binary companion star. These objects suddenly brighten in absolute B magnitude from greater than 10 to less than −7 and then fade away in a period of tens of days.[1] Supernovae are now known to achieve absolute B magnitudes in the range from −16 to −20; they are thus at least about 10^4 times brighter than novae. Theoretically, supernovae are entirely separated from the classical novae events.

It was early recognized that there were two observationally distinct classes of supernovae: type I and type II. Type I supernovae have no detectable hydrogen. Type II supernovae have prominent hydrogen lines. At least two subclasses have been distinguished for both main classes. Theoretical understanding of these two classes is quite different; therefore discussion of supernovae must soon become class specific. In section (b) of this chapter the observational data and the theoretical model of type I supernovae will be discussed. Section (c) does the same for type II supernovae.

Before going to the class specific discussion there are some general conventions and facts that should be introduced.

A supernova is named by the year in which it is discovered with a letter appended that gives the order of discovery by alphabetical ordering: e.g., the fourteenth supernova discovered in 1983 is named SN 1983n, or often just 1983n. If only one supernova is discovered in a year, then the appended letter may be omitted. If a supernova has not yet received a formal designation it may be identified only by noting the supernova's parent galaxy; e.g., SN 1981b was called a 1981 supernova in NGC 4536 by Branch *et al.* (1982). Historic supernovae may have names given in honor of a discoverer or famous observer: e.g., SN 1572 is sometimes called Tycho, and SN 1604 is sometimes called Kepler.

The total electromagnetic luminosity of a supernova is not an observed quantity, though it can be inferred from extensive observations. Since the color temperature of the supernova during the period for which observations are available implies that a Planck spectrum would be peaked in the visible, the B and V magnitudes are probably quite good indicators of the total luminosity. Since these color

[1] Magnitudes are a logarithmic measure of radiation intensity. A magnitude is related to intensity by

$$M = -2.5\log(I) + K,$$

where K is a constant. A color magnitude measures the weighted average of intensity over a wavelength band. The B (blue) color measures the intensity at $\approx 4400\,\text{Å}$, and the V (visual) color measures the intensity at $\approx 5500\,\text{Å}$. Apparent magnitude is what is measured for an object from Earth. Absolute magnitude is what would be measured for an object by an observer located at 10 pc from the object. Conventionally, the magnitude scales on graphs run from high numbers at the bottom to low numbers at the top. Thus a low magnitude corresponding to a high intensity will be plotted high on a graph.

magnitudes are observables, they are the customary quantities to plot in lieu of the unobservable total luminosity. Supernova magnitudes plotted versus time (the time evolution of luminosity) are called light curves. The maximum of the light curve (the magnitude minimum) is called maximum light. Fig. 1.1 shows examples of mean supernova light curves for type Ia supernovae, and the two common subclasses of type II supernovae.

Since the discovery of supernovae as distinct events, over 500 supernovae have been discovered.[2] The rate of discovery is roughly 10 per year. They are usually discovered on photographic plates well after maximum light has passed. Usually only very prominent supernovae that have been discovered near or especially before maximum light have merited extensive observation. Due to insufficient observational data most supernovae are not even assigned a type classification.

Recently there have been two promising developments in supernova discovery procedure. Amateur astronomer Rev. Robert Evans has demonstrated that visual discovery of supernovae is a feasible and rewarding procedure (Evans 1986). Visual discovery involves the examination of a galaxy by telescope and eye, and comparison to a photograph or chart of the galaxy in a catalogue. This procedure clearly requires a dedicated instrument and astronomer. However, visual discovery has the important advantage that a discovered supernova can be reported without the delay involved in photographic discovery. The delay in photographic discovery usually means that a discovery is only reported after the supernova has waned which decreases the supernova's observational value. An additional advantage is that amateurs can devote attention to nearer galaxies which produce the brightest supernovae. Through 1985, 13 supernovae had been discovered visually by amateurs of which 11 were by Evans. Of these supernovae 5 were discovered before maximum light.

The second development is the use of automated systems for supernova search. In this procedure a computer controlled telescope provides a galaxy image that is compared by computer to a reference image; the supernovae are then picked out by an algorithm. Such a system promises to discover on the order of 100 supernovae per year (Kare *et al.* 1982). The attempt to develop such an automated system has been going since at least 1968 (Colgate 1982). In 1986 an automated search system discovered a supernova in M99 (Pennypacker *et al.* 1986; Piel *et al.* 1986). Unfortunately that system has not, apparently, become fully operational. The high supernova discovery rate remains an expectation.

---

[2] By 1980, 474 supernovae had been discovered (Barbon 1980). The rate of discovery indicates that more than 500 have been discovered by 1987.

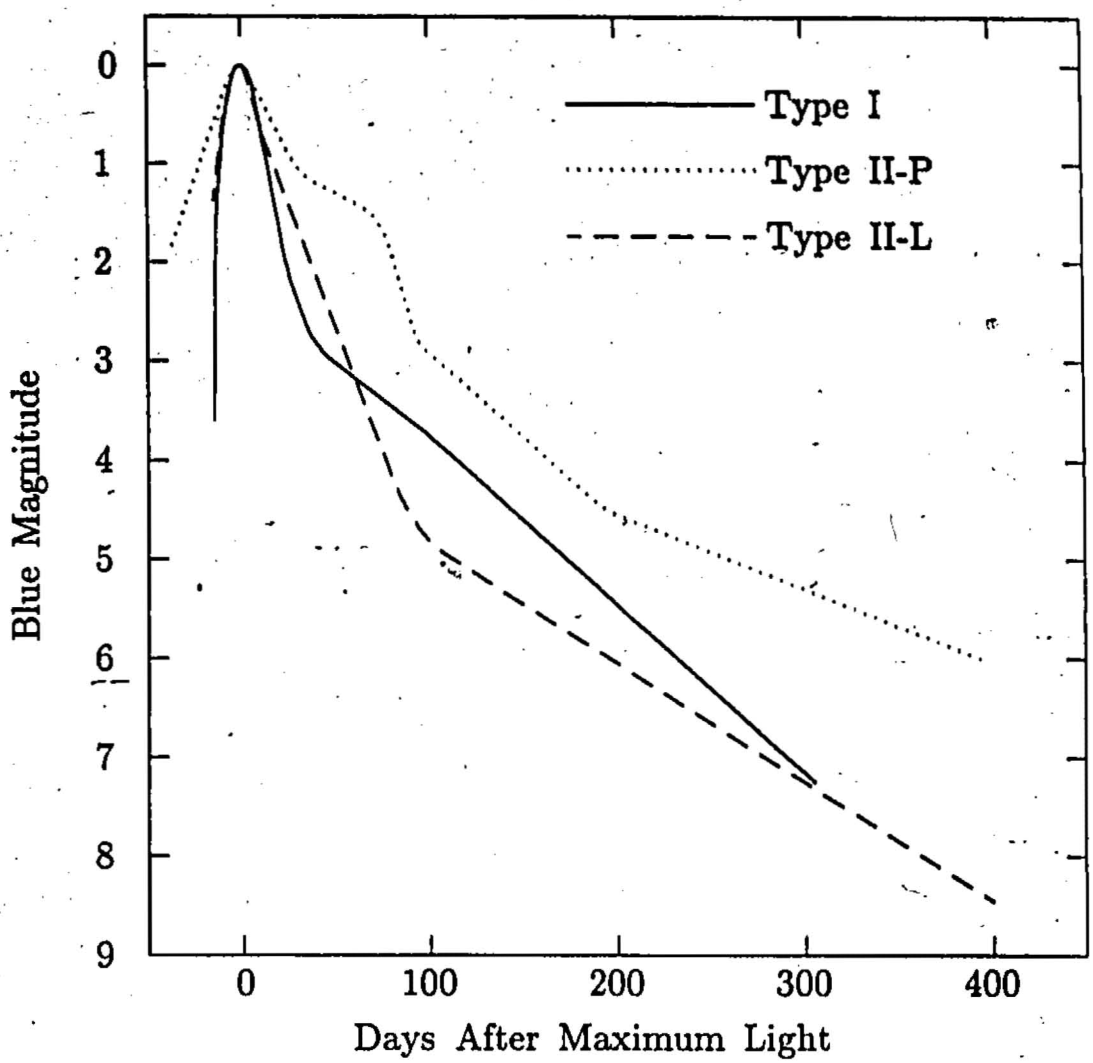

Fig. 1.1. Mean blue light curves for supernovae taken from Doggett and Branch (1985). The mean curves were drawn by eye through a compilation of supernova observations. The vertical scale is arbitrary; the curves are all normalized to their maximum light values. The observations show some scatter about the mean curves; the scatter is partially observational, but to an uncertain degree owes to intrinsic variation in supernovae. The type I curve is drawn through a collection of data given by Barbon *et al.* (1973); presumably all these events were classic type Ia supernovae. After 40 days the type I curve enters a slower phase of decline; after 100 days Doggett and Branch find that the decline becomes 0.017 mag day^{-1}. On the basis of light curves Barbon *et al.* (1979) divided type II supernovae in two subclasses: plateau (type II-P) and linear (type II-L). Doggett and Branch find that the late time decline rate for type II-P is 0.0075 mag day^{-1}, and for type II-L is 0.012 mag day^{-1}. The similarity in the light curves of SNe type I and SNe type II-L lead Doggett and Branch to suggest that these two classes may be related events.

b) Type I Supernovae

The type I class of supernova has in the 1980's become divided into two subclasses. Both subclasses, of course, have the observational type I distinction: an absence of detectable hydrogen. The classical type I supernovae for which most observation and theory exists are now called type Ia or sometimes just type I. The new subclass is called type Ib. There are also a few peculiar supernovae not confidently assigned to either subclass.

A general observational fact about type Ia supernovae is that they are a remarkably homogeneous class of events. Authors Kowal (1968) Tammann (1978) and Elias *et al.* (1981) have noted that well observed type I light curves are very similar. Recently Cadonau *et al.* (1985) have claimed that there is "no photometric evidence for light curve variations of SNe I", and therefore the type Ia class are excellent standard candles. Branch (1982) reports that type I optical spectra are also very uniform at all phases. Thus it may be that all type Ia data can be averaged together to obtain the intrinsic type Ia properties. However, intrinsic type Ia variations may just be small or comparatively rare. Branch (1987a) reports that the photospheric velocity (see Chapter 2 section (c)) near maximum light of type I supernova SN 1984a was 35% higher than that of the well-observed and typical type I SN 1981b. This evidence indicates that there may be some intrinsic variation in the type Ia class.

The evolution of a type Ia supernova light curve can be seen in Fig. 1.1 taken from Doggett and Branch (1985). This mean curve was just drawn by eye through a set of old data points (Barbon *et al.* 1973). This particular curve is presented as representative, not as the best obtainable. From Fig. 1.1 the rapid evolution toward maximum light can be seen. It is strongly assumed that there is a sharp supernova ignition time which of course has never been observed. Pskovskii (1977), from a survey of data, determined the time from ignition to maximum light to be 15.5 ± 1.5 days. More recently Cadonau *et al.* (1985) report the rise time to be greater than 20 days. It should be noted that there are few observations for supernovae before maximum light, and so there is statistically low accuracy for the rise phase.

The average absolute B magnitude at maximum light has been determined to be

$$\langle M_B^{max} \rangle = -19.69 \pm .13 + 5\log(H_0/50) \tag{1.1}$$

(Cadonau *et al.* 1985). The H_0 is Hubble's constant which sets the scale size of the universe. At present H_0 is not well determined; values between 40 km s^{-1} Mpc^{-1} and 120 km s^{-1} Mpc^{-1} have been reported. Cadonau *et al.* find $H_0 = 43^{+10}_{-7}\,\mathrm{km\,s^{-1}\,Mpc^{-1}}$, but cautiously, like many others, prefer to report quantities that depend on H_0 in terms of H_0.

Following maximum light the light curve decreases rapidly with a slope $\sim .1\,\mathrm{mag\,day^{-1}}$. After about 30 days there is a sharp change in the average decline and the slope becomes $\sim .01\,\mathrm{mag\,day^{-1}}$. From about 100 to 500 days the mean slope is found to be $.017\,\mathrm{mag\,day^{-1}}$ by Cadonau *et al.* (1985) and by Doggett and Branch (1985). This slope corresponds to a luminosity half-life of

$$t_{1/2} = 44\,\mathrm{days}. \tag{1.2}$$

Of course, for the later light curve the number of data points become fewer, since only the supernovae with high apparent brightness can be observed so late. Thus the late-time light curve is increasingly less certainly determined as time increases beyond maximum light.

As remarked above, the optical spectra of supernovae are remarkably alike at all phases that are well-observed. Near maximum light the spectra are mainly made up of the P-Cygni lines (see Chapter 2 section (b)) of singly ionized species such as Ca II, Si II, Mg II, and S II along with O I and perhaps He I (Branch *et al.* 1982). In the near UV, Co II features have been identified near maximum light (Branch *et al.* 1985; Harkness 1985, 1986). After maximum light many Fe II lines begin to appear in the spectrum; by about 120 days after maximum light Fe II lines dominate the spectrum.

In the picture of a supernova atmosphere developed by Branch (1980) and Branch *et al.* (1981, 1982, 1983, 1985) the lines arise from resonance transition scattering of continuum radiation emitted by a photosphere. The photosphere is a surface (assumed spherical by Branch *et al.*) from which a photon has approximately an even chance of escaping to infinity without interacting with any sources of continuous opacity. The photon interaction with the sources of line opacity above the photosphere results in the line spectrum. The changes that occur in the spectrum as time passes must owe to a large degree to the falling density of the expanding supernova matter. Falling density causes the opacities to fall. The decreasing continuous opacity causes the photosphere to recede into the supernova matter as time passes: i.e., the photosphere encloses a decreasing fraction of the supernova mass.[3] Thus compositional variation with mass fraction may be changing the strengths

[3] The radius of the photosphere actually increases for about 30 days after maximum light due to the overall expansion of the supernova; thereafter the radius decreases with time (Branch *et al.* 1983). In terms of supernova mass fraction, the photosphere is always receding.

of the sources of line opacity. The increasing strength of Fe II lines in the spectra of type I supernovae may indicate that their interiors are iron rich. However, this is not necessarily the case. The recession of the photosphere causes the line scattering atmosphere to become geometrically extended. In such extended atmospheres, local thermodynamic equilibrium (LTE) may not obtain; non-LTE effects may change the spectrum even if the composition is uniform (Feldt 1980, p. 32; Branch *et al.* 1983). The changing temperature of the expanding matter could also affect the line spectrum.

Type I supernovae occur in galaxies of all morphological type though with varying rates (Tammann 1982). There is evidence from the characteristics of the parent galaxies that type I progenitors are old low mass stars.[4] In spiral galaxies, type I supernovae are not confined to the spiral arms (Maza and van den Bergh 1976). Spiral arms are density waves in spiral galaxies where there is a concentration of stars and gas. The concentration of gas causes star formation in the spiral arms. However, because a spiral arm is a wave, stars formed in the spiral arm will be left behind in time by the moving wave crest. Assuming the supernova progenitors are born in the spiral arms their lack of confinement to the spiral arms indicates that the progenitor lifetimes must be greater than $\sim 10^7$ years and the progenitor masses less than $\sim 6\,M_\odot$ (Biermann and Tinsley 1974). In elliptical galaxies, the stars have ages $\sim 10^{10}$ years, and therefore have masses that are $\lesssim 1\,M_\odot$. Thus it is plausible that type I progenitors in elliptical galaxies have ages that are of the order of the universe's age. A contrary conjecture to old low mass progenitors has, however, been made by Oemler and Tinsley (1979).

The above is just a short and very incomplete review of type Ia observations. However, it should sufficiently give the context for the current theoretical understanding of type Ia supernovae.

At present a standard model of type Ia supernovae exists. This model explains the spectra and light curves very well. Its difficulties are in finding a plausible scenario for evolution to explosion, and in understanding the element abundances resulting from the type Ia supernova rate.

The model explosion begins with a carbon-oxygen white dwarf. White dwarfs are supported by the pressure of a degenerate electron gas. Such a system has an absolute upper mass limit, called the Chandrasekhar mass, of approximately $1.4\,M_\odot$; the exact value depends slightly on composition. Above the Chandrasekhar mass the pressure of a degenerate electron gas cannot support the system;

[4] In drawing inferences about type I progenitors, there is the complication of the existence of two subclasses of type I supernovae. The conjecture of old low mass progenitors applies to the type Ia supernovae, since they are the most abundant subclass and since there is evidence that all type I events seen in ellipticals are type Ia's (Panagia 1985).

heavier cold objects must be neutron stars or black holes. The existence of such a rather exact upper bound on the mass of the progenitor helps to explain the uniformity of type Ia events. A dwarf star near this mass limit has such a high central density that it is close to the regime where pycnonuclear carbon ignition can take place at or near the center. Pycnonuclear burning occurs due to high density with only a slight temperature dependence.

Ignition occurs when the rate of energy released due to burning exceeds the losses due to neutrino cooling processes, and heat transport due to conduction or convection. The heat build up due to the carbon burning cannot be dissipated by adiabatic expansion, since the degenerate electron gas pressure is only slightly affected by the increasing temperature. Thus there is a rapid increase in temperature in the central region of the dwarf. This temperature increase stimulates thermonuclear burning of carbon and oxygen which in turn causes increasing temperature. A thermonuclear runaway occurs that takes all the central matter to the state of nuclear statistical equilibrium (NSE). The heat released by the burning lifts the degeneracy of the central matter and an over-pressure develops that becomes an outgoing shock wave. The shock wave though it accelerates and expands the dwarf matter is insufficiently strong to heat and compress the matter to the point of nuclear burning. Rather the nuclear burning front moves outward at slower speed than the shock and is propagated by convective transport. This convectively driven burning front is usually called a deflagration or sometimes a flame. The energy released by the deflagration is sufficient to explode the white dwarf. The rapid adiabatic cooling of expansion causes the matter in NSE, at least in the inner regions of the white dwarf, to freeze out of NSE as ^{56}Ni.

The physics of the deflagration is one of the great uncertainties of the standard model. Convection in these extreme conditions is not well understood. Convection is inherently a 3-d (3 dimensional) process and 3-d hydrodynamic calculations are at present too computer intensive to be undertaken. Müller and Arnett (1982) have done a 2-d hydrodynamical calculation. The results show angular inhomogeneity in the propagation of the deflagration, with the creation of large fingers expanding out from a spherically burnt core. Such calculations are sensitive to the grid size used for the difference equations; a finer grid may well produce different results. Müller and Arnett suggested that a finer grid might cause the deflagration front to become more spherically symmetric again.

Most deflagration calculations (Nomoto *et al.* 1976; Nomoto 1980a,b, 1981; Jeffery 1983; Nomoto *et al.* 1984; Woosley *et al.* 1984; Sutherland and Wheeler 1984; Jeffery and Sutherland

1985) have simulated convection with some modified mixing-length theory that provides a subsonic velocity for the deflagration propagation. Mixing-length theories have a free parameter that controls the propagation speed. This parameter is adjusted in deflagration calculations to give the correct energy to the white dwarf matter. Observations of supernova spectra determine the maximum light photospheric velocity to be $\sim 12000\,\mathrm{km\,s^{-1}}$ (Branch *et al.* 1982). Energies near 10^{51} erg must be released in the white dwarf to produce such velocities. If the deflagration velocity is too fast, too much of the white dwarf is burnt releasing too much energy before the cooling due to expansion turns off the burning; the resulting model explosion is moving too fast. If the deflagration velocity is too slow, burning is turned off before enough energy is released.

The nuclear burning, when the deflagration is turning off in the outer regions of the white dwarf, is incomplete and intermediate mass elements such as Ca, Mg, and Si are produced (Nomoto *et al.* 1984). It is clear that the elements in type I supernova spectra are produced in at least approximately the right regions by model calculations. Moreover, Branch *et al.* (1985) using the Nomoto *et al.* 's W7 deflagration model created synthetic spectra that were in good agreement with observed type Ia spectra.

More important than the spectra, deflagration models are successful in reproducing the type Ia light curve. Most of the energy released by the deflagration burning is transformed into the kinetic energy of the explosion. The electromagnetic radiation luminosity that is the whole of the observed supernova display can be provided by the delayed energy released by the decay of the radioactive ^{56}Ni (Pankey 1962; Colgate and McKee 1969; Meyerott 1978; Arnett 1979; Colgate *et al.* 1980; Axelrod 1980a,b). The ^{56}Ni, produced in the inner regions of the exploding white dwarf, is beta unstable and decays with a 6.1 day half-life to ^{56}Co; the ^{56}Co decays with a 78.76 day half-life to ^{56}Fe. The gamma rays and positrons released by the decays reheat the supernova matter and power the light curve. Axelrod (1980a,b) has shown that the late-time spectra and light curve can be well accounted for by such a radioactive source. The luminosity requires that something like .5 to 1 $M_\odot$ of ^{56}Ni be produced in the deflagration. Such amounts can be produced by adjustment of the deflagration model parameters.

As the supernova matter expands and its opacity falls some of the gamma rays should escape. Ambwani (1986), and Ambwani and Sutherland (1988) have calculated expected gamma ray spectra for deflagration models. Observations of such gamma ray spectra would be a strong confirmation of the deflagration model.

The successes of the standard model with regard to light curve and spectra are considerable. However, as noted above, there are difficulties. The amount of iron produced per type Ia supernova times the type I rate seems to over-produce the amount of iron observed in the interstellar medium (Woosley *et al.* 1986). Another difficulty is understanding the evolutionary scenario that brings the white dwarf progenitor to carbon ignition.

The traditional evolutionary scenario was that the white dwarf accreted mass from a binary companion. The accreted matter heated and compressed the white dwarf, driving it to ignition. This scenario and other suggested scenarios are all subject to theoretical objections; for a review of these objections see Woosley and Weaver (1986). An alternative to the white dwarf progenitor, suggested by Wheeler (1978), was the R Cor Bor type star. These stars have helium envelopes surrounding a degenerate carbon-oxygen core; the core takes the place of the white dwarf in the standard model. Glen (1985) largely ruled out this class of progenitor. However, Glen (private communication) has recently retreated and finds that R Cor Bor stars may be viable progenitors after all.

Observationally and theoretically, considerably less is known about the type Ib subclass of supernovae than is known about the type Ia subclass. The prototypical type Ib supernovae are SN 1983n and SN 1984l; SN 1961l and SN 1964l are also be members of this subclass (Branch 1986). The spectra of the type Ib supernovae are superficially similar to type Ia subclass, but are different in detail. The type Ib spectra at maximum light resemble type Ia spectra from 2 months after maximum light. The type Ib maximum light is roughly one fourth as bright as the type Ia maximum light (see the review of Woosley and Weaver 1986). Massive stars that have lost their hydrogen envelopes have been suggested as type Ib progenitors (Wheeler and Levreault 1985). If this suggestion is correct, type Ib events may bear only a superficial resemblance to type Ia events. However, Woosley and Weaver (1986) conjecture that the type Ib supernovae may be only variations of the type Ia supernovae.

There are some type I events that do not fit well into either the a or b subclass. Some of these supernovae may actually be type Ib supernovae. The type Ib subclass would then be less homogeneous and more varied than at first supposed (Wheeler *et al.* 1987).

Type Ia supernovae are not likely candidates for being asymmetric supernovae. Asymmetry implies variability in observational characteristics; at present type Ia supernovae show no suggestive observational variability. Since little is still known about type Ib and peculiar type I supernovae, they must be considered as candidates for being asymmetric. In fact it is noteworthy that the prototypical type Ib SN 1983n did have an interesting polarization feature associated with a P-Cygni line (McCall 1985; see also Chapter 5 section (a)). Such polarization features may be indicative of shape asymmetry as argued in the Introduction.

c) Type II Supernovae and Supernova 1987a

Type II supernovae are not as homogeneous a class as are type Ia supernovae. The maximum light B magnitude for type II supernovae can be as bright as about -19, which is as bright as a type Ia (Branch *et al.* 1981). More commonly, maximum light B magnitudes are found between -16 and -18 (Tammann 1982). The light curve behavior varies considerably between different events. These facts indicate that type II supernovae cannot be explained by a uniquely characterized progenitor as seems to be the case for type Ia supernovae.

From a sample of 23 well-observed type II supernovae Barbon *et al.* (1979) have distinguished type II events, on the basis of light curve, into two subclasses called type IIP and type IIL: the "P" stands for plateau and "L" for linear. The type IIP supernovae have a distinct plateau region in their light curves subsequent to maximum light; the type IIL light curves lack this feature and bear a resemblance to type I supernovae light curves. Of the 23 supernovae in Barbon *et al.* 's sample 15 were assigned to the IIP subclass (65 %), and 6 to the IIL subclass (26 %); the remaining 2 supernovae showed peculiar features and so were classed as peculiar. Even within the established subclasses variations in behavior among events are noted. It may be that the subclasses are not distinct, but represent average groupings from two ends of a continuous range of plateau sizes (Doggett and Branch 1985). Fig 1.1 displays the mean IIP and IIL curves given by Doggett and Branch (1985).

As noted previously, type II supernova are observationally distinguished from type I supernovae by the presence of strong hydrogen Balmer lines in their spectra. Near maximum light the type II spectra indicate roughly solar composition with helium lines accompanying the hydrogen lines. In later evolution, lines of some intermediate mass elements and Fe II appear (Branch *et al.* 1981).

The optical display of type II supernovae can be produced in calculations by initiating a central point explosion in a simplified model red giant atmosphere (Imshennik and Nadëzhin 1964; Grassberg *et al.* 1971; Falk and Arnett 1973, 1977; Arnett and Falk 1976; Chevalier 1976; Arnett 1980). Suitable models have an explosive energy of $\sim 10^{51}$ erg with radius between 10^{13} and 10^{14} cm. Weaver and Woosley (1980) found excellent agreement between calculated quantities (light curves, photospheric temperatures, photospheric velocities, and photospheric radii) and corresponding observational quantities for type IIP supernovae. In such model calculations the injection of the explosion energy in the center of the atmosphere initiates a shock wave that explodes and heats the atmosphere. Most of the injected energy (99 %) becomes kinetic energy of the expanding matter; the energy radiated is only about 10^{49} erg. At first the expanding atmosphere has increasing luminosity due to the expanding photosphere radius. However, soon the decreasing density and cooling starts the photosphere to contract in mass fraction. When the temperature is too low to ionize hydrogen, the opacity of the hydrogen falls and the matter becomes very transparent. Thus the optical depth to the photosphere tends to be fixed at the radius at which hydrogen recombination is occurring. The recombination front and thus the photosphere recede into the atmosphere mass as the atmosphere cools. Since hydrogen recombines at about 6000 K, the photospheric temperature remains relatively constant. Even though the photosphere is receding in mass fraction, the spatial radius of the photosphere is approximately constant due to the expansion of the atmosphere. With approximately constant radius and temperature at the photosphere, the supernova luminosity is approximately constant. Recall that a spherical black body has luminosity given by

$$L = 4\pi r^2 \sigma T^4, \tag{1.3}$$

where σ is the Stefan-Boltzmann constant. The plateau region of the light curve is explained by this recombination front effect. Eventually the photosphere recedes into slower moving non-hydrogenic matter, and the nature of the radiative emission changes. The later part of the light curve can be explained by the presence in the supernova ejecta of ^{56}Ni that provides a radioactive source for the luminosity just as in the supernova type Ia case.

The type IIL supernovae have not been as extensively studied as the type IIP supernovae. The type IIL events may result from massive stars that have lost much, but not all, of their hydrogen envelopes (Chevalier 1984). Alternatively the type IIL events could be more closely related to type Ia events with their light curve being mostly powered by the ^{56}Ni decay scenario (Iben and Renzini 1983; Doggett and Branch 1985).

The current theoretical understanding of the energy source of the type II supernova is summarized below. The summary is brief and is given almost without references. A better account (along with references) is given in a review paper by Woosley and Weaver (1986).

The initial explosion energy for type II supernovae is thought to result from the collapse of the degenerate core of an old massive star. The late evolutionary (post-main sequence) history of massive stars is rather complex. It is thought that stars less massive than $\sim 8\,M_\odot$ lose enough mass that they become stable white dwarf stars. Above $\sim 40\,M_\odot$ it is thought that a star loses all of its hydrogen. Such massive stars may explode, but because they have lost their hydrogen they would not be classed as type II supernova. Since stars more massive than $40\,M_\odot$ are rare, their rate of explosion would be small.

For type II supernovae theoretical interest is focused on the stars with main sequence masses in the range 8–40 $M_\odot$. The cores of these massive stars are the result of previous burning phases, and can no longer burn exothermically. The overlying layers of the star continue to burn and accrete burnt matter onto the core. These overlying layers can be divided in mantle and atmosphere. The mantle consists mainly of helium in its outer part and of intermediate elements in its inner part. The atmosphere is mostly hydrogen and is much less dense than the mantle. The elements tend to be stratified, but are mixed to an uncertain degree by convection. For stars with main sequence mass greater than about $10\,M_\odot$ the core is iron; for the 8–10 $M_\odot$ range the core is oxygen and neon. When the core density is sufficiently high there are two instabilities that tend to rob it of pressure support: electron capture by nuclei and photodisintegration of nuclei. Which of these two effects dominates depends on the main sequence mass of the star. The removal of pressure support initiates a collapse that cannot be stopped until the density is of the order of nuclear density: i.e., $\rho \sim 10^{14}\,\mathrm{g\,cm^{-3}}$. The collapse occurs on a time scale of about a second. The collapse event is thought to be the origin of neutron stars.

The large binding energy of a neutron star, $\sim 10^{53}$ erg, is released in a core collapse. Most of this released binding energy escapes in the form of neutrinos. Only about 1 % of the energy is required to power the supernova explosion. Unfortunately, there has been considerable difficulty in coupling a small fraction of the released binding energy to the matter in the mantle and atmosphere of the star. Without this coupling the outer matter would just collapse onto the neutron star, increase its mass, and convert it into a black hole. Currently there are two favoured scenarios for how the supernova explosion occurs. Both these scenarios have been made to yield marginally successful explosions only within the last few years.

In the first scenario, the equation of state of the collapsing core stiffens as the core matter reaches approximately nuclear density and the collapse of the inner core is suddenly stopped. The exact core density at which the core is stopped is somewhat uncertain, since it depends on the equation of state of nuclear matter. As the collapse stops, an outgoing shock wave is initiated. The stopping of the core and the production of the shock is called the bounce. If the shock wave has enough energy, the outer layers of matter will attain escape velocity and an explosion ensues. Most of the core remains behind as a neutron star. This scenario is called the prompt explosion, since the exploding shock wave is formed by the bounce.

The second mechanism is called the delayed explosion. In this sort of event the bounce shock wave is formed, but is insufficiently strong to cause an explosion: the shock stalls. However, the neutrino flux from the core re-heats the matter behind the shock and re-starts the shock (Wilson 1985). The opacity of matter for neutrinos is small, but the capture of $\lesssim 5\,\%$ of the neutrino flux of $10^{53}\,\mathrm{erg\,s^{-1}}$ is sufficient to re-start the shock. The time scale for the re-starting to occur is hundreds of milliseconds. The delayed shock mechanism may explain the explosion of larger massive stars.

On 1987 Feb. 24 a type II supernova in the Larger Magellanic Cloud (LMC) was discovered by Ian Shelton of the University of Toronto working at Las Campanas Observatory in Chile (1987). The LMC, a small irregular galaxy, is the nearest neighbor to the Galaxy. The distance to the LMC is $50 \pm 7\,\mathrm{kpc}$ (Laney and Stobie 1986); this is roughly twice the diameter of the Galaxy. It is clear that an LMC supernova would have an apparent luminosity that was comparable to that of a Galactic supernova. In fact, due to dust and gas in the plane of the Galactic disk some Galactic supernovae would be poorer observational objects than an LMC supernova. No Galactic supernovae have been observed since SN 1604 which was observed by Kepler and others (for a review of historical Galactic supernovae see Clark and Stephenson (1982)). Thus the LMC supernova is the best observational opportunity ever for supernova research. Since the LMC supernova was the first supernova discovered in 1987 it has been designated SN 1987a.

SN 1987a has already proven an astonishing confirmation of and stimulus to type II supernovae research. Probably the most impressive and satisfying observation was the detection of a strong neutrino flux on 1987 Feb. 23 by the Kamiokande (Hirata *et al.* 1987) and IMB (Bionta *et al.* 1987) neutrino observatories. This flux of neutrinos is naturally explained by the neutrino burst expected when a core collapse occurs. The neutrino flux thus confirms the hitherto purely theoretical picture of core collapse (Bahcall *et al.* 1987; Burrows and Lattimer 1987). The neutrino flux also gives an exact time for the ignition of the explosion; never before has the ignition time of a supernova event been determined.

Another important feature of SN 1987a is that the progenitor has been identified as the previously observed star Sanduleak–69 202 (Gilmozzi *et al.* 1987; and others). Only for one other supernova has a supernova progenitor been identified; that supernova was the remarkable SN 1961v (see Doggett and Branch 1985). The SN 1987a progenitor star, contrary to expectations for type II supernovae, was a blue supergiant rather than a red supergiant. Another, probably related, surprise has been the unusual light curve and rather dim maximum light of SN 1987a. These unexpected features of SN 1987a may find their explanation in the low metallicity of the LMC. The low metallicity may cause a massive star to end its evolution as a blue rather than as a red star (Woosley 1987). It seems probable that SN 1987a will become the prototype of a new subclass of type II supernovae.

A startling discovery is that there is a companion source close to SN 1987a. This discovery was made using speckle imaging techniques by Karovska *et al.* (1987) on Mar. 25 and Apr. 2. It has subsequently been confirmed by Matcher *et al.* (1987). The companion source had a 6560 Å magnitude that was $2.7 \pm .2$ dimmer than the supernova (i.e., it was $.085 \pm .015$ times as bright) and was 5 magnitudes brighter than any pre-SN 1987a source in the field (Nisenson *et al.* 1987). The companion source is clearly associated somehow with the SN 1987a outburst. It may be that the companion is a large gas or dust cloud that is reflecting supernova radiation as suggested by Nisenson *et al.* They caution, however, that such a cloud would have to be so large that it ought to have been resolved by observation; this was not the case. Another possibility is that the companion is part of a jet emitted by the supernova explosion. The angular distance of the companion from the supernova was $.059 \pm .008$ arcseconds Using the distance to the LMC, the angular separation indicates that companion and supernova are separated by about 4×10^{16} cm. If the companion source was associated with a jet, the jet velocity would be $\approx c/2$. There is no experimental evidence or theoretical reason (see Symbalisty 1984) for jets of such a high velocity from a supernova. Another possibility is that the companion source is not real; speckle imaging techniques are difficult and a misinterpretation is possible. At present the companion source remains a mystery.

There have been and will be many other SN 1987a observations of great importance. Of particular relevance to this thesis are spectropolarimetric observations. Many spectropolarimetric observations have already been done (Walsh *et al.* 1987; Magalhaes and Velloso 1987; Schwarz and Mundt 1987; Cropper *et al.*), and analyses of the data have already been given by Jeffery (1987) and Cropper *et al.* (1987). In Chapter 5 a further analysis of some of the early data is given. The analysis indicates that SN 1987a has considerable shape asymmetry.

In general type II supernovae are more likely candidates for being asymmetric than type I supernovae. The variability of type II events, though explainable in terms of the large mass differences among the expected progenitors, may owe in part to shape asymmetry. There are calculations and observations that indicate that asymmetry will be present. Section (d) below briefly reviews some of these calculations and observations.

d) Asymmetric Supernovae

In this section a brief survey of some of the asymmetric supernova calculations is given. None of these calculations was a complete explosion calculation. Each calculation followed the explosion in only one of the following: core, mantle, or atmosphere. The physical scale and the time scale for important dynamic events are very different for each of these regimes. Formidable numerical difficulties would need to be overcome to perform a unified calculation. In addition some discussion is given of observational evidence from supernova remnants (SNRs) for asymmetric explosions.

Müller and Hillebrandt (1981), and Hillebrandt (1982) reported 2-dimensional hydrodynamic calculations of core collapses. Their primary interest was to see if the difficulties in getting core collapse models to explode would be alleviated by the introduction of rotation. They gave the cores (i.e. the inner $1.4\,M_{\odot}$) of their initial models rotational energies of order 10^{49} erg. Rotational energies of this order are are expected for newly formed pulsars, the presumed remnants of type II supernovae (Gunn and Ostriker 1969; see also Shapiro and Teukolsky 1983, p. 279). The core collapse was initiated by reducing the core entropies by 5%. For models with core rotational energy of about 5×10^{48} erg the effects of rotation were modest. There was roughly a 5 % oblate asymmetry in the density contours at a few milliseconds after the core bounce when the calculation was halted. For a model with rotational energy 6.2×10^{49} erg the contours showed 50 % oblate asymmetry about 7 milliseconds after the bounce when the calculation was halted. The flow patterns in this model were rather complex and showed the formation of vortices. The reason for halting the calculations was that the rotational effect did not give these models sufficient additional kinetic energy to become supernova explosions, and also because such 2-dimensional calculations are computationally very demanding.

Livio *et al.* (1980) considered a 2-dimensional model to study the effects of Rayleigh-Taylor instabilities in core collapse. The Rayleigh-Taylor instability occurs in situations where the pressure and density gradients have different signs. Such instabilities do obtain in the bouncing core collapse. Livio *et al.* hoped that the instability would result in a massive overturn of the core that would enhance the release of neutrinos; the neutrinos would then help to power an explosion. They found that there was a large overturn of most of the core matter by the time they halted their calculation, 30 milliseconds after the bounce. The overturn took the form of a large vortex. Livio *et al.* expected that some enhancement of the neutrino flux would occur.

Symbalisty (1984, 1985) considered 2-dimensional rotating core collapse models with and without strong magnetic fields. He used models with rotational energies comparable to those used by Müller and Hillebrandt. In Symbalisty's rotation-only calculations he obtained flow patterns and density contours not dissimilar to those of Müller and Hillebrandt. Symbalisty ran his models for about 20 milliseconds after the bounce, and the scale of his flow patterns was about 10 times larger than the scale of Müller and Hillebrandt's flow patterns. He found no explosion for these models; he did find, due to a vortex flow, that a small mass of $4 \times 10^{-4} M_{\odot}$ had obtained escape velocity. This mass was roughly directed along the polar axis of his model and he interpreted it as a jet.

To study magnetorotational effects, Symbalisty considered models with dipole magnetic fields. For the weaker fields there was no significant difference from the rotation-only models. For a model with a 10^{13} gauss field there was a strong polar jet with escape velocity and with a mass of $6.9 \times 10^{-3} M_{\odot}$. There was no overall explosion. (The jet result was discovered earlier by LeBlanc and Wilson (1970) using a now obsolete model.) The Symbalisty jet is impressive, but the magnetic field generated in the core was of order 10^{16} gauss. This is roughly 1000 times stronger than the $\sim 10^{12}$–10^{13} gauss fields inferred for pulsars. Symbalisty concluded that the "magnetorotational explosion does not seem likely".

The three core collapse calculations discussed above were done without the delayed explosion mechanism discovered by Wilson (1985). How the asymmetry of the reported models would have evolved with the inclusion of delayed explosion is an open question.

Bodenheimer and Woosley (1983) found that rotation of the mantle could cause an explosion even when the core shock had stalled. To obtain a value for the total angular momentum of their model mantle they considered the inner $8\,M_\odot$ of a model O star ($M = 30\,M_\odot$ and $R = 7.5\,R_\odot$). Assuming rigid rotation and assigning a surface rotational velocity of of $200\,\mathrm{km\,s^{-1}}$ (typical for O stars) gave the inner $8\,M_\odot$ an angular momentum of 4.5×10^{51} erg-s. Bodenheimer and Woosley used parameterized boundary conditions to simulate the core and atmosphere boundaries. The model was run for 15 s. A vortex flow pattern was set up that lead to an equatorial explosion. In order to achieve this explosion there had to be an injection of energy from oxygen burning as well as rotation. The material in the equatorial outburst was enriched with oxygen and oxygen burning products. The outflowing matter had velocities considerably smaller than those attributed to supernovae. Bodenheimer and Woosley estimated that the optical display of such an event would be less luminous than that of a typical supernova. Of course, if the delayed explosion mechanism had been included in their calculation, a more conventional supernova explosion might have been recovered, possibly with an oblate asymmetry. Without the delayed explosion mechanism the Bodenheimer and Woosley model may describe a undiscovered, subluminous class of supernovae. Bodenheimer and Woosley cite some evidence from SNR observations that this might be the case.

Most young galactic SNR's have a rather spherical shell shape. It should be noted that a spherical remnant does not necessarily indicate a spherically symmetric explosion. It has been shown that a uniform interstellar medium (ISM) may spherize an originally asymmetric remnant on a time scale of thousands of years (Bisnovatyi-Kogan and Blinnikov 1983). There are, however, some remnants that resemble what might be expected from a Bodenheimer and Woosley type explosion. Lasker (1980) reports that SNR N132 D in the LMC has a toroidal ring of oxygen enriched knots. A similar interpretation can be made for the galactic remnant G292.0+1.8 (Tuohy *et al.* 1980; Clark and Tuohy 1983), and perhaps for the famous galactic remnant Cas A (Markert *et al.* 1981). The supernova that caused the Cas A remnant should have been visible to the eye sometime about the year 1667, but it was not observed. This indicates that Cas A supernova may have been an subluminous event; if that were so it could be consistent with a Bodenheimer and Woosley type explosion.

Chevalier and Klein (1978) examined the effect of Rayleigh-Taylor instabilities on the explosion of a red supergiant type atmosphere in 2-dimensional calculations. Their models showed large clumps containing 20–30 % of the atmosphere mass form by 10 days after the explosion. The density ratio of clump to non-clump was about 3 to 1. Chevalier and Klein concede that the discretization of their models may not have been fine enough to remove all discretization effects. However, they concluded that the large scale clumping effect was real. They considered that the mass clumps observed in the Cas A remnant may be evidence for the effect.

The above survey of 2-dimensional calculations shows that asymmetric effects may be relevant in the cores, mantles and atmospheres of supernova explosions. A unified 2-dimensional supernova calculation would be a mammoth undertaking, but would probably be necessary to understand the net effect of these asymmetries. More observational evidence of supernova asymmetry would be of considerable aid. Spectropolarimetry of supernova may provide some of this evidence. A discussion of available spectropolarimetry data is given in Chapter 5. As noted in the Introduction, this thesis was undertaken to provide an interpretation technique for spectropolarimetry.

Chapter 2

The Sobolev Method

And the Sobolev-H Method for Polarizing Resonance Scattering

In section (a) of this chapter a derivation of the Sobolev method is presented. Section (b) discusses the validity of the method in general, and section (c) its application to supernova calculations. Section (d) develops a version of the Sobolev method, called the Sobolev-H method, that includes the polarizing effect of resonance scattering. Section (e) discusses the validity of the Sobolev-H method. Section (f) considers the application of the Sobolev-H method to closely spaced lines and multiplets.

a) The Sobolev Method

The Sobolev method or escape-probability method originated with Sobolev (1947) and has been extended by others (Castor 1970; Rybicki 1970; Lucy 1971; Rybicki and Hummer 1978; Olson 1982; Hummer and Rybicki 1985; Bartunov and Mozgovoi 1987). The method is used to calculate line radiative transfer in moving atmospheres with large velocity gradients. In this presentation of the Sobolev method the discussion, derivation, and notation of Rybicki and Hummer (1978) have been followed. The general concepts and terms of radiative transfer can be found in the book *Stellar Atmospheres* by Mihalas (1978).

Consider an atmosphere in which the opacity is due to only one infinitely sharp ion transition line. If this atmosphere is at rest, then only incident radiation with frequency equalling the transition frequency would interact with the scattering ions. The radiation at other frequencies would pass through the atmosphere unimpeded. The calculation of the emergent radiation flux at the transition frequency (a line transfer problem) requires the solution of a differential equation due to the radiative coupling of all regions of the atmosphere. In systems more complicated than that presently considered the solution of the emergent radiation by differential equations can become computationally very demanding. If the atmosphere has a velocity flow with velocity gradients, then the ion transition frequency is no longer the rest-frame frequency and is not a constant. The gradients of the velocity field cause a spatially varying Doppler shift of the transition frequency of the ions. Thus the transition frequency depends both on the location of the ion in the flow and on the direction of any incident photons. The opacity of the atmosphere is no longer confined to a single frequency; there is a global continuum opacity, since the velocities of the ions give rise to a continuum of Doppler shifts. However, the opacity at a given frequency for a given direction of incidence is localized. Provided the velocity gradient does not go to zero in the given direction, the ions providing this opacity lie on a surface called a velocity surface. The velocity surfaces can also be referred to by the more general term resonance regions. The atmosphere can be considered as being made up of these velocity surfaces. The problem of radiative transfer through such an atmosphere becomes a problem of following radiation of a given initial frequency through scatterings in, it is hoped, a limited number of velocity surfaces. In simple flow cases only one velocity surface per atomic transition need be considered for each frequency of the emergent flux.

There are two types of velocity surface that it is useful to consider: common-direction (CD) and common-point (CP). CD surfaces are formed by the set of material points having a common velocity in a given direction. The defining equation for a CD velocity surface that interacts with photons of frequency ν and contains ions with rest-frame transition frequency ν_0 is

$$\hat{n} \cdot \vec{v}(\vec{r}) = v_{\delta\nu}, \tag{2.1}$$

where $\vec{r}$ is a position vector that traces out the surface, $\hat{n}$ defines the common direction, and $v_{\delta\nu} = c(\nu - \nu_0)/\nu$ is the magnitude of the velocity that Doppler shifts the transition frequency (assuming only the first order Doppler shift is required). The $\hat{n}$-direction is usually one to a distant observer. Photons scattered from such a surface in the $\hat{n}$-direction emerge with the common frequency ν due to the common Doppler shifted transition frequency. If the velocity flow is not monotonic in the direction defined by $\hat{n}$, or if multiple ion transitions are being considered, then multiple surfaces satisfying equation (2.1) are possible. Such surfaces are radiatively coupled and this coupling must, of course, be considered in solving for the emergent flux. A CP surface is formed by material points that are radiatively coupled to a specified material point (the common point). The defining equation is

$$\frac{(\vec{r} - \vec{r}\,')}{|\vec{r} - \vec{r}\,'|} \cdot (\vec{v}(\vec{r}) - \vec{v}(\vec{r}\,')) = v_{\delta\nu}, \tag{2.2}$$

where $\vec{r}$ traces out the surface and $\vec{r}\,'$ locates the common point. The surface and the common point are radiatively coupled if $v_{\delta\nu} = 0$, since there is no relative Doppler shift between the transition frequency of any point on the surface and the transition frequency of the common point. If there is more then one ion transition, there will also be radiatively coupled CP surfaces for the $v_{l\nu}$ values that give Doppler shifts equal to the frequency differences between different transitions.

Real line transitions are not infinitely sharp. Ions can absorb or emit photons over some range of frequencies. The probabilities of absorption or emission at any frequency are described by absorption and emission probability distributions called profiles. Mathematically, the profiles allow a transition at any frequency, but with vanishingly small probability outside of an interval centered on the frequency with the maximum transition probability. This interval of high probability is made quantitative by defining it as the full-width at half maximum, or, if appropriate, the standard deviation of the profile. The interval is often called the line-width, or simply the width of the line transition. The frequency of maximum probability is called the line center frequency, or simply the line frequency.

The broadening of the line transition frequency into a frequency line-width is due to several effects: the intrinsic broadening due to the quantum nature of the transition, thermal Doppler broadening due to the thermal motion of the ions, Doppler broadening from random turbulent flow of fluid elements in the atmosphere, and collisional broadening. The profiles arising from this mixture of effects are not simple in general. In astrophysical systems the thermal broadening effect is often most important and this results in a Gaussian profile for absorption and emission. The effects of turbulence broadening may also be important in the mass loss winds from early type stars, and possibly in supernovae.

A consequence of finite line-width is that the velocity surfaces are not sharp, but have finite spatial width. To first order in v/c the Doppler shift of a line frequency is given by

$$\nu(l) = \nu_0(1 + v_l/c), \tag{2.3}$$

where ν_o is the rest line frequency, l is a distance parameter measuring backward along a ray path (see Fig. 2.1), and v_l is the macroscopic velocity of the ions in the direction of the ray path. A photon of frequency $\nu(l)$ travelling along the ray path can interact with the ions at l, but due to the finite line-width $\Delta\nu$ the photon can also interact over a finite range Δl of the l-parameter. The symmetry between frequency and spatial parameter can be seen if v_l is expanded to first order about l:

$$\delta\nu = \nu(l + \delta l) - \nu(l) = -\frac{\nu_0}{c}\frac{dv_l}{dl}\delta l = -\frac{\nu_0}{c}Q\delta l, \tag{2.4a}$$

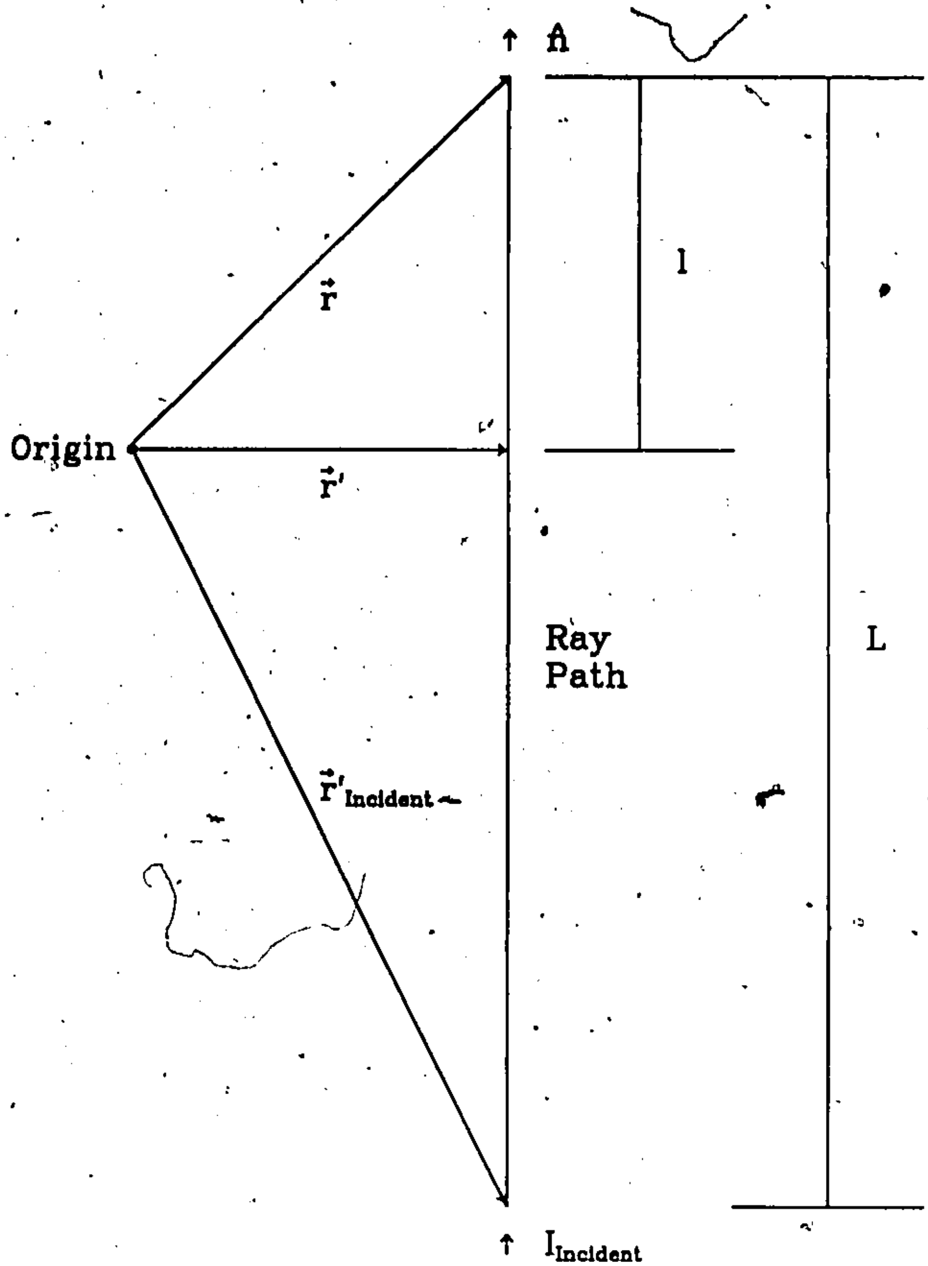

Fig. 2.1. Geometry of a ray path and the variables describing the path.

where

$$Q \equiv \frac{dv_l}{dl}. \tag{2.4b}$$

It follows that the spatial width of the velocity surface (resonance region) corresponding to the frequency line-width is given by

$$\Delta l = \frac{c}{\nu_0}\frac{\Delta\nu}{|Q|}. \tag{2.5}$$

The Sobolev method exploits the functional relationship between spatial coordinate and frequency that is established by the spatially varying Doppler shift. The spatial coordinate-frequency relationship is assumed to be linear over distances the size of the spatial resonance width Δl. Thus it is assumed that only the first order Doppler shift is required and that the velocity gradient is a constant over Δl. The Sobolev method also assumes that the thermodynamic quantities that determine the integrated line opacity (the integral of the monochromatic line opacity integrated over all frequency) and line source function (line emissivity divided by the monochromatic line opacity) do not vary significantly over Δl. The only quantities allowed to vary over Δl are the line absorption and emission profiles, which are functions of the spatial coordinate since they are functions of frequency, and velocity. A rough criterion for the validity of these assumptions can be given. If l_{ch} is a characteristic distance over which the thermodynamic quantities vary and v_{ch} is the change in velocity over l_{ch}, then one can set $|dv_l/dl| \approx v_{ch}/l_{ch}$. The line-width, assuming it owes to thermal Doppler broadening, is given by $\Delta\nu = \nu_0 v_{th}/c$, where v_{th} is the thermal root mean square velocity. From (2.5) one obtains

$$\Delta l/l_{ch} \approx v_{th}/v_{ch}. \tag{2.6}$$

The Sobolev method demands $\Delta l \ll l_{ch}$, and therefore requires that $v_{th} \ll v_{ch}$. Thus the spatial resonance regions will be relatively sharp when the macroscopic velocity gradient is relatively large.

To derive the Sobolev expressions consider the radiative transfer equation (see Mihalas 1978, p. 30) for the specific intensity directed along the ray path depicted in Fig 2.1:

$$\hat{n}\cdot\nabla I(\vec{r},\hat{n},\nu) = -\frac{dI}{dl} = -k(\vec{r})\phi(\nu')[I-S], \tag{2.7}$$

where I is the specific intensity, $k(\vec{r})$ the integrated line opacity, ϕ is the normalized line absorption profile, S is the line source function, and $\nu' = \nu(1-\hat{n}\cdot\vec{v}(\vec{r})/c)$ is the frequency of the $\hat{n}$-directed radiation observed in the local frame at $\vec{r}$. The assumption has been made that $|\hat{n}\cdot\vec{v}(\vec{r})|/c \ll 1$ so that only the first order Doppler shift formula is required. The correction factor for stimulated emission following the usual practice can be thought of as having been absorbed into the opacity k (Mihalas 1978, p. 80).

Note that

$$\nu' = \nu(1 - \hat{n} \cdot \vec{v}/c) = \nu(1 - v_l/c) = \nu - (\nu + \nu_0 - \nu_0)(v_l/c)$$
$$= \nu - \nu_0(1 + \delta)(v_l/c),$$

where $\delta = (\nu - \nu_0)/\nu_0$. Subtracting ν_0 from each side gives

$$\nu' - \nu_0 = \nu - \nu_0 - \nu_0(1 + \delta)(v_l/c) \qquad \text{or} \qquad \delta' = \delta - (1 + \delta)(v_l/c),$$

where $\delta' = (\nu' - \nu_0)/\nu_0$. Re-arranging gives

$$\delta = \frac{\delta' + (v_l/c)}{1 - (v_l/c)} \approx (\delta' + (v_l/c))(1 + (v_l/c))$$
$$\approx \delta' + (v_l/c) + \delta'(v_l/c) + (v_l/c)^2,$$

where the assumption that $(v_l/c) \ll 1$ has been used. For significant scattering $|\delta'| \lesssim \Delta\nu/\nu_0$, where it is recalled that $\Delta\nu$ is the line-width. Usually $\Delta\nu/\nu_0 \ll 1$, and thus for significant scattering $|\delta'| \ll 1$. Therefore it follows that $\delta \ll 1$, and thus to first order in small quantities

$$\nu' = \nu - \nu_0(v_l/c). \tag{2.8}$$

This expression for the Doppler shifted frequency will be employed in all the subsequent derivations.

Equation (2.7) can now be written as

$$\frac{dI}{dl} = k(l)\phi(\nu - \nu_0(v_l/c))[I(l) - S(l)] \, ,$$

where the distance parameter l is taken as the independent variable (see Fig. 2.1 for the geometry of the ray path being considered). The integrating factor for this differential equation is

$$u(l) = \exp\left[- \int_0^l dl' k(l')\phi(\nu - \nu_0(v_{l'}/c)) \right],$$

and thus the formal solution is

$$I(\vec{r}, \hat{n}, \nu) = I(l = 0) = \int_0^L dl u(l)k(l)\phi(\nu - \nu_0(v_l/c))S(l) \quad + \quad I_{inc}u(L), \tag{2.9}$$

where I_{inc} is the specific intensity of frequency ν incident on the medium at the point label L on the ray path. For the present it is assumed that the velocity along the ray path is strictly increasing or decreasing so that there can be at most one resonance point per frequency. Thus the integrand of equation (2.9) will be significantly different from zero only in a spatial resonance region of thickness Δl centered on a resonance point located at l_{res}. The Sobolev assumption is that the thermodynamic quantities should be approximately constant over the resonance region. Therefore $k(l)$ and $S(l)$ can be set to $k = k(l_{res})$ and $S = S(l_{res})$, and removed from the integrals. If the frequency ν is specified, then the resonance point coordinate l_{res} can be obtained by solving

$$\nu_0 = \nu - \nu_0(v_{res}/c), \tag{2.10}$$

where $v_{res} = v_{l_{res}}$. Alternatively, if the resonance point coordinate is specified, equation (2.10) can be used to solve for the local resonance frequency ν. Recalling the Sobolev assumption that the velocity gradient does not vary significantly over the spatial resonance width, the velocity at l_{res} can be expanded in a Taylor's series to first order:

$$v_l = v_{res} + Q(l - l_{res}), \tag{2.11}$$

where, recalling equation (2.4b), $Q = (dv_l/dl)$. Using equation (2.11) the expression for the specific intensity at point $\vec{r}$, in direction $\hat{n}$, and with frequency ν becomes

$$\begin{aligned} &I(\vec{r}, \hat{n}, \nu) = \\ &kS \int_0^L dl\, \phi\Big(\nu - (\nu_0/c)\big(v_{res} + Q(l - l_{res})\big)\Big) \exp\left[-k \int_0^l dl'\, \phi\Big(\nu - (\nu_0/c)\big(v_{res} + Q(l' - l_{res})\big)\Big)\right] \\ &\quad + I_{inc} \exp\left[-k \int_0^L dl\, \phi\Big(\nu - (\nu_0/c)\big(v_{res} + Q(l - l_{res})\big)\Big)\right]. \end{aligned} \tag{2.12}$$

The following transformation of the variables will be made:

$$\lambda = \frac{|Q| l}{(c/\nu_0)\Delta\nu} = \frac{l}{\Delta l}, \qquad \text{and} \qquad \xi = \frac{\nu - \nu_0(v_{res}/c) + Q(l_{res})(\nu_0/c)}{\Delta\nu}, \tag{2.13}$$

where equation (2.5) for Δl has been used. The following definition is also needed:

$$\varphi(\xi) = \Delta\nu\, \phi(\xi \Delta\nu). \tag{2.14}$$

Note that

$$1 = \int_0^\infty d\nu\, \phi(\nu) = \int_0^\infty d\xi\, \varphi(\xi) \approx \int_{-\infty}^\infty d\xi\, \varphi(\xi),$$

where the last integration has been extended to negative infinity, since the extension makes a negligible contribution. Another required definition is

$$\tau \equiv k\frac{\Delta l}{\Delta \nu} = \frac{kc}{\nu_0|Q|}, \tag{2.15}$$

where τ is the Sobolev line optical depth of the resonance region. Using all these transformations and definitions, equation (2.12) is rewritten as

$$\begin{aligned} I(\vec{r},\hat{n},\nu) =& S\tau\int_0^\infty d\lambda\varphi(\xi\mp\lambda)\exp\left[-\tau\int_0^\lambda d\lambda'\varphi(\xi\mp\lambda')\right] \\ &+ I_{inc}\exp\left[-\tau\int_0^\infty d\lambda\varphi(\xi\mp\lambda)\right] \qquad \text{where} \quad \begin{cases} -\lambda & \text{is for } Q>0; \\ +\lambda & \text{is for } Q<0, \end{cases} \end{aligned} \tag{2.16}$$

and where it has been assumed that the point labeled by L is sufficiently far from the resonance region that L can be replaced by infinity. The further transformation

$$t = \xi \mp \lambda = \left(\frac{\nu - \nu_0(\vec{v}_{res}/c) - Q(l-l_{res})(\nu_0/c)}{\Delta\nu}\right)$$

leads to the expression

$$I(\vec{r},\hat{n},\nu) = S\tau\int_\xi^{\mp\infty}(\mp dt)\,\varphi(t)\exp\left[-\tau\int_\xi^t(\mp dt')\,\varphi(t')\right] \quad + \quad I_{inc}\exp\left[-\tau\int_\xi^{\mp\infty}(\mp dt)\,\varphi(t)\right]. \tag{2.17}$$

Defining

$$w(\xi) \equiv \begin{cases} \int_{-\infty}^{\xi} dt'\,\varphi(t') & \text{for } Q>0; \\ \int_{\xi}^{\infty} dt'\,\varphi(t') & \text{for } Q<0, \end{cases}$$

where $w(\pm\infty) = 1$ and $w(\mp\infty) = 0$. Integrating equation (2.17) gives the result

$$I(\vec{r},\hat{n},\nu) = S(1-\exp[-\tau w(\xi)]) + I_{inc}\exp[-\tau w(\xi)]. \tag{2.18}$$

From equation (2.13) it can be seen that if ν is fixed, then ξ depends linearly on the distance l_{res} from the point $\vec{r}$ to the resonance point for frequency ν. In limiting cases of l_{res} equation (2.18) becomes

$$I(\vec{r},\hat{n},\nu) = \begin{cases} I_{inc}, & l_{res}\to-\infty; \\ I_{inc}\exp[-\tau] + S(1-\exp[-\tau]), & l_{res}\to\infty. \end{cases} \tag{2.19}$$

The two cases correspond to the specific intensity before and after the resonance region. The first and second terms in the $l_{res}\to\infty$ case are called, respectively, the direct and diffuse contributions to the specific intensity.

Equations (2.18) and (2.19) are only of use if the source function S can be specified. In obtaining S a useful quantity is the integrated specific intensity defined by

$$\bar{I}(\vec{r},\hat{n}) = \int_0^\infty d\nu\phi(\nu - (\nu_0/c)(\hat{n}\cdot\vec{v}(\vec{r})))\, I(\vec{r},\hat{n},\nu). \tag{2.20}$$

The integrated specific intensity is proportional to the rate a which $\hat{n}$-directed photons are scattered out of the beam by the line transition. The quantity $k\bar{I}$ is energy per unit volume per unit time scattered out of the beam by the line transition. Using equations (2.13) and (2.14), and substituting from equation (2.18) gives

$$\bar{I}(\vec{r},\hat{n}) = \int_{-\infty}^\infty d\xi\varphi(\xi)\Big(S(1-\exp[-\tau w(\xi)]) + I_{inc}\exp[-\tau w(\xi)]\Big), \tag{2.21}$$

where the lower integration limit has been extended to negative infinity with negligible effect. It is assumed that the incident specific intensity I_{inc} and the line source function S do not vary significantly over the ξ-range where $\varphi(\xi)$ is significantly different from zero. It is important to note that I_{inc} should be evaluated at the local resonance frequency ν which is obtained from the equation

$$\nu_0 = \nu - (\nu_0/c)(\hat{n}\cdot\vec{v}(\vec{r})); \tag{2.22}$$

this is the frequency where $\varphi(\xi)$ is a maximum. Performing the integration gives

$$\bar{I}(\vec{r},\hat{n}) = S\left(1 - \frac{1-\exp[-\tau]}{\tau}\right) + I_{inc}\frac{1-\exp[-\tau]}{\tau}. \tag{2.23}$$

The first term gives the contribution to the integrated specific intensity from the photons that are created locally in the resonance region centered on $\vec{r}$ by downward line transitions. The second term is the contribution from the incident photons. The quantity defined by

$$\beta_d \equiv \frac{1-\exp[-\tau]}{\tau}, \tag{2.24}$$

is called the directional escape probability. The probabilistic interpretation of β_d is considered below.

A general expression for the source function for bound-bound transitions (Hummer 1969) adapted to a moving atmosphere system is

$$S(\vec{r},\hat{n},\nu) = \frac{(1-\epsilon)}{\phi(\nu - (\nu_0/c)(\hat{n}\cdot\vec{v}(\vec{r})))}\oint\frac{d\Omega'}{4\pi}\int_0^\infty d\nu' R(\nu,\hat{n};\nu',\hat{n}')I(\vec{r},\hat{n}',\nu') \quad + \quad \tilde{G}(\vec{r}), \tag{2.25}$$

where Ω is solid angle, $\hat{n}$ gives the propagation direction, ϵ is the probability per scattering that a photon leaves the line, $\phi(\nu-(\nu_0/c)(\hat{n}\cdot\vec{v}(\vec{r})))$ is the normalized line emission profile, R is redistribution function, and G is the non-resonance source of line photons. The quantity ϵ is a measure of the coupling of the line transition to other transitions (including those to the continuum) and to the local thermal conditions. In the two-level atom approximation (see Mihalas 1978, p. 336) ϵ is referred to as the thermal coupling constant, since only the local thermal conditions through collisional excitation and de-excitation of the transition are allowed to couple to the line radiation field. In the two level-atom approximation

$$G(\vec{r}) = \epsilon B_{\nu_0}(T_e), \tag{2.26}$$

where B_{ν_0} is the thermodynamic equilibrium Planck specific intensity evaluated at the line rest frequency and the local electron temperature T_e:

$$B_{\nu_0} = \frac{2h\nu_0^3}{c^3}\frac{1}{\exp[h\nu_0/kT_e]-1}. \tag{2.27}$$

In this approximation ϵ is given by

$$\epsilon = \frac{C_0(1-\exp[h\nu_0/kT_e])}{A_0 + C_0(1-\exp[h\nu_0/kT_e])}, \tag{2.28}$$

where C_0 is the collisional de-excitation rate from the upper level of the transition and A_0 is the spontaneous emission rate. For multi-level atoms the simple expressions for G and ϵ do not obtain.

Ordinarily in the Sobolev method the redistribution of photons is assumed to be what is called complete redistribution (sometimes abbreviated to CRD) where the redistribution function is given by

$$R(\nu,\hat{n};\nu',\hat{n}') = \phi(\nu-(\nu_0/c)(\hat{n}\cdot\vec{v}(\vec{r})))\phi(\nu'-(\nu_0/c)(\hat{n}'\cdot\vec{v}(\vec{r}))). \tag{2.29}$$

In this form of redistribution the incident and scattered photon frequency are independent, the absorption and emission profiles are the same, and the scattering is isotropic in the static atmosphere case. Polarizing effects are not included. Substituting equation (2.29) into equation (2.25) gives

$$S(\vec{r}) = (1-\epsilon)\oint\frac{d\Omega'}{4\pi}\int_0^\infty d\nu'\phi(\nu'-(\nu_0/c)(\hat{n}'\cdot\vec{v}(\vec{r})))I(\vec{r},\hat{n}',\nu') \quad + \quad G(\vec{r}) \tag{2.30}$$

This expression satisfies the Sobolev condition on S of no strong dependence on ν. This condition was required in deriving equations (2.19) and (2.23). Assuming equation (2.30) is valid, equation (2.23) can be substituted into equation (2.30) to give

$$S = (1-\epsilon)[(1-\beta)S + I_\beta] + G, \tag{2.31}$$

where

$$\beta = \oint \frac{d\Omega}{4\pi} \frac{1 - \exp[-\tau]}{\tau} = \oint \frac{d\Omega}{4\pi} \beta_d \tag{2.32}$$

and

$$I_\beta = \oint \frac{d\Omega}{4\pi} \frac{1 - \exp[-\tau]}{\tau} I_{inc}. \tag{2.33}$$

The quantity β, called the escape probability, is discussed below. Solving equation (2.31) for S gives

$$S(\vec{r}) = \frac{(1-\epsilon)I_\beta + G(\vec{r})}{\epsilon + (1-\epsilon)\beta}. \tag{2.34}$$

That an explicit solution for the source function can be obtained from the Sobolev method is very useful in actual line calculations. In fact the Sobolev source function has been found to be more accurate than the formal Sobolev solution given by equation (2.19) (Hamann 1981).

An important special case of equation (2.34) occurs when ϵ and G are zero (i.e., a case of pure two-level atom resonance scattering), and the incident specific intensity emerges from a spherical surface of radius r_c and is independent of the angle of emergence. The source function is then

$$S(r) = W(r) I_{inc}, \tag{2.35}$$

where

$$W(r) = \frac{1}{2}\left(1 - \sqrt{1 - (r_c/r)^2}\right). \tag{2.36}$$

$W(r)$ is called the dilution factor.

Equations (2.19) and (2.23) can readily be generalized to the case of non-monotonic velocity fields or the case of multiple ion transitions. In both cases multiple velocity surfaces must be considered. The generalized expression for the emergent specific intensity for frequency ν is

$$I(\nu)_{Emg} = I(\nu)_{inc} \exp\left[-\sum_{i=1}^{N} \tau_i\right] + \sum_{i=1}^{N} S_i(1 - \exp[-\tau_i]) \exp\left[-\sum_{j=1}^{i-1} \tau_j\right], \tag{2.37}$$

where the CD velocity surfaces for frequency ν are number 1 through N backward along the ray path of the specific intensity beam. The τ_i and S_i are the velocity surface optical depths and source functions for frequency ν. The integrated specific intensity for a transition labelled A at some common point $\vec{r}_1$ is

$$\begin{aligned}\bar{I}(\vec{r}_1, \hat{n}) = &\left(I_{inc} \exp\left[-\sum_{i=2}^{N} \tau_i\right] + \sum_{i=2}^{N} S_i(1 - \exp[-\tau_i]) \exp\left[-\sum_{j=2}^{i-1} \tau_j\right]\right)\left(\frac{1 - \exp[-\tau_1]}{\tau_1}\right) \\ &+ S_1\left(1 - \frac{1 - \exp[-\tau_1]}{\tau_1}\right),\end{aligned} \tag{2.38}$$

where the CP surfaces for common point $\vec{r}_1$ are numbered 2 through N backward along the ray path of the specific intensity beam. Note that the CP velocity surfaces can be resonance regions for transitions different from transition A or for transition A itself if the velocity field is non-monotonic along the ray path. Thus the indexing of the optical depths and source functions in equation (2.38) is for geometrical purposes. The source function for transition A (i.e. source function S_A) may correspond to several indices in equation (2.38). Substituting from equation (2.38) into equation (2.30) gives an expression for S_A. This expression will, however, in general be an integral equation for S_A if the velocity field is non-monotonic. Solving for the source functions for a multiple transition case with a non-monotonic velocity field thus involves solving coupled integral equations.

Explicit solutions for the source functions are recovered if an atmosphere is in a state of general expansion or general contraction. If only one transition is present in the atmosphere then general expansion or contraction is a sufficient and usually a necessary condition for a single velocity surface (and therefore explicit) solution to the radiative transfer of a given frequency (Rybicki and Hummer 1978). A photon emitted by the transition that escapes the resonance region of emission cannot interact with that transition again. The general expansion or contraction causes the transition frequency along the ray path to be monotonically Doppler shifted away from the photon's frequency. The photon must escape the atmosphere. However, if there are multiple transitions the photon can interact with lower frequency transitions in the general expansion case and higher frequency transitions in the general contraction case. Therefore the source function for each transition at every point $\vec{r}$ in the general expansion case can be explicitly constructed using equation (2.30) from the source functions of the higher frequency transitions (Olson 1982); in the general contraction case the source function can be constructed from the lower frequency transitions. Supernova atmospheres are in general expansion (see section (c) below), and so their source functions can be constructed in this way.

The Sobolev formalism can be given a probabilistic interpretation when applied to individual photons (Rybicki 1970; de Jong, Chu, and Dalgarno 1975). The differential loss from a specific intensity beam is given by

$$dI(s,\hat{n},\nu) = -\kappa(s,\nu)I(s,\hat{n},\nu)ds, \tag{2.39}$$

where $\kappa(s,\nu) = k(s)\phi(\nu - \nu_0(v_s/c))$ is the monochromatic line opacity and ds is a differential path element. The solution to this equation is

$$I(s_{max}, \hat{n}, \nu) = I(0, \hat{n}, \nu) \exp\left[-\int_0^{s_{max}} ds'\, \kappa(s', \nu)\right]. \tag{2.40}$$

For a single photon of frequency ν, the probability of travelling from 0 to s_{max} along the path without interacting with the line transition is

$$P(s_{max}, \hat{n}, \nu) = \exp\left[-\int_0^{s_{max}} ds'\, \kappa(s', \nu)\right]. \tag{2.41}$$

Consider a system where the Sobolev formalism applies, where $s = 0$ is taken to be a resonance point and where only a single velocity surface solution is required. Setting s_{max} to infinity and using the previously given transformations and expressions, equation (2.41) becomes

$$P(\infty, \hat{n}, \nu) = \exp\left[-\tau w\left(\xi(\nu)\right)\right]. \tag{2.42}$$

In this case

$$\xi = \frac{\nu - \nu_0(v_{res}/c) + Q(s_{res})(\nu_0/c)}{\Delta\nu} = \frac{\nu - \nu_0(v_{res}/c)}{\Delta\nu}, \tag{2.43}$$

where ν is being allowed to vary. (Note that the Q-cases of $w(\xi)$ are interchanged from the earlier derivation, since the present derivation has the specific intensity direction the same as the direction in which the coordinate s increases.) Equation (2.42) gives the probability that a photon of frequency ν escapes to infinity from the resonance point $s = 0$. By changing Q to $-Q$ equation (2.42) also gives the probability that a photon of frequency ν comes in from infinity to $s = 0$.

Assuming that the emission profile is the same as the absorption profile, then the average escape probability for a line photon emitted at the resonance point in direction $\hat{n}$ is

$$\begin{aligned} P(\infty, \hat{n}) &= \int_{-\infty}^{\infty} d\xi\, \varphi(\xi) P(\infty, \hat{n}, \xi) = \int_{-\infty}^{\infty} d\xi\, \varphi(\xi) \exp\left[-\tau w(\xi)\right] \\ &= \frac{1 - e^{-\tau}}{\tau} \\ &= \beta_d(\hat{n}). \end{aligned} \tag{2.44}$$

The reason for the earlier designation of β_d as the directional escape probability should now be clear. The direction-average escape probability is

$$\beta = \int \frac{d\Omega}{4\pi} \beta_d(\hat{n}) = \int \frac{d\Omega}{4\pi} \frac{1 - e^{-\tau}}{\tau}, \tag{2.45}$$

where the integration is over all solid angle. Usually, as mentioned above, β is just called the escape probability. Note that β_d and β can range from 0 to 1. Note also that $kI_{inc}\beta$ is the energy scattered per unit volume per unit time at the resonance point from a specific intensity beam that is incident on the resonance region and that is constant over the frequency range where $\phi(\nu)$ is significantly different from zero.

It is interesting to investigate the number of scatterings that a line-emitted photon undergoes inside a resonance region before escaping to infinity. For this discussion pure two-level resonance scattering will be assumed. Thus photons interact only with the line transition and any photon absorbed in the line is re-emitted by the line. Since β is the probability that a line-emitted photon escapes the resonance region without scattering again, it follows that $(1-\beta)$ is the probability that the photon is absorbed in the line again. The probability that a line-emitted photon is absorbed, re-emitted, and escapes is clearly $(1-\beta)\beta$. It is easily seen that the probability distribution for the number of scattering events a line-emitted photon undergoes before escaping to infinity is

$$P(n) = (1-\beta)^n\beta, \tag{2.46}$$

where the Sobolev method assumes that β is a constant. This distribution is quite easily understood. If the escape probability β is large (i.e. $\beta \approx 1$), then $P(0)$ is large, and the $P(n>0)$ values are small. Thus a line-emitted photon would escape the resonance region without being scattered in almost all cases. The chance of scattering n times decreases rapidly as n increases. If $\beta \ll 1$, then the probability of any particular n-scattering event is small, and the distribution decreases rather slowly with n. In this situation there would be a large variation in the number of scatterings that line-emitted photons would undergo.

A formal analysis of the scattering probability distribution can be given. Note that

$$\sum_{n=0}^{\infty} P(n) = \sum_{n=0}^{\infty}(1-\beta)^n\beta = \frac{\beta}{1-(1-\beta)} = 1, \tag{2.47}$$

and so the distribution is properly normalized. For convenience let

$$\upsilon = 1-\beta. \tag{2.48}$$

The mean, or first moment of the distribution, is

$$\begin{aligned} <n> &= \sum_{n=0}^{\infty} nP(n) = \sum_{n=1}^{\infty} nP(n) = \beta\sum_{n=1}^{\infty} n\upsilon^n = \beta\upsilon\sum_{n=1}^{\infty} n\upsilon^{n-1} \\ &= \beta\upsilon\frac{d}{d\upsilon}\left(\sum_{n=1}^{\infty}\upsilon^n\right) = \beta\upsilon\frac{d}{d\upsilon}\left(\frac{1}{1-\upsilon}-1\right) = \beta\upsilon\left(\frac{1}{(1-\upsilon)^2}\right) = \frac{(1-\beta)}{\beta}. \end{aligned} \tag{2.49}$$

This expression for the mean shows that when the escape probability is large then $< n >$ is small; when the escape probability is small then $< n >$ is large. The second moment of the distribution is

$$\begin{aligned}
< n^2 > &= \sum_{n=0}^{\infty} n^2 P(n) \\
&= \sum_{n=0}^{\infty} [n(n-1)P(n) + nP(n)] = \sum_{n=0}^{\infty} n(n-1)P(n) \quad + \quad < n > \\
&= \sum_{n=2}^{\infty} n(n-1)P(n) \quad + \quad < n > \quad = \beta \upsilon^2 \sum_{n=2}^{\infty} n(n-1)\upsilon^{n-2} \quad + \quad < n > \\
&= \beta \upsilon^2 \frac{d^2}{d\upsilon^2} \left(\sum_{n=2}^{\infty} \upsilon^n \right) \quad + \quad < n > \quad = \beta \upsilon^2 \frac{d^2}{d\upsilon^2} \left(\frac{1}{1-\upsilon} - 1 - \upsilon \right) \quad + \quad < n > \\
&= \beta \upsilon^2 \left(\frac{2}{(1-\upsilon)^3} \right) \quad + \quad < n > \quad = \frac{2(1-\beta)^2}{\beta^2} \quad + \quad < n > .
\end{aligned} \tag{2.50}$$

The standard deviation is

$$\begin{aligned}
\sigma &= \sqrt{< n^2 > - < n >^2} \\
&= \frac{1-\beta}{\beta} \sqrt{1 + \frac{\beta}{1-\beta}} \\
&= < n > \sqrt{1 + \frac{1}{< n >}} .
\end{aligned} \tag{2.51}$$

For small β, $< n >$ is large, and so

$$\sigma \approx < n > . \tag{2.52}$$

The fact that the standard deviation is approximately equal to the mean is consistent with the expectation that probability distribution is rather flat for small β.

A useful characteristic quantity of a scattering system is the effective optical depth τ_{eff}. Consider the Sobolev optical depth

$$\tau(\vec{r}, \hat{n}) = \frac{kc}{\nu_0 |Q|} \approx \frac{\kappa \Delta \nu c}{\nu_0 |Q|}, \tag{2.53}$$

where κ is the line center monochromatic opacity, and $\Delta\nu$ is the line-width of the line profile. Now as indicated by equation (2.5) the velocity width of a resonance region is

$$\Delta v = (c/\nu_0)\Delta\nu, \tag{2.54}$$

and thus

$$\tau(\vec{r}, \hat{n}) \approx \frac{\kappa \Delta v}{|Q|}. \tag{2.55}$$

If the line-width is a result of thermal or turbulence broadening, Δv is a characteristic thermal or turbulence velocity. If a characteristic macroscopic velocity v_{ch} and a characteristic length l_{ch} can be found for the scattering atmosphere, then the approximation

$$|Q| \approx \frac{v_{ch}}{l_{ch}} \tag{2.56}$$

can be made. Thus

$$\tau(\vec{r}) \approx \frac{\kappa \Delta v}{v_{ch}/l_{ch}}, \tag{2.57}$$

where the $\hat{n}$ dependence of τ as been effectively averaged away by using a crude approximation for $|Q|$, but $\vec{r}$ dependence still remains due to the κ. Averaging $\tau(\vec{r})$ over the characteristic length gives

$$\tau_{eff} = \frac{\tau_{ch}}{v_{ch}/\Delta v}, \tag{2.58}$$

where

$$\tau_{ch} = \int dr\, \kappa(\vec{r}) \tag{2.59}$$

is the static atmosphere line center optical depth along the characteristic length.

The effective optical depth can be seen to be a sort of average or characteristic Sobolev opacity for the atmosphere. It is certainly a rather crude quantity since it incorporates little information about the geometry or opacity distribution in an atmosphere. However, an estimate of the average number of scatterings per scattered photon for the whole atmosphere can be obtained from τ_{eff}. The global average escape probability can be approximated by

$$\beta_{glo} \approx \frac{1 - \exp[-\tau_{eff}]}{\tau_{eff}}. \tag{2.60}$$

The global average scatterings per scattered photon is then

$$< n >_{glo} \approx \frac{1 - \beta_{glo}}{\beta_{glo}} + 1, \tag{2.61}$$

where 1 has been added to the formula of equation (2.49) to account for the condition that the photon has been scattered once at least in the resonance region. In the limits of small and large τ_{eff}

$$< n >_{glo} \approx \begin{cases} 1 + \frac{1}{2}\tau_{eff} & \text{for } \tau_{eff} \ll 1; \\ \tau_{eff} & \text{for } \tau_{eff} \gg 1, \end{cases} \tag{2.62}$$

where small and large τ expansions for β_d have been used (see Appendix 1, section (a)). In section (b) of this chapter τ_{eff} and $< n >_{glo}$ will be considered again.

It is interesting to recall that in a random walk process the number of scatterings necessary to traverse some medium is approximately proportional to the square of the optical depth of the medium:

$$n_{random\ walk} \propto \tau^2_{medium}. \tag{2.63}$$

In a random walk a photon is thought of as travelling a finite fixed distance (the mean free path) between scattering events; the photon cannot escape to infinity except when it is a mean free path from the surface. Also the random walking photon is free to move toward or away from the edge of the medium. A photon trapped in a spatial resonance region (a Sobolev type situation) is a contrasting case; the photon has a finite chance of escaping to infinity after each scattering event. The difference of the Sobolev case from the random walk case leads to the linear dependence on optical depth when the optical depth is large of the average number of scattering events needed to traverse a medium (see equation (2.62)).

b) The Physical Validity of the Sobolev Method

To test the physical validity of the Sobolev method comparisons can be made to the results of more exact radiative transfer calculations. In this section an examination will be made of the calculations and conclusions of Hamann (1981), Natta and Beckwith (1986), and Beckwith and Natta (1987). Hamann's paper directly confronted Sobolev calculation results with the results of calculations done with the co-moving frame formalism (Mihalas *et al.* 1975; Mihalas 1978, p. 490). Natta and Beckwith (hereafter referred to as NB) performed Monte-Carlo scattering calculations in expanding atmospheres, and made comparisons to the Sobolev method. Hamann and NB's calculations were done with mass flow in early type stars in mind. Such mass flows are rather complicated in comparison to the homologous expansion of supernova atmospheres.

Recall equation (2.6)

$$\Delta l/l_{ch} \approx \Delta v/v_{ch}, \tag{2.64}$$

where

$$\Delta v = v_{th} \quad \text{or} \quad v_{turb} \tag{2.65}$$

The v_{th} quantity is the full-width of the Gaussian thermal Doppler profile and is given by

$$v_{th} = \sqrt{2kT/m} = 12.85\sqrt{\frac{T}{10^4 A}}\,\mathrm{km\,s^{-1}}, \tag{2.66}$$

where A is the atomic mass in amu. If small scale turbulence (microturbulence) is present in the atmosphere then random motions by the turbulent elements can cause a turbulent Doppler shift profile that is usually presumed to be Gaussian. The turbulence velocity v_{turb}, that gives the full-width of the profile, may be supersonic. Hamann reports that v_{turb} may be of order of 100's of $km\,s^{-1}$ in early type stars. In this case turbulence would be the principal source of line broadening.

In the Sobolev method a principle assumption is that the width of the resonance region, Δl, can be approximated as zero in comparison to the length scale l_{ch} over which quantities such as the source function, and opacity vary significantly. Thus the Sobolev method demands that

$$\Delta l/l_{ch} \approx \Delta v/v_{ch} \ll 1. \tag{2.67}$$

The question of how small this ratio has to be cannot be answered adequately by considering the Sobolev method alone. Recourse must be made to more general methods of radiative transfer. Hence Hamann's use of the co-moving frame formalism.

The co-moving frame formalism (hereafter CMF) is able to treat large and small velocity flows unlike the Sobolev method. It can thus treat accurately systems with wide ranging velocity conditions. CMF also has in principle formal and computational advantages: opacity, emissivity, and redistribution functions recover their static forms; the calculations can be done with a great deal of parallelism. The disadvantages of CMF are that it is computationally intensive, and that it would become more so if extended to treat asymmetric systems.

To understand the effects Hamann found in his study it is useful to see an example of the line profile that emerges from an expanding atmosphere. Fig. 2.2 shows such profiles for a homologously expanding atmosphere where there is only one line transition supplying opacity in the atmosphere. In this case the line is artificial, and has a line center frequency of 5000 Å. The profile is produced by scattering in a spherical atmosphere surrounding a spherical source of continuum radiation, usually called the photosphere. Fig. 2.3 displays a schematic representation of such a scattering atmosphere. Radiation emitted with frequencies far from the line center frequency cannot interact with the atmosphere, because it is never Doppler shifted into resonance with the local line frequencies in the expanding atmosphere. Thus far from the line center a distant observer sees radiation with the continuum distribution of the photosphere.

Radiation emitted by the photosphere and scattered through nearly 90° toward a distant observer tends to be scattered from regions that have small velocity components along the line of

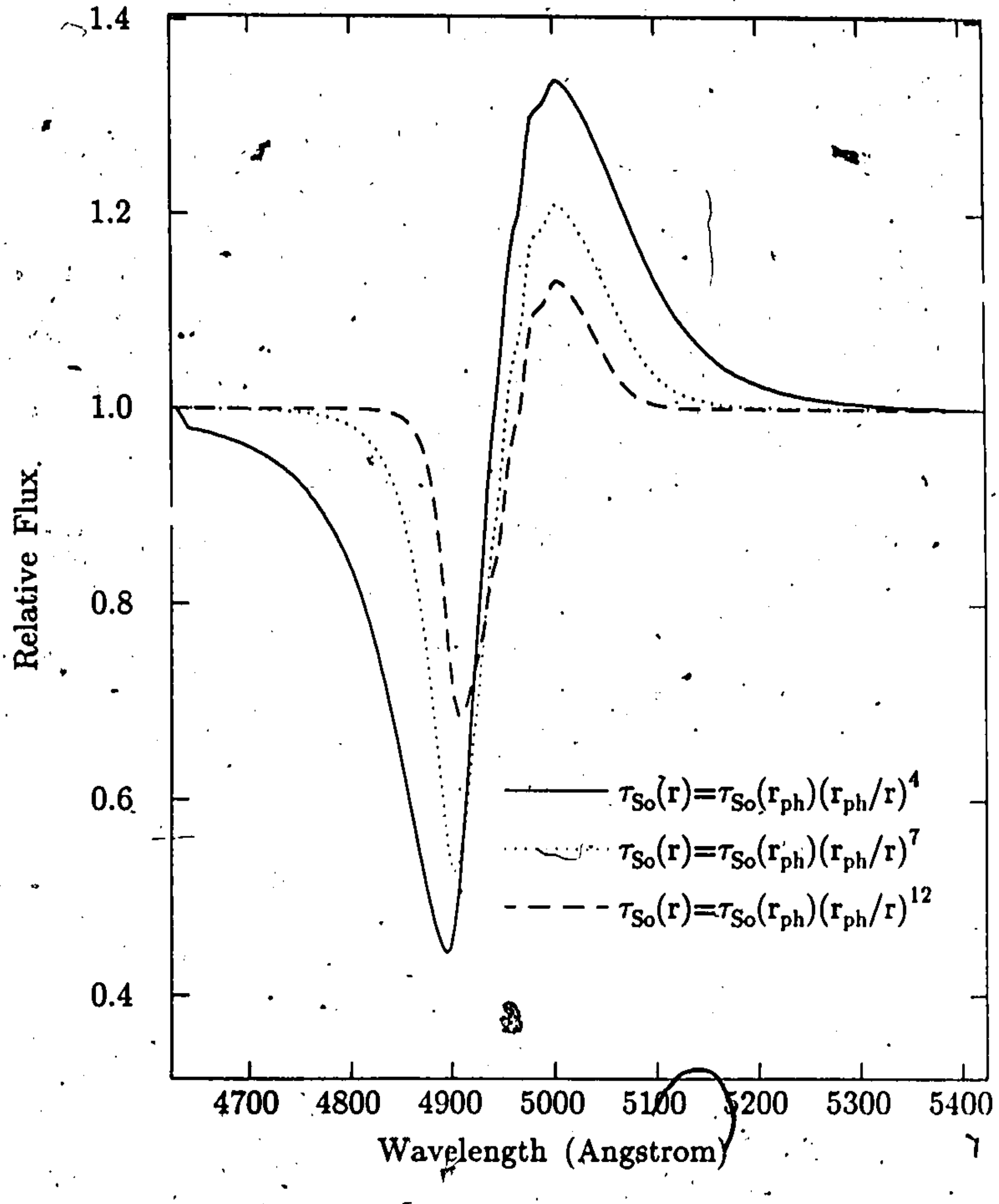

Fig. 2.2. Sample line profiles for a spherically-symmetric, homologously expanding atmosphere calculated with the Sobolev method. A continuum flux emerges from a photosphere of radius r_{ph}, and is resonantly scattered in the outer atmosphere. The Sobolev optical depths are parameterized as inverse powers of the radius, and the value $\tau_{S_o}(r_{ph}) = 5$. The profiles are typical of all expanding atmospheres, and are called P-Cygni profiles.

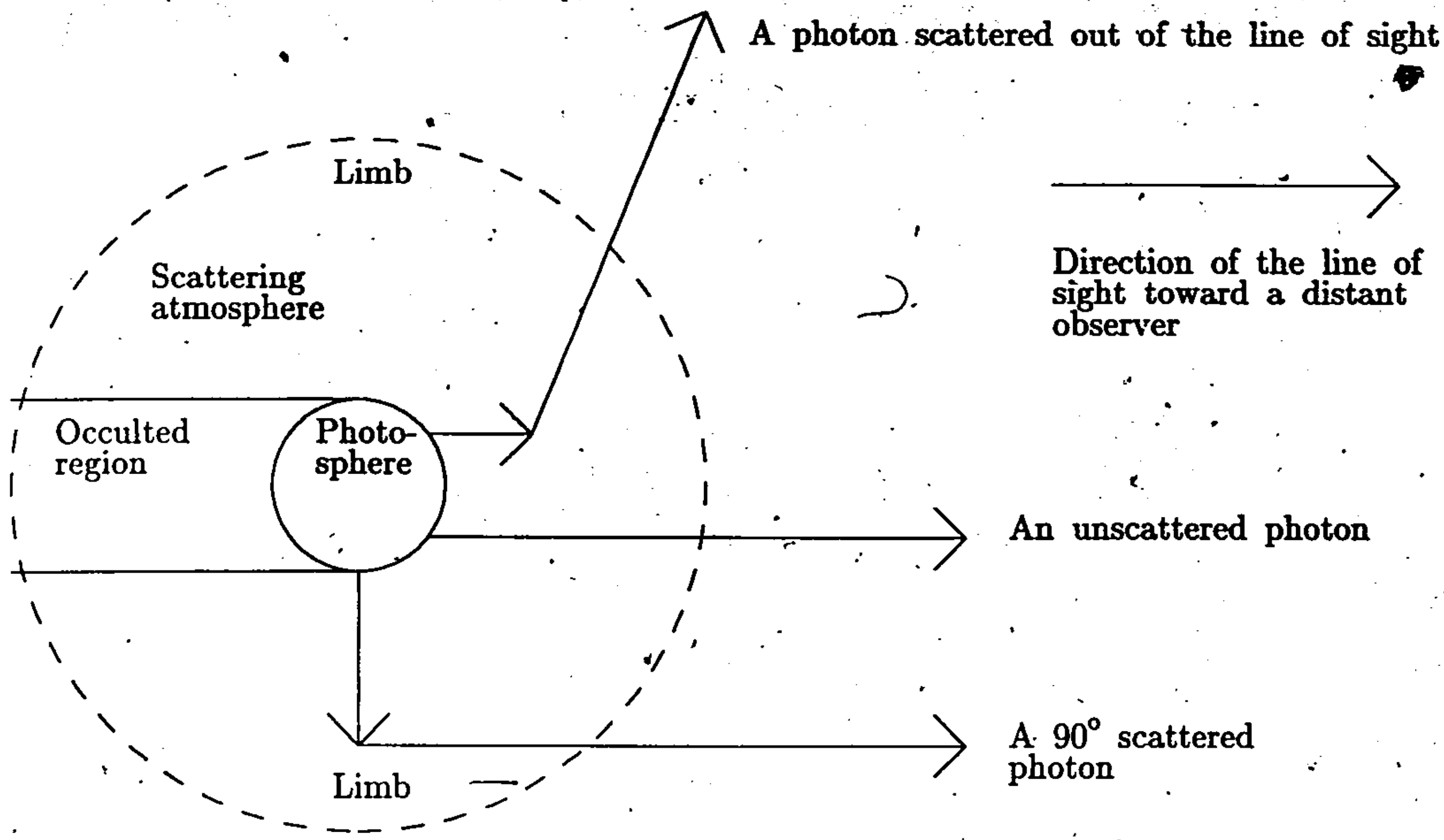

Fig. 2.3. A schematic representation of a scattering atmosphere.

sight to the distant observer. Thus this scattered emission as seen by the observer has only a small Doppler shift from the line center frequency (assuming the net Doppler shift of the whole system has been corrected for). The region of emission is rather near the plane perpendicular to the line of sight that contains the center of the whole system. This region and its projection are usually called the limb.

Radiation emitted by the photosphere directly toward the observer near the line center frequency is redshifted in the local frame of the expanding atmosphere through which it must pass to reach the observer. Such radiation therefore does not interact with the atmosphere, but streams freely toward the observer. In the terms of the Sobolev method one would say that the CD velocity surface for line center frequency emission is behind the photosphere. Therefore there is an excess emission over the continuum near the line center frequency since there is both full continuum emission, and limb scattered emission. This excess emission appears in Fig. 2.2. In fact the emission feature maximum can be redshifted from the line center. This effect is not obtained with a pure Sobolev calculation and so the profiles in Fig. 2.2 have their maxima at the line center frequency.

Radiation emitted from the photosphere directly toward the observer with frequencies higher than the line center frequency can be redshifted into resonance with the local line center frequencies of the expanding atmosphere. Thus there will be scattering out of the line of sight from frequencies higher than the line center frequency. This scattering is uncompensated for, and thus there is an absorption feature in the line profiles seen in Fig. 2.2. The combined blue shifted absorption, and near line center emission features are called P-Cygni profiles.

Hamann did not examine homologously expanding atmospheres, but qualitatively expanding atmospheres always produce P-Cygni profiles. The argument given above indicates why this is so. Hamann applied CMF to a set of models designed to encompass extreme cases of spherically symmetric mass outflow from stars. He investigated the effect of varying $\Delta v/v_{th}$, the effects of varying opacity over orders of magnitude, and the effect of varying the distribution of opacity and velocity. The non-Sobolev effects he obtained when $\Delta v/v_{th}$ was increased from .1 to .3 were: (1) a redward shift of the emission feature maximum from the line center wavelength, (2) that the blue edge of the absorption feature was shifted blueward, and (3) that there was a general broadening and softening of the line profile. A Sobolev calculated profile appeared as the $\Delta v/v_{th} = 0$ profile in this sequence; it was sharp edged and narrow compared to the CMF profiles. The effects of increasing the opacity by orders of magnitude were qualitatively similar to the effects of increasing $\Delta v/v_{th}$ by a factor of order 2. There is no need here to discuss the effects of the peculiar opacity and velocity distributions Hamann considered.

The effects of increasing $\Delta v/v_{th}$ and opacity can be understood fairly simply. The formal solution for the flux of wavelength λ that arises only from the source function is

$$I_{emg} = \int_0^{\tau_{\lambda\,max}} d\tau_\lambda\, S(\vec{r}(\tau_\lambda)) \exp[-\tau_\lambda], \tag{2.68}$$

where monochromatic optical depth has been used as the dummy variable rather than spatial distance.[1] Earlier this function was simplified in the Sobolev limit.

If $\tau_{\lambda\,max} \ll 1$, then the exponential factor in the integrand is never very different than 1, and the integrand can be approximated by the source function, weighted by the line profile that is absorbed in the differential $d\tau$. If the profile is symmetric about the line center in the local frame of the resonance, which is the usual case, then odd terms in an expansion for S about $\vec{r}_{res}$ will not contribute to the integral. Thus if the variation in S is no stronger than linear in the resonance region the Sobolev method continues to be plausible. If the variation in S is stronger than linear then the Sobolev method begins to be inadequate. The flux contribution to each wavelength no longer arises from a spatially localized region.

If $\tau_{\lambda\,max} \gtrsim 1$, then there is a strong tendency for the I_{emg} to equal $S(\vec{r}(\tau_\lambda = 1))$. This can be seen by expanding S to first order in $(\tau_\lambda - 1)$ about $\tau_\lambda = 1$:

$$S(\tau_\lambda) = S_0 + S_1(\tau_\lambda - 1), \tag{2.69}$$

where $S_0 = S(\vec{r}(\tau_\lambda = 1))$. Setting $\tau_{\lambda_{max}} = \infty$ and solving the integral of equation (68) for the emergent specific intensity with this limited expansion gives

$$I_{emg} = S_0, \tag{2.70}$$

with the first order term giving no contribution. The spatial point where $\tau_\lambda = 1$ is not likely in general to be coincident with the resonance point. If Δl is wide then the two points could be very different, and the Sobolev method which treats them as coincident would begin to fail.

---

[1] The monochromatic optical depth is defined by

$$d\tau_\lambda = k(\vec{r})\phi(\nu')dl$$

(see equation (2.7)). The monochromatic optical depth is not the same as the Sobolev optical depth which has been denoted by τ throughout this thesis.

If $\tau_{\lambda\ max} \geq 2$, then the source function that contributes most to the emergent intensity $I(\lambda)$ lies nearer to the observer than the resonance point for λ. Thus the flux at λ is enhanced or diminished relative to the Sobolev case depending on whether the source function increases or decreases in the direction toward the observer. In the atmospheres that Hamann considered the source function is a strong decreasing function of the radius; this is the usual case. Since the atmospheres were expanding the redder line scattered flux came from the hemisphere further from the observer, and the bluer flux from the nearer hemisphere. In the further hemisphere, moving toward the observer decreases radius, and thus increases the source function. Thus red flux is enhanced. In the nearer hemisphere, moving toward the observer increases the radius, decreases the source function, and thus decreases the blue flux. Therefore the redward shift of emission maximum in Hamann's profiles can be explained.

The blueward shift of the edge of the absorption feature is also due to the broadening of the line profile. There can be considerable scattering of radiation of wavelength $\lambda < \lambda_0$ at points of greater radius than the radius of the λ-resonance point.

The above discussion shows why increasing either $\Delta v/v_{th}$ or opacity can affect the profiles in a similar way. However, the profiles are much more sensitive to changing $\Delta v/v_{th}$. Why this is so can be seen by using the Sobolev approximation for the exponential factor in equation (2.68). From equation (2.17)

$$\exp[-\tau_\lambda] = \exp\left[-\tau \int_{\pm\infty}^{t} (\mp dt')\, \varphi(t')\right] \tag{2.71}$$

where the unsubscripted τ is the Sobolev optical depth defined by equation (2.15), where

$$t = \left(\frac{\nu_0 - Q(l - l_{res})(\nu_0/c)}{\Delta\nu}\right) \tag{2.72}$$

(the ν has been set to the local resonance frequency in the expression for t), and where l_{res}, the distance from the resonance point to the observation point, is so large that $\xi \rightarrow \pm\infty$. Of course, the Sobolev optical depth varies over the width of the resonance region, but since the variation of the line profile is stronger, τ can be approximated as a constant for an order of magnitude result. As argued above, the emergent intensity tends to equal the source function evaluated where $\tau_\lambda = 1$. Thus setting

$$1 \simeq \tau \int_{\pm\infty}^{t} (\mp dt')\, \varphi(t') \tag{2.73}$$

will allow an order of magnitude determination of the displacement between l_{res} and $l(\tau_\lambda = 1)$. Setting

$$\varphi(t) = \psi\left(t - \frac{\nu_0}{\Delta\nu}\right), \tag{2.74}$$

where ψ is assumed to be the Gaussian function

$$\psi(s) = \frac{\exp[-s^2]}{\sqrt{\pi}}, \tag{2.75}$$

changing the variable of integration in equation (2.74) with

$$t = s + \frac{\nu_0}{\Delta\nu}, \tag{2.76}$$

and defining

$$x = -\frac{|Q|(l - l_{res})}{(c/\nu_0)\Delta\nu} \tag{2.77}$$

gives

$$1 = \tau \int_x^\infty ds\, \psi(s), \tag{2.78}$$

where the fact has been used that ψ is an even function of s to eliminate the $\pm$ case distinction. To obtain an analytic result, τ will be assumed to be large. The integral of the Gaussian must then be small, and can be replaced by the first term of an asymptotic series to obtain

$$1 = \tau\left(\frac{e^{-x^2}}{2\sqrt{\pi}x}\right). \tag{2.79}$$

This replacement will cause x to be over-estimated by about 10 % for $\tau \approx 10$, and is increasingly accurate as τ increases from 10. From equation (2.79) the iterative expression

$$x = \sqrt{\ln\left(\frac{\tau}{2\sqrt{\pi}}\right) - \ln(x)} \tag{2.80}$$

can be obtained. For $\tau \geq 10$, there is only a further over-estimate of at most 10 % in using

$$x \approx \sqrt{\ln\left(\frac{\tau}{2\sqrt{\pi}}\right)}. \tag{2.81}$$

Using

$$|Q| \approx v_{ch}/l_{ch} \qquad \text{and} \qquad (c/\nu_0)\Delta\nu = \Delta v, \tag{2.82}$$

gives

$$\frac{\delta l_{res}}{l_{ch}} \approx \frac{\Delta v}{v_{ch}}\sqrt{\ln\left(\frac{\tau}{2\sqrt{\pi}}\right)} \tag{2.83}$$

for $\tau \geq 10$. Here δl_{res} is the distance between the resonance point for a wavelength λ and the point where most of the flux of wavelength λ originates. The distance δl_{res} increases linearly with $\Delta v/v_{ch}$, but as the square root of the logarithm of τ. It is now clear why Hamann's profiles were much more sensitive to changes in $\Delta v/v_{ch}$ than to changes in opacity.

If equation (2.83) is evaluated for the effective optical depth, a global diagnostic for the usefulness of the Sobolev method can be defined:

$$R_v = \begin{cases} \approx (\Delta v/v_{ch})\sqrt{\ln\left(\frac{\tau_{eff}}{2\sqrt{\pi}}\right)}, & \text{if } \tau_{eff} \gtrsim 10; \\ \approx (\Delta v/v_{ch}) & \text{if } \tau_{eff} \lesssim 10. \end{cases} \tag{2.84}$$

When R_v is sufficiently small the Sobolev method should be adequate, provided that l_{ch} is a characteristic distance for the source function and opacity variation as well as for the velocity variation. The criterion for smallness, however, depends strongly on the geometry, velocity distribution, and opacity distribution of the atmosphere considered. Also, important regions of the atmosphere may have τ's much greater than 10 even though τ_{eff} is evaluated to be less than 10; different definitions of τ_{eff} from that of section (a) may be more appropriate in such cases. Given these considerations it is not surprising that evaluating R_v for Hamann's models, and comparing the relative quality of his Sobolev models, leads to no general criterion for the smallness of R_v. However, Hamann's models are not inconsistent with the notion that increasing $\Delta v/v_{ch}$ and $\ln(\tau)$ cause comparable decreases in the accuracy of Sobolev method calculations. R_v is probably most useful in analyzing a well defined class of models.

Hamann only considered models where $\Delta v/v_c \geq .1$. Except for the lowest opacity cases the Sobolev profiles could only be considered qualitatively accurate. However, the limited nature of his survey does not allow a general conclusion about a $\Delta v/v_c$ criterion for the adequacy of the full Sobolev method. Hamann did find that the Sobolev source function was more accurate than the formal Sobolev solution, and used it as a first approximation in his CMF calculations. However, he also found that the Sobolev source function for two blended lines was rather poor for the redward line. Recall that the redward line in an expanding atmosphere can interact with photons scattered by the blueward line. This conclusion must be discounted, since Hamann used the older blending rule of Castor and Lamers (1979). Olson's prescription for line blending (1981) makes the Sobolev line blends as accurate as the single line Sobolev calculations.

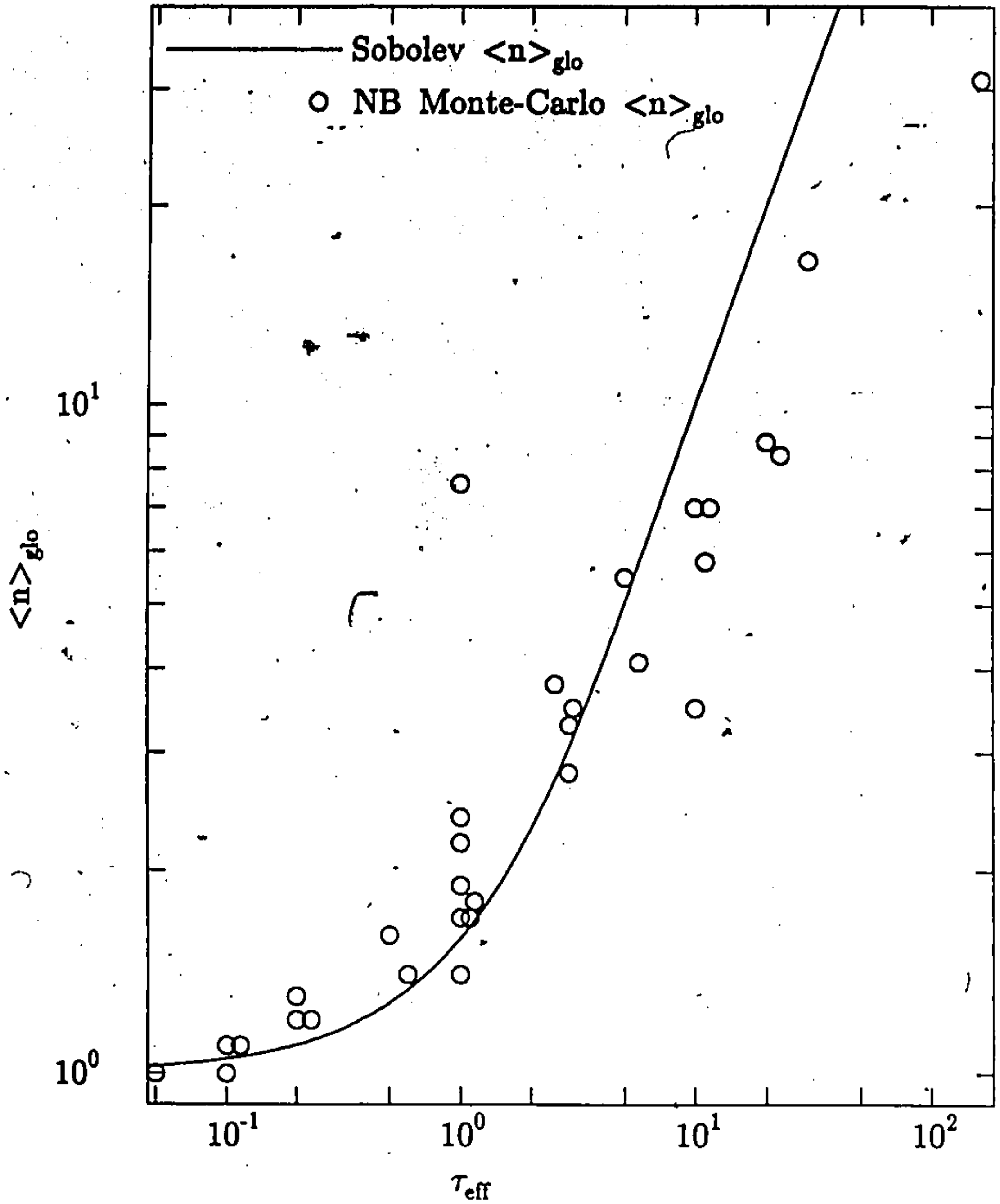

Fig. 2.4. Monte-Carlo global averages for number of scatterings per scattered photon from the calculations of Natta and Beckwith (1986), and the global average function calculated from an approximation of the Sobolev method. This figure reproduces Natta and Beckwith's Fig. 15. Note there is considerable clustering of the Monte-Carlo points about the Sobolev curve. The points tend to fall below the Sobolev curve at large τ_{eff} due to diffusion of photons in a density gradient. The Sobolev method does not include this diffusion effect.

NB made Monte-Carlo calculations of line profiles from expanding spherical atmospheres. They concluded, as they had expected to, that the Sobolev picture of radiative transfer was qualitatively correct. They discovered non-Sobolev effects in their profiles similar to those found by Hamann. However, their method allowed them to keep track of the behavior of individual photons. One quantity they computed was the average number of scatterings per scattered photon. This was compared to the global average number of scatterings per scattered photon calculated using the Sobolev method, and τ_{eff}. Equation (2.62) gives the Sobolev prescription for the global average. Fig. 2.4 reproduces Fig. 15 of NB's paper I. The points are the Monte-Carlo results, and the curve is the Sobolev prescription. It can be seen that there is considerable clustering of the Monte-Carlo results about the Sobolev curve. It should be recalled that even in terms of the Sobolev model the prescription for the global average is approximate, and that since the points arise from a multi-parameter class of models, no one parameter function could be expected to give them an exact fit. It can be seen that for $\tau_{eff} \gtrsim 10$ the Monte-Carlo points tend to fall below the Sobolev curve. NB attribute this to the outward diffusion of photons due to decreasing density of scatterers with radius. Of course, the Sobolev method treats the resonance regions where the scattering occurs as uniform in density.

A conservative general conclusion that can be drawn from the results of Hamann and NB is that for $\Delta v/v_{ch} \lesssim .1$, and $\tau_{eff} \lesssim 10$ there is no reason to believe that the Sobolev method is not qualitatively accurate. Since the Sobolev method is computationally much less intensive than CMF, or Monte Carlo methods, it is an obvious method of first approach to problems in this regime that are not spherically symmetric, and are without complete redistribution of scattered photons.

c) The Application of the Sobolev Method to Supernova Calculations

The foremost exploiters of the Sobolev method for the calculation of line spectra for supernovae have been David Branch and his collaborators (Branch 1980; Branch *et al.* 1981, 1982, 1983, 1985). In this section their procedure will be summarized, and then discussed in detail. Examples of the results of their synthetic spectra calculation will also be discussed.

The primary interest in doing Sobolev calculations is to fit observed spectra from supernovae. Thus a model of a supernova explosion and a fitting procedure are needed. Branch and collaborators (1981, 1982, 1983) used a model and procedure summarized in the following statements. (1) The exploded supernova matter is in homologous expansion. (2) The Sobolev method (Sobolev 1947; Castor 1970) in the generalized form of Rybicki and Hummer (1978), and Olson (1982) is employed to calculate the spectra. (3) There is a spherically symmetric photosphere surrounded by a spherically symmetric atmosphere. (4) The photosphere is well defined, and produces a black-body continuum. The photospheric temperature is determined by fitting the observed supernova continuum to a reddened black-body curve. The reddening of the curve accounts for the wavelength dependent effect of interstellar absorption. (5) The opacity of the atmosphere is taken to be due only to line transitions. The radiative transfer is treated as pure two-level atom resonance scattering. (6) The Sobolev optical depth for each transition as a function of radius is parameterized by the expression

$$\tau(r) = \tau_{ph}(r_{ph}/r)^{p}, \tag{2.85}$$

where τ_{ph} is the Sobolev optical depth at the photosphere, and p is a parameter that is normally set to 7. The τ_{ph} for the strongest line arising from a given ion is used as a fitting parameter. The τ_{ph}'s for the other lines arising from the same ion are determined by assuming the occupation numbers of the lower levels of these lines are determined by the Boltzmann distribution (LTE distribution) evaluated at the photospheric temperature. Note that

$$\tau_l \propto k_l \propto n_l, \tag{2.86}$$

where n_l is the occupation number of the lower level l of a transition. (7) Estimates of the element abundances are obtained from the fitted τ_{ph}'s, and the photospheric temperature. (8) The velocity of the photosphere is determined from P-Cygni absorption minima of weak lines. (9) A selection of ion transitions for the model atmosphere is made by recognition or on the basis of reasonable expectations about supernova element abundances. For instance, in the case of type II supernovae there is no doubt that the hydrogen Balmer lines are present. The selected transitions can be verified to some degree by the agreement of the synthetic spectra with observations.

By the time that supernovae have expanded to several times their initial size, the gravitational and internal energy of the supernova matter has fallen to near zero relative to the kinetic energy of the macroscopic motion. As a result no strong forces act on mass elements, and they are set in uniform motion. This form of expansion is called homologous expansion. The position of mass element i as a function of time becomes

$$\vec{r}_i(t) = \vec{v}_i t + \vec{r}_i(initial). \tag{2.87}$$

The initial radii of type I supernovae's presumed white dwarf progenitors are of order 10^9cm. The initial radii of type II supernovae's presumed red giant progenitors are of order 10^{13}cm. The velocity of supernova mass elements are known to be of order 10^9 cm s^{-1}. It is clear that long before maximum light $r_i(initial) \ll r_i(t)$. Thus after early times

$$r_i(t) \approx v_i t, \tag{2.88}$$

where the vector notation has been suppressed since the elements are approximately moving only radially with respect to the ignition point. The distance between mass element i and j is

$$r_{ij} = \sqrt{r_i^2 + r_j^2 - 2r_i r_j \cos\theta}, \tag{2.89}$$

where θ is the angle between the directions to the elements. Since there are no forces, θ is a constant. The time t can be extracted from the square root of equation (2.89) to give

$$r_{ij} = v_{ij} t, \tag{2.90}$$

where v_{ij} is time-independent. Thus

$$v_{ij} \sim r_{ij}, \tag{2.91}$$

where t^{-1} is the constant of proportionality. This condition defines the state of homologous expansion. The expanding universe models are, of course, another case of homologous expansion.

The homologous expansion of supernovae is the macroscopic velocity field needed for the Sobolev method. It should be noted that the atoms have random thermal velocity, and there may be random microturbulent motions superimposed on the homologous expansion. The macroscopic velocities of supernovae are of order 10^9 cm s^{-1}. This size scale can be deduced from the P-Cygni profiles of supernovae with only a Sobolev picture of the atmosphere, and without a formal calculation. Since the Sobolev picture is qualitatively well verified (see section (b) of this chapter) there is no reason to doubt this estimate. The highest temperatures of supernova are estimated to be of order 10^4 K. These estimates are based on fitting the continuum to a black-body spectrum. Since the continuum source may not radiate like a black-body these estimates may be in error (Wagoner, 1981). However, the estimates are not likely to be in error by orders of magnitude, and so equation (2.66) indicates that

$$v_{th} \lesssim 10^6 \text{ cm s}^{-1}. \tag{2.92}$$

If emission and absorption profile widths of transitions are determined by the thermal velocity, then $\Delta v/v_{eh} = v_{th}/v_{eh} \approx 10^{-3}$. This ratio is much smaller than the ratios for which Hamann (1981), and Natta and Beckwith (1986) found the Sobolev method to be qualitatively correct (see section (b) of this chapter). Thus supernova atmospheres may be an exellent system for the application of the Sobolev method. However, microturbulence velocity v_{turb} may determine the transition profiles, and v_{turb} may be greater than v_{th}. The quality of the fits to supernova lines obtained by Branch *et al.* (1981, 1982, 1983, 1985) indicate that $\Delta v/v_{eh} < .1$, whatever the origin of the width of transition profiles. Branch *et al.* used the multi-line formulation of the Sobolev method of Rybicki and Hummer (1978), and Olson (1982) after 1982; this formulation is presented in section (a) of this chapter. Before 1982 they used the older formulations of Sobolev (1960) and Castor (1970), and the less accurate line blending prescription of Castor and Lamers (1979).

Homologous expansion presents a very simple system for the application of the Sobolev method. The CD velocity surface for frequency ν is determined by the equation

$$\hat{n} \cdot \vec{v}(\vec{r}) = v_{s\nu}, \tag{2.93}$$

where $\hat{n}$ defines the direction, and $v_{s\nu}$ is the velocity required to Doppler shift the transition frequency to ν from the rest atom frequency ν_0 (see section (a) of this chapter). In the homologous expansion case this equation becomes

$$\hat{n} \cdot \vec{r} Q = v_{s\nu}, \tag{2.94}$$

where $Q = t^{-1}$ for supernovae; thus Q is a constant for the whole atmosphere at a given time. Thus

$$\hat{n} \cdot \vec{r} = Q^{-1} v_{s\nu} = \text{constant} \tag{2.95}$$

which is the equation of a plane. Therefore the CD surfaces for homologous expansion are just planes. The CP surfaces are determined by

$$\frac{(\vec{r} - \vec{r}')}{|\vec{r} - \vec{r}'|} \cdot (\vec{v}(\vec{r}) - \vec{v}(\vec{r}')) = v_{s\nu}, \tag{2.96}$$

where $\vec{r}$ traces out the surface, $\vec{r}'$ locates the common point, and $v_{s\nu}$ is the velocity difference needed to shift the transition on the surface into resonance with the transition at the common point. In the homologous expansion case this becomes

$$|\vec{r} - \vec{r}'| = Q^{-1} v_{s\nu} \tag{2.97}$$

which is the equation of a sphere. Therefore the CP surfaces for homologous expansion are spheres.

A further simplification of homologous expansion occurs for the expressions for the escape probabilities. Recall that the Sobolev optical depth is defined by

$$\tau = \frac{kc}{\nu_0|Q|} \tag{2.98}$$

which in general depends on direction through the $|Q|$ factor. The Q is independent of direction for homologous expansion. Thus the escape probability given by

$$\beta = \oint \frac{d\Omega}{4\pi} \frac{1 - \exp[-\tau]}{\tau} \tag{2.99}$$

(see section (a) of this chapter) becomes simply

$$\beta = \frac{1 - \exp[-\tau]}{\tau}. \tag{2.100}$$

The assumption of Branch *et al.* that the photosphere and atmosphere are spherically symmetric may be valid in many cases. The question of supernova asymmetry is discussed in Chapter 1 section (d). The present thesis, of course, does not assume spherical symmetry.

The assumption that a well defined, black-body producing photosphere exists is somewhat problematic. Neither for supernova type I or II is the continuum spectrum well fit by a black-body curve at a single temperature. The UV (ultraviolet) continuum of type I supernova is well known to be deficient compared to the optical continuum. The IR (infrared) continuum also appears to be deficient. The UV and IR continuum of type I supernova SN 1981b near maximum light can be fit by a black-body curve with temperature 9400 K, whereas the optical continuum is fit by a black-body curve with temperature 15800 K (Panagia 1985). These results indicate that the opacity is much higher in the UV and IR than in the optical. On the other hand, the well observed type II supernova 1980k showed a UV excess at all times (Benvenuti *et al.* 1982), and IR excess (Dwek *et al.* 1983). The UV excess may be due to the effects of circumstellar matter (Fransson 1984), and IR excess to extended atmosphere effects. These results for particular supernovae may not hold for all supernovae, but they do show that a single black-body continuum producing photosphere is not tenable in general.

There is another difficulty with the notion of a black-body continuum photosphere even with the restriction to a limited part of the spectrum. Wagoner (1981) argues that type II supernova atmospheres may be scattering dominated, and this changes the spectrum into a diluted black-body spectrum. For such a spectrum, the color temperature obtained by trying to fit a black-body curve would be higher than the effective temperature. Wagoner's considerations may also apply to type I supernovae as well.

At later times the supernova matter becomes rarefied, and the photosphere must recede into the expanding matter. At some point the whole supernova will become optically thin, and a black-body radiation field may not exist at any depth. Harkness (1986) suggests the possibility that the radiation field in type I supernovae may never be black-body at any depth at any time.

The fact that Branch *et al.* (1981, 1983) can fit the P-Cygni line profiles quite well until late times indicates that the assumption of a photosphere is probably quite good. For instance, SN 1981b's spectrum was adequately fitted by a synthetic spectrum 116 days after maximum light (Branch *et al.* 1983). The fact that the continuum produced by the photosphere may not be black-body does not really effect the quality of the fits. The problem with not having a black-body continuum lies in the interpretation of the fitted τ_{ph} parameters in terms of abundances. With a black-body continuum it is reasonable, at least at the photosphere, that the occupation numbers of the energy states of the ions are determined by thermodynamic equilibrium. Without a black-body continuum, extracting the abundances becomes more difficult.

The assumption of Branch and his collaborators that the scattering in the atmosphere is pure two-level atom resonance scattering is an admitted approximation. In a two-level atom resonance scattering, a photon is absorbed by an ion causing a transition to an upper level. That ion subsequently makes a transition (spontaneous or induced) to the original level emitting a photon with nearly the same frequency as the original photon. There are no collisional interactions, and no radiative transitions involving other levels. Electron scattering, free-free transitions, and bound-free transitions are also ignored. The proper treatment of radiative transfer in a non-LTE system involves solving the equations of statistical equilibrium (or rate equations) in order to obtain correct expressions for the source functions. Feldt (1980) undertook the task of comparing rate equation source functions for supernovae atmospheres to those obtained assuming two-level atom resonance scattering. In most of the cases he examined, the two-level atom resonance scattering source functions agreed to within a factor of 2 with the rate equation source functions. In view of the fact that there is considerable uncertainty in the temperature, density, and abundance distributions for supernova atmospheres an uncertainty of a factor of 2 in the source functions is acceptable for extracting approximate information about the atmosphere.

Along with the source function, the other important quantity required by the Sobolev method is the Sobolev optical depth given by

$$\tau = \frac{kc}{\nu_l |Q|}, \tag{2.101}$$

where k is the line integrated opacity, ν_l is the line center frequency for transition l, and Q is the derivative of velocity with respect to distance (see section (a) of this chapter).

The integrated line opacity is given by

$$k = \frac{\pi e^2}{mc} f_{lu} n_l \left(1 - \frac{g_l n_u}{g_u n_l}\right), \tag{2.102}$$

where l indicates the lower state of the transition, u the upper state, f_{lu} is the oscillator strength of the transition, n_l is the density of ions in state l (occupation number), and g_l is the degeneracy or statistical weight of state l (see Mihalas, 1978, p. 80–84). Accurate values of k are obtained by solving the rate equations. Branch and collaborators avoided solving the rate equations by making some highly simplifying assumptions.

First, the stimulated emission effect is neglected. The quantity $(g_l n_u / g_u n_l)$ is the correction for stimulated emission, and in thermodynamic equilibrium equals $\exp[-h\nu_{lu}/kT]$. The exponent has the value

$$\frac{h\nu_{lu}}{kT} = \frac{1.4390}{T_4 \lambda_\mu}, \tag{2.103}$$

where T_4 is photospheric temperature in units of 10^4 K, and λ_μ is the transition wavelength in microns. The temperatures estimated for supernova photospheres give $T_4 \lesssim 3$ near maximum light, and cooler later (for type II supernova see Kirshner and Kwan 1974; for type I see Branch *et al.* 1983). For optical lines $\lambda_\mu < .7$. Thus the exponent will be larger than $\approx .6$ for these conditions, and the correction term smaller than $\approx e^{-.6} = 0.55$. Since the temperature for both types of supernovae falls below ≈ 10000 K about 20 days after maximum light, the correction term drops below $\approx e^{-2} = .135$ for later times. If the thermodynamic equilibrium result is even approximately valid in supernova atmospheres, stimulated emission should not be an overwhelming effect after maximum light, and not an important effect at all after about 20 days.

Branch and collaborators assumed that all the occupation numbers were proportional to the density:

$$n_i(r) \propto \rho(r). \tag{2.104}$$

Several factors could cause deviation from this simple relation: temperature gradients in the atmosphere, non-LTE effects even if the electron temperature is a constant, and element stratification. The further assumption was made that

$$\rho(r) \propto r^{-7}. \tag{2.105}$$

This density dependence for the outer atmosphere has some support in explosion calculations. Hydrodynamic calculations by Colgate and McKee (1969) showed that

$$v(r) \propto F(r)^{-1/4}, \tag{2.106}$$

where

$$F(r) \propto \int_r^\infty dr' \, r'^2 \rho(r')$$

is the mass fraction above radius r. If it is assumed that

$$\rho(r) \propto r^{-p}, \tag{2.107}$$

then

$$F(r) \propto r^{-p+3}, \tag{2.108}$$

and then

$$v(r) \propto r^{(p-3)/4}. \tag{2.109}$$

Equation (2.88) shows that at a given time

$$v(r) \propto r, \tag{2.110}$$

and so consistency requires that

$$p = 7. \tag{2.111}$$

This result is often invoked to obtain an analytic expression for the density distribution. Some numerical calculations of supernova explosions do offer partial confirmation of this sort of density distribution. Nomoto *et al.* 's W7 deflagration model (1984) for a type I supernova from a carbon-oxygen white dwarf progenitor, has a density profile that can be approximated by an inverse power 7 law (see Branch *et al.* 1985). Glen (1985, p. 77) showed that degenerate core models surrounded by low density non-degenerate envelopes when exploded produced outer density distributions that were inverse power laws of between 6 and 10.

With the inverse power 7 law, the assumption that occupation numbers are proportional to density, and the neglect of stimulated emission, the parameterisation

$$\tau(r) = \tau_{ph}(r_{ph}/r)^7 \quad . \tag{2.112}$$

is obtained for the Sobolev optical depths. The τ_{ph} of the strongest line of an ion was taken as a fitting parameter. The assumption of LTE populations at the photospheric temperature gives the occupation numbers, and hence optical depths for the other lines of the ion. The fitted τ_{ph}'s, again assuming LTE, allow estimates of the relative element densities and abundances to be made using equations (2.101), (2.102) and (2.105). If $Q = t^{-1}$ can be specified, then absolute estimates can be made. The time t is, of course, usually not known, but observations and hydrodynamic calculations allow it to be estimated if sufficient photometry is obtained for a supernova event. The photospheric radius can be estimated from $r_{ph} = v_{ph}t$. All these estimates are, of course, rather uncertain.

The photospheric velocity, v_{ph}, can be rather accurately determined provided the density gradient is rather steep; i.e., $p \gtrsim 7$ (Branch 1980). The CD velocity plane tangent to the photosphere, and perpendicular to the line of sight has an observer frame resonance wavelength that is Doppler shifted by an amount corresponding to the velocity of the photosphere toward the observer. For weak lines the absorption minima form at this tangent velocity surface, and thus an immediate determination of the photospheric velocity can be made. In this context weak lines are those with $\tau_{ph} \lesssim 10$. A demonstration of this feature of weak lines is given in Chapter 4 section (b).

The line transitions to include in a synthetic spectrum calculation can be determined partially by recognition, and partially by theoretical expectation. In type II supernova spectra the Balmer series can easily be recognized by their relative strength, and spacing. The assumption of solar composition can be used to identify other lines in type II supernova.

Branch (1980) and Branch *et al.* (1981) produced synthetic spectra for type II supernova SN 1979c. Qualitative fits obtained with H I, He I, Na I, Ca II, and Fe II lines give reasonable confidence in the identification. The discrepancy between the synthetic and observed spectra was attributed to thermal emission. The Hα was notably discrepant in that it lacked a P-Cygni absorption feature. Not all type II supernovae Hα lines lack the P-Cygni absorption, but it seems to be common that there is more flux gained in the emission feature than is lost in the absorption feature; for pure P-Cygni resonance lines the reverse obtains (see Chapter 4 section (b)).

Type I supernovae show no evidence of Balmer lines, and are thus understood to be very hydrogen deficient. At maximum light the lines are attributed to intermediate mass species such as Si II, Mg II, Ca II, and OI (Branch 1980; Branch *et al.* 1982; 1983). Before the work of Branch *et al.* the identity of these lines was quite uncertain. Deflagration calculations for carbon-oxygen white dwarfs by Nomoto *et al.* (1984) show that such intermediate elements are produced.

A variation on the procedure outlined above was made by Branch *et al.* (1985) by using the abundances and density profile of Nomoto *et al.* 's W7 model. By using model calculated quantities some of the freedom that parameters have in the basic procedure was restricted. In this Sobolev calculation synthetic spectra were produced that closely matched the spectra of the prototypical type I SN 1981b. In order to obtain the best fits, the upper layers (matter moving with $v \geq 8000\,\mathrm{km\,s^{-1}}$) of the W7 model had to be completely mixed artificially. The physical origin of the mixing was taken to be convection. The theoretical expectation that large amounts of ^{56}Ni should be produced in the ignition of a type I supernova, suggests that ^{56}Ni decay products, ^{56}Co, and ^{56}Fe, may contribute lines. In the maximum light spectrum of SN 1981b a UV line has been attributed to Co II by Branch *et al.* In model W7, the ^{56}Co matter is mostly below the photosphere; Branch *et al.* determined the maximum light photospheric velocity to be $10000\,\mathrm{km\,s^{-1}}$ by line fitting. The artificial layer mixing was necessary to give a good fit to the Co II line. Fe II lines appear in the post-maximum light spectra of SN 1981b. These lines may owe largely to iron that existed before the deflagration rather than to the iron expected from the ^{56}Ni decay. However, Branch *et al.* found that the mixing which dredged up some of the decay product iron improved the Fe II line fits.

On the whole, the quality of fits of Sobolev calculated synthetic spectra to observed spectra obtained by Branch and collaborators is quite good. This gives reasonable confidence in the identification of lines. Obviously weak lines that are fit assuming LTE occupation numbers are less certain, and alternate identifications are possible. Interpreting the fitted τ_{ph}'s in terms of abundances is also somewhat uncertain, though useful.

Improvements on the basic fitting procedure for creating synthetic spectra have been made. As discussed above, Branch *et al.* (1985) improved the method by using a model density and abundance distribution rather than relying purely on simple atmosphere assumptions. Hempe (1985) used the co-moving frame formalism (CMF). Harkness (1985; 1986) used CMF with LTE populations, and included continuous absorption opacities. Harkness *et al.* (1987) present CMF models with a first order correction for non-LTE effects. Improved calculational methods and models offer improved understanding, but at the cost of greater computational effort.

For this thesis the procedure of Branch (1980) and Branch *et al.* (1981; 1982; 1983) has been adopted with the modifications that the assumption of spherical symmetry has been replaced by axial symmetry, and the Sobolev method has been generalised to allow for the polarising effect of resonance scattering (see section (d) below). The improvements on the procedure noted above would be even more computationally demanding with these modifications. For instance, generalising from spherical symmetry to axial symmetry in model calculations has the effect of squaring the number of operations in a calculation. The thesis author is also not aware of any aspherical version of the CMF formalism in the literature. Should any such verison appear it would probably be confined to some simple asymmetries. The Sobolev method, on the other hand, should be easily generalisable to complicated asymmetric atmospheres. A Monte-Carlo method such as that used by Natta and Beckwith (1986), and Beckwith and Natta (1987) is probably the superior alternative to the Sobolev method for asymmetric atmospheres. Monte-Carlo calculations are, of course, also computationally intensive.

d) The Sobolev-H Method for Polarizing Resonance Scattering

In this section the Sobolev method is generalized to include the polarizing effect of resonance scattering. This generalized Sobolev method, for reasons given below, has been called the Sobolev-H method. The physical validity of the approximation used to introduce a polarizing effect will be considered in section (e).

In order to describe polarization, Chandrasekhar's version of the Stokes parameters (1960, p. 24) has been adopted. The parameters are (1) I_l, the specific intensity of the radiation field component along an axis labelled l, (2) I_r, the specific intensity of the radiation field component along an axis labelled r which is 90° clockwise from axis l, (3) U, the difference between the specific intensities of radiation field components along a system of axes rotated 45° clockwise from the l-r system, and (4) V, which describes the circular polarization. The specific intensity I considered in section (a) of this chapter is the total specific intensity and is given by

$$I = I_l + I_r. \tag{2.113}$$

Angle-dependent linear polarization is defined as

$$P(\phi) = (I_\phi - I_{\phi+\pi/2})/I, \tag{2.114}$$

for an arbitrary choice of orthogonal axes along which I_ϕ, and $I_{\phi+\pi/2}$ are measured. $I = I_\phi + I_{\phi+\pi/2}$ is the total specific intensity and is independent of angle. The value of $P(\phi)$ varies with ϕ and so the linear polarization is defined as an extremum value of $P(\phi)$. From Chandrasekhar (1960, p. 34),

$$P(\phi) = ((I_l - I_r)\cos 2\phi + U \sin 2\phi)/I, \tag{2.115}$$

gives the ϕ dependence of $P(\phi)$ in terms the Stokes parameters measured with some standard axes which have been label by l, and r as before. The angle ϕ is measured clockwise from axis l. From equating the derivative of equation (2.115) to zero, the angle of the extremum, called the position angle of polarization, is found to be given by

$$\tan 2\phi = U/(I_l - I_r) = U/Q, \tag{2.116}$$

where $Q \equiv I_l - I_r$. The extremum polarization, hereafter called simply the polarization, is

$$P = \pm\sqrt{Q^2 + U^2}/I. \tag{2.117}$$

If the projected image of a radiating system has symmetry about the l axis, it follows for the total emergent flux that the net U field is zero, and that

$$P = Q/I, \tag{2.118}$$

where P can be positive or negative.

The net polarization of the total flux of a radiating system can be found by integrating the Stokes parameters over a surface. It is often easiest to calculate the Stokes vector components for a point on the surface in a convenient local coordinate system, but then the vectors need to be transformed to general coordinates in order to integrate.

For radiation fields described by the Stokes parameters, the general expression for the source function for bound-bound transitions, as adapted from equation (2.25), is

$$\mathbf{S}(\vec{r}, \hat{n}, \nu) = \frac{(1-\epsilon)}{\phi(\nu + (\nu_0/c)(\hat{n}\cdot\vec{v}(\vec{r})))} \oint \frac{d\Omega'}{4\pi} \int_0^{+\infty} d\nu' \mathbf{R}(\nu, \hat{n}; \nu', \hat{n}')\mathbf{I}(\vec{r}, \hat{n}', \nu') \quad + \quad \mathbf{G}(\vec{r}), \tag{2.119}$$

where the source function, the specific intensity, and the thermal source are now vectors whose components are the Stokes parameters, and the redistribution function is now, in general, a matrix.

The Stokes vectors have the form

$$\begin{pmatrix} S_l \\ S_r \\ S_U \\ S_V \end{pmatrix}, \quad \begin{pmatrix} I_l \\ I_r \\ U \\ V \end{pmatrix}, \quad \text{and} \quad \begin{pmatrix} G_l \\ G_l \\ 0 \\ 0 \end{pmatrix},$$

where $G_I = G_l = G_r$ since the thermal source is assumed to be isotropic and nonpolarising, and where the total thermal source $G = G_l + G_r = 2G_I$. For complete redistribution (CRD) the redistribution function is

$$\mathbf{R}(\nu, \hat{n}; \nu', \hat{n}') = \mathbf{g}_I(\hat{n}, \hat{n}')\phi(\nu + (\nu_0/c)(\hat{n} \cdot \vec{v}(\vec{r})))\phi(\nu' - (\nu_0/c)(\hat{n}' \cdot \vec{v}(\vec{r}))), \tag{2.120}$$

where $\mathbf{g}_I$ is the isotropic scattering phase-matrix:

$$\mathbf{g}_I(\hat{n}, \hat{n}') = \frac{1}{2} \begin{pmatrix} 1 & 1 & 0 & 0 \\ 1 & 1 & 0 & 0 \\ 0 & 0 & 0 & 0 \\ 0 & 0 & 0 & 0 \end{pmatrix}. \tag{2.121}$$

The isotropic scattering phase-matrix g_I is assumed in the ordinary Sobolev method. Hamilton (1947) has given a prescription for a non-isotropic, polarising scattering phase-matrix for resonance scattering. Replacing the isotropic phase-matrix by the Hamilton phase-matrix in the redistribution function allows the derivation of a polarizing version of the Sobolev method. The polarising Sobolev method has been called the Sobolev-H method, where the "H" is for Hamilton. The new redistribution function has been called the hybrid redistribution (HRD) function. In section (e) of this chapter the physical applicability of the Hamilton phase-matrix, and validity of the Sobolev-H method will be discussed.

The Hamilton phase-matrix, in Chandrasekhar's version (1960, p. 51), is

$$\mathbf{g}_H(\hat{n}, \hat{n}') = E_1 \left(\frac{3}{2}\right) \begin{pmatrix} \cos^2\Theta & 0 & 0 & 0 \\ 0 & 1 & 0 & 0 \\ 0 & 0 & \cos\Theta & 0 \\ 0 & 0 & 0 & (E_3/E_1)\cos\Theta \end{pmatrix} + E_2 \left(\frac{1}{2}\right) \begin{pmatrix} 1 & 1 & 0 & 0 \\ 1 & 1 & 0 & 0 \\ 0 & 0 & 0 & 0 \\ 0 & 0 & 0 & 0 \end{pmatrix}, \tag{2.122}$$

where Θ is the angle between the incident beam and the scattered beam. The incident and scattered beams define the scattering plane. In order to use equation (2.122), the incident and scattered radiation fields must be described by l and r axes that are parallel and perpendicular to the scattering plane, respectively. The first matrix in equation (2.122) is the Rayleigh phase-matrix which also applies to Thomson scattering from electrons. The second matrix is the isotropic phase-matrix that is given in equation (2.121). The E_1, E_2, and E_3 are constant coefficients that depend on J, the total angular momentum of the lower level of the transition, and $J + \Delta J$, the total angular momentum of the upper level of the transition. Hamilton only considered allowed trantions and so $\Delta J = \pm 1$ or 0. Table 2.1 gives the prescriptions for the coefficients. It can be deduced from the table that $E_1 + E_2 = 1$; this is a requirement for conservative scattering. For $J = 0$ and $\Delta J = 1$ the coefficients are

$$E_1 = 1, \qquad E_2 = 0, \qquad \text{and} \qquad E_3 = 1,$$

and the Hamilton phase-matrix reduces to the Rayleigh phase-matrix. For $J = 1$ and $\Delta J = -1$ the coefficients are

$$E_1 = 0, \qquad E_2 = 1, \qquad \text{and} \qquad E_3 = 0,$$

and the isotropic phase-matrix is recovered. For reference Table 2.2 displays the E_i coefficients for small total angular momentum cases.

For use in scattering calculations, the Rayleigh phase-matrix must be transformed so that the incident and scattered beams can be located with respect to a general orthogonal coordinate system with the scattering center at the origin. The isotropic phase-matrix is unchanged by the transformation. The scattered beam in the general coordinate system is located by $\mu = \cos\theta$, where θ is the meridian angle measured from the z-axis and by ϕ, the azimuthal angle measured from the x-axis. The incident beam is located by primed versions: μ', and ϕ'. The beam axes l, and r are tangent to the meridian, and to the azimuth, respectively. Chandrasekhar's version (1960, p. 42) of the generalized Rayleigh phase-matrix is

$$\mathbf{P}(\mu,\phi:\mu',\phi') = Q\Big[\mathbf{P}^{(0)}(\mu,\mu') + \sqrt{1-\mu^2}\sqrt{1-\mu'^2}\,\mathbf{P}^{(1)}(\mu,\phi;\mu',\phi') + \mathbf{P}^{(2)}(\mu,\phi;\mu',\phi')\Big], \tag{2.123a}$$

where

$$\mathbf{P}^{(0)}(\mu,\mu') = \frac{3}{4}\begin{pmatrix} 2(1-\mu^2)(1-\mu'^2) + \mu^2\mu'^2 & \mu^2 & 0 & 0 \\ \mu'^2 & 1 & 0 & 0 \\ 0 & 0 & 0 & 0 \\ 0 & 0 & 0 & \mu\mu' \end{pmatrix}, \tag{2.123b}$$

$$\mathbf{P}^{(1)}(\mu,\phi;\mu',\phi') = \frac{3}{4}\begin{pmatrix} 4\mu\mu'\cos(\phi'-\phi) & 0 & 2\mu\sin(\phi'-\phi) & 0 \\ 0 & 0 & 0 & 0 \\ -2\mu'\sin(\phi'-\phi) & 0 & \cos(\phi'-\phi) & 0 \\ 0 & 0 & 0 & \cos(\phi'-\phi) \end{pmatrix}, \tag{2.123c}$$

TABLE 2.1.—Prescriptions for the E_1, E_2, and E_3 coefficients.

ΔJ	E_1	E_2	E_3
1	$\frac{(2J+5)(J+2)}{10(J+1)(2J+1)}$	$\frac{3J(6J+7)}{10(J+1)(2J+1)}$	$\frac{J+2}{2(J+1)}$
0	$\frac{(2J-1)(2J+3)}{10J(J+1)}$	$\frac{3(2J^2+2J+1)}{10J(J+1)}$	$\frac{1}{2J(J+1)}$
−1	$\frac{(2J-3)(J-1)}{10J(2J+1)}$	$\frac{3(6J^2+5J-1)}{10J(2J+1)}$	$\frac{J-1}{2J}$

SOURCE: Chandrasekhar (1960, p. 52).

TABLE 2.2—The E_i phase-matrix coefficients for small total angular momentum cases.

$J_1 - J_2$	E_1	E_2	E_3	$J_1 - J_2$	E_1	E_2	E_3
$\frac{1}{2} - \frac{1}{2}$	0	1	$\frac{2}{3}$				
$\frac{1}{2} - 1\frac{1}{2}$	$\frac{15}{30}$	$\frac{15}{30}$	$\frac{5}{6}$	0 − 1	1	0	1
$1\frac{1}{2} - \frac{1}{2}$	0	1	$\frac{1}{6}$	1 − 0	0	1	0
$1\frac{1}{2} - 1\frac{1}{2}$	$\frac{24}{75}$	$\frac{51}{75}$	$\frac{2}{15}$	1 − 1	$\frac{5}{20}$	$\frac{15}{20}$	$\frac{1}{4}$
$1\frac{1}{2} - 2\frac{1}{2}$	$\frac{28}{100}$	$\frac{72}{100}$	$\frac{7}{10}$	1 − 2	$\frac{21}{60}$	$\frac{39}{60}$	$\frac{3}{4}$
$2\frac{1}{2} - 1\frac{1}{2}$	$\frac{3}{150}$	$\frac{147}{150}$	$\frac{3}{10}$	2 − 1	$\frac{1}{100}$	$\frac{99}{100}$	$\frac{1}{4}$
$2\frac{1}{2} - 2\frac{1}{2}$	$\frac{64}{175}$	$\frac{111}{175}$	$\frac{2}{35}$	2 − 2	$\frac{21}{60}$	$\frac{39}{60}$	$\frac{1}{12}$
$2\frac{1}{2} - 3\frac{1}{2}$	$\frac{45}{210}$	$\frac{165}{210}$	$\frac{9}{14}$	2 − 3	$\frac{36}{150}$	$\frac{114}{150}$	$\frac{4}{6}$
$3\frac{1}{2} - 2\frac{1}{2}$	$\frac{10}{280}$	$\frac{270}{280}$	$\frac{5}{14}$	3 − 2	$\frac{6}{210}$	$\frac{204}{210}$	$\frac{2}{6}$
$3\frac{1}{2} - 3\frac{1}{2}$	$\frac{120}{315}$	$\frac{195}{315}$	$\frac{2}{63}$	3 − 3	$\frac{45}{120}$	$\frac{75}{120}$	$\frac{1}{24}$
$3\frac{1}{2} - 4\frac{1}{2}$	$\frac{66}{360}$	$\frac{294}{360}$	$\frac{11}{18}$	3 − 4	$\frac{55}{280}$	$\frac{225}{280}$	$\frac{5}{8}$
$4\frac{1}{2} - 3\frac{1}{2}$	$\frac{21}{450}$	$\frac{429}{450}$	$\frac{7}{18}$	4 − 3	$\frac{15}{360}$	$\frac{345}{360}$	$\frac{3}{8}$
$4\frac{1}{2} - 4\frac{1}{2}$	$\frac{192}{495}$	$\frac{303}{495}$	$\frac{2}{99}$	4 − 4	$\frac{77}{200}$	$\frac{123}{200}$	$\frac{1}{40}$
$4\frac{1}{2} - 5\frac{1}{2}$	$\frac{91}{550}$	$\frac{459}{550}$	$\frac{13}{22}$	4 − 5	$\frac{78}{450}$	$\frac{372}{450}$	$\frac{6}{10}$
$5\frac{1}{2} - 4\frac{1}{2}$	$\frac{36}{660}$	$\frac{624}{660}$	$\frac{9}{22}$	5 − 4	$\frac{28}{550}$	$\frac{522}{550}$	$\frac{4}{10}$
$5\frac{1}{2} - 5\frac{1}{2}$	$\frac{280}{715}$	$\frac{435}{715}$	$\frac{2}{143}$	5 − 5	$\frac{117}{300}$	$\frac{183}{300}$	$\frac{1}{60}$
$5\frac{1}{2} - 6\frac{1}{2}$	$\frac{120}{780}$	$\frac{660}{780}$	$\frac{15}{26}$	5 − 6	$\frac{105}{660}$	$\frac{555}{660}$	$\frac{7}{12}$
$6\frac{1}{2} - 5\frac{1}{2}$	$\frac{55}{910}$	$\frac{855}{910}$	$\frac{11}{26}$	6 − 5	$\frac{45}{780}$	$\frac{735}{780}$	$\frac{5}{12}$
$6\frac{1}{2} - 6\frac{1}{2}$	$\frac{384}{975}$	$\frac{591}{975}$	$\frac{2}{195}$	6 − 6	$\frac{165}{420}$	$\frac{255}{420}$	$\frac{1}{84}$
$6\frac{1}{2} - 7\frac{1}{2}$	$\frac{153}{1050}$	$\frac{897}{1050}$	$\frac{17}{30}$	6 − 7	$\frac{136}{910}$	$\frac{774}{910}$	$\frac{9}{14}$

$$\mathbf{P}^{(2)}(\mu,\phi;\mu',\phi') = \frac{3}{4}\begin{pmatrix} \mu^2\mu'^2\cos 2(\phi'-\phi) & -\mu^2\cos 2(\phi'-\phi) & \mu^2\mu'\sin 2(\phi'-\phi) & 0 \\ -\mu'^2\cos 2(\phi'-\phi) & \cos 2(\phi'-\phi) & -\mu'\sin 2(\phi'-\phi) & 0 \\ -\mu\mu'^2\sin 2(\phi'-\phi) & \mu\sin 2(\phi'-\phi) & \mu\mu'\cos 2(\phi'-\phi) & 0 \\ 0 & 0 & 0 & 0 \end{pmatrix}, \quad (2.123d)$$

and

$$\mathbf{Q} = \begin{pmatrix} 1 & 0 & 0 & 0 \\ 0 & 1 & 0 & 0 \\ 0 & 0 & 2 & 0 \\ 0 & 0 & 0 & 2 \end{pmatrix}. \quad (2.123e)$$

With the general coordinate version of the Hamilton phase-matrix a derivation of the Sobolev-H formalism can proceed. Substituting the HRD redistribution function into equation (2.119), and integrating over frequency gives

$$\mathbf{S}(\vec{r},\hat{n}) = (1-\epsilon)\oint \frac{d\Omega'}{4\pi}\mathbf{g}_H(\hat{n},\hat{n}')\bar{\mathbf{I}}(\vec{r},\hat{n}') \qquad + \qquad \mathbf{G}(\vec{r}), \quad (2.124)$$

where $\bar{\mathbf{I}}$ is the integrated specific intensity Stokes vector; $\bar{\mathbf{I}}$ corresponds to the result of equation (2.20) for the integrated specific intensity. The derivation and conditions of section (a) for the formal Sobolev expression for the integrated specific intensity (see equation (2.23)) can be repeated without change for the integrated specific intensity Stokes vector. Thus

$$\bar{\mathbf{I}}(\vec{r},\hat{n}) = \mathbf{S}(1-\beta_d) + \mathbf{I}_{ext}\beta_d, \quad (2.125)$$

where β_d is the directional escape probability of equation (2.24), and $\mathbf{I}_{ext}(\vec{r},\hat{n})$ is the Stokes vector incident on the resonance region that owes to all sources external to the resonance region backward along the ray defined by $\hat{n}$. An integral equation for the source function is thus obtained:

$$\mathbf{S}(\vec{r},\hat{n}) = (1-\epsilon)\Lambda[(1-\beta_d)\mathbf{S}(\vec{r},\hat{n}')] + (1-\epsilon)\Lambda[\beta_d\mathbf{I}_{ext}] + \mathbf{G}(\vec{r}), \quad (2.126)$$

where the following integral operator has been defined

$$\Lambda[\mathbf{f}(\hat{n}')] \equiv \oint \frac{d\Omega'}{4\pi}\mathbf{g}_H(\hat{n},\hat{n}')\mathbf{f}(\hat{n}'). \quad (2.127)$$

In principle equation (2.126) can be solved for S given $\mathbf{I}_{ext}$, and G. However, only a special system with the following characteristics will be examined here. (1) The macroscopic flow of the system is considered to be homologous motion: either expansion or contraction. Recall from section (c) of this chapter that homologous expansion is a characteristic of supernova explosions. For homologous motion, the directional escape probability is independent of direction, and so $\beta = \beta_d = (1 - e^{-\tau})/\tau$. (2) The system will be considered to be axially symmetric about an axis parallel to the z-axis of the scattering coordinate system, and the negative x-axis of the scattering coordinate system will chosen to intersect the symmetry axis. (3) The incident V Stokes field will be set to zero. Since the Rayleigh phase-matrix does not couple the V Stokes field to the other fields there is no scattered V field either (see equations (2.123)). Thus the V field will always be zero for this system. In consequence, only three-component Stokes vectors and a 3×3 phase-matrix need be considered. (4) As a consequence of the axial symmetry of the system, the I_l and I_r fields must be even functions of the azimuthal coordinate ϕ, and the U field must be an odd function of ϕ. Similarly, S_l and S_r must be even functions of ϕ, and S_U an odd function of ϕ.

What can be called the direct contribution to the source function vector is given by

$$\mathbf{D}(\vec{r}, \hat{n}) = \Lambda[\mathbf{I}_{ext}]. \tag{2.128}$$

The symmetries of component fields of the $\mathbf{I}_{ext}$ vector result in the following functional forms for the direct contribution field components:

$$D_l = D_1 + D_2\mu^2 + D_3\mu\sqrt{1-\mu^2}\cos\phi + D_4\mu^2\cos 2\phi, \tag{2.129a}$$

$$D_r = D_5 - D_4\cos 2\phi, \tag{2.129b}$$

and

$$D_U = D_3\sqrt{1-\mu^2}\sin\phi + 2D_4\mu\sin 2\phi, \tag{2.129c}$$

where the D_i coefficients are obtained from the integrals

$$D_1 = \oint \frac{d\Omega'}{4\pi}\left[(\tfrac{3}{2}(1-\mu'^2)E_1 + \tfrac{1}{2}E_2)I_l \quad + \quad \tfrac{1}{2}E_2 I_r\right], \tag{2.130a}$$

$$D_2 = \tfrac{3}{4}E_1\oint \frac{d\Omega'}{4\pi}\left[(-2+3\mu'^2)I_l \quad + \quad I_r\right], \tag{2.130b}$$

$$D_3 = \tfrac{3}{4}E_1\oint \frac{d\Omega'}{4\pi}\left[(4\mu'\sqrt{1-\mu'^2}\cos\phi')I_l \quad + \quad (2\sqrt{1-\mu'^2}\sin\phi')U\right], \tag{2.130c}$$

$$D_4 = \tfrac{3}{4}E_1\oint \frac{d\Omega'}{4\pi}\left[(\mu'^2\cos 2\phi')I_l \quad - \quad (\cos 2\phi')I_r \quad + \quad (\mu'\sin 2\phi')U\right], \tag{2.130d}$$

and

$$D_5 = \oint \frac{d\Omega'}{4\pi}\left[(\tfrac{3}{4}\mu'^2 E_1 + \tfrac{1}{2}E_2)I_l \quad + \quad (\tfrac{3}{4}E_1 + \tfrac{1}{2}E_2)I_r\right]. \tag{2.130e}$$

The D_i can be constructed from eight simple integrals:

$$d_1 = \oint \frac{d\Omega'}{4\pi} I_l, \tag{2.131a}$$

$$d_2 = \oint \frac{d\Omega'}{4\pi} I_r, \tag{2.131b}$$

$$d_3 = \oint \frac{d\Omega'}{4\pi} \mu'^2 I_l, \tag{2.131c}$$

$$d_4 = \oint \frac{d\Omega'}{4\pi} (\mu' \sqrt{1-\mu'^2} \cos\phi') I_l, \tag{2.131d}$$

$$d_5 = \oint \frac{d\Omega'}{4\pi} (\sqrt{1-\mu'^2} \sin\phi') U, \tag{2.131e}$$

$$d_6 = \oint \frac{d\Omega'}{4\pi} (\mu'^2 \cos 2\phi) I_l, \tag{2.131f}$$

$$d_7 = \oint \frac{d\Omega'}{4\pi} (\cos 2\phi) I_r, \tag{2.131g}$$

and

$$d_8 = \oint \frac{d\Omega'}{4\pi} (\mu' \sin 2\phi') U. \tag{2.131h}$$

In general the integrals of equations (2.131) must be solved numerically. The expressions for the D_i become

$$D_1 = \tfrac{1}{2}(1+2E_1)d_1 \quad + \quad \tfrac{1}{2}(1-E_1)d_2 \quad - \quad \tfrac{3}{2}E_1 d_3, \tag{2.132a}$$

$$D_2 = \tfrac{3}{4}E_1(-2d_1 + d_2 + 3d_3), \tag{2.132b}$$

$$D_3 = \tfrac{3}{4}E_1(4d_4 + 2d_5), \tag{2.132c}$$

$$D_4 = \tfrac{3}{4}E_1(d_6 - d_7 + d_8), \tag{2.132d}$$

and

$$D_5 = \tfrac{1}{2}(1-E_1)d_1 \quad + \quad \tfrac{1}{2}(1+\tfrac{1}{2}E_1)d_2 \quad + \quad \tfrac{3}{4}E_1 d_3. \tag{2.132e}$$

where the fact that $E_2 = 1 - E_1$ has been used. Note that

$$D_1 - D_5 = \tfrac{3}{4}E_1(2d_1 - d_2 - 3d_3), \tag{2.133}$$

and

$$D_1 + D_2 - D_5 = 0. \tag{2.134}$$

The diffuse contribution to the source function vector is given by an expression exactly analogous to equation (2.128):

$$\mathbf{F} = \Lambda[\mathbf{S}]. \tag{2.135}$$

Since the components of the S vector have the same symmetries as those of the $\mathbf{I}_{ext}$ vector, the expressions for S_l, S_r and S_U must have the same functional forms as equations (2.129). Thus

$$S_l = S_1 + S_2\mu^2 + S_3\mu\sqrt{1-\mu^2}\cos\phi + S_4\mu^2\cos 2\phi, \tag{2.136a}$$

$$S_r = S_5 - S_4\cos 2\phi, \tag{2.136b}$$

and

$$S_U = S_3\sqrt{1-\mu^2}\sin\phi + 2S_4\mu\sin 2\phi. \tag{2.136c}$$

By substituting the expressions for S_l, S_r, and S_U into equation (2.135) the following expression for the F_i are obtained:

$$F_1 = S_1\tfrac{1}{2}[1+E_1] \quad + \quad S_2\tfrac{1}{6}[1+\tfrac{1}{5}E_1] \quad + \quad S_5\tfrac{1}{2}[1-E_1], \tag{2.137a}$$

$$F_2 = S_1[-\tfrac{3}{4}E_1] \quad + \quad S_2[-\tfrac{1}{20}E_1] \quad + \quad S_5[\tfrac{3}{4}E_1], \tag{2.137b}$$

$$F_3 = S_3[\tfrac{7}{10}E_1], \tag{2.137c}$$

$$F_4 = S_4[\tfrac{7}{10}E_1], \tag{2.137c}$$

and

$$F_5 = S_1\tfrac{1}{2}[1-\tfrac{1}{2}E_1] \quad + \quad S_2\tfrac{1}{6}[1-\tfrac{1}{10}E_1] \quad + \quad S_5\tfrac{3}{2}[1+\tfrac{1}{2}E_1]. \tag{2.137c}$$

The direct contributions D_i, and the diffuse contributions F_i can now be substituted into equation (2.126),

$$\mathbf{S}(\vec{r},\hat{n}) = (1-\epsilon)(1-\beta)\Lambda[\mathbf{S}(\vec{r},\hat{n}')] + (1-\epsilon)\beta\Lambda[\mathbf{I}_{ext}] + \mathbf{G}(\vec{r}), \tag{2.138}$$

where the fact that $\beta_d = \beta$ has been used. From equation (2.138),

$$S_1 = (1-\epsilon)\beta D_1 \quad + \quad (1-\epsilon)(1-\beta)F_1 \quad + \quad G_l, \tag{2.139a}$$

$$S_2 = (1-\epsilon)\beta D_2 \quad + \quad (1-\epsilon)(1-\beta)F_2, \tag{2.139b}$$

$$S_3 = (1-\epsilon)\beta D_3 + (1-\epsilon)(1-\beta)(\tfrac{7}{10})E_1S_3, \tag{2.139c}$$

$$S_4 = (1-\epsilon)\beta D_4 + (1-\epsilon)(1-\beta)(\tfrac{7}{10})E_1S_4, \tag{2.139d}$$

and

$$S_5 = (1-\epsilon)\beta D_5 \quad + \quad (1-\epsilon)(1-\beta)F_5 \quad + \quad G_r. \tag{2.139e}$$

Now

$$\begin{aligned} S_1 - S_5 = &(1-\epsilon)\beta(D_1 - D_5) \quad + \\ &(1-\epsilon)(1-\beta)[\tfrac{3}{4}E_1S_1 + \tfrac{1}{20}E_1S_2 - \tfrac{3}{4}E_1S_5], \end{aligned} \tag{2.140}$$

where it should be recalled that $G_l - G_r = 0$. Recalling equations (2.137b), (2.134), and (2.139b), it follows that

$$S_1 + S_2 - S_5 = 0. \tag{2.141}$$

Substituting for S_2 in equation (2.140) from equation (2.141) gives

$$S_1 - S_5 = \frac{(1-\epsilon)\beta(D_1 - D_5)}{1-(1-\epsilon)(1-\beta)(\frac{7}{10})E_1} = -\frac{(1-\epsilon)\beta D_2}{1-(1-\epsilon)(1-\beta)(\frac{7}{10})E_1} = -S_2. \tag{2.142}$$

The expression for $S_1 + S_5$ is

$$\begin{aligned} S_1 + S_5 &= (1-\epsilon)\beta(D_1 + D_5) \quad + \quad G \\ &\qquad (1-\epsilon)(1-\beta)[(1+\tfrac{1}{4}E_1)S_1 + \tfrac{1}{3}(1+\tfrac{1}{20}E_1)S_2 + (1-\tfrac{1}{4}E_1)S_5] \\ &= (1-\epsilon)\beta(D_1 + D_5) \quad + \quad G \\ &\qquad (1-\epsilon)(1-\beta)[(S_1 + S_5) + \tfrac{1}{3}(1-\tfrac{7}{10}E_1)S_2)], \end{aligned} \tag{2.143}$$

where $G = G_l + G_r$. Re-arranging and substituting for S_5 gives

$$\begin{aligned} S_1 = \frac{1}{2}\Bigg[-S_2 + \frac{\gamma S_2 \frac{1}{3}(1-\frac{7}{10}E_1)}{1-\gamma} \\ \frac{(1-\epsilon)\beta(D_1 + D_2)}{1-\gamma} + \frac{G}{1-\gamma}\Bigg], \end{aligned} \tag{2.144}$$

where

$$\gamma \equiv (1-\epsilon)(1-\beta). \tag{2.145}$$

Substituting for S_2, and collecting powers of γ gives

$$\begin{aligned} S_1 = &\frac{(1-\epsilon)\beta}{(1-\gamma)\,(1-\gamma(\frac{7}{10})E_1)}\left[D_1 + \tfrac{1}{2}\gamma[D_2 + \tfrac{1}{3}(1-\tfrac{7}{10}E_1)D_2 - \tfrac{7}{10}E_1(D_1 + D_5)]\right] \\ &+ \quad \frac{\frac{1}{2}G}{1-\gamma}. \end{aligned} \tag{2.146a}$$

The other S_i are now simply found:

$$S_2 = \frac{(1-\epsilon)\beta D_2}{1-\gamma(\frac{7}{10})E_1}, \tag{2.146b}$$

$$S_3 = \frac{(1-\epsilon)\beta D_3}{1-\gamma(\frac{7}{10})E_1}, \tag{2.146c}$$

$$S_4 = \frac{(1-\epsilon)\beta D_4}{1-\gamma(\frac{7}{10})E_1}, \tag{2.146d}$$

and, using equation (2.141),

$$S_5 = \frac{(1-\epsilon)\beta}{(1-\gamma)\left(1-\gamma(\frac{7}{10})E_1\right)}\left[D_5 + \tfrac{1}{2}\gamma\left[-D_2 + \tfrac{1}{3}(1-\tfrac{7}{10}E_1)D_2 - \tfrac{7}{10}E_1(D_1+D_5)\right]\right]$$
$$+ \quad \frac{\frac{1}{2}G}{1-\gamma}. \tag{2.146e}$$

Note from equations (2.132) that the D_i are dependent on the phase-matrix coefficients E_i.

It is illuminating to consider two special cases for the source function coefficients S_i. First, in the case of extremely weak scattering, where the escape probability $\beta \to 1$ and $\gamma \to 0$, expressions for the source function coefficients are

$$S_1 = (1-\epsilon)D_1 + \tfrac{1}{2}G, \tag{2.147a}$$

$$S_2 = (1-\epsilon)D_2, \tag{2.147b}$$

$$S_3 = (1-\epsilon)D_3, \tag{2.147c}$$

$$S_4 = (1-\epsilon)D_4, \tag{2.147d}$$

and

$$S_5 = (1-\epsilon)D_5 + \tfrac{1}{2}G. \tag{2.147e}$$

These source function coefficients are just the direct contribution depolarized by the effect of the thermal coupling constant ϵ, and the thermal source G. The polarizing effect is strongest in this limit since the photons scatter at most once and there is no depolarizing effect from multiple scattering. The second case is that of extremely strong scattering, where $\beta \to 0$ and $\gamma \to (1-\epsilon)$. The expressions for the source function coefficients become

$$S_1 = G/(2\epsilon), \qquad S_2 = S_3 = S_4 = 0, \qquad \text{and} \qquad S_5 = G/(2\epsilon). \tag{2.148}$$

With the escape probabililty $\beta \to 0$ no photons enter or leave the the resonance region; they are all created and destroyed locally. The source function is coupled to the thermal source only, and is thus isotropic and unpolarized.

Source function expressions for the special case of a sphérically symmetric atmosphere are relegated to Appendix 2.

The procedure to obtain the Sobolev-II source functions, the Sobolev-II formal solution for the emergent flux, and the net polarization of the emergent flux can now be presented. Recall that the following assumptions have been made previously: the atmosphere is axisymmetric and in homologolous motion.

Recall from the discussion in section (a) that the case of general expansion (or contraction), of which homologous motion is a special case, allows explicit source functions to be determined for all the blueward (or redward) transitions of the transition under consideration. Thus an expression (the Stokes parameter generalization of equation (2.37)) can be written down for the specific intensity vector incident on a resonance point $\vec{r}$ of a transition labelled 1:

$$\mathbf{I}(\vec{r},\hat{n})_{ext} = \mathbf{I}_{inc}\exp\left[-\sum_{i=2}^{N}\tau_i\right] + \sum_{i=2}^{N}\mathbf{S}_i(1-\exp[-\tau_i])\exp\left[-\sum_{j=2}^{i-1}\tau_j\right], \tag{2.149}$$

where the $\mathbf{S}_i$, the source function vectors of the blueward (or redward) transitions, are already known, and are evaluated on the CP (common point) velocity surfaces of point $\vec{r}$. Using equation (2.149) for $\mathbf{I}_{ext}$, the integrals of equations (2.130) can be done to obtain the $(D_i)_1$ coeffients at $\vec{r}$. Equations (2.146) then give the $(S_i)_1$ coeffients at $\vec{r}$. Repeating the integrations at all points $\vec{r}$ constructs the source function vector $\mathbf{S}_1$ for the whole atmosphere. The procedure can then be repeated for the construction of the source function vectors of all transitions blueward (or redward) of transition 1.[2]

Having obtained the source function vectors for all transitions, the formal Sobolev solution can be written down, again using using the Stokes parameter generalization of equation (2.37):

$$\mathbf{I}(\nu)_{Em_t} = \mathbf{I}(\nu)_{inc}\exp\left[-\sum_{i=1}^{N}\tau_i\right] + \sum_{i=1}^{N}\mathbf{S}_i(1-\exp[-\tau_i])\exp\left[-\sum_{j=1}^{i-1}\tau_j\right], \tag{2.150}$$

where the $\mathbf{S}_i$ are evaluated on CD (common direction) surfaces in this case. The velocity surfaces of the transitions are ordered spatially by increasing distance from the observer from the reddest (lowest wavelength transition) velocity surface to the bluest (highest wavelength transition) velocity surface in the case of an expanding atmosphere; the ordering is reversed in the case of a contracting atmosphere. The components of $\mathbf{I}(\nu)_{Em_t}$ can be integrated over the velocity surfaces appropriate for frequency ν to obtain the net Stokes parameters. Applying equations (2.117), or (2.118) then gives the net polarization.

It is clear from the above derivations that polarization of radiation emitted from any location in an atmosphere depends, in a complicated manner, on several factors. If the original source of

[2] In order to simplify the derivation of the source function coefficients, the coordinate system for which they were defined has its x-axis, from which the angle ϕ is measured, passing through the the symmetry axis. Thus for a system with an arbitrary x axis an angular transformation must be applied when evaluating the S_I, S_r, and S_U components of the source function vector.

unpolarized radiation subtends finite solid angle at a point $\vec{r}$, then the D_l coefficients, and thus the S_l coefficients evaluated at $\vec{r}$, will depend on this solid angle and on distance from the original source. For large distances from the original source the coefficients will decrease as the inverse square of the distance. This is a purely geometric dependence. The polarization depends on the angle, $\Theta_{(average\ scatter)}$ between the line of sight to a distant observer, and some sort of average line drawn to the original source. Polarization will tend to be large if $|\Theta_{(average\ scatter)} - 90°|$ is small, since the polarization of scattered radiation for Rayleigh scattering is given by

$$P(\Theta) = \frac{1 - \cos^2\Theta}{1 + \cos^2\Theta}, \tag{2.151}$$

where Θ is the angle between the incident, and scattered beams (see equation (2.122)). The geometric shape of the atmosphere is an important consideration; if the atmosphere has circular symmetry about the line of sight then the net polarization will be zero at all frequencies. The polarization depends on the optical depth τ which may in turn depend on location in the atmosphere. The polarization can also depend on multi-line (multi-velocity surface) effects.

It is of interest to try to determine the particular τ value that maximizes the absolute value of the polarization of the radiation emitted toward a distant observer. The determination of the maximizing τ may for a specified system allow the determination of the location from which the most polarized radiation is emitted. For a moving atmosphere, this location will help to determine the frequencies of the extrema of the polarization spectrum. Only the Sobolev formalism and a few other assumptions are needed to obtain a qualitative determination. The qualitative solution has practical use in analyzing calculated model atmospheres.

The net polarization from a velocity surface of an axially symmetric atmosphere is given by

$$P_{net} = \frac{\int dA\,(S_l - S_r)(1 - e^{-\tau})}{\int dA\, I(\nu)}, \tag{2.152}$$

where the integration is over the velocity surface, and where single-velocity surfaces have been assumed. The integration x axis is chosen parallel to the symmetry axis of the atmosphere so that $U_{net} = 0$, and thus there is no need to consider the U field at all. The integrand of the denominator of equation (2.152) is given by

$$I(\nu) = \begin{cases} (S_l + S_r)(1 - e^{-\tau}), & \text{if the beam path does not intersect the original source;} \\ (S_l + S_r)(1 - e^{-\tau}) + I(\nu)_{inc} e^{-\tau}, & \text{if the beam path does intersect the original source;} \\ I(\nu)_{inc}, & \text{if the beam path intersects the original source, but no velocity surface.} \end{cases} \tag{2.153}$$

Note for reasonable atmosphere models the integrand in the denominator will be either

$$I(\nu)_{inc} \quad \text{or} \quad (S_l + S_r)(1-e^{-\tau}) + I_{inc}e^{-\tau}$$

for some region on the velocity surface. If S varies less strongly with position than τ, then at some level of approximation

$$(S_l + S_r)(1-e^{-\tau}) + I_{inc}e^{-\tau} \approx I_{inc}(1-e^{-\tau}) + I_{inc}e^{-\tau} = I_{inc}. \tag{2.154}$$

It will be assumed that equation (2.154) is valid, and thus it follows that the denominator of equation (2.152) will depend less strongly on the functional behaviour of τ than numerator.[3] With this assumption maximizing the integrand of the numerator of equation (2.152) with respect to τ will give a crude result for the τ value that maximizes the polarization. Using equations (2.136), and (2.146), the integrand is

$$(S_l - S_r)(1-e^{-\tau}) = \Big(-D_2(1-\mu^2) + D_3\mu\sqrt{1-\mu^2}\cos\phi + D_4(1+\mu^2)\cos 2\phi\Big)\frac{(1-\epsilon)\beta(1-e^{-\tau})}{\big(1-(1-\epsilon)(1-\beta)(\frac{7}{10})E_1\big)}. \tag{2.155}$$

The D_i depend only on the original source since the velocity surfaces are assumed to be single. They depend on the solid angle subtended by the original source at the position where equation (2.155) is evaluated. However, the assumption that the variation of the integrand in the denominator of equation (2.152) is small, implies that the variation of the D_i is also unimportant. All the τ dependence in equation (2.155) is contained in the expression

$$\frac{(1-\epsilon)\beta(1-e^{-\tau})}{\big(1-(1-\epsilon)(1-\beta)(\frac{7}{10})E_1\big)}.$$

To obtain a one parameter expression it will be assumed that the thermal coupling constant ϵ is 0, and the phase-matrix coefficient E_1 is 1. Thus for a pure Rayleigh, pure resonance scattering atmosphere the τ expression will defined to be $\Pi(\tau)$, a measure of the polarization:

$$\Pi(\tau) = \frac{\beta}{1-(\frac{7}{10})(1-\beta)}(1-e^{-\tau}) \tag{2.156}$$

[3] For a spherical supernova atmosphere with a sharp photosphere and with a single pure resonance transition, $S(r) = W(r)I_{inc}$, where $W(r) = (1/2)[1-\sqrt{1-(r_{ph}/r)^2}]$ (see equations (2.35) and (2.36)). Recall from section (c) of this chapter that a useful approximation is $\tau = \tau_{ph}(r_{ph}/r)^7$. Note for $r/r_{ph} = 1.5$, $S(r)/I_{inc} = .1273$; thus $S(r)$ is decreased by only one order of magnitude below I_{inc}. Since $S(r)/I_{inc} \approx (1/4)(r_{ph}/r)^2$ for $r/r_{ph} \gtrsim 1.5$, it is clear that equation (2.154) is valid to within two orders of magnitude over a large range of r where τ varies much more strongly. Thus the result for the polarization maximizing τ obtained in this section should apply approximately to supernova models of the sort discussed in section (c).

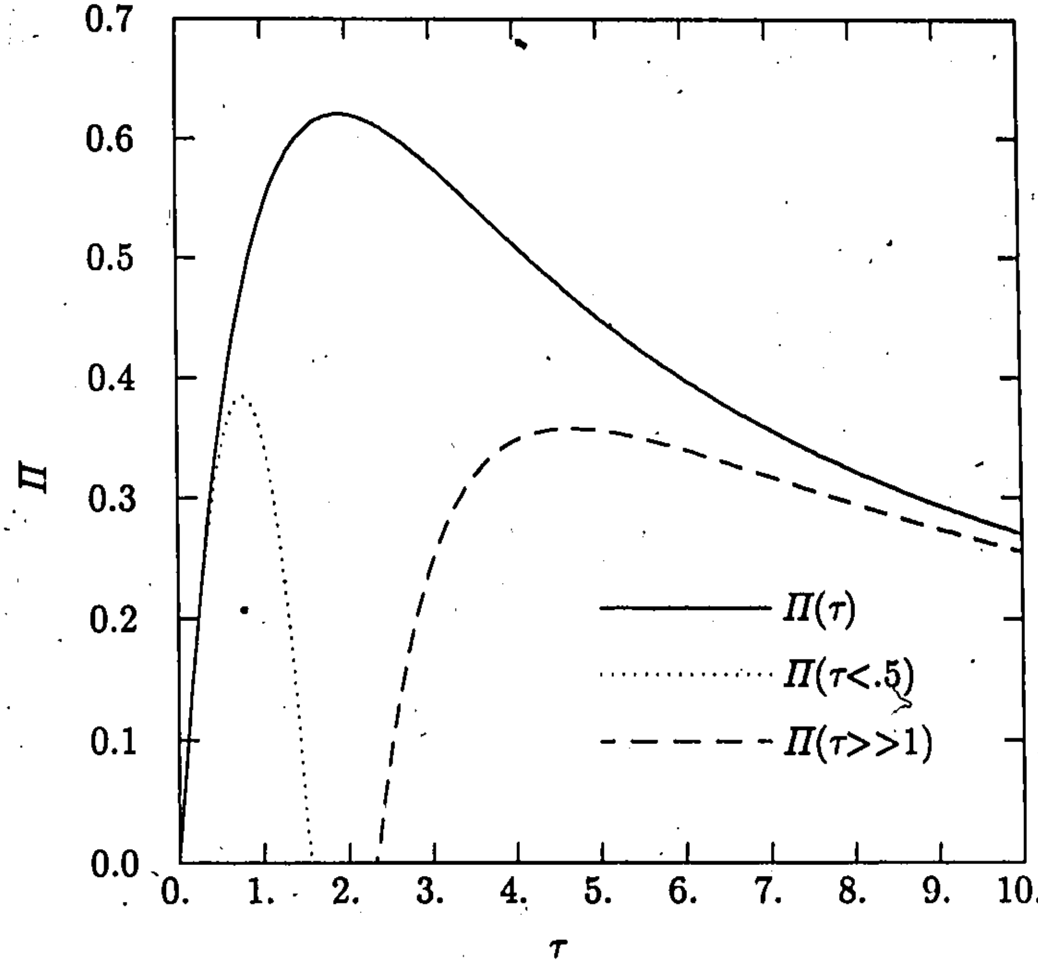

Fig. 2.5. The polarization measure $\Pi(\tau)$, and small and large τ approximations for $\Pi(\tau)$.

Recalling that $\beta = (1 - e^{-\tau})/\tau$ for homologous motion, then for $\tau \lesssim .5$

$$\Pi(\tau) = \tau\left(1 - \frac{13}{20}\tau\right), \tag{2.157a}$$

and for $\tau \gg 1$

$$\Pi(\tau) = \frac{10}{3}\frac{1}{\tau}\left(1 - \frac{7}{3}\frac{1}{\tau}\right). \tag{2.157b}$$

The $\Pi(\tau)$ function has its maximum at $\tau_{max} = 1.922294$ with a value of .6206712 (see Appendix 1). Fig. 2.5 shows $\Pi(\tau)$ and the approximate $\Pi(\tau)$'s for the interval $[0, 10]$.

The physical picture that explains the $\Pi(\tau)$ function's dependence on τ is, of course, one of scattering. Physically, small τ means few polarizing scattering events, and thus low polarization. As τ increases there is more scattering, and thus higher polarization. However, further increases in optical depth in a resonance region leads to multiple scatterings before a photon escapes the region. The multiple scatterings tend to make the radiation field isotropic and depolarize the escaping radiation. The Sobolev method approximates this physical picture by using escape probabilities, and related quantities. The escape probability and related quantities in turn give rise to the simple expression for $\Pi(\tau)$.

The $\Pi(\tau)$ function's dependence on τ is not especially strong. However if, as has already been assumed, τ has a strong position dependence, then $\Pi(\tau(\vec{r}))$ may be strongly peaked in a relatively well defined region where $\tau(\vec{r}) \approx 2$. In this case the region in the atmosphere of maximum polarized emission may be relatively small, and determinable. Clearly, however, the other factors affecting polarization will strongly affect the location of maximum polarized emission. Therefore it is not possible in general to predict how closely the actual maximizing τ will be to 2. The foregoing discussion is thus mainly of use in analyzing already calculated model results.

e) The Physical Validity of the Sobolev-H Method

In this section the physical validity of the Sobolev-H method will be discussed. This discussion requires some explanation of partial redistribution functions. Partial redistribution (PRD), in contrast to complete redistribution, allows correlation between absorbed, and emitted photons in both direction and frequency.

Hummer (1962; see also Mihalas 1978, p. 411) has given four standard partial redistribution functions corresponding to four different physical cases. In each of these cases there is an intrinsic atomic redistribution in frequency, and angle. For the intrinsic redistribution the angular and frequency dependencies are decoupled. The angular dependence appears as a phase-matrix coefficient to the frequency redistribution function. Since the discussion of this section will compare the Hummer redistribution functions to the HRD redistribution function used by the Sobolev-H method, a brief description of Hummer's intrinsic atomic redistribution functions is useful. (I) The first redistribution function is for the case of a transition between two perfectly sharp states. Thus the absorbed and emitted photons have exactly the same well defined frequency. Since only a ground state can be considered perfectly sharp, this case is an idealization. (II) The second redistribution function is for the case of a transition with a broadened upper state, and a perfectly sharp lower state. Since the upper state is broadened the transition has a Lorentzian absorption profile, and can absorb a range of frequencies. However, the emitted photon's frequency is the same as the absorbed photon frequency. (III) The third redistribution function is for the case of a perfectly sharp lower state, and broadened upper state where the absorption and emission profiles are independent Lorentzians. Thus there is no correlation between the absorbed and emitted photons' frequencies; this is complete redistribution in frequency. The physical picture usually assumed for this case is that collisions reshuffle the atom among the upper substates of the transition, and thus destroy any correlation. If collisions are responsible for this redistribution function then the appropriate phase-matrix may be the isotropic phase-matrix; no polarizing effect would then be present. (IV) The fourth redistribution function is for the case of a transition between a broadened upper state and a broadened lower state. This sort of redistribution function applies to transitions that are not to ground states. Since the redistribution function is rather complex, it is seldom actually considered, and simpler redistribution functions are used for the cases where it would apply.

The intrinsic redistributions need to be averaged over the thermal distribution of atoms to obtain the laboratory frame redistribution. The four thermal averaged redistribution functions are labeled R_I, R_{II}, R_{III}, and R_{IV}. The functions increase greatly in complexity with subscript index. A physically appropriate phase-matrix can be included in the prescriptions for the R-functions.

An effect of the thermal averaging on the redistribution functions is to introduce an angular dependence into the frequency redistribution function, thereby coupling angle and frequency redistribution. Also, the absorbed and emitted photon frequencies are coupled even in the case of R_{III} where there is complete frequency redistribution in the atom's frame. Thus in none of the four cases is complete redistribution obtained. Since complete redistribution in frequency, and angle (CRD) is the simplest and computationally the least demanding redistribution, it is fortunate that in many calculations CRD is an adequate approximation to Hummer's redistribution functions. In other cases angle-averaged versions of Hummer's redistribution functions are adequate. For a discussion of the adequacy of these approximations see Mihalas (1978, p. 411). Of course, if the polarization of scattered radiation is the subject of interest, then a non-isotropic scattering phase-matrix must be used as a coefficient to the Hummer redistribution functions.

In principle, some improvement in calculating supernova spectra would be obtained if each transition were treated with the Hummer redistribution function that most adequately describes it. However, the degree of potential improvement does not seem to researchers to have been adequate compensation for the much greater computation involved in using partial redistribution functions. As indicated in section (c), the Sobolev method calculations, which assume CRD, seem to produce very adequate fits to observed spectra. Thus there may be no need to go beyond CRD if only the flux spectra is of interest. However, to calculate polarization spectra some partial redistribution function is required. An expert opinion (Rybicki 1984, p. 23) is that it is unclear whether or not escape probability methods, such as the Sobolev method, can be used to treat cases of partial redistribution in frequency. The derivation of the Sobolev method presented in section (a) required the complete frequency redistribution in a very fundamental manner. However, as the derivation of the Sobolev-H method demonstrated in section (d), it is possible to include angular redistribution, and a non-isotropic phase matrix, provided complete frequency redistribution is maintained.

For the Sobolev-H method derivation the HRD redistribution function introduced in section (d) was used. The HRD redistribution function has a complete redistribution function for frequency multiplied by the Hamilton scattering phase-matrix. This gave a polarizing redistribution for the photons. For HRD to be physically justified two questions must be considered. (1) Is HRD an adequate approximation to the Hummer's standard redistribution functions when these functions include a polarizing phase-matrix? (2) Do Hummer's redistributions and the Hamilton phase-matrix adequately represent the physics of transition scattering in supernova atmospheres?

In considering the first question two extreme cases provide some evidence that the answer is yes: (1) the case of an optically thick atmosphere, and (2) the case of an atmosphere where photons scatter at most only once.

McKenna (1985) considered a static, semi-infinite, plane-parallel, isothermal atmosphere where the deviation from LTE (local thermodynamic equilibrium), the ratio of continuous to integrated line opacity, and the ratio of the natural line width to thermal Doppler width were all held constant. The ratio of natural line width to thermal Doppler width is given by

$$a = \nu_N/\nu_{th}; \tag{2.158}$$

a is a parameter of R_{II}, R_{III}, and R_{IV}. McKenna set $a = 10^{-3}$. McKenna calculated the emergent specific intensity and polarization profiles from his model atmosphere using a selection of redistribution functions. He used the full and angle-averaged R_I, R_{II}, and R_{III} functions multiplied by the Rayleigh phase-matrix. Recall from section (d) of this chapter that the Rayleigh phase-matrix is the most anisotropic limiting case of the Hamilton phase-matrix. What has been called the hybrid

(HRD) redistribution in this thesis was also used. The differences between the results from the full and angle-averaged versions for each R-function were less than .5 %. This is strong evidence that the angle-averaged versions of the $\bar{R}$-functions are adequate approximations at least for the sort of atmosphere McKenna considered. The emergent specific intensity profiles of the R-functions, and the HRD function were all virtually identical. The polarization profiles for the four cases were qualitatively quite similar. The three R-function polarization profiles were very similar with the HRD function profile being smaller by $\approx 50\,\%$ in some, but not all, parts of the profile. Thus the HRD redistribution function can be considered to be a very good qualitative approximation to the R-functions for McKenna's atmosphere. It is also clear that the distinction between the R_I, R_{II}, and R_{III} is not very great for these atmospheres. Apparently McKenna considered the R_{IV} function difficult too treat.

The atmosphere McKenna considered is far removed from the homologously expanding, non-homogeneous, spheroidal atmospheres of supernovae. The comparison of the HRD functions, and the R-functions for his atmosphere can therefore be considered an extreme case from the point of view of supernovae. The other extreme is the case where photons are only scattered once in a supernova atmosphere before escaping. For this thesis numerical experiments have been performed with a supernova atmosphere in which photons are artificially limited to scattering once only. With only one scattering it is fairly easy to implement the first two R-functions in equation (2.110) for the source function. Comparisons of the flux, and polarization profiles for a line with this sort of calculation showed that the HRD, R_I, and R_{II} redistributions gave virtually the same flux and polarization profiles when the ratio $a \leq .1$. For $a = .5$ the R_{II} results deviated by as much as 30 % from the HRD flux profile, and by as much as 10 % from the HRD polarization profile. It is worth noting that the SN 1987a lines for which early spectropolarimetric data were available (Schwarz and Mundt 1987), the hydrogen Balmer lines, and the Na D lines, have lifetimes of order 10^{-8} s; thus their ν_N's are of order $10^{8}\,s^{-1}$. The thermal Doppler widths using equation (2.65) are given by

$$\nu_{th} = 1.285 \times 10^{10} \times \lambda_{\mu}^{-1} \sqrt{\frac{T}{10^4 A}}\, s^{-1}, \tag{2.159}$$

where λ_{μ} is the wavelength of the transition in micrometers. For reasonable supernova temperature, the observed lines should have a's of order 10^{-2}.

The fact that the two extreme cases show that the R_I and R_{II} functions are reasonably well approximated by the HRD function allows some confidence that in general lines well represented by these two redistribution functions are well represented by the HRD function. McKenna's result also gives some confidence that the R_{III} function is well represented by the HRD function. Unfortunately, comparisons of the HRD function to the R_{IV} function are difficult to perform.

The second question in justifying HRD concerns its correctness as a physical description of the transition scattering in supernova atmospheres. Cooper *et al.* (1982) have shown that the redistribution part of an angle-averaged source function for a multi-line atom can be expressed as linear combinations of Hummer's redistribution functions R_{II} and R_{III}, and of the complete redistribution function. Since CRD functions are in many cases adequate approximations to the angle-averaged R_{II} and R_{III}, Cooper *et al.* 's result provides some confidence in the complete frequency redistribution of HRD. In a more modern, and elaborate calculation than Hamilton (1947), Ballagh and Cooper (1977) have shown that scattering in transitions does polarize radiation. They also considered quantitatively the effects of collisions in destroying the polarizing effect by destroying the alignment of the atom; Hamilton considered collisions only qualitatively. Lombardi and Kelleher (1985) using the Ballagh and Cooper formalism calculate that right angle scattering from He in the 2^1P-3^1D transition by incident radiation polarized perpendicular to the plane of scattering gives scattered radiation with .45 polarization. This agrees with .4468 polarization that can be determined using Hamilton's phase-matrix. Their calculated polarization for the Hα is .34, which disagrees with the .4430 calculated from the Hamilton phase-matrix using the equal occupation probability average E_1 coefficient calculated in section (f) of this chapter. Lombardi and Kelleher performed measurements that found agreement with their He and Hα predictions within experimental uncertainty. They also measured, in agreement with quantitative expectations, the destruction of the polarizing effect by collisions.

The results of these recent authors indicate that the Hamilton phase-matrix and HRD redistribution offer qualitatively correct descriptions of the physics of resonance scattering. However, since the polarizing effect can be destroyed by collisions an investigation of the conditions needed to allow the polarizing effect is warranted. Hamilton gave the following conditions for his prescription: (1) there should be no transitions between the total angular momentum m_j-substates of the upper level of the line transition, and (2) the states of the lower level of the line transition have equal occupation probability. The first condition means that there must be no effect, such as collisions, to reshuffle the excited ion among the upper states. Clearly in practice there would still be some polarising effect provided the average time between collisions were not too much smaller than the radiative lifetime of the upper level. Lombardi and Kelleher (1985) show the decreasing polarization of transition line emission as a function of time from a set of transitions excited simultaneously using a laser pulse; the longer lived upper levels have their alignment increasingly destroyed by collisions as time passes. The second condition requires that there is a reshuffling effect among the lower states that destroys any coherence between successive photon scatterings. If the second condition were violated, there would still presumably be a polarising effect, but the Hamilton phase-matrix would not strictly apply.

Hamilton also mentions that the hyperfine precession of the atomic total angular momentum vector about the nuclear spin would tend to alter the alignment of the excited atom. Rough estimates of the ratio of lifetime to precession time of the states giving rise to the hydrogen Balmer lines and the Na D lines indicate that this hyperfine-structure effect should not overwhelm the Hamilton polarizing effect. The hyperfine-structure effect on the polarization of the Hα transition is considered by Lombardi and Kelleher (1983).

A criterion can be established for when collisions will destroy the alignment of the upper levels of the Balmer transitions in hydrogen dominated atmospheres. In such atmospheres the H^+ ions are mostly responsible for the alignment destroying collisions. Thus the density of H^+ ions is the relevant quantity for deciding whether or not polarization is destroyed. For hydrogen dominated atmospheres $n(H^+) \approx n_e$, where n_e is the free electron density. Pengelly and Seaton (1964) calculated the critical electron densities for which the rate of $nl \rightarrow nl'$ ($l' = l \pm 1$) transitions in H atoms due to H^+ collisions equalled the rate of radiative transition out of the levels of principal quantum number n. They used first order time-dependent perturbation theory, and found that the collisional transition rates depended on a sum of dipole transition matrix elements

$$\langle nl'm_l'|\vec{r}|nlm_l\rangle, \tag{2.160}$$

where a selection rule forbids $nlm \rightarrow nlm'$ transitions (Baym 1978, p. 285). It is clear from the Pengelly and Seaton derivation that transitions among the states $|lsjm_j\rangle$ also involve dipole transition matrix elements of the form

$$\langle l'sj'm_j'|\vec{r}|lsjm_j\rangle, \tag{2.161}$$

where $lsjm_j \rightarrow lsj'm_j'$ transitions are likewise forbidden. Therefore, to first order in perturbation theory, the atom cannot change its j-state or m_j-substate without changing the l quantum number.

also. Thus the $nl \rightarrow nl'$ collisional transition rates considered by Pengelly and Seaton are the relevant collisional rates for the destruction of the alignment that polarizes the scattered radiation.

At Pengelly and Seaton's critical density for principal quantum number n approximately half the scattered photons are polarized. The other half are unpolarized, since the alignments of the excited states from which they arise have been destroyed by collisions. At lower densities there is more polarization; at higher densities the polarization will be less. Pengelly and Seaton's Fig. 4 displays the l-averaged critical electron densities for $n > 3$. Table 2.3 shows the critical densities for $n = 4$ through 8.

TABLE 2.3—The critical electron densities for the destruction of the polarizing effect of the Balmer transitions in a hydrogen dominated atmosphere.

Transition	n_{upper}	$n_{e\ crit}$ (cm^{-3})
Hα	3	–
Hβ	4	4×10^{8}
Hγ	5	1×10^{8}
Hδ	6	2.5×10^{7}
Hϵ	7	8×10^{6}
Hζ	8	2×10^{6}

SOURCE: The critical density values were measured from Fig. 4 of Pengelly and Seaton (1964).

For many other important transitions in a hydrogen dominated atmosphere the critical density for destroying the polarizing effect should be somewhat higher than for the Balmer transitions. Most ion levels are not nearly as degenerate as are the levels giving rise to the Balmer transitions; therefore the collisions must be more energetic to cause transitions among the m_j substates of a level. For example, the separation between the upper levels of the Na D lines is 6 Å, whereas the largest separation in wavelength between the levels of any n for the hydrogen atom is .0053 Å. The upper levels of the Na D lines are also ≈ 3 eV below the continuum, whereas the $n = 3$ level of the H atom are only ≈ 1.5 eV below the continuum. The excited states of the Na D line transitions are more tightly bound than the upper state of the Hα transition, and thus are more protected from collisional depolarization.

An estimate of the free electron density in supernova atmospheres can be made. It will be assumed that the electron density obeys the same inverse power law as density. This assumption is clearly valid sometimes. For type II supernovae near maximum light the temperatures are of order 25000 K; the hydrogen, which makes up the bulk of the matter, should be fully ionised and thus electron density should be proportional to atomic densities. Feldt (1980, p. 35) provides some evidence that the power law holds for electron density in the atmospheres of type I supernovae. There is reason to believe that the continuous opacity in supernova atmospheres is scattering dominated (Wagoner, 1981). Here it is assumed that electron scattering provides all of this continuous opacity. This assumption is very probably incorrect, since many thousands of weak lines also contribute a significant continuous opacity in an expanding atmosphere due to Doppler enhancement (Karp *et al.* 1977). The assumption that the continuous opacity is entirely due to electron scattering will lead to an over-estimate of the electron density. The over-estimate should not be worse than a factor of order 2. Considering the other uncertainties in the density estimate this is not a significant problem.

With the above assumptions the continuum optical depth to the photosphere is then given by

$$\begin{aligned}\tau_e &= \int_{r_{ph}}^{\infty} dr\, n_e(r)\sigma \\ &= \frac{n_e(r_{ph})\sigma r_{ph}}{p-1},\end{aligned} \tag{2.162}$$

where $n_e(r)$ is the electron density, p is the power parameter, and σ is the Thomson cross-section:

$$\sigma = \frac{8\pi e^4}{3m_e^2c^4} = 6.65 \times 10^{-25}\,\mathrm{cm}^2. \tag{2.163}$$

The continuum optical depth to the photosphere, τ_e, is ≈ 1. This depth defines the smallest spherical shell (photosphere) from which a radially directed photon can emerge and pass through the atmosphere with an average number of scatterings that is less than 1. Thus the electron density is given by

$$n_e(r) = \frac{(p-1)\tau_e}{\sigma r_{ph}}(r_{ph}/r)^p \tag{2.164a}$$

$$= 1.74 \times 10^{10}\frac{(p-1)\tau_e}{v_9 t_d}(r_{ph}/r)^p\ \mathrm{cm}^{-3} \tag{2.164b}$$

where equation (2.88) has been used, v_9 is the photospheric velocity in units of 10^9 cm, and t_d is the time in days since the supernova exploded. In section (d) of this chapter a crude estimate was made of the Sobolev optical depth for a line that maximizes the polarization. Since it has been assumed that the Sobolev optical depths vary as $\tau(r) = \tau_{ph}(r_{ph}/r)^p$, the radial region that is probably most important in producing the polarization spectrum can be determined from

$$(r_{ph}/r)^p = \tau_{max}/\tau_{ph}. \tag{2.165}$$

Thus the density of the most polarizing region of the supernova is approximately given by

$$n_{e\ pol} \approx 1.74 \times 10^{10} \frac{(p-1)\tau_e}{v_9 t_d} (\tau_{max}/\tau_{ph})\ \mathrm{cm}^{-3}. \tag{2.166}$$

Since $\tau_{max} \approx 2$, and $\tau_e \approx 1$

$$n_{e\ pol} \approx 3.5 \times 10^{10} \frac{(p-1)}{v_9 t_d} (1/\tau_{ph})\ \mathrm{cm}^{-3}. \tag{2.167}$$

If p is set to 7, and v_{ph} is set to .5 (a typical type II supernova value) then

$$n_{e\ pol} \approx 4 \times 10^{11} \frac{1}{t_d \tau_{ph}}\ \mathrm{cm}^{-3}. \tag{2.168}$$

The time since the supernova explosion is usually not known. Observational evidence indicates the time to maximum light for type II supernovae is some tens of days (Doggett and Branch 1985). For type I supernovae the time to maximum light is observationally estimated to be about 15 ± 2 days (Pskovskii 1977). Typical large τ_{ph} values from synthetic spectra are about 10 to 15 (Branch *et al.* 1981, 1982). Thus for times after maximum light, but before the photosphere has receded out of the region of inverse power law density distribution,

$$n_{e\ pol} \lesssim 10^9\ \mathrm{cm}^{-3}. \tag{2.169}$$

This value is sufficiently small that given the uncertainties in its estimation a significant polarizing effect due to scattering by Balmer lines in type II supernova atmospheres near maximum light and thereafter cannot be ruled out. Other lines such as the Na D lines are more likely to be polarizing. It is also plausible to believe that there will be some polarizing effect due to line scattering in type I supernova atmospheres.

Since polarization structure associated with line structure in the spectra of supernovae may arise from several sources, it is important to have some means of estimating whether or not collisional effects will destroy the polarizing effect of resonance scattering. The analysis, given above, gives confidence that this polarizing effect will not be totally destroyed. For specific cases a better analysis can be done. In Chapter 5 a collisional depolarization analysis is done for the special case of SN 1987a.

f) Closely Spaced Lines and Multiplets

In this section some spectroscopy terminology will be needed. An atomic or ionic state is specified by four quantum numbers L, S, J, and M_J, or L, S, M_L, and M_S. A transition between states is called a line component. A level is a set of states specified by L, S, and J. The set of transitions between levels is called a line. The set of levels specified by L and S is called a term. The set of transitions between two terms is called a multiplet. Giving the n and l quantum numbers for all the electrons of the atom specifies the atom's configuration. The set of all transitions between two configurations is called a transition array. The set of states specified by the principal quantum number n is called an energy level.

In some cases the lines of a multiplet may be too closely spaced in wavelength for the multi-line Sobolev method to be appropriate. The Sobolev method treats line photons as if they were scattered from infinitely thin velocity surfaces. However, the resonance region for a line actually has a finite width as discussed in section (a). If lines are too closely spaced then their resonance regions can overlap. There can in this case be a two-way flow of photons between the bluer and redder line. Recall for a generally expanding or contracting atmosphere the multi-line Sobolev method assumes only a one way flow of photons: from the bluer line to the redder line for the generally expanding case, and vice versa for the generally contracting case. If the lines are very closely spaced then they can simply be treated as a single line. This can be done without much difficulty by using an average wavelength, and average oscillator strength, and average phase-matrix coefficient if necessary. If the lines are sufficiently far apart then they can be referred to as Sobolev-separated, and treated by the multi-line Sobolev method. A simple intermediate treatment for lines that cannot be treated as a single, or as Sobolev-separated, may be rather hard to obtain, and may not often be needed.

The problem of very closely spaced lines may not be too important. Recall that the thermal velocity width of a resonance region is

$$v_{th} = \sqrt{2kT/m} = 12.85\sqrt{\frac{T}{10^4 A}}\,\mathrm{km\,s^{-1}}, \tag{2.170}$$

and so the corresponding wavelength width would be

$$\Delta\lambda = .4286\left(\frac{\lambda_0}{10^4}\right)\sqrt{\frac{T}{10^4 A}}\ \text{Å}, \tag{2.171}$$

where λ_0 is in Ångstroms. Since supernova atmosphere temperatures are no more than a few 10^4 K, it is clear that optical lines separated by a few Ångstroms should be Sobolev separate if the thermal velocity width applies. If a microturbulence velocity width is greater than the thermal velocity width, then the corresponding wavelength width of a line could be larger. Since Sobolev-calculated fits to supernova lines are often quite good, the microturbulence velocity is probably much less a tenth of the expansion velocity which is of order 5000 to 10000 km s^{-1}. If the microturbulence velocity was of order 100 km s^{-1}, then the wavelength widths of lines would be a few Ångstroms. Some important lines, such as the Na D lines, may be verging on being non-Sobolev-separated if a microturbulence velocity of this size obtains.

The hydrogenic atom is one important case where the nearly degenerate states specified by the principal quantum number n can be grouped together. The largest wavelength separation between levels for a given n for the hydrogen atom is .0053 Å between the $2s\,^2P_{\frac{1}{2}}$ and $2s\,^2P_{1\frac{1}{2}}$ levels. Thus all the hydrogen transitions between configurations are strongly overlapping and need to be treated as single lines. It is therefore important to be able to obtain average values for the oscillator strength and the phase-matrix E_1 coefficients. The method for getting these averages will be reviewed here.

Consider a set of lower energy states labelled by the index i and a set of upper states labelled by j. The transition probability between a state i and a state j is the oscillator strength f_{ij}, aside from some factor common to all the f_{ij}'s. The probability of a photon inducing this transition is

$$\rho_i f_{ij}, \tag{2.172}$$

where ρ_i is the probability of the atom being in state i. The average transition probability is

$$f = \sum_{i,j} \rho_i f_{ij}. \tag{2.173}$$

If ρ_i is a constant value for all the states i, then

$$g^{-1} = \rho_i, \tag{2.174}$$

where g is the number of states i. The average probability is then

$$f = g^{-1} \sum_{i,j} f_{ij}. \tag{2.175}$$

If a subset of transitions labeled kl can be assigned an average oscillator strength, $f_{kl} = \langle f_{ij} \rangle$, then

$$f = g^{-1} \sum_{k,l} g_k f_{kl}, \tag{2.176}$$

where g_k is the number of lower states of the transition subset kl. The net transition of the kl subset can be interpreted as a line transition, and the net transition of the whole set of ij transitions as a multiplet. Thus line oscillator strength times the number of lower states in the line transition summed over all the lines in a multiplet equals the multiplet oscillator strength times the number of lower states of the multiplet:

$$g_t f_{mult} = \sum_{line} g_l f_{line}. \tag{2.177}$$

The quantity g_t is called the statistical weight of the term that gives rise to the multiplet, and g_l is called the statistical weight of the level that gives rise to the line. The product gf is called the weighted oscillator strength. It should be apparent for the hydrogenic atom that if all the states in an energy level had equal occupation probability (EQP), then the weighted oscillator strength of the set of transitions between energy levels would be

$$g_n f_{ener} = \sum_{mult} g_t f_{mult} = \sum_{line} g_l f_{line}, \tag{2.178}$$

where g_n is the statistical weight of the lower energy level. The statistical weights are given by

$$g_l = 2J + 1, \tag{2.179a}$$

$$g_t = (2L+1)(2S+1), \tag{2.179b}$$

and

$$g_n = 2n^2. \tag{2.179c}$$

Since the weighted oscillator strengths are additive for combinations of transitions, they are convenient quantities to work with and are often tabulated.

The weighted oscillator strengths can be regarded as the unnormalized probabilities of their respective transitions. The sum of the weighted oscillator strengths is the normalization constant of the probability distribution. Now the Hamilton prescription assigns a set of E_i coefficients to each line transition. The average E_i coefficients for a multiplet or an energy level transition can therefore be obtained from

$$< E_i >_{mult/ener} = \frac{1}{(gf)_{mult/ener}} \sum_{line} (gf)_{line} (E_i)_{line}. \tag{2.180}$$

The crucial assumption made in obtaining the expressions for the weighted oscillator strengths and average E_i coefficients was that the states of the collection had equal occupation probability.

For nearly degenerate states in thermodynamic equilibrium, the assumption is valid; thermodynamic equilibrium guaranteeing that the occupation probability of a state depends only on its energy. However, in non-equilibrium systems, such as scattering dominated atmospheres, the assumption may not hold. The average quantities must, in a rigorous treatment, be obtained by solving for the occupation numbers of the all the levels using the rate equations or equations of statistical equilibrium (for the method see Mihalas p. 127). Such a calculation is computer intensive. A first approach to the problem would be to assume an occupation probability. EQP is a natural first assumption, but the characteristics of a particular case might indicate other occupation probabilities that should be investigated.

A case very relevant to the polarization spectrum of SN 1987a is that of the Balmer transitions. The lower energy level of the Balmer transitions has $n = 2$ and consists of two terms: $2\,^2S$, and $2\,^2P$. Since the transition from the ground state to the $2S$ term is forbidden, it is easy to understand that there may not be EQP for the $2s$ and $2p$ states. To investigate the consequences of unequal occupation three cases can be considered: (1) the $2s$ states have EQP and the $2p$ states have zero occupation probability (the s-case), (2) the $2p$ states have EQP and the $2s$ states have zero occupation probability (the p-case), and (3) there is EQP for all the states (the e-case). The average oscillator strengths, and E_i coefficients for these three cases are given in Table 2.4 for the first six Balmer lines. The s-case results are just those for the ^2S-^2P multiplet. The p-cases are designated by $\mathrm{H}\alpha_{\mathrm{p}}$, $\mathrm{H}\beta_{\mathrm{p}}$, etc. The e-cases are designated by $\mathrm{H}\alpha$, $\mathrm{H}\beta$, etc.

The oscillator strength varies between the s-case and p-case by $\approx 40\,\%$ for the $\mathrm{H}\alpha$ transitions; by $\approx 25\,\%$ for the $\mathrm{H}\beta$ transitions; and by rapidly diminishing amounts for the higher order transitions. The E_1, E_2, and E_3 vary by approximately 5 %, 5 %, 2.5 %, and 10 % respectively between the two cases for all the lines examined. The conclusion can be drawn that EQP may not be an adequate approximation for obtaining the oscillator strengths of the $\mathrm{H}\alpha$, and $\mathrm{H}\beta$ transitions. For the E_i coefficients, EQP is probably always adequate.

Table 2.4 also contains transition quantities for the Na D lines. Their multiplet average quantities are also displayed. However, as the Na D lines are separated by ≈ 7 Å they are Sobolev-separated, and ought to be treated as separate lines in any calculation.

TABLE 2.4—Transition quantities for lines, multiplets, and energy level transitions.

Designation	λ(Å)	gf	g	f	$\lambda_\mu f$	E_1	E_2	E_3
				Hα				
$\frac{1}{2}$-$\frac{1}{2}$	6562.	0.2899	2	0.14495	0.09512	0.0000	1.0000	0.6667
$\frac{1}{2}$-$1\frac{1}{2}$	6562.	0.5798	2	0.28990	0.19023	0.5000	0.5000	0.8333
^{2}S-^{2}P	6562.	0.8697	2	0.43485	0.28535	0.3333	0.6667	0.7778
$\frac{1}{2}$-$\frac{1}{2}$	6562.	0.0272	2	0.01358	0.00891	0.0000	1.0000	0.6667
$1\frac{1}{2}$-$\frac{1}{2}$	6562.	0.0543	4	0.01358	0.00891	0.0000	1.0000	0.1667
^{2}P-^{2}S	6562.	0.0815	6	0.01358	0.00891	0.0000	1.0000	0.3333
$\frac{1}{2}$-$1\frac{1}{2}$	6562.	1.3916	2	0.69578	0.45657	0.5000	0.5000	0.8333
$1\frac{1}{2}$-$1\frac{1}{2}$	6562.	0.2783	4	0.06958	0.04566	0.3200	0.6800	0.1333
$1\frac{1}{2}$-$2\frac{1}{2}$	6562.	2.5048	4	0.62620	0.41092	0.2800	0.7200	0.7000
^{2}P-^{2}D	6562.	4.1747	6	0.69578	0.45657	0.3560	0.6440	0.7067
Hα_p	6562.	4.2562	6	0.70937	0.46549	0.3492	0.6508	0.6995
Hα	6562.	5.1260	8	0.64075	0.42046	0.3465	0.6535	0.7128
				Hβ				
$\frac{1}{2}$-$\frac{1}{2}$	5.	0.0685	2	0.03425	0.00002	0.0000	1.0000	0.6667
$\frac{1}{2}$-$1\frac{1}{2}$	5.	0.1370	2	0.06850	0.00003	0.5000	0.5000	0.8333
^{2}S-^{2}P	5.	0.2055	2	0.10275	0.00005	0.3333	0.6667	0.7778
$\frac{1}{2}$-$\frac{1}{2}$	5.	0.0061	2	0.00305	0.00000	0.0000	1.0000	0.6667
$1\frac{1}{2}$-$\frac{1}{2}$	5.	0.0122	4	0.00305	0.00000	0.0000	1.0000	0.1667
^{2}P-^{2}S	5.	0.0183	6	0.00305	0.00000	0.0000	1.0000	0.3333
$\frac{1}{2}$-$1\frac{1}{2}$	5.	0.2436	2	0.12180	0.00006	0.5000	0.5000	0.8333
$1\frac{1}{2}$-$1\frac{1}{2}$	5.	0.0487	4	0.01218	0.00001	0.3200	0.6800	0.1333
$1\frac{1}{2}$-$2\frac{1}{2}$	5.	0.4385	4	0.10962	0.00005	0.2800	0.7200	0.7000

TABLE 2.4—*Continued.*

Designation	λ(Å)	gf	g	f	$\lambda_\mu f$	E_1	E_2	E_3
^2P-^2D	5.	0.7308	6	0.12180	0.00006	0.3560	0.6440	0.7067
$H\beta_p$	5.	0.7491	6	0.12485	0.00006	0.3473	0.6527	0.6975
$H\beta$	5.	0.9546	8	0.11932	0.00006	0.3443	0.6557	0.7148
				$H\gamma$				
$\frac{1}{2}$-$\frac{1}{2}$	4340.	0.0280	2	0.01398	0.00607	0.0000	1.0000	0.6667
$\frac{1}{2}$-$1\frac{1}{2}$	4340.	0.0559	2	0.02797	0.01214	0.5000	0.5000	0.8333
^2S-^2P	4340.	0.0839	2	0.04195	0.01821	0.3333	0.6667	0.7778
$\frac{1}{2}$-$\frac{1}{2}$	4340.	0.0024	2	0.00122	0.00053	0.0000	1.0000	0.6667
$1\frac{1}{2}$-$\frac{1}{2}$	4340.	0.0049	4	0.00122	0.00053	0.0000	1.0000	0.1667
^2P-^2S	4340.	0.0073	6	0.00122	0.00053	0.0000	1.0000	0.3333
$\frac{1}{2}$-$1\frac{1}{2}$	4340.	0.0887	2	0.04437	0.01926	0.5000	0.5000	0.8333
$1\frac{1}{2}$-$1\frac{1}{2}$	4340.	0.0177	4	0.00444	0.00193	0.3200	0.6800	0.1333
$1\frac{1}{2}$-$2\frac{1}{2}$	4340.	0.1597	4	0.03993	0.01733	0.2800	0.7200	0.7000
^2P-^2D	4340.	0.2662	6	0.04437	0.01926	0.3560	0.6440	0.7067
$H\gamma_p$	4340.	0.2735	6	0.04558	0.01978	0.3465	0.6535	0.6967
$H\gamma$	4340.	0.3573	8	0.04466	0.01938	0.3435	0.6568	0.7159
				$H\delta$				
$\frac{1}{2}$-$\frac{1}{2}$	4101.	0.0144	2	0.00720	0.00295	0.0000	1.0000	0.6667
$\frac{1}{2}$-$1\frac{1}{2}$	4101.	0.0288	2	0.01440	0.00591	0.5000	0.5000	0.8333
^2S-^2P	4101.	0.0432	2	0.02160	0.00886	0.3333	0.6667	0.7778

TABLE 2.4—*Continued.*

Designation	λ(Å)	gf	g	f	$\lambda_\mu f$	E_1	E_2	E_3
$\frac{1}{2}$- $\frac{1}{2}$	4101.	0.0012	2	0.00062	0.00025	0.0000	1.0000	0.6667
$1\frac{1}{2}$- $\frac{1}{2}$	4101.	0.0025	4	0.00062	0.00025	0.0000	1.0000	0.1667
^{2}P-^{2}S	4101.	0.0037	6	0.00062	0.00025	0.0000	1.0000	0.3333
$\frac{1}{2}$-$1\frac{1}{2}$	4101.	0.0433	2	0.02163	0.00887	0.5000	0.5000	0.8333
$1\frac{1}{2}$-$1\frac{1}{2}$	4101.	0.0087	4	0.00216	0.00089	0.3200	0.6800	0.1333
$1\frac{1}{2}$-$2\frac{1}{2}$	4101.	0.0779	4	0.01947	0.00798	0.2800	0.7200	0.7000
^{2}P-^{2}D	4101.	0.1298	6	0.02163	0.00887	0.3560	0.6440	0.7067
Hδ_p	4101.	0.1335	6	0.02225	0.00912	0.3461	0.6539	0.6963
Hδ	4101.	0.1767	8	0.02209	0.00906	0.3430	0.6570	0.7162
				Hϵ				
$\frac{1}{2}$- $\frac{1}{2}$	3970.	0.0085	2	0.00425	0.00169	0.0000	1.0000	0.6667
$\frac{1}{2}$-$1\frac{1}{2}$	3970.	0.0170	2	0.00850	0.00337	0.5000	0.5000	0.8333
^{2}S-^{2}P	3970.	0.0255	2	0.01275	0.00506	0.3333	0.6667	0.7778
$\frac{1}{2}$- $\frac{1}{2}$	3970.	0.0007	2	0.00037	0.00015	0.0000	1.0000	0.6667
$1\frac{1}{2}$- $\frac{1}{2}$	3970.	0.0015	4	0.00037	0.00015	0.0000	1.0000	0.1667
^{2}P-^{2}S	3970.	0.0022	6	0.00037	0.00015	0.0000	1.0000	0.3333
$\frac{1}{2}$-$1\frac{1}{2}$	3970.	0.0247	2	0.01233	0.00490	0.5000	0.5000	0.8333
$1\frac{1}{2}$-$1\frac{1}{2}$	3970.	0.0049	4	0.00123	0.00049	0.3200	0.6800	0.1333
$1\frac{1}{2}$-$2\frac{1}{2}$	3970.	0.0444	4	0.01110	0.00441	0.2800	0.7200	0.7000
^{2}P-^{2}D	3970.	0.0740	6	0.01233	0.00490	0.3560	0.6440	0.7067
Hϵ_p	3970.	0.0762	6	0.01270	0.00504	0.3457	0.6543	0.6959
Hϵ	3970.	0.1016	8	0.01270	0.00504	0.3430	0.6580	0.7171

TABLE 2.4—*Continued.*

Designation	λ(Å)	gf	g	f	$\lambda_\mu f$	E_1	E_2	E_3
				Hζ				
$\frac{1}{2}$-$\frac{1}{2}$	3889.	0.0055	2	0.00273	0.00106	0.0000	1.0000	0.6667
$\frac{1}{2}$-$1\frac{1}{2}$	3889.	0.0109	2	0.00547	0.00213	0.5000	0.5000	0.8333
^{2}S-^{2}P	3889.	0.0164	2	0.00820	0.00319	0.3333	0.6667	0.7778
$\frac{1}{2}$-$\frac{1}{2}$	3889.	0.0005	2	0.00023	0.00009	0.0000	1.0000	0.6667
$1\frac{1}{2}$-$\frac{1}{2}$	3889.	0.0009	4	0.00023	0.00009	0.0000	1.0000	0.1667
^{2}P-^{2}S	3889.	0.0014	6	0.00023	0.00009	0.0000	1.0000	0.3333
$\frac{1}{2}$-$1\frac{1}{2}$	3889.	0.0155	2	0.00775	0.00301	0.5000	0.5000	0.8333
$1\frac{1}{2}$-$1\frac{1}{2}$	3889.	0.0031	4	0.00078	0.00030	0.3200	0.6800	0.1333
$1\frac{1}{2}$-$2\frac{1}{2}$	3889.	0.0279	4	0.00698	0.00271	0.2800	0.7200	0.7000
^{2}P-^{2}D	3889.	0.0465	6	0.00775	0.00301	0.3560	0.6440	0.7067
Hζ_p	3889.	0.0479	6	0.00798	0.00310	0.3456	0.6544	0.6958
Hζ	3889.	0.0643	8	0.00804	0.00313	0.3425	0.6575	0.7167
				Na D Lines				
$\frac{1}{2}$-$\frac{1}{2}$	5896.	0.6500	2	0.32500	0.19162	0.0000	1.0000	0.6667
$\frac{1}{2}$-$1\frac{1}{2}$	5889.	1.3100	2	0.65500	0.38573	0.5000	0.5000	0.8333
^{2}S-^{2}P	5891.	1.9600	2	0.98000	0.57735	0.3342	0.6658	0.7781

SOURCE: The weighted oscillator strengths for the multiplet, and energy level transitions were taken from Allen p. 70, except the weighted oscillator strength of the Hγ, ^2P-^2D multiplet which was taken from Green (1957). The weighted oscillator strengths for the lines were obtained from the multiplet oscillator strengths using tables that assumed LS coupling (Allen p. 61). The LS coupling approximation is very accurate for the hydrogen atom.

NOTE: The designation indicates type of transition: (1) the $J_1 - J_2$ designation indicates a line transition between levels with total angular momentum J_1 and J_2, (2) the ${}^{2S+1}L - {}^{2S'+1}L'$ designation indicates a multiplet transition where the terms are specified by L and S, and (3) well known designations are given for well known transitions, such as the Balmer series. For the Balmer series the transition designations subscripted by p indicate the combined transition that arises from p terms. The quantities in the other columns have the meanings discussed in the text. The $\lambda_\mu f$ quantity is used to calculate the Sobolev optical depths.

Chapter 3

Earlier Supernova Polarization Calculations

Shapiro and Sutherland (1982) and McCall (1985) have presented supernova polarization calculations. In section (a) of this chapter, the models and results of Shapiro and Sutherland are discussed. McCall's expression for supernova polarization is derived and discussed in section (b).

a) The Shapiro and Sutherland Polarization Calculation

Shapiro and Sutherland (1982; hereafter referred to as SS) calculated the continuum polarization for asymmetric model supernova atmospheres. They considered axially symmetric atmospheres with ellipsoidal shape asymmetry, and atmospheres with non-uniform surface flux.

SS adopted the plane-parallel, semi-infinite atmosphere solutions of Chandrasekhar (1960, p. 248), and Harrington (1969). These solutions give the angular distribution of specific intensity that emerges from an atmosphere surface (i.e., the darkening law), and the polarization of this specific intensity. The solutions are given in tabulated form with the darkening law and polarization given as functions of $\mu = \cos\zeta$, where ζ is the angle measured from the normal to the plane. In the solutions the specific intensity decreases as ζ increases. In the two Harrington solutions the decline is steeper. The Stokes parameters of the emergent specific intensity are specified in a two dimensional coordinate system attached to the beam with the axes labelled l and r. The l axis is in a plane with the beam and with the normal to the surface; the r axis is perpendicular to this plane. The Stokes parameter $Q/I = (I_r - I_l)/I$ is tabulated. The symmetry of the plane-parallel system indicates that the U parameter is zero, and so polarization is just $P = Q/I$. All the solutions have $Q > 0$, and show P increasing monotonically from zero at $\zeta = 0°$ to a maximum at $\zeta = 90°$. The Chandrasekhar polarization maximum is 11.7%, and the two Harrington maxima are 22.9% and 28.33%.

The Chandrasekhar solution is for the case of a pure continuous scattering opacity atmosphere. The scattering does not affect photon frequency and obeys the Rayleigh scattering law. An atmosphere with only electron scattering is, of course, an example of such a system. A quasi-continuous scattering opacity can also be provided in expanding atmospheres by the Doppler enhancement of thousands of weak lines (Karp *et al.* 1977). Such a quasi-continuous scattering would not obey the Rayleigh phase-matrix, but rather the Hamilton phase-matrix with some sort of average E_1 coefficient (see Chapter 2 section (d)). SS only consider solutions that use the Rayleigh phase-matrix since these would be the solutions with the maximum polarizing effect.

Wagoner (1981) suggested that the continuous scattering opacity of a type II supernova atmosphere may be at least as great as the absorption opacity; this may also apply to type I supernova atmospheres. If continuous scattering is important, then the thick scattering atmosphere required by the Chandrasekhar and Harrington solutions may obtain. However, a substantial portion of the continuous scattering opacity could owe to the quasi-continuous opacity provided by Doppler enhancement effect. If the Doppler enhancement effect is important, SS's results would tend to lead to under-estimates of supernova asymmetry when used to analyze observed supernova polarization.

The Chandrasekhar solution was obtained for a static atmosphere, where the frequency of a photon was unchanged by scattering. Thus each frequency of radiation propagates through the atmosphere independently. In a moving atmosphere, the directions of incidence, and scattering affect the frequency of the photons due to the Doppler effect. However, since electron scattering is frequency-independent, photons always encounter the same opacity distribution as if the atmosphere were static. The effect on the frequency distribution of radiation is small if the continuum, which is formed deep in the atmosphere, is fairly constant with frequency. A specific intensity beam scattered through some angle has its frequency shifted from ν_0. Another beam of nearly equal strength with the first is shifted to ν_0 by scattering through the same angle. Thus there is a replacement effect. Therefore the Chandrasekhar solution can be taken as applying to a moving plane-parallel atmosphere.

The two Harrington solutions are for plane-parallel atmospheres with continuous scattering, and continuous absorption and emission. The continuous absorption could be provided by photoionization, or by collisional de-excitation of a photo-excited bound state, and the emission by the reverse processes. These processes strengthen the coupling of the radiation to the local thermal state of the atmosphere. The effect of thermal coupling would, as a first expectation, lead to a decrease in the polarization of emergent radiation, since thermal emission is isotropic and unpolarized. However, Code (1950) showed that thermal coupling could enhance the polarization if there was increased anisotropy of the radiation field. This possible enhancement in polarization can be demonstrated by an argument adapted from SS.

In the diffusion approximation (see Mihalas 1978, p. 50), where the thermal coupling is assumed strong,

$$I_\nu(\tau_\nu, \mu) \approx B_\nu(\tau_\nu) + \mu \frac{dB_\nu}{d\tau_\nu}, \tag{3.1}$$

where τ_ν is the continuum optical depth from the surface for radiation of frequency ν, and B_ν is the Planck function. Using the diffusion approximation result, a measure of the radiation field anisotropy is

$$\rho \equiv \left(\frac{dB_\nu}{d\tau_\nu} \bigg/ B_\nu\right). \tag{3.2}$$

From equation (3.1), it can be seen that ρ is specifically a measure of the outward peaking of the radiation field. Assuming radiative equilibrium and LTE (local thermodynamic equilibrium), then the Eddington approximation (see Mihalas 1978, p. 61) gives

$$T^4 = \frac{3}{4} T_{eff}^4 \left(\tau + \frac{2}{3}\right), \tag{3.3}$$

where T_{eff}, called the effective temperature, is determined by assuming that the net flux is radiated by a black-body of temperature T_{eff}. Using the Eddington approximation,

$$\rho \approx \frac{x}{(1 - e^{-x})} \left(\frac{1}{4}\right) \frac{1}{(\tau_\nu + \frac{2}{3})}, \tag{3.4}$$

where $x \equiv h\nu/(kT)$. For large x, ρ can become large indicating a large outward peaking of the radiation field. This argument for outward peaking has been developed for a strong thermal coupling case (i.e., an LTE case). However, the argument should still have some validity even when the coupling is not strong, i.e, when the effect of scattering is strong. The scattering of radiation at angles near 90° is highly polarizing (see Chapter 2 section (d)). Thus the outward peaking of the radiation field could enhance the polarization of radiation scattered at angles near 90° to the normal to the surface, since the dilution by the unpolarized, thermalized radiation field is lessened in those directions.

Following Code, Harrington considered two illustrative solutions to the plane-parallel atmosphere with $x \approx 20$. In the first solution, the ratio of absorption opacity to total opacity ϵ was set to 1/6. For this solution the $\zeta = 90°$ polarization was 22.90%. The second solution used

$$\epsilon = \frac{\tau}{(\tau + 1)}. \tag{3.5}$$

This expression for ϵ is physically more plausible since increasing optical depth is expected to be accompanyed by increasing density in supernovae. The increasing density will usually cause increasing ϵ (i.e., increasing thermal coupling of radiation and matter). For the second solution the $\zeta = 90°$ polarization was 28.33%.

Since the Harrington solutions were only for model atmospheres, and these were not expanding supernova model atmospheres, their use for supernova modelling is heuristic. However, it is possible that some degree of Code's polarization enhancement effect will be present. A month after maximum light supernovae have $T_{photosphere} \approx 5000$ K. For radiation with $\lambda \approx 5000$ Å, $x \approx 6$; an x of this size may cause some polarization enhancement for the optical radiation. It should also be noted that continuous absorption is not frequency independent as is electron scattering; thus the velocity fields in a supernova atmosphere are also a factor to consider.

By using scattering atmosphere results SS assumed that the continuum optical depth to the region where the continuum radiation is thermalized is rather large: i.e., $\tau_{continuum} \gg 1$. This assumption is rather different from the assumption that Branch *et al.* (1982) made for the calculation of supernova P-Cygni lines. Branch *et al.* assume $\tau_{continuum} \approx 1$ for the optical depth to a black-body radiation (thermalized radiation) producing photosphere. However, the understanding of supernova atmospheres is still so rudimentary that the two pictures may be reconcilable (see the discussion in Chapter 2 section (c)).

Another assumption SS have made is that plane-parallel solutions are appropriate to describe the extended atmospheres of supernova. This assumption requires that the spatial depth to the thermalizing region be rather small compared to the radius of the supernova. The discussion in Chapter 2 section (c) indicated that the continuous opacity of a spherical supernova atmosphere can be adequately approximated by a power 7 decay law. For such a decay law, the ratio of tangential to radial optical depth from the photosphere to infinity is 4.35. Formally this ratio should be infinity for a plane-parallel atmosphere. A ratio of 4.35 seems too small to be certain that the plane-parellel solutions will be valid. Cassinelli and Hummer (1971; hereafter referred to as CH) showed that plane-parallel solutions do not in general adequately describe spherical, scattering atmospheres.

CH considered a spherical, scattering atmosphere with a wavelength independent opacity given by $k(r) = r^{-p}$. (The unit of radial measure was chosen so that k(r=1)=1.) CH's model had a central point source that produced an unpolarized continuum flux. Thus their model was all atmosphere for $r > 0$. They considered the polarization of the specific intensity emitted by the atmosphere as a function of impact parameter. Impact parameter was defined as

$$\delta = \sqrt{y^2 + z^2}, \tag{3.6}$$

where y, and z are coordinates of a point in a plane perpendicular to the line of sight to a distant observer. The point source was located at the origin of the coordinate system. CH demonstrated that the polarization of the specific intensity as a function of δ would rise to a plateau value for δ greater than some $\delta_{critical} > 1$. If the atmosphere extended to infinity, the polarization would stay at the plateau value as $r \rightarrow \infty$. If the atmosphere had a cut-off radius R, then the polarization would rise sharply from the plateau value to unity when $\delta \approx R$. The plateau polarization value is given by

$$P(p) = \frac{p+1}{p+3}, \tag{3.7}$$

where p is the power of the opacity decay law, and where the polarization is aligned with the tangent line to the circle defined by δ. Recall for supernovae that $p \sim 7$ has been found appropriate. With p values of this size, the polarization given by equation (3.7) is much greater than the 11.7% maximum polarization given by the Chandrasekhar solution, and the 22.9% and 28.33% maximum polarizations of the Harrington solutions.

CH's results make it clear that in general the plane-parallel solutions cannot account for all the features of spherical atmospheres. However, CH did not consider scattering atmospheres with finite central sources of unpolarized flux. Having a finite source reduces the polarizing effect of a scattering atmosphere. To illustrate this effect, consider a scattering point in an atmosphere and consider two sources with equal source strength: a point source and a finite source. For the point source there are directions for which all the scattered flux from the scattering point is right-angle scattered; for the finite source there are no such directions, since every scattered beam is the sum of beams scattered out of a finite portion of solid angle. Since right-angle scattering is most highly polarizing (see Chapter 2 section (d)), it seems probable that point source atmospheres would tend to produce flux of higher polarization than finite source atmospheres. Since supernovae are thought to have finite sources for unpolarized flux (i.e. photospheres), it is not clear that the CH solution is more appropriate for supernovae than the plane-parallel solutions. This is question for further investigation.

SS considered axisymmetric ellipsoids for their shape asymmetric models. They parameterized the asymmetry with a parameter ξ where

$$\xi_{pro} = 1 - (a/c), \qquad a < c \quad \text{(prolate)}; \tag{3.8a}$$

$$\xi_{obl} = 1 - (c/a), \qquad a > c \quad \text{(oblate)}, \tag{3.8b}$$

where c is the semi-axis along the axis of symmetry of the ellipsoid, and a is the semi-axis perpendicular to the axis of symmetry. For their surface flux asymmetry they considered a distribution of the form

$$f(\theta) = f_{pole}(1 - \alpha \sin^2 \theta)^{\beta}, \tag{3.9}$$

where f is the astrophysical flux, θ is the angle measured from the symmetry axis of the ellipsoid, α is a parametdr that can be varied from $-\infty$ to $+1$, and β is a parameter that can be varied from 0 to $+\infty$.

Since supernova cannot be resolved, only the net quantities can be observed. Therefore to obtain results that can be compared to observations, SS integrated the Chandrasekhar and Harrington solutions over the projected area of their model atmospheres. The Stokes fields for these solutions must, of course, be transformed to a common coordinate system in order to be integrated. Some analytical results required for this integration are presented in Appendix 3. The asymmetric models will yield a net polarization. The edge of the projection of the ellipsoid is called the limb. Radiation emitted from the limb is highly polarized because it is emitted at a large angle ζ with respect to the local surface normal. From the central region of the projection the radiation is emitted at smaller angles ζ, and so is less polarized. A projection that is circularly symmetric about the line of sight yields zero net polarization. Asymmetry leads to net polarization due to incomplete cancelation between the polarized radiation from the long edge and the short edge of the limb. The central region of the projection acts as a source of relatively unpolarized radiation which dilutes the polarized radiation from the limb, and so reduces the net polarization.

The net polarization as a function of ξ for the models with shape asymmetry, uniform surface flux, and $\theta = 90^{\circ}$, are shown in Fig. 3.1. The oblate models have negative polarization indicating that their net polarization is aligned perpendicular to the symmetry axis of the ellipsoid. The polarizations of prolate models are positive indicating that the polarization is aligned with the symmetry axis. Other alignments of the polarization are precluded by the symmetry of the system:

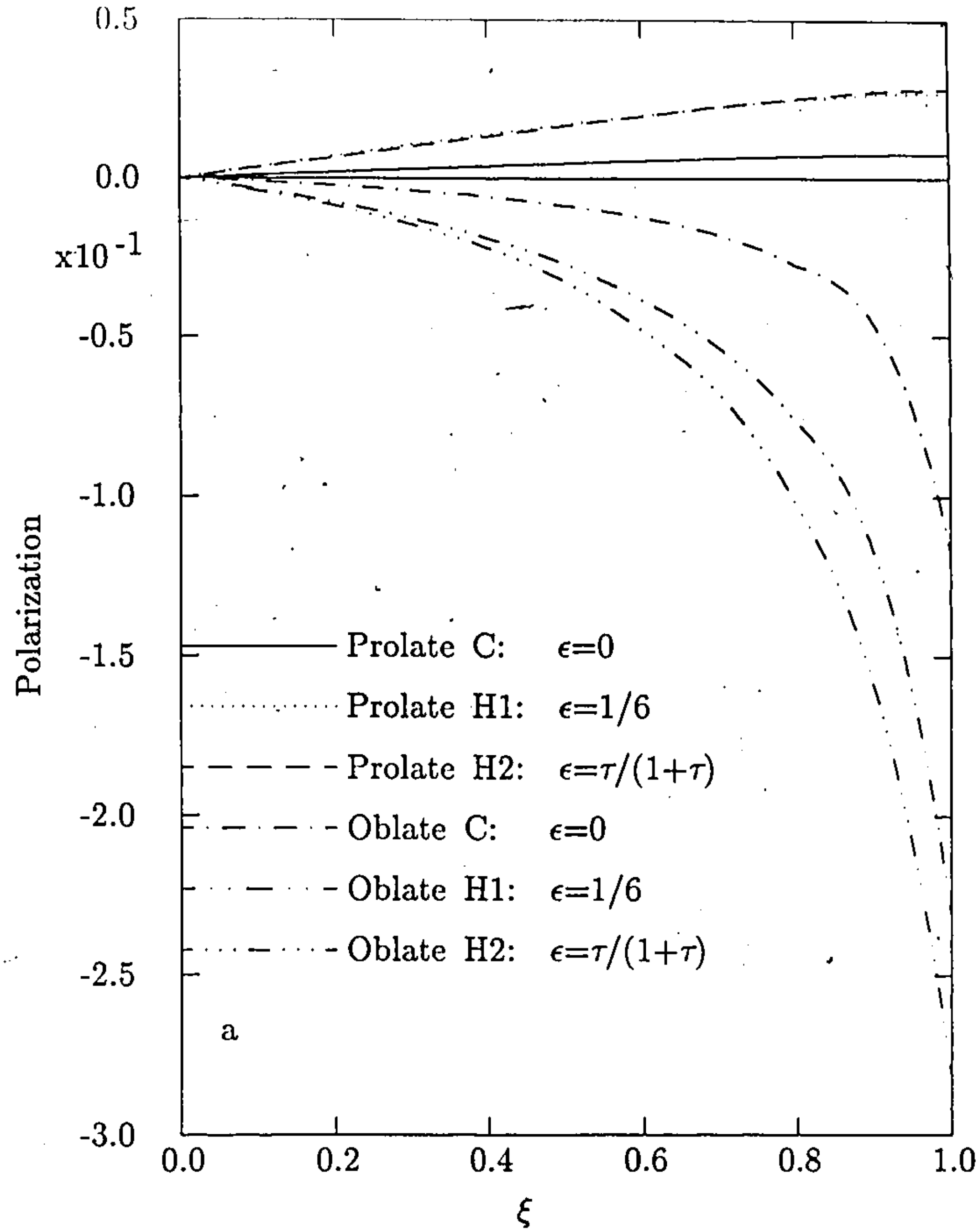

Figure 3.1. The net polarization as a function of the asymmetry ξ for Shapiro and Sutherland's (1982) oblate, and prolate models. The Chandrasekhar solution models are labeled C. The Harrington solution models are labeled H1 and H2. The oblate models have greater polarization magnitudes than the prolate models for the same asymmetry. The Harrington solution models have greater polarization magnitudes than the Chandrasekhar solution models

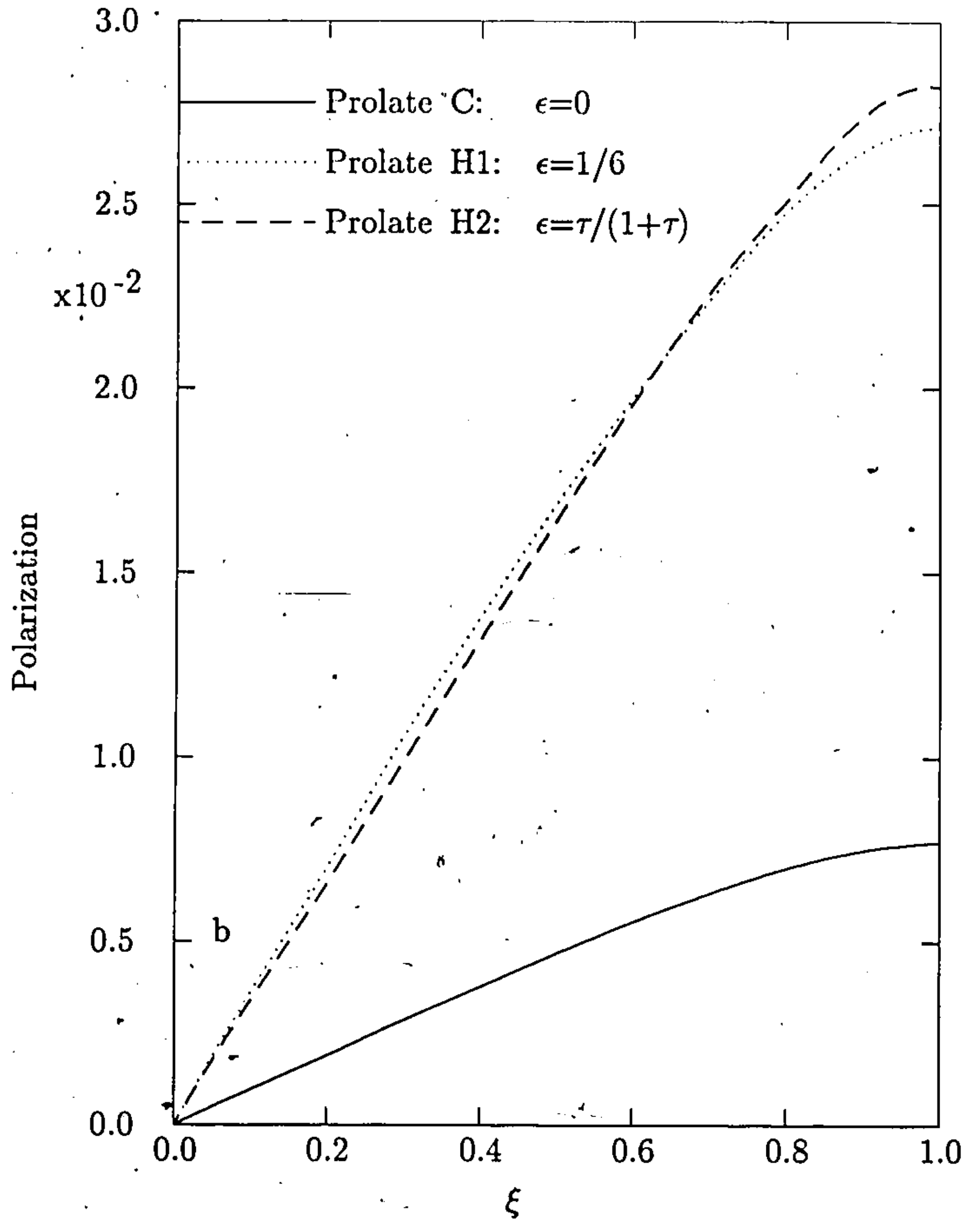

Figure 3.2. The net polarization as a function of the asymmetry ξ for Shapiro and Sutherland's (1982) prolate models. Chandrasekhar solution models are labeled C. The Harrington solution models are labeled H1 and H2. The Harrington solution models have greater polarization magnitudes than the Chandrasekhar solution models.

i.e., the net U Stokes field is zero. The Harrington solution models, as one could have expected, have greater polarization magnitudes than the Chandrasekhar solution models. For a given solution case, the oblate model polarization magnitude is greater than the prolate model polarization magnitude for all ξ. This difference in polarization magnitude increases with ξ, and becomes quite large in the limit $\xi \rightarrow 1$. This result can be understood by considering the dilution effect of the relatively unpolarized radiation from the central region of the projection of the ellipsoid. For oblate models as ξ_{obl} increases, the central region of the projection decreases relative to the limb region, and vanishes in the limit that $\xi_{obl} \rightarrow 1$. Also, the limb region in the limit that $\xi_{obl} \rightarrow 1$ becomes entirely polar. Thus the limiting case of the oblate models is one of viewing a plane edge on. The polarization values of the plane-parallel solutions for $\zeta = 90°$ are thus recovered: 11.7% for the Chandrasekhar solution, 22.90% for Harrington 1, and 22.83% for Harrington 2. For the prolate models the increasing asymmetry does not lead to a vanishing of the diluting central region of the projection relative to the limb region; thus the dilution effect is present for all ξ. The prolate polarizations are plotted on an expanded scale in Fig. 3.2. The limiting polarizations are .77% for the Chandrasekhar solution, 2.7% for Harrington 1, and 2.8% for Harrington 2.

The polarization results for the models with non-uniform surface flux will not be discussed at length here, since the present thesis is concerned with shape asymmetry. It is sufficient to note, that for what SS considered to be comparable degrees of asymmetry, that non-uniform flux asymmetry gave substantially smaller polarizations than shape asymmetry.

SS also considered the effect of shape asymmetry on the determination of supernova luminosity. Clearly, viewing an oblate supernova with uniform surface flux at a small inclination angle to the axis of symmetry would lead to an over-estimate of total luminosity if spherical symmetry is assumed. With a large inclination angle the luminosity would be under-estimated. For prolate models the polar view leads to an under-estimate, and the equatorial view to an over-estimate.

In their paper SS also consider the effects of intervening matter on polarization, and review the supernova polarization measurements made up to 1982.

b) McCall's Prescription for the Polarization for Asymmetric Supernovae

McCall (1984, 1985) considered a very simple model of a supernova atmosphere in order to attempt to assess supernova asphericity from the flux and polarization profiles of supernova P-Cygni lines. The reason for examining line polarization was, as for the present thesis, to obviate as far as possible the need to consider the effects of interstellar polarization on radiation from supernovae. The motivation of McCall's study was to discover if supernova asphericity would eliminate the discrepancies between distance determinations to galaxies by the Baade-Wesselink method (Baade 1926; Wesselink 1949; Branch *et al.* 1981) using supernova as distance indicators, and distances determined by other means.

McCall assumes a simple two-component model of the projection of a supernova atmosphere onto the plane perpendicular to the line of sight. The model consists of an elliptically symmetric, polarizing limb region, and a similar elliptically symmetric, non-polarizing central region. These two regions will be referred to as the limb and photodisk, respectively throughout this thesis (see Fig. 3.3). The limb is the projection of a scattering, aspherical atmosphere that surrounds the aspherical photosphere. The photosphere produces unpolarized continuum radiation. The photodisk is the projection of the photosphere which is, of course, covered by the scattering atmosphere. The radiation from the limb is polarized since it has all been scattered in the direction of the line sight by continuous scattering by electrons or by resonance scattering by ions. The photodisk radiation is taken to be entirely unpolarized since the atmosphere above the photosphere tends mainly to scatter radiation out of the line of sight. This assumption can at best be only partially true since there is clearly some scattering in the direction of the line of sight from the photodisk.

The nature of the asphericity of the photosphere and atmosphere is not specified further than by giving the ratio of the semi-minor to semi-major axes of their elliptical projections. This ratio will be defined here to be

$$\eta = a/c, \tag{3.10}$$

where c is the semi-major axis and a is the semi-minor axis. The convention established for this derivation is that elliptical projection is centered in a coordinate system with orthogonal y and z axes. The x axis is along the line of sight. Without loss of any generality the semi-major axis of the ellipse is taken to be along the z axis, and the semi-minor axis along the y axis. If $\eta = 1$, then the net flux is unpolarized since the atmosphere is circularly symmetric about the line of sight. If $\eta \neq 1$, then there will be a net polarization.

The elliptical symmetry of a projected atmosphere model requires the polarization to be aligned

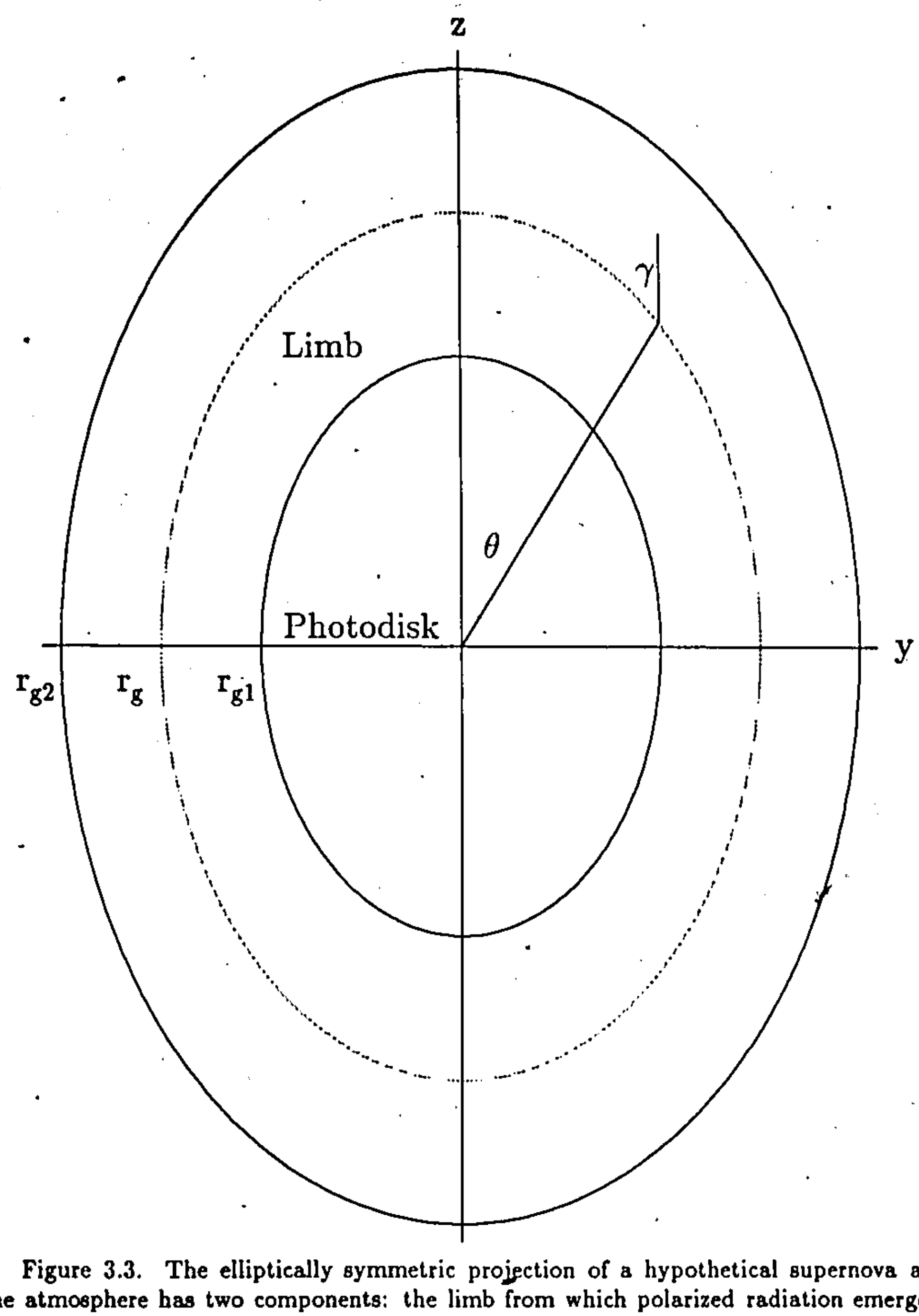

Figure 3.3. The elliptically symmetric projection of a hypothetical supernova atmosphere. The atmosphere has two components: the limb from which polarized radiation emerges, and the photodisk from which unpolarized radiation emerges. The parameter r_g is a generalized radius given by $r_g = \sqrt{(y/a)^2 + (z/c)^2}$. The polarization of the radiation emitted from a point on the limb is aligned with the tangent to an ellipse of symmetry drawn through that point.

either with the short or long axis of projection. The polarization of a specific intensity beam is

$$P(\lambda, y, z) = \frac{I_l - I_r}{I_l + I_r}, \tag{3.11}$$

where I_l and I_r are specific intensities of the Stokes fields aligned with the z and y axes respectively. The net polarization is found by integrating I_l and I_r over the whole elliptical projection to obtain

$$F_l = \int dx dy\, I_l \qquad \text{and} \qquad F_r = \int dx dy\, I_r, \tag{3.12}$$

and thus

$$P(\lambda) = \frac{F_l - F_r}{F_l + F_r}. \tag{3.13}$$

There is no circular polarization, since no source of circular polarization is included in the model.

Scattering by electrons is wavelength independent. Thus the flux from the atmosphere will have a wavelength independent continuum polarization. The scattering by resonant transitions of ions in the homologously expanding supernova atmosphere creates the P-Cygni profiles that are superimposed on the supernova flux continuum. Resonance scattering is also polarizing, and so it is expected that polarization features associated with the P-Cygni flux profile will be superimposed on the continuum polarization. The additional scattered flux in the emission feature increases the fraction of polarized radiation emitted near the rest wavelength of the resonant transition. The resonant scattering out of the line of sight of unpolarized radiation in the photodisk forms the blue-shifted P-Cygni absorption feature. Thus in the wavelength region of the absorption feature there is less diluting unpolarized radiation, and so again the fraction of polarized radiation is increased. There will also be some polarizing resonance scattering into the line of sight of photons with wavelengths in the absorption feature wavelength region. McCall's model ignores this contribution by resonance scattering, and assumes that it is continuum scattered radiation that is the source of polarization of the absorption feature.

McCall's intention was not to calculate model results, but to obtain a simple analytic prescription for the polarization of the emission maximum flux of a P-Cygni line, and a simple prescription for η in terms of measurable quantities. To this end, he simply assumed that the plateau polarization result obtained by CH (see section (a) of this chapter) applied to all the specific intensity beams emitted from the limb. The CH result was obtained for spherical, scattering atmospheres with central point sources of unpolarized flux. Having a finite central source of unpolarized flux may reduce the polarization of the net flux scattered by the atmosphere. Furthermore, the plateau result was obtained only for some of the atmosphere scattered flux; it is not clear that it should be applied to all limb-scattered flux even if it is appropriate for some of the limb-scattered flux. Thus McCall's prescriptions will probably lead to over-estimates of polarization and under-estimates of asymmetry. The CH result was derived for continuous scattering in a static atmosphere. Thus, it should be applicable to continuous scattering due to electrons in moving atmospheres (see section (a) of this chapter). ~~However~~, it is not clear that it adequately describes the polarization of resonance scattering in moving atmospheres where the scattering for each wavelength is confined to velocity surfaces as described in Chapter 2 section (a). Nevertheless, to avoid complications McCall applied the result to all the resonance scattered limb radiation with an additional depolarization factor to correct for the depolarization effect of resonance scattering.

The McCall prescription for the polarization of a specific intensity emitted by the limb of his model is

$$P_0(p) = \left(\frac{p+1}{p+3}\right) D(E_1), \tag{3.14}$$

where the first factor is the CH plateau polarization result and where $D(E_1)$ is a depolarization factor that depends on E_1, the phase-matrix coefficient of the Hamilton scattering phase-matrix. Using equation (2.122) of Chapter 2 section (d), the polarization of a beam scattered by a transition obeying the Hamilton phase-matrix is

$$\begin{aligned} P(\Theta) &= \frac{\frac{3}{2}E_1(1-\cos^2\Theta)}{\frac{3}{2}E_1(1+\cos^2\Theta)+2(1-E_1)} = \frac{(1-\cos^2\Theta)}{(1+\cos^2\Theta)}\left(\frac{\frac{3}{2}E_1(1+\cos^2\Theta)}{\frac{3}{2}E_1(1+\cos^2\Theta)+2(1-E_1)}\right) \\ &= P(\Theta)_{Rayleigh}\left(\frac{\frac{3}{2}E_1(1+\cos^2\Theta)}{\frac{3}{2}E_1(1+\cos^2\Theta)+2(1-E_1)}\right) = P(\Theta)_{Rayleigh}D(E_1,\Theta), \end{aligned} \tag{3.15}$$

where the polarization is aligned perpendicular to the scattering plane. The second factor of equation (3.15) is a depolarization correction for resonant scattering where the E_1 is determined by the prescription given in Chapter 2 section (d). McCall set $\Theta = 90°$ to obtain the one parameter depolarization factor

$$D(E_1) = \frac{3E_1}{4-E_1}. \tag{3.16}$$

This is probably the optimum choice for three reasons. First, right-angle scattering is the most highly polarizing scattering, and is thus probably most important in establishing the CH polarization plateau. Second, the ratio $D(E_1)/D(E_1,\Theta)$ can vary only between 0.5 and 1; thus $D(E_1)$ is never wrong by more than 50%. Lastly, $D(E_1)/D(E_1,\Theta)$ is monotonically increasing with E_1, and thus is least in error for the most polarizing resonance transitions; lines resulting from the most polarizing transitions are likely to be the best observational objects.

CII derived their polarization result for a spherically symmetric system. Their result has the polarization of a specific intensity beam aligned with the tangent to a circle of symmetry that passes through the point from which the specific intensity beam is emitted. Since McCall considered elliptical symmetry, he assumed that the polarization alignment of a specific intensity beam at any point in the limb is tangent to an ellipse of symmetry that passes through the point from which the specific intensity beam is emitted (see Fig. 3.3). In the untransformed local coordinate system the Stokes parameters of the specific intensity beam from a point are

$$I_l' = I(1+P_0)/2, \qquad I_r' = I(1-P_0)/2 \qquad \text{and} \qquad U' = 0, \tag{3.17}$$

where I is the total specific intensity from the point, and P_0 is the plateau polarization. The tangent ellipse can be defined by the equation

$$r_g = \sqrt{(z/c)^2 + (y/a)^2}, \tag{3.18}$$

where r_g can be thought of as a generalized radius. The local system must be rotated clockwise by an angle γ with

$$\begin{aligned} \tan\gamma &= \frac{\sqrt{r_g^2 - (y/a)^2}}{(c/a)(y/a)} \\ &= (a/c)^2(z/y) \\ &= (a/c)^2 \cot\theta, \end{aligned} \tag{3.19a}$$

$$\cos\gamma = \frac{(c/a)^2 \tan\theta}{\sqrt{1 + (c/a)^4 \tan^2\theta}}, \tag{3.19b}$$

and

$$\sin\gamma = \frac{\pm 1}{\sqrt{1 + (c/a)^4 \tan^2\theta}}, \tag{3.19c}$$

where θ is the angle measured from the z axis to the vector (y, z). The transformation equations for the Stokes parameters are

$$I_l = I_l' \cos^2\gamma + I_r' \sin^2\gamma + (1/2)U' \sin 2\gamma, \tag{3.20a}$$

$$I_r = I_l' \sin^2\gamma + I_r' \cos^2\gamma - (1/2)U' \sin 2\gamma, \tag{3.20b}$$

and

$$U = -I_l' \sin 2\gamma + I_r' \sin 2\gamma + U' \cos 2\gamma \tag{3.20c}$$

(Chandrasekhar, 1960, p. 34). McCall assumed that the primed Stokes parameters were constants over the elliptical limb region. Thus symmetry and the fact that $U' = 0$ reduces the necessary integrands to

$$I_l = I_l' \cos^2\gamma + I_r' \sin^2\gamma, \tag{3.21a}$$

$$I_r = I_l' \sin^2\gamma + I_r' \cos^2\gamma, \tag{3.21b}$$

and

$$U = 0. \tag{3.21c}$$

The required integrals are

$$\int dy \int dz \cos^2\gamma \qquad \text{and} \qquad \int dy \int dz \sin^2\gamma, \tag{3.22}$$

where the region of integration is the area of the elliptically symmetric limb. Using the transformations

$$y = ar_g \sin\xi \qquad \text{and} \qquad z = cr_g \cos\xi, \tag{3.23}$$

the integrals become

$$\int_{r_{g1}}^{r_{g2}} dr_g \int_0^{\pi/2} d\xi \, \frac{acr_g (c/a)^2 \tan^2\xi}{1 + (c/a)^2 \tan^2\xi} \qquad \text{and} \qquad \int_{r_{g1}}^{r_{g2}} dr_g \int_0^{\pi/2} d\xi \, \frac{acr_g}{1 + (c/a)^2 \tan^2\xi}, \tag{3.24}$$

where the symmetry requires that the ξ integral be done only from 0 to $\pi/2$ and then a multiplication by 4 for the final result, and where r_{g1} and r_{g2} are the bounding generalized radii of the limb. The r_g integral can be done at once to yield the coefficient

$$2ac(r_{g2}^2 - r_{g1}^2), \tag{3.25}$$

where the factor of 4 has been included. Using the transformation

$$\xi = \tan^{-1} s, \tag{3.26}$$

the ξ integrals become

$$\int_0^\infty ds \, \frac{(s/\eta)^2}{(1 + (s/\eta)^2)(1 + s^2)} \qquad \text{and} \qquad \int_0^\infty ds \, \frac{1}{(1 + (s/\eta)^2)(1 + s^2)}. \tag{3.27}$$

Using partial fractions the integrals become

$$\left(\frac{-1}{1-\eta^2}\right)\left(\int_0^\infty ds\,\frac{1}{1+(s/\eta)^2}\right)+\left(\frac{1}{1-\eta^2}\right)\left(\int_0^\infty ds\,\frac{1}{1+s^2}\right) \tag{3.28a}$$

and

$$\left(\frac{1}{1-\eta^2}\right)\left(\int_0^\infty ds\,\frac{1}{1+(s/\eta)^2}\right)+\left(\frac{-\eta^2}{1-\eta^2}\right)\left(\int_0^\infty ds\,\frac{1}{1+s^2}\right). \tag{3.29b}$$

The solutions are

$$\frac{\pi}{2}\left(\frac{1}{1+\eta}\right) \quad \text{and} \quad \frac{\pi}{2}\left(\frac{\eta}{1+\eta}\right) \tag{3.30}$$

respectively. Thus the net limb Stokes parameters are

$$F_l=\frac{\pi}{2}ac(r_{g2}^2-r_{g1}^2)\left(\frac{(1+\eta)I+(1-\eta)P_0I}{(1+\eta)}\right), \tag{3.31a}$$

$$F_r=\frac{\pi}{2}ac(r_{g2}^2-r_{g1}^2)\left(\frac{(1+\eta)I+(\eta-1)P_0I}{(1+\eta)}\right), \tag{3.31b}$$

and

$$U=0. \tag{3.31c}$$

The polarization of the limb flux is then

$$P(limb)=\left(\frac{1-\eta}{1+\eta}\right)P_0. \tag{3.32}$$

A consequence of equation (3.32), that is independent of many assumptions made by McCall, is that radiation originating on an elongated source and scattered at right angles toward a distant observer will tend to have its net polarization aligned with the long axis of the source.

McCall's prescriptions for the polarization of the emission maximum flux of a P-Cygni line, and for η can now be obtained. Definitions of quantities needed are listed for convenience in Table 3.1. The observed continuum polarization is given by

$$P(cont)=\frac{F_c(limb)P_c}{F_c(net)}. \tag{3.33}$$

The polarization of the emission maximum of the P-Cygni line is given by

$$P(emis)=\frac{F_c(limb)P_c+F_l(limb)P_l}{F_c(net)+F_l(limb)}. \tag{3.34}$$

The assumption is being made that the effects of continuous and resonant line scattering are independent. This assumption is really only valid when one or both of continuous and resonant scattering

TABLE 3.1.—Quantities appearing in McCall's prescriptions.

Quantity	Description	Determination
P_c	The polarization of the continuum radiation emerging from the limb.	Equations (3.17) and (3.35) with the $E_1 = 1$ for electron scattering and some appropriate average E_1 for the quasi-continuous opacity due to the Doppler enhancement effect (see section (a) of this chapter).
P_l	The polarization of the resonantly scattered radiation emerging from the limb.	Equations (3.17) and (3.35) with the appropriate E_1 coefficient for the resonance line under consideration.
$F_c(limb)$	The net continuum flux from the limb.	Solved for from observed quantities.
$F_c(net)$	The net continuum flux from the limb and photodisk.	Observed
$F_l(limb)$	The P-Cygni emission maximum flux for a resonant line.	Observed.
$P(cont)$	The continuum polarization.	Observed.
$P(emis)$	The P-Cygni emission maximum polarization.	Observed.

effects are weak. If both effects are so weak that a photon passing through the atmosphere has only a small chance of scattering even once by either mechanism, then clearly the effects are additive. If one effect is extremely weak compared to the other, then its contribution is sufficiently small that it can be approximated crudely. When $P_c = 0$, the polarization of the emission maximum is

$$P(emis) = \frac{F_l(limb)P_l}{F_c(net) + F_l(limb)}. \tag{3.35}$$

This prescription is used in Chapter 4 to obtain McCall emission polarizations that are compared to the corresponding Sobolev values.

Substituting for $F_c(limb)P_c$ in equation (3.34) from equation (3.33) gives

$$P(emis) = \frac{P(cont) + fP_l}{1+f}, \tag{3.36}$$

where

$$f \equiv \frac{F_l(limb)}{F_c(net)}. \tag{3.37}$$

Thus

$$P_l = \frac{P(emis)(1+f) - P(cont)}{f}. \tag{3.38}$$

Recalling equation (3.32),

$$\begin{aligned} \eta &= \frac{P_0 f - P(emis)(1+f) + P(cont)}{P_0 f + P(emis)(1+f) - P(cont)} \\ &= \frac{f[P_0 - P(emis)] - [P(emis) - P(cont)]}{f[P_0 + P(emis)] + [P(emis) - P(cont)]}. \end{aligned} \tag{3.39}$$

Thus using observable quantities and McCall's depolarization corrected version of the CH result (see equation (3.14)) an expression is obtained for the ratio of the semi-minor to semi-major axes of the projection of a supernova atmosphere.

The prescription for η has the advantage of simplicity. However, the assumptions made in obtaining it are not obviously justifiable. Three major weaknesses in the assumptions can be recapitulated here. (1) The application of the CH polarization plateau result to all the limb-scattered radiation of a system with a finite central source of unpolarized radiation will probably lead to over-estimates of the amount of polarized limb flux, and under-estimates of the asymmetry of the supernova atmosphere. The over-estimates and under-estimates may be quite significant. (2) The CH result was derived for a spherical atmosphere. Its use for an asymmetric model is plausible, but clearly an approximation of uncertain accuracy. (3) The CH result applies to a continuous scattering atmosphere. It is not clear that it would be any more than order of magnitude correct for resonant scattering in a moving atmosphere.

The weaknesses of McCall's assumptions indicates that his expressions are probably not very useful in estimating supernova asymmetry from observational data. In Chapter 4 results obtained from Sobolev-II calculations are compared to values obtained from McCall expressions.

Chapter 4
Polarizing Atmosphere Models
And a Parameter Survey

Section (a) of this chapter discusses the model supernova atmospheres considered in this thesis. The results of flux and polarization line spectra calculations for a parameter survey of spherically symmetric, prolate, and oblate models are given sections (b), (c), and (d), respectively. Figures for the spectra calculations are gathered at the ends of the appropriate section. The general conclusions for each section are given at the end of the section.

a) Discussion of the Model Supernova Atmospheres

This thesis considers axially symmetric, expanding atmospheres as possible models of supernovae. The asymmetry of a supernova can be detected from the polarization spectra of the supernova lines. The calculation of polarization spectra for a parameter survey of models has been done, and this chapter reports and discusses the results. To calculate the polarization spectra a computer program was written using the Sobolev-H formalism derived in Chapter 2. The program can calculate flux and polarization spectra for expanding, multi-line-resonance scattering atmospheres. The remainder of this section discusses the features, parameters, and limitations of the computer program. The program is listed in Appendix 4. Some analytical results pertaining to axially symmetric ellipsoids that were used in the program are presented in Appendix 3.

The discussion of asymmetric supernova calculations given in Chapter 1 section (d) suggests that rotation may lead to oblate explosions, and that rotation with magnetic fields may lead to prolate explosions. It is plausible to assume that if an asymmetric core or mantle exists in a supernova explosion, then density asymmetry along with kinetic energy will be transferred to the outer layers. Therefore supernova atmospheres with oblate or prolate density distributions may occur. The assumption can be made that the temperature and other thermodynamic distributions would have the same asymmetry as that of the density distribution. It then follows that the photosphere of a supernova would also tend to have the same asymmetry. In view of current ignorance of the behavior of asymmetric supernova explosions, all of the above assumptions have been made in order to have a simple model atmosphere for calculations. This kind of model atmosphere is used in all the polarization spectra calculations for this thesis.

The exact specification of the models is given in the following. The photosphere and the thermodynamic state of the models were considered to have regular axially symmetric ellipsoidal symmetry. Axisymmetric ellipsoidal shapes were considered as they are relatively easy to implement in a computer code, and as only a single parameter controls their shape variation. Following Shapiro and Sutherland (1982) the ellipsoids are parameterized by an asymmetry parameter ξ:

$$\xi_{pro} = 1 - (a/c), \quad a < c \quad \text{(prolate);} \tag{4.1a}$$

$$\xi_{obl} = 1 - (c/a), \quad a > c \quad \text{(oblate),} \tag{4.2b}$$

where c and a are the lengths of the symmetry and perpendicular semiaxes, respectively. The same ξ is used for both photosphere and atmosphere. Since spherical supernova models and spectra fits (see Chapter 2 section (c)) indicate that a useful parameterization of the density distribution is a power law decay with radius, a generalized version may be assumed for asymmetric supernovae:

$$\rho(r_g) = \rho_{ph}(r_{g_{ph}}/r_g)^p, \tag{4.3}$$

where ρ_{ph} is the photospheric density, p is the power index, and r_g is a generalized radius parameter given by

$$r_g = \sqrt{(x/a)^2 + (y/a)^2 + (z/c)^2}. \tag{4.4}$$

When r_g is held constant, equation (4.4) defines an axisymmetric ellipsoid. The power index p was set to 7 in all but one of the model calculations. Spherically symmetric hydrodynamic calculations indicate that a power index of 7 gives a good representation of supernova atmospheres. (see Chapter 2 section (c)). For practical calculations a maximum generalized radius, $r_{g_{max}}$, had to be implemented. For all reported calculations $r_{g_{max}}$ was set to $4r_{g_{ph}}$, which is effectively at infinity for $p = 7$ models.

In the model calculations the density is never used, rather the Sobolev optical depth is the density-related quantity that appears. In correspondence to the assumption of Branch and collaborators (see the discussion in Chapter 2 (c)), it has been assumed that the Sobolev optical depths are proportional to the density and are given by the expression

$$\tau(r_g) = \tau_{ph}(r_{g_{ph}}/r_g)^p, \tag{4.5}$$

where τ_{ph} is the Sobolev optical depth at the photosphere. Most of the models considered are single-line models. Strongly blended line models would be more difficult to uniquely parameterize and thus would give a less sure diagnostic of supernova characteristics. Observers should, if possible, do spectropolarimetry on strong isolated lines to allow the clearest interpretation of data.

Again following Branch and collaborators, no continuous opacity has been included in the calculations reported in this chapter. However, continuous opacity is thought of as establishing the photosphere at a continuum optical depth of approximately 1. Continuous opacity can be provided by electron scattering, ionizing transitions or the quasi-continuous opacity due to the Doppler enhancement of thousands of weak lines (Karp *et al.* 1977). The inclusion of continuous opacity does not have a drastic effect on the morphology of line profiles that emerge from a supernova atmosphere (Harkness 1986); however, the model parameters needed to fit a spectrum may well change when continuous opacity is included. Without continuous opacity there is no source of continuum polarization in the calculations. Recall from Chapter 3 that the Shapiro and Sutherland (1982) calculations gave net continuum polarizations on the order of a few percent for $\xi \sim .5$. Anticipating the results of the present chapter, P-Cygni line polarizations can also be of the order of a few percent for $\xi \sim .5$. It might be conjectured that the line polarization features would simply be superimposed on the continuum polarization. However, an experimental investigation of the convolution of continuum and line polarization indicates that the net effect is more complicated than simple superposition. This investigation is reported in Chapter 5 section (b).

The photosphere is considered to be a well defined surface. It is the original source of the continuum radiation that is then scattered in the atmosphere. Two sorts of continuum have been considered: (1) an artificial continuum that is constant with wavelength, and (2) a Planck black-body continuum that depends on wavelength and photospheric temperature, T_{ph}. The constant continuum is used because it does not bias the models with regard to the slope of the continuum which, for the Planck continuum, depends on temperature. Wien's displacement law gives the wavelength of the maximum of the Planck distribution:

$$\lambda_{max} = \frac{28978.}{T_3}\,\text{Å}, \tag{4.6}$$

where λ_{max} is in Ångstroms, and T_3 is the temperature in units of 10^3 K. Since supernova photospheric temperatures range from ≈ 30000 K to ≈ 5000 K, it is clear that the maximum of the Planck continuum can occur at any wavelength in the optical region, and therefore the slope of the continuum may be positive or negative in the optical region. Thus it is preferable to examine models with zero slope continuum, unless the effect of the continuum slope is itself being investigated. Most of the models reported in this chapter have the zero slope, constant continuum.

The constant ϵ, as explained in Chapter 2 section (a), gives the coupling of the resonance transition to the other transition processes. When $\epsilon = 0$, pure two-level atom resonance scattering obtains. For non-zero ϵ (and the Planck continuum), the calculations assume the two-level atom approximation, and thus the non-resonance source of photons is collisional excitation by particles obeying a Maxwell-Boltzmann distribution evaluated at the local electron temperature. This thermal source is given by the Planck function B_ν multiplied by ϵ (see Chapter 2 section (a)). The Planck function is evaluated at the photospheric temperature T_{ph} which is assumed to be equal to the electron temperature everywhere in the atmosphere. The thermal emission provided by non-zero ϵ only adds flux: it tends to fill in the P-Cygni absorption feature and it increases the emission feature. Since the particle collisions are random, the thermal emission is isotropic and unpolarized. The effect of adding a thermal source is simply to diminish polarization. No non-zero ϵ calculations are reported in this chapter.

The radiative transfer in the models was treated with the the Sobolev-H method derived in Chapter 2 section (d). The polarizing effect arises from the use of the Hamilton phase-matrix. Since this chapter is only reporting a parameter survey, there is no need to consider the validity of Hamilton scattering for the models. The E_1 coefficient of the Hamilton phase-matrix controls the polarizing effect: $E_1 = 0$ gives isotropic non-polarizing scattering, and $E_1 = 1$ pure Rayleigh scattering. The effect on the flux profiles of varying E_1 is examined in the reported models. The effect on the polarization profiles of decreasing E_1 from 1 is clearly to cause a decrease in polarization. In fact, the polarization of the net flux of a supernova atmosphere tends to be linearly dependent on E_1. The only nonvanishing terms that occur in the numerator of the net polarization ratio are those in which the S_2, S_3 and S_4 coefficients appear linearly in the integrands; recall from equation (2.141) that $S_5 - S_1 = S_2$. From equations (2.146) and (2.130), it can be seen that for the S_2, S_3 and S_4 coefficients, the most important E_1 dependence is linear. The denominator of the the net polarization ratio has a large contribution of flux that is unscattered and thus has no dependence on E_1. Thus the net polarization tends to be linearly dependent on E_1. No reported polarization calculations used $E_1 \neq 1$, since the effect on polarization is fairly clear from the above argument.

TABLE 4.1.—Descriptions of the model calculation parameters.

Continuum$_{ph}$:	This determines the nature of the continuum radiation emergent from the photosphere. It can have two values: "Constant" for a wavelength independent continuum, and "Planck" for a Planck distribution of temperature T_{ph}.
E_1:	This is the phase-matrix coefficient discussed in Chapter 2 section (d). $E_1 = 0$ gives isotropic, nonpolarizing scattering, and $E_1 = 1$ gives pure Rayleigh scattering.
p:	This is the power in the function that determines the optical depth as a function of r_g: $\tau(r_g) = \tau_{ph}(r_{g_{ph}}/r_g)^p$.
Pro/Oblate:	This determines whether the model is prolate or oblate.
$r_{g_{max}}$:	This is the atmosphere's limiting outer generalized radius in units of $r_{g_{ph}}$, the generalized radius of the photosphere.
T_{ph}:	This is the photospheric temperature when a Planck continuum is specified. It is also the temperature of the atmosphere when the thermal coupling parameter ϵ is non-zero.
v_{ph}:	This is the line of sight velocity toward a distant observer of that part of the photosphere nearest the observer.
ϵ:	This is the thermal coupling parameter in the two-level atom approximation. $\epsilon = 0$ indicates a pure resonance-scattering atmosphere, and $\epsilon = 1$ indicates an atmosphere from which emitted radiation owes to collisional excitations of the ions.
θ_{incl}:	This is the inclination angle between the axis of symmetry of the ellipsoidal atmosphere and the line of sight to a distant observer. $\theta_{incl} = 0°$ means that the projection of the atmosphere on a plane perpendicular to the line of sight is circularly symmetric about the line of sight. $\theta_{incl} = 90°$ maximizes the asymmetry of the projection of the atmosphere.
λ_{rest}:	This the rest wavelength of the ion transition that gives the resonance scattering.
ξ:	This is the ellipsoid asymmetry parameter. $\xi_{pro} = 1-(a/c)$ for prolate models, and $\xi_{obl} = 1-(c/a)$ for oblate models. $\xi_{pro/obl} = 0$ gives a spherical atmosphere. $\xi_{pro} = 1$ gives an infinite cylindrical atmosphere. $\xi_{obl} = 1$ gives an infinite disk atmosphere.
τ_{ph}:	This is the Sobolev optical depth at the photosphere. See Chapter 2 section (a) for the definition of Sobolev optical depths.

In section (b) of this chapter, the effect of varying E_1 on the flux profile of a P-Cygni line has been investigated.

The inclination angle between the symmetry axis of the ellipsoid and the line of sight to the observer has been labeled θ_{incl}. For a given model the polarization is maximized for $\theta_{incl} = 90°$ and is zero for $\theta_{incl} = 0°$. Calculations showing the effects of varying θ_{incl} are reported.

For this parameter study artificial lines with rest wavelengths labeled by λ_{rest} were considered. For the constant continuum models the choice of a particular λ_{rest} has no significance. For convenience, λ_{rest} was usually chosen to be 5000 Å.

The velocity along the line of sight to a distant observer of that part of the photosphere nearest the observer is labeled v_{ph}, and is referred to as the photospheric velocity. Since supernova explosions are in homologous expansion, the velocity between two matter elements is proportional to the distance between the elements (Chapter 2 section (c)). Thus the velocity gradient Q is a constant. The Q value is obtained by dividing v_{ph} by the distance along the line of sight from the point where $v = 0$ to the point where $v = v_{ph}$. The Doppler shift of specific intensity originating at any point in the atmosphere is proportional to Q. Thus varying v_{ph} or Q causes a linear variation in the horizontal scale of the flux and polarization profiles. The choice of a particular v_{ph} has no real significance to the parameter survey. The photospheric velocity v_{ph} has been set to $6 \times 10^8\,\mathrm{cm\,s^{-1}}$ for all models of the survey. This velocity is representative of supernova velocities, and it conveniently corresponds to a Doppler shift of 100 Å for a rest wavelength of 5000 Å.

For convenience, Table 4.1 lists the model calculation parameters alphabetically and gives brief descriptions of them.

b) Spherically Symmetric Models

Spherically symmetric models have been examined in this survey in order to demonstrate and explain the flux profile behavior that is not dependent on asymmetry. The polarization of the net flux from spherically symmetric models is, of course, zero. For convenience the models are labeled by their figure number. Thus the results of model 4.1 are displayed in Figures 4.1. Models 4.1, 4.2, and 4.6 largely repeat work done by Branch (1980). The parameters for all the spherical models examined are given in Table 4.2. All the flux profiles displayed have been normalized to the flux value at the lowest wavelength shown on the figures. The figures labeled "a" display the net flux profiles. The figures labeled "b" display the limb component of the flux profiles, and those labeled "c" the photodisk component of the flux profiles. (For the definition of limb and photodisk see Chapter 3 section (b).)

To explain the models, it is useful to recall from Chapter 2 section (a) the formal Sobolev solution for emergent specific intensity given by equation (2.19). This solution is appropriate for systems where single velocity surfaces are adequate to describe the radiative transfer. Such a system is one in general expansion or contraction with isolated lines. The solution can be adapted for the case where a distant observer views both the projection of an atmosphere covering a photosphere, and the projection of an atmosphere alone. The first projection has been called the photodisk of the projected object, and the latter the limb. The emergent specific intensity is then

$$I(\nu)_{emg} = \begin{cases} S(\nu)(1-e^{-\tau}) + I(\nu)_{ph}e^{-\tau}, & \text{for the photodisk;} \\ I(\nu)_{ph}, & \text{for the photodisk when the velocity surface is below the the photosphere surface;} \\ S(\nu)(1-e^{-\tau}), & \text{for the limb.} \end{cases} \tag{4.7}$$

The source function $S(\nu)$, and the optical depths τ are evaluated on the velocity surface corresponding to the frequency ν. With homologous expansion the CD velocity surfaces are planes perpendicular to the line of sight. Taking x as the coordinate along the line of sight with the positive direction toward the observer and using the first order Doppler shift, the location of a velocity surface corresponding to frequency ν is

$$\begin{aligned} x(\nu) &= (\nu/\nu_{rest} - 1)/(Q/c) \\ &= (\lambda_{rest}/\lambda - 1)(Q/c), \end{aligned} \tag{4.8}$$

where ν_{rest} is the rest frame frequency of the line transition and Q is the velocity gradient. The Q value is, of course, a constant for homologous expansion. The net emergent flux at frequency ν, $F(\nu)$, is evaluated by integrating $I(\nu)_{emg}$ over the whole velocity surface. A distant observer cannot resolve the atmosphere, and so only measures the net flux. Thus it is important to interpret the net flux profiles in terms of underlying physical parameters. In this survey the net flux profiles have been calculated and are presented in the figures.

It should be remembered that frequency (or wavelength), velocity, and position coordinates are approximated as linearly related quantities for the model supernova atmospheres at any particular

TABLE 4.2.—Parameters for the spherical models of section (b).

Model (Figure)	Continuum$_{ph}$ / E_1 / p	Pro/Oblate / $r_{g_{max}}$ / T_{ph}	v_{ph} / ϵ / θ_{incl}	λ_{rest} / ξ / τ_{ph}
4.1	Constant 0 7	Spherical $4 \times r_{g_{ph}}$ †	$.6 \times 10^9\,\mathrm{cm\,s^{-1}}$ 0 †	5000 Å 0 *
4.2	Constant 0 *	Spherical $4 \times r_{g_{ph}}$ †	$.6 \times 10^9\,\mathrm{cm\,s^{-1}}$ 0 †	5000 Å 0 5
4.3[a]	Constant 0 7	Spherical $4 \times r_{g_{ph}}$ †	$.6 \times 10^9\,\mathrm{cm\,s^{-1}}$ 0 †	5000 Å 0 *
4.4	Constant * 7	Spherical $4 \times r_{g_{ph}}$ †	$.6 \times 10^9\,\mathrm{cm\,s^{-1}}$ 0 †	5000 Å 0 10
4.5	Planck 0 7	Spherical $4 \times r_{g_{ph}}$ *	$.6 \times 10^9\,\mathrm{cm\,s^{-1}}$ 0 †	5000 Å 0 10
4.6	Constant 0 7	Spherical $4 \times r_{g_{ph}}$ †	$.6 \times 10^9\,\mathrm{cm\,s^{-1}}$ 0 †	* 0 10

NOTE: The "*" indicates that the parameter is being varied for this model. The "†" indicates that the parameter is irrelevant for this model.

[a]Model 4.3 has an artificially transparent photosphere.

time. The use of one or other of these at any point in the discussion is a matter of convenience. Recall for example that

$$r_{ph} = v_{ph} t, \tag{4.9}$$

where t is the time since the supernova explosion.

The flux profile of a line from an expanding atmosphere with macroscopic velocities exceeding thermal velocities has a typical shape called a P-Cygni profile (see also the discussion in Chapter 2 section (b)). The P-Cygni profile consists of an emission feature centered on the rest frequency and a blue shifted absorption feature. The emission feature owes mainly to nearly right angle scattering from the limb region of the atmosphere. The ions in the limb have most of their velocity directed perpendicular to the line of sight, and so photons scattered into the line of sight from this region have only small Doppler shifts. For axisymmetric atmospheres treated in the Sobolev approximation, the flux profile component owing to the limb is a symmetric function about the rest frequency. The absorption feature owes to scattering out of the line of sight of photons emitted by the photosphere toward the distant observer. The scattering ions are moving toward the observer and have blue shifted transition frequencies. Thus photons removed from the flux toward the observer are higher frequency or bluer than the rest frequency, and thus the absorption feature is blueshifted from the rest frequency. The absorption feature mainly owes to the photodisk region. The flux components from the photodisk, and limb have been plotted separately in the figures so that their separate effects can be analyzed.

To gain a quantitative understanding of Sobolev-calculated P-Cygni profiles for the case of a homologously expanding supernova atmosphere, the emission maximum and absorption minimum will be examined analytically for a simple spherically symmetric system. The atmosphere is considered to be a pure resonance scattering atmosphere. The photosphere emits a constant continuum. The source function is then given by

$$S(r) = W(r) I_{ph}, \tag{4.10}$$

where $W(r)$ is the dilution factor and is given by

$$W(r) = \frac{1}{2}\left(1 - \sqrt{1 - (r_{ph}/r)^2}\right). \tag{4.11}$$

The emission maximum occurs for $\nu = \nu_{rest}$, where the velocity surface is defined by $x(\nu = \nu_{rest}) = 0$. For $\nu \leq \nu_{rest}$, the photodisk flux component is clearly as large as it can be, since the observer-facing hemisphere of the photosphere lies entirely above the velocity surface, and thus the photodisk flux component has no flux lost due to scattering. The limb component is a maximum, since only for the velocity surface at $x = 0$ does the limb region touch the photosphere where the source function is a largest. The limb component is

$$F(\nu_{rest})_{limb} = 2\pi \int_{r_{ph}}^{r_{max}} dr\, r S(r)(1 - e^{-\tau}), \tag{4.12}$$

where for all the models considered

$$\tau = \tau_{ph}(r_{ph}/r)^p. \tag{4.13}$$

This integral has no simple analytic solution. However, the upper limit is clearly

$$F_{limit} = 2\pi \int_{r_{ph}}^{r_{max}} dr\, r S(r). \tag{4.14}$$

The solution to the limiting integral is

$$\begin{aligned}
F_{limit} &= \pi I_{ph} \int_{r_{ph}}^{r_{max}} dr\, r \left(1 - \sqrt{1 - (r_{ph}/r)^2}\right) \\
&= \pi I_{ph}(r^2/2) \left[1 - \sqrt{1 - (r_{ph}/r)^2} + (r_{ph}/r)^2 \ln\left(r\left(1 + \sqrt{1-(r_{ph}/r)^2}\right)\right)\right]_{r_{ph}}^{r_{max}} \\
&= \pi I_{ph}(r_{max}^2/2)\Big[1 - (r_{ph}/r_{max})^2 - \sqrt{1-(r_{ph}/r_{max})^2} \\
&\qquad + (r_{ph}/r_{max})^2 \ln(r_{max}/r_{ph}) \\
&\qquad + (r_{ph}/r_{max})^2 \ln\left(1 + \sqrt{1-(r_{ph}/r_{max})^2}\right)\Big].
\end{aligned} \tag{4.15}$$

For $r_{ph}/r_{max} \ll 1$,

$$F_{limit} = \pi r_{ph}^2 I_{ph}(1/2)\left[\ln(r_{max}/r_{ph}) + \ln(2) - \frac{1}{2} - \frac{1}{8}(r_{ph}/r_{max})^2\right]. \tag{4.16}$$

The limiting emission maximum relative to the continuum flux is then

$$\frac{F_{net\,limit}}{F_{continuum}} = 1 + (1/2)\left[\ln(r_{max}/r_{ph}) + \ln(2) - \frac{1}{2} - \frac{1}{8}(r_{ph}/r_{max})^2\right]. \tag{4.17}$$

In the model calculations $r_{max} = 4r_{ph}$, and thus

$$\frac{F_{net\,limit}}{F_{continuum}} = 1.78575 \tag{4.18}$$

is the maximum relative flux that can be obtained in any calculation. It is clear that if $r_{max} \to \infty$, F_{limit} diverges logarithmically. The correct limb flux integral, given by equation (4.12), will not diverge due to the $(1 - e^{-\tau})$ factor. This factor behaves rather like a step function: for $\tau > 1$, $(1 - e^{-\tau}) \approx 1$, and for $\tau < 1$, $(1 - e^{-\tau}) \approx 0$. Thus there is an effective maximum radius given by

$$r_{Max\,effective} \approx (\tau_{ph})^{(1/p)} r_{ph}. \tag{4.19}$$

To obtain $r_{Max\,effective} > 4$ with p=7, τ_{ph} must be greater than 16384. Thus the maximum relative flux given by equation (4.18) would be expected for model calculations with $\tau_{ph} \gtrsim 16000$. If $r_{Max\,effective}$ is substituted into equation (4.17), then an expression is obtained for the maximum relative flux as a function of τ_{ph} for $\tau_{ph} \gg 1$:

$$\frac{F_{net\,limit}}{F_{continuum}} \approx 1.1 + \frac{\ln(\tau_{ph})}{2p}. \tag{4.20}$$

Thus the relative flux grows as the logarithm of τ_{ph}.

The location of the absorption minimum can be approximately determined by considering the specific intensity beam emitted along the radius collinear with the line of sight through the center of the spherical system:

$$I(r(\nu))_{emg} = \begin{cases} S(r(\nu))(1-e^{-\tau}) + I_{ph}e^{-\tau}, & \text{for } r > r_{ph}; \\ I_{ph}, & \text{for } r < r_{ph}, \end{cases} \tag{4.21}$$

where $r(\nu) = (\nu/\nu_{rest} - 1)/(Q/c)$. Note that since $S(r)$ is always less than I_{ph}, it follows that $I(r > r_{ph}) < I(r < r_{ph})$. The strongest radial dependence of $I(r)$ is in the exponential factors. The source function term starts to fall rapidly and the direct term starts to rise rapidly when $\tau \approx 1$. Thus the radius giving the minimum emergent intensity is given approximately by

$$r_{min} \approx (\tau_{ph})^{(1/p)} r_{ph}. \tag{4.22}$$

A more exact result can be easily derived. Taking the derivative of equation (4.21) for $r > r_{ph}$ gives

$$\frac{dI(r)}{dr} = (I_{ph} - S(r))\frac{p\tau_{ph} r_{ph}^{p}}{r^{p+1}}e^{-\tau} + S'(1-e^{-\tau}). \tag{4.23}$$

Setting the derivative to zero, re-arranging, and cancelling common factors gives

$$0 = \left[2\sqrt{1-(r_{ph}/r)^2}\,(1-W(r))\frac{(r/r_{ph})^2 p\tau_{ph}}{(r/r_{ph})^p} + 1\right]e^{-\tau} - 1 \tag{4.24}$$

If $r_{min} \gg r_{ph}$ and $\tau_{ph} > 1$, then $(1 - W(r)) \to 1$ and $(r/r_{ph})^2$ can be approximated by $(\tau_{ph})^{2/p}$. The resulting expression for r_{min} is

$$r_{min} = \left(\frac{(\tau_{ph})^{(1/p)}}{\left[\ln(1 + 2(\tau_{ph})^{(2/p)}p)\right]^{(1/p)}}\right) r_{ph}. \tag{4.25}$$

Alternatively, for $\tau \ll 1$ the exponential in equation (4.24) can be expanded to first order, and after some cancelation the equation

$$1 = \left(\sqrt{1-(r_{ph}/r)^2} + 1 - (r_{ph}/r)^2\right) p(r/r_{ph})^2 \tag{4.26}$$

is obtained. The resulting for expression r_{min} is

$$r_{min} = \left(\frac{1+1/p}{\sqrt{1+2/p}}\right) r_{ph}, \tag{4.27}$$

where there is no dependence on τ_{ph}. The actual minimum net flux in a line profile is the result of the integration over the all the specific intensity beams from the photodisk and limb. It seems unlikely that the r_{min} of the net flux should be very different from the r_{min} of the radial specific intensity. The other beams from the photodisk have a slower source function decay with the x coordinate as their beam paths along the line of sight are not radial; this compensates somewhat for the beam paths emerging from the photosphere at $x < r_{ph}$. Furthermore, it is clear that the minimum cannot occur for $x \lesssim r_{ph}$, since as x decreases from r_{ph} more and more of the photosphere surface is above the scattering velocity surface. The limb component of the flux has no minimum, and thus should not affect the above argument.

In model 4.1 flux profiles for a large range of τ_{ph} values were calculated with $p = 7$. The other parameters for the model can be found in Table 4.2. Fig. 4.1a displays the profiles. Fig. 4.1b, and 4.1c display the limb, and photodisk components of the profiles, respectively. From Fig. 4.1a it can be seen that the flux maximum increases in a roughly linear manner with the logarithm of τ_{ph} until $\tau_{ph} = 10^5$. The logarithmic growth with τ_{ph} was predicted by equation (4.20). When $\tau_{ph} = 10^5$, $r_{Max\ effective} \approx 5.2r_{ph}$ which exceeds the $r_{max} = 4r_{ph}$ used in calculating the model. Further increases of τ_{ph} would not change the profile any further unless r_{max} were increased. The ratio of the saturated maximum flux to the continuum flux is ≈ 1.78 which is in good agreement with the value 1.78575 obtained analytically for $r_{max} = 4r_{ph}$ (see equation (4.18)).

The v_{ph} parameter was chosen so that the Doppler shift associated with r_{ph} would be 100 Å. It is clear from Fig. 4.1a that the flux minimum wavelengths for $\tau_{ph} = 1$ and $\tau_{ph} = 10$ are about 100 Å below the rest wavelength of 5000 Å. Thus $r_{min} \approx r_{ph}$. From equation (4.27) for small τ_{ph}, the predicted value is $r_{min} = 1.00791r_{ph}$. The two values are quite consistent. It is clear that for low τ_{ph} values the flux minimum forms right at the photosphere. Thus unblended, weak supernova lines should allow immediate determination of the photospheric velocity from a measurement of the flux minimum wavelength (Branch 1980). It should be recalled, however, that the models assume that a well defined photosphere exists.

As larger τ_{ph} values are applied to model 4.1, the wavelength difference between the rest wavelength and the wavelength of the flux minimum increases slowly. In Table 4.3 a comparison is made of the model values for the flux minimum x coordinate, and the values obtained from minimizing the radial specific intensity beam equation exactly and in the various approximations. The agreement between the model ~~4.1 results~~ and the analytic exact x_{min} is quite good.

The results of model 4.2 are displayed in Fig. 4.2a, 4.2b, and 4.2c. This model has $\tau_{ph} = 5$,

TABLE 4.3.—Comparison of the x_{min} values from minimizing the radial specific intensity equation, and the x_{min} values from model 4.1.

τ_{ph}	$\tau_{ph}^{(1/p)}$	$\frac{(\tau_{ph})^{(1/p)}}{[\ln(1+2(\tau_{ph})^{(2/p)}p)]^{(1/p)}}$	Exact x_{min}	Model 4.1 x_{min}
10^{-4}	0.268270	0.282471	1.00791	—
10^{-3}	0.372759	0.368673	1.00795	—
10^{-2}	0.517947	0.486096	1.00801	—
10^{-1}	0.719686	0.646854	1.00861	—
10^{0}	1.00000	0.867345	1.01789	0.94
10^{1}	1.38950	1.16993	1.17359	1.02
10^{2}	1.93070	1.58530	1.54917	1.40
10^{3}	2.68270	2.15570	2.09402	2.01
10^{4}	3.72759	2.93931	2.85211	2.80
10^{5}	5.17947	4.01641	3.89877	3.56
10^{6}	7.19686	5.49770	5.34251	—

NOTE: The x_{min} values are all expressed in units of r_{ph}. The parameter $p = 7$.

and the power parameter p set to 4, 7, and 12. The $p = 4$ case has an extended blue wing to its absorption feauture that is not observed for supernova lines of moderate strength, and so 4 may not be an acceptable p value; the values of 7, and 12 have profiles that appear acceptable as supernova line profiles (Branch 1980). The value $p = 7$ is used for all the other model calculations since 7 is the favoured value in simple models of supernova atmospheres (see Chapter 2 section (c)).

The typical pure resonant scattering P-Cygni line loses more energy in the absorption feature than is added by the emission feature. In the physical picture assumed, this lost energy is due to scattered photons striking the photosphere and being thermalized there. These lost photons contribute to setting the thermal continuum emitted by the photosphere. Thus pure resonant scattering lines can be called non-energy-conserving. The only photons scattered toward the observer that strike the photosphere are those that are emitted in that part of atmosphere occulted by the photosphere. Therefore making the photosphere artificially transparent will make the P-Cygni line energy-conserving. Fig. 4.3a shows the behavior of resonance line profiles when the photosphere is made transparent to scattered radiation. Instead of having a relatively sharp flux maximum there is flux plateau that extends from roughly $\lambda(x = 0) = 5000\,\text{Å}$ to roughly $\lambda(x = -x_{ph}) = 5100\,\text{Å}$. The flux contribution of the atmosphere's source function is nearly constant when the velocity surface is touching the photosphere. The photospheric flux contribution is constant when the velocity surfaces are entirely behind the observer-facing hemisphere of the photosphere. For the non-transparent photosphere these contributions are never constant simultaneously, but for the transparent photosphere they are for the wavelength range corresponding to velocity surfaces between $x = 0$ and $x = -x_{ph}$, whence the plateau. Due to the numerical integration the plateau in Fig. 4.3a has small wiggles. The model conserved energy to better than 5% for the four cases of τ_{ph} that were examined.

Model 4.4 was calculated to study the effects on flux profiles of using the Hamilton phase-matrix. Recall that with the phase-matrix coefficient E_1 set to 0 the phase-matrix reduces to isotropic non-polarizing scattering, and that set to 1 the scattering is pure Rayleigh scattering. Fig. 4.4a shows that the profiles are not greatly altered when E_1 is varied from 0 to 1. There is a slight decrease in the flux maximum as anisotropic scattering is increased, and a slight increase in the absorption minimum. These alterations can be understood from the Rayleigh phase function that describes the scattered total specific intensity as a function of the angle Θ between the incident and scattered beams:

$$p(\Theta) = \frac{3}{4}(1 + \cos^2 \Theta). \tag{4.28}$$

This function shows that there is a 2-to-1 ratio in magnitude between forward and right angle scattered beams. Thus forward scattering should be stronger for Rayleigh scattering than for isotropic scattering. The absorption feature of a P-Cygni line, which owes in part to forward scattering (as well as to unscattered flux), would therefore tend to be filled in as the scattering phase-matrix became more Rayleigh-like. Furthermore, the emission feature, due more to nearly right angle scattering, would tend to be diminished when there is less right angle scattering. However, the effects of increasing E_1 are not very dramatic as Figures 4.4 show. The lack of striking effects is partially due to the fact that most of the scattering occurs close to the photosphere where the source function is rather isotropic since it is an average of specific intensity beams over the large solid angle subtended by the photosphere. The lack of striking effects is also partially due to the fact that the net flux is the integral of all the specific intensity beams emitted by a velocity surface; this tends to average away the effects of anisotropic scattering. Since the effects of anisotropic scattering are so small for flux profiles, they probably cannot be detected. Isotropic Sobolev calculations, such as those done by Branch and collaborators (1980; Branch *et al.* 1982, 1983, 1985), and the anisotropic calculations are equally adequate in describing supernova flux spectra.

Fig. 4.5a displays the results of a model with a Planck rather than a constant continuum. The three Planck continua used for the model had photospheric temperature T_{ph} set to 7244 K, 5796 K, and 4830 K. These temperatures were chosen so the wavelength of the maxima of the Planck continua would be 4000 Å, 5000 Å, and 6000 Å, respectively. Recall that all the profiles have been normalized to their value at the lowest wavelength displayed in the figures. Without the normalization the 7244 K profile's average height would be roughly 6 times greater than that of the 4830 K. It is clear that introducing slopes to the photospheric continua of the magnitude considered for these profiles has little qualitative affect on the profile shape or on the interpretation of the profile shape.

Fig. 4.6a displays the effect of blending two weak P-Cygni lines of equal strength. At a separation of 400 Å, the profiles are largely independent. At a separation of 100 Å, the lines are strongly blended. In this case the minimum of the absorption feature of the 5100 Å line falls exactly on the location of what would have been the emission flux maximum of the 5000 Å line if no blending had been present. The emission maximum of 5000 Å line is largely suppressed. However, the absorption minima of the two lines are quite apparent. Absorption minima are probably of greater usefulness than emission maxima in line identification (Branch 1980). At zero wavelength separation, the two lines are fully blended, and give the appearance of a single line. The two lines are not, however, effectively one line of double strength, since the calculation continues to treat their resonance regions as non-overlapping. (Closely spaced lines are discussed in Chapter 2 section (f).)

A summary of important conclusions that can be drawn from spherical model calculations will now be given. Most of these conclusions were well known before this survey was done. (1) For weak to moderate lines with $\tau_{ph} \lesssim 100$ the wavelength of the flux minimum is Doppler shifted from the line rest wavelength by approximately the photospheric velocity v_{ph}. This allows v_{ph} to be easily obtained from spectral data provided a sharp photosphere is assumed. (2) The difference for flux profiles between assuming isotropic nonpolarizing scattering or assuming Rayleigh scattering is slight. (3) Flux profiles are not affected qualitatively by the slope of the continuum. (4) In fitting supernova lines with Sobolev calculations it is probably best to give more weight to fitting the absorption features. The absorption features for pure resonance scattering are slightly more prominent than the emission features, since more energy is lost in the absorption than is gained in the emission. Also, as indicated above, the absorption minima are less obscured when lines are strongly blended.

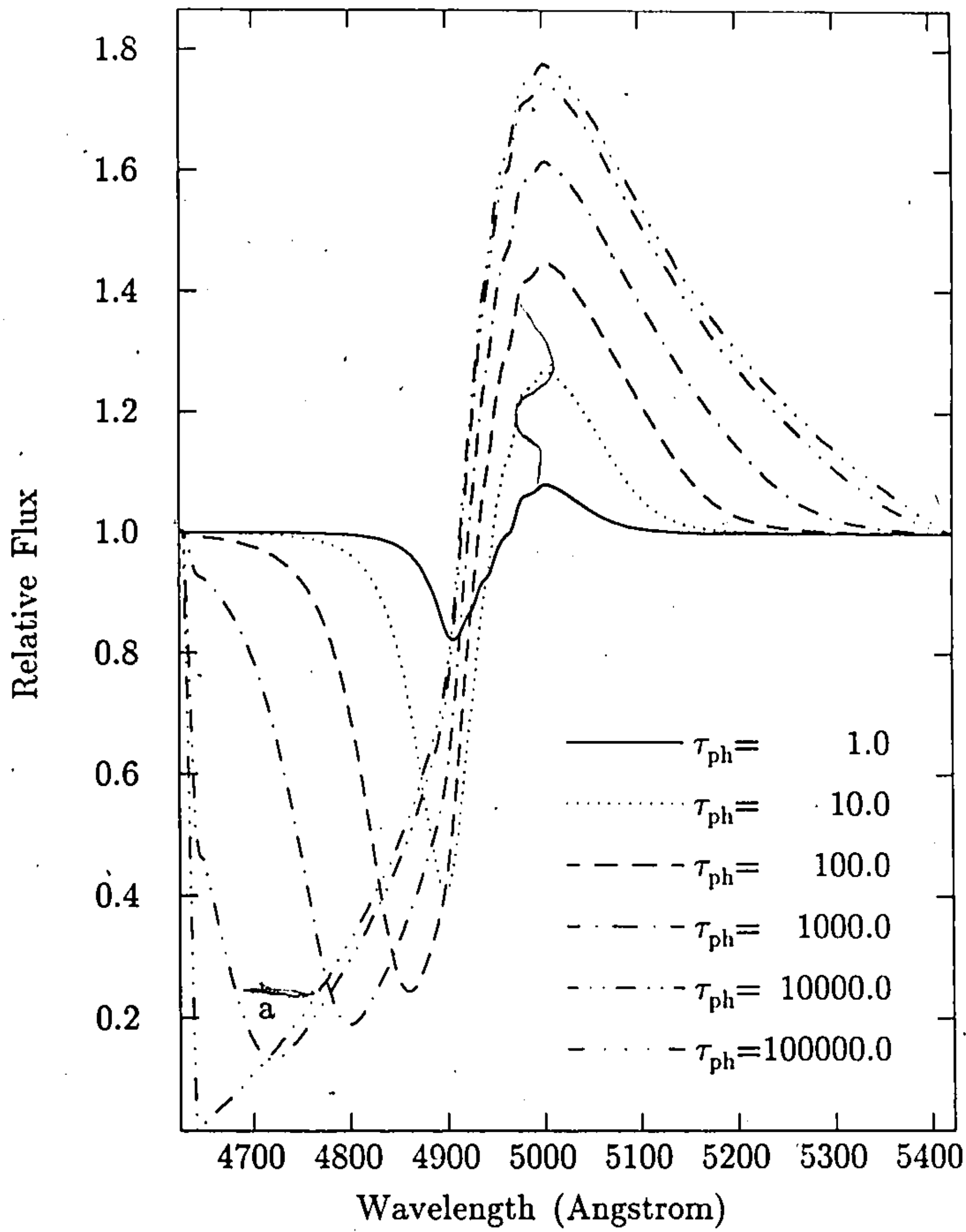

Fig. 4.1a. Flux profiles for a spherical model with varied photospheric optical depth, τ_{ph}. The absorption minimum wavelength of 4900 Å for the $\tau_{ph} \leq 10$ cases is Döppler shifted from the rest wavelength by a velocity v_{ph}. This shows for weaker lines that the absorption minimum wavelength can be used to determine the photospheric velocity. For stronger lines ($\tau_{ph} > 10$) the absorption minimum wavelength corresponds to velocities greater than v_{ph}.

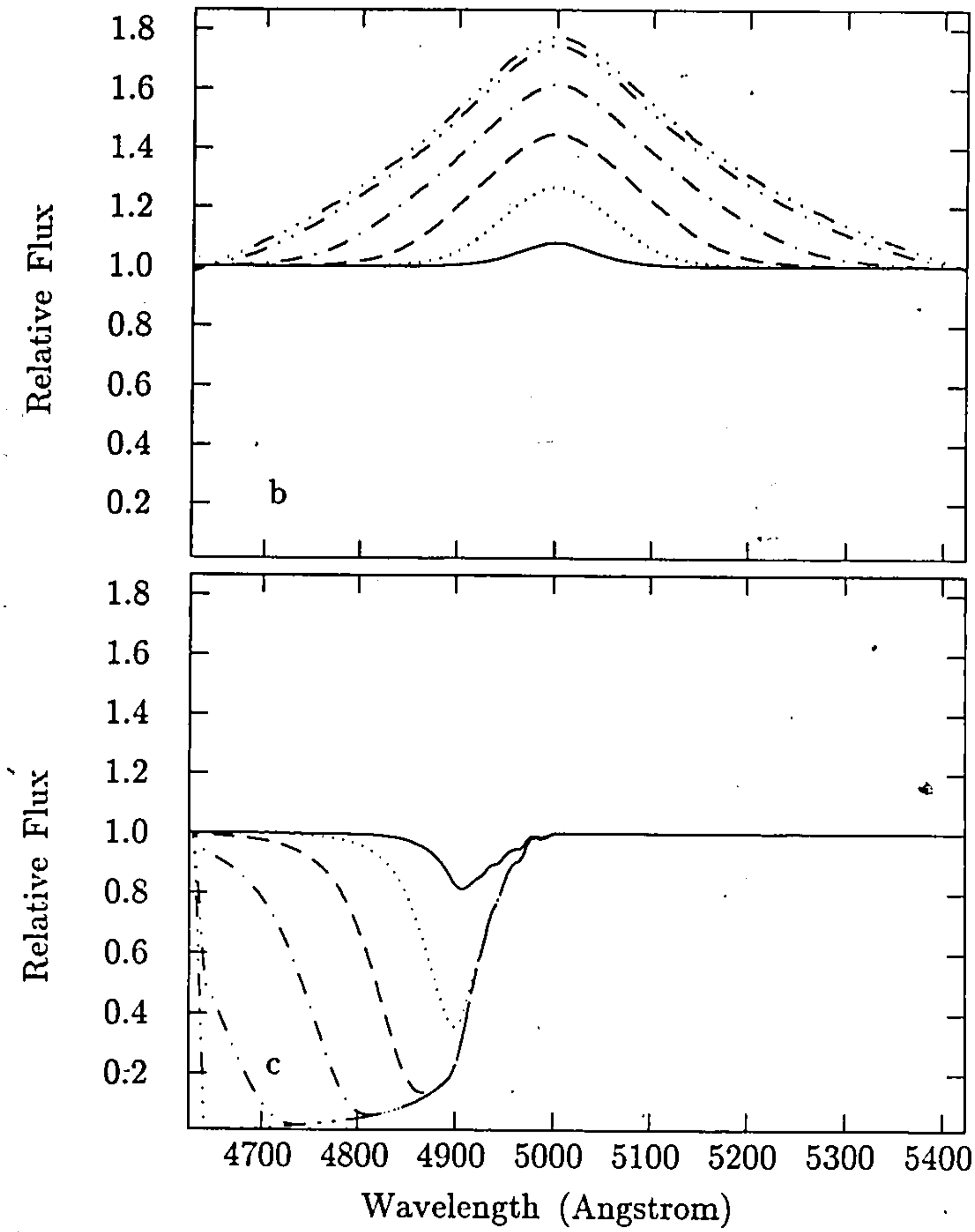

Fig. 4.1b and c. The limb and photodisk components of the flux profiles of Fig. 4.1a. The small wrinkles in the photodisk profiles near 5000 Å are artifacts of the numerical integration for the flux.

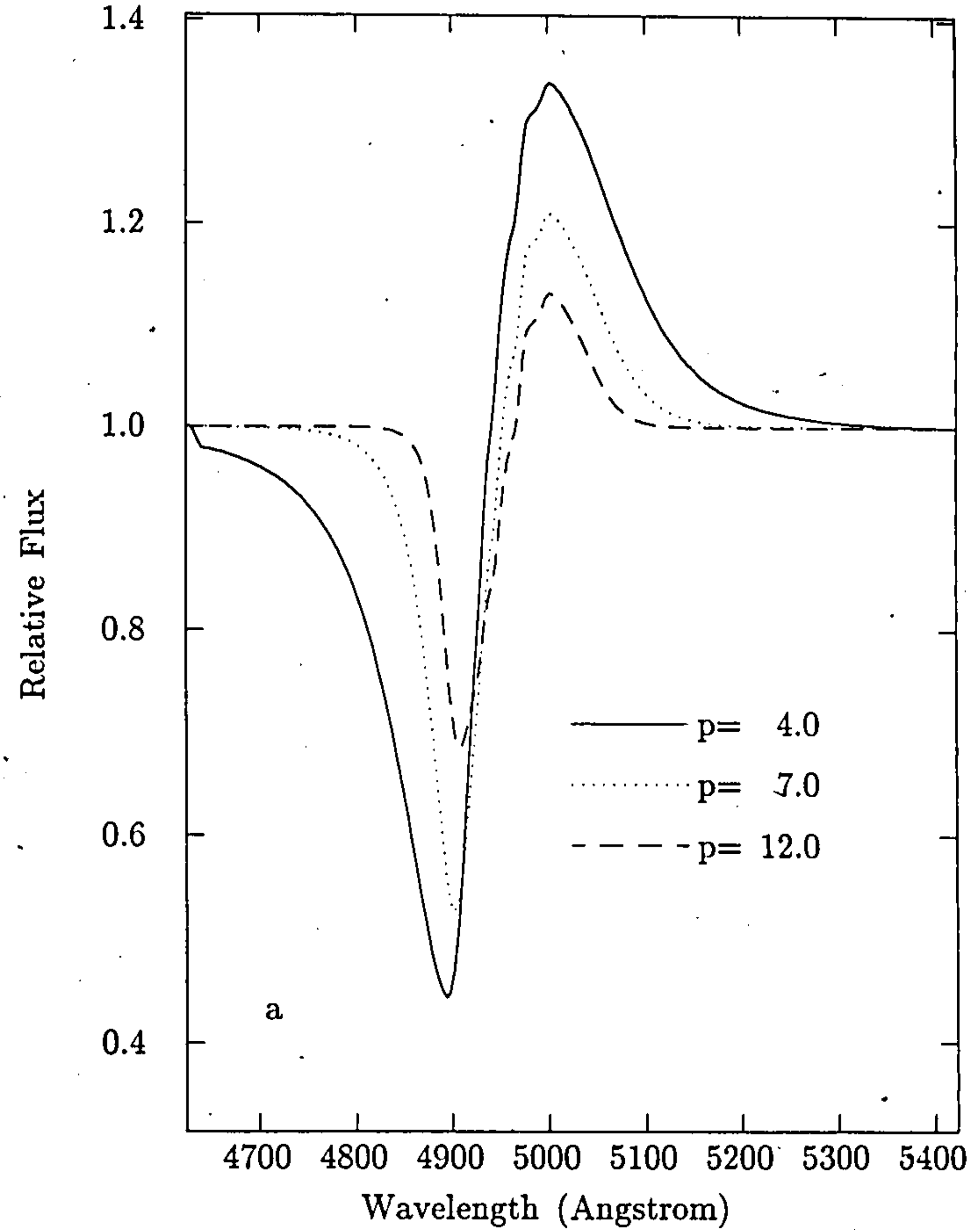

Fig. 4.2a. Flux profiles for a spherical model with varied power p, where the optical depth function is $\tau(r_g) = \tau_{ph}(r_{g_{ph}}/r_g)^p$. The extended blue wing of the absorption feature for the $p = 4$ case is not observed for supernovae lines of moderate strength (Branch 1980).

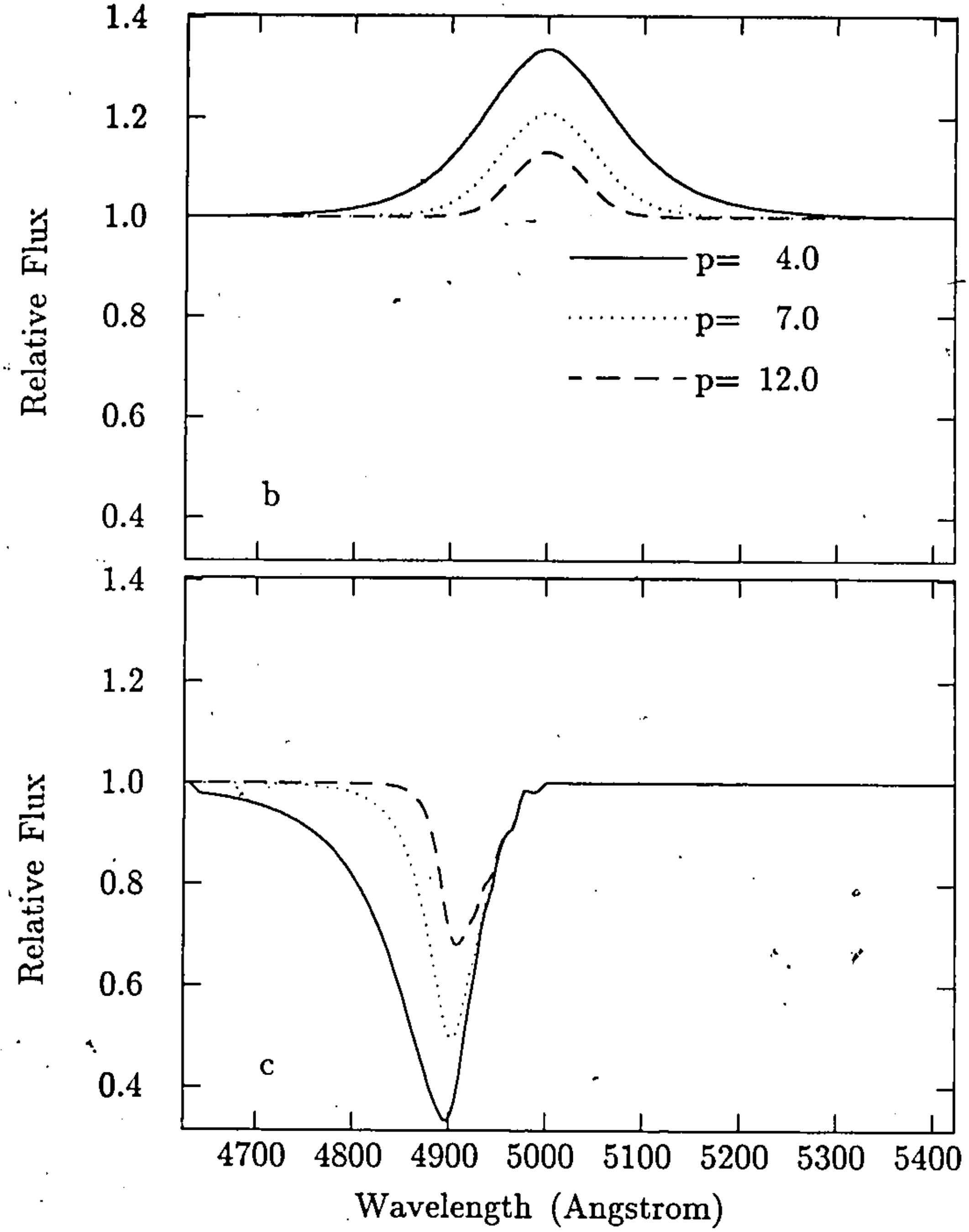

Fig. 4.2b and c. The limb (Fig. 4.2b), and photodisk (Fig. 4.2c) components of the flux profiles of Fig. 4.2a. The small wrinkles in Fig. 4.2c near 5000 Å are artifacts of the numerical integration for the flux.

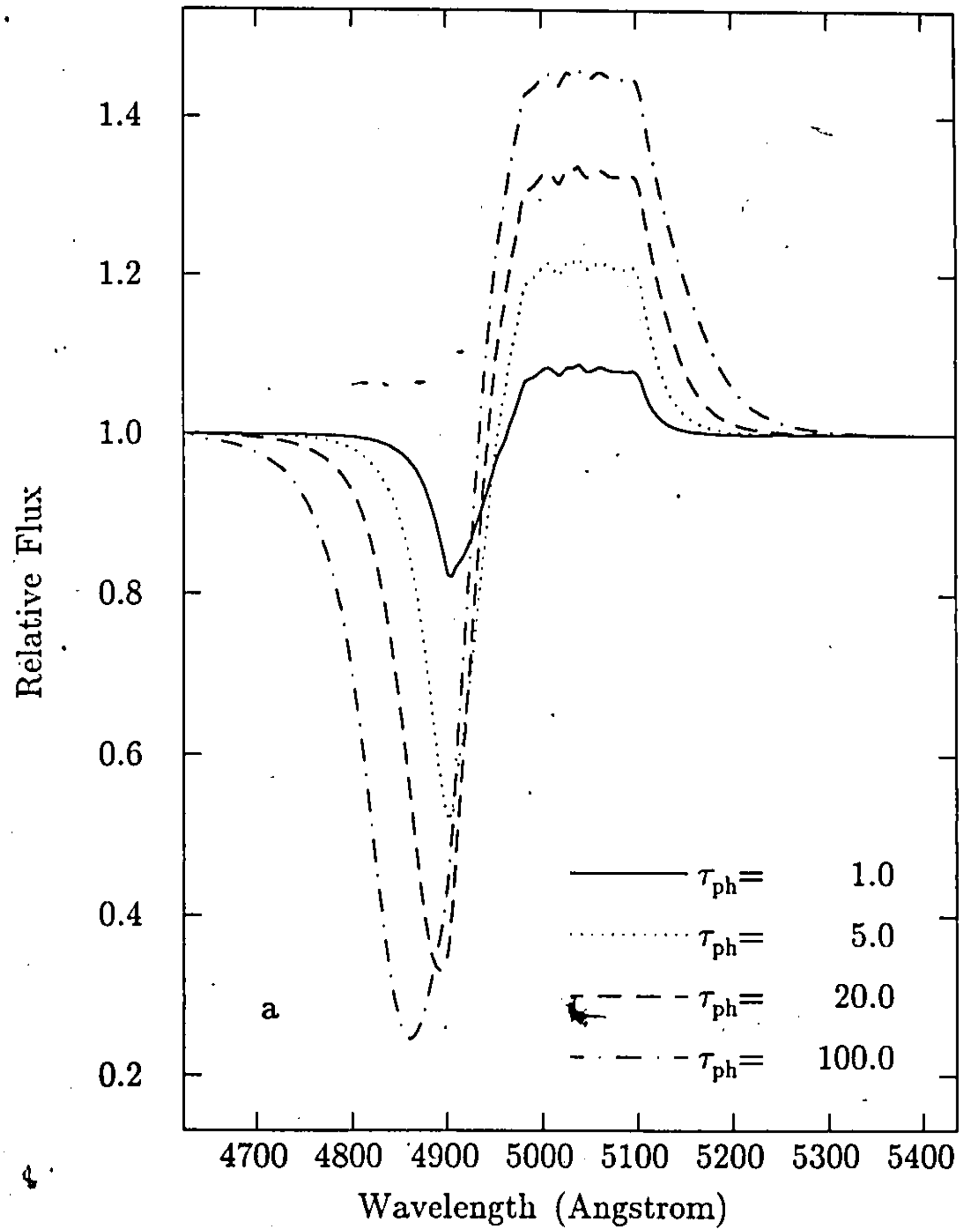

Fig. 4.3a. Flux profiles for a transparent-photosphere spherical model with varied photospheric optical depth τ_{ph}. Transparent-photosphere model is not physical, but is used to demonstrate energy conservation; the integrated emission flux ought to equal the integrated flux lost to absorption. The models shown in the figure conserved energy to better than 5%. The small wrinkles in the emission plateaus are artifacts of the numerical integration.

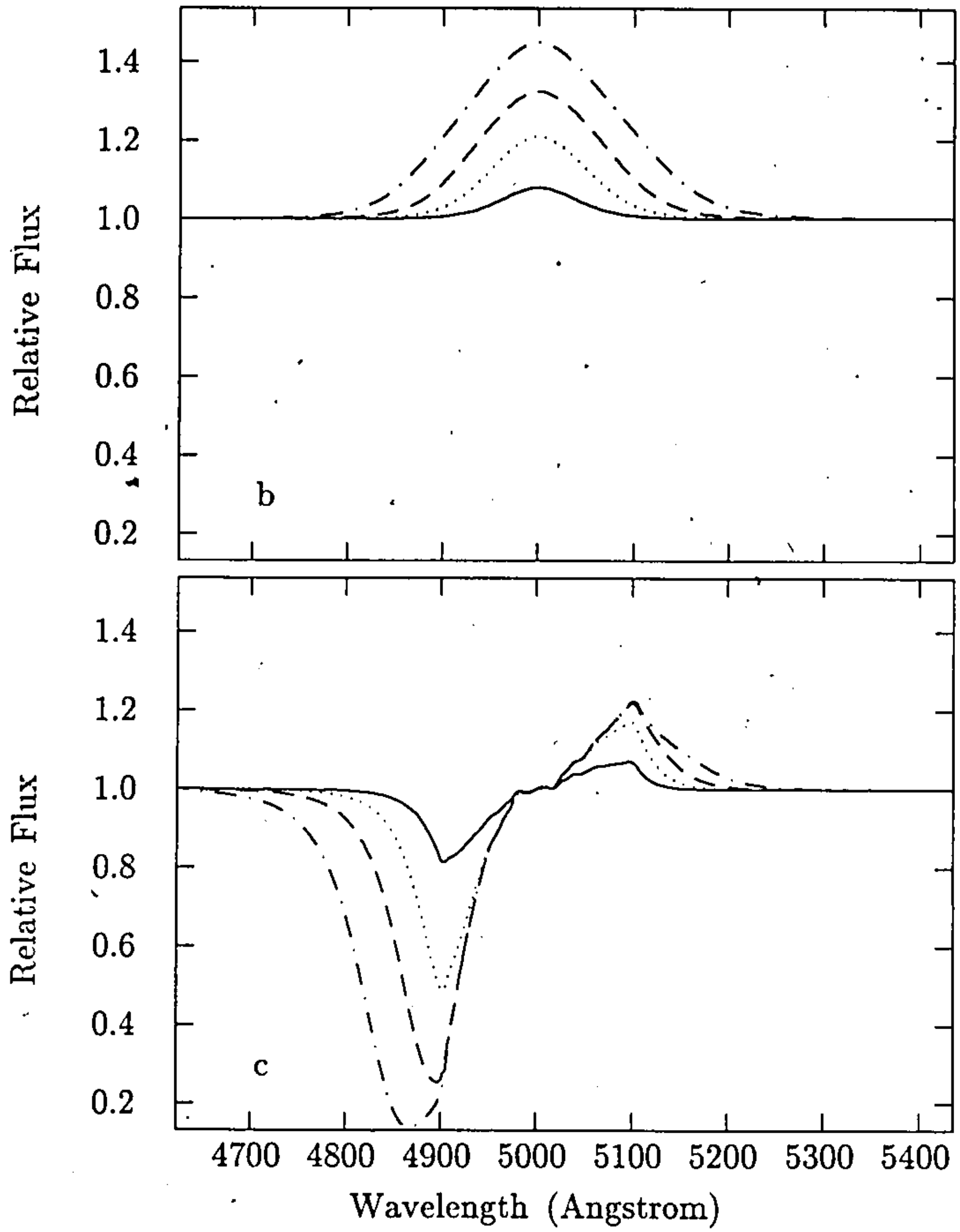

Fig. 4.3b and c. The limb and photodisk components of the flux profiles of Fig. 4.3a.

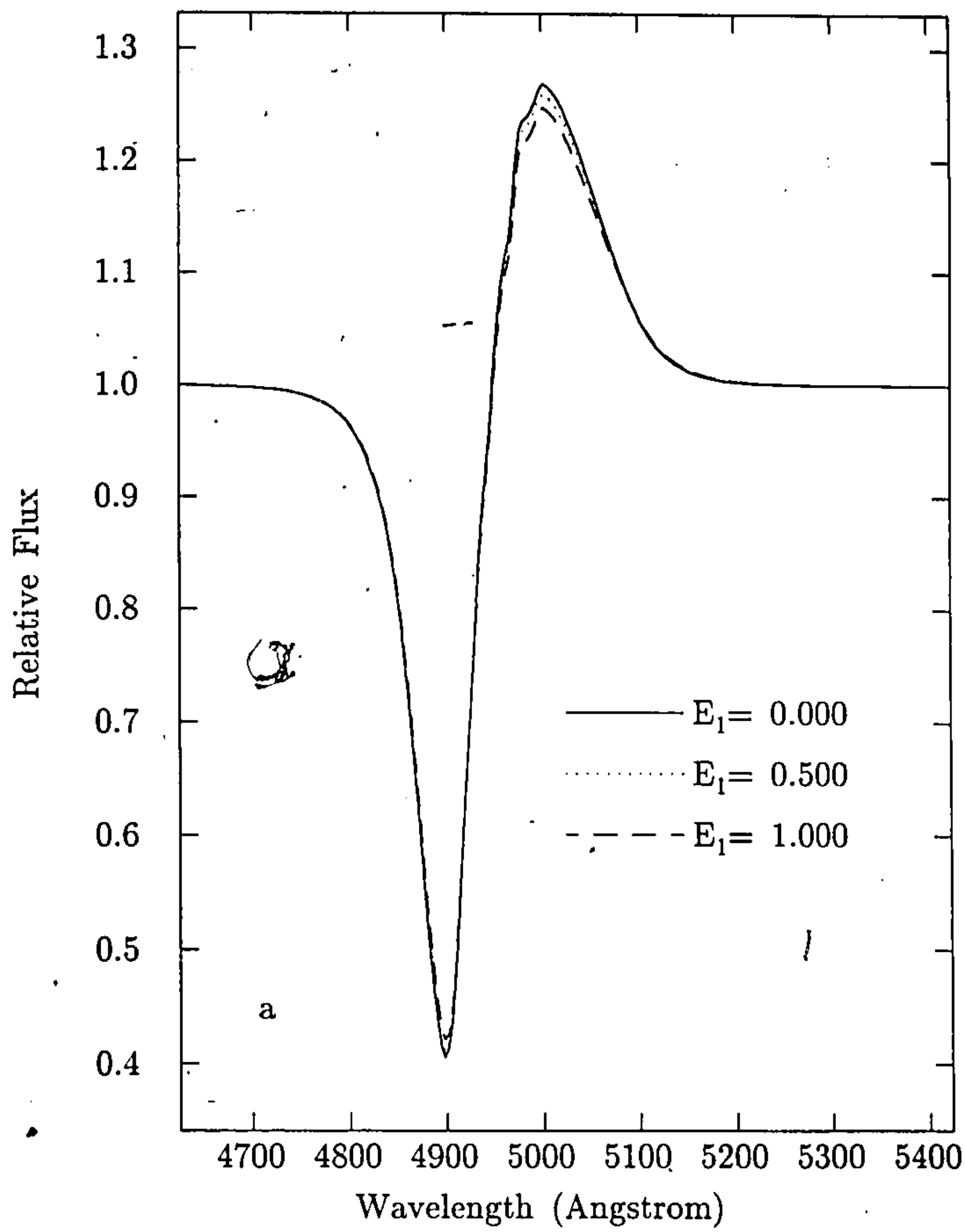

Fig. 4.4a. Flux profiles for a spherical model with varied phase-matrix coefficient E_1. $E_1 = 0$ for isotropic, nonpolarizing scattering, and $E_1 = 1$ for pure Rayleigh scattering. There is little change in flux profiles as the E_1 coefficient is varied over its full range.

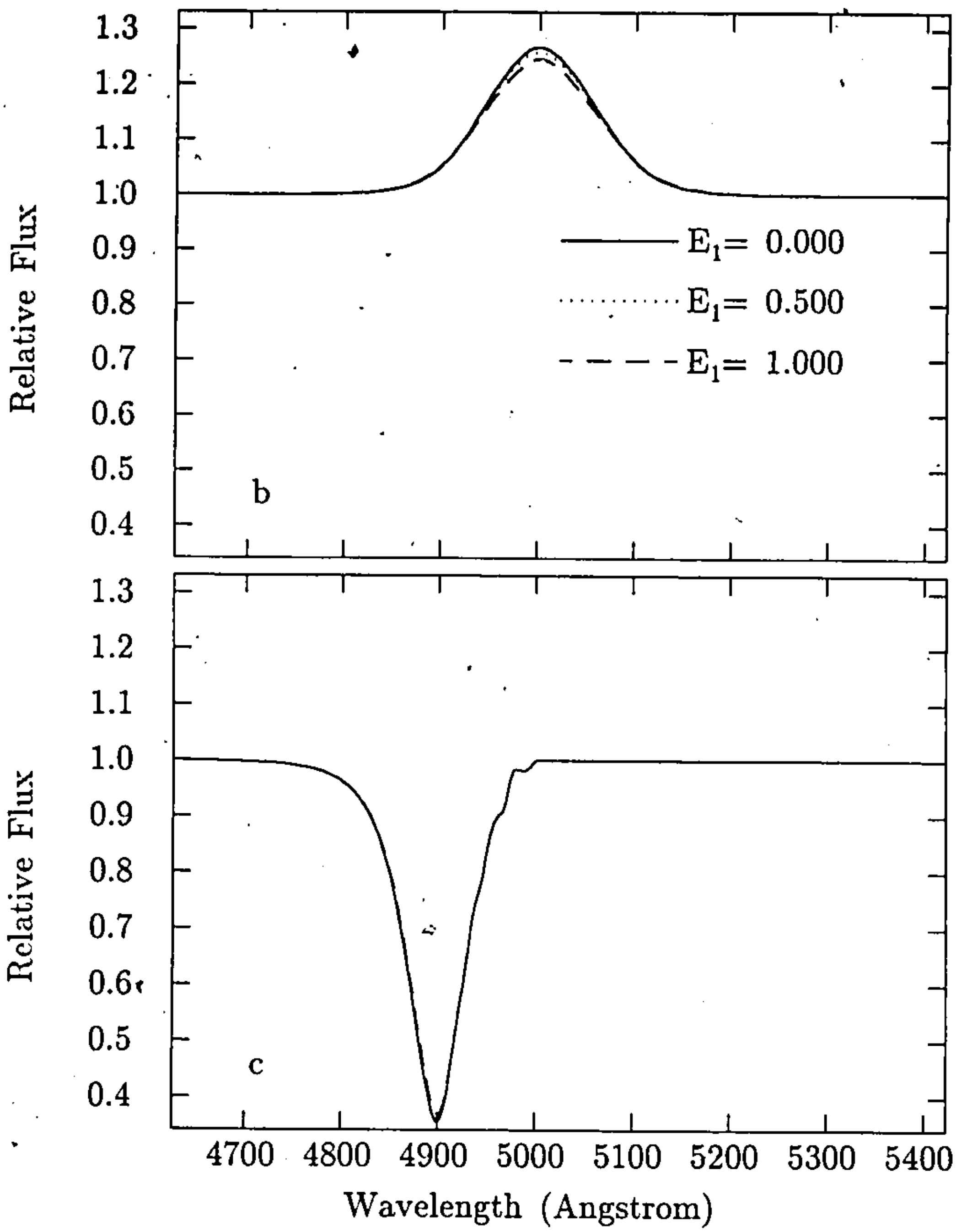

Fig. 4.4b and c. The limb and photodisk components of the flux profiles of Fig. 4.4a.

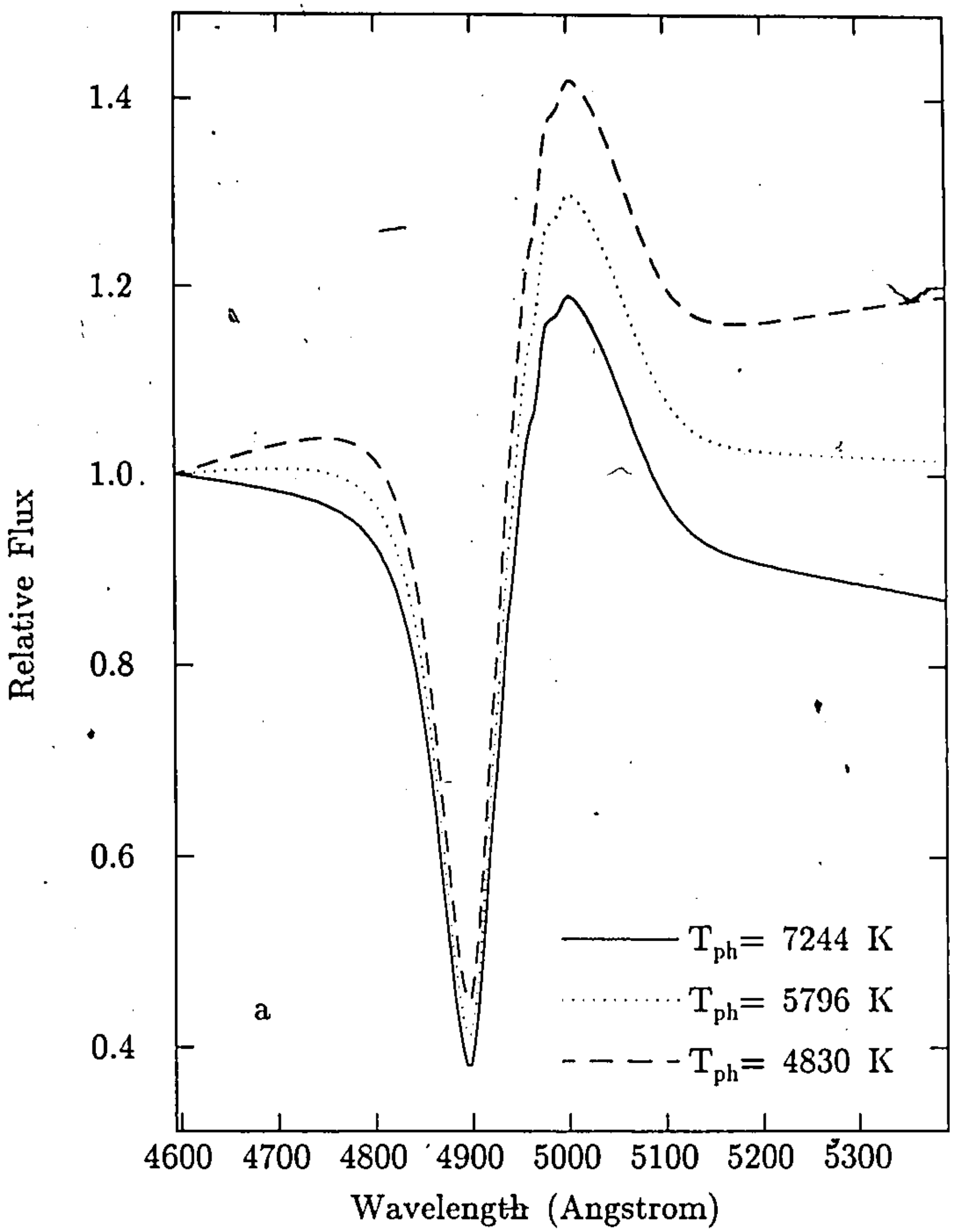

Fig. 4.5a. Flux profiles for a spherical model with a Planck continuum emitting photosphere and varied photospheric temperature T_{ph}. The profiles are each normalized to their values at smallest wavelength shown on the figure.

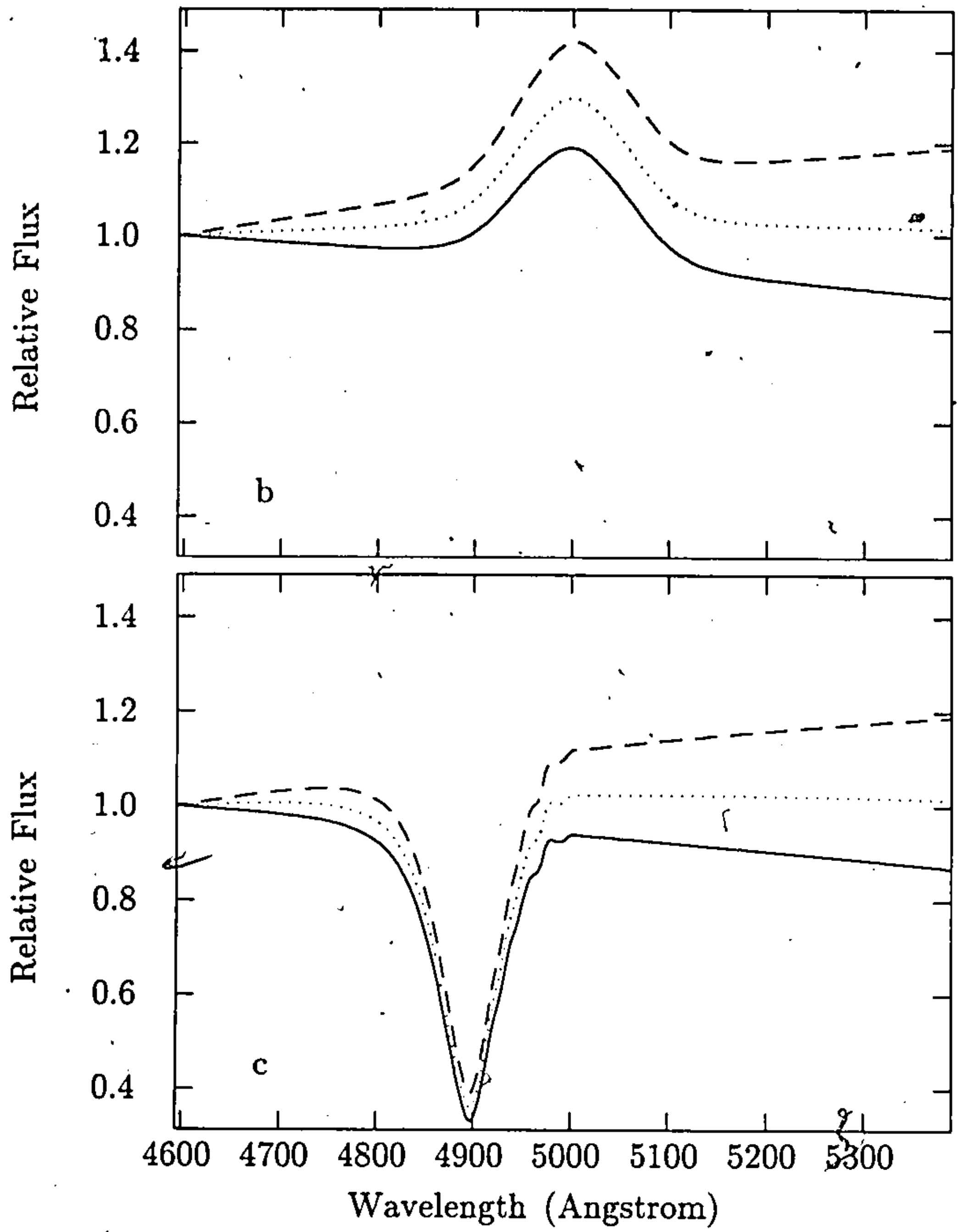

Fig. 4.5b and c. The limb and photodisk components of the flux profiles of Fig. 4.5a.

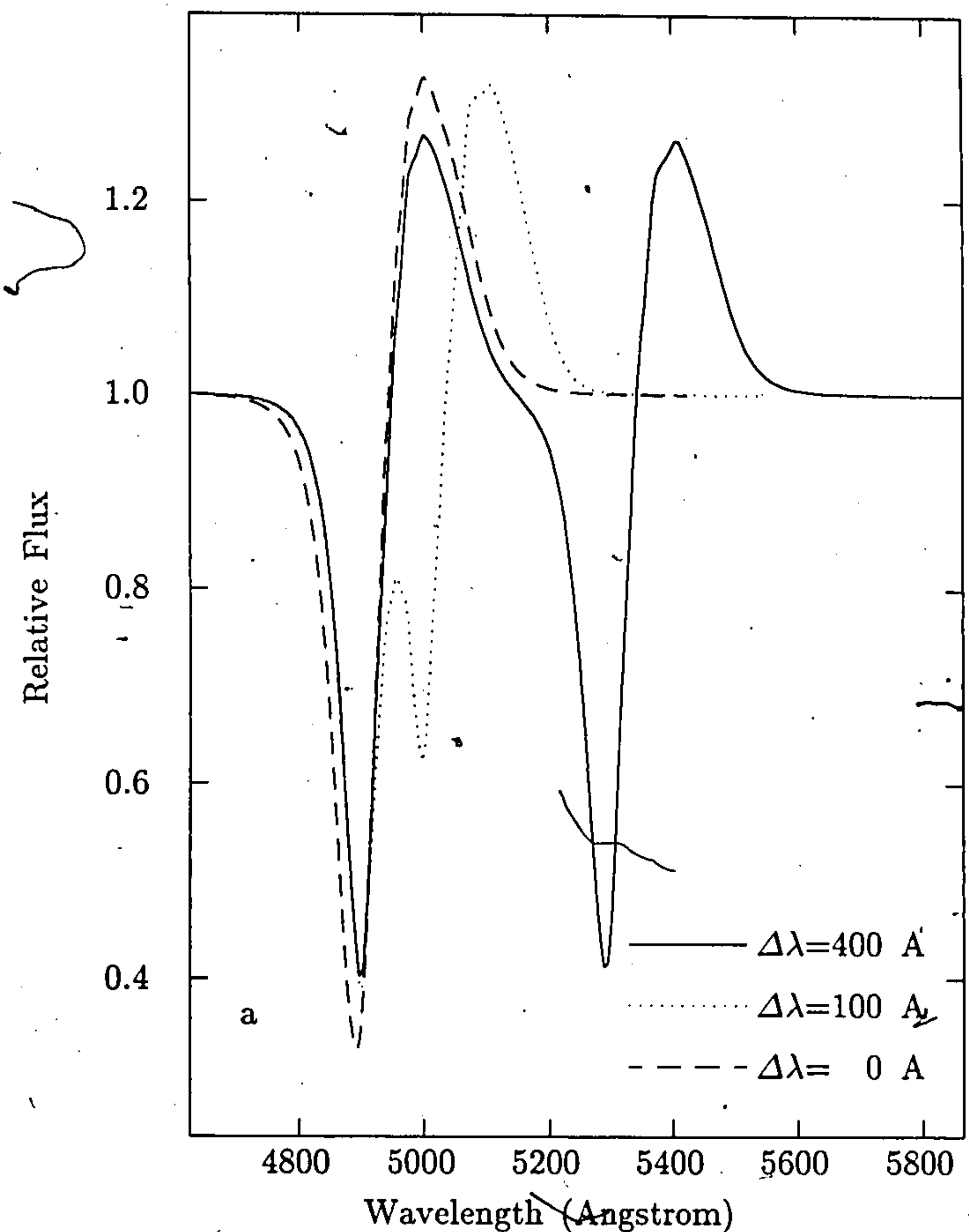

Fig. 4.6a. Flux profiles for a spherical model with two lines and varied separation between the lines. For $\Delta\lambda = 400\,\text{Å}$ the lines are nearly independent. For $\Delta\lambda = 100\,\text{Å}$ the lines are strongly blended, and the emission maximum of the 5000 Å line is largely suppressed. For $\Delta\lambda = 0\,\text{Å}$ the two lines give the appearance of being a P-Cygni single line.

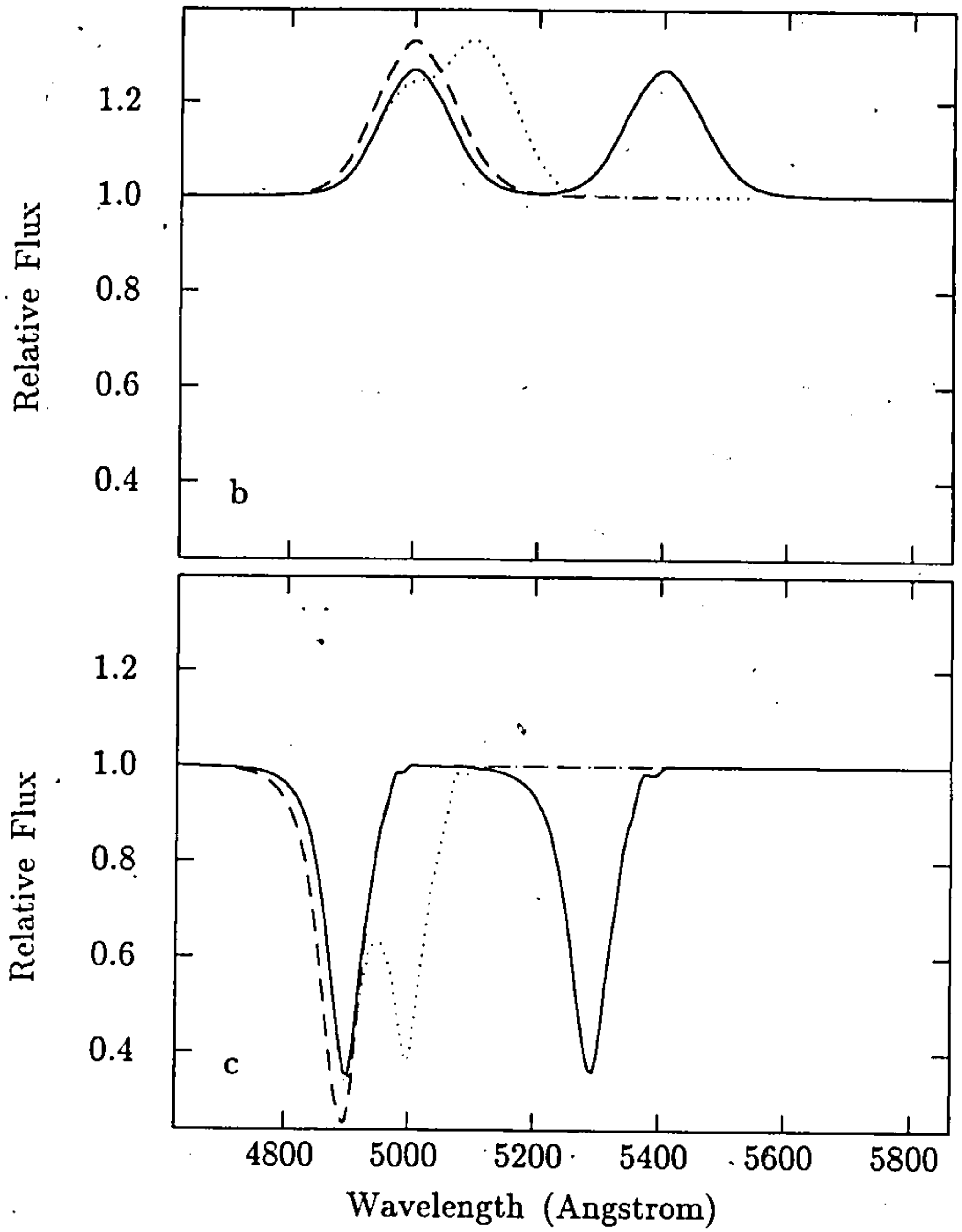

Fig. 4.6b and c. The limb and photodisk components of the flux profiles of Fig. 4.6a.

c) Prolate Ellipsoid Models

In this section the flux and polarization profiles of prolate ellipsoid models are presented and discussed. For convenience the models are labeled by their figure number. Thus the results of model 4.7 are displayed in Figures 4.7. The parameters for all the prolate models examined are given in Table 4.4. All the flux profiles displayed have been normalized to the flux value at the lowest wavelength shown on the figures.

For convenience in the following discussion it is useful to set some conventions about the geometry of the atmosphere and photosphere. The symmetry axis of the ellipsoid is along the z axis. The x axis lies in the plane containing the z axis and the line of sight to a distant observer. The y axis is perpendicular to this plane. The x' axis is along the line of sight and the z' axis is perpendicular to the x' axis and to the y axis. There is no need for a primed y axis as all the inclinations are rotations about the y axis. When the inclination angle is set to 90° the primed axes are the same as the unprimed axes. When expressions "in front of the photosphere" and "behind the photosphere" are used, what is meant are those points in the photodisk region with positive and negative x' coordinates, respectively. The expression "beside the photosphere" refers to those points in the limb region that have $|z'| \lesssim c'$, where c' is the semi-major axis of the projection of the photosphere. The expressions "above the photosphere" and "below the photosphere" refer to those points in the limb region that have $z' \gtrsim c'$ and $z' \lesssim -c'$, respectively.

For each model eight figures have been prepared displaying different calculated features of the model. These eight figures are labeled alphabetically. The a-figures display the net flux profiles. The b-figures display the net polarization profiles. The c-, d-, e-, and f-figures display the limb flux component, the limb polarization component, the photodisk flux component, and the photodisk polarization component, respectively. The g-figures displays the maximum and minimum polarization of the Sobolev-H calculation as a function of a varied parameter. The emission maximum polarization calculated by McCall's prescription (see Chapter 3 section (b)) is also displayed in the g-figures. The g-figure for the model with varied asymmetry also plots the Shapiro and Sutherland results for continuum polarization calculated using the Chandrasekar solution (see Chapter 3 section (a)). The h-figures display the same results as those of the g-figures, but with the scale chosen to make the Sobolev-H results more prominent.

Note that for each model not all of the eight figures are discussed, but only the figures that

TABLE 4.4.—Parameters for the prolate models of section (c).

Model (Figure)	Continuum$_{ph}$ E_1 p	Pro/Oblate $r_{g_{max}}$ T_{ph}	v_{ph} ϵ θ_{incl}	λ_{rest} ξ τ_{ph}
4.7	Constant 1 7	Prolate $4 \times r_{g_{ph}}$ †	$.6 \times 10^9\,\mathrm{cm\,s^{-1}}$ 0 90°	5000 Å * 10
4.8	Constant 1 7	Prolate $4 \times r_{g_{ph}}$ †	$.6 \times 10^9\,\mathrm{cm\,s^{-1}}$ 0 *	5000 Å .5 10
4.9	Constant 1 7	Prolate $4 \times r_{g_{ph}}$ †	$.6 \times 10^9\,\mathrm{cm\,s^{-1}}$ 0 90°	5000 Å .5 *
4.10	Planck 1 7	Prolate $4 \times r_{g_{ph}}$ *	$.6 \times 10^9\,\mathrm{cm\,s^{-1}}$ 0 90°	5000 Å .5 10
4.11	Constant 1 7	Prolate $4 \times r_{g_{ph}}$ †	$.6 \times 10^9\,\mathrm{cm\,s^{-1}}$ 0 90°	* .5 10

NOTE: The "*" indicates that the parameter is being varied for this model. The "†" indicates that the parameter is irrelevant for this model.

present features of interest. However, for reference all eight figures are presented.

The convention used in plotting the polarization is that positive polarization means that the radiation field component aligned with the z' axis is larger than the component aligned with the y axis. Thus the quantity displayed in the b-figures is

$$P(net) = \frac{F_z(net) - F_y(net)}{F(net)}, \tag{4.29}$$

where

$$F(net) = F_z(net) + F_y(net). \tag{4.30}$$

The quantity displayed in the d-figures is

$$P(limb) = \frac{F_z(limb) - F_y(limb)}{F(net)}, \tag{4.31}$$

rather than

$$P(limb \quad alone) = \frac{F_x(limb) - F_y(limb)}{F(limb)}. \tag{4.32}$$

This choice was made to retain the same plotting scale for the b-figures and the d-figures since clearly $P(limb \quad alone) \gg P(limb)$. Similarly, the quantity displayed in f-figures is

$$P(photodisk) = \frac{F_x(photodisk) - F_y(photodisk)}{F(net)}. \tag{4.33}$$

The model 4.7 has a varied asymmetry parameter ξ_{pro}. The photospheric optical depth $\tau_{ph} = 10$ and the inclination angle $\theta_{incl} = 90°$. The photospheric optical depth is typical of supernova lines of moderate strength. The choice of $\theta_{incl} = 90°$ maximizes the asymmetry of the projection of the atmosphere, and thus maximizes polarization. The other parameters are shown in Table 4.4. Recall

$$\xi_{pro} = 1 - (a/c) \qquad \text{for} \quad a < c \qquad \text{(prolate)}, \tag{4.34}$$

and

$$(c/a) = \frac{1}{1 - \xi_{pro}}. \tag{4.35}$$

Thus the case with $\xi_{pro} = .5$ is a spheroid with a 50% asymmetry. The case with $\xi_{pro} = .998$ is 500 times longer than it is wide. It is wrong, however, to think of the $\xi_{pro} = .998$ case as a one dimensional object. Recall that an atmosphere with $r_{s_{max}} = 4r_{s_{ph}}$ is 4 times bigger than the photosphere in all dimensions. Thus the $\xi_{pro} = .998$ case has a long extended atmosphefe above and below a long extended photosphere.

Fig. 4.7a displays the flux profiles for model 4.7. Qualitatively, the profiles are not greatly affected by the asymmetry variation. However, the total increase in asymmetry causes the absorption minimum to increase by $\approx .05$ in relative flux, and the emission maximum to decrease by $\approx .075$. The two extrema vary in a roughly linear manner with ξ_{pro}. These changes in the flux profiles do not owe to the Rayleigh scattering, nor to the choice of $r_{s_{max}}$. The ratio of limb to photodisk area does not change, and so that is not a factor. The variation in the extrema probably owes to the changes in the relative amounts of solid angle subtended at points in the limb and photodisk regions.

In Fig. 4.7b the net polarization profiles are displayed. The polarization magnitude over most of the wavelength interval appears to increase from zero in a roughly linear manner with increasing asymmetry. The profile consists of two distinct features: a positive emission polarization feature and a negative absorption polarization feature. A comparison of the profiles of Fig. 4.7b to the limb components in Fig. 4.7d and the photodisk components in Fig. 4.7f shows that the emission feature owes almost entirely to the limb and the absorption feature to the photodisk. The profiles of Fig. 4.7d show that the limb polarization is largely symmetric about the rest wavelength. The slight asymmetry owes to $F(net)$ in the denominator of equation (4.31) for P(limb); $F(net)$ is asymmetric due to occultation by the photosphere. The comparison of the flux and polarization components both for the limb and the photodisk show a strong correlation between the flux and polarization features. This is not surprising since the flux features owe to scattering, and scattering is, of course, the origin of all the polarized radiation in these models.

The emission polarization feature owes to scattering from the sides, and above and below the photosphere. The scattering into the direction of the line of sight tends to be right-angle scattering which has a maximum polarizing effect. The alignment of polarized radiation from right-angle scattering from an elongated source tends to be along the long axis of the source. To demonstrate this consider an infinite cylindrically symmetric, unpolarized source emitting a constant specific intensity. Consider also a Rayleigh scattering point that could be either a resonance scattering ion with $E_1 = 1$ in the weak scattering limit where equations (2.147) apply, or a free electron. A coordinate system has its origin at the point, its z axis parallel to the axis of symmetry of the source, and its x axis is a line of sight to an observer. The cylindrical source is centered at some point $(0, y_{cyl})$ in the x-y plane. Using equations (2.129), radiation scattered from the point toward the observer has the polarization

$$P = \frac{D_1 - D_5 + D_4}{D_1 + D_5 - D_4}, \tag{4.36}$$

where $\mu = \cos\theta = 0$ and $\phi = 0$. Using equations (2.130) gives

$$\begin{aligned} P &= \frac{\oint d\Omega' \, (1 - 3\mu'^2 + (\mu'^2 - 1)\cos 2\phi')}{\oint d\Omega' \, (3 - \mu'^2 - (\mu'^2 - 1)\cos 2\phi')} \\ &= \frac{-\int_{\pi/2-\Delta/2}^{\pi/2+\Delta/2} d\phi' \, \cos 2\phi'}{4\Delta + \int_{\pi/2-\Delta/2}^{\pi/2+\Delta/2} d\phi' \, \cos 2\phi'} = \frac{-(1/2)\sin 2\phi|_{\pi/2-\Delta/2}^{\pi/2+\Delta/2}}{4\Delta + (1/2)\sin 2\phi|_{\pi/2-\Delta/2}^{\pi/2+\Delta/2}} \\ &= \frac{\sin\Delta}{4\Delta - \sin\Delta}, \end{aligned} \tag{4.37}$$

where Δ is the ϕ-angle subtended by the cylindrical source at the scattering point. For $\Delta = \pi$, the scattered beam is unpolarized. For $\Delta < \pi$, the scattered flux is polarized and the polarization is positive (i.e., the polarization is aligned with the z axis). The maximum polarization is 1/3 for $\Delta = 0$ (i.e. a line source). This simple demonstration shows why the polarization is aligned with the long axis of the prolate ellipsoid model. The calculated emission polarization feature never reaches the 1/3 value for several reasons: (1) the photosphere is not a line source, (2) the model photosphere is not an infinite cylindrical source, even when $\xi_{pro} \to \infty$, since there is always some radiation with cancelling polarization scattered from the short ends of the photosphere, (3) the scattering is not extremely weak, and so there is the depolarization effect of multiple scattering, and (4) there is dilution of the polarized flux by the strong unpolarized flux from the photodisk.

There is a large negative polarization feature associated with the flux absorption feature (see Figures 4.7a and 4.7b). Note that most of the scattered flux that forms the absorption feature is scattered from points that are in front of the photosphere. To explain the negative polarization feature consider again the infinite cylindrical system introduced above with the exception that the cylindrical source is now centered at $(x_{cyl}, 0)$, where $x_{cyl} < 0$. Allowing for the change in the centering of the cylindrical source, equation (4.37) yields

$$P = \frac{-\sin\Delta}{4\Delta + \sin\Delta}. \tag{4.38}$$

The polarization of the radiation scattered from the scattering point is aligned perpendicular to the symmetry axis of the cylindrical source; i.e. the polarization is negative by the convention established in this chapter. The absolute value of the polarization has a minimum of 0 for $\Delta = \pi$, and a maximum of 1/5 for $\Delta = 0$. This simple demonstration shows why the absorption polarization feature in Fig. 4.7b is negative: it owes to scattering toward the observer from points in the atmosphere that lie roughly in front of the photosphere. The reasons why the absorption polarization feature never reaches the $-1/5$ value are similar to those given above in the discussion of the height of the emission polarization feature. However, it should be noted that the dilution effect of the unpolarized flux from the photodisk is reduced, since much of the flux emitted by the photosphere is scattered out of the line of sight. It is probably this reduction in dilution that causes the absolute value of the absorption polarization minima to be greater than the emission polarization maxima (see Fig. 4.7b). The small negative wings of the limb polarization component profile (see Fig. 4.7d) owe to the same geometrical scattering effect that causes the negative absorption feature; however, the competing geometrical effect that leads to positive polarization makes these negative wings relatively small in absolute value.

In Fig. 4.7e and 4.7f it can be seen that the absorption polarization feature's minimum is at a slightly lower wavelength than the flux minimum. The offset would be an interesting characteristic to check for when analyzing supernova data.

Fig. 4.7g and 4.7h display the Sobolev-H polarization extrema for the model as a function of the asymmetry ξ_{pro}. The emission polarization calculated from McCall's prescription and the SS pure scattering (Chandrasekhar solution) result for continuum polarization are also plotted on the figures. The Sobolev-H polarization extrema increase monotonically with ξ_{pro}, and are limited to the range of approximately -3% to 1.5%. The McCall prescription leads to much larger polarizations. This is a consequence of assuming that the Cassinelli and Hummer (1971) polarization plateau result applies to all the radiation scattered from the limb. The SS continuum polarization results are of the same order of magnitude as the Sobolev-H maxima polarizations. The close agreement between the SS and Sobolev-H maxima from $\xi_{pro} = 0$ to $\xi_{pro} \approx .2$ is accidental; the Sobolev-H maxima would change if τ_{ph} were changed.

Model 4.8 has the inclination angle parameter varied from 90° to 0°. The asymmetry parameter $\xi_{pro} = .5$; this asymmetry was chosen because .5 seems a plausible large value for supernova asymmetry (see the discussion in Chapter 1 section (d)). The parameter $\tau_{ph} = 10$, and the other parameters can be found in Table 4.4.

Fig. 4.8a shows the variation in the flux profile as the inclination angle is decreased. The absolute values of the flux maximum and flux minimum at first decrease somewhat and then rise steeply. The ratio of photodisk area to limb area remains the same as the inclination angle changes, and so that cannot be the cause of the changes in the flux profiles. The difference between the 90° case and the 0° case for the flux maximum is probably due to changes in the solid angle subtended by the photosphere at scattering points. Recall that the source function depends strongly on solid angle. At $\theta = 90°$ the maximum flux is produced by scattering points at the poles and equator of the ellipsoid. At $\theta = 0°$ the maximum flux is produced only by the equatorial scattering points. At a given r_s equatorial points see more solid angle than the polar points, and thus the $\theta = 0°$ case would be expected to have a larger emission maximum flux. The other changes in the flux profile are harder to explain. Probably, the explanation would require an analysis that isolated the effects of the various features of the model.

As inclination angle is decreased the expectation is that the polarization at each wavelength should, in general, be decreased: at 90° the polarization should be maximized, and at 0°, where the projected atmosphere is circularly symmetric, the polarization should be zero everywhere. Fig. 4.8b shows that these expectations are confirmed by the model calculation. Note that the absolute value of the emission polarization maximum is smaller than the absolute value of the absorption polarization minimum for inclination angles greater than 60°, and that the reverse is true for inclination angles less than 60°. This reversal may allow some information about inclination to be deduced from spectropolarimetric data.

In Fig. 4.8b there is an interesting shift in the location of the polarization maximum as the inclination decreases. This shift to higher wavelengths can be understood by examining the limb and photodisk components of the polarization profiles. In Fig. 4.8d the limb component maximum is seen to bifurcate into two maxima as inclination angle decreases. The bifurcation is caused by the forward and backward extension of the lobes of the ellipsoid for inclination angles other than 90° and 0°. These lobes cause the polarizing asymmetry to maximize at symmetric points about the $x' = 0$ coordinate. The higher wavelength limb polarization maximum is apparent in the net polarization profiles. The lower wavelength maximum is suppressed due to the effect of the photodisk polarization shown in Fig. 4.8f. The original photodisk polarization minimum decreases monotonically as the inclination decreases, but a second minimum appears that is formed on a velocity surface that has $V_{surface} \approx (1/2)v_{ph}$. This second photodisk minimum is at approximately the same wavelength as the lower wavelength limb maximum. These two component extrema partially cancel each other when combined to obtain the net polarization. This cancelation causes there to be only the single shifted polarization maximum in the net polarization profiles. The shift is possibly quite important as it may allow some distinction to be made between asymmetry and inclination effects in spectropolarimetric data.

The net polarization extrema are plotted as a function of inclination angle in Fig. 4.8g, and 4.8h. The figures show that the absolute value of the extrema increase monotonically with inclination angle. The dependence of the polarization extrema on inclination angle can be approximated by two lines: one line for the $\theta_{incl} \lesssim 30°$ and one for $\theta_{incl} \gtrsim 30°$. The polarizations for the emission feature obtained from the McCall prescription are greater in absolute value than the Sobolev-II results by at least a factor of 4 or 5.

Model 4.9 has a varied photospheric optical depth τ_{ph}. The asymmetry parameter $\xi_{pro} = .5$ and the inclination angle is 90°. The flux behavior as τ_{ph} changes (see Fig. 4.9a) is qualitatively the same and quantitatively very similar to the flux behavior of the spherically symmetric model 4.1.

The discussion of this behavior is given in section (b) of this chapter, and need not be repeated here.

The polarization profiles are given in Fig. 4.9b. As τ_{ph} increases the absorption polarization feature shifts to lower wavelength and deepens (for $\tau_{ph} < 10^5$). This behavior is readily explained. Recall from Chapter 2 section (d) that the polarization maximizing τ should be of order 2. Recall from section (b) of this chapter that the flux minimum occurs for $\tau(x) \approx 1$. Thus regions where the flux minimum forms and where polarizing scattering is maximized should be strongly overlapping. The dilution effect of unpolarized radiation is most reduced at the flux minimum, and thus a polarization maximum at the same wavelength is to be expected. As τ_{ph} increases, the region where $\tau \approx 1$ gets moved to larger x implying lower wavelengths for the resulting flux and polarization features. Since the flux minimum deepens with increased τ_{ph}, the dilution effect is decreased, and a deepening of the polarization minimum is to be expected.

Table 4.5 shows the $x_{pol\ min}$ coordinates that correspond to the wavelengths of the absorption polarization minima and shows the optical depths $\tau(x_{pol\ min})$. It is clear for $\tau_{ph} < 10^5$ that $\tau(x_{pol\ min})$ is only approximately 2. The fact that τ varies widely over the velocity surface defined by $x_{pol\ min}$ is probably the main cause of the lack of close agreement with the predicted value of 2. Some sort of average of $\tau(r)$ over the velocity surface specified by $x_{pol\ min}$ may be a more appropriate test of the prediction for the polarization maximizing τ.

TABLE 4.5.—The polarization minimizing $\tau(x)$ values from the model 4.9.

τ_{ph}	$x_{pol\ min}$	$\tau(x_{pol\ min}) = \tau_{ph}(x_{ph}/x_{pol\ min})^p$
10^0	1.02	0.871
10^1	1.09	5.47
10^2	1.44	7.79
10^3	2.01	7.54
10^4	2.75	8.41
10^5	3.35	21.1

NOTE: The $x_{pol\ min}$ values are all expressed in units of r_{ph}. The parameter $p = 7$.

By comparing Fig. 4.9d for limb polarization, and Fig. 4.9f for photodisk polarization, it can be seen that for larger τ_{ph} the limb contributes the most to the polarization minimum. This is because angles of scattering for observer-directed photodisk radiation in the $x_{pol\ min}$ region become small when $x_{pol\ min}$ becomes large. Recall that Rayleigh scattering is unpolarizing when the angle of scattering is 0°. Thus most of the polarizing scattering on the velocity surface that gives the polarization minimum is at the larger angles found in the limb.

The second negative polarization feature that occurs at wavelengths higher than the rest wavelength exhibits similar behavior as the absorption polarization feature. This similarity is due, of course, to the fact that the limb radiation fields are symmetric about the rest wavelength. The photodisk radiation for wavelengths higher than the rest wavelength is unscattered, undiminished photosphere radiation. Dilution by this photodisk radiation reduces the size of the higher wavelength negative polarization feature compared to the size of absorption polarization feature.

The behavior of the the emission polarization feature, for $\tau_{ph} < 10^5$, (see Fig. 4.9b) can also be explained: The polarization increases strongly with τ_{ph} for a while and has its maximum at the rest wavelength. Then for $\tau_{ph} > 100$, the polarization does not increase much, and the maximum of the feature shifts to a lower wavelength. The reason for the polarization not increasing further with τ_{ph} is probably that much of the increasing scattered flux comes from regions of high τ, and thus is mostly unpolarized. High τ implies that photons have multiple scatterings in resonance regions. Multiple scattering makes the radiation field more isotropic and less polarized (see Chapter 2 section (d)). This scattered unpolarized flux dilutes the polarized flux, and thus halts the increase in polarization as τ_{ph} increases. Note that the absorption polarization feature is less affected by dilution of scattered unpolarized radiation, since the polarized aborption feature radiation is Doppler decoupled from the scattered unpolarized radiation.

The shift in the maximum of the emission polarization feature from 5000 Å to about 4900 Å (see Fig. 4.9b) probably results from a decrease in cancelling negative polarized radiation from the photodisk (see Fig. 4.7f) and the near photodisk region of the limb (see Fig. 4.9d) at 4900 Å. The amount of positively polarized limb flux is nearly as great at 4900 Å as at 5000 Å, but at 4900 Å the positively polarized limb flux is diluted by negatively polarized photodisk flux and at 5000 Å the diluting flux is unpolarized unscattered photosphere emission. When the increasing τ_{ph} moves the region of negatively polarized radiation production to smaller wavelengths (see Fig. 4.9d and f) then both the 4900 Å and 5000 Å positively polarized fluxes are being diluted by unpolarized flux. At 4900 Å the diluting flux is diminished by scattering out of the line of sight, and so a higher positive polarization can be expected at 4900 Å.

There is a strong decrease in the absolute values of polarization of both the emission and absorption features when $\tau_{ph} = 10^5$. This is due to the choice of $r_{s_{max}} = 4r_{s_{ph}}$. For $\tau_{ph} \gtrsim 33000$, the optical depth τ never falls to 2 for $r \le r_{s_{max}} = 4r_{s_{ph}}$ when $p = 7$. Thus there ceases to be a highly polarizing region in the atmosphere as τ_{ph} increases above $\tau_{ph} \approx 33000$. For large enough τ_{ph} there would be no polarization at all.

Model 4.10 has a Planck continuum with varied photospheric temperature rather than a constant continuum. The Sobolev optical depth $\tau_{ph} = 10$, and the inclination angle is set to 90°. The temperatures chosen for the variation are the same as for the spherically symmetric model 4.5: 7244 K, 5796 K, and 4830 K. These temperatures give the continuum maximum flux at 4000 Å, 5000 Å, and 6000 Å, respectively. The flux profiles, which are displayed in Fig. 4.10a, are not changed qualitatively by the variations in the slope of the continuum. The behavior of the flux profiles is qualitatively the same as behavior of the flux profiles of the spherically symmetric model 4.5.

The polarization profiles displayed in Fig 4.10b show a slight increase in the emission polarization feature as the slope of the continuum flux changes from negative to positive (i.e., as the temperature decreases). This effect is entirely due to flux from the limb, since the limb polarization shows the increase (see Fig. 4.10d), but the photodisk polarization is unchanged by the continuum slope variation (see Fig. 4.10f). The slight polarization increase arises from the prescription for the continuum specific intensity. This specific intensity is integrated over the solid angle subtended by the photosphere to obtain the D_i coefficients. The Stokes source function fields, as shown in Chapter 2 section (d), depend linearly on the D_i coefficients. A specific intensity beam arises at some point on the photosphere, and travels a distance d along a beam path to some point $\vec{r}$ where the D_i coefficients are to be evaluated. A continuum specific intensity beam is evaluated at a wavelength such that the Doppler-shifted wavelength it has when it reaches the point $\vec{r}$ is equal to the rest wavelength of the transition λ_0 in the local frame at point $\vec{r}$. Since the atmospheres considered are in homologous expansion, the Doppler shift is a red shift, and is proportional to the distance d. Therefore the continuum specific intensity beam must be evaluated at lower wavelengths than λ_0. The greater the path distance d the beam must travel, the lower the wavelength at which the specific intensity beam is evaluated. The cone of beams that arrive at point $\vec{r}$ from a convex photosphere are therefore from lower wavelengths of the continuum near the edge of the cone than near the center of the cone. Thus the slope of the photospheric continuum affects the relative contribution of edge and center specific intensity beams: a negative slope increases the contribution of the edge beams, and a positive slope the contribution of the center beams. Recall that right-angle scattering is the most polarizing scattering (see Chapter 2 section (d)). For the case where center beams scatter through angles closer to right-angles than the angles the edge beams scatter through, then a change in continuum slope from negative to positive will cause some increase in the polarization of the emitted radiation. This case corresponds roughly to the situation that gives rise to the limb polarization, and hence the slight increase in polarization as the continuum slope is varied from negative to positive. The photodisk polarization arises from a case where nearly right angle scattering of radiation is not necessarily from center beams of the cone of specific intensity beams. Thus an increase polarization could not be predicted. The results in Fig. 4.10f show that the photodisk polarization is not significantly affected by the continuum variation at all. The effect of the variation is probably averaged away in the integration over the photodisk to obtain the net photodisk polarization.

Fig. 4.10g and 4.10h show the variation in polarization extrema as temperature is varied. The emission polarization increases slightly with decreasing temperature (increasing flux continuum slope). The absorption polarization minimum shows an even slighter increase as temperature is decreased. The McCall emission polarization shows no significant variation with temperature. This lack of variation in the McCall emission polarization is due to the lack in variation of the ratio of emission flux to continuum flux at the rest wavelength. Recall that it is this ratio that is used in McCall's prescription (see Chapter 3 section (b)). The McCall polarization, as for all other models, is much larger than the Sobolev-H polarization.

Model 4.11 has two identical scattering transitions with varied wavelength separation between them. The separations correspond to weakly blended, strongly blended, and exactly overlapping lines. The flux profiles are given in Fig. 4.11a; they are qualitatively the same as the flux profiles of the spherically symmetric model 4.6 (see section (b) of this chapter). The polarization profiles are given in Fig. 4.11b. For the weakly blended case with $\Delta\lambda = 400\,\text{Å}$, the polarization profile seems to be just that of two typical P-Cygni lines. Actually there is some blending effect, since the polarization minimum and maximum of the 5400 Å line are both somewhat lower than those of the 5000 Å line. The strongly blended case with $\Delta\lambda = 100\,\text{Å}$ has the polarization minima at approximately the same wavelengths that they would have if the lines were independent, but the maxima are displaced. The polarization maximum of the independent 5000 Å line is suppressed by the overlapping minimum of the 5100 Å . This effect is analogous to the suppression of the flux maximum seen in Fig. 4.11a. The maximum of the independent 5100 Å line is suppressed and a new maximum appears at an intermediate wavelength between 5000 Å and 5100 Å. This effect is not analogous to the flux behavior where the 5100 Å maximum is retained after blending. The case of exactly overlapping lines gives a polarization profile that appears the same as that of a single line with only slightly greater polarization features than either of the two lines that form it. The exactly overlapping lines are not, however, the same as one line with twice the photospheric Sobolev optical depth (see the discussion in Chapter 2 section (f)).

Figures 4.11c through 4.11f show the behavior of the limb and photodisk components of the flux and polarization profiles. Fig. 4.11g and 4.11h show that the polarization extrema do not vary strongly with wavelength separation. The McCall emission polarization is calculated for a 5000 Å line. The McCall values again are much larger than the Sobolev results and also show more and non-monotonic variation with the variation in separation. The non-monotonic behavior is a consequence of the fact that the McCall prescription does not include anything to account for line-blending. Recall from Chapter 3 section (b) that the McCall prescription contains the factor $F(limb)/F(net)$ evaluated at the rest wavelength, λ_0, of a line. Now $F(net) = F(photodisk) + F(limb)$, and the McCall picture supposes $F(photodisk) = F(continuum)$ at λ_0 since the photodisk region of the velocity surface of the line evaluated at the rest wavelength is entirely occulted by the photosphere. However, when a velocity surface of a second line has $x(\lambda = \lambda_0) = x_{ph}$ then $F(photodisk) < F(continuum)$, since the second line's velocity surface is in front of the photosphere scattering photodisk flux out of the line of sight. This situation is precisely the case for the separation of 100 Å, where the 5100 Å line's 5000 Å velocity surface is at x_{ph}. In other words the 5100 Å line's flux minimum is suppressing the maximum of the 5000 Å line. The McCall result in this situation is not very meaningful.

Several general conclusions can be drawn from this survey of prolate ellipsoid atmospheres. (1) There is polarization structure associated with P-Cygni lines emitted by prolate asymmetric atmospheres. (2) There is a change of sign in the polarization between the emission feature and absorption feature. This change of sign was not predicted by McCall (1984, 1985). (3) The polarization extrema increase monotonically with asymmetry ξ_{pro} and inclination angle θ_{incl}. (4) The flux profiles vary somewhat with asymmetry, and inclination. A procedure for fitting spectropolarimetric data would be to fit τ_{ph} values to the flux data for a spherically symmetric model, then fit the observed polarization profiles by adding asymmetry. The flux profiles would be somewhat altered, but they could be re-fit for the asymmetric model. Then the asymmetry could be changed to re-fit the polarization profiles, and so on until some convergence is reached. (5) The Sobolev-H polarizations obtained are not very large. They are of the order of a few per cent even in rather extreme cases. The McCall emission feature polarizations are larger than the Sobolev polarization by roughly an order of magnitude. This discrepancy undoubtedly owes to the simplicity of the McCall prescription for the polarization. A simple correction to the McCall prescription seems unlikely, since several physical and geometrical features need to be included in the prescription. The simplicity of Sobolev-H calculations probably obviates any need for an improved McCall prescription. (6) The absorption polarization feature minimum is larger in absolute value than the emission polarization feature maximum for large inclinations and smaller for small inlination angles. This characteristic may allow an approximate determination of inclination angle. (7) For inclination angles different from 90° the emission polarization feature's maximum is shifted to wavelengths greater than the line rest wavelength. The flux maximum is also shifted to higher wavelengths. These shifts may allow detection of the inclination angle from spectropolarimetric and flux data. (8) The effects of line blending on polarization profiles do not quite mimic the effects on the flux profiles. The blending behavior may make it harder to obtain a unique fit to any data. Observers should thus concentrate their efforts on obtaining the spectra of pure, unblended P-Cygni lines.

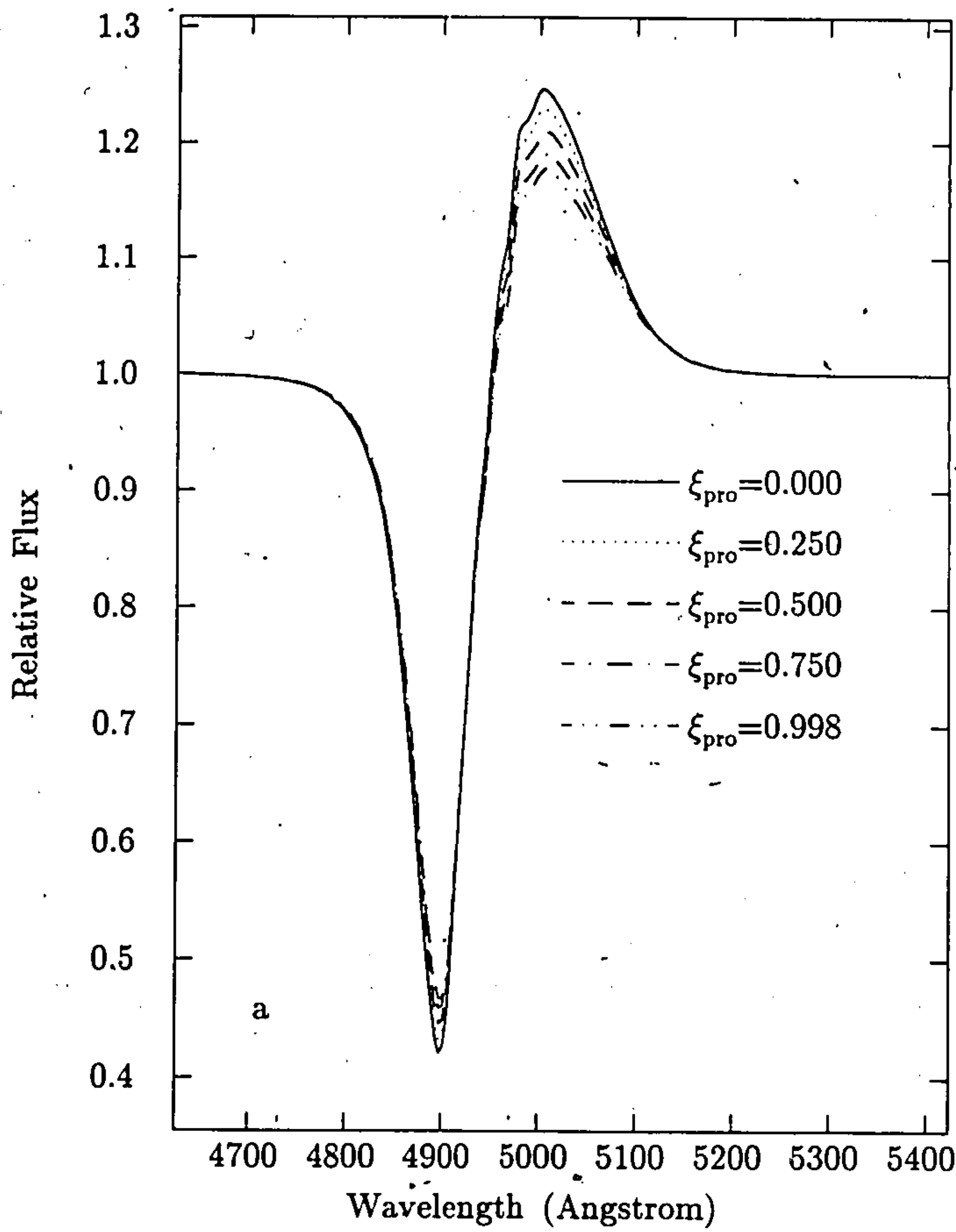

Fig. 4.7a. The flux profiles for a typical prolate model with varied asymmetry ξ_{pro}. The profiles show some alteration with increasing asymmetry, but remain qualitatively the same.

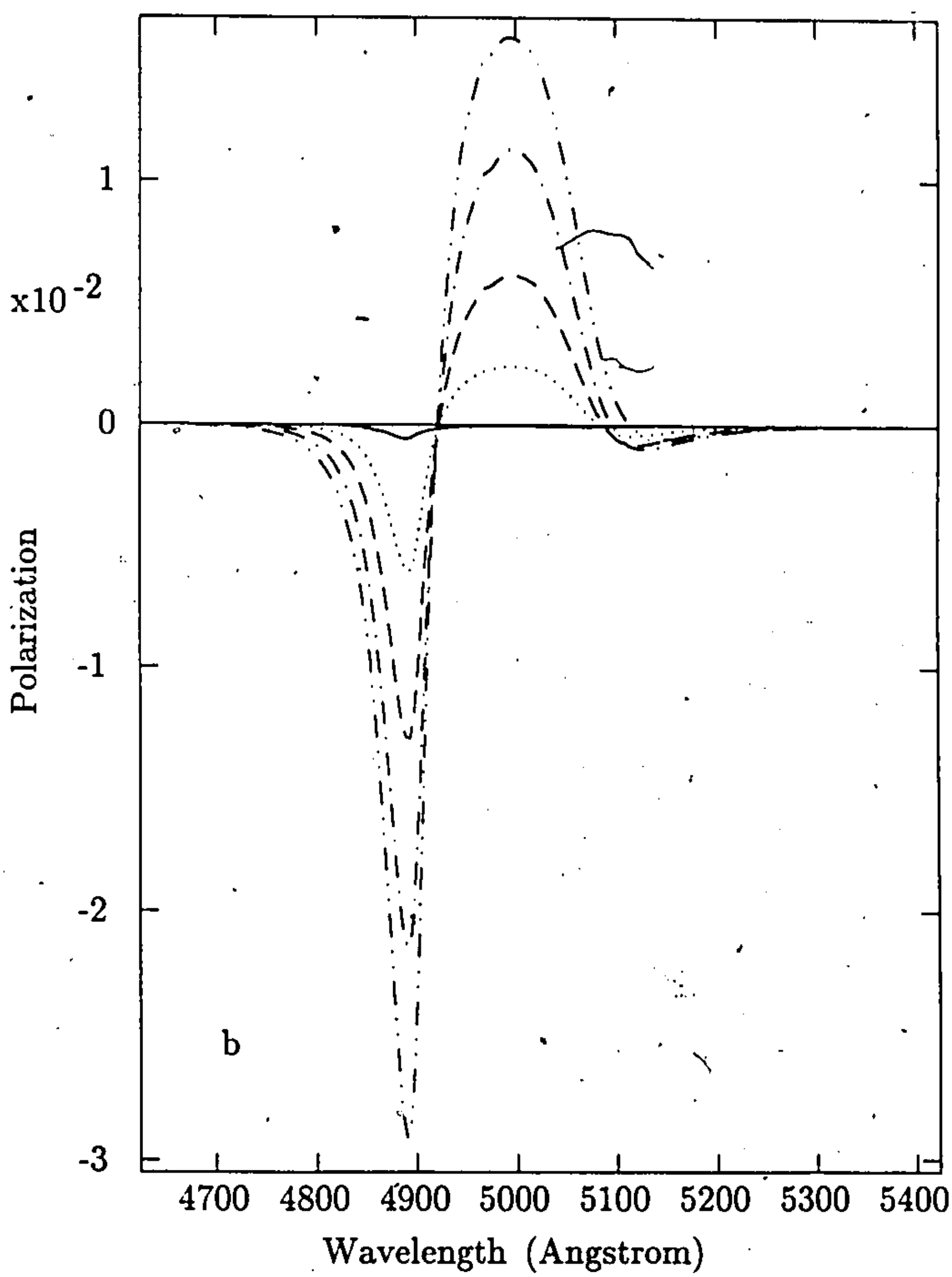

Fig. 4.7b. The polarization profiles corresponding to the flux profiles of Fig. 4.7a. There is a general increase in the absolute value of the polarization with increasing prolate asymmetry. The profiles show an inversion between absorption and emission features. The small non-zero polarization result for the $\xi_{pro} = 0$ case is a result of the numerical uncertainty in the model calculation.

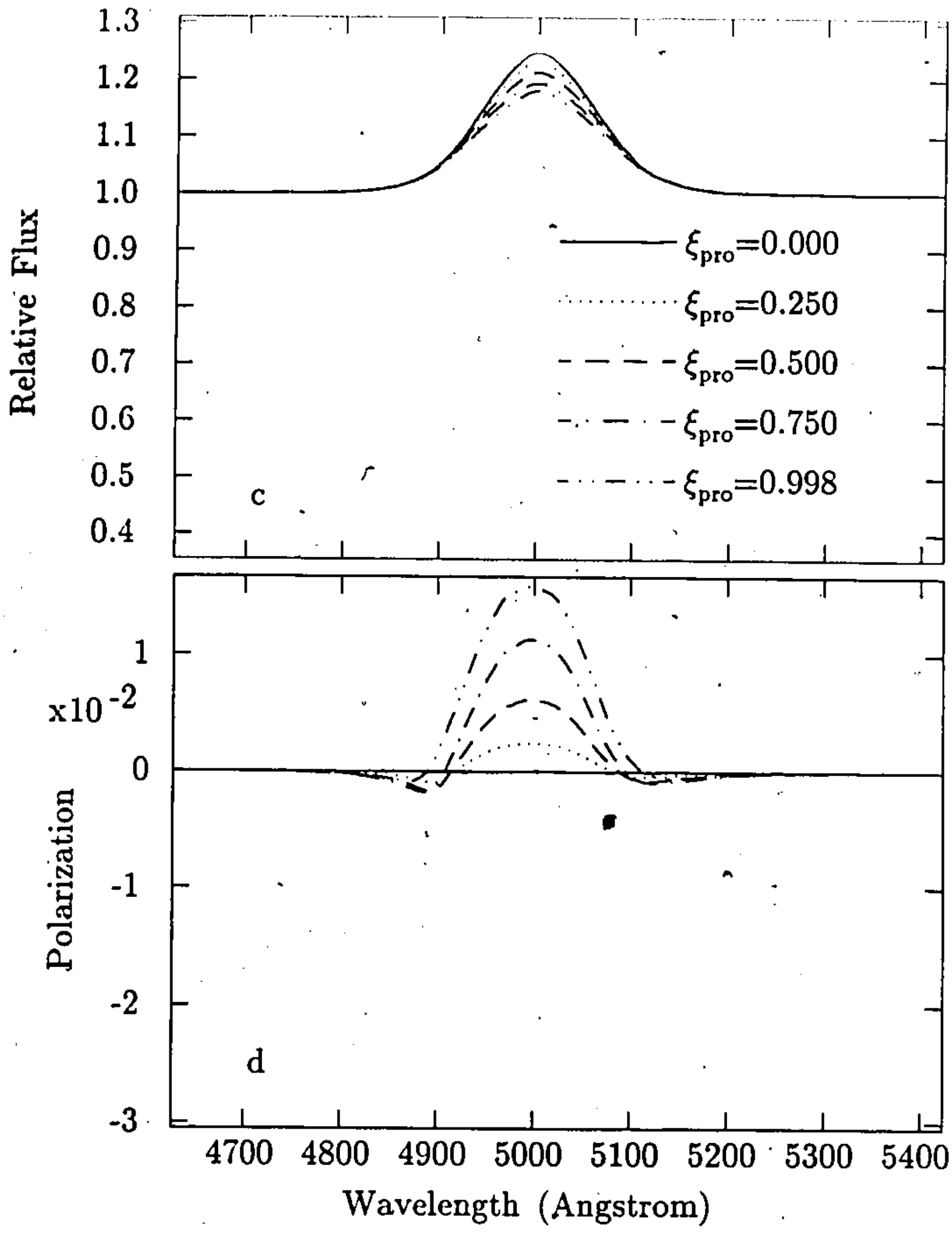

Fig. 4.7c and d. The limb components of the flux and polarization profiles of Fig. 4.7a and b. The limb flux profiles have complete symmetry about the line center; this owes to the symmetry of the ellipsoid shape and to the lack of occultation for the limb contribution. The polarization profiles lack the complete symmetry because they are calculated from $(F_x(limb) - F_y(limb))/F(net)$, where $F(net)$ is not symmetric due to occultation.

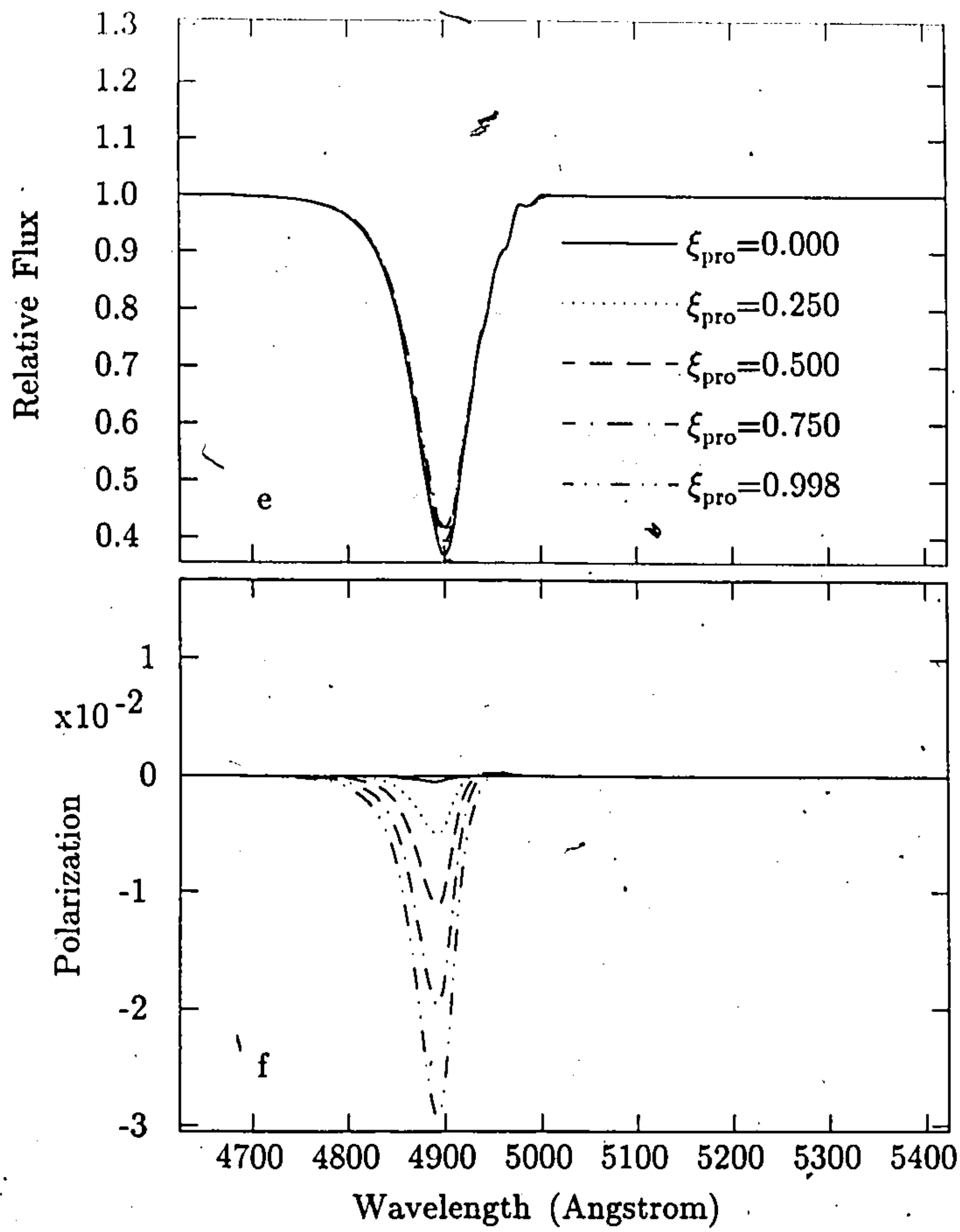

Fig. 4.7e and f. The photodisk components of the flux and polarization profiles of Fig. 4.7a and b.

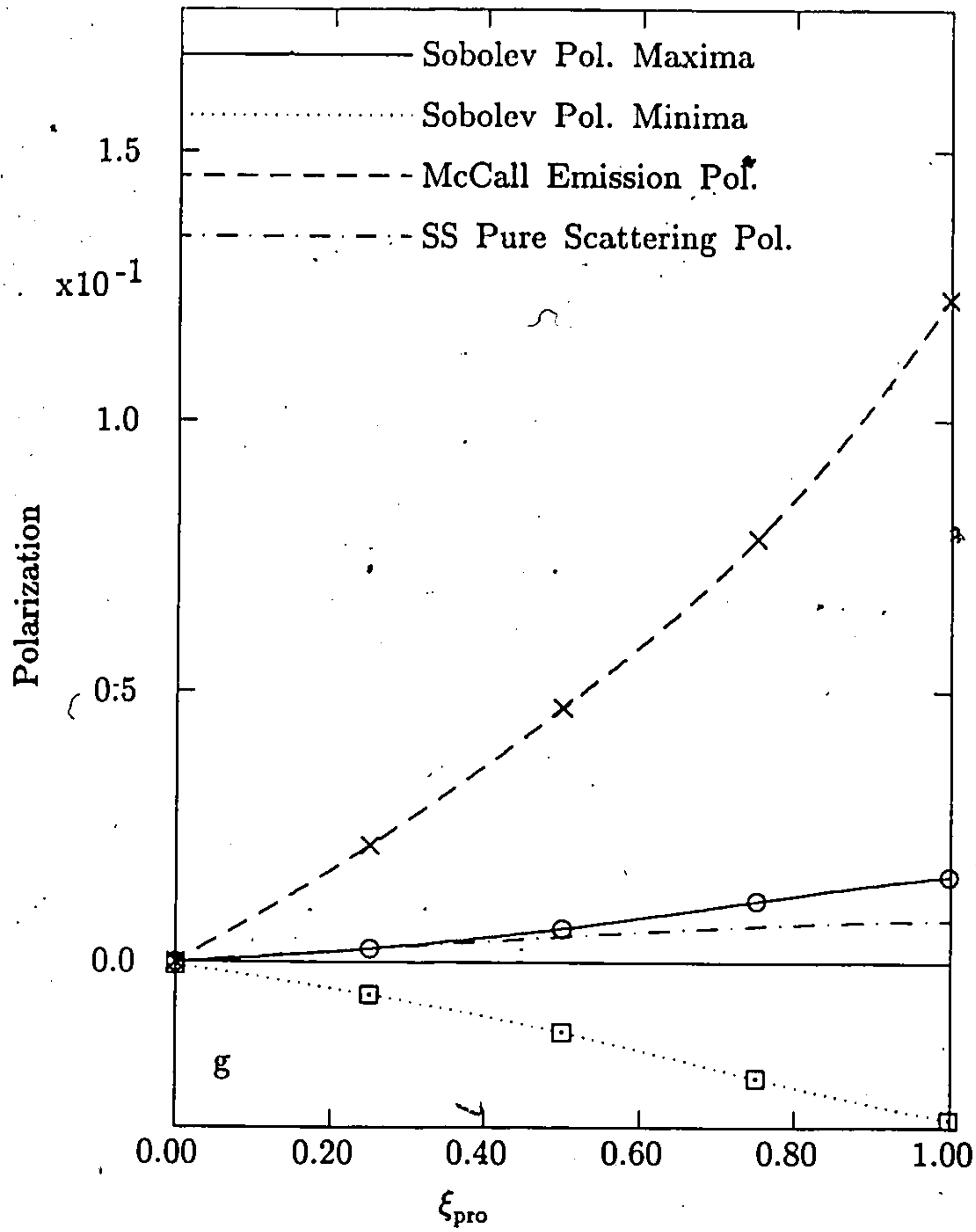

Fig. 4.7g. The maximum and minimum polarizations for each of the profiles of Fig. 4.7b as a function of asymmetry ξ_{pro}. The absolute value of the polarization extrema increase roughly linearly for $\xi_{pro} \lesssim .5$. The SS continuum polarization for the pure scattering case and the McCall emission polarization maxima are also shown for comparison.

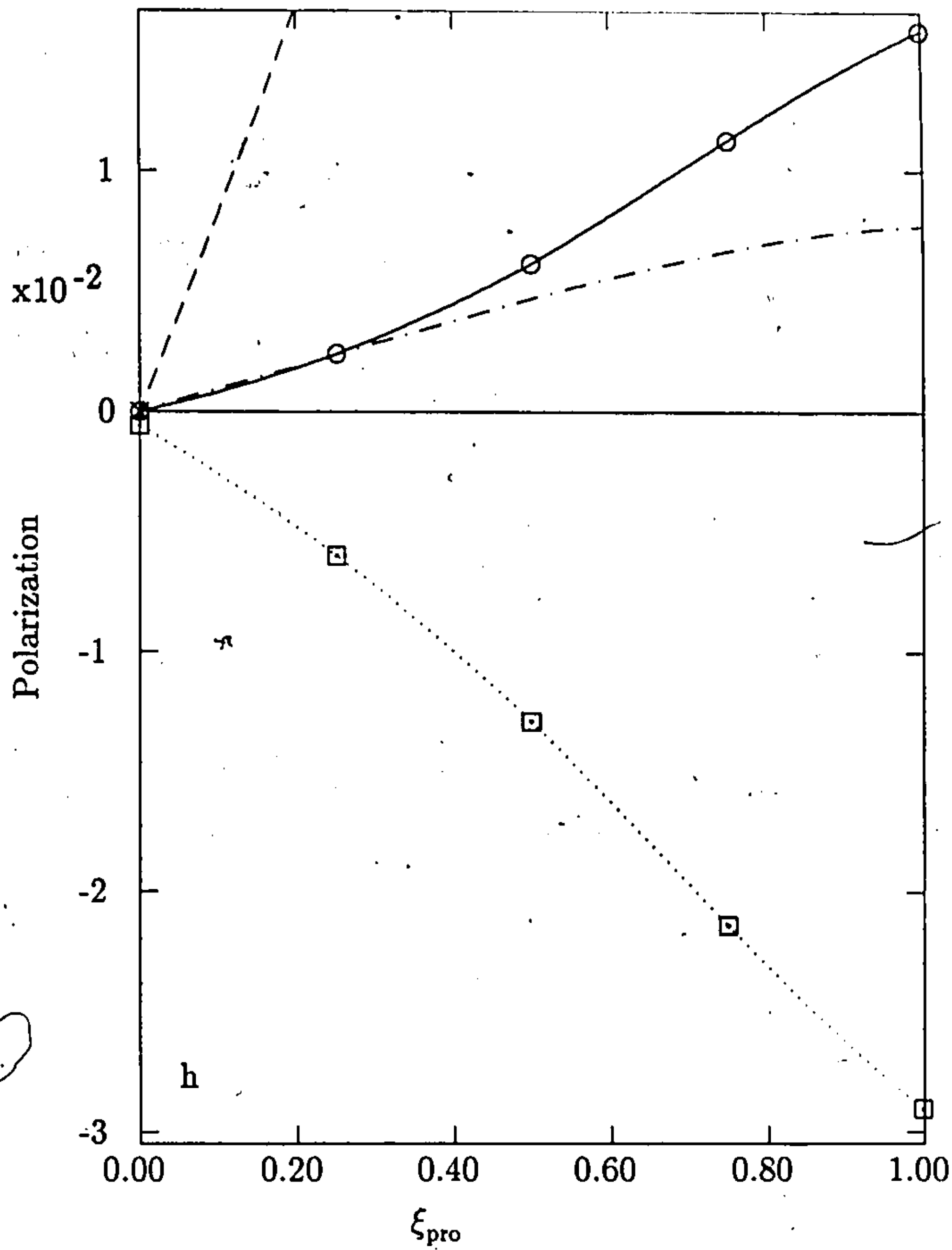

Fig. 4.7h. This is the same as Fig. 4.7g., but with a smaller vertical range in order to better display the Sobolev-H calculation results.

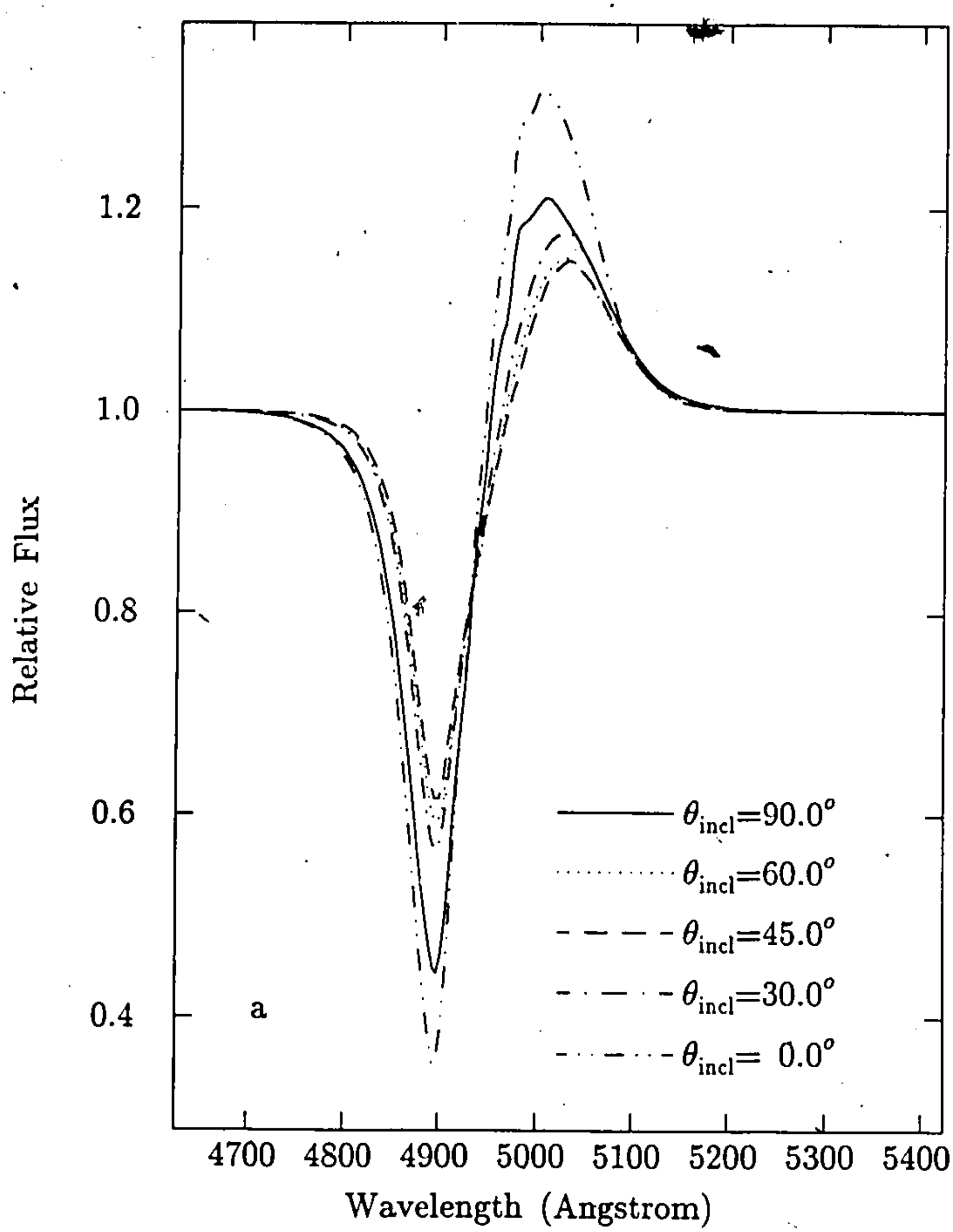

Fig. 4.8a. The flux profiles for a typical prolate model with varied inclination angle θ_{incl} and with ξ_{pro} = .5. The flux profiles are all normalized with respect to the continuum; in absolute value the flux decreases by a factor of 2 as θ_{incl} goes from 90° to 0°. The flux profiles change non-monotonically with θ_{incl}. There is also a shift in the flux maximum to wavelengths higher than the rest wavelength for θ_{incl} not equal to 90° or 0°.

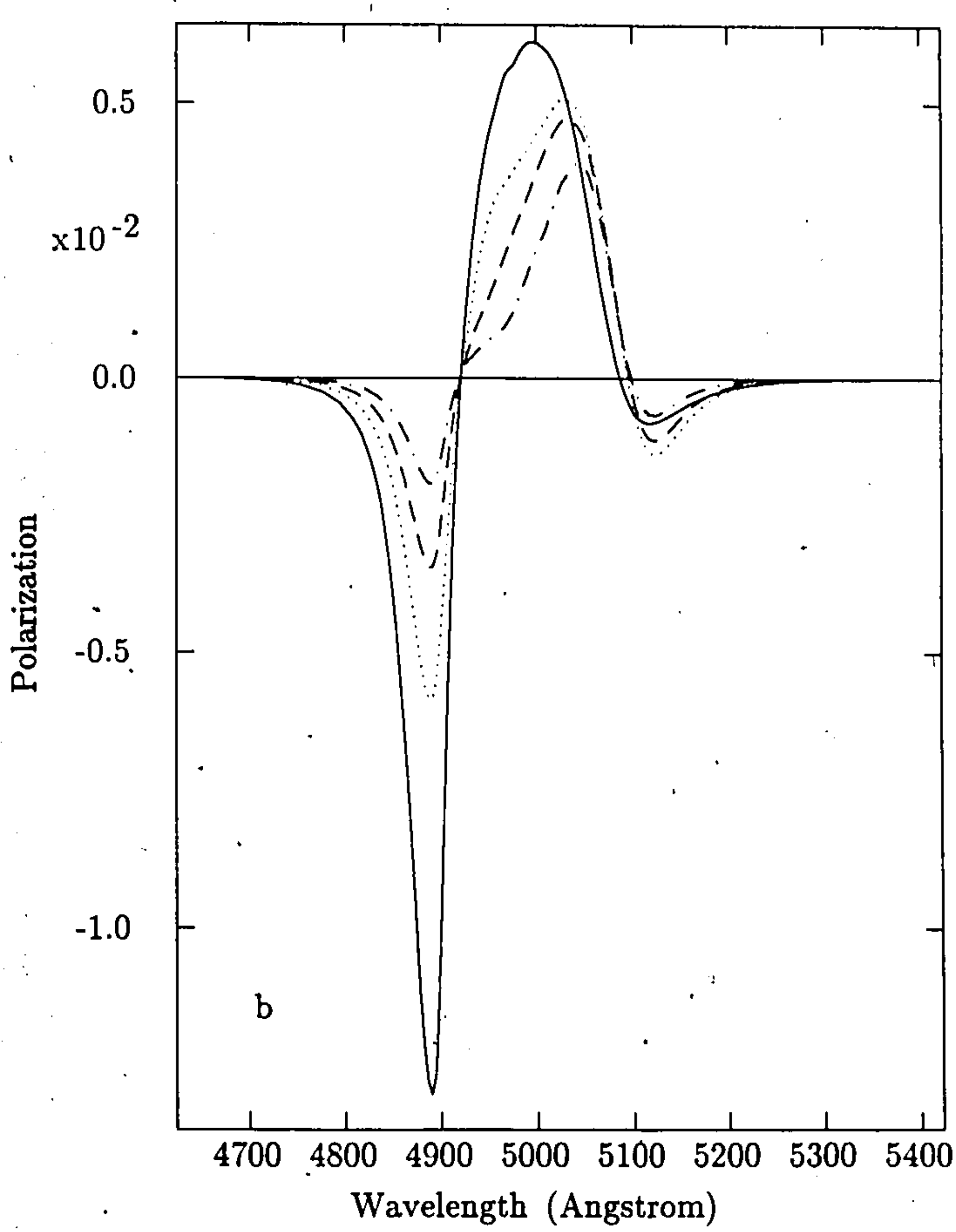

Fig. 4.8b. The polarization profiles corresponding to the flux profiles of Fig. 4.8a. The overall scale size of the polarization profiles declines as the inclination angle is decreased. The polarization profiles go to zero everywhere as the inclination angle goes to zero. The polarization profiles show a shift in the the polarization maximum to wavelengths greater than the rest wavelength as inclination angle decreases.

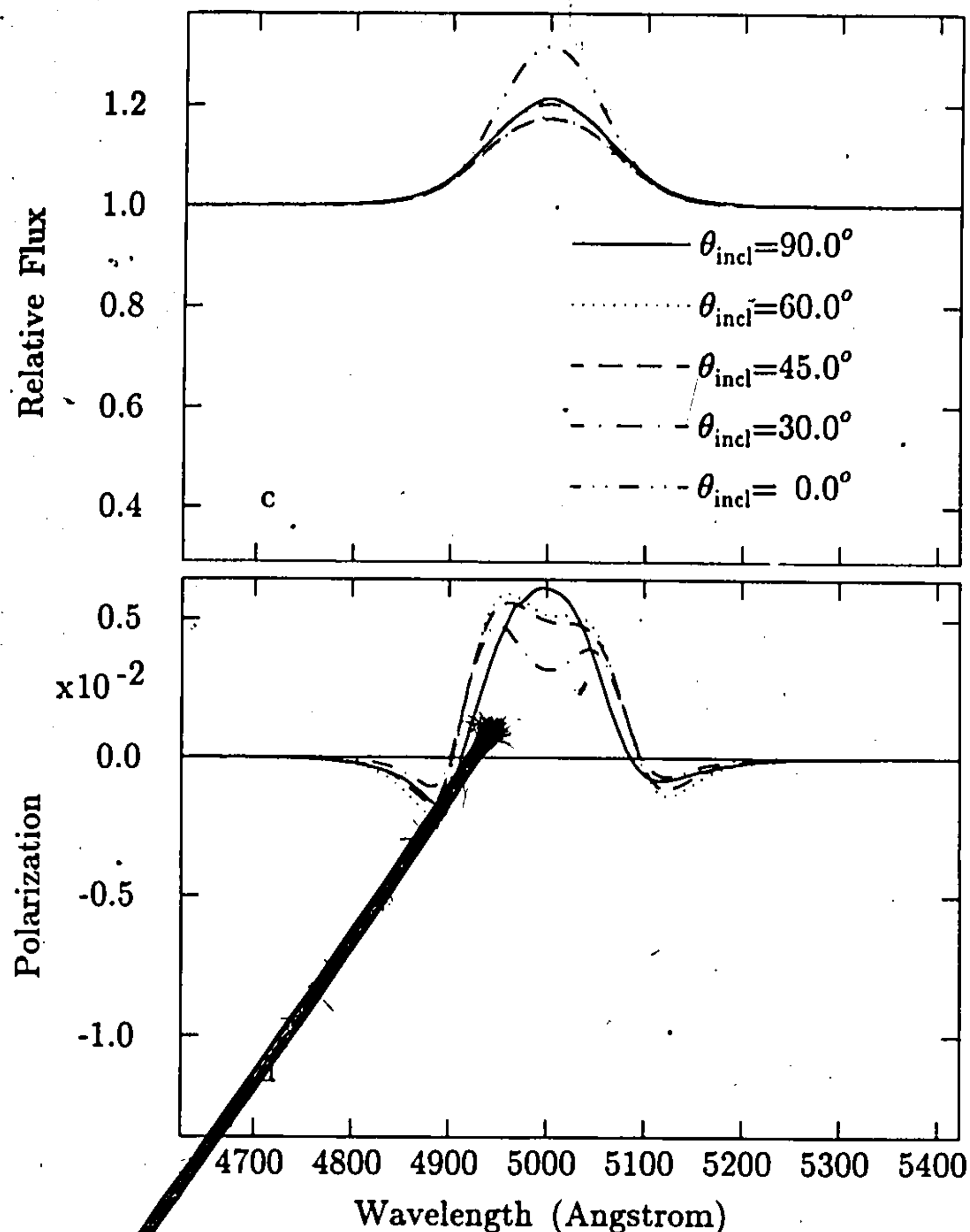

Fig. 4.8c and d. The limb components of the flux and polarization profiles of Fig. 4.8a and b. The polarization emission feature maximum bifurcates into two maxima when the inclination angle is changed from 90°.

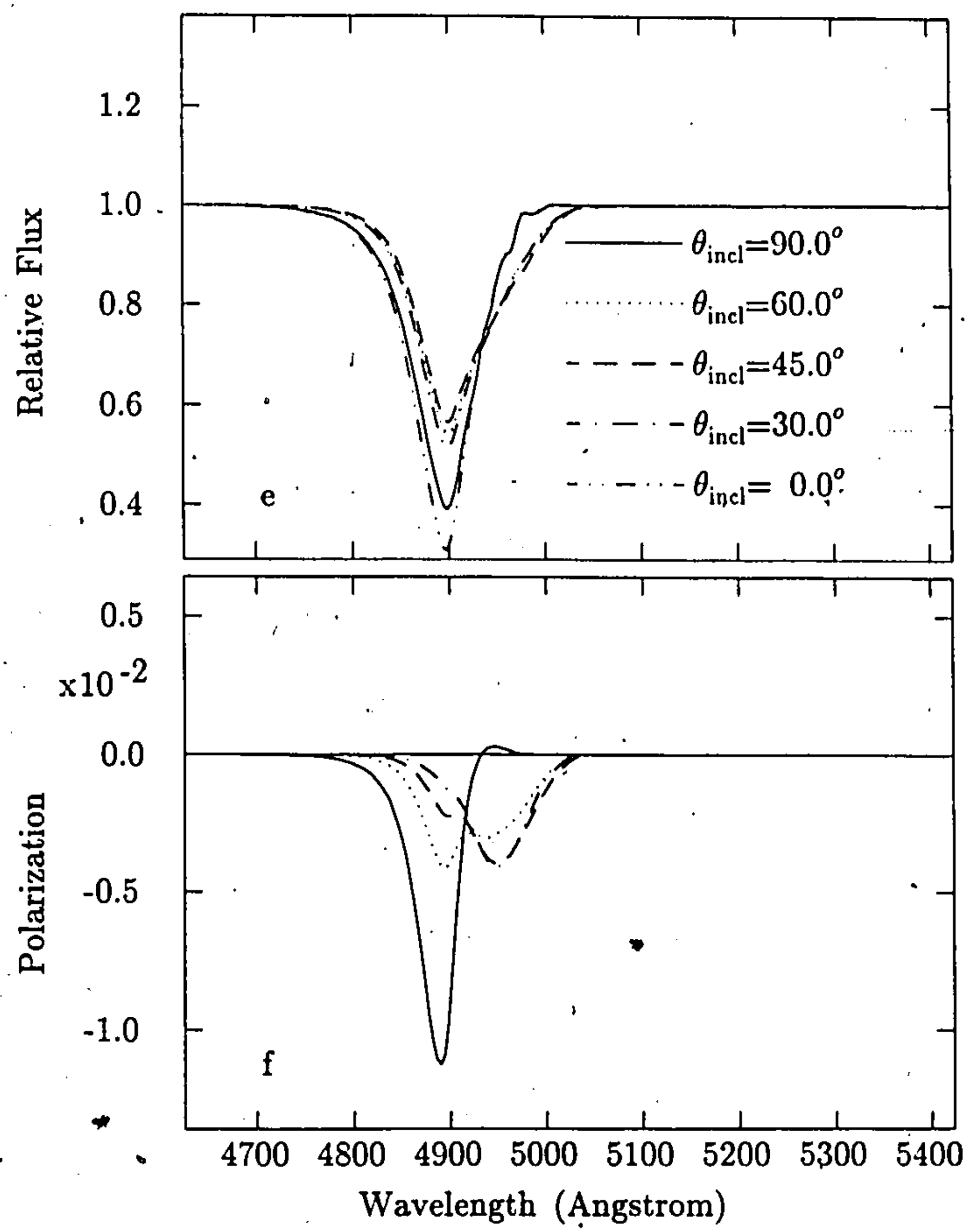

Fig. 4.8e and f. The photodisk components of the flux and polarization profiles of Fig. 4.8a and b. Note that a second polarization minimum develops as the inclination angle is reduced from 90°.

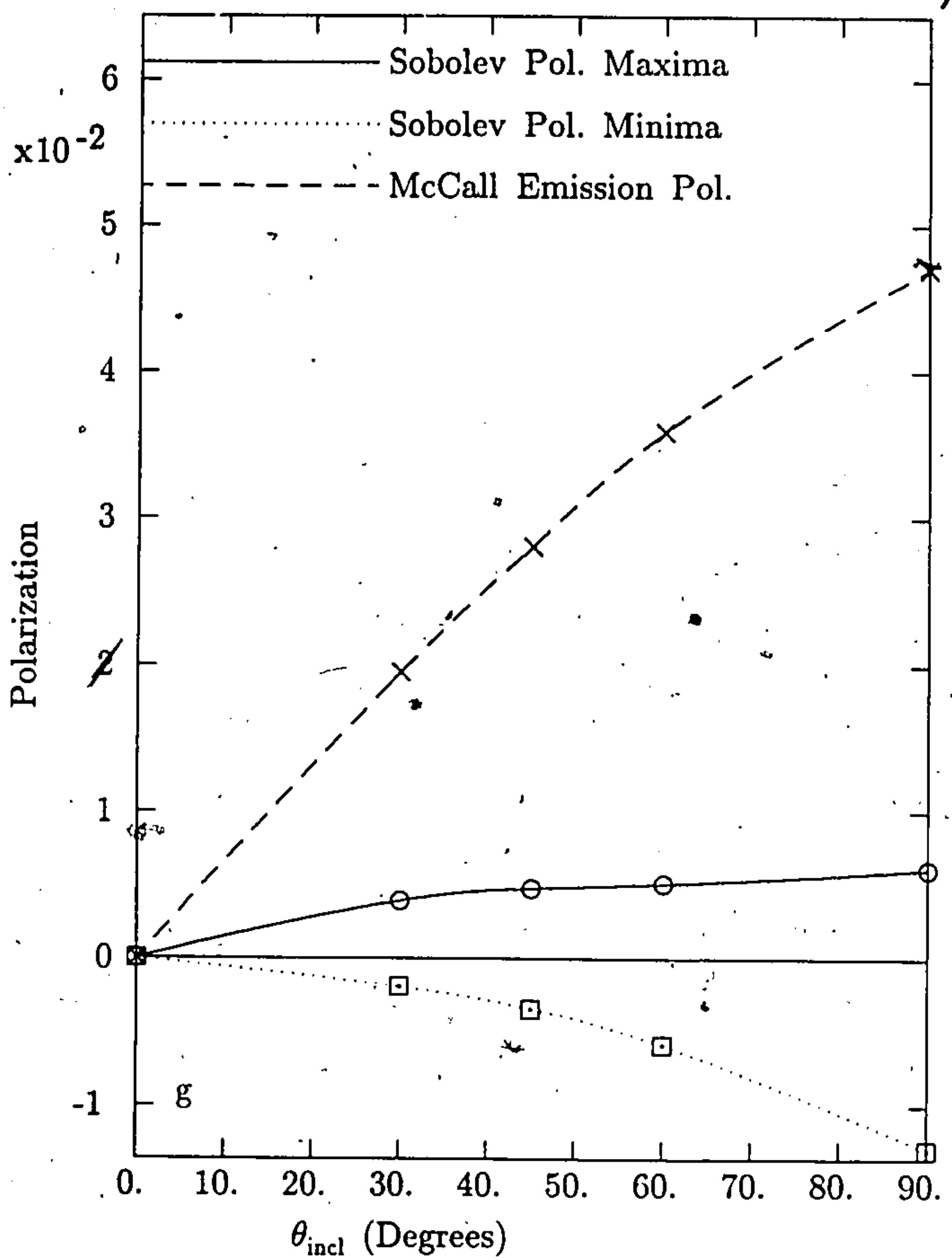

Fig. 4.8g. The maximum and minimum polarizations for the profiles of Fig. 4.8b as a function of inclination angle θ_{incl}. The polarization extrema increase monotonically in absolute value as the inclination angle increases. The McCall emission polarization maxima are also shown for comparison.

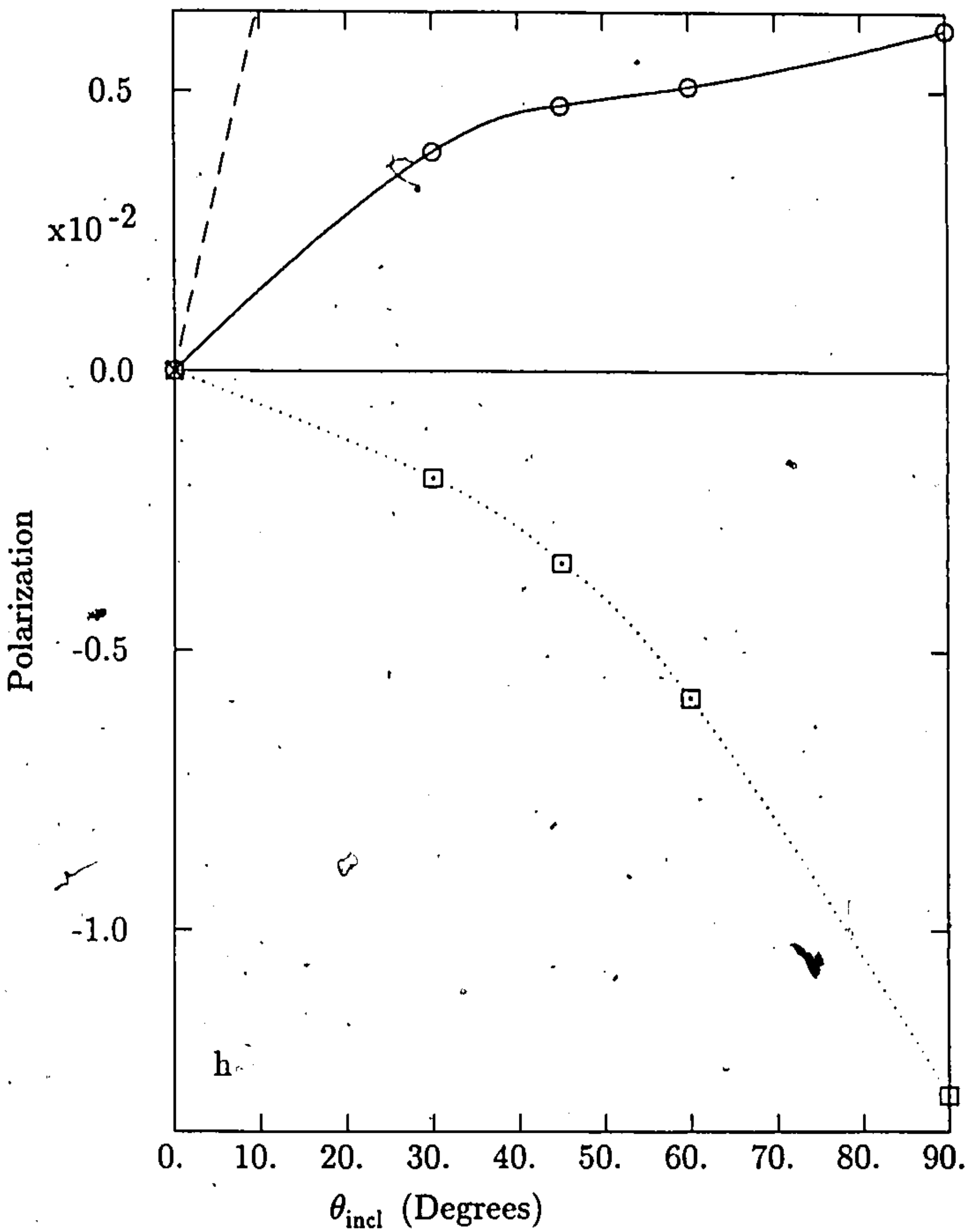

Fig. 4.8h. This is the same as Fig. 4.8g, but with a smaller vertical range in order to better display the Sobolev-H calculation results.

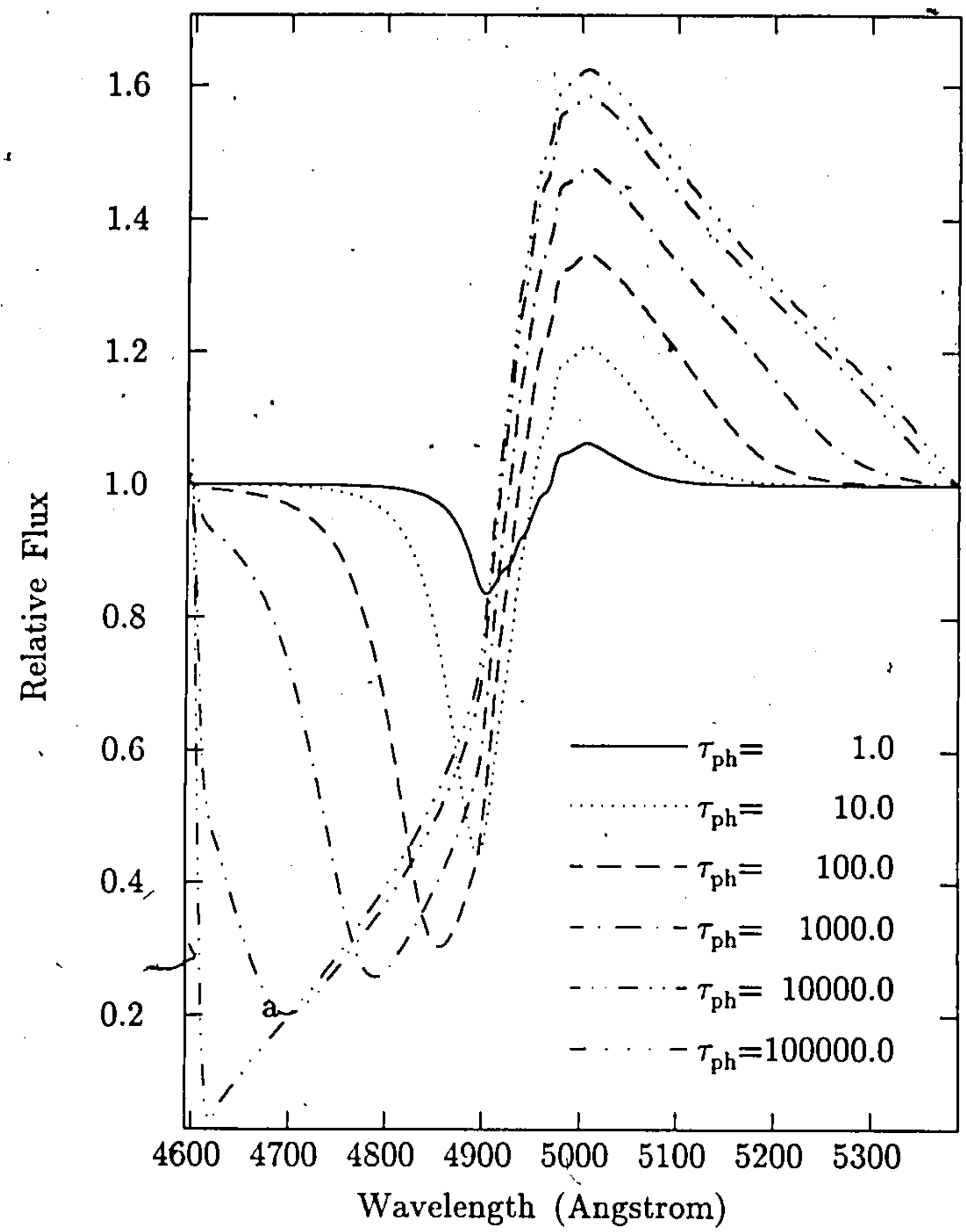

Fig. 4.9a. Flux profiles for a model with varied Sobolev photospheric optical depth τ_{ph}. The flux maximum increases roughly the logarithm of τ_{ph}. The wavelength separation between the rest wavelength and the wavelength of the flux minimum increases roughly as $(\tau_{ph})^{(1/p)}$.

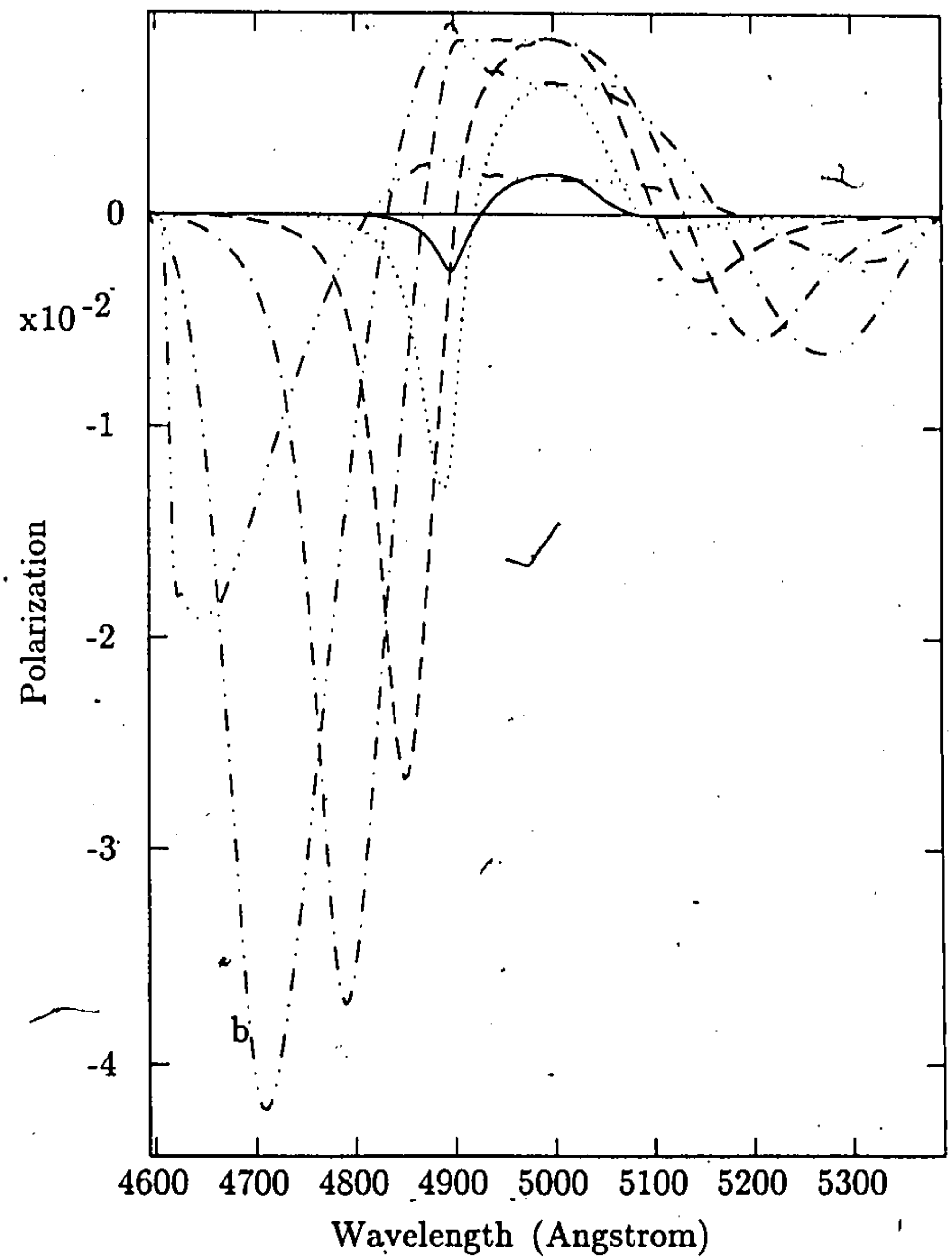

Fig. 4.9b. The polarization profiles corresponding to the flux profiles of Fig. 4.9a. The absorption polarization feature's minimum is closely correlated to the flux minimum. The decrease in polarization for $\tau_{ph} = 10^5$ is due to the choice of $r_{g_{max}} = 4r_{ph}$. The emission polarization feature increases, and then reaches a rough plateau as τ_{ph} is increased. The emission polarization maximum shifts to lower wavelengths as τ_{ph} is increased.

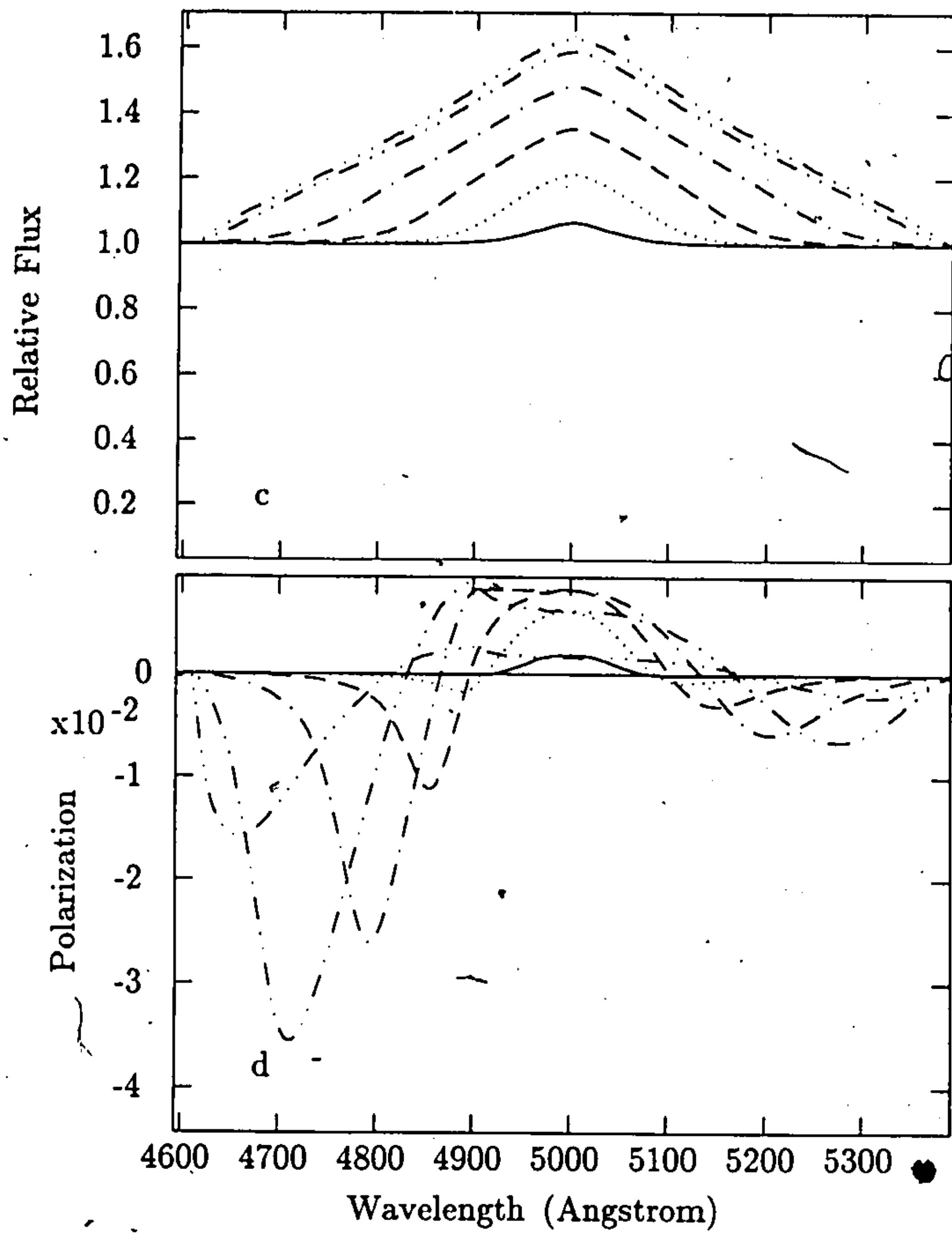

Fig. 4.9c and d. The limb components of the flux and polarization profiles of Fig. 4.9a and b. Note that for large τ_{ph} that the limb polarization profile is similar to the net polarization for both emission and absorption features.

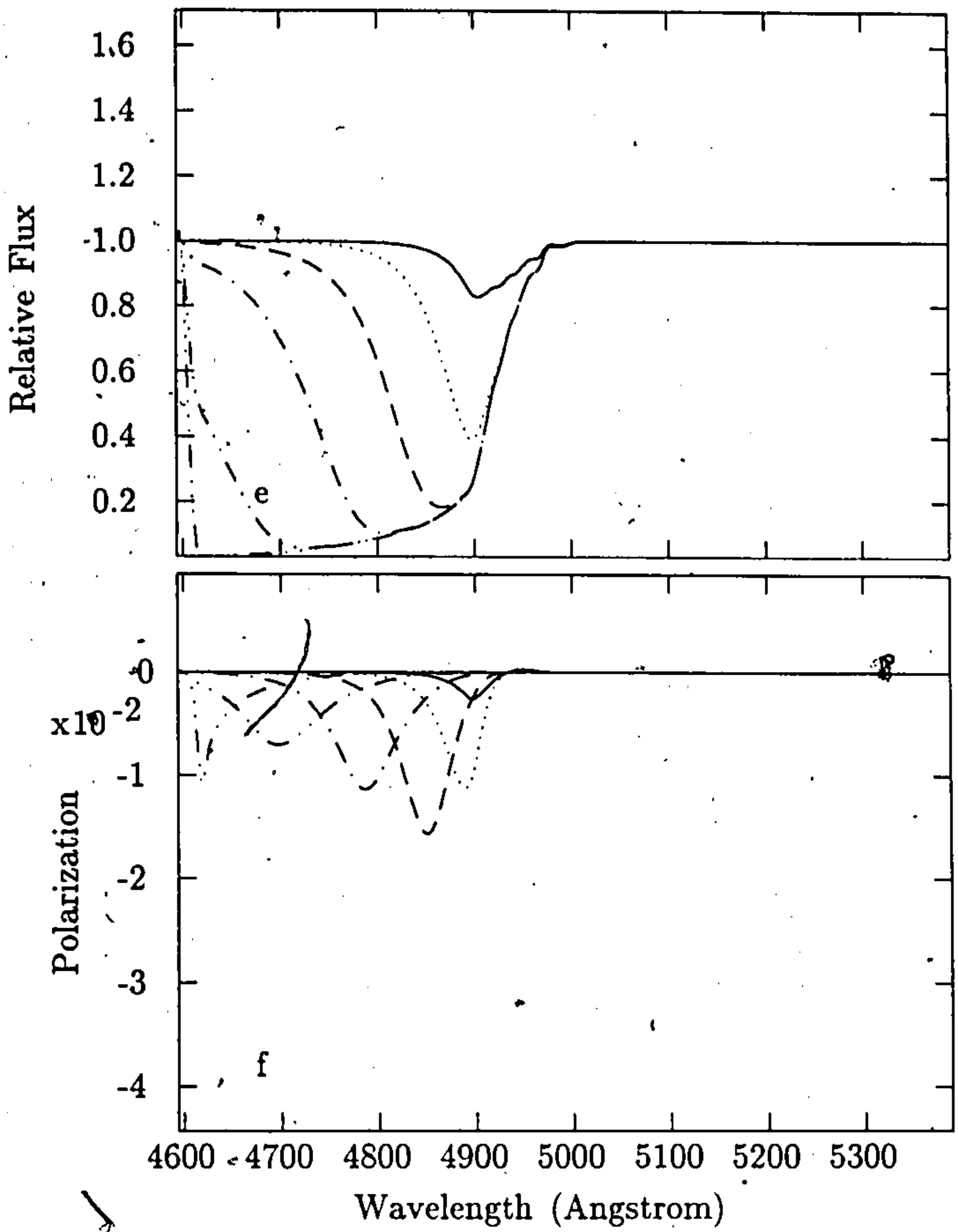

Fig. 4.9e and f. The photodisk components of the flux and polarization profiles of Fig. 4.9a and b. Note that for large τ_{ph} the photodisk polarization is not a large contributor to the net polarization profile.

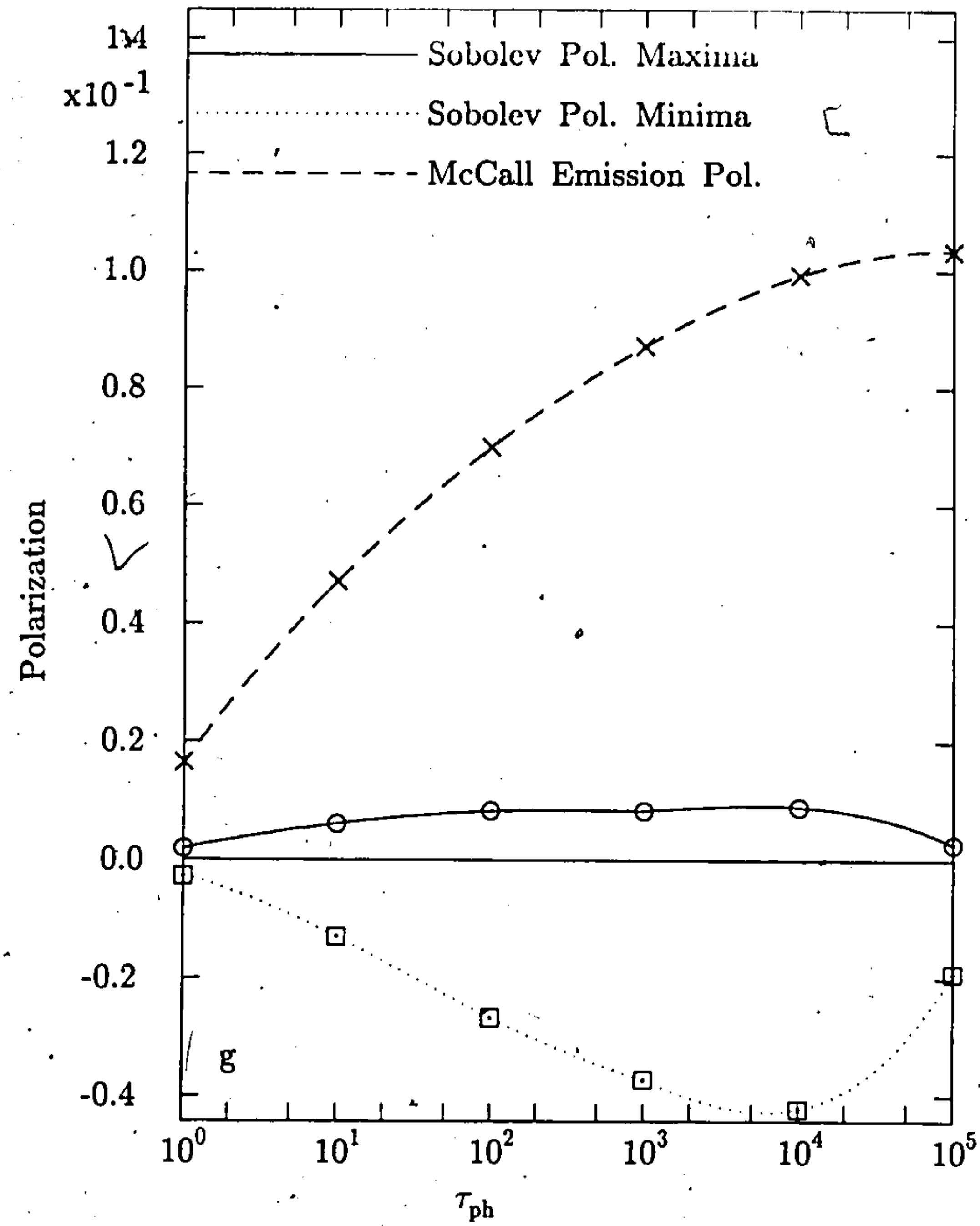

Fig. 4.9g. This shows the maximum and minimum polarizations for the profiles of Fig. 4.9b as a function of τ_{ph}. The McCall emission polarization maxima are also shown for comparison.

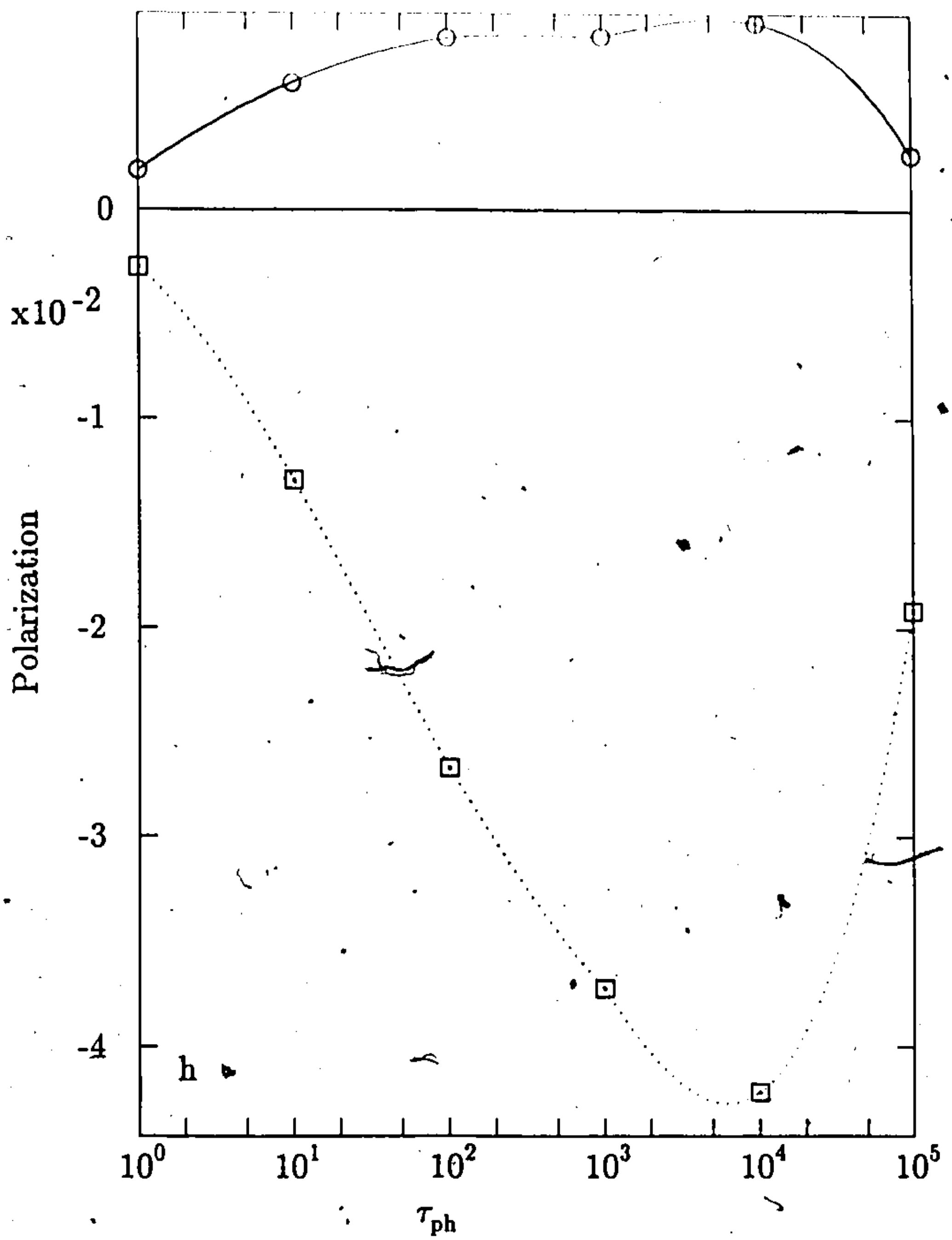

Fig. 4.9h. This is the same as Fig. 4.9g., but with a smaller vertical range in order to better display the Sobolev-H calculation results. Note that the absorption polarization feature's minimum decreases linearly with the logarithm of τ_{ph}, until the finite outer radius of the atmosphere begins to affect the polarization profiles. The emission polarization feature's maximum rises to a plateau, and then decreases due to the finite outer radius.

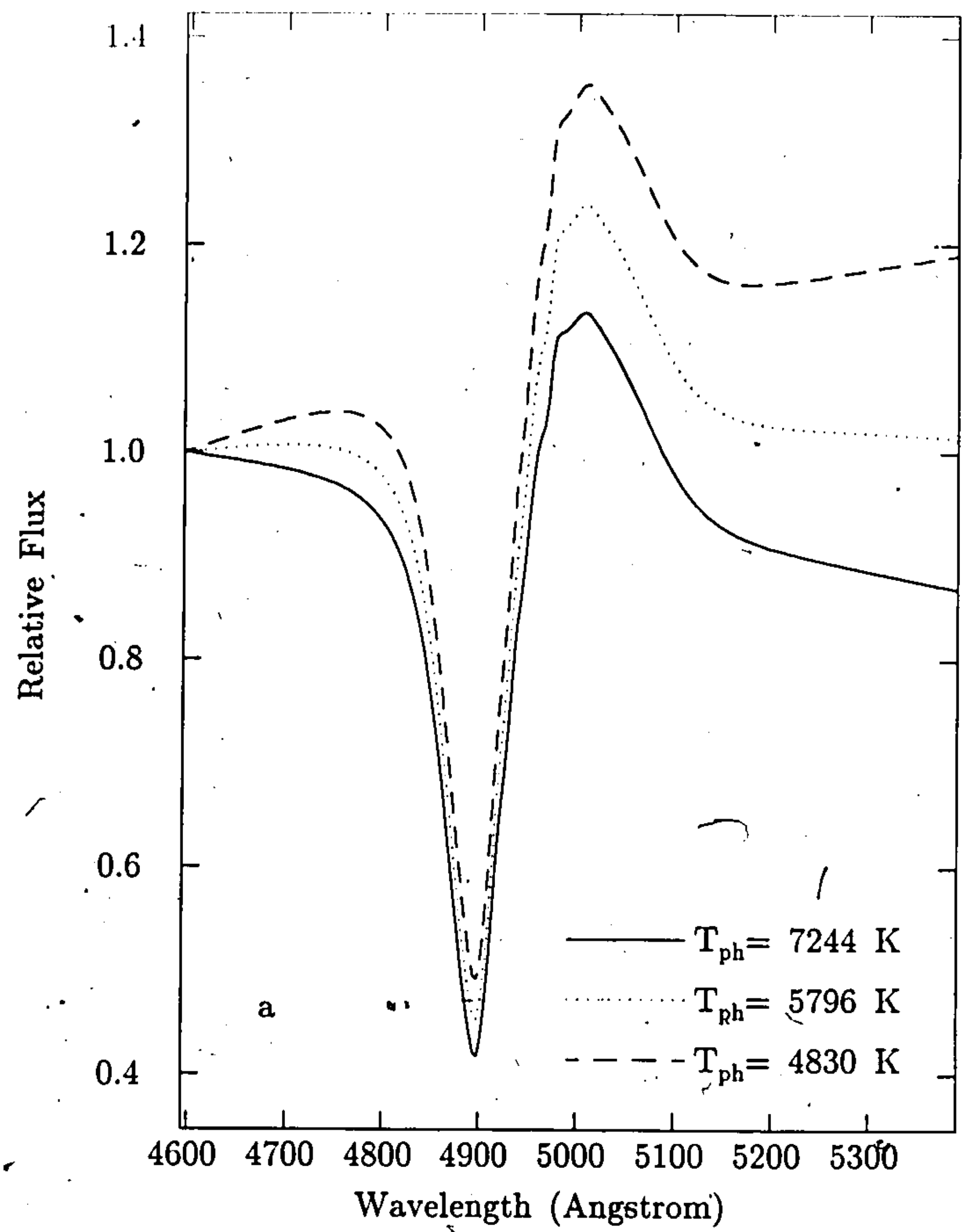

Fig. 4.10a. Flux profiles for a model with a Planck continuum producing photosphere with varied photospheric temperature. The varied temperature causes a varied continuum slope. The varied slope has little qualitative affect on the P-Cygni profiles.

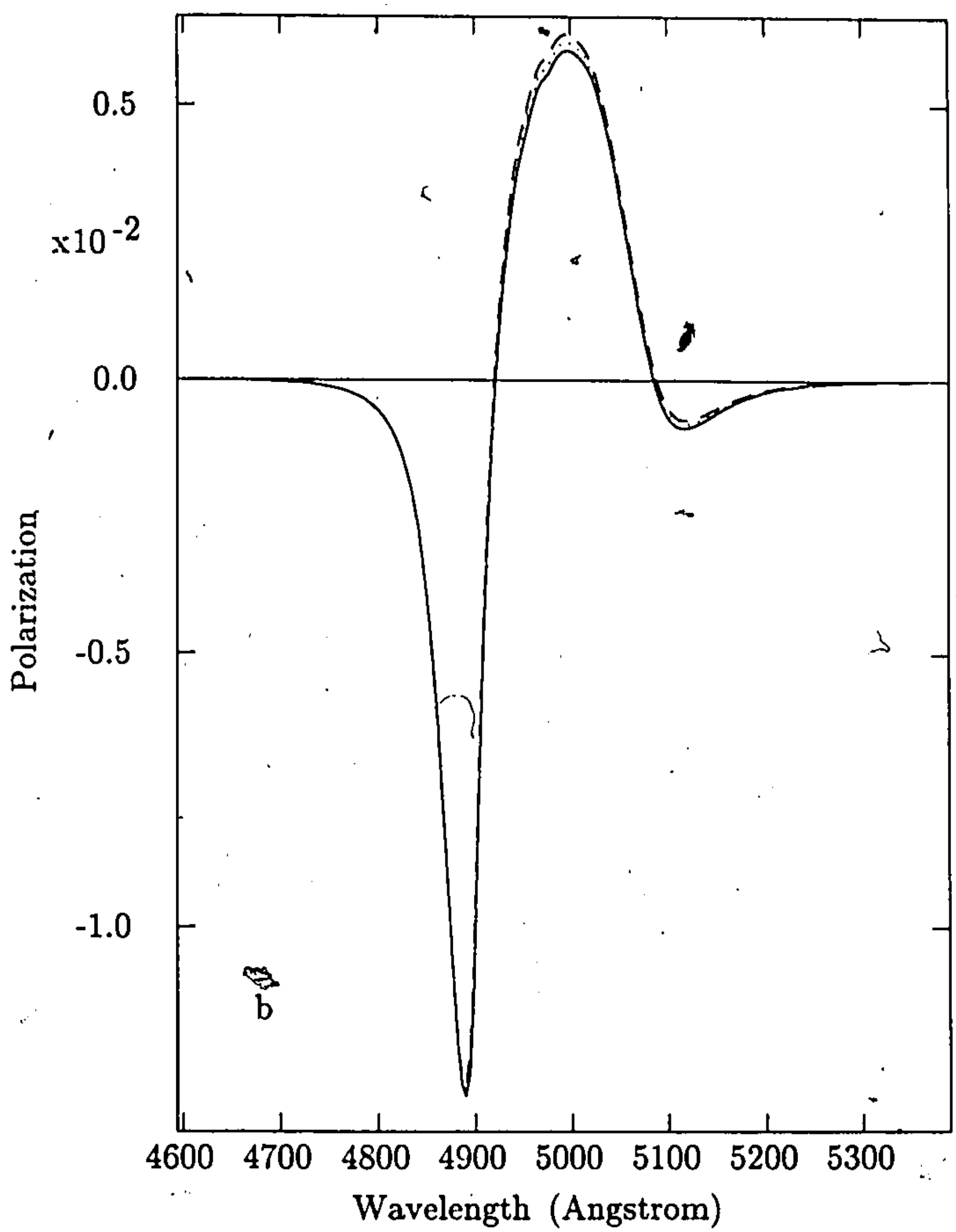

Fig. 4.10b. Polarization profiles for a model with a Planck continuum producing photosphere with varied photospheric temperature. The profiles are nearly unaffected by the changing slope of the photospheric continuum flux. There is a slight increase in the emission feature polarization as temperature is reduced (i.e. as the flux continuum slope changes from negative to positive).

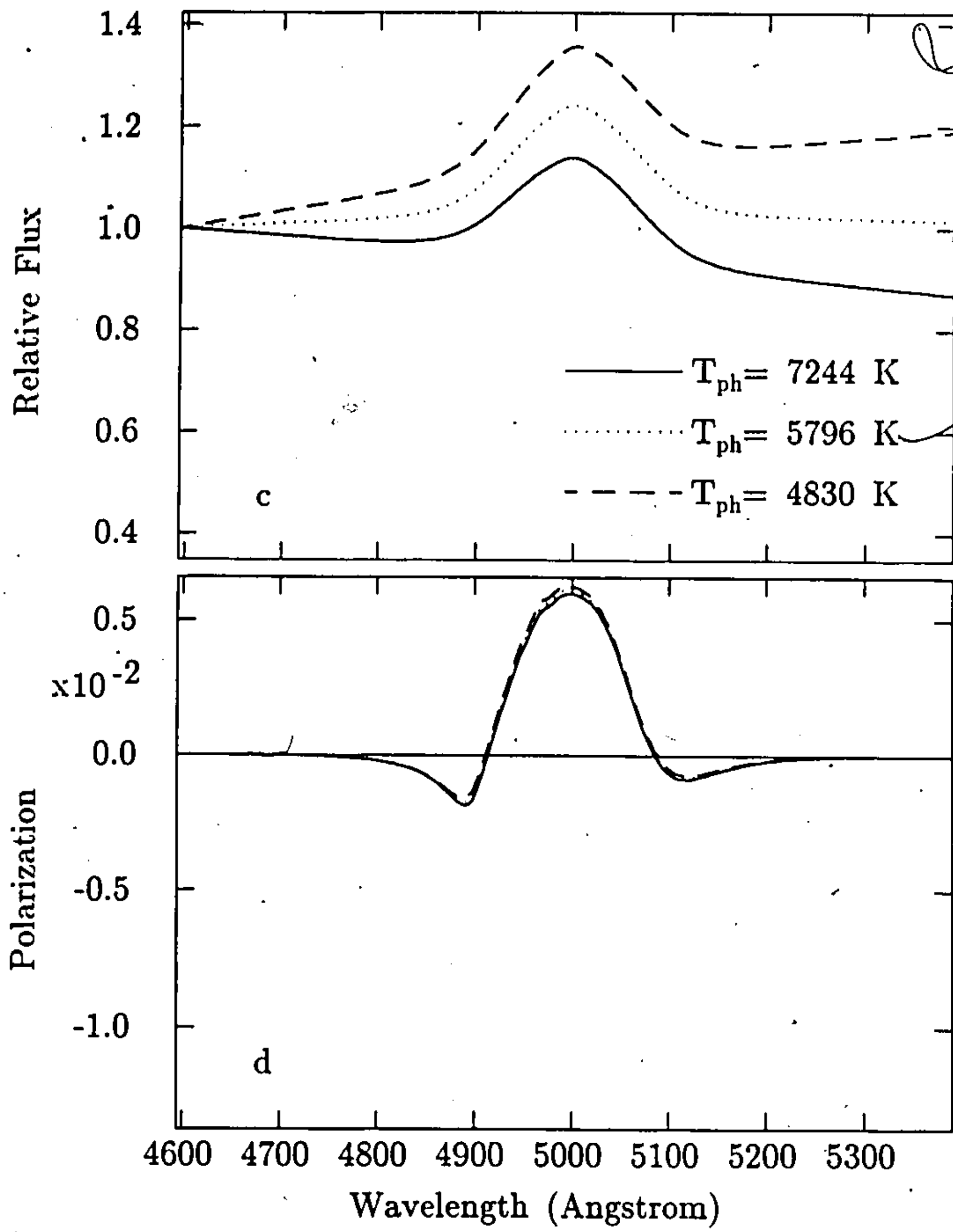

Fig. 4.10c and d. The limb components of the flux and polarization profiles of Fig. 4.10a and b. The varied continuum slope has little affect on the limb polarization profiles.

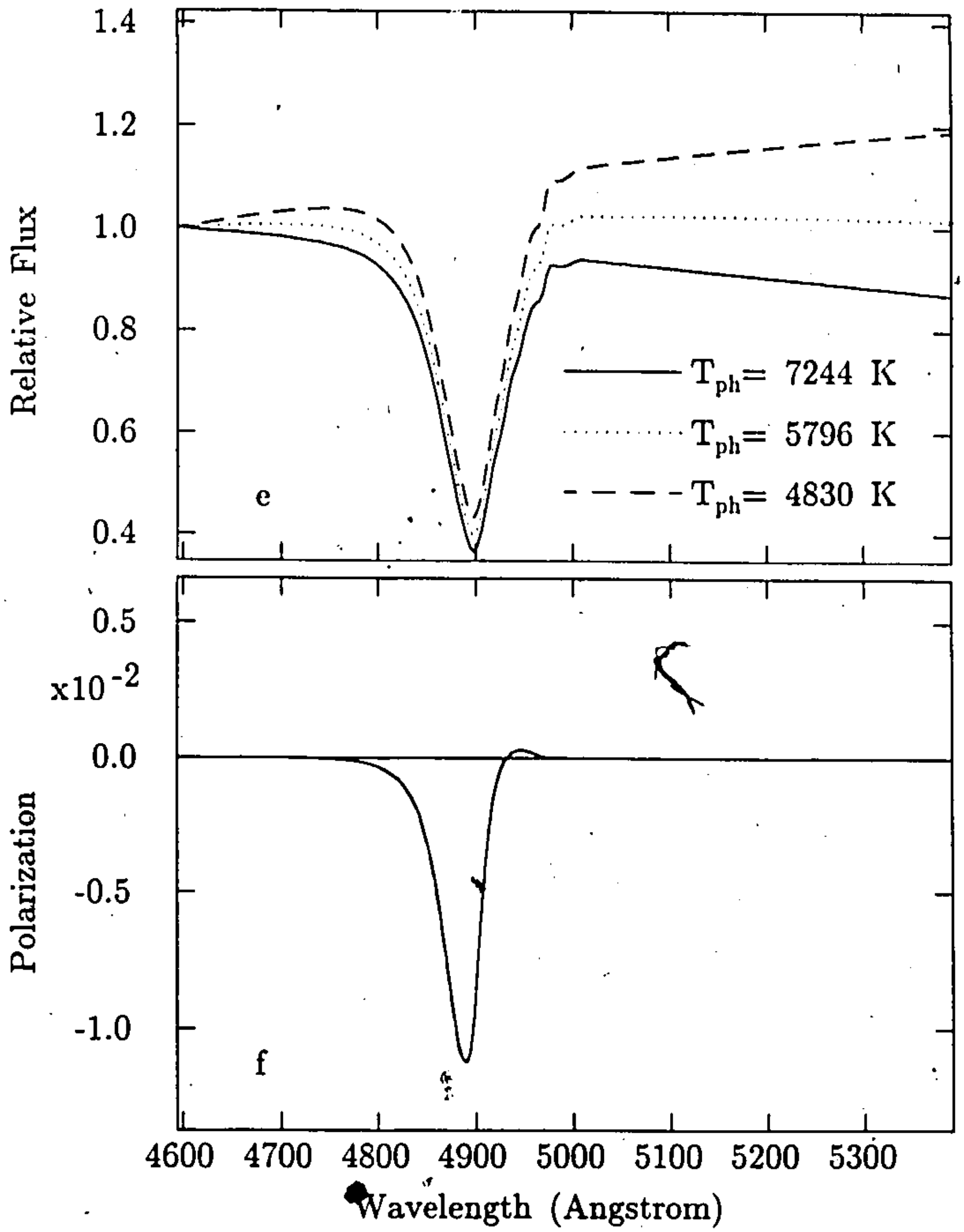

Fig. 4.10e and f. The photodisk components of the flux and polarization profiles of Fig. 4.10a and b. The varied continuum slope has no significant affect on the photodisk polarization profiles.

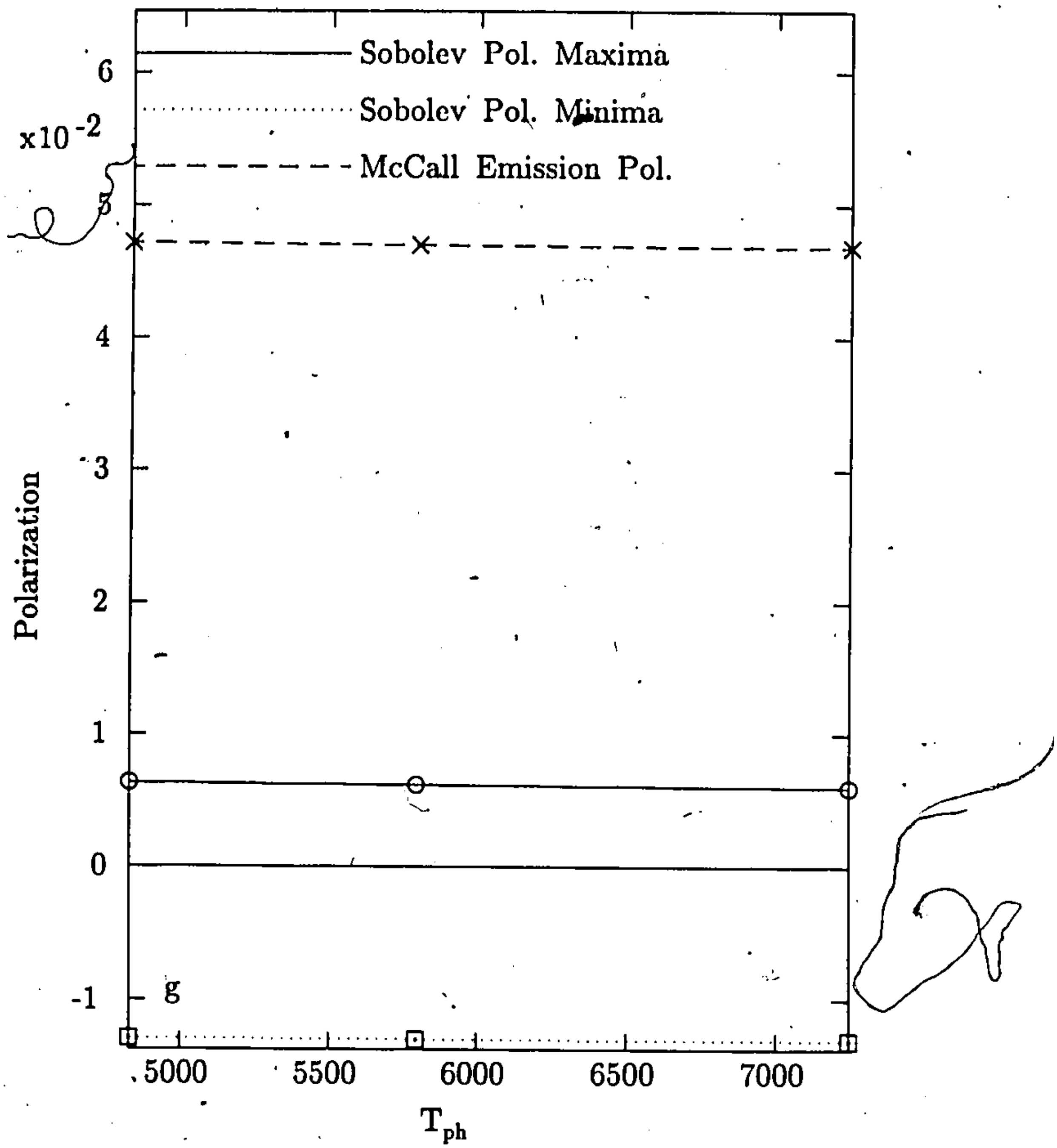

Fig. 4.10g. The maximum and minimum polarizations of the profiles of Fig. 4.10b as a function of photospheric temperature T_{ph}. The McCall emission polarization maxima are also shown for comparison. There is very little variation with temperature.

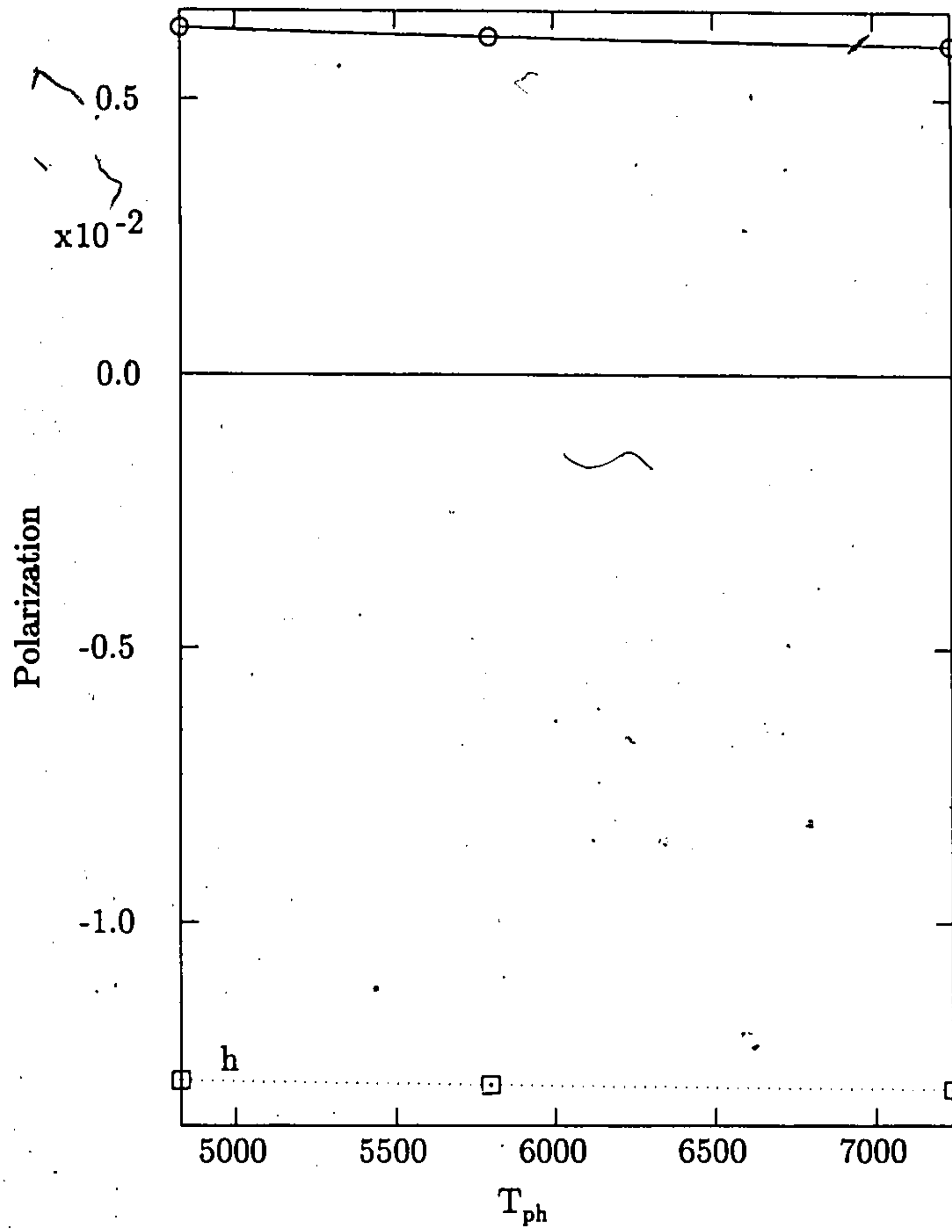

Fig. 4.10h. This is the same as Fig. 4.10g., but with a smaller vertical range in order to better display the Sobolev-H calculation results. There is very little variation in the polarization extrema with variation in the photospheric temperature T_{ph}.

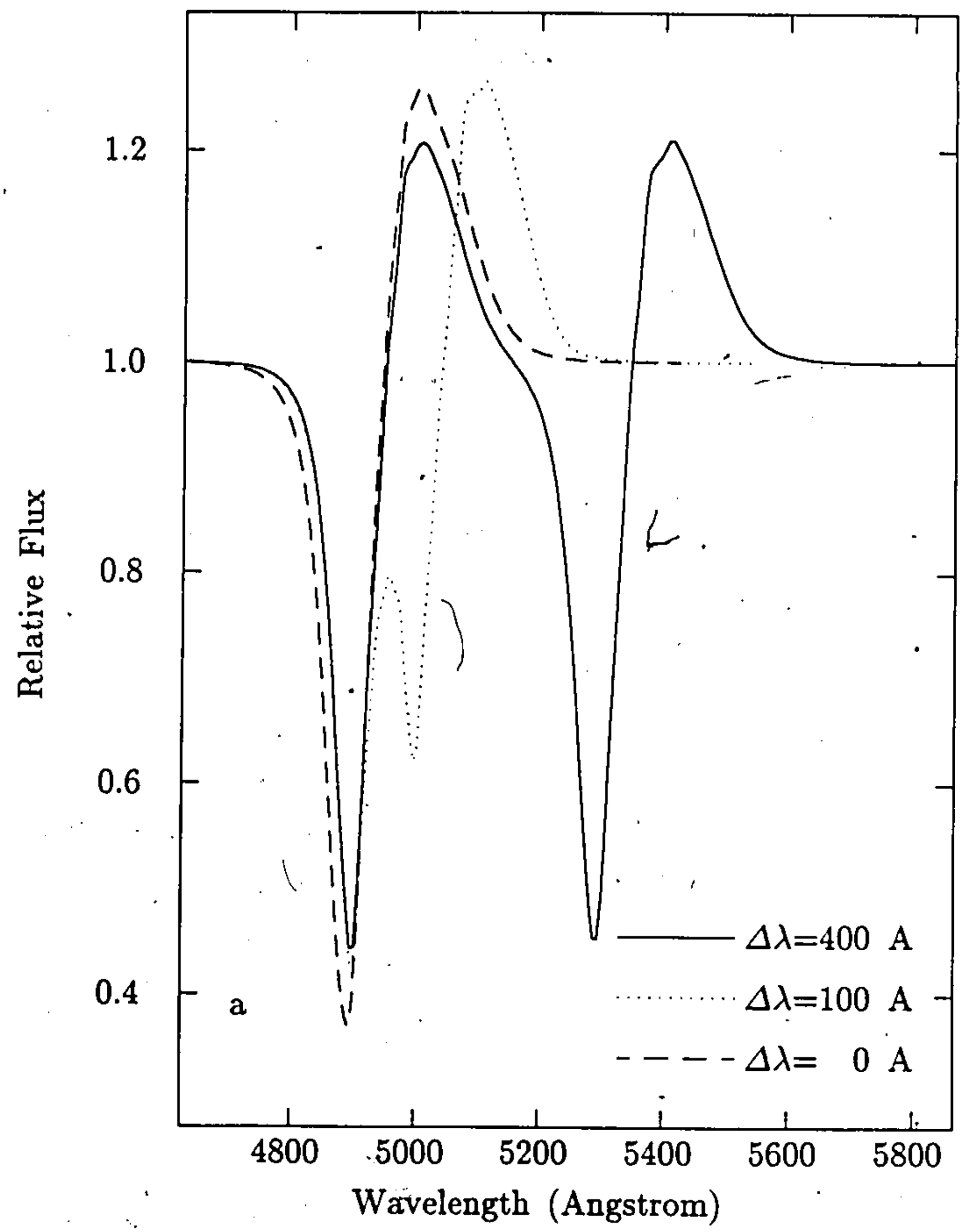

Fig. 4.11a. Flux profiles for a model with two lines, and varying wavelength separation between the lines. The profiles appear completely independent for $\Delta\lambda = 400\,\text{Å}$. For $\Delta\lambda = 100\,\text{Å}$, the lines are strongly perturbing each other. For $\Delta\lambda = 0\,\text{Å}$, the lines appear to be a single P-Cygni line. The $\Delta\lambda = 0\,\text{Å}$ case is not equivalent, however, to a single line with τ_{ph} doubled (see the discussion in Chapter 2 section (f)).

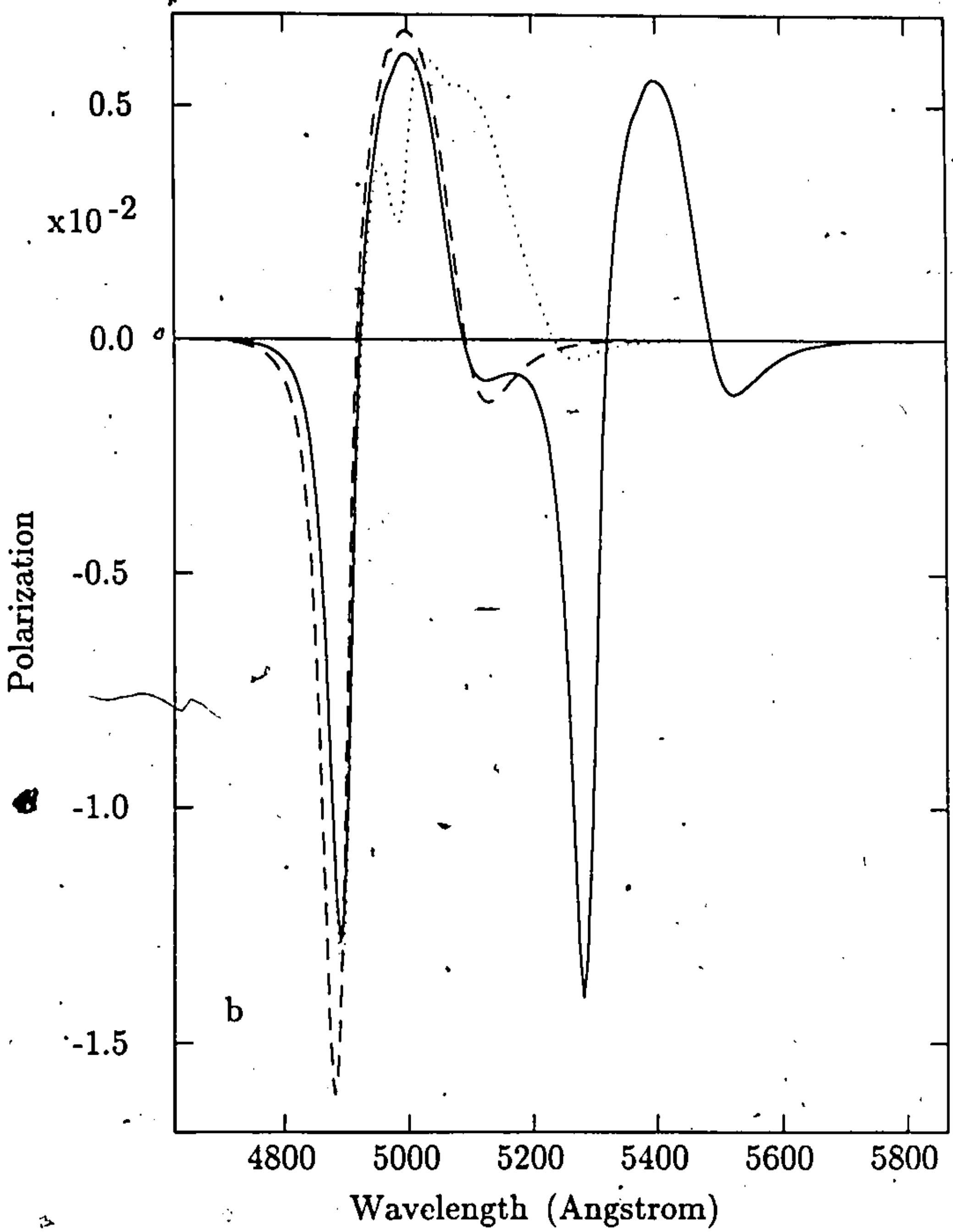

Fig. 4.11b. Polarization profiles for a model with two lines, and varying wavelength separation between the lines. The profiles only slightly affect each other for $\Delta\lambda = 400\,\text{Å}$. For $\Delta\lambda = 100\,\text{Å}$, the lines are strongly perturbing each other. For $\Delta\lambda = 0\,\text{Å}$, the lines appear to have a single P-Cygni line polarization profile.

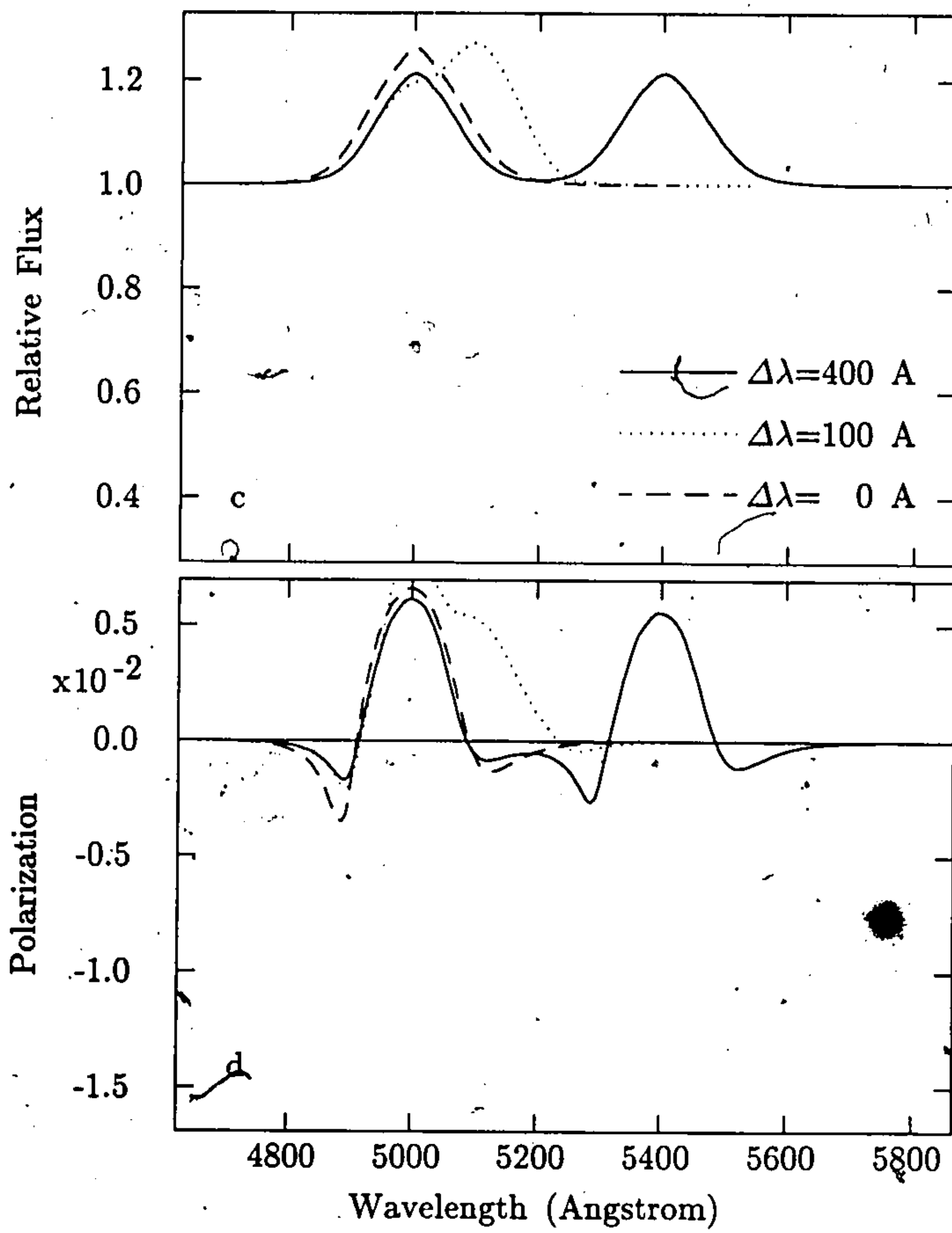

Fig. 4.11c and d. The limb components of the flux and polarization profiles of Fig. 4.11a and b.

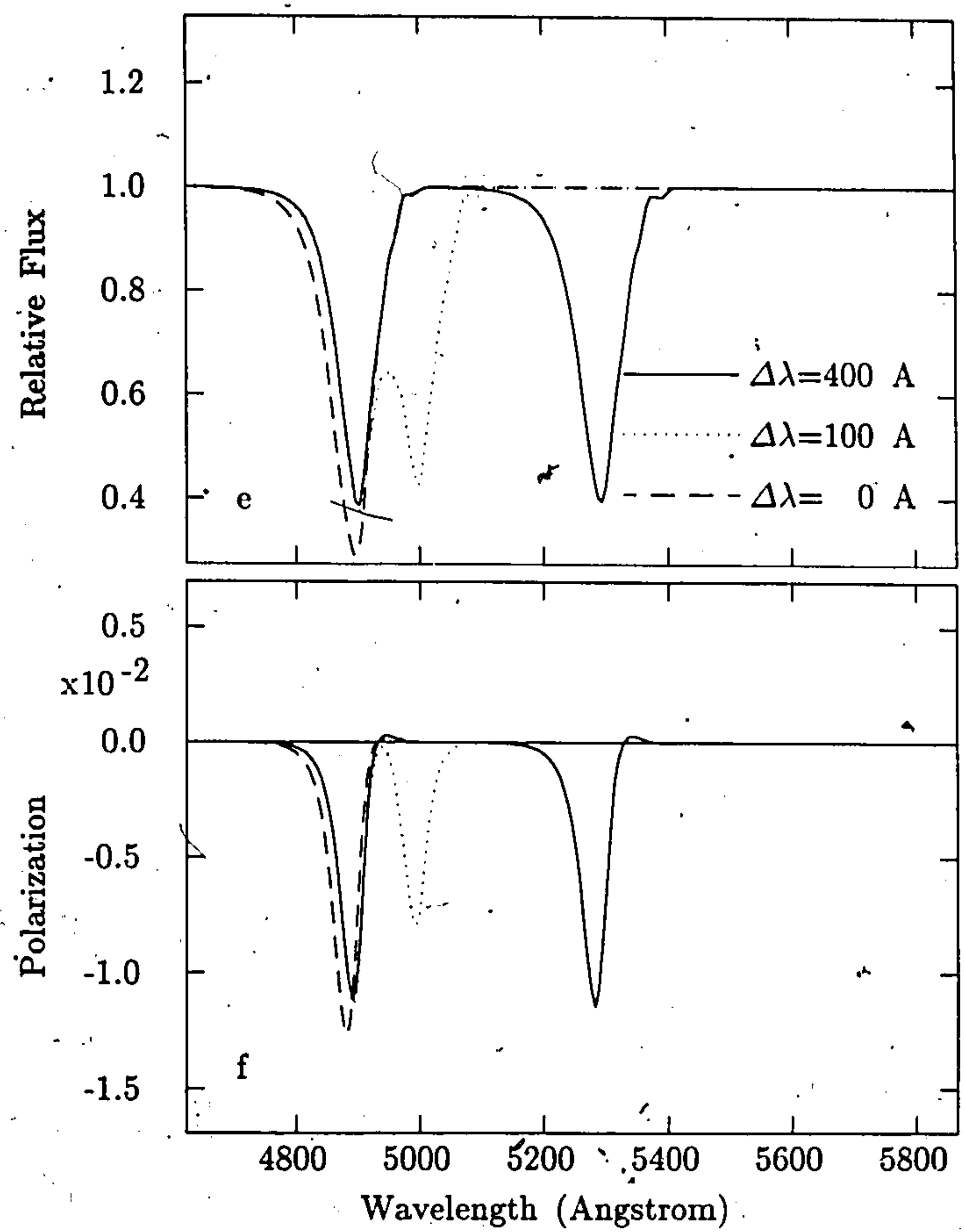

Fig. 4.11e and f. The photodisk components of the flux and polarization profiles of Fig. 4.11a and b.

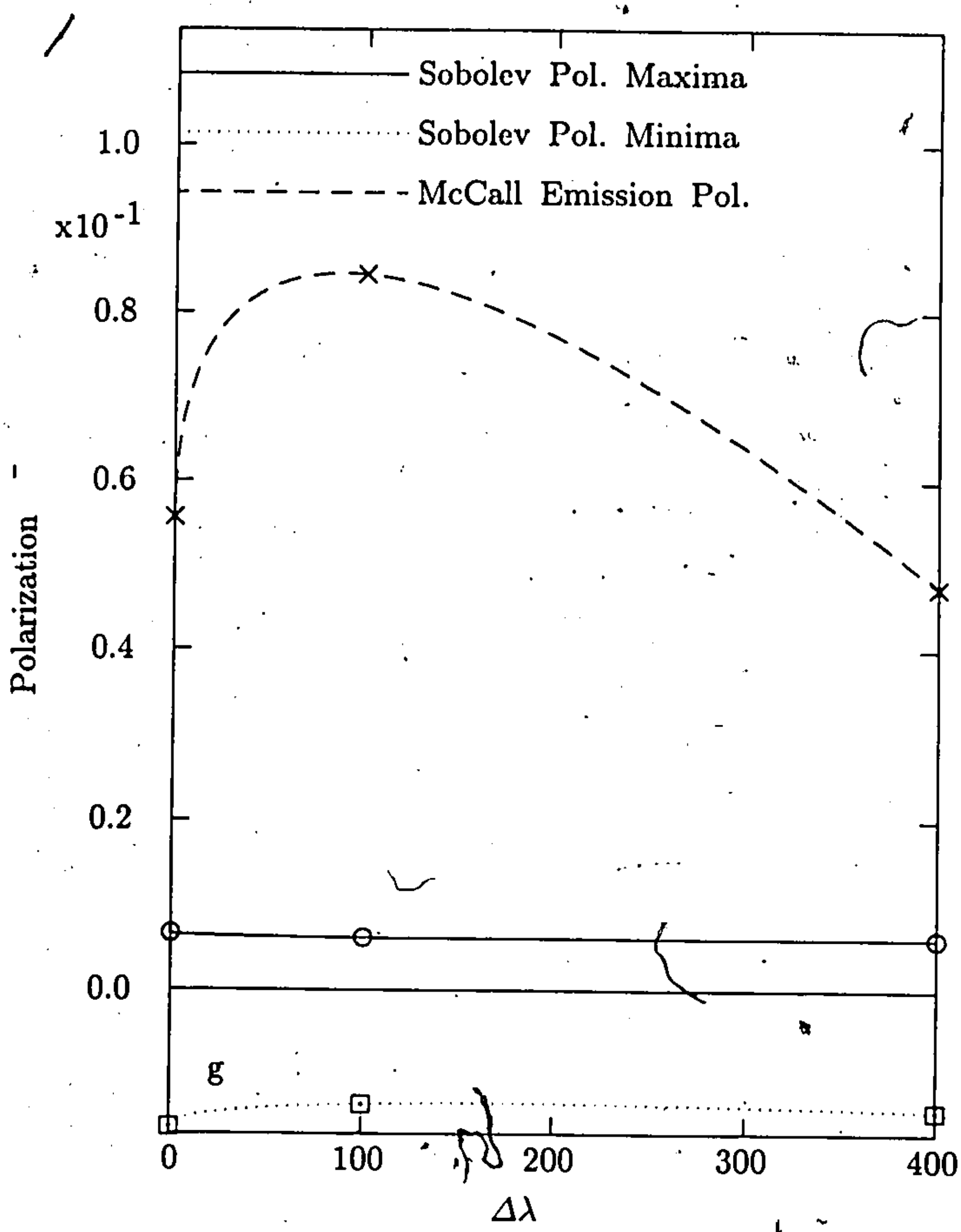

Fig. 4.11g. The maximum and minimum polarizations for the profiles of Fig. 4.11b as a function of the wavelength separation of the lines. The extrema are not greatly affected by the various degrees of blending. McCall emission polarization maxima are also shown for the 5000 Å line. In this case the McCall results are not very significant, since line blending is not included in the McCall prescription.

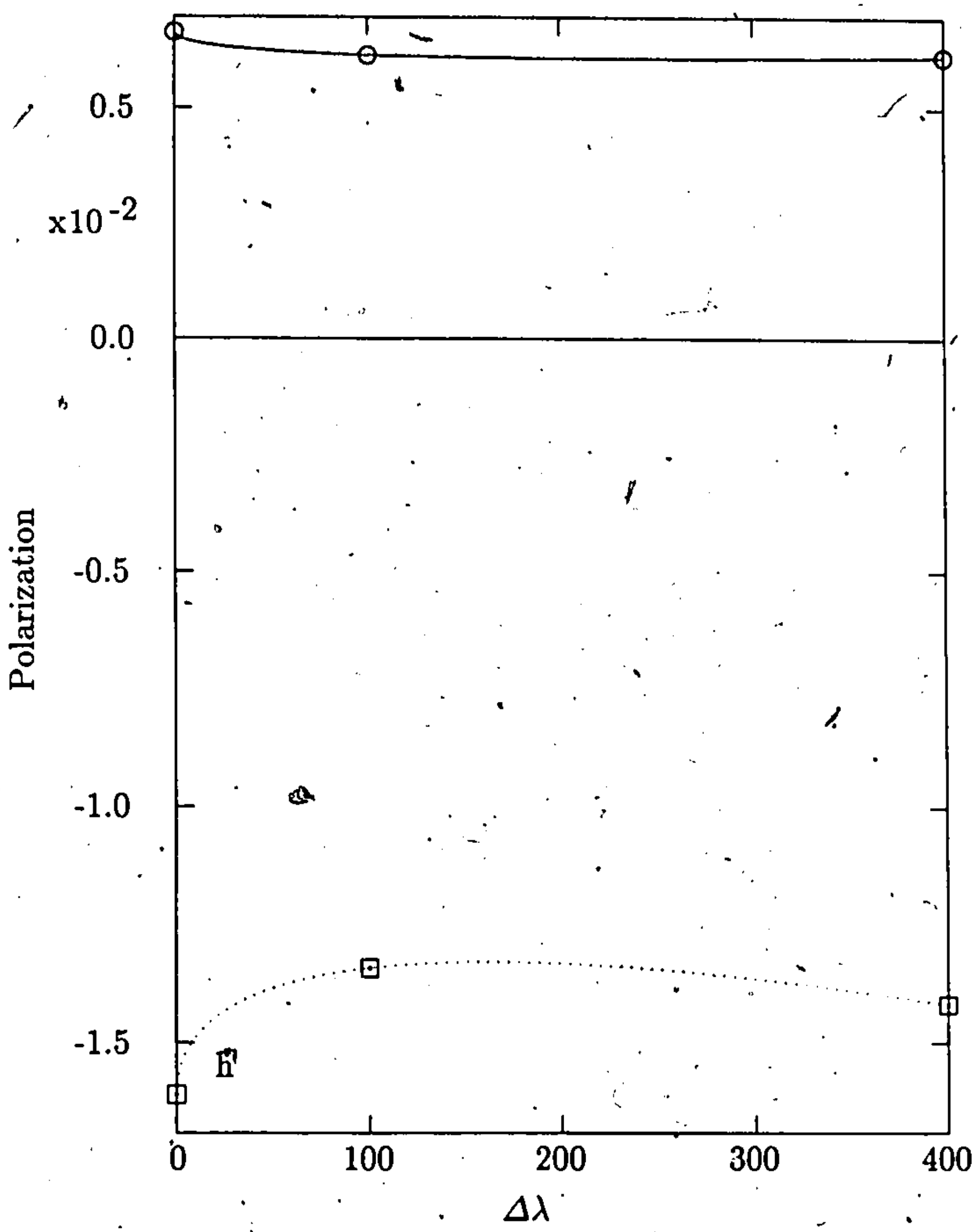

Fig. 4.11h. This is the same as Fig. 4.11g., but with a smaller vertical range in order to better display the Sobolev-H calculation results.

d) Oblate Ellipsoid Models

In this section the flux and polarization profiles of oblate models are presented and discussed. The oblate models considered have exactly the same parameters as the prolate models of section (c) of this chapter, except that the asymmetry is oblate asymmetry (i.e. ξ_{obl} rather than ξ_{pro}). These parameters are given in Table 4.6. All the conventions established for discussing prolate models in section (c) are maintained for the discussion of oblate models.

Except for the cases of extreme asymmetry, oblate models tend to give results that are similar to the results given by prolate models. The reason is clearly that the projections of both oblate and prolate models are elliptical. Both flux and polarization profiles depend strongly on this elliptical symmetry. It is clear that much of the discussion given for the prolate models need not be repeated for their counterpart oblate models. Therefore the discussion in this section will concentrate only on those features of the oblate models that differ from those of the prolate models. Nonetheless all eight figures for each oblate model are presented for completeness and reference.

The major distinction in appearance between the prolate and oblate polarization profiles is an inversion of their behavior about the zero polarization axis: positive and negative prolate features become negative and positive oblate features, respectively. Recall that positive polarization means that the polarization is aligned with the symmetry axis, and negative polarization means that the polarization is aligned perpendicular to the symmetry axis. The inversion between the oblate and prolate models arises because the semi-major axis of the projection of an oblate model is perpendicular to the symmetry axis of the model, whereas the reverse is true for a prolate model. In the discussion of the prolate model 4.7 in section (c) of this chapter, it was shown how an elongated object could give rise to negative and positive polarization features; the same discussion applies to oblate models.

The model 4.12 has a varied asymmetry parameter ξ_{obl}. The $\tau_{ph} = 10$ and the inclination angle $\theta_{incl} = 90°$. This photospheric optical depth is typical of a moderate strength supernova line. The choice of $\theta_{incl} = 90°$ maximizes the asymmetry of the projection of the atmosphere, and thus maximizes polarization. The other parameters are shown in Table 4.6. Recall

$$\xi_{obl} = 1 - (c/a), \qquad a > c \qquad \text{oblate}, \tag{4.39}$$

and

$$(c/a) = 1 - \xi_{obl}. \tag{4.40}$$

TABLE 4.6.—Parameters for the oblate models of section (d).

Model (Figure)	Continuum$_{ph}$ E_1 p	Pro/Oblate $r_{g_{max}}$ T_{ph}	v_{ph} ϵ θ_{incl}	λ_{rest} ξ τ_{ph}
4.12	Constant 1 7	Oblate $4 \times r_{g_{ph}}$ †	$.6 \times 10^9\,\mathrm{cm\,s^{-1}}$ 0 90°	5000 Å * 10
4.13	Constant 1 7	Oblate $4 \times r_{g_{ph}}$ †	$.6 \times 10^9\,\mathrm{cm\,s^{-1}}$ 0 *	5000 Å .5 10
4.14	Constant 1 7	Oblate $4 \times r_{g_{ph}}$ †	$.6 \times 10^9\,\mathrm{cm\,s^{-1}}$ 0 90°	5000 Å .5 *
4.15	Planck 1 7	Oblate $4 \times r_{g_{ph}}$ *	$.6 \times 10^9\,\mathrm{cm\,s^{-1}}$ 0 90°	5000 Å .5 10
4.16	Constant 1 7	Oblate $4 \times r_{g_{ph}}$ †	$.6 \times 10^9\,\mathrm{cm\,s^{-1}}$ 0 90°	* .5 10

NOTE: The "*" indicates that the parameter is being varied for this model. The "†" indicates that the parameter is irrelevant for this model.

The flux profiles for model 4.12 are shown in Fig. 4.12a. Varying the asymmetry has some affect on the profile, but the P-Cygni shape is maintained. The flux maximum increases as ξ_{obl} increases, and the flux minimum decreases. The counterpart prolate model 4.7's flux profiles have the opposite behavior with increasing asymmetry. The oblate model behavior can be explained by the varying amounts of solid angle the photosphere subtends at points in the atmosphere. Recall the source function depends strongly on solid angle. As the photosphere becomes more oblate the points above and below the photosphere see more and more solid angle. The points before, behind, and beside the photosphere see less and less solid angle. In the limit where $\xi_{obl} \to 1$ the photosphere becomes an infinite plane. All points above and below the photosphere then see 2π of solid angle, and the other points see none. Since the emission feature results mainly from points above, below, and beside the photosphere it is clear that the emission flux should tend to increase with increasing oblateness.

The absorption feature's flux results mainly from scattering from points with $x \gtrsim x_{ph}$. These points see less solid angle with increasing asymmetry, and thus the absorption feature becomes deeper. Another feature of the oblate flux profiles in the limit of extreme asymmetry (e.g., $\xi_{obl} = .999$) is that the there is a sharp corner of the profile at the wavelength corresponding to $x = -x_{ph}$. In the limb component profiles, shown in Fig. 4.12c, there are sharp corners at $x = \pm x_{ph}$. These corners are also explainable from the solid angle argument. The limb points before and behind the photosphere have so little solid angle contributing to their source functions that there is a sharp decline to nearly zero for scattered flux from velocity surfaces just before or behind the photosphere.

Model 4.12's polarization profiles are shown in Fig. 4.12b. The profiles are similar to those of the counterpart prolate model 4.7's profiles after allowing for the overall inversion in the zero polarization axis. However, there is some distinction at large asymmetries. This is understandable since the prolate models tend to become quasi-1-dimensional line objects at large asymmetries, whereas the oblate models tend to become quasi-2-dimensional disk objects. The oblate model profiles have a general increase in the absolute value of polarization as ξ_{obl} increases until about $\xi_{obl} \approx .85$, then the profiles decrease rapidly (see Fig 4.12h). It should also be noted for the $\xi_{obl} = .85$ profile that the emission feature minimum has become bifurcated. Both these behaviors can be explained by the fact that the atmosphere is approaching being plane-parallel as asymmetry increases. The polarization of radiation emitted from a point $\vec{r}$ is directly proportional to the difference between the source function fields $S_x(\vec{r})$ and $S_y(\vec{r})$, providing that the Stokes U field need not be considered. From equation (2.155)

$$S_x - S_y \propto -D_2(1-\mu^2) + D_3\mu\sqrt{1-\mu^2}\cos\phi + D_4(1+\mu^2)\cos 2\phi, \tag{4.41}$$

where the D_i are the direct contributions to the source function that are discussed in Chapter 2 section (d). For a point above a planar photosphere that emits a uniform, angle-independent, unpolarized specific intensity the D_2, D_3, and D_4 coefficients are all zero (see equations (2.130)). Thus the radiation emitted from a plane-parallel atmosphere above such a photosphere would be unpolarized. This is precisely the situation that the model 4.12 is tending toward as asymmetry increases. This depolarizing effect is first noticed for limb emission flux that is emitted from the atmosphere above and below the central region of the disk-like oblate photosphere. Thus near the rest wavelength the emission feature of the polarization profile stops growing so rapidly with increasing asymmetry, and starts to decline for $\xi_{obl} \gtrsim .85$. The polarization is becoming confined to the radiation emitted near the edge of the disk. However, with increasing asymmetry the flux contribution from the edges declines relative to the flux contribution from above and below the photosphere. For $\xi_{obl} \gtrsim .85$, the relative decrease in polarized flux becomes a more important effect than the polarizing effect of asymmetry. Polarization thus declines for all wavelengths when ξ_{obl} is increased above approximately .85. When $\xi_{obl} = .999$, the polarization is nearly zero everywhere compared to all the other non-zero asymmetry profiles.

The Figures 4.12c, 4.12d, 4.12e, and 4.12f display the flux and polarization profiles of the limb and photodisk. Figures 4.12g and 4.12h show the polarization extrema as a function of asymmetry. The McCall emission polarization and the SS (Shapiro and Sutherland, 1982) continuum pure scattering polarization are also shown. The McCall values are an order of magnitude greater in absolute value than ~~the~~ the Sobolev-H results. This is the same as for prolate models. The SS results do not seem to have any close relation to the Sobolev-H results. It is interesting to contrast the extreme asymmetry limit for the Sobolev model and the SS model. In the Sobolev-H case, for the reasons explained above, the polarization goes to zero. In the SS case the polarization goes to 11.7% when the atmosphere becomes a disk viewed edge on. The SS model uses Chandrasekhar's plane-parallel continuum scattering atmosphere result (1960, p. 248). The Chandrasekhar result for polarization of radiation emitted at 90° to the normal of the symmetry plane is 11.7%. SS simply recovered this result for their extremely oblate model. The difference between the Sobolev-H and the SS extreme oblate results, of course, arises from the difference in the physical systems. The Sobolev system consists of velocity surfaces in which initially unpolarized radiation is scattered a few times, and then escapes to infinity. The Chandrasekhar system consists of an infinitely deep plane-parallel atmosphere with frequency independent scatterers; only the radiation emitted at the surface plane escapes to infinity without being scattered again.

Model 4.13 has the inclination angle varied from 90° to 0°. The asymmetry parameter $\xi_{obl} = .5$. This asymmetry was chosen because it seems a plausible large value for supernova asymmetry (see the discussion in Chapter 1 section (d)). The optical depth at the photosphere $\tau_{ph} = 10$. This τ_{ph} value produces a line of moderate strength. The other parameters are given in Table 4.6.

The flux profiles for model 4.13 are shown in Fig. 4.13a. The height of the emission maximum and absorption minimum vary in a non-monotonic manner with decreasing inclination angle. At 0°, the absolute values of the emission maximum and absorption minimum are less than at 90°.

Recalling that the strength of the source function at scattering points depends on the solid angle the photosphere subtends at those points, the change in the height of the emission maximum between the 90° and the 0° cases can be accounted for. Points near the equator of the photosphere see less solid angle than points that are nearer the poles. At 90° some of the velocity surface points that give rise to the emission flux are polar and some equatorial; at 0° all the points contributing to the emission flux are equatorial. Thus it is not surprising that the emission flux is larger at 90° than at 0°. The other behavior of the flux profile as inclination angle varies is more difficult to explain; the explanation probably requires an analysis that isolates the various effects that give rise to the flux.

The polarization profiles for model 4.13 are shown in Fig. 4.13b. The polarization declines to zero everywhere as the inclination angle goes to zero. At $\theta_{incl} = 0°$ the projection of the atmosphere has circular symmetry about the line of sight and hence the net polarization must be zero at all wavelengths. The effect on the profiles of decreasing the inclination is rather interesting. The emission polarization minimum is shifted to a wavelength below the rest wavelength. The subsidiary local maximum that is at $\lambda(-v_{ph})$ for $\theta_{incl} = 90°$ shifts to a lower wavelength. Also, a second polarization minimum appears at a wavelength greater than that of the subsidiary maximum. These effects might allow the determination of inclination angle from spectropolarimetric data. None of the effects is present for the counterpart prolate model 4.8, and so their presence in spectropolarimetric data may allow differentiation between prolate and oblate asymmetry.

The limb and photodisk component profiles in Figures 4.13d and 4.13f give some insight into how the inclination effects on the profiles arise. Recall the limb and photodisk polarization components combine to create the features of the polarization profiles. The limb component polarization profile (see Fig. 4.13d) becomes roughly inverted with respect to the zero polarization axis as the inclination angle increases, and the central polarization minimum bifurcates into two polarization maxima. The new maximum with the higher wavelength gives rise to the shifted subsidiary maximum in the net polarization profile (see Fig. 4.13b). The bifurcating extremum is explained by the fact that the ellipsoid atmosphere viewed at an oblique inclination angle has projecting and retreating lobes that cause the polarizing asymmetry to maximize at symmetric x' positions. This same bifurcation effect, but not the profile inversion, was noted for the limb polarization of the obliquely viewed prolate model 4.8 in section (c). The inversion of the oblate model profile probably owes to the increasing strength of scattering from the sides of the photosphere relative to scattering from above and below it. This increasing relative strength owes to the fact that the limb regions near the sides of the photosphere stay closer to the photosphere than the limb regions above and below the photosphere as inclination angle is decreased. Recall from the prolate model 4.9 that for $\tau_{ph} \lesssim 100$ most of the polarizing scattering occurs very near the photosphere. Thus it is the rapid decay of the Sobolev optical depth with generalized radius rather than solid angle, which determines the behavior.

The photodisk component of the source function (see Fig. 4.13f) shows a negative polarization feature growing and then shrinking as inclination angle is decreased. This photodisk negative polarization feature dominates the net polarization, causing the shifted net emission polarization feature (see Fig. 4.13b). This negative feature probably arises from the increasing area of velocity surfaces near $x(v = .5 \times v_{ph})$ as inclination angle is decreased. The unocculted parts of these velocity surfaces are scattering surfaces that are elongated along the y axis. A main result of all the Sobolev-H calculations and the expectation from the elliptical symmetry polarization calculation of Chapter 3 section (b) indicate that scattering from the sides of an elongated photospheric surface tend to polarize parallel to the direction of elongation. This is the effect that leads to the development of the negative polarization feature of the photodisk polarization component.

Fig. 4.13g and 4.13h show the Sobolev-H polarization extrema as a function of asymmetry. The maximum increases and the minimum decreases monotonically with ξ_{obl}. The McCall emission polarization is also shown. The McCall results are roughly an order of magnitude greater in absolute value than the Sobolev-H results; this is the same as for all the other models.

Model 4.14 has a varied photospheric optical depth τ_{ph}. The flux profiles, given in Fig. 4.14a, are qualitatively very similar to the counterpart prolate model 4.9 flux profiles (see the discussion in section (c) of this chapter). A noticeable difference is that the redward side of the emission feature is rather concave for the oblate model, and rather linear with wavelength for the prolate model. The spherical model with varied τ_{ph} (model 4.1) has an intermediate shape for the redward side of its emission flux features. The polarization profiles for model 4.14 are given in Fig. 4.14b. Except, of course, for the inversion of the profiles about the zero polarization axis the polarization profiles are similar to the counterpart prolate model's profiles, and are similarly explained. There are, however, two distinctions. (1) The oblate profiles are noticeably affected by the finite outer radius of the atmosphere for $\tau_{ph} \geq 10^4$, whereas the prolate profiles seemed unaffected for $\tau_{ph} = 10^4$. (2) The oblate model's polarization emission feature extremum does not develop the shift and the cusp-like appearance that the prolate model's emission feature extremum develops as τ_{ph} increases. The other figures for model 4.14 are similar to the figures for the counterpart prolate model 4.9.

Model 4.15 has a Planck continuum with varied photospheric temperature T_{ph}. The figures 4.15 display the results for this model. These results are entirely analogous to the results of the counterpart prolate model 4.10. Therefore the discussion of model 4.10 given in section (c) of this chapter applies here without any alteration.

Model 4.16 has two identical scattering transitions with varied wavelength separation between them. The figures 4.16 display the results for this model. These results are largely analogous to the results of the counterpart prolate model 4.11. Therefore the discussion of model 4.11 given in section (c) of this chapter applies here.

Several general conclusions can be drawn from this survey of oblate ellipsoid atmospheres. These conclusions are mainly the same as for the prolate models, but there are some differences. (1) There is polarization structure associated with P-Cygni lines emitted by oblate asymmetric atmospheres. (2) There is a change in sign in polarization between the emission feature and absorption feature. This change of sign was not predicted by McCall (1985). The absorption feature has polarization aligned with the symmetry axis, and the emission feature has polarization aligned perpendicular to the symmetry axis. These alignments are the reverse of those of the prolate models. In both cases, however, the emission polarization, and the absorption polarization are aligned parallel, and perpendicular, respectively, to the semi-major axis of the elliptical projection of the atmosphere. (3) The absolute values of the polarization extrema grow monotonically with ξ_{obl} until $\xi_{obl} \approx .85$; then they decline rapidly to zero as $\xi_{obl} \rightarrow 0$. The absolute values of the polarization extrema increase monotonically with increasing inclination angle θ_{incl}. The flux profiles also vary somewhat with asymmetry and inclination. A procedure for fitting spectropolarimetric data would be to fit τ_{ph} values to the flux data for a spherically symmetric model, then fit the observed polarization profiles by adding asymmetry. The flux profiles would be somewhat altered, but they could be re-fit for the asymmetric model. Then the asymmetry could be changed to re-fit the polarization profiles, and so on until some convergence is reached. (4) The Sobolev-H polarizations obtained are not very large. They are of the order of a few per cent even in rather extreme cases. The McCall emission feature polarizations are larger than the Sobolev-H polarizations by about an order of magnitude. This discrepancy undoubtedly owes to the simplicity of the McCall prescription for the polarization. A simple correction to the McCall prescription seems unlikely, since several physical and geometrical features need to be included in prescription. The simplicity of Sobolev-H calculations probably obviates any need for an improved McCall prescription. (5) For inclination angles different from 90° the emission polarization feature's minimum is shifted to wavelengths less than the line rest wavelength. The subsidiary local polarization maximum is shifted to lower wavelengths and a second polarization minimum appears. The flux maximum is shifted to higher wavelengths than the rest wavelength for inclination angles that are not 90° or 0°. These changes may allow detection of the inclination angle from spectropolarimetric and flux data. (6) The effects of line blending on polarization profiles do not quite mimic the effects on the flux profiles. The blending behavior may make it harder to obtain a unique fit to any data. Observers should thus concentrate their efforts on obtaining the spectra of pure, unblended P-Cygni lines.

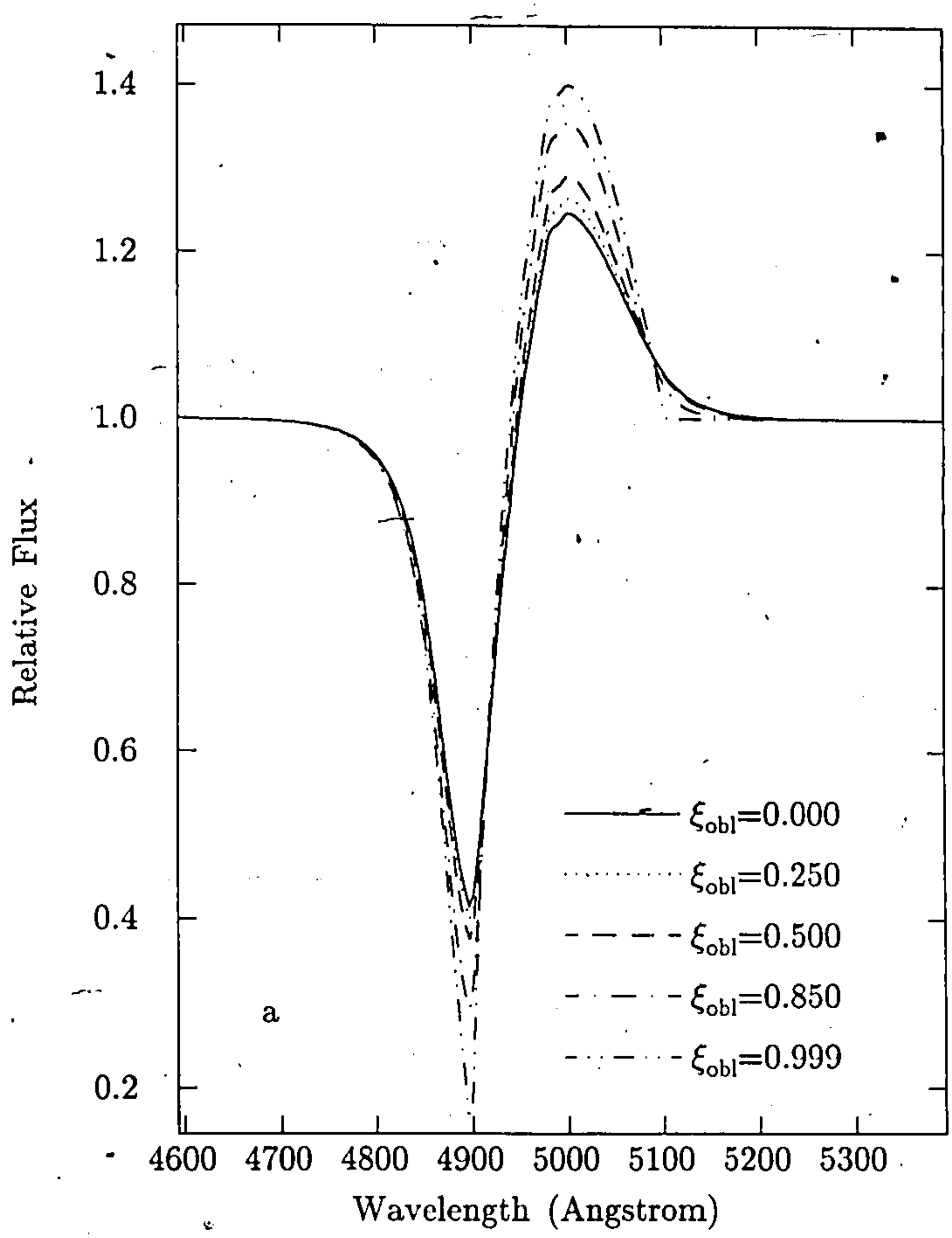

Fig. 4.12a. The flux profiles for a typical oblate model with varied asymmetry ξ_{obl}. The profiles show some alteration with increasing asymmetry, but remain qualitatively the same.

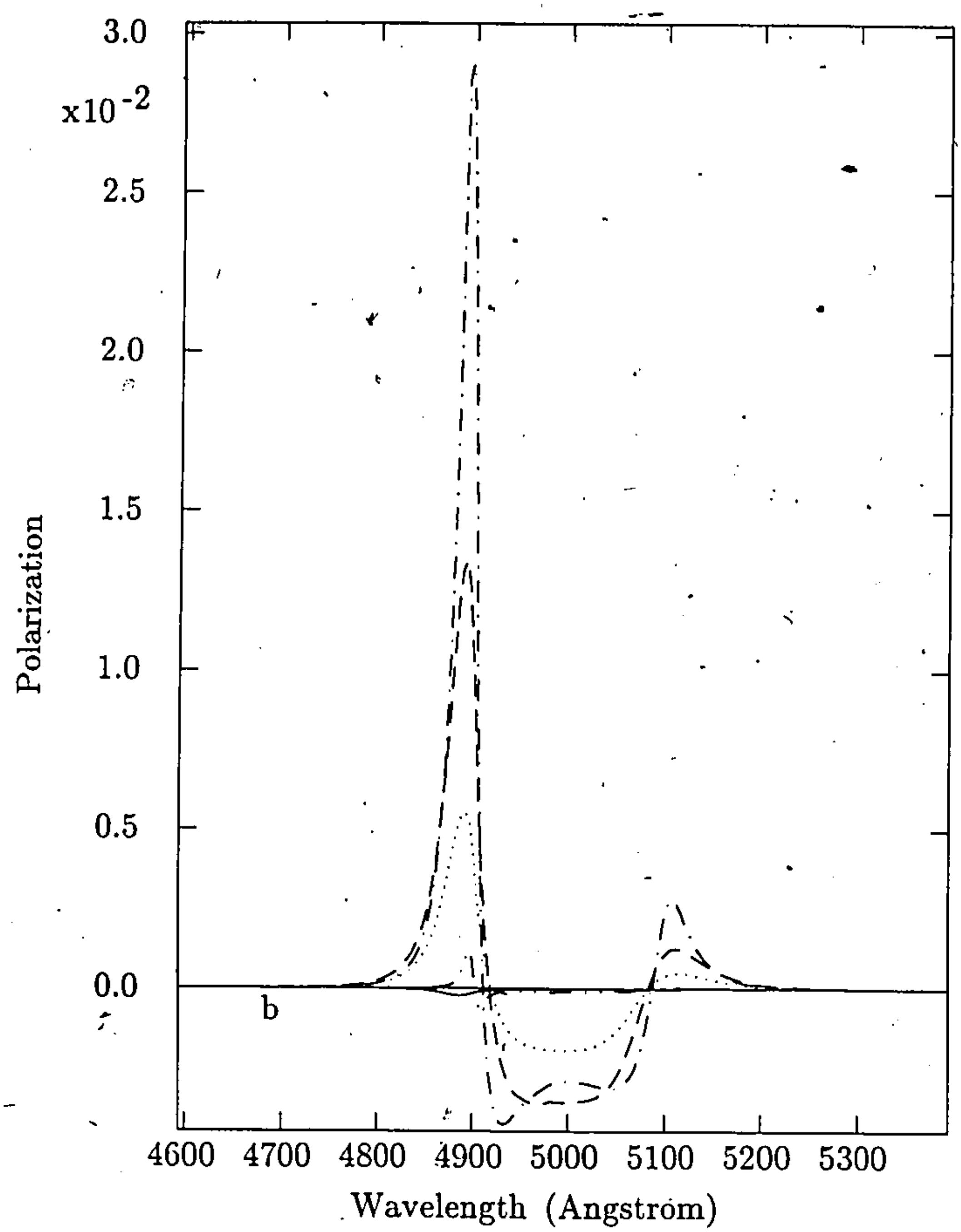

Fig. 4.12b. The polarization profiles corresponding to the flux profiles of Fig. 4.12a. There is a general increase in the absolute value of polarization with increasing oblate asymmetry. The profiles show a change in sign between absorption and emission features.

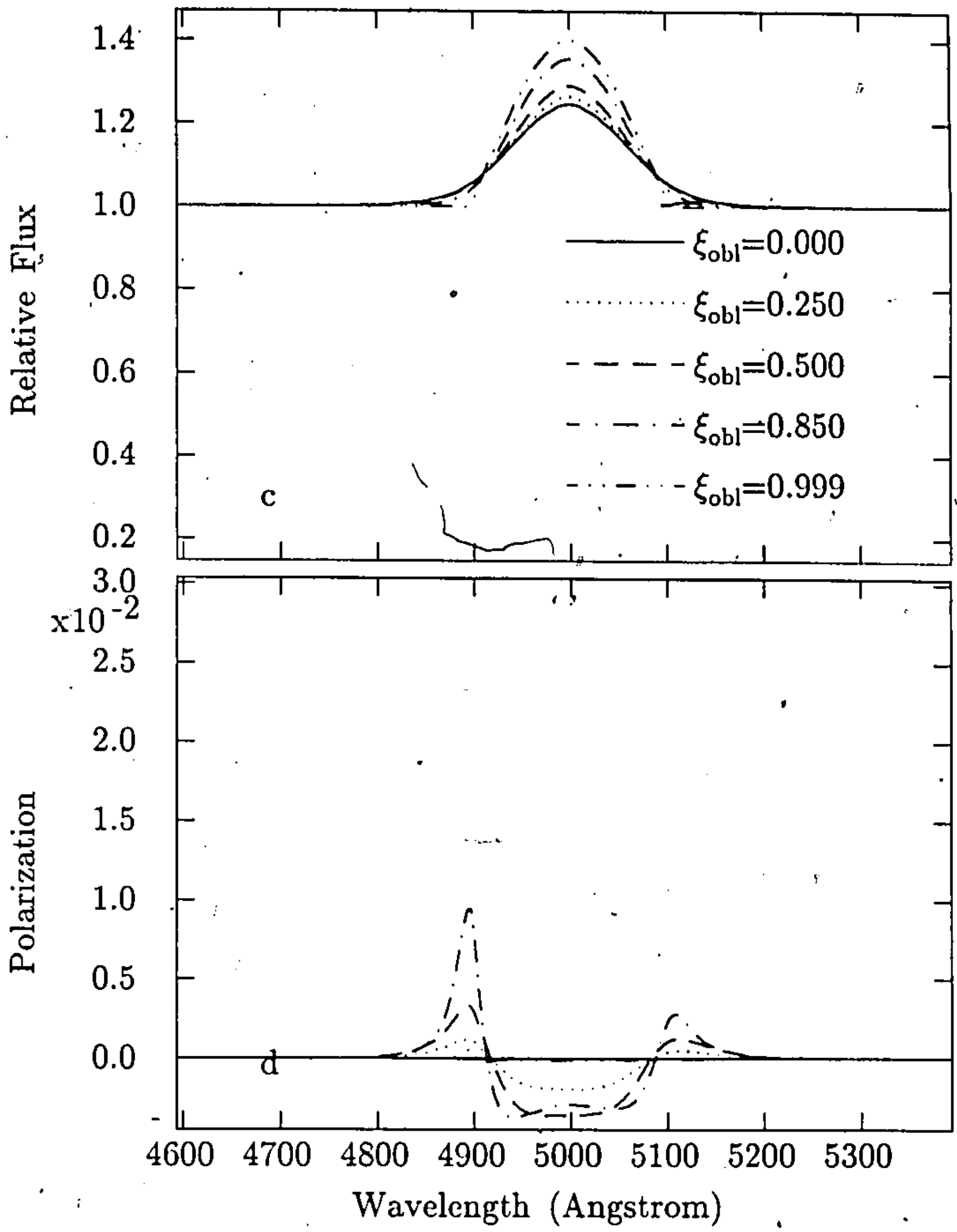

Fig. 4.12c and d. The limb components of the flux and polarization profiles of Fig. 4.12a and b. The limb flux profiles have complete symmetry about the line center; this owes to the symmetry of the ellipsoid shape and to the lack of occultation for the limb contribution. The polarization profiles lack the complete symmetry because they are calculated from $(F_x(limb) - F_y(limb))/F(net)$, where $F(net)$ is not symmetric due to occultation.

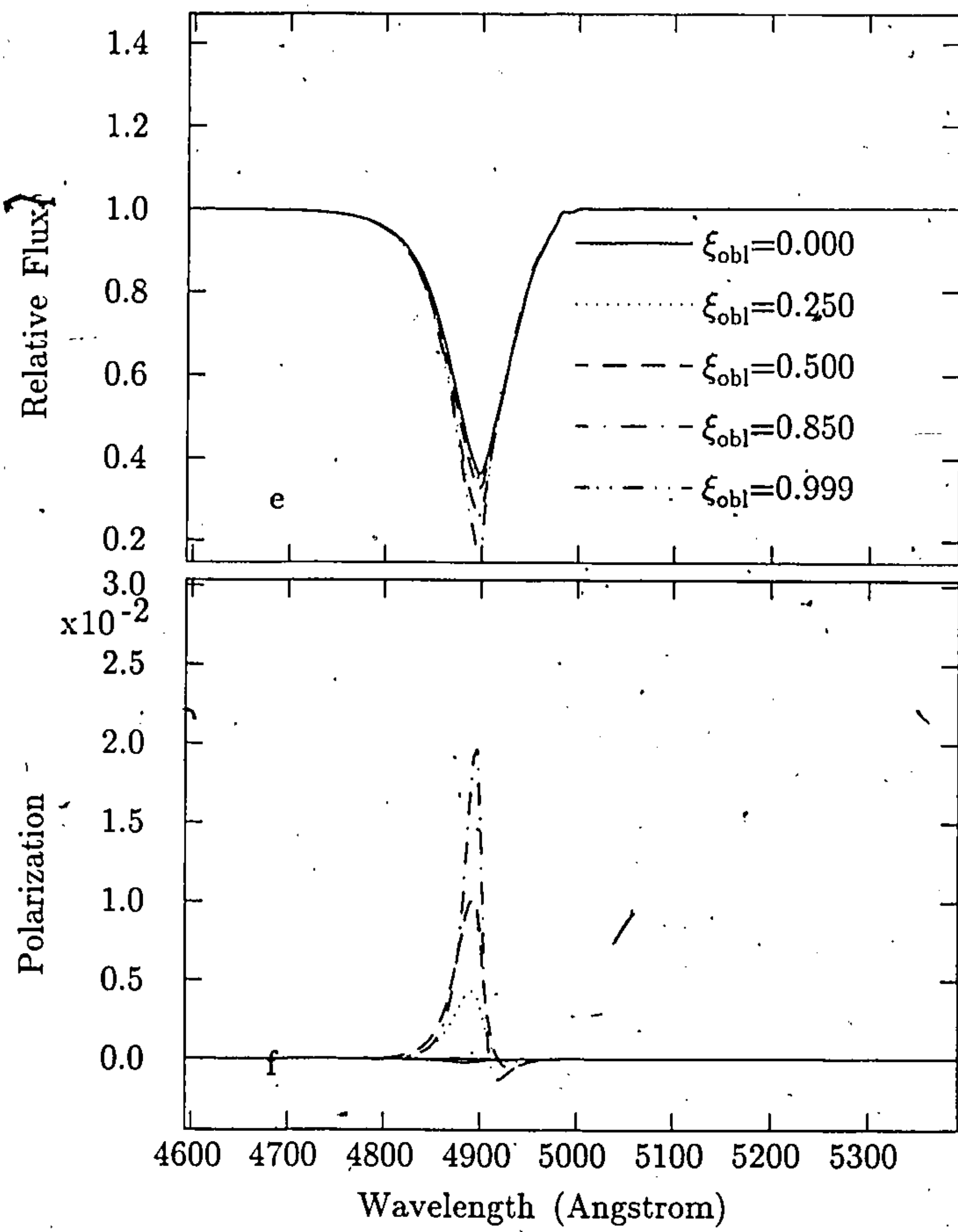

Fig. 4.12e and f. The photodisk components of the flux and polarization profiles of Fig. 4.12a and b.

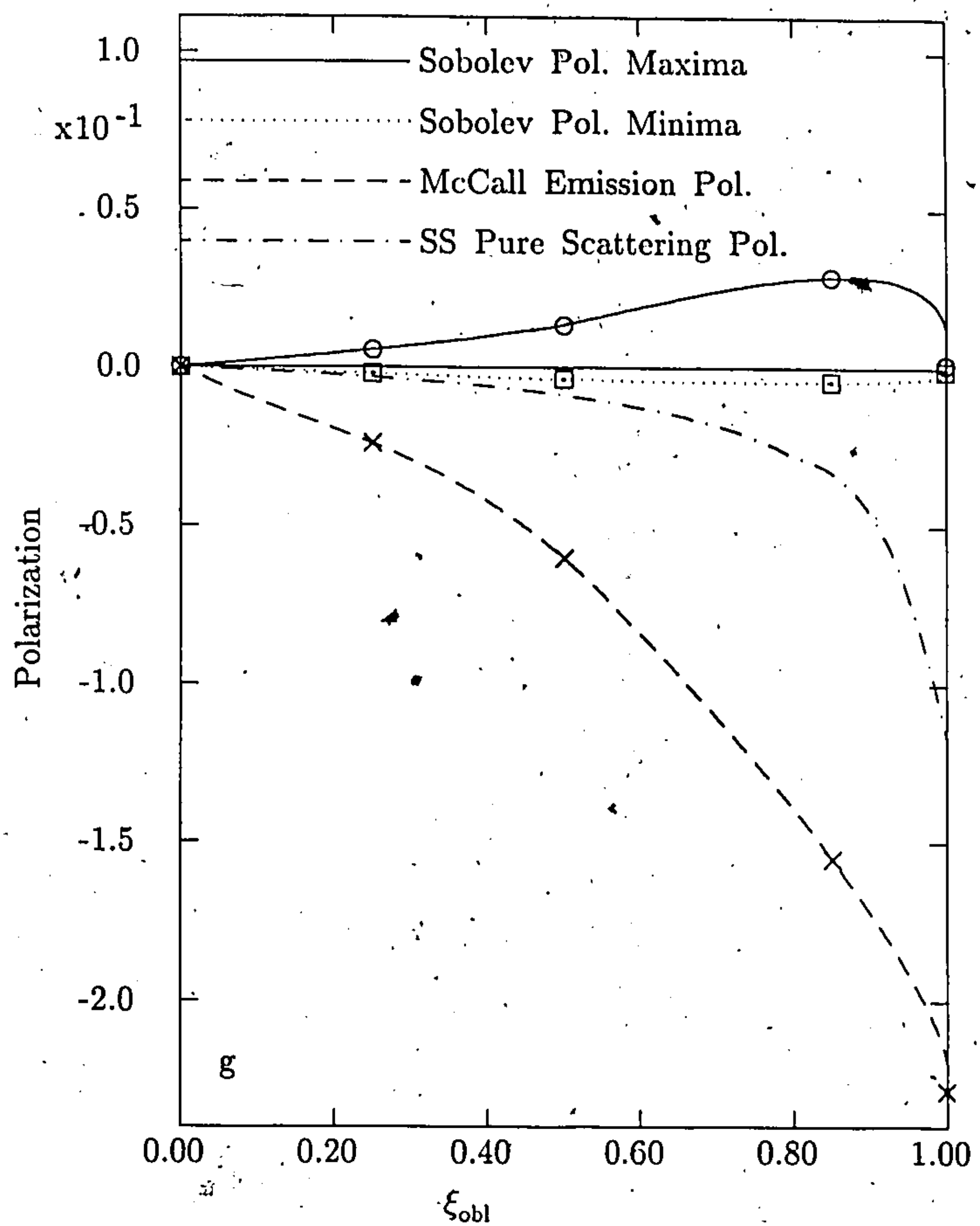

Fig. 4.12g. The maximum and minimum polarizations for each of the profiles of Fig. 4.12b as a function of asymmetry ξ_{obl}. The SS continuum polarization for the pure scattering case and the McCall emission polarization minima are also shown for comparison.

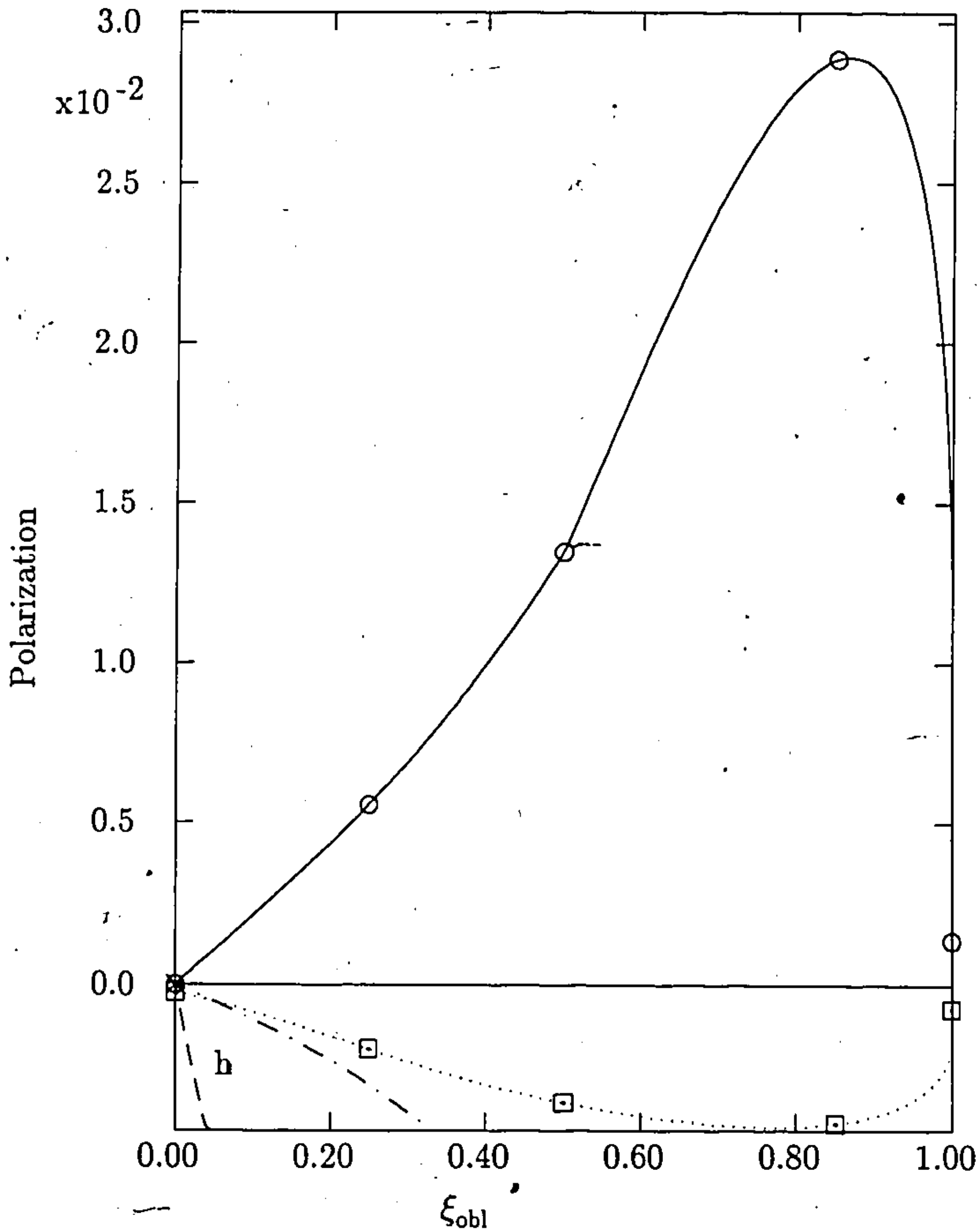

Fig. 4.12h. This is the same as Fig. 4.12g., but with a smaller vertical range in order to better display the Sobolev-H calculation results. Note that the Sobolev-H polarization extrema are roughly linear with ξ_{obl} for $\xi_{obl} \lesssim .5$.

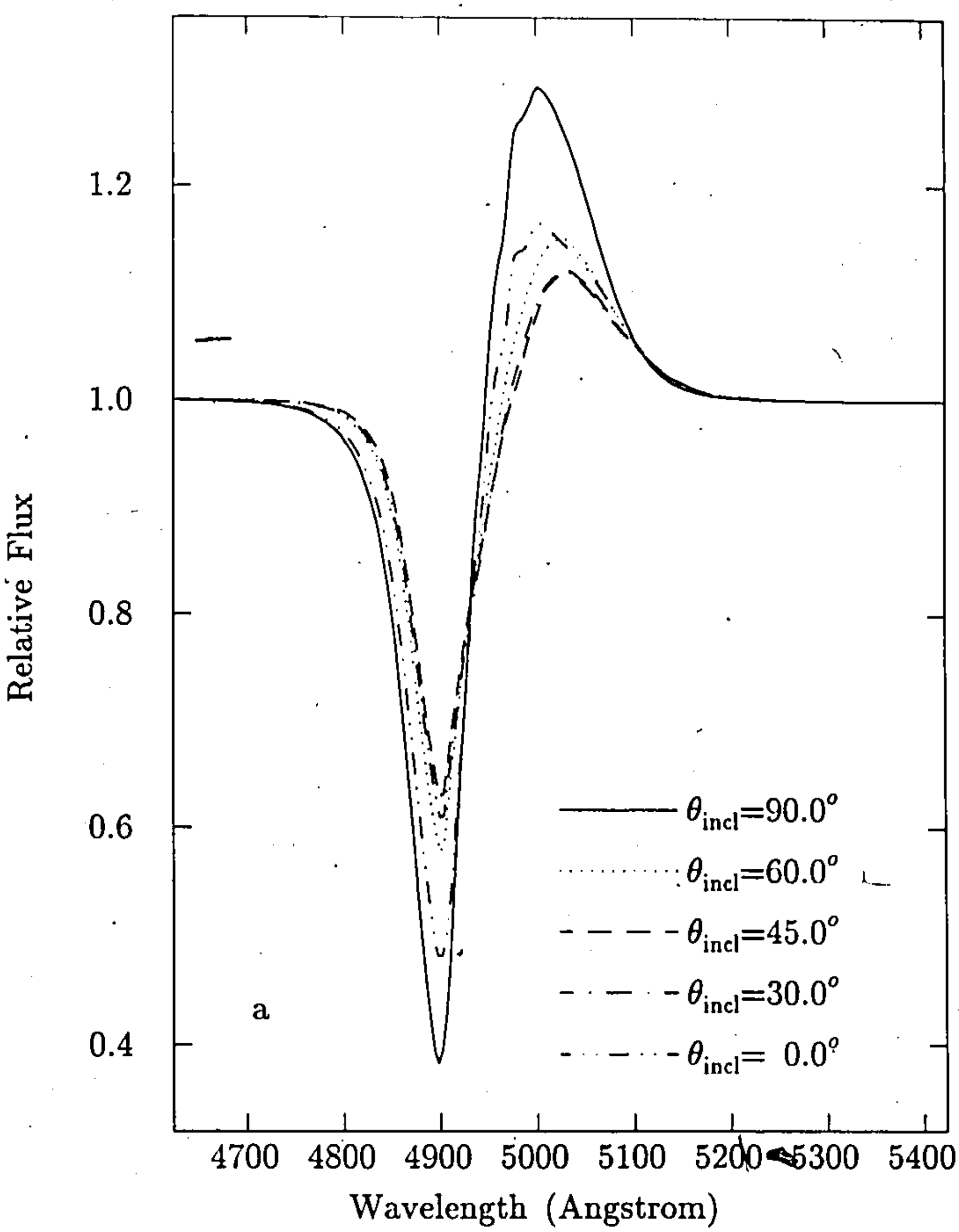

Fig. 4.13a. The flux profiles for a typical oblate model with varied inclination angle θ_{incl} and with ξ_{obl} = .5. The flux profiles are all normalized with respect to the continuum; in absolute value the flux increases by a factor of 2 as θ_{incl} goes from 90° to 0°. The flux profiles change non-monotonically with θ_{incl}. There is also a shift in the flux maximum to wavelengths higher than the rest wavelength for θ_{incl} not equal to 90° or 0°.

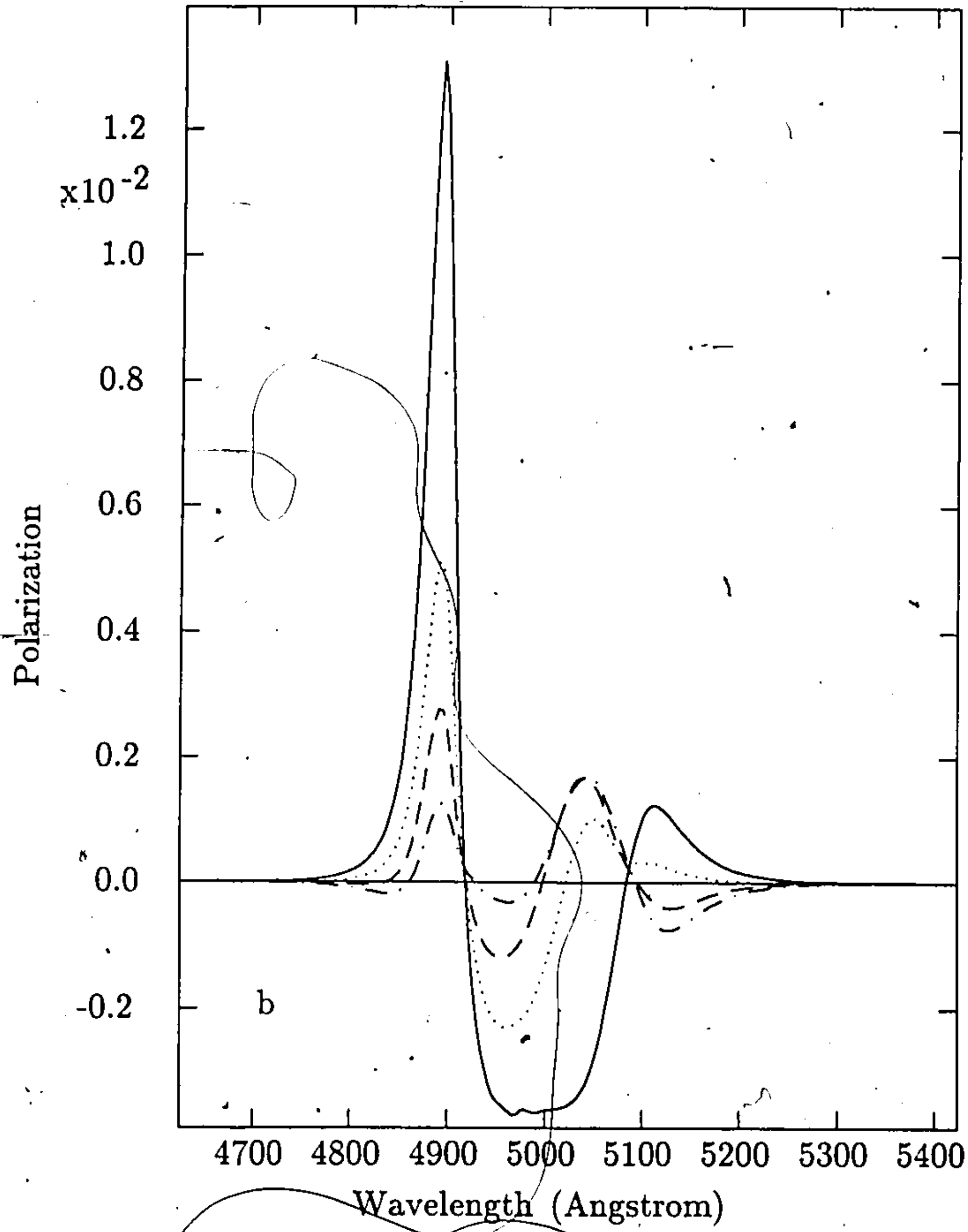

Fig. 4.13b. The polarization profiles corresponding to the flux profiles of Fig. 4.13a. ~~The overall~~ scale size of the polarization profiles declines as the inclination angle ~~is decreased~~. The polarization profiles go to zero everywhere as the inclination angle goes to zero. The polarization profiles show a shift in the polarization minimum to wavelengths less than the rest wavelength as inclination angle decreases. The subsidiary local maximum shifts to lower wavelengths and a second local minimum appears as inclination angle decreases.

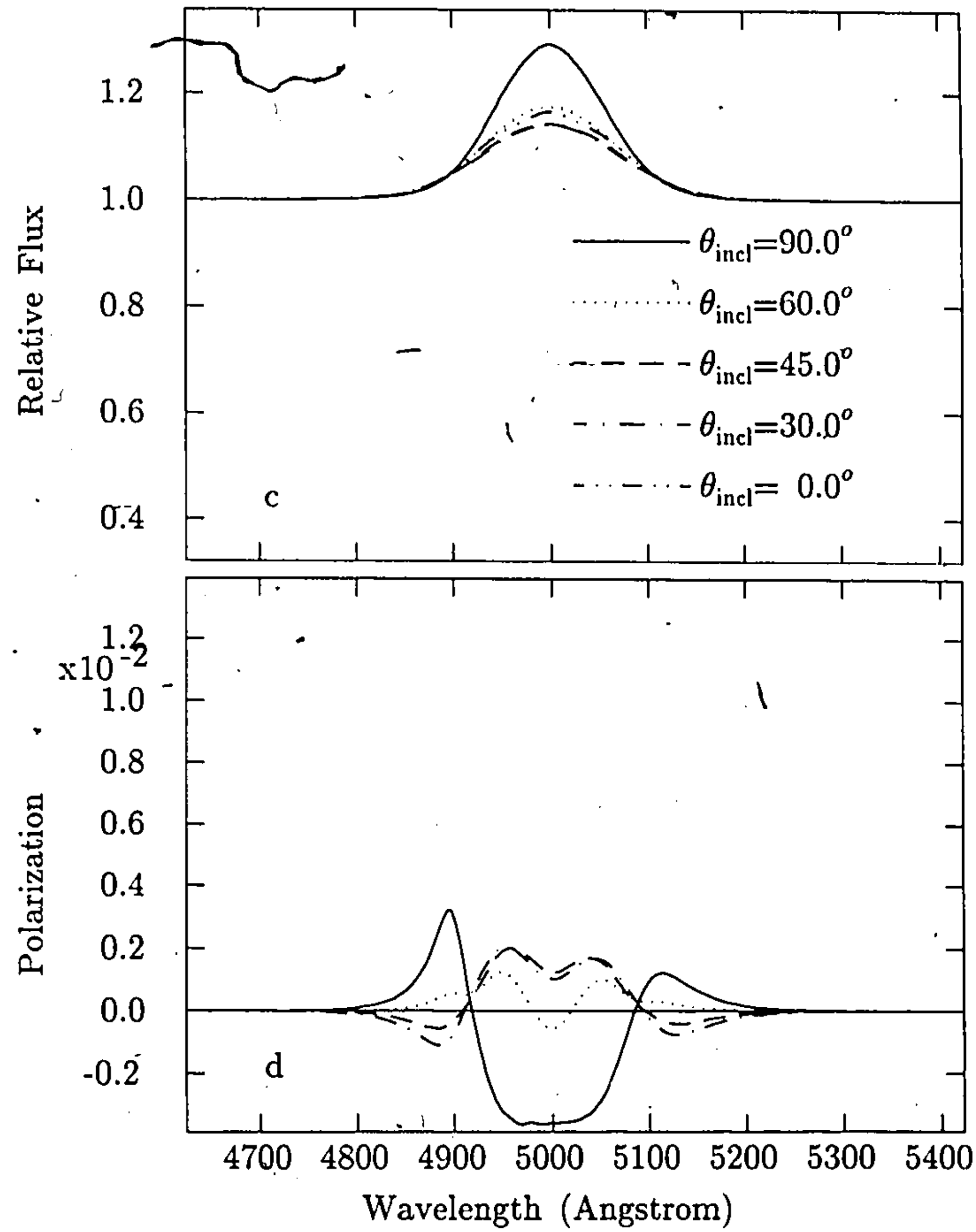

Fig. 4.13c and d. The limb components of the flux and polarization profiles of Fig. 4.13a and b. The polarization emission feature minimum bifurcates into two maxima when the inclination angle is changed from 90°.

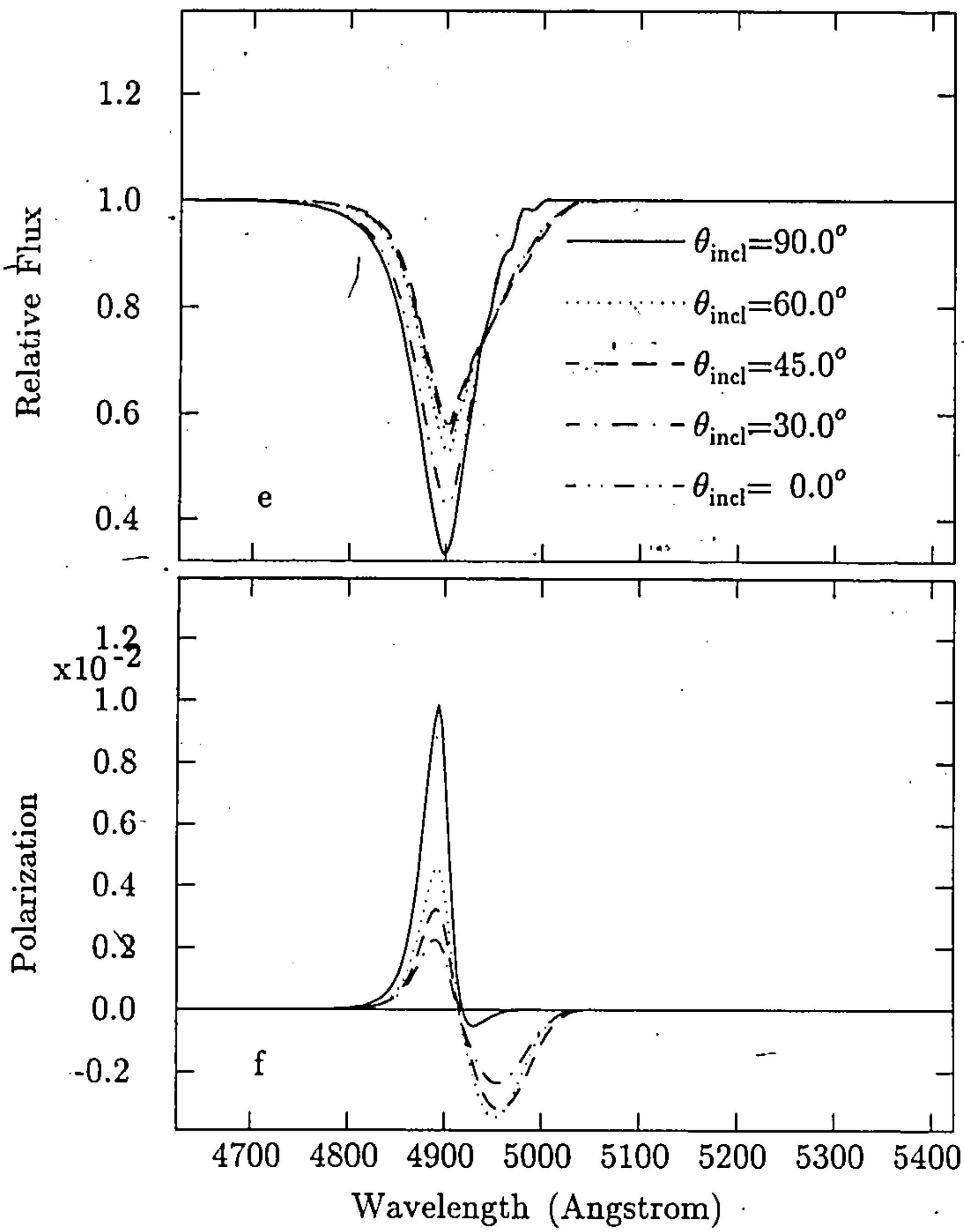

Fig. 4.13e and f. The photodisk components of the flux and polarization profiles of Fig. 4.13a and b. Note that a polarization minimum develops as the inclination angle is reduced from 90°.

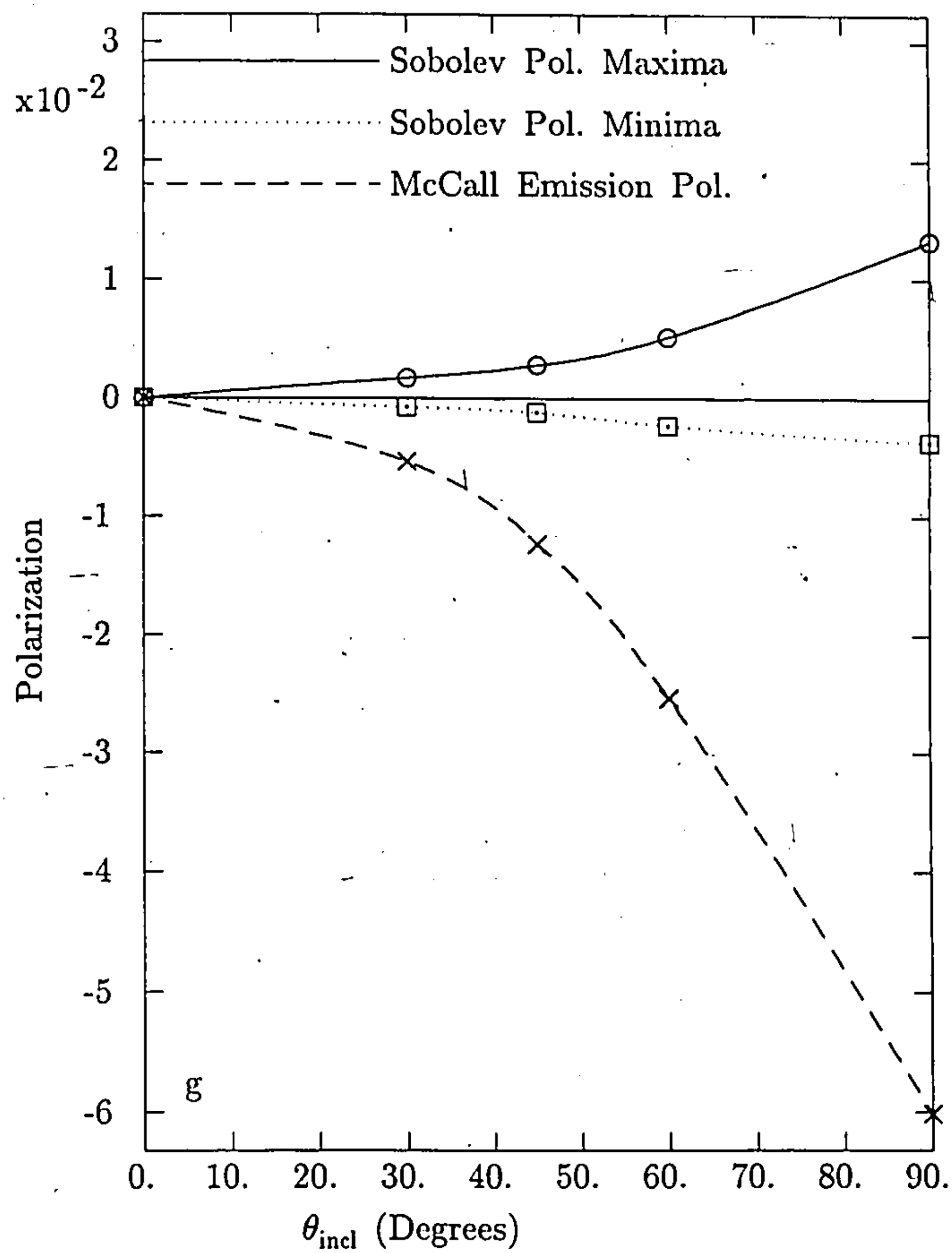

Fig. 4.13g. The maximum and minimum polarizations for the profiles of Fig. 4.13b as a function of inclination angle θ_{incl}. The polarization extrema increase monotonically in absolute value as the inclination angle increases. The McCall emission minima are also shown for comparison.

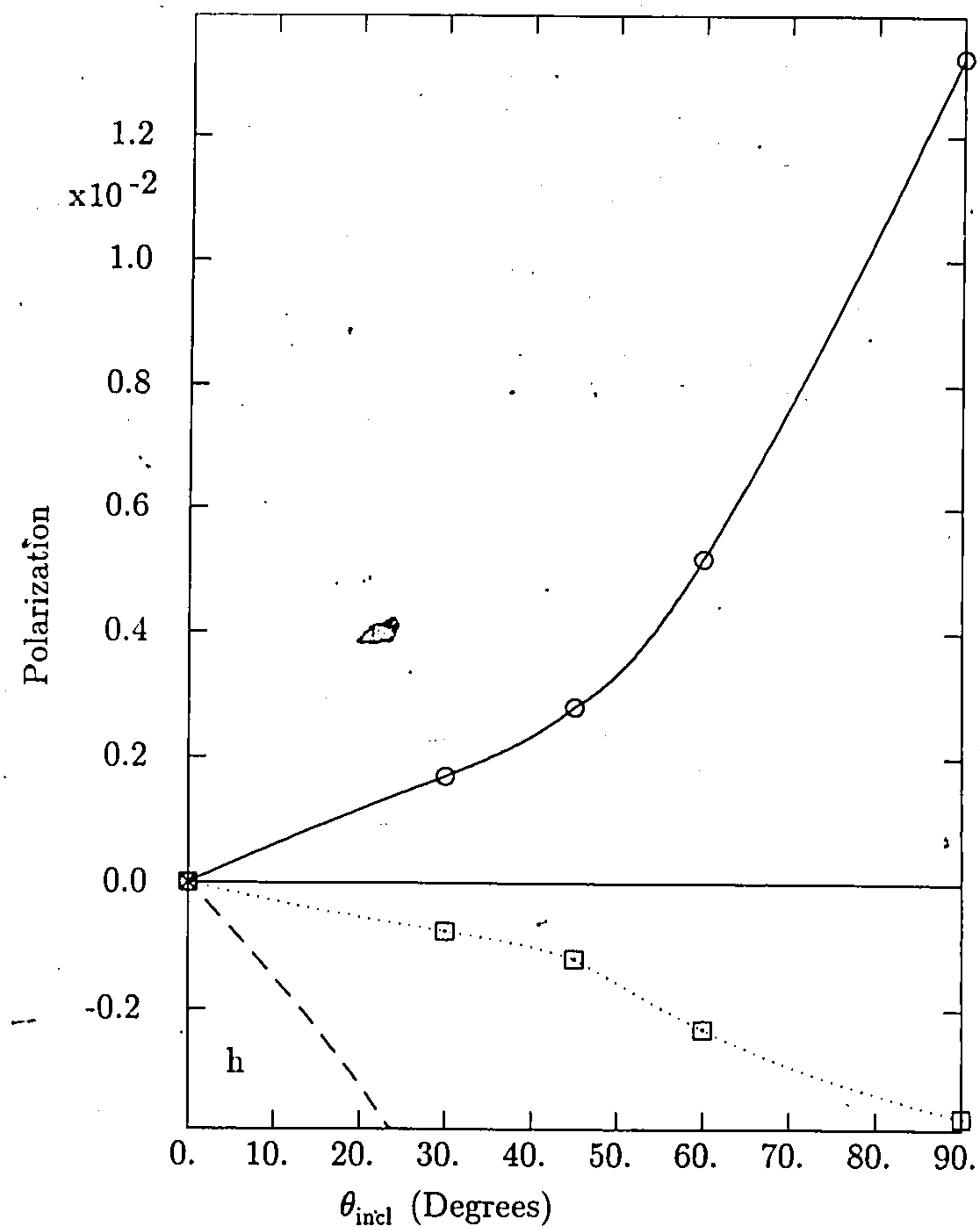

Fig. 4.13h. This is the same as Fig. 4.13g., but with a smaller vertical range in order to better display the Sobolev-H calculation results.

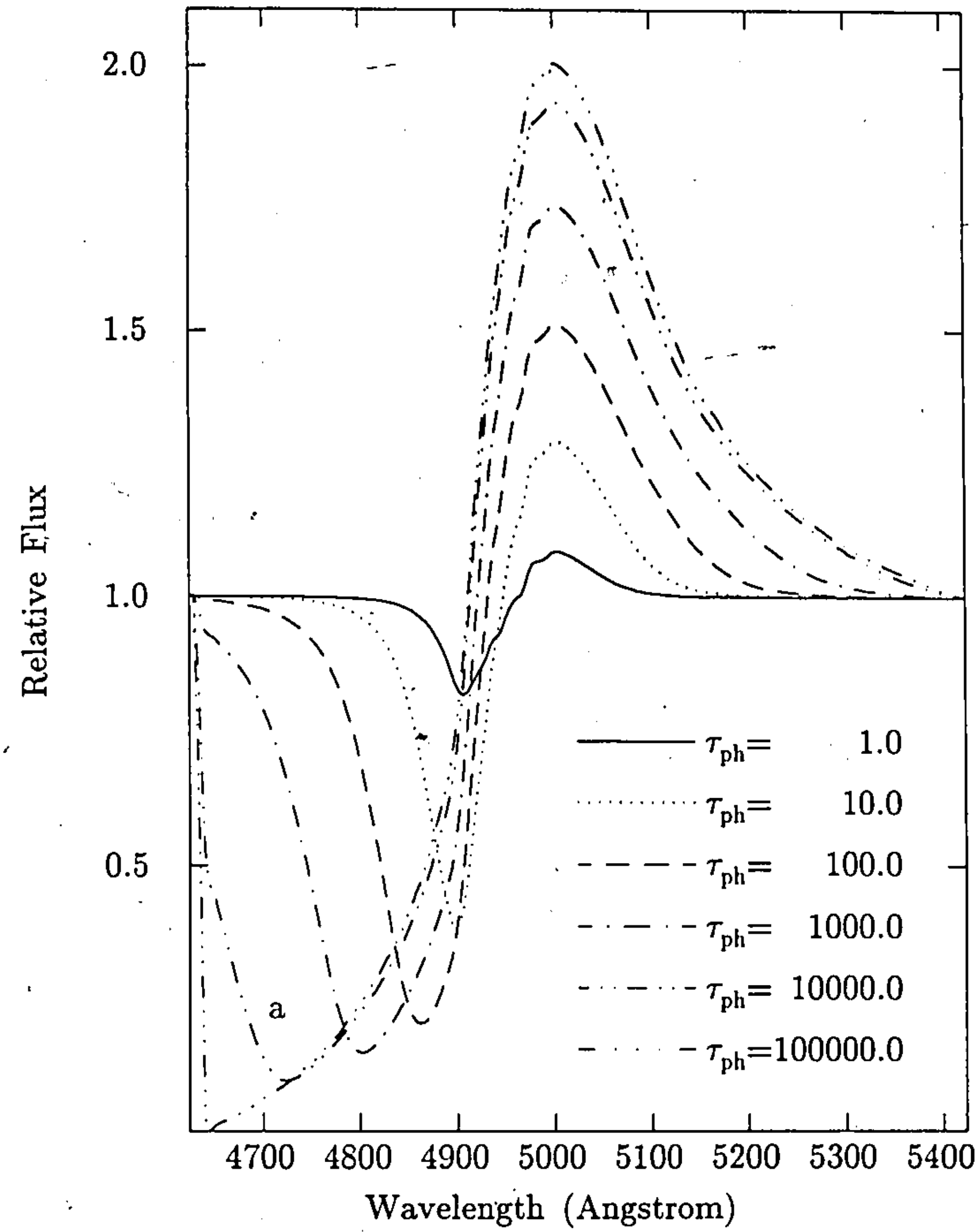

Fig. 4.14a. Flux profiles for a model with varied Sobolev photospheric optical depth τ_{ph}. The flux maximum increases roughly as the logarithm of τ_{ph}. The wavelength separation between the rest wavelength and the wavelength of the flux minimum increases as $(\tau_{ph})^{(1/p)}$.

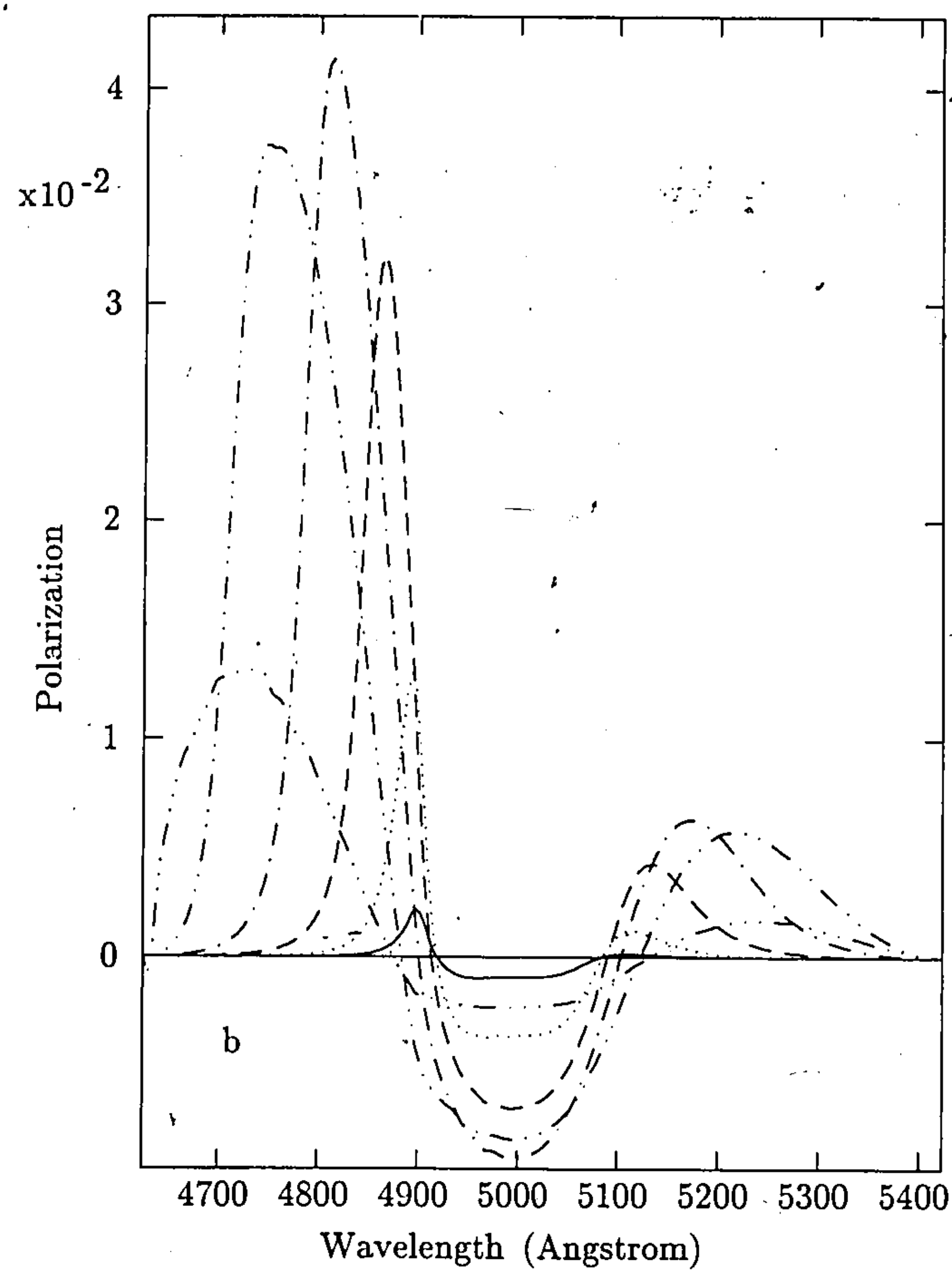

Fig. 4.14b. The polarization profiles corresponding to the flux profiles of Fig. 4.14a. The absorption polarization feature's maximum is closely correlated to the flux minimum. The decrease in polarization for $\tau_{ph} \gtrsim 10^4$ is due to the choice of $r_{g_{max}} = 4r_{ph}$. The emission polarization feature's minimum at first increases and then decreases with τ_{ph}.

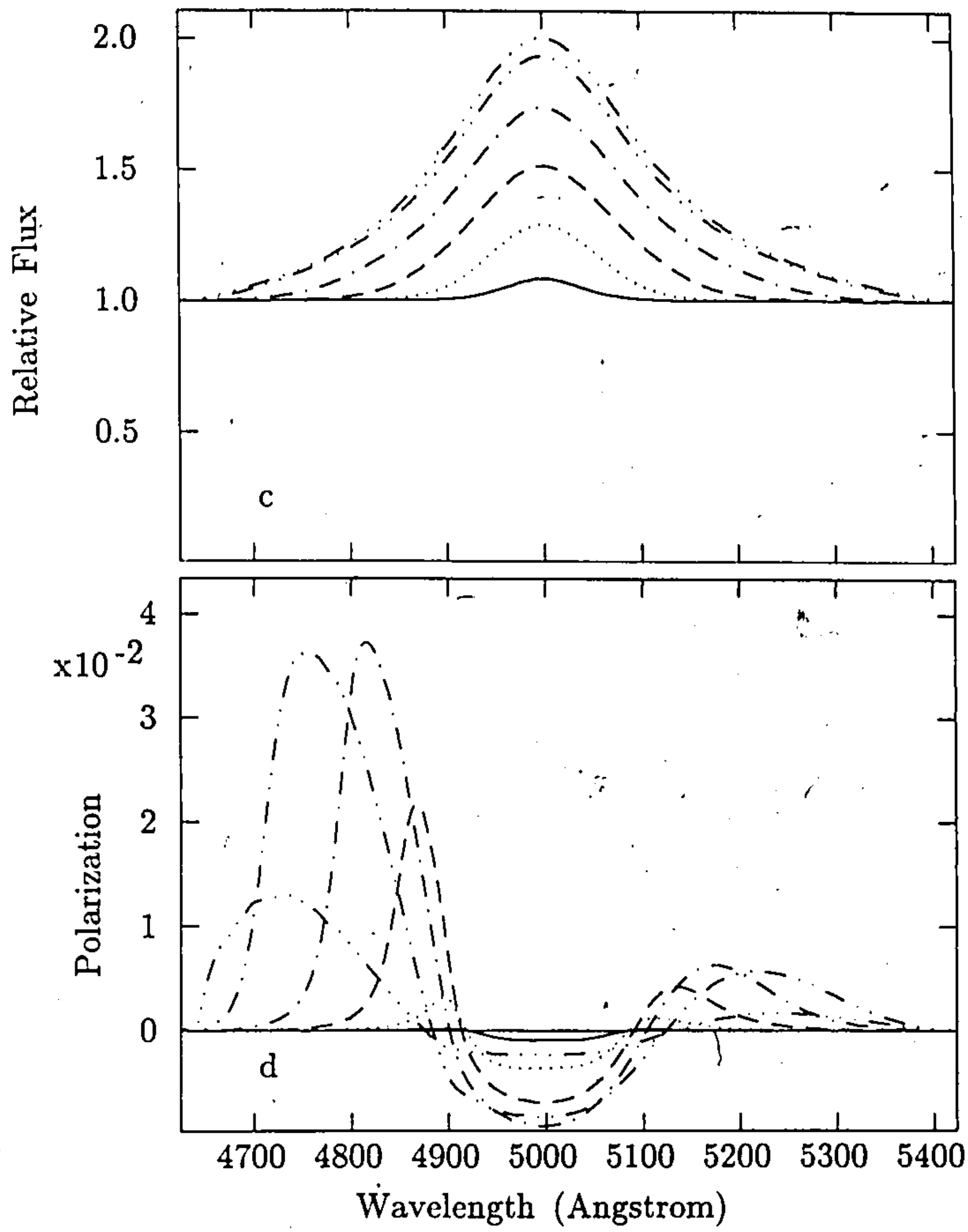

Fig. 4.14c and d. The limb components of the flux and polarization profiles of Fig. 4.14a and b. Note that for large τ_{ph} that the limb polarization is nearly the same as the net polarization for both emission and absorption features.

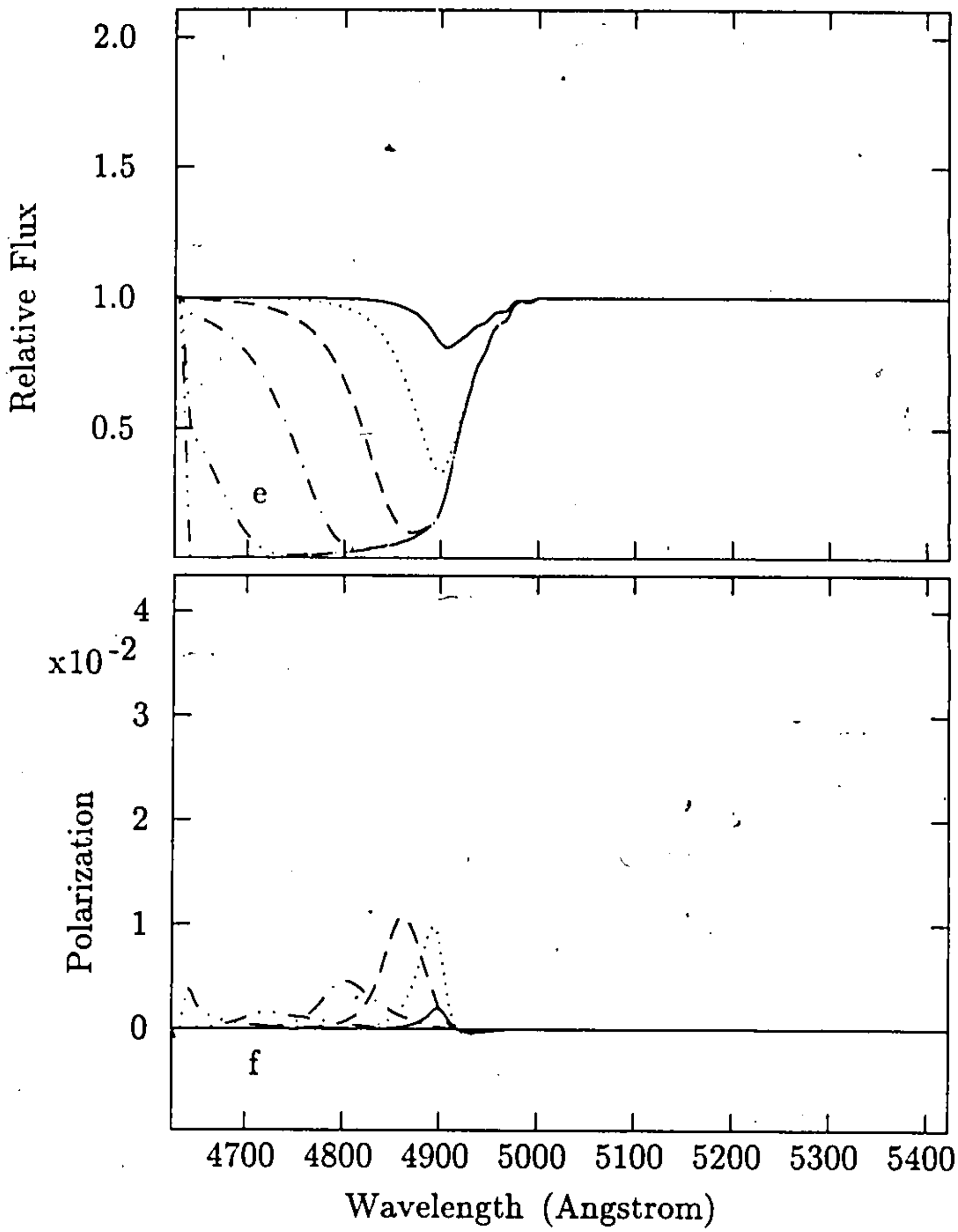

Fig. 4.14e and f. The photodisk components of the flux and polarization profiles of Fig. 4.14a and b. Note that for large $\tau_{p\lambda}$ the photodisk polarization is not a large contributor to the net polarization profile.

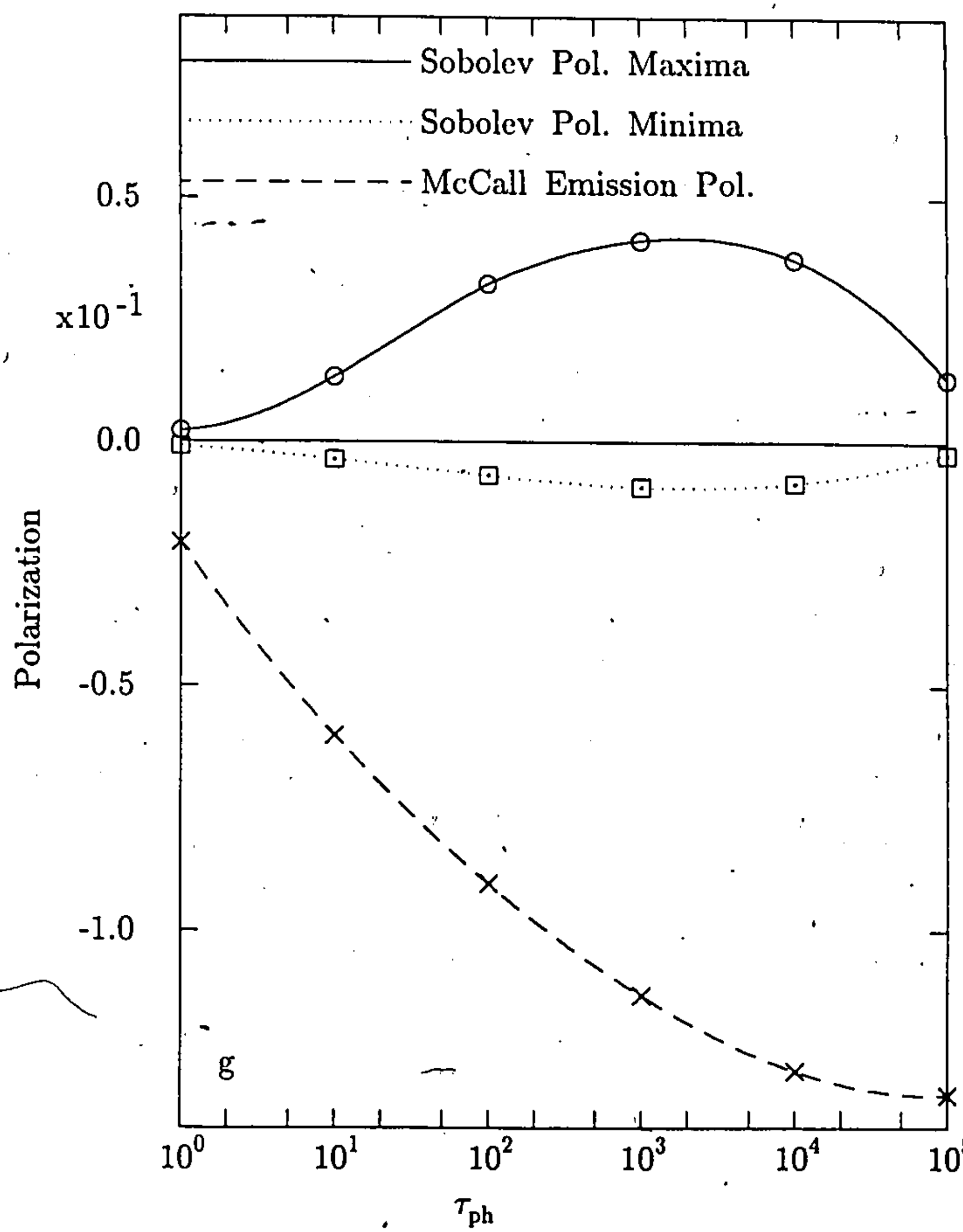

Fig. 4.14g. This shows the maximum and minimum polarizations for the profiles of Fig. 4.14b as a function of τ_{ph}. The McCall emission polarization minima are also shown for comparison.

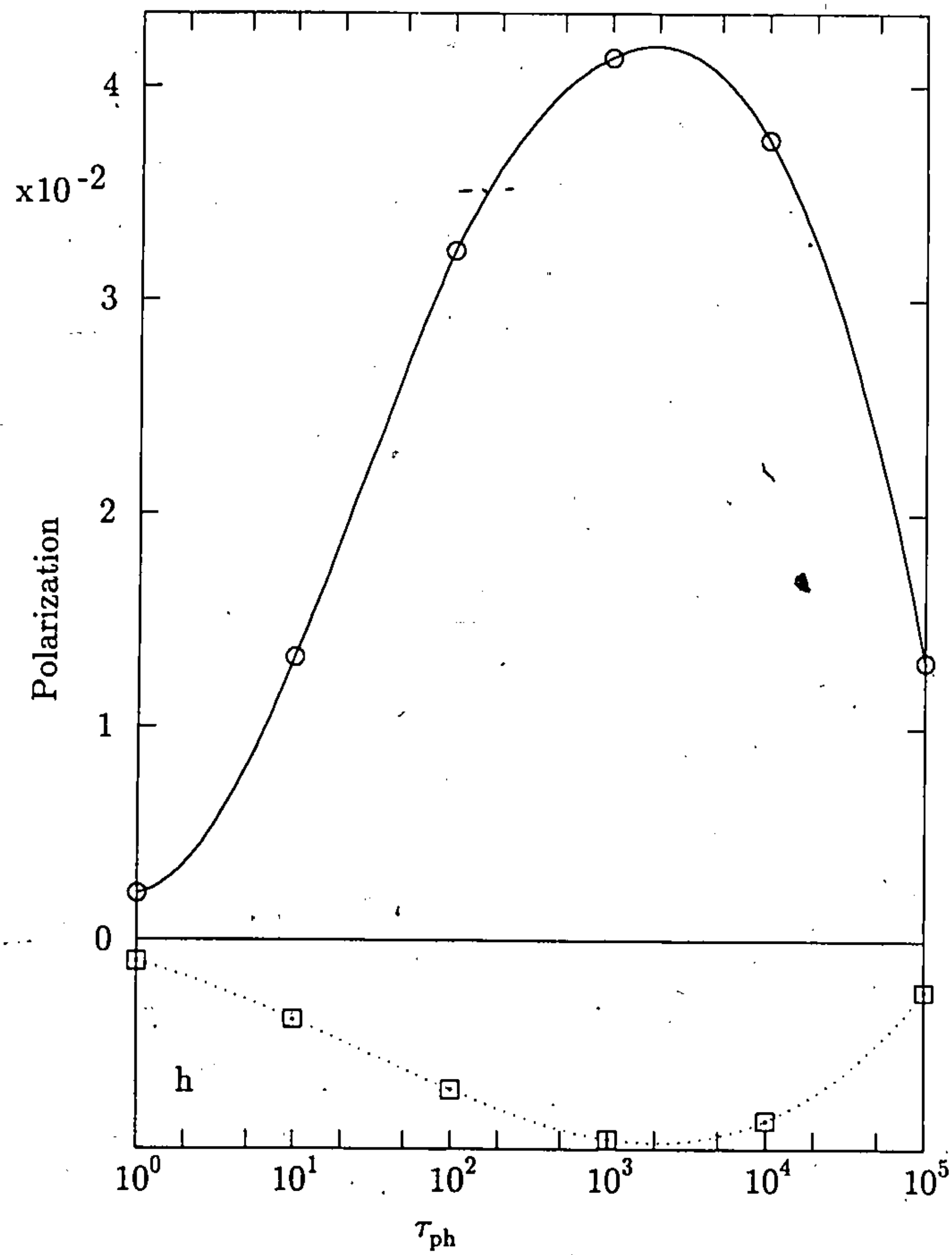

Fig. 4.14h. This is the same as Fig. 4.14g., but with a smaller vertical range in order to better display the Sobolev-H calculation results. Note that the absolute value of the extrema increase with τ_{ph} until the the finite outer generalized radius of the atmosphere begins to affect the polarization profiles.

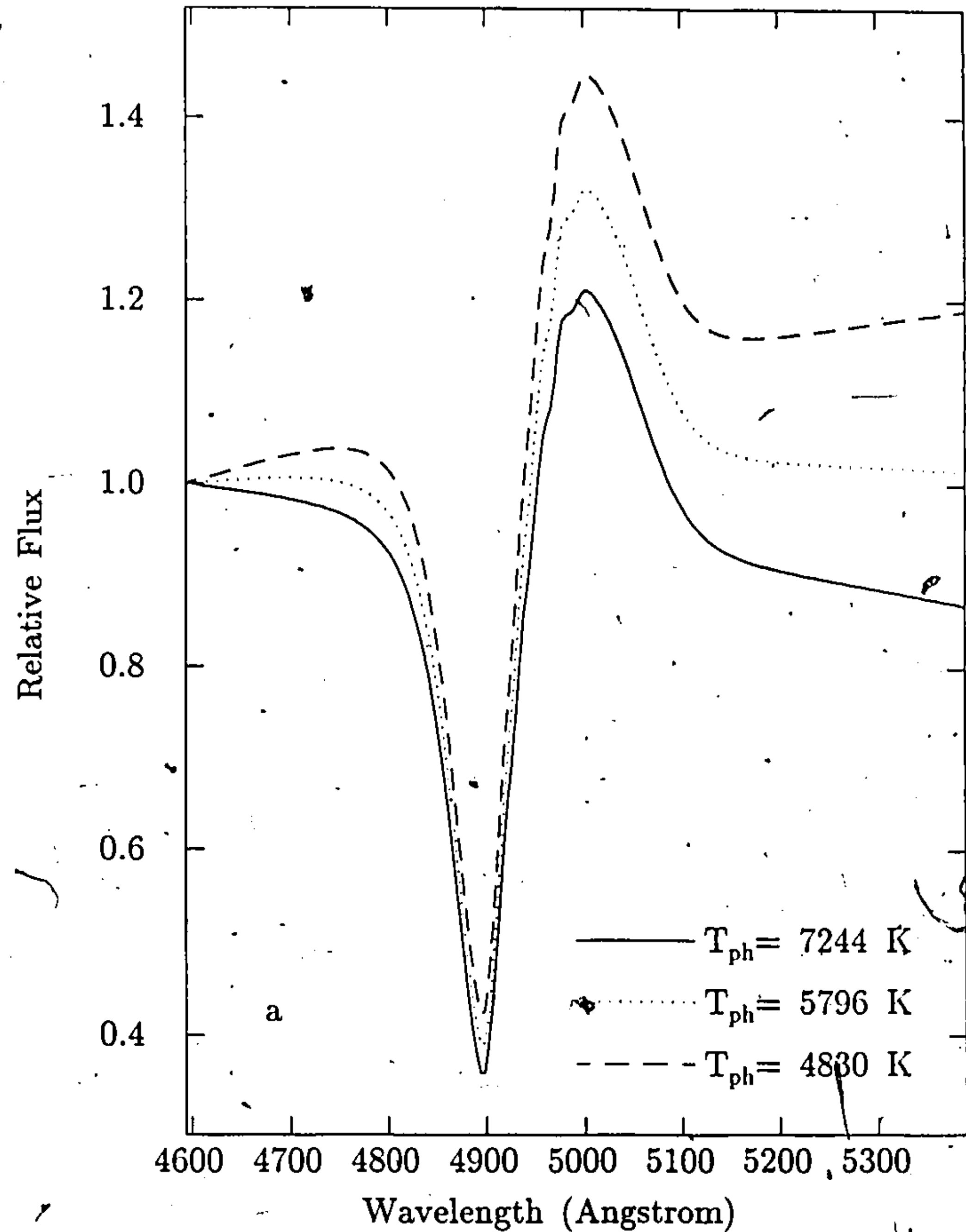

Fig. 4.15a. Flux profiles for a model with a Planck continuum producing photosphere with varied photospheric temperature. The varied temperature causes a varied continuum slope. The varied slope has little qualitative affect on the P-Cygni profiles.

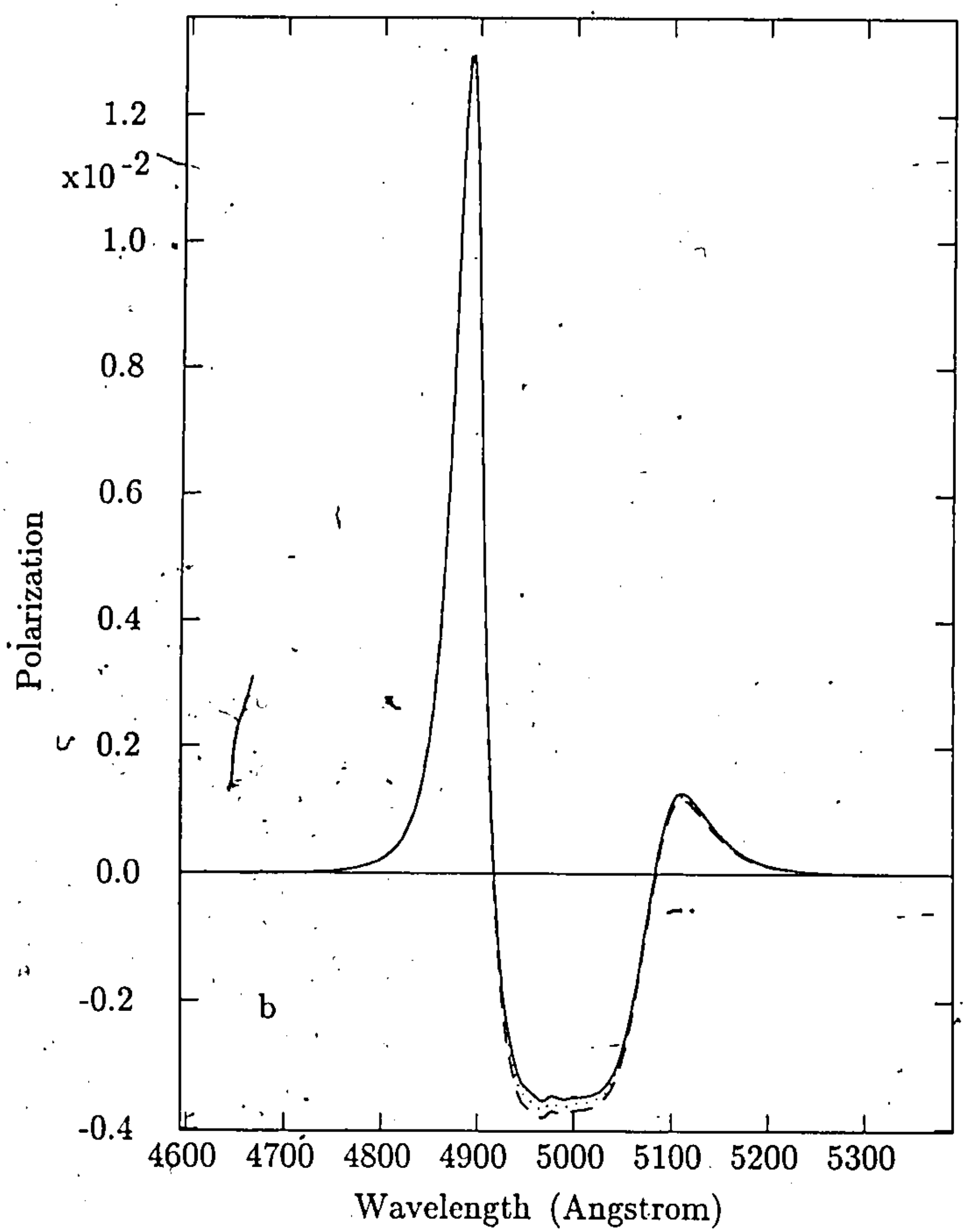

Fig. 4.15b. The polarization profiles corresponding to the flux profiles of Fig. 4.15a. The profiles are nearly unaffected by the changing slope of the photosphere's continuum.

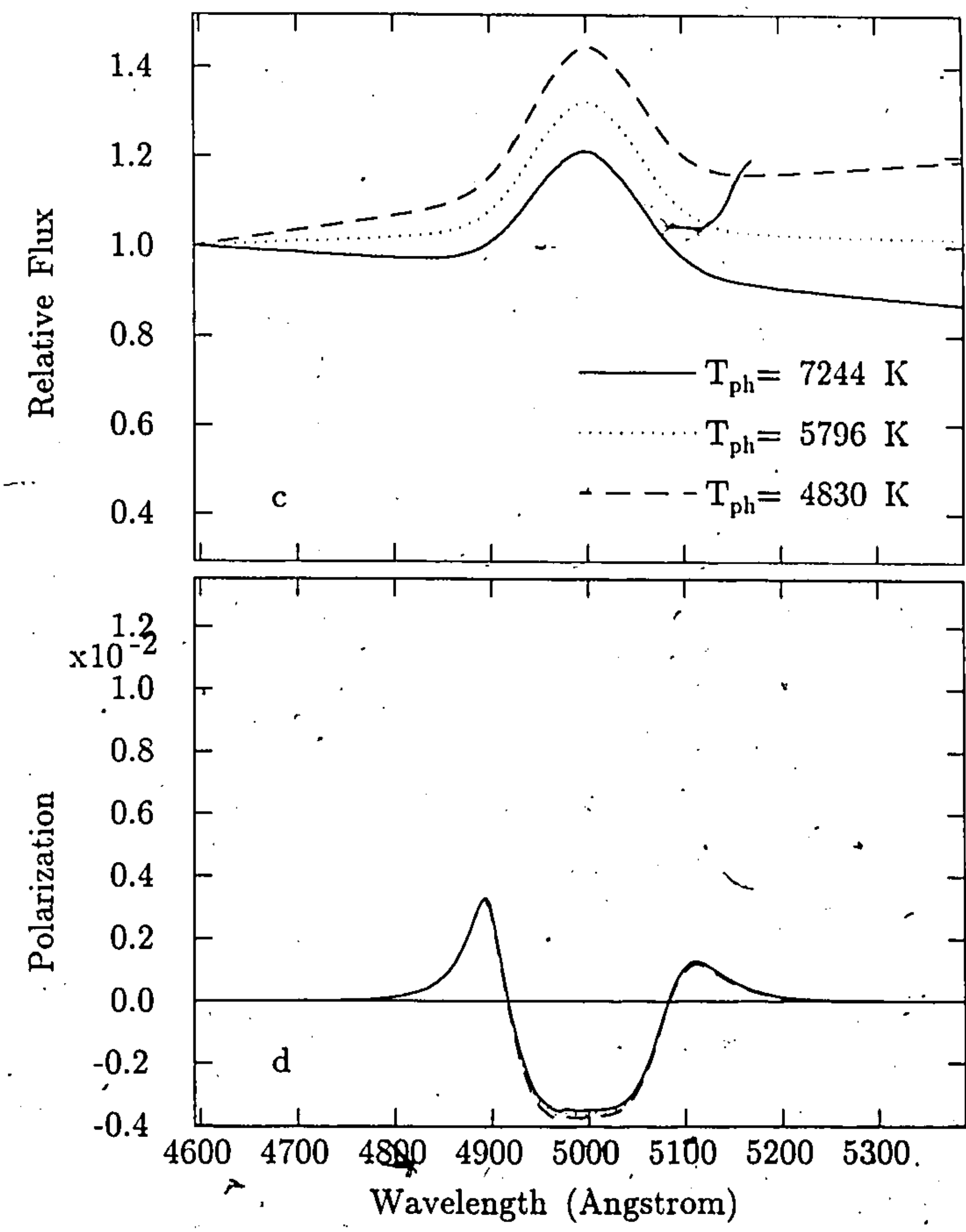

Fig. 4.15c and d. The limb components of the flux and polarization profiles of Fig. 4.15a and b. The varied continuum slope has little affect on the limb polarization profiles.

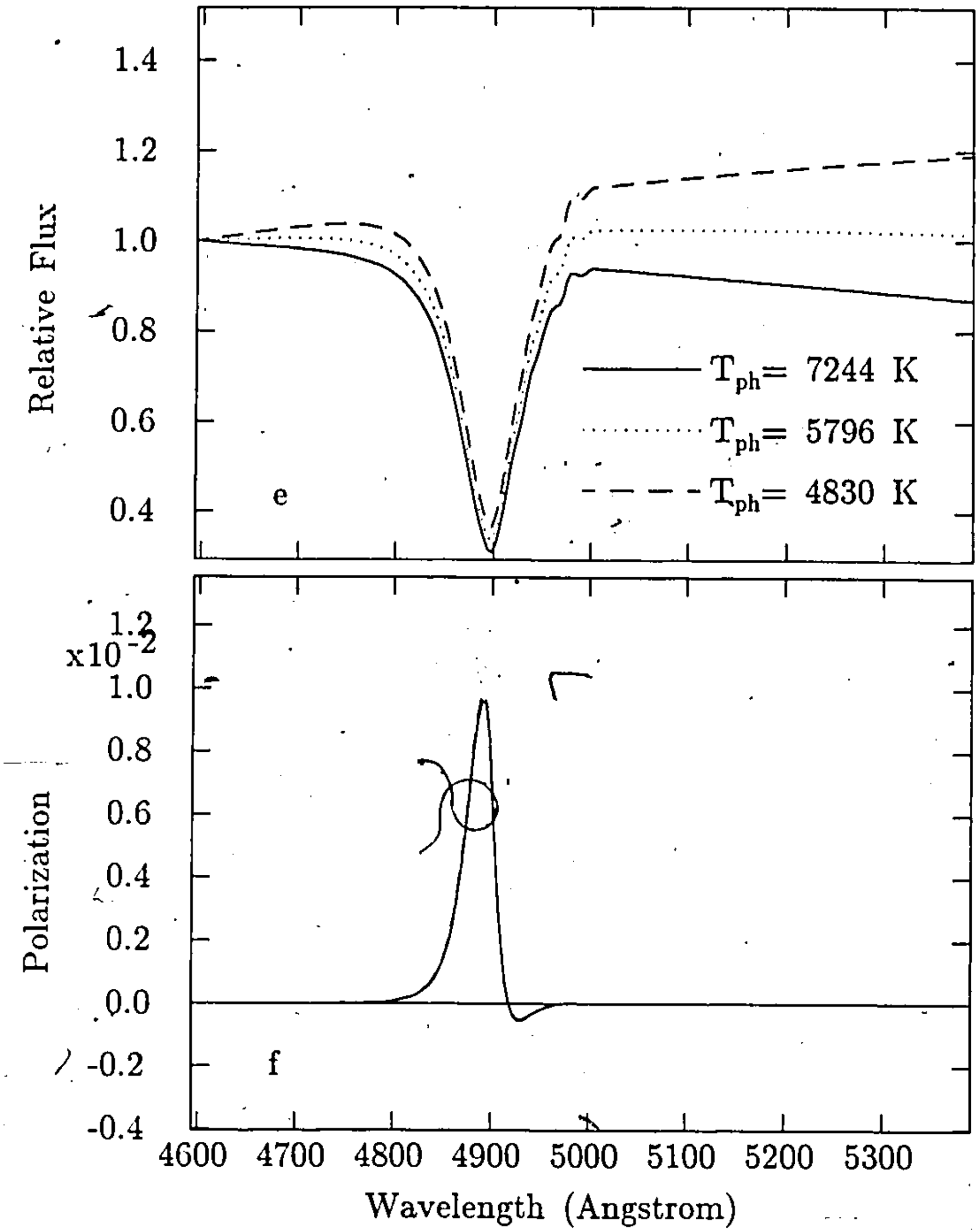

Fig. 4.15e and f. The photodisk components of the flux and polarization profiles of Fig. 4.15a and b. The varied continuum slope has no significant affect on the photodisk polarization profiles.

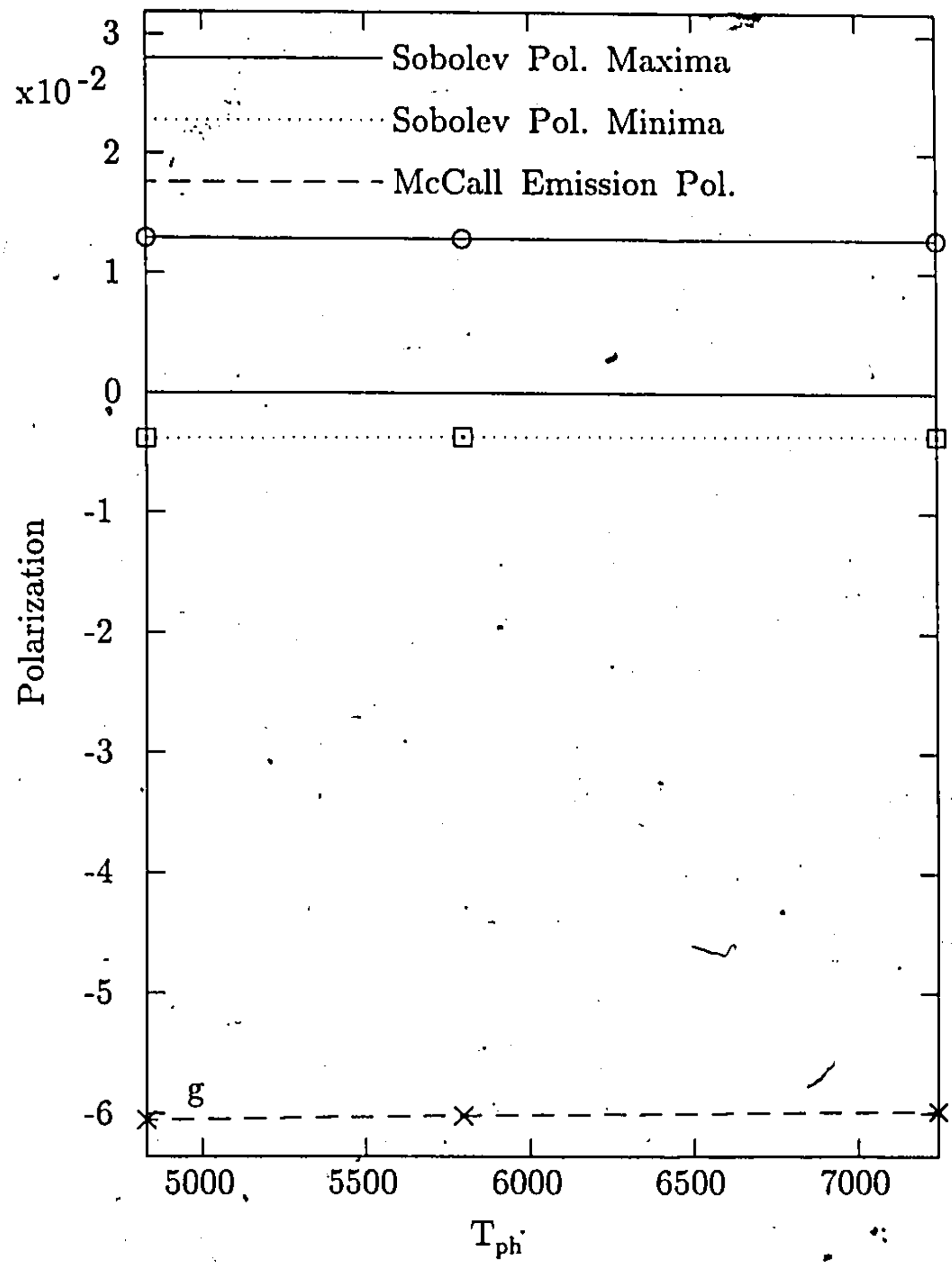

Fig. 4.15g. The maximum and minimum polarizations for the oblate model profiles of Fig. 4.15b as a function of photospheric temperature T_{ph}. The McCall emission polarization minima are also shown for comparison. There is very little variation with temperature.

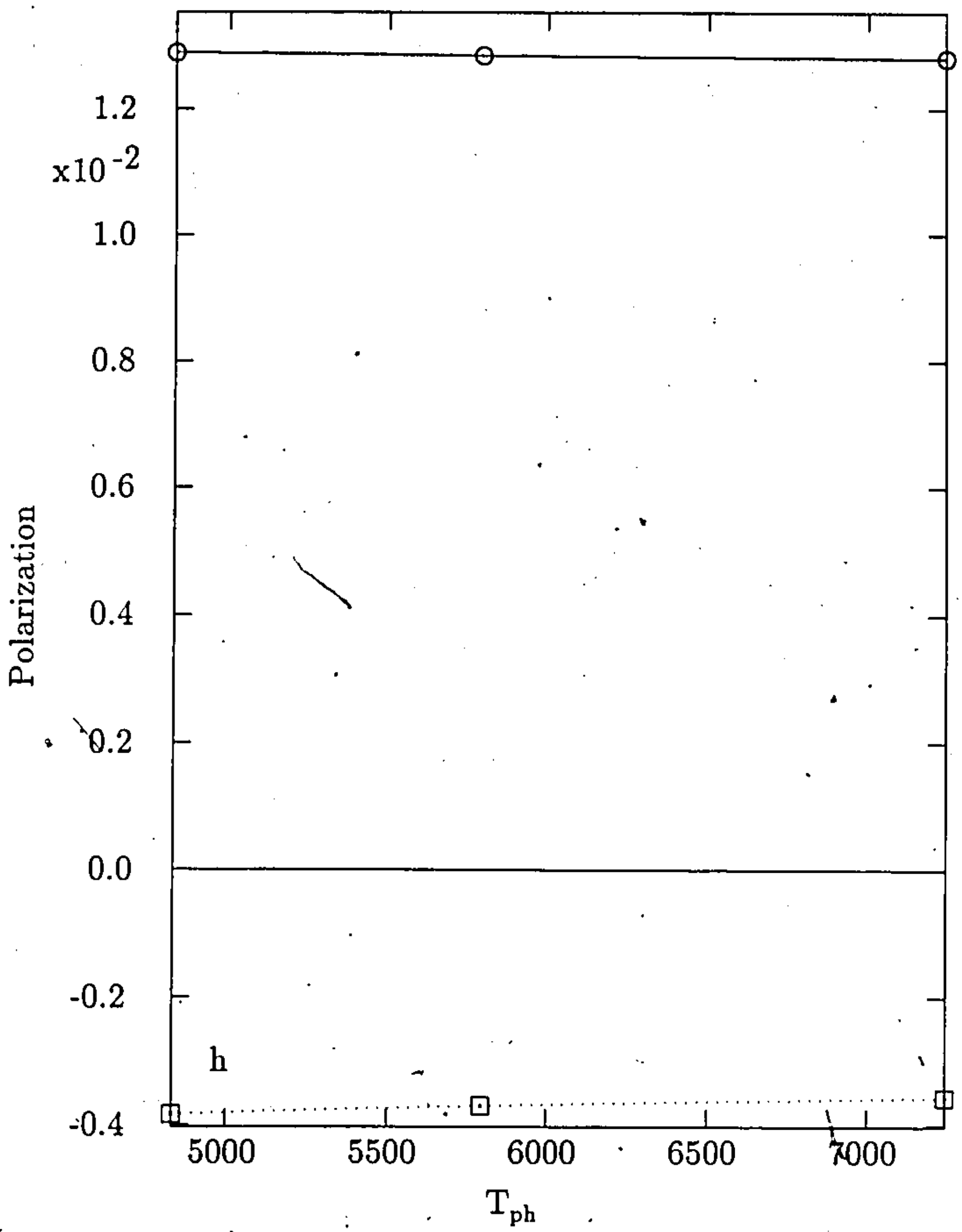

Fig. 4.15h. This is the same as Fig. 415g., but with a smaller vertical range in order to better display the Sobolev-H calculation results. There is very little variation in the polarization extrema with variation in the photospheric temperature T_{ph}.

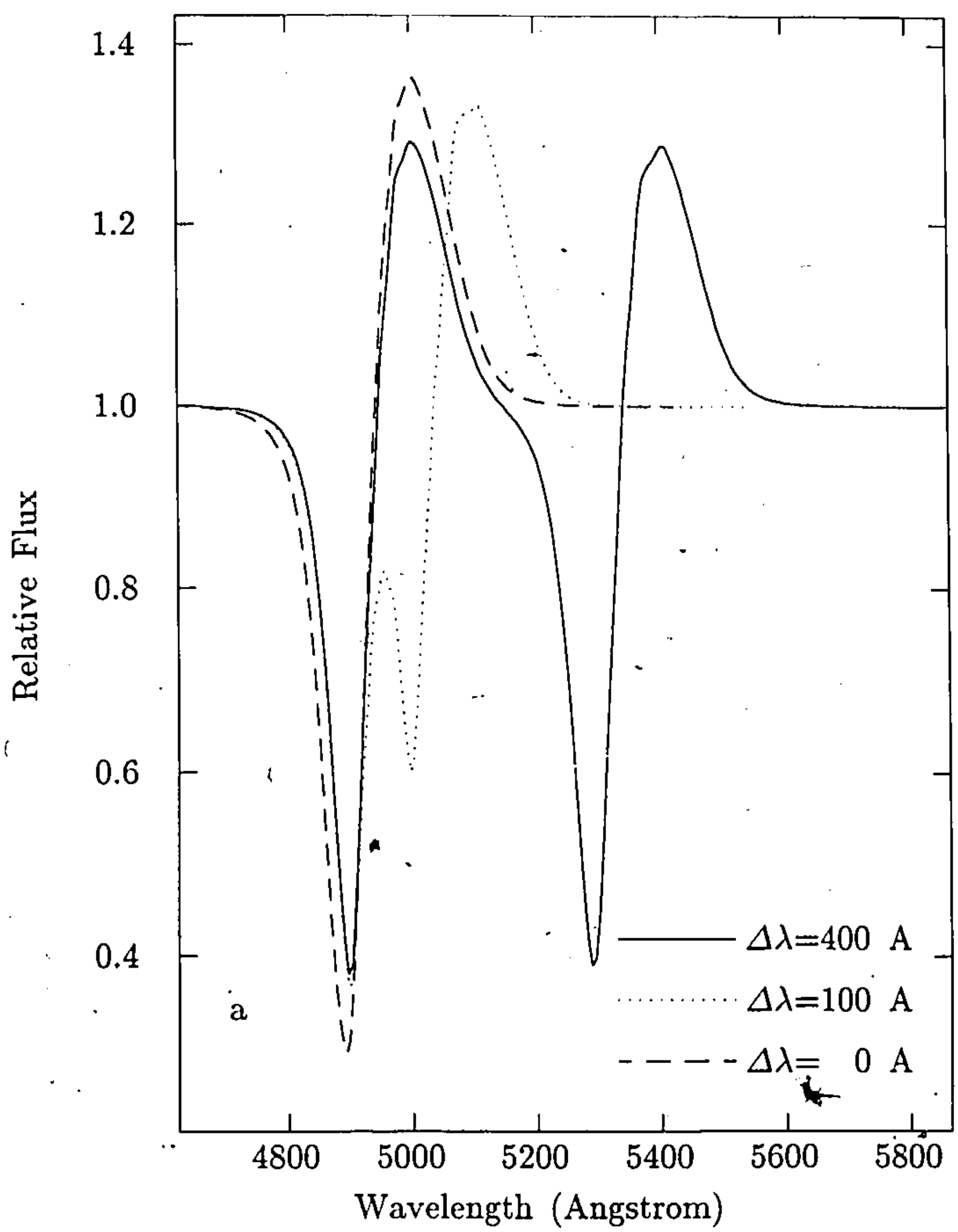

Fig. 4.16a. Flux profiles for a model with two lines and varying wavelength separation between the lines. The profiles appear completely independent for $\Delta\lambda = 400\,\text{Å}$. For $\Delta\lambda = 100\,\text{Å}$, the lines are strongly perturbing each other. For $\Delta\lambda = 0\,\text{Å}$, the lines appear to be a single P-Cygni line. The $\Delta\lambda = 0\,\text{Å}$ case is not equivalent, however, to a single line with τ_{ph} doubled (see the discussion in Chapter 2 section (f)).

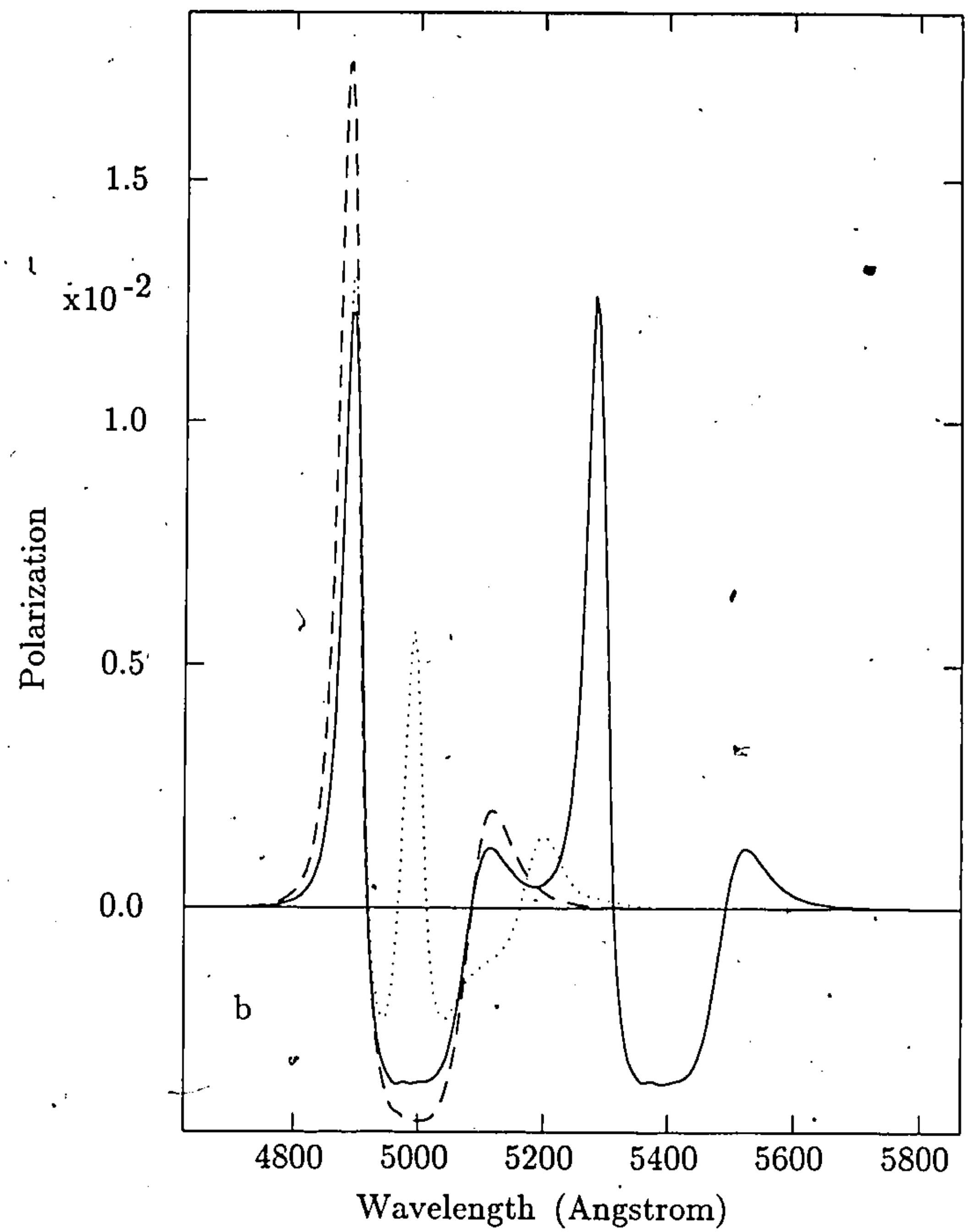

Fig. 4.16b. Polarization profiles for a model with two lines, and varying wavelength separation between the lines. The profiles only slightly affect each other for $\Delta\lambda = 400\,\text{Å}$. For $\Delta\lambda = 100\,\text{Å}$, the lines are strongly perturbing each other. For $\Delta\lambda = 0\,\text{Å}$, the lines appear to have a single P-Cygni line polarization profile.

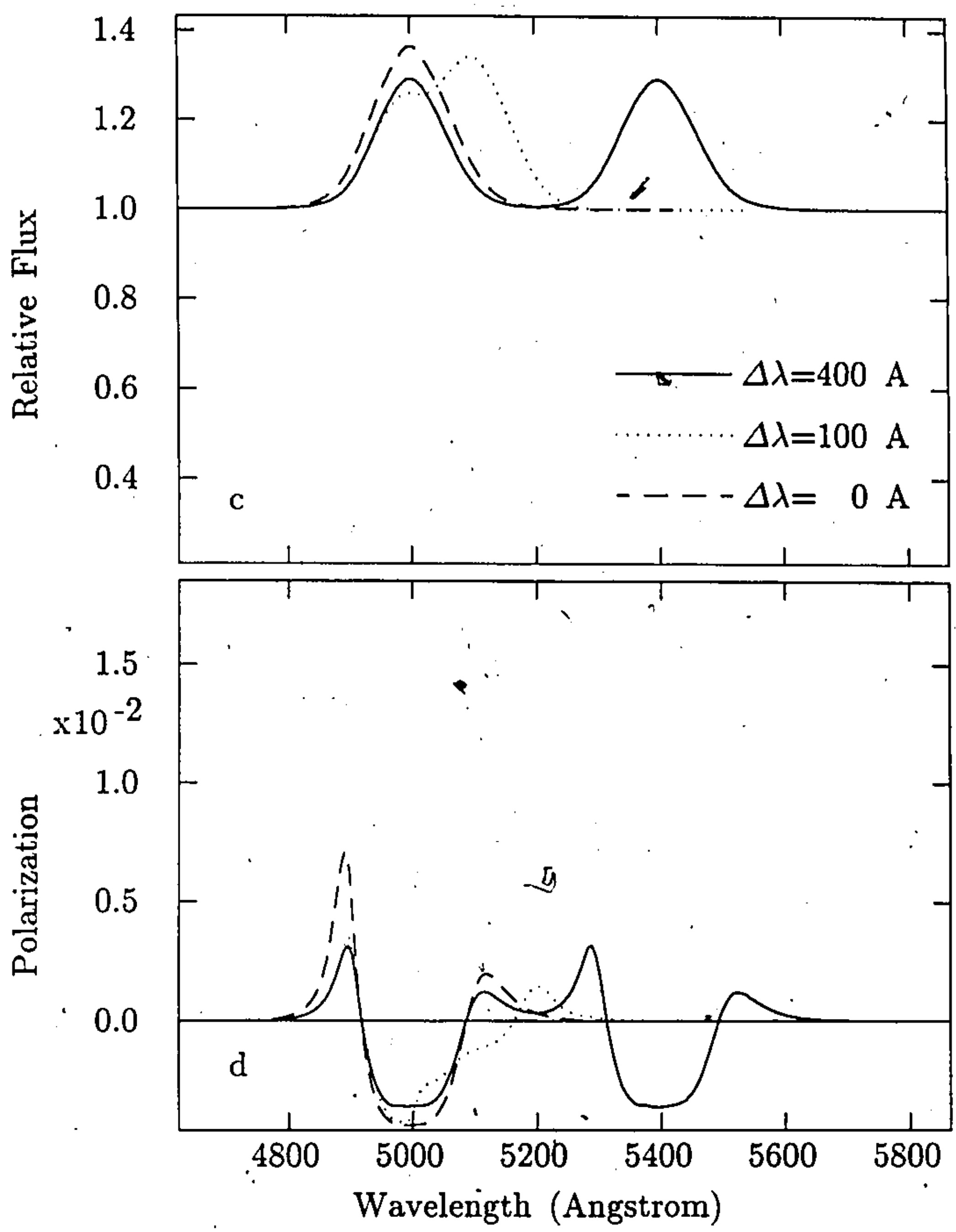

Fig. 4.16c and d. The limb components of the flux and polarization profiles of Fig. 4.16a and b.

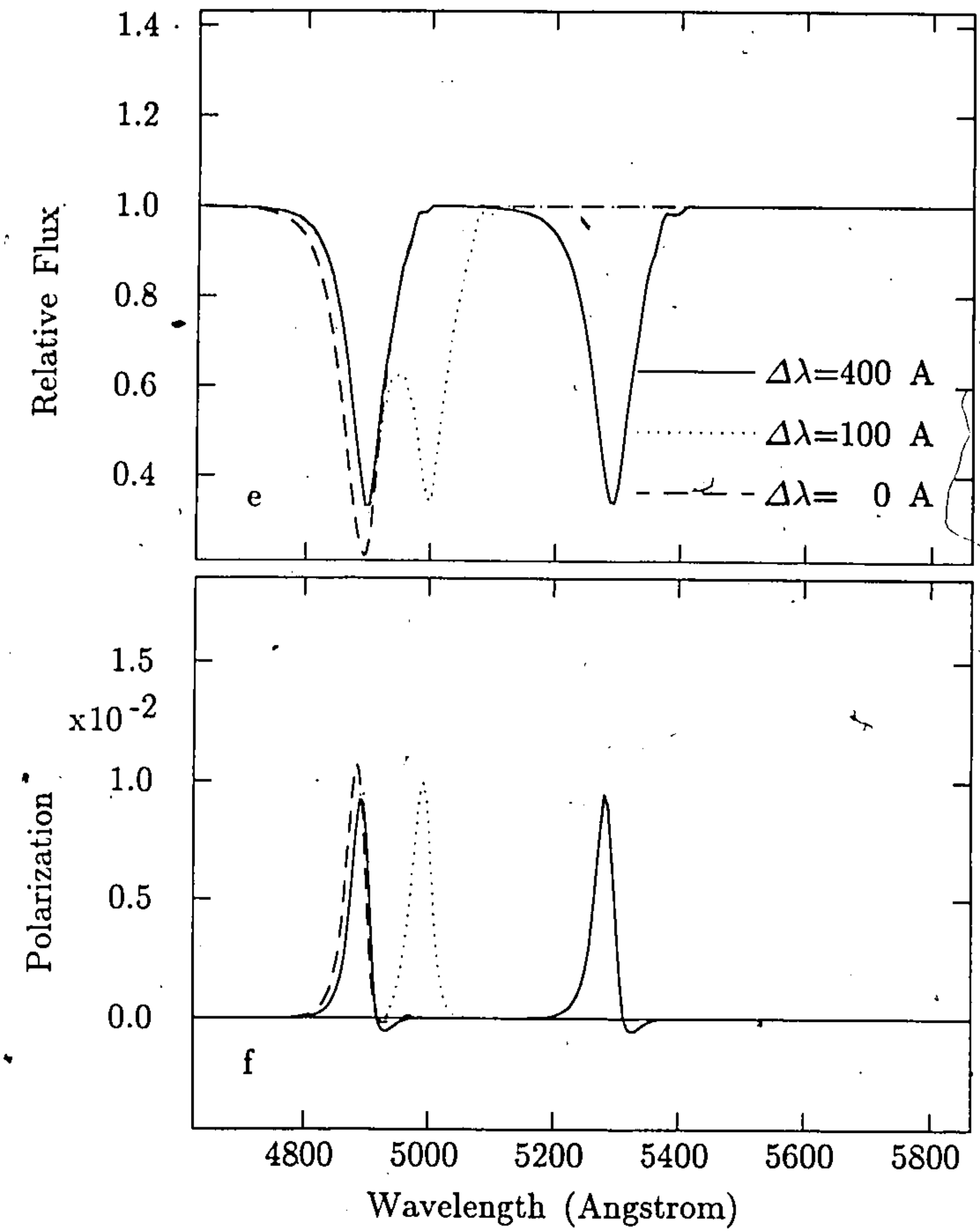

Fig. 4.16e and f. The photodisk components of the flux and polarization profiles of Fig. 4.16a and b.

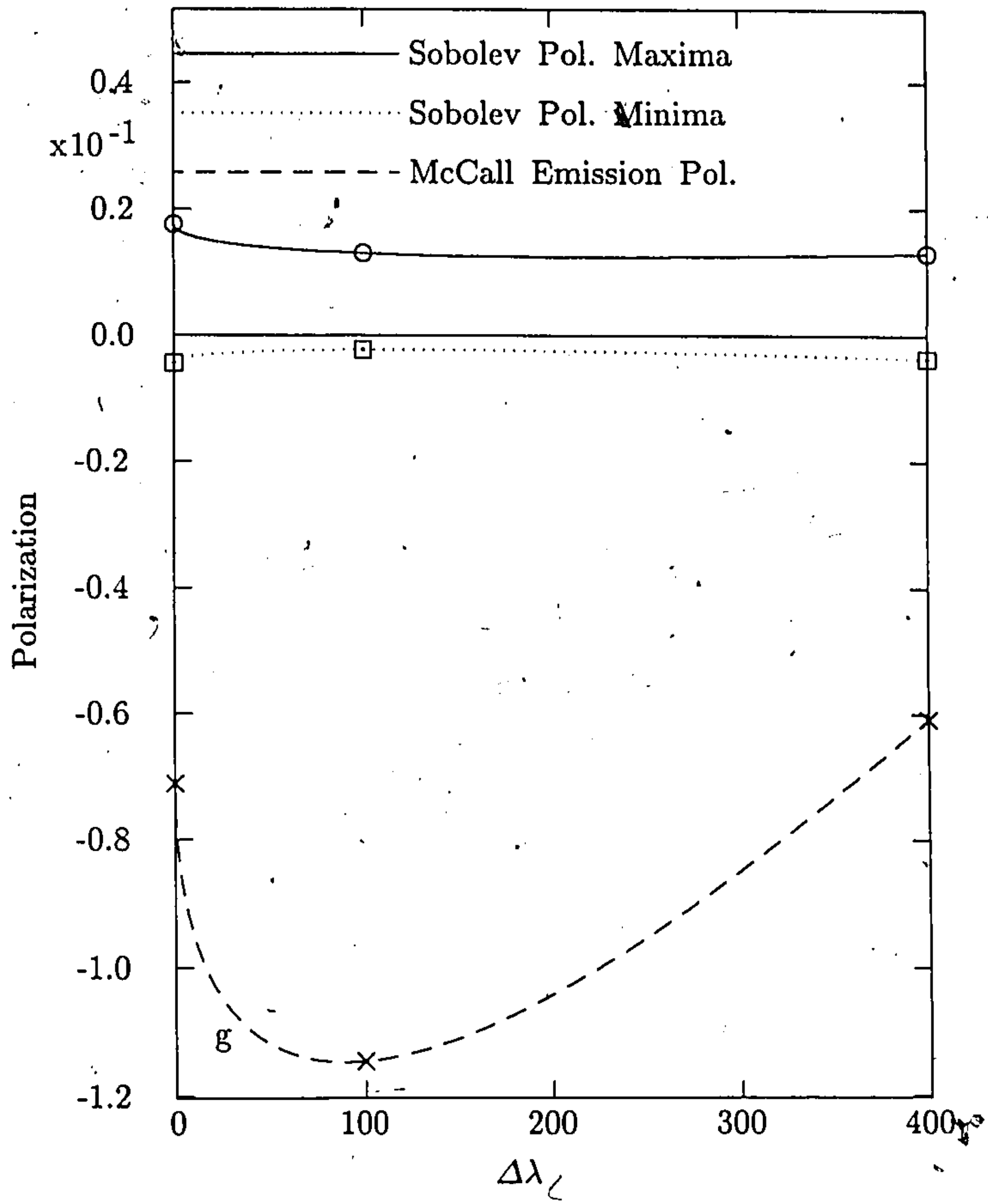

Fig. 4.16g. The polarization extrema for the oblate model profiles of Fig. 4.16b as a function of the wavelength separation of the two lines. The extrema are affected somewhat by the various degrees of blending. McCall emission polarization minima are also shown for the 5000 Å line. In this case the McCall results are not very significant, since line blending is not included in the McCall prescription.

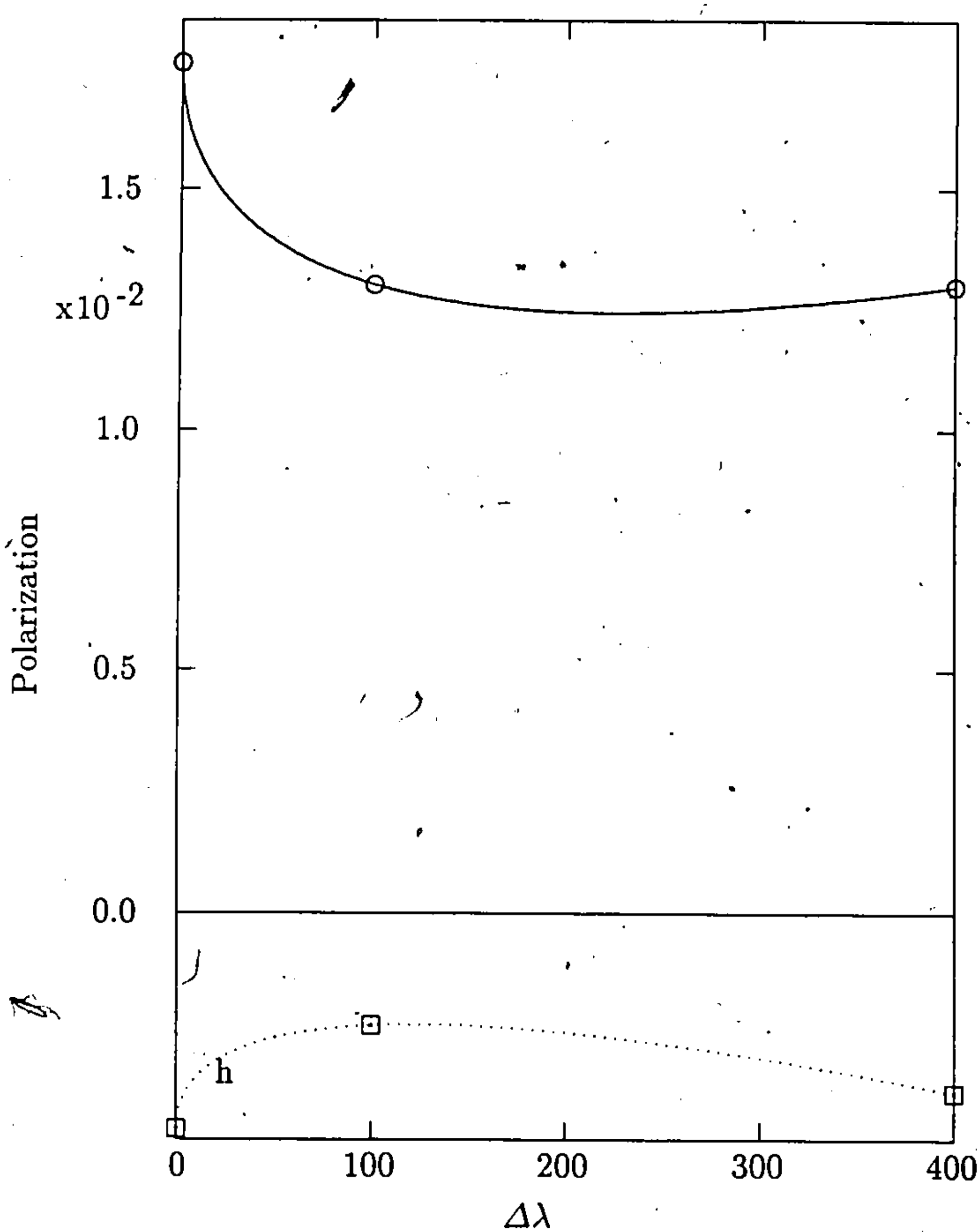

Fig. 4.16h. This is the same as Fig. 416g., but with a smaller vertical range in order to better display the Sobolev-H calculation results.

Chapter 5

Analysis of Supernova 1987a Spectropolarimetry

In section (a) of this chapter a brief review is given of supernova polarization data and analyses that antedate SN 1987a. Section (b) presents an analysis of some of the early SN 1987a spectropolarimetry.

a) Pre-1987a Supernova Polarization Data

Before SN 1987a there were few observations of supernova polarization. Some color and broad band polarization measurements have been reported (Serkowski 1970; Shakhovskoi and Efimov 1978; Wolstencroft and Kemp 1972; Shakhovskoi 1976). These measurements are discussed in Shapiro and Sutherland (1982) along with an unpublished measurement by M. Breger. Shapiro and Sutherland conclude that in three of the five observations there is evidence for intrinsic supernova polarization.

As far as the thesis author is aware, there have been only two pre-1987a spectropolarimetric observations of supernovae. McCall *et al.* (1984) obtained spectropolarimetry for the type I SN 1983g in NGC 4753 near maximum light. They found a mean polarization of about 2 %; the uncertainty in their data points was also about 2 %. No estimate of the interstellar polarization was given. McCall *et al.* identified no significant correlation of the polarization structures with the P-Cygni line profiles. To the eye of the thesis author there is a suggestion of a correlation between the polarization structures near 4850 Å and 5500 Å, and the absorption features of a Si II line blend and S II line, respectively. A re-analysis of this data using the Sobolev-H method might be of some interest. The uncertainties in the data would, however, probably prohibit any strong conclusions.

McCall (1985) mentions that an interesting polarization feature was found in spectropolarimetry of type Ib SN 1983n taken within one night of maximum light. The most prominent flux feature was a blend of Fe II lines with an emission peak near 4600 Å. Preliminary reductions of spectropolarimetry showed a dip in polarization from 1.4 % to .8 % at the Fe II emission peak. No significant change in the position angle of the polarization was found indicating that the intrinsic and interstellar polarization vectors were nearly orthogonal. Unfortunately the data from this observation have never been published nor fully reduced (McCall, private communication). An analysis with the Sobolev-H method would be of considerable interest especially as SN 1983n is the prototype for the type Ib subclass of supernovae. The type Ia supernovae (the classical type I events) have remarkably uniform observational characteristics (Cadonau *et al.* 1985), and so are unlikely candidates for asymmetric supernovae. Much less is certain about the common characteristics of type Ib supernovae, since only a few supernovae have been assigned to the type Ib subclass (see the discussion in Chapter 1 section (b)). Thus the type Ib supernovae are potential candidates for being asymmetric supernovae.

b) Analysis of Supernova 1987a Spectropolarimetry

The discovery of SN 1987a in the LMC has provided an unprecedented opportunity for many supernova observations including spectropolarimetry. Reports of spectropolarimetry have become available (Walsh *et al.* 1987; Magalhaes and Velloso 1987; Schwarz and Mundt 1987; Cropper *et al.* 1987; Schwarz 1987). Preliminary analyses of the spectropolarimetry in terms of supernova shape asymmetry have been provided by Jeffery (1987; hereafter Paper I) and Cropper *et al.* (1987). In addition, color polarimetry data and an analysis in terms of shape asymmetry have been given by Méndez *et al.* (1987). In this section an analysis is given of the Schwarz and Mundt Mar. 6–7 observations (1987).[1] A set of synthetic flux and polarization spectra will be presented and compared to the Mar. 6–7 observations. These synthetic spectra are superior to those presented in Paper I, since a multi-line Sobolev-II computer program only became available subsequent to the calculations of Paper I. There is also some discussion and reference to the data and analysis of Cropper *et al.*

Before considering the spectropolarimetric data some of the conventions used for describing the data should be mentioned. Recall that in Chapter 2 section (d) the Stokes parameters were introduced. In this chapter the normalized Stokes parameters are used without explicitly writing the qualifier "normalized" all the time. The normalized Stokes parameters are given by dividing the ordinary Stokes parameters by the total specific intensity. The Stokes parameters and the polarizations will usually be expressed as percentages except in the figures. Also recall from Chapter 2

[1] The data from Schwarz and Mundt (1987) has been supplemented by H. E. Schwarz (private communication) and from a preprint by Schwarz (1987). The Schwarz and Mundt data and the supplementary data were partly based on observations collected at the European Southern Observatory.

section (d) that the polarization and position angle are given by

$$P = \sqrt{Q^2 + U^2}, \tag{5.1a}$$

and

$$\phi = \frac{1}{2}\arctan(U/Q), \tag{5.1b}$$

respectively. It should be clear that

$$Q = P\cos 2\phi \quad \text{and} \quad U = P\sin 2\phi. \tag{5.2}$$

The normalized Q parameter is given by

$$Q = (I_l - I_r)/I, \tag{5.3}$$

where the l and r axes are along the celestial meridian and celestial latitude, respectively. The U parameter is also determined from equation (5.3), but in a coordinate system rotated 45° in the clockwise direction (Chandrasekhar 1960, p. 34). It follows that the position angle is measured from clockwise from the celestial meridian.

In order to analyze the spectropolarimetry the interstellar polarization (ISP) must be considered. This interstellar polarization arises from interstellar dust in the Galaxy and in the LMC. The dust grains are aligned by interstellar magnetic fields, and so create a polarizing medium. The effect on a radiation beam of passing through the dust medium can be described by a set of differential equations for the normalized Stokes parameters (Martin 1974). Solving the differential equations is not necessary if values can be obtained for the Q_{ISP} and U_{ISP} Stokes parameters that initially unpolarized radiation acquires in its passage from some specified location to Earth. These ISP values are then simply subtracted from the net Stokes parameters measured for an object at the specified location to obtain the intrinsic Stokes parameters of the radiation field of the object:

$$Q_{int} = Q_{net} - Q_{ISP}, \tag{5.4a}$$

and

$$U_{int} = U_{net} - U_{ISP}. \tag{5.4b}$$

Determining the ISP components can be difficult, however. The contribution from the Galaxy might be determined from the polarization of starlight along the line of sight. The contribution from the parent galaxy of a supernova may be harder to determine. It is this difficulty that originally motivated the consideration of spectropolarimetry for supernova rather than broad band polarimetry (McCall 1984). Interstellar polarization varies slowly with wavelength compared to the polarization structure expected to be associated with supernova P-Cygni lines. Therefore intrinsic polarization features should be easily identifiable from spectropolarimetry. However, to extract quantitative information about the supernova asymmetry from spectropolarimetry requires that the interstellar polarization be known. Unfortunately the ISP value in the direction to SN 1987a is rather uncertain. The ISP values suggested by several authors vary over a considerable range. Barrett (1987) gives an ISP of .97% at 37°. Cropper *et al.* (1987) estimate .7% at 25°, while conceding considerable uncertainty. Méndez *et al.* (1987) give ISP values that range from .39% to .50% at about 1° for the UBVRI color wavelength bands. Schwarz (private communication) provides ISP values that range from .90% to 1.09% at about 3° for the the UBVRI color wavelength bands and for several line wavelengths. For this thesis the ISP values given by Schwarz have been adopted. These are given in Table 5.1 in the form of interstellar Q and U parameters.

The Mar. 6–7 spectropolarimetry taken by Schwarz and Mundt (1987) along with some data provided by the courtesy of H. E. Schwarz (private communication) and some data from Schwarz (1987) appear in Table 5.1. The values subscripted by "ISP" are the estimates Schwarz gives for the interstellar polarization; those subscripted by "net" are his measured values. The values subscripted by "int" for intrinsic are the supernova values corrected for interstellar polarization. Since the interstellar polarization values are uncertain, the given intrinsic values may have a large systematic error.

The position angles of the intrinsic polarizations in Table 5.1 agree with each other within estimated uncertainties. However, the uncertainties in the position angles are large, and it is noteworthy that there appears to be a systematic difference of about 20° between the emission feature's position angle and the absorption feature's position angle. For axisymmetric emitting systems the position angle should be constant or have 90° shifts only. There is some evidence that SN 1987a has a strong axisymmetric component. Polarization position angle measurements were performed with high wavelength resultion by Cropper *et al.* on Mar. 7 and from May into July. Their measurements show complicated variation of net position angle with wavelength. Cropper *et al.* show, however, that the position angles do cluster about a value $16.5° \pm 3°$. While it is clear that the supernova

TABLE 5.1.—Polarization data for SN 1987a for Mar. 6–7 1987.

Feature	Q_{ISP} (%)	U_{ISP} (%)	Q_{net} (%)	U_{net} (%)	Q_{int} (%)	U_{int} (%)
U	0.09	0.90	0.32±.07	0.75±.07	0.23±.07	-0.15±.07
B	0.11	1.03	0.22	0.67	0.11	-0.36
V	0.11	1.08	0.31	0.64	0.20	-0.44
R	0.10	0.98	0.19	0.65	0.09	-0.33
I	0.09	0.90	0.28	0.57	0.19	-0.33
$H\alpha_{rest}$	0.10	0.98	0.13	0.94	0.03	-0.04
$H\alpha_{abs}$	0.10	0.98	0.11	0.61	0.01	-0.37
$H\beta_{rest}$	0.11	1.05	0.28	0.70	0.17	-0.35
$H\beta_{abs}$	0.11	1.05	-0.31	-0.15	-0.42	-1.20
$H\gamma_{rest}$	0.11	1.03	0.26	0.70	0.15	-0.33
$H\gamma_{abs}$	0.11	1.03	-0.06	0.45	-0.17	-0.58
Na D_{rest}	0.10	1.00	0.48	—0.66	0.38	-0.34
Na D_{abs}	0.10	1.00	-0.01	0.31	-0.11	-0.69
(OIII)	-	-	0.30	0.84	0.20	-0.14

Feature	$\lambda_{filter}\|\delta\lambda$ (Å)	P_{net} (%)	θ_{net} (°)	P_{int} (%)	θ_{int} (°)
U		0.82±.07	33.±15.	0.27±.07	-17.±20.
B		0.71	36.	0.38	-36.
V		0.71	32.	0.48	-33.
R		0.68	37.	0.34	-37.
I		0.64	32.	0.38	-30.
$H\alpha_{rest}$	6565|10	0.95	41.	0.05	-27.
$H\alpha_{abs}$	6251|33	0.62	40.	0.37	-44.
$H\beta_{rest}$	4867|34	0.75	34.	0.39	-32.
$H\beta_{abs}$	4697|10	0.34	103.	1.27	-55.
$H\gamma_{rest}$	4340|28	0.75	35.	0.36	-33.
$H\gamma_{abs}$	4188|33	0.45	49.	0.60	-53.
Na D_{rest}	5897|56	0.82	27.	0.51	-21.
Na D_{abs}	5757|20	0.31	46.	0.70	-50.
(OIII)		0.89	35.	0.24	-18.

SOURCE: The Q_{ISP}, U_{ISP}, Q_{net}, and U_{net} values were supplied by H. E. Schwarz (private communication). The Q_{int} and U_{int} were calculated using the *ISP* and *net* values; the Q_{int} and U_{int} can also be found in Schwarz and Mundt (1987) or, in a more convenient form, in Schwarz (1987). The $\lambda_{filter}|\delta\lambda$ are the central wavelengths and FWHM's of the filters used by Schwarz and Mundt. The uncertainty estimates were also taken from Schwarz and Mundt.

NOTE: The Q_{ISP}, and U_{ISP} values are estimates for the interstellar values toward SN 1987a. The *net* values are the actual observed values for SN 1987a. The Q_{int} and U_{int} are obtained by subtracting the *ISP* values from the net values. The uncertainties assigned to the data are rather approximate, and do not include the systematic error due to the uncertainty in the *ISP* values. The uncertainty in the *ISP* values may be quite large.

cannot be purely axisymmetric, there is probably a strong axisymmetric component.

The symmetry axis for axisymmetric models would be either $\approx -40^\circ$ or $\approx 50^\circ$ if Schwarz and Mundt's intrinsic position angles are taken at face value. Cropper *et al.* 's data indicate the symmetry axis should be $\approx 15^\circ$ or $\approx -75^\circ$. The companion source (see Chapter 1 section (c)) discovered by Karovska *et al.* (1987) using speckle imaging techniques is located at a position angle of $194^\circ \pm 2^\circ$ relative to the supernova (Nisenson *et al.* 1987). It may be that this position angle is also the angle of the symmetry axis of the supernova. This suggestion supports Cropper *et al.* 's assignment of the symmetry axis, since 180° shifts in polarization position angle are of no physical significance. The discrepancy between the two assignments of the approximate symmetry axis may owe to evolution of the supernova. Schwarz and Mundt's data are from Mar. 6–7, and the bulk of Cropper *et al.* 's data are from May 5 and later.

The speckle imaging observations reported by Nisenson *et al.* (1987) for Mar. 25 and Apr. 2 reveal a possible shape asymmetry for the supernova. Their reconstructed images of the supernova show an elongation. The reference star images also show elongation, but not so much as the supernova images. Nisenson *et al.* suggest that the elongation of the supernova images may indicate an intrinsic elongation of the supernova; the uncertainty in the data are too great to be sure. The axis of the elongation of the 6560 Å image is roughly along the celestial latitude (position angle 90°). The direction of elongation is thus roughly perpendicular to the position angle of the companion source. The ratio of height to length for this image is $\approx .8$. The shape asymmetry suggested by the speckle image offers some support to an interpretation of the polarization spectrum in terms of shape asymmetry.

The companion source is probably not a major contributor to the polarization of the net flux of the supernova and companion. These P-Cygni profiles are major structures in the net flux spectrum and are strongly dependent on the velocity distribution of the scattering regions. It seems unlikely that the line flux profiles of the companion source would have the same P-Cygni shapes as the supernova since the companion almost certainly has a different velocity distribution; the companion may not have any significant macroscopic velocity at all. Since the companion source is a weaker source by 2.7 magnitudes than (.08 as bright as) the supernova (Nisenson *et al.* 1987), its line flux profiles can contribute only weakly to the net line flux spectrum. Thus the net flux profiles owe mainly to the supernova, not the companion. The polarization and position angle data are strongly correlated with these flux profiles (Cropper *et al.*) indicating that the polarization is due mainly to the supernova. This argument is taken from Cropper *et al.*

A series of models have been examined to try to fit the flux spectrum and the Schwarz and Mundt polarization data for Mar. 6–7. The synthetic flux spectra have been fitted to an observed spectrum using the procedure outlined in Chapter 2 section (c) and models of the type described in Chapter 4 section (a). The asymmetry ξ, inclination angle to the axis of symmetry, and Sobolev photospheric optical depths have been varied to try to fit the polarization data. The goodness criterion for these fits is merely judgement by eye. Therefore the fits are not uniquely good, and must be considered as reasonable fits rather than best fits. Following the convention established in Chapter 4, the models are labelled by the same number as the figure that displays their spectra: e.g., Fig. 5.2 displays the spectra for model 5.2. All the figures are collected at the end of the chapter.

The first step in fitting the polarization data for Mar. 6–7 is to fit the flux spectrum for that epoch. An observed flux spectrum for Mar. 6 from Blanco *et al.* (1987), provided by the courtesy of J. Matthews (private communication), is displayed in Fig. 5.1. Spherically symmetric model 5.1 was used to calculate a synthetic spectrum to fit the observed spectrum. The model parameters and the reasoning behind their selection for model 5.1 are given in Table 5.2.

The fit to the observed spectrum is quite good in some wavelength regions. Below about 4500 Å it is probable that more lines are needed to fit the observed spectrum. There is in fact a considerable deficiency relative to the black body curve in the UV region of the supernova spectrum after Feb. 26 (Danziger 1987). This deficiency may owe to the opacity of many thousands of weak lines as is speculated for the UV deficiency of type I supernova (Harkness 1986). Above 6700 Å the observed curve falls considerably below the synthetic reddened black body curve. For the V band and longer wavelengths the supernova spectrum is known to obey the black body curve quite well (Bouchet *et al.* 1987); thus adding a few more strong lines above 6700 Å would probably remedy the discrepancy.

The absorption and emission features of the synthetic Hα and Hβ lines are not as extreme as the observed features. Trying to strengthen these lines shifts unacceptably the location of their absorption minima. It is possible that some thermal emission accounts for the excess of the observed Hα emission feature above the synthetic pure resonance scattering emission feature. The lack of a synthetic Hβ emission feature is due to the Fe II 5018 Å line. This line's absorption feature falls on the Hβ's emission feature and destroys it. The destruction of emission features by coincident

TABLE 5.2.—Parameters for the model 5.1 which is used to calculate a synthetic flux spectrum for SN 1987a for Mar. 6 (see Fig 5.1).

Parameter	Value	Comment or Source
E_{B-V}	.20	This value for the color excess was adopted from the estimate $E_{B-V} = .20 \pm .05$ given by Cropper *et al.* (1987) The reddening (extinction) curve was taken from Code *et al.* (1976).
Normalization		The synthetic spectrum was normalized to a reddened black body curve (T=5500 K) at 5900 Å. The observed spectrum was normalized by demanding the integrated flux between 4600 Å and 6400 Å be the same for observed and synthetic spectra.
$r_{g_{max}}$	$4r_{g_{ph}}$	For $p = 7$, a line with $\tau_{ph} = 600$ has the nearly insignificant optical depth of $\approx .04$ at $r_g = 4r_{g_{ph}}$. Thus $4r_{g_{ph}}$ seems a reasonable cut off radius.
p	7	p is the power for the optical depth decay law. 7 is the standard choice for p (see Chapter 2 section (c) and Chapter 4 section (a)).
symmetry	spherical	As an unprejudiced first choice for spectrum fitting a spherically symmetric model is considered.
$\tau_{ph}(\mathrm{H}\alpha)$ $\lambda = 6562$ Å	600	This optical depth provides reasonable fits to the observed Balmer series lines. The optical depths for the other Balmer lines are obtained using the procedure described in Chapter 2 section (c). The first 6 Balmer lines are included in the synthetic spectrum.
$\tau_{ph}(\mathrm{Na\ D})$ $\lambda = 5890$ Å	2.25	Only the Na D lines were included for Na I. The other Na I lines made negligible contribution to the shape of the synthetic spectrum.
$\tau_{ph}(\mathrm{Fe\ II})$ $\lambda = 4233.16$ Å	10	The 33 strongest Fe II between 4173 Å and 6248 Å were included in the synthetic spectrum.
T_{ph}	5500 K	This photospheric temperature was obtained by interpolating from the temperatures of black body curve fits to SN 1987a optical and IR data given by Bouchet *et al.* (1987).
v_{ph}	6000 Km s^{-1}	This photospheric velocity was determined by fitting the absorption feature of the weak Na D lines (see Chapter 2 section (c) and Chapter 4 section (b)).

NOTE: The line wavelengths and energy levels were taken from Striganov and Sventitskii (1968, p. 73, 231, 465). The weighted oscillator strengths for the Balmer and Na I lines were taken from Allen (1976, p. 70). The weighted oscillator strengths for the Fe II lines were taken from Phillips (1979).

absorption features was discussed in Chapter 4 section (b). The Fe II 5018 Å line is necessary to create the emission feature near 5000 Å. Trying to add a line strong enough to restore the emission near 4900 Å destroys the fit of the Hβ absorption feature. It may be that the observed feature near 4900 Å is a thermal emission feature also.

It seems likely that some additional weak lines near 6000 Å would reduce the synthetic Na D line emission feature and improve the fit in that region.

Having obtained τ_{ph} values for the Balmer series lines, a collisional depolarization analysis can be done. In Chapter 2 section (e) an equation for the electron density of the most polarizing region in a supernova atmosphere was derived:

$$n_{e\ pol} \approx 3.5 \times 10^{10} \frac{(p-1)}{v_9 t_d} (1/\tau_{ph})\, cm^{-3}, \tag{5.5}$$

where v_9 is the photospheric velocity in units of $10^9 \mathrm{cm\,s^{-1}}$, and t_d is the time in days since the supernova exploded. From the synthetic spectrum fit $v_9 = .6$. The Mar. 6–7 data was taken approximately 12 days after the neutrino burst that marked the supernova explosion. The p parameter was set to 7 for the model. The τ_{ph} and $n_{e\ pol}$ values are given in Table 5.3 along with the critical density values. Recall from Chapter 2 section (e) that if the $n_{e\ pol}$ values greatly exceed the critical density values, then the polarizing effect of scattering would be expected to be destroyed by collisions.

TABLE 5.3—The critical electron densities for the destruction of the polarizing effect of the Balmer transitions in a hydrogen dominated atmosphere and the $n_{e\ pol}$ values for SN 1987a on Mar. 6–7 1987.

Transition	n_{upper}	$n_{e\ crit}$ (cm^{-3})	τ_{ph}	$n_{e\ pol}$ (cm^{-3})
Hα	3	–	600.	5×10^7
Hβ	4	4×10^8	83.	3.5×10^8
Hγ	5	1×10^8	28.	1×10^9
Hδ	6	2.5×10^7	13.	2.2×10^9
Hϵ	7	8×10^6	7.2	4×10^9
Hζ	8	2×10^6	4.5	6×10^9

SOURCE: The critical density values were measured from Fig. 4 of Pengelly and Seaton (1964).

It is clear from Table 5.3 that the polarizing effect cannot be ruled out for either the Hα or Hβ lines. Considering the equation (5.5) is rather approximate even the Hγ line's polarizing effect may survive collisional destruction. As argued in Chapter 2 section (e) some other lines, such as the Na D lines, are probably safer than the Hα line from collisional depolarization. These conclusions provide confidence that the observed polarization structure associated with the line flux profiles does in fact owe to resonance scattering.

To try to fit the polarization data the asymmetric models 5.2, 5.3, 5.4, 5.5 and 5.7 were considered. These models, except as indicated, have the same parameters as model 5.1. Except for model 5.5 the Fe II lines were not included in these models in order to reduce the computational effort while examining parameter space.

For model 5.2, oblate asymmetry was introduced and varied between $\xi_{obl} = .2$ and $\xi_{obl} = .8$. Recall from Chapter 4 section (a) that

$$(c/a) = 1 - \xi_{obl}, \tag{5.6}$$

where c and a are the semiaxes parallel and perpendicular to the axis of symmetry, respectively. Only oblate asymmetry was considered since oblateness seems the most plausible asymmetry for supernova. Rotation of an exploding supernova core or mantle is a plausible source of oblateness (see Chapter 1 section (d)). The oblateness is assumed to be communicated somehow to the atmosphere (see the discussion in Chapter 4 section (a)). The inclination angle of the line of sight to the symmetry axis of the model was set to 90°. The position angle of the model's symmetry axis on the plane of the sky was taken to be either $-40°$ or 50° as indicated by Schwarz and Mundt's position angles.

Except for the absence of Fe II lines, the synthetic flux spectrum for model 5.2 (see Fig 5.2a) is not greatly changed from that of model 5.1. It is noteworthy that the absorption features of the Hα and Hβ lines are somewhat better fit by the oblate model curves; the $\xi_{obl} = .4$ to .6 curves fit the absorption feature of the Hα best, and the extreme $\xi_{obl} = .8$ curve fits the absorption feature of the Hβ best. Remarkably the $\xi_{obl} = .8$ curve improves the fit of the emission feature of the Hα line.

The synthetic polarization spectra for model 5.2 are displayed in Fig. 5.2b along with Schwarz and Mundt's spectropolarimetric data (corrected for ISP using Schwarz's ISP value). As mentioned above, the data have shifts in postion angle between the absorption and emission polarizations that are consistent, within uncertainty, with being 0°; however, there appears to be a systematic shift of about 20°. An axisymmetric interpretation of the data requires that the shifts be assumed to be either 0° or 90°. As mentioned above, Cropper *et al.* conclude that there is some evidence for an approximate symmetry axis. Since only axisymmetric models have been considered for this thesis, it is assumed that there is a symmetry axis. Therefore it seems best to regard the position angle shifts found in the Schwarz and Mundt data as being 0°. Synthetic polarization spectra for resonance lines show 90° shifts in position angle across the P-Cygni profile; the 90° shifts are expressed graphically as changes in the sign of polarization (see Chapter 4). Thus there is a considerable discrepancy between the Sobolev-II calculated polarization spectra and the Schwarz and Mundt data. In Fig. 5.2b, this discrepancy appears as a polarization difference between the baseline of the synthetic spectra (i.e., the zero axis) and the average polarization of the Schwarz and Mundt data. Some of the discrepancy may be remedied by a better estimate of the ISP. Also, intrinsic continuuum polarization could provide a non-zero baseline for the resonance polarization profiles. Intrinsic continuum polarization almost certainly exists for 1987a (see the discussion of Fig. 5.5b below). Models 5.6 and 5.7 (see below) are used to investigate the effects of continuum polarization. For the models 5.2 through 5.5 the discrepancy between the average polarization of the data points and the baseline of the synthetic polarization profiles will not be considered further. Instead these models will be used to try to fit the absorption-emission polarization differences of the data. For brevity these differences will be labelled by ΔP.

The observed ΔP and those obtained from the calculations for model 5.2 are given in Table 5.4. Due to the large uncertainties, all the asymmetric models produce ΔP values that are consistent with the observed values for the Hα, Hγ, and Na D lines; however the closest fit for these lines is given by the $\xi_{obl} = .4$ model. For the Hβ line, there are no fits within the estimated uncertainties; the model ΔP are always too small. Note from Fig. 5.2b that the difference between the polarization maximum and minimum of the Hβ line is about .5 % for $\xi_{obl} = .4$ and about 1.2 % for $\xi_{obl} = .6$. The reason why the Hβ line's ΔP values are too small is that the wavelength where the absorption polarization datum was measured is not the wavelength of the model maximum polarization. Since the model absorption polarization feature is rather narrow, a small offset in wavelength changes the ΔP value dramatically. The position of the polarization maximum is not very certain, since it depends sensitively on the photospheric velocity and very probably on the actual supernova photosphere shape. Thus it seems reasonable to suggest that since a model with $\xi_{obl} \approx .5$ would produce a polarization difference of order .8% between the maximum and minimum of the polarization profile, that asymmetry of this size may explain the Hβ polarization data. This difficulty with the Hβ line data is not too disappointing, since it is already understood from the lack of a constant position angle of polarization that simple oblate models cannot completely explain the polarization data.

Table 5.4. The observed ΔP and the ΔP taken from model 5.2.

Line	ΔP_{obs} (%)	ΔP_{model} (%)			
		$\xi_{obl} = .2$	$\xi_{obl} = .4$	$\xi_{obl} = .6$	$\xi_{obl} = .8$
Hα	$.32 \pm .14$	$.17 \pm .03$	$.35 \pm .03$	$.49 \pm .03$	$.45 \pm .03$
Hβ	.88	.20	.42	.61	.56
Hγ	.24	.11	.25	.35	.32
Na D	.19	.08	.17	.26	.30

NOTE: The ΔP_{obs} are taken from Table 5.1. The ΔP_{model} are taken from the calculations for model 5.2. The wavelengths at which the polarization values were taken for the ΔP_{model} are those given by Schwarz and Mundt (1987) for their filter central wavelengths. The uncertainties in the ΔP_{model} values are due to the numerical integrations and to truncation errors that occur when subtracting flux components to get polarization and when subtracting polarization values to get the ΔP values.

Since an asymmetry $\xi_{obl} \approx .5$ can explain the Hβ data, and since the polarization profiles of a $\xi_{obl} = .5$ model would give reasonably good fits to the other line data, the asymmetry ξ_{obl} has been set to .5 for the rest of the models investigated. The oblate asymmetries obtained by Müller and Hillebrandt (1981), and Bodenheimer and Woosley (1983) in their rotating supernova explosions indicate that $\xi_{obl} = .5$ (or 50% asymmetry) is physically plausible (see Chapter 1 section (d)).

The inclination angle of the line of sight to the symmetry axis of model 5.2 was set to 90° degrees. This choice of inclination angle maximizes the polarizing effect of the asymmetry. The inclination angles of supernovae, however, should be randomly distributed between 0° and 90°. It is clear that the effect of varying the inclination angle should be investigated. Model 5.3 was calculated with inclination angles of 90°, 60°, and 15°. The 60° inclination was chosen since the mean of random inclinations is nearly 60°:

$$\langle \theta_{incl} \rangle = \int_0^{\pi/2} d\theta\, \theta \sin\theta = 1 \approx 57.3^\circ. \tag{5.7}$$

The 15° inclination was chosen to examine a low inclination case. The 90° inclination was for comparison. Model 5.3 had $\xi_{obl} = .5$.

The flux spectra for model 5.3 are shown in Fig. 5.3a. It is clear that decreasing the inclination while holding the optical depths constant worsens the flux spectrum fit to the observations. Most of the worsening occurs as the inclination angle is reduced from 90° to 60°. The polarization spectra are shown in Fig. 5.3b. The fit to the polarization data for the Hβ and Na D lines is lost when inclination angle is decreased significantly below 90° . The fit for all the lines is lost when inclination angle is decreased to 15°. The loss of fit to both flux and polarization data may be recovered either by increasing the asymmetry (see Fig. 4.12a and 4.12b Chapter 4 section (d)) or by increasing the optical depths (see Fig. 4.14a and 4.14b Chapter 4 section (d)). Since an asymmetry of $\xi_{obl} = .5$ seems physically rather extreme, the option of increasing optical depths has been considered with model 5.4.

Model 5.4 has $\xi_{obl} = .5$ and the inclination angle is set to 60°. ~~The~~ optical depths of the Balmer lines are increased by factors of 10 and 50 over the values fitted for the spherically symmetric model. Fig. 5.4a shows that increasing the optical depth does improve the fit to the depth of the absorption features and the height of the emission features. The locations of the absorption minima have been shifted, but these can be recovered by reducing the photospheric velocity. Increasing the Balmer line optical depths also recovers Balmer line polarization features of size comparable to the observed features (see Fig. 5.4b).

It is clear from the examination of models 5.3 and 5.4 that unique values for asymmetry, inclination, optical depths, and photospheric velocity might be very difficult to determine. Other observational evidence or theoretical guidance may help to determine unique values.

Model 5.5 was created to examine the effects of introducing the Fe II lines into the spectrum of an oblate model. The asymmetry $\xi_{obl} = .5$, the inclination angle is set to 90°, and the optical depths from the spherically symmetric model 5.1 are used. Fig. 5.5a shows that the model 5.5 synthetic flux spectrum fits the observed spectrum at least as well as the spectrum of the spherically symmetric model 5.1. The ΔP_{model} values are reasonable fits to the ΔP_{obs} values (see Fig. 5.5b).

The effect on the synthetic polarization spectrum of introducing the Fe II lines is not very large (see Fig. 5.5b). The smallness of the polarizing effect of the Fe II lines owes in part to the smallness of their optical depths: the strongest lines have optical depths of order 10, and most of the lines have optical depths of order 1. However, it is not only the weakness of the Fe II lines, but also the smallness of their E_1 coefficients that makes their polarizing effect weak: of the 33 Fe II lines included in the synthetic spectrum, 18 lines have $E_1 < .1$. The cumulative polarizing effect of the Fe II lines is not enough to account for the intrinsic continuum polarization that the Schwarz and Mundt data indicates exists. This experience with the Fe II lines indicates that it may not be possible to build up a continuum polarization from identifiable spectrum lines. It may be that thousands of weak lines provide a quasi-continuous scattering opacity due to Doppler enhancement (Karp *et al.* 1977), and these may contribute to a continuum polarization; however, nearly all of these lines would have $E_1 < .5$ (see Table 2.2 in Chapter 2 section (d)). It is not clear that resonance lines can provide much continuum polarization. However, intrinsic continuum polarization is almost certainly present for SN 1987a. Cropper *et al.* observed a continuum polarization of .8% on Mar. 7 in the region of the Hα line; by May 5 the continuum polarization had dropped to about .5%. This time variation is naturally attributed to a variation in an intrinsic continuum polarization. The introduction of continuous opacity would provide a source for this continuum polarization.

The Sobolev calculations of Branch (Branch 1980; Branch *et al.* 1981, 1982, 1983, 1985) and Paper I, and all the Sobolev calculations previously presented in this thesis ignore continuous opacity. Continuous opacity is wavelength independent, at least over wavelength intervals of interest to line calculations. It has thus been assumed that it has little effect on the morphology of the line flux profiles. The continuous opacity is merely thought of as establishing the photospheric radius at optical depth of order 1 in the continuum. Co-moving frame calculations (Harkness 1986) with continuous opacity, including electron scattering, show that the assumption that continuous opacity has little effect on the morphology of line profiles is valid. Thus the identification of lines, and order of magnitude estimates of line strengths can probably be safely made while ignoring continuous opacity. However, the effects of combining sources of continuum and line polarization are less certain. Some preliminary study of these effects ought to be made since they could clearly be important in interpreting SN 1987a's polarization spectra.

It seems most probable that the source of continuum polarization is Thomson scattering by free electrons. Free electrons are a major source of continuous opacity in supernovae (Wagoner 1981). Electron scattering obeys a Rayleigh phase-matrix (a Hamilton phase-matrix with E_1=1), and so is highly polarizing. Since electron scattering is wavelength-independent, velocity fields have little effect on radiative transfer involving electrons. This fact was invoked by Shapiro and Sutherland (1982) and McCall (1984, 1985) so that they could use static atmosphere solutions for their polarization calculations (see Chapter 3). Unfortunately, there seems to be no simple way to merge existing static atmosphere, continuum solutions with moving atmosphere, line calculations; McCall's method for doing so was very qualitative. Instead of merging a static atmosphere, continuum solution, a simple expedient is to discretize the continuous (and wavelength-independent) electron opacity into a series of weak, closely spaced pseudo-lines. Here, this method is called the discretized continuous opacity method or the DCO method. The DCO method is developed below, and some exploratory results are presented for models 5.6 and 5.7.

The assumption is made that all the continuous opacity owes to free electrons; this is probably not valid (see Wagoner 1981). However, as argued in the discussion of model 5.4, another source of continuous opacity, Doppler enhancement of thousands of weak resonant lines, may not produce much polarizing effect. Also the continuous opacity provided by ionization processes will not be polarizing. Thus for an exploratory treatment the limitation to electron continuous opacity seems reasonable.

The discretization procedure requires a prescription for the Sobolev optical depths for the pseudo-lines. The Sobolev optical is given by

$$\tau = \frac{k_\nu c}{\nu_0 |Q|} = \frac{k_\lambda c}{\lambda_{rest}|Q|}, \tag{5.8}$$

where λ_{rest} is the rest frame line center wavelength, and k_λ is the integral of the monochromatic line opacity over all wavelength. For the electron pseudo-lines, let

$$k_\lambda = n_e \sigma \Delta\lambda, \tag{5.9}$$

where n_e is the electron density, σ is the Thomson cross-section, and $\Delta\lambda$ is the discretization increment in wavelength. Assuming the expression for n_e from equation (2.164a) in Chapter 2 section (e) gives

$$\tau_{pseudo} = \frac{(p-1)c\tau_e}{r_{ph}|Q|}\frac{\Delta\lambda}{\lambda_{rest}}(r_{ph}/r)^p, \tag{5.10}$$

where τ_e is the optical depth to the photosphere and λ_{rest} is interpreted as the wavelength of a pseudo-line. The optical depth to the photosphere is usually taken to be 1. Recall from Chapter 2 section (c) that for supernova

$$|Q| \approx t^{-1} \qquad \text{and} \qquad r_{ph} \approx v_{ph} t, \tag{5.11}$$

where t is the time since the explosion and v_{ph} is the photospheric velocity. Thus the equation for pseudo-line Sobolev optical depth is

$$\tau_{pseudo} = \frac{(p-1)c\tau_e}{v_{ph}} \frac{\Delta\lambda}{\lambda_{rest}} (r_{ph}/r)^p = \tau_{pseudo(ph)} (r_{ph}/r)^p. \tag{5.12}$$

With this expression for the pseudo-line optical depths it is a simple matter to implement the discretized continuous opacity in the multi-line Sobolev program.

It should be noted that there is no need to think of the continuous electron opacity as discretized in wavelength. The macroscopic motion of the atmosphere implies that wavelength discretization is equivalent to spatial discretization of the opacity due to the Doppler effect. Note that

$$\Delta\lambda = \lambda_{rest}(\Delta v/c) = \lambda_{rest}(|Q|\Delta l/c), \tag{5.13}$$

where Δl is a spatial discretization increment for the continuous opacity. Substituting equation (5.13) into equation (5.10) gives the prescription

$$\tau_{pseudo} = (p-1)\tau_e \left(\frac{\Delta l}{r_{ph}}\right) (r_{ph}/r)^p \tag{5.14}$$

for the optical depths to be used at the spatial discretization points. Since both line and continuous opacity are being treated, it is most convenient to think in terms of wavelength discretization and to use equation (5.12) in computer calculations.

In order to form a continuum scattered flux and a continuum polarization, the pseudo-lines have to be sufficiently dense. One would expect that the individual flux and polarization features of the pseudo-lines would have to be strongly overlapping. From models 4.1, 4.9 and 4.14 of Chapter 4, it can be seen for weak and moderate lines ($\tau_{ph} \lesssim 100$) that the flux and polarization emission and absorption features have widths of order $\lambda_{rest}(v_{ph}/c)$. Thus to overlap the features, the separation of the pseudo-line rest wavelengths should be of order $\lambda_{rest}(v_{ph}/c)$ or smaller. This condition is the same as requiring the spatial discretization increment to be of order r_{ph} or smaller. Numerical experiments show that for $\Delta\lambda \gtrsim 2\lambda_{rest}(v_{ph}/c)$, the line structure has not been suppressed in either flux or polarization. For $\Delta\lambda \lesssim \lambda_{rest}(v_{ph}/c)$ the line structure is largely suppressed and continuum-like flux and polarization regions are present; some small oscillations due to the lines remain superimposed on the continua. As $\Delta\lambda$ is reduced further the line structure is further reduced and the flux and polarization continua become smoother. For $\Delta\lambda \lesssim \lambda_{rest}(v_{ph}/c)$ the average height and slope of the continuum flux and polarization are roughly constant as $\Delta\lambda$ is decreased.

It should be noted that the pseudo-lines can only be introduced over a finite range of wavelengths. Thus spurious structure is to be expected near the low and high ends of the range; at the ends of the range there is a step-function-like change in scattering opacity. Therefore the wavelength range must be made wide enough that the spurious structure is not important in the central region of the range where the continuum effects are to be studied. The spurious structure extends over a few times $\lambda_{rest}(v_{ph}/c)$ at the ends of the wavelength range.

In order to test the physical validity of DCO, a comparison has been made between model results calculated using DCO and results obtained by Cassinelli and Hummer (1971; hereafter CH). CH considered models that consisted of spherical, electron scattering atmospheres with central point sources of unpolarized flux. The opacity of the CH models is given by $k(r) = r^{-p}$; the radial unit of measure was chosen so that k(r=1)=1. The atmospheres have a cut-off radius R. CH plotted the polarization of specific intensity beams emitted from an atmosphere as a function of the logarithm of the impact parameter. The impact parameter is the distance on the projected atmosphere (as seen by a distant observer) measured from the center of the projection. The CH results, taken from CH's Fig. 6., for a calculation with $p = 3$ and $R = 10$ are shown in Fig. 5.6. The polarization plateau region mentioned in Chapter 3 section (a) is not present; R must be greater than 10 for the plateau region to be evident. The plateau region is beginning to form before the inflection point near log(impact parameter) $\approx$ .6 causes the polarization curve to rise rapidly to unity. A DCO calculation was done with a model that was the same as the CH model, except that a finite central source for unpolarized continuum flux was used. The agreement between the CH and the DCO curve is good. This gives confidence in using DCO for supernova models. Further comparisons of DCO and CH results should be made to give additional confirmation of the DCO method.

The DCO model used for producing the curve in Fig. 5.6 required a finite central source of unpolarized radiation for numerical reasons. The central source had a radius $r_{source} = (1/3)$. The pseudo-lines must have a spatial discretization increment of the same size as the radius of the central source in order for their P-Cygni profiles to overlap. Thus for an atmosphere of diameter $2R = 20 = 60r_{source}$, 60 pseudo-lines are required. A present, the practical upper limit on lines in the existing Sobolev-H program (see Appendix 4) is about 60. Models with smaller central sources and only 60 pseudo-lines gave poorer agreement to the CH curve. Smaller central sources with more pseudo-lines would probably improve the agreement of the DCO and CH curves.

Before presenting results of supernova model calculations with DCO, it is useful to consider what results were expected and qualitatively what was found. For resonance scattering the absorption and emission polarizations are aligned perpendicular to each other for both prolate and oblate atmospheres. The absorption feature has a higher absolute value of polarization in general than the emission feature (see Chapter 4). However, the emission flux is more diluted by unscattered, unpolarized radiation; thus the emission flux may include more polarized radiation in absolute quantity than the absorption flux. Therefore it is not certain which polarization alignment would dominate if the absorption and emission flux were summed. Continuum polarized fluxes from the photodisk and limb regions of the atmosphere are not separated by wavelength as is the case for the P-Cygni line fluxes. Thus what can be called emission and absorption continuum fluxes are summed to give the emergent continuum flux. Therefore there can only be one continuum polarization alignment. McCall's treatment (1984, 1985) of the scattered continuum flux using the CH continuum polarization result indicates that continuum polarization should be aligned with the long axis of an elongated scattering atmosphere (see Chapter 3 section (b)). Thus one expects that the continuum polarization should have the same polarization alignment that the emission feature polarization of a resonance line has in the absence of continuous opacity. With the convention used in all the figures of Chapter 4, the continuum polarization is expected to be positive for prolate atmospheres and negative for oblate atmospheres. Numerical experiments for oblate atmospheres with DCO confirm the expectation for oblate atmospheres.

The effect of the DCO on the polarization profiles of the resonance lines turned out to be contrary to expectations. It was expected that the profiles would be superimposed on the continuum polarization without very profound modifications. This was a supposition of Paper I. The result of numerical experiments with oblate atmospheres was that the continuum polarization caused an inversion of the profile; the positive absorption feature became a dip on the continuum polarization spectrum and the negative emission feature became a hump. This inversion effect is certainly valid for a dense spectrum of lines. The good agreement between the DCO and CH calculation, discussed above, indicates that the inversion effect may well be valid for the convolution of electron and resonant line scattering. Further numerical experiments are needed to understand how the inversion effect arises and how it varies with the model parameters.

If valid, the inversion effect explains a previously puzzling feature of the SN 1987a polarization data: the fact that the absorption features were apparently humps on a continuum polarization. The absorption hump is the oblate atmosphere absorption dip after a 90° shift of the conventional position angle of polarization. With this interpretation the Schwarz and Mundt data would indicate an oblate supernova atmosphere with its symmetry axis at a position angle between about 35° and 70°. If Cropper *et al.* 's correction for interstellar polarization is applied to the uncorrected data of Schwarz and Mundt, then the position angle of the symmetry axis would be between about $-25°$ and 20°.

Supernova model 5.7 was calculated using DCO. The model has $\xi_{obl} = .5$, inclination angle 90°, no Fe II lines, and all other parameters the same as model 5.1. The average pseudo-line wavelength increment is given by $\Delta\lambda_{ave} = 67.3\,\text{Å} \approx .7 \times \lambda_{rest}(v_{ph}/c)$. This wavelength increment was chosen since only about 50 pseudo-lines could be used for the wavelength range 3700-7200 Å due to computational limitations. The wavelength increment gives an adequate scattered continuum flux and polarization; however, these continua are less than ideal, since some pseudo-line structure remains. The continuum optical depth to the photosphere $\tau_e = 7$. With $\tau_e = 7$ the Sobolev optical depth of a pseudo-line $\tau_{pseudo(ph)} = 27$. Model 5.7 was used only for an exploratory calculation. The calculated spectra were only intended to be rough fits to the data, not exact fits. More exploration of parameter space is required for exact fits.

The synthetic flux spectrum for model 5.7 appears in Fig. 5.7a. It can be seen that the fit of the synthetic spectrum is considerably worsened by the introduction of DCO. Note that the Na D lines in the synthetic spectrum are barely disguishable from the spurious pseudo-line structure. The line fits could probably be improved easily by increasing the line Sobolev optical depths. The large emission feature near 7200 Å is spurious, and is due to there being no pseudo-lines beyond 7200 Å. The synthetic polarization spectrum in Fig. 5.7b is qualitatively a fit to the data. The polarization features for wavelengths less than about 4000 Å and greater than about 6700 Å are probably spurious results due to the ends of the range of the pseudo-lines.

To fit the average height of the data points τ_e had to be set to 7 rather than to the more usual value of 1. Since some of the continuum polarization in the supernova data may still owe to *ISP*, τ_e values that are less than 7 are plausible. However, it seems likely that $\tau_e > 1$ will be required to fit the continuum polarization data. This is not implausible. In an atmosphere in which true absorption dominates the opacity, the optical depth to the region where the thermal continuum radiation is formed is of order 1. In general, however, the optical depth to the thermalization region (the thermalization depth) is $\sim \zeta^{-1/2}$, where ζ is the ratio of absorption to total opacity (see Mihalas 1978, p. 149). Since Wagoner (1981) argues that type II supernova atmsopheres may be scattering dominated, ζ may be much less than 1, and the thermalization depth much greater than 1. Recall that the photosphere is usually defined to be the optical depth from which outward moving photons have equal probability of scattering again or of escaping the atmosphere without scattering again. If $\tau_e = 7$ is required, then all the quantities labelled photospheric (e.g. v_{ph} and r_{ph}) ought to be re-labelled to indicate that they are quantities at the thermalization depth. Of course, it should be noted that the region of thermalization may not have a sharp boundary.

The conclusions of this exploratory investigation of the continuum polarization must be tentative. Continuum polarization of the right order can be generated. The rough shape of the polarization data can be approximated. Better fits to the flux and polarization data could undoubtedly be achieved by varying the parameters. However, further study of the physical validity of the DCO method ought to be done. Also more study is needed to understand how the continuum polarization affects the P-Cygni line polarization.

The conclusions of the analysis of Schwarz and Mundt's Mar. 6–7 data must also be tentative. Assuming oblate shape asymmetry is the origin of the polarization, then an asymmetry of about 50 % ($\xi_{obl} = .5$) seems to be necessary to fit the polarization data's variations across the P-Cygni line profiles. If SN 1987a were prolate, then a similar degree of asymmetry would be needed to fit the data's variations. A more definite analysis requires the following: (1) a confident value for the interstellar polarization, (2) a better understanding of the effects of continuum polarization, and (3) more sophisticated model atmospheres.

Other investigators, as mentioned above, have attempted to interpret SN 1987a polarization data in terms of shape asymmetry. Cropper *et al.* (1987), using the results of Shapiro and Sutherland (1982), find $\xi_{obl} = .23$ (23 % oblate asymmetry) or $\xi_{pro} = .29$ (29 % prolate asymmetry). Using McCall's prescription (1984, 1985) for the axis ratio of the atmosphere, Cropper *et al.* find approximately a 10 % asymmetry. These asymmetry estimates are given tentatively, since Cropper *et al.* conclude that the Shapiro and Sutherland, and McCall models of a supernova atmosphere are too simple to explain all the behavior of the SN 1987a data. The limitations of the Shapiro and Sutherland, and McCall results are discussed in Chapter 3. In Chapter 4, it was found that the McCall prescription for resonance line polarization gave polarization values that were about an order of magnitude greater than the Sobolev-H polarization values. Thus it is to be expected that McCall's prescription for asymmetry would lead to smaller asymmetry estimates than the asymmetry estimates determined from Sobolev-H calculations.

Méndez *et al.* (1987), interpreting their color polarimetry, find for their most favoured supernova models that the asymmetries required are less than 1 %. Méndez *et al.* rely on a polarization result given by Brown and McLean (1977) for an optically thin, electron scattering atmosphere with a central point source of unpolarized radiation. By optically thin it is meant that photons that are scattered more than once make negligible contribution to the emergent flux. Since multiple scattering has a depolarizing effect on scattered radiation, the use of the Brown and McLean result may lead to an underestimate of the asymmetry required to reproduce the observed SN 1987a polarization data. Additionally the fact that the Brown and McLean atmosphere has a point source would tend toward underestimating the supernova asymmetry; a finite source causes a scattering atmosphere model to be less polarizing (see the discussion in Chapter 3 section (a)). The supernova has a finite central source of unpolarized radiation. If the application of the Sobolev-H method to SN 1987a is correct, then the results presented in this chapter show that Méndez *et al.* have severely under-estimated the asymmetry of SN 1987a.

The analysis given in this chapter has been restricted to the Schwarz and Mundt polarization data from Mar. 6–7. Schwarz (private communication, 1987) has continued to take polarization data at intervals throughout the year 1987. This data should be available soon. Cropper *et al.* (1987) have already reported an impressive collection of spectropolarimetric data for the period from Feb. 27 through July 8 1987. By the courtesy of the authors (especially J. Bailey), and the Anglo-Australian Observatory this data has been supplied to the thesis author. It is hoped that a more sophisticated analysis will be done on all the SN 1987a spectropolarimetry in the near future. Whatever the final interpretation, the spectropolarimetric data is likely to prove important to the understanding of SN 1987a.

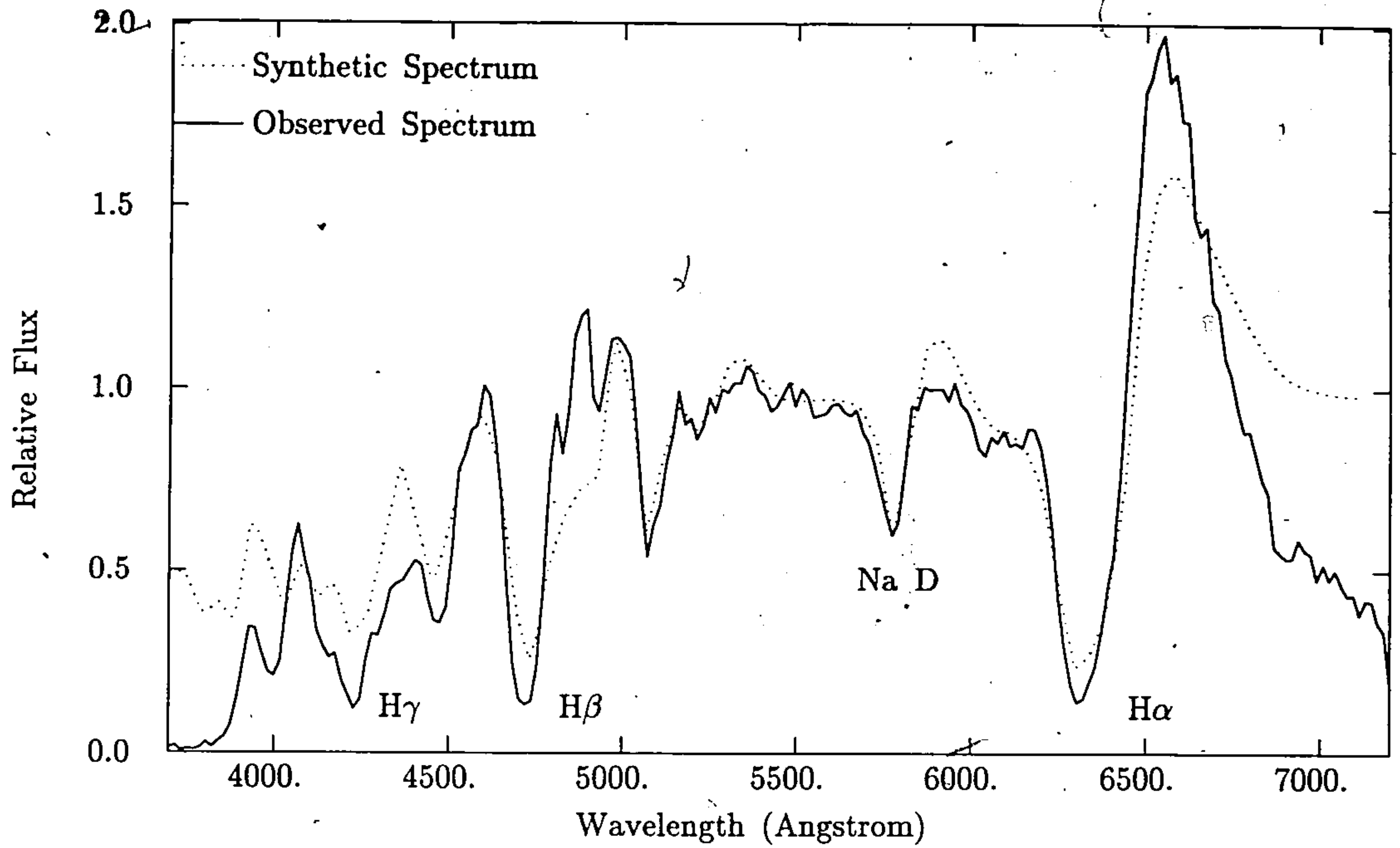

Fig. 5.1. Observed and synthetic SN 1987a flux spectra (spherical model; Fe II lines; Mar. 6).

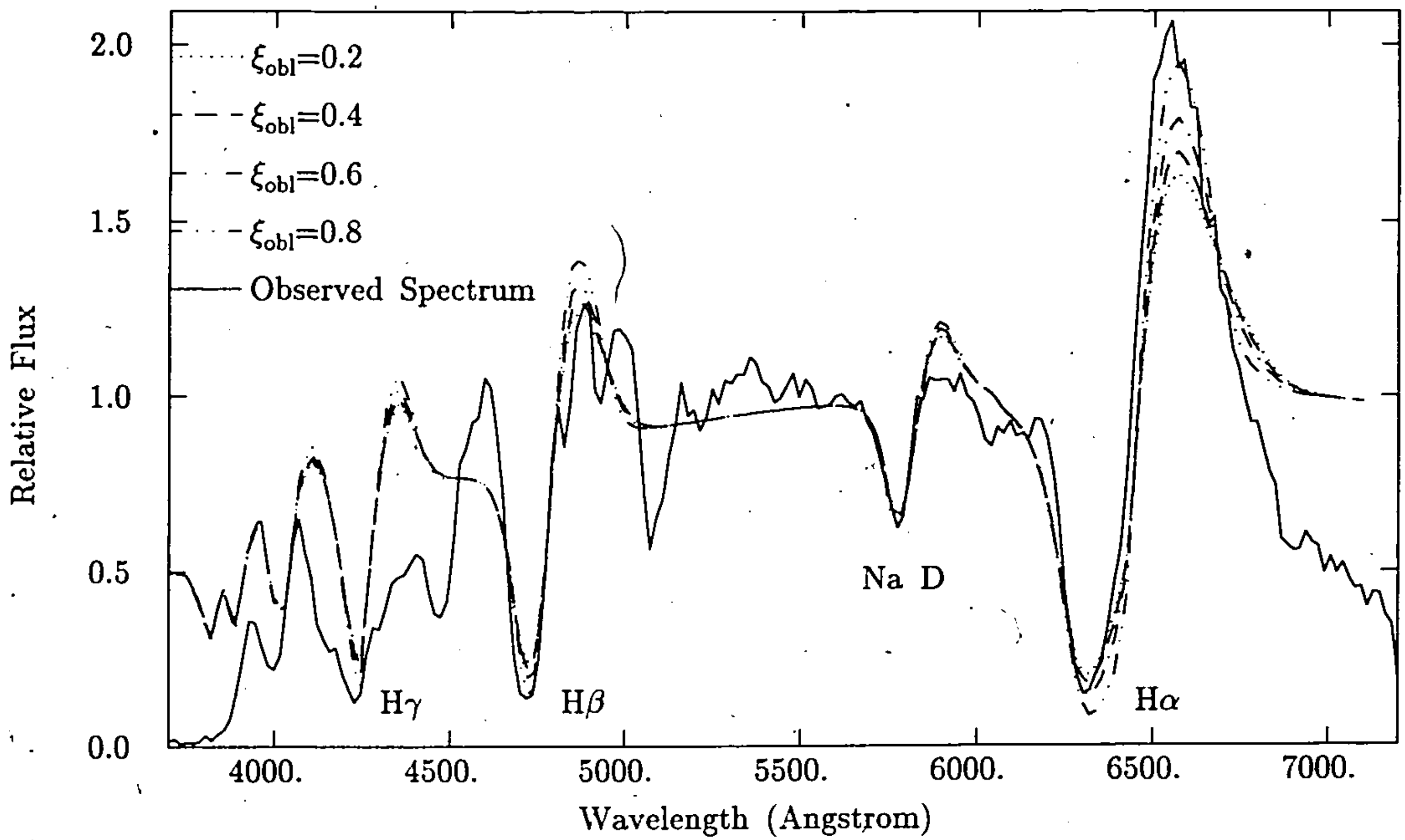

Fig. 5.2a. Observed and synthetic SN 1987a flux spectra (oblate model; θ=90°; varied asymmetry; no Fe II lines; Mar. 6).

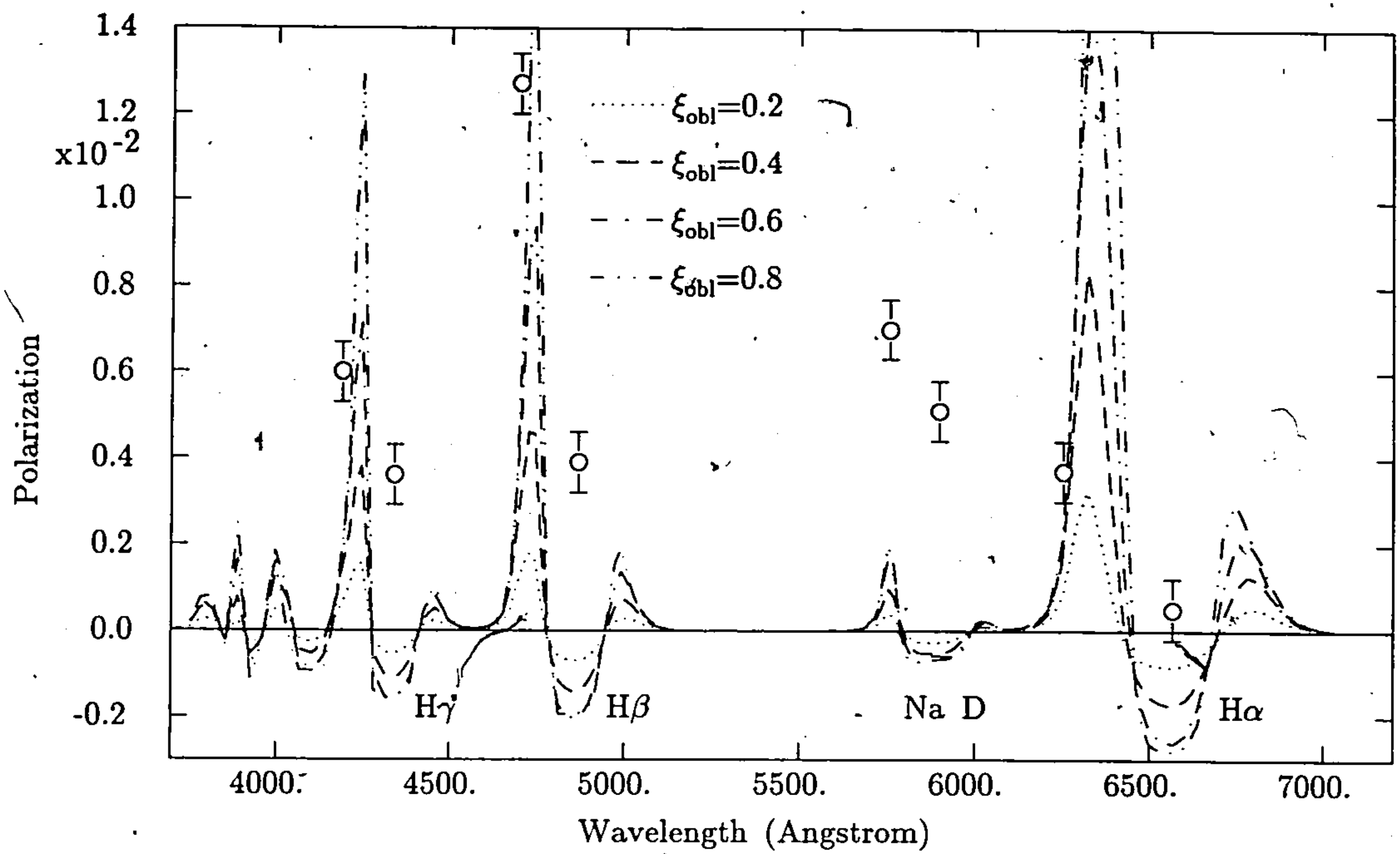

Fig. 5.2b. Polarization data for SN 1987a (Mar. 6-7) and synthetic polarization spectra for model 5.2.

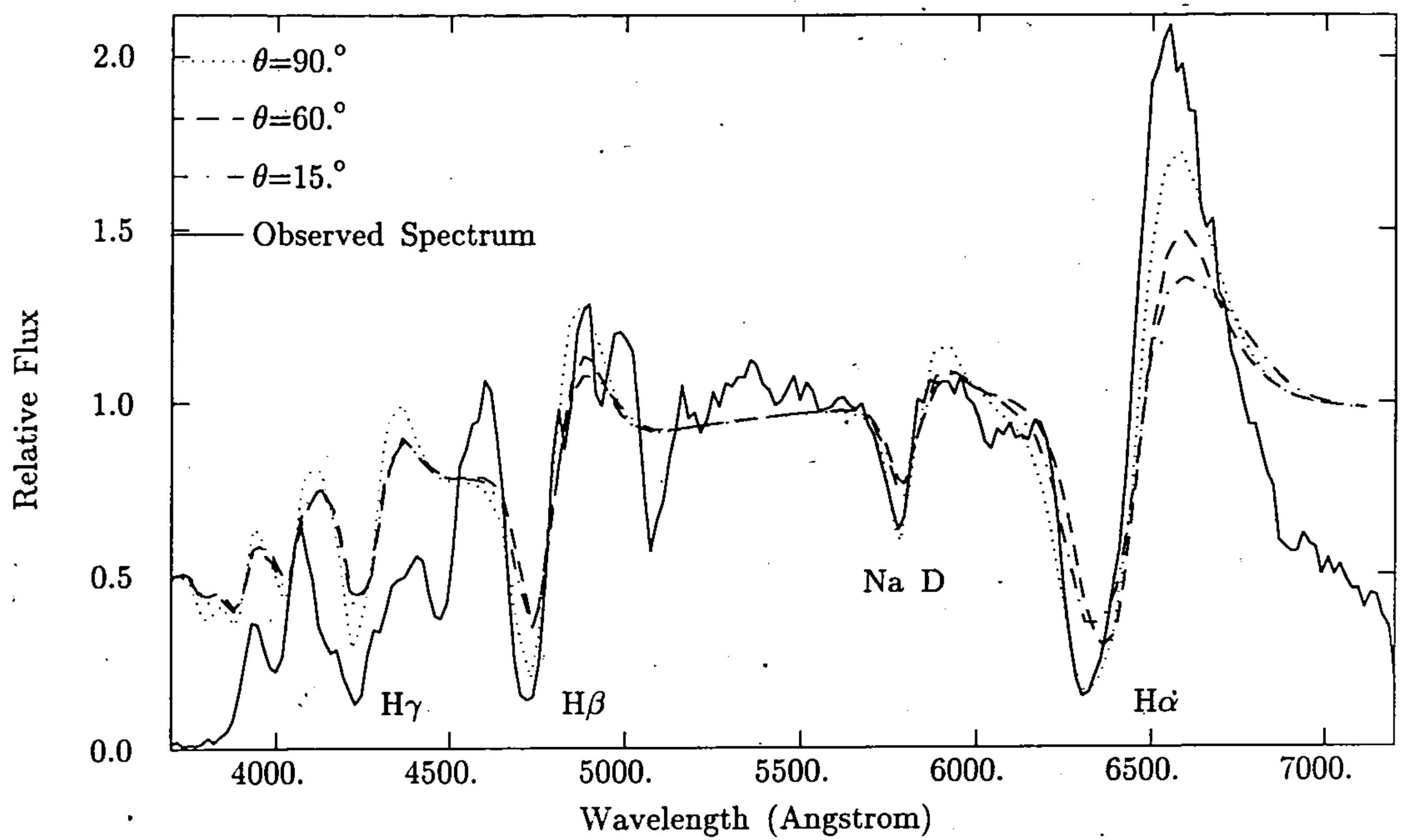

Fig. 5.3a. Observed and synthetic SN 1987a flux spectra (oblate model; varied θ_{incl}; ξ_{obl}=.5; no Fe II lines; Mar. 6).

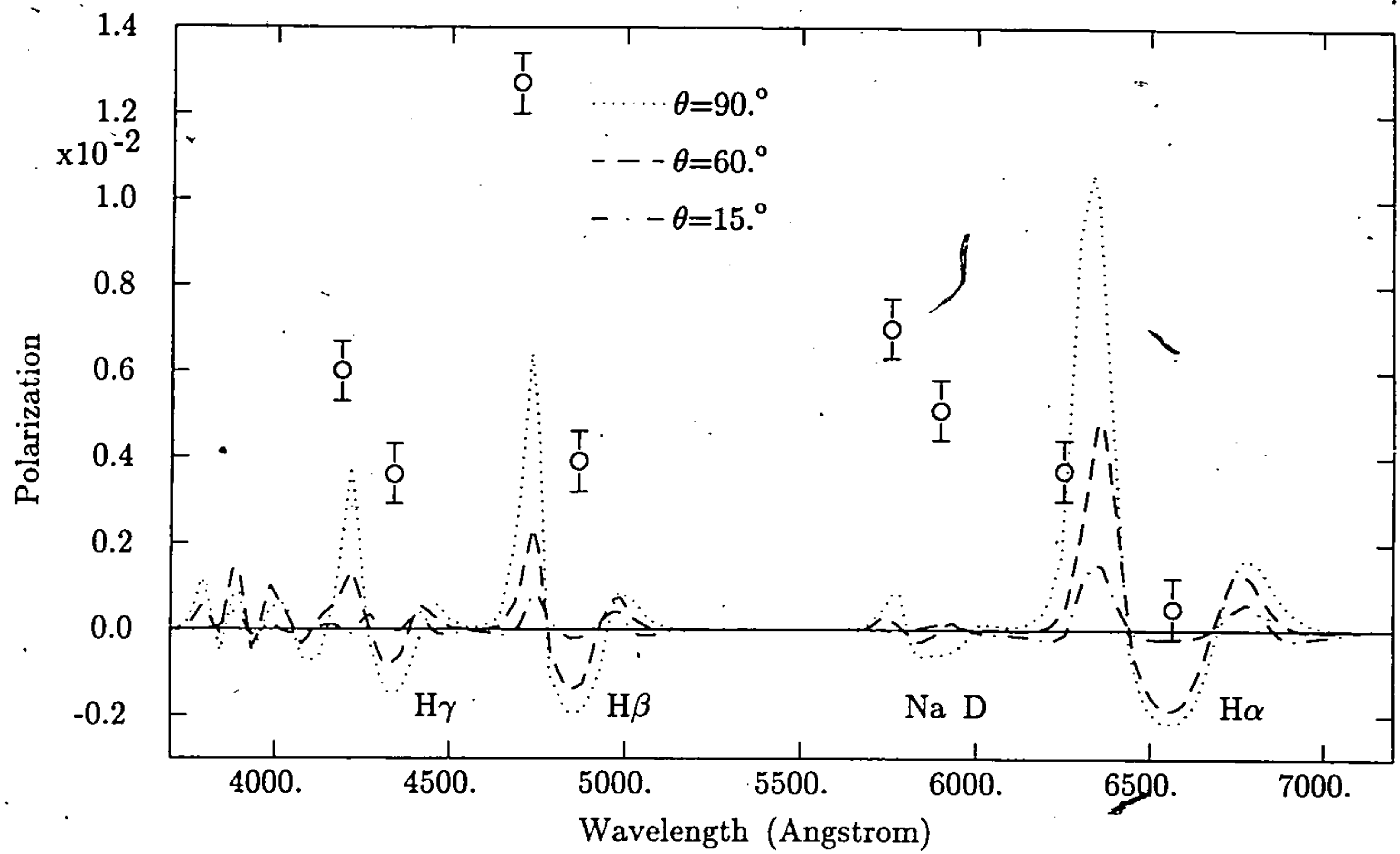

Fig. 5.3b. Polarization data for SN 1987a (Mar. 6-7) and synthetic polarization spectra for model 5.3.

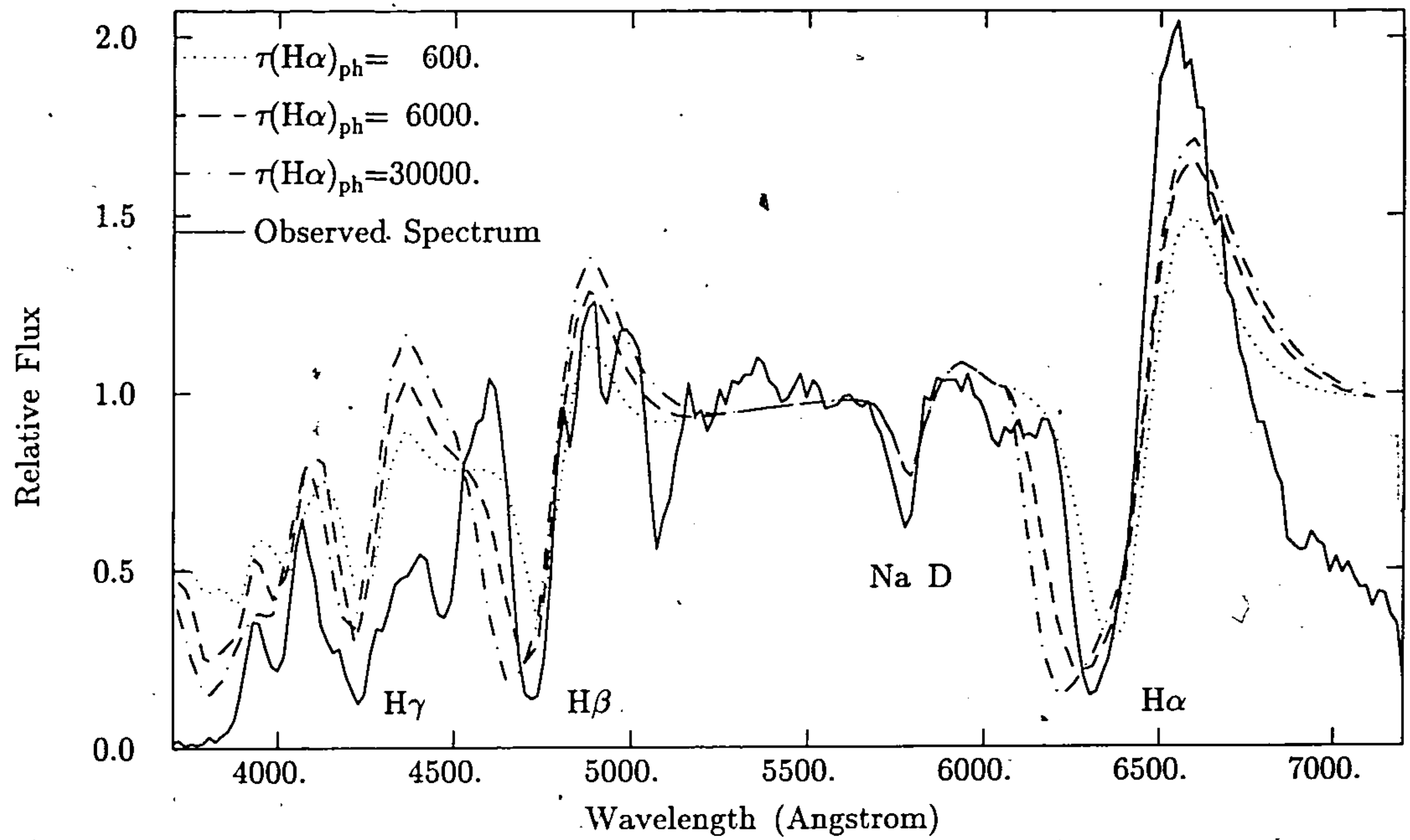

Fig. 5.4a. Observed and synthetic SN 1987a flux spectra (oblate models; $\theta_{incl}=60^{\circ}$; $\xi_{obl}=.5$; no Fe II lines; varied $\tau(H\alpha)_{ph}$; Mar. 6).

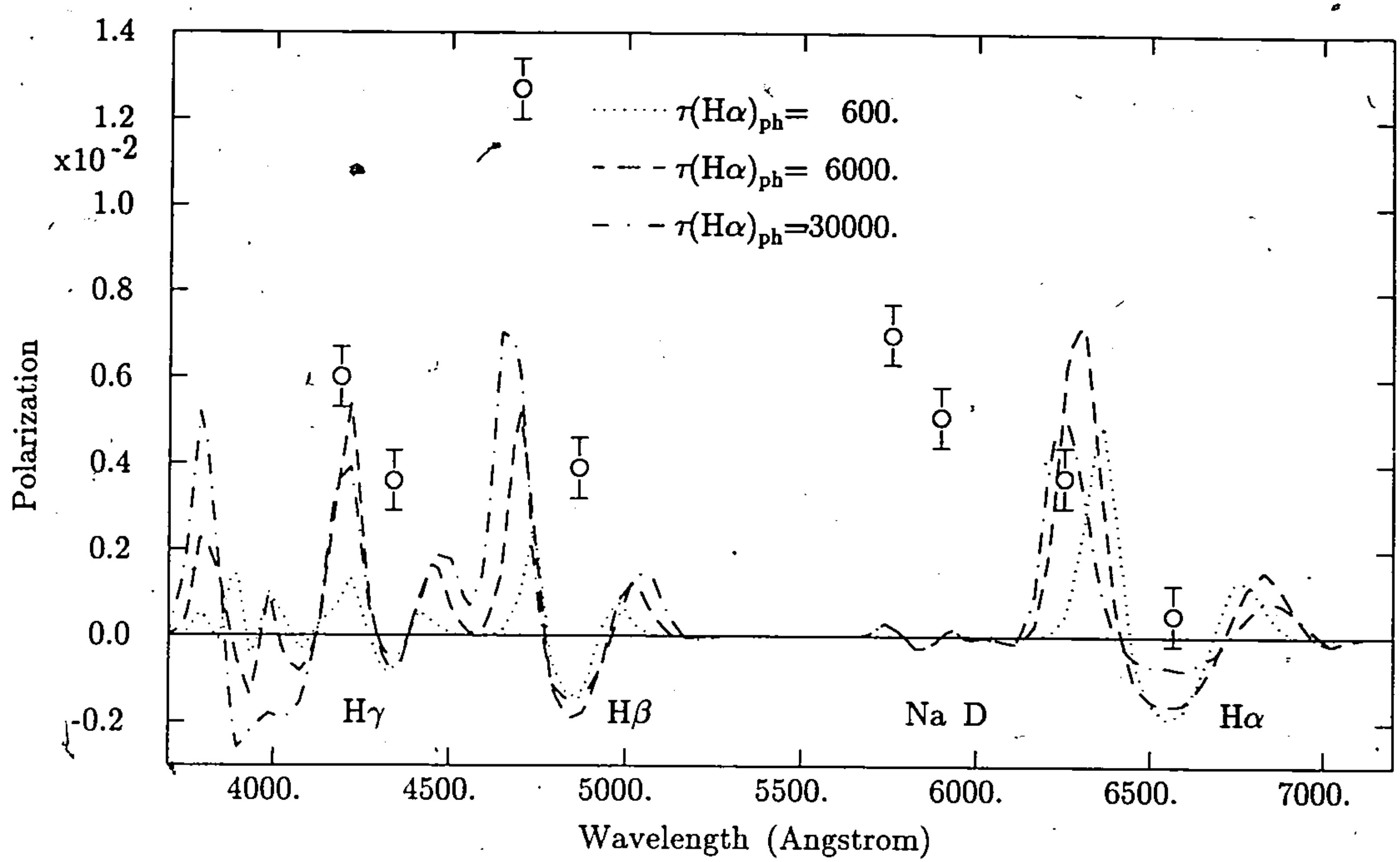

Fig. 5.4b. Polarization data for SN 1987a (Mar. 6-7) and synthetic polarization spectra for model 5.4.

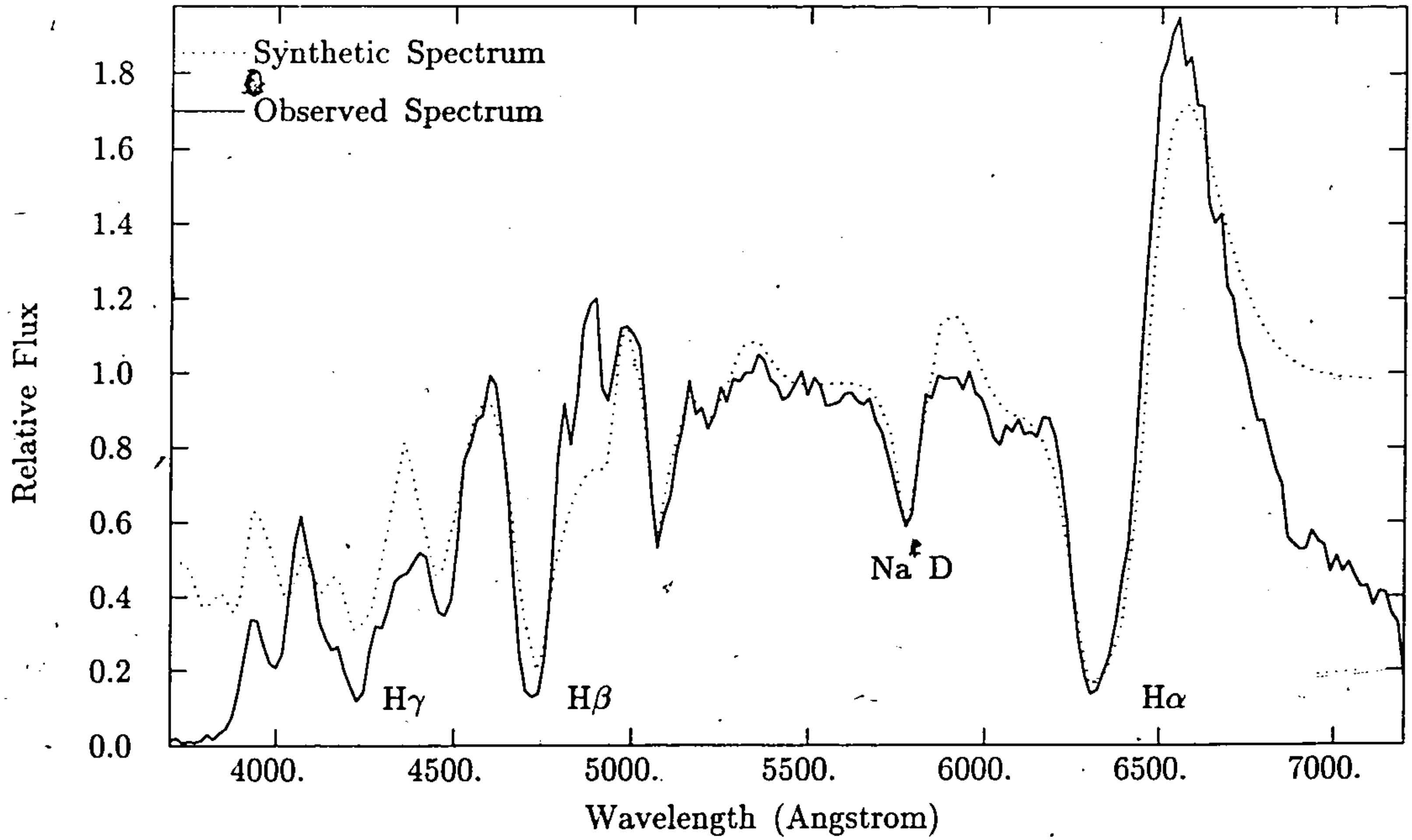

Fig. 5.5a. Observed and synthetic SN 1987a flux spectra (oblate model; $\theta=90^{\circ}$; $\xi_{\rm obl}=.5$; Fe II lines; Mar. 6).

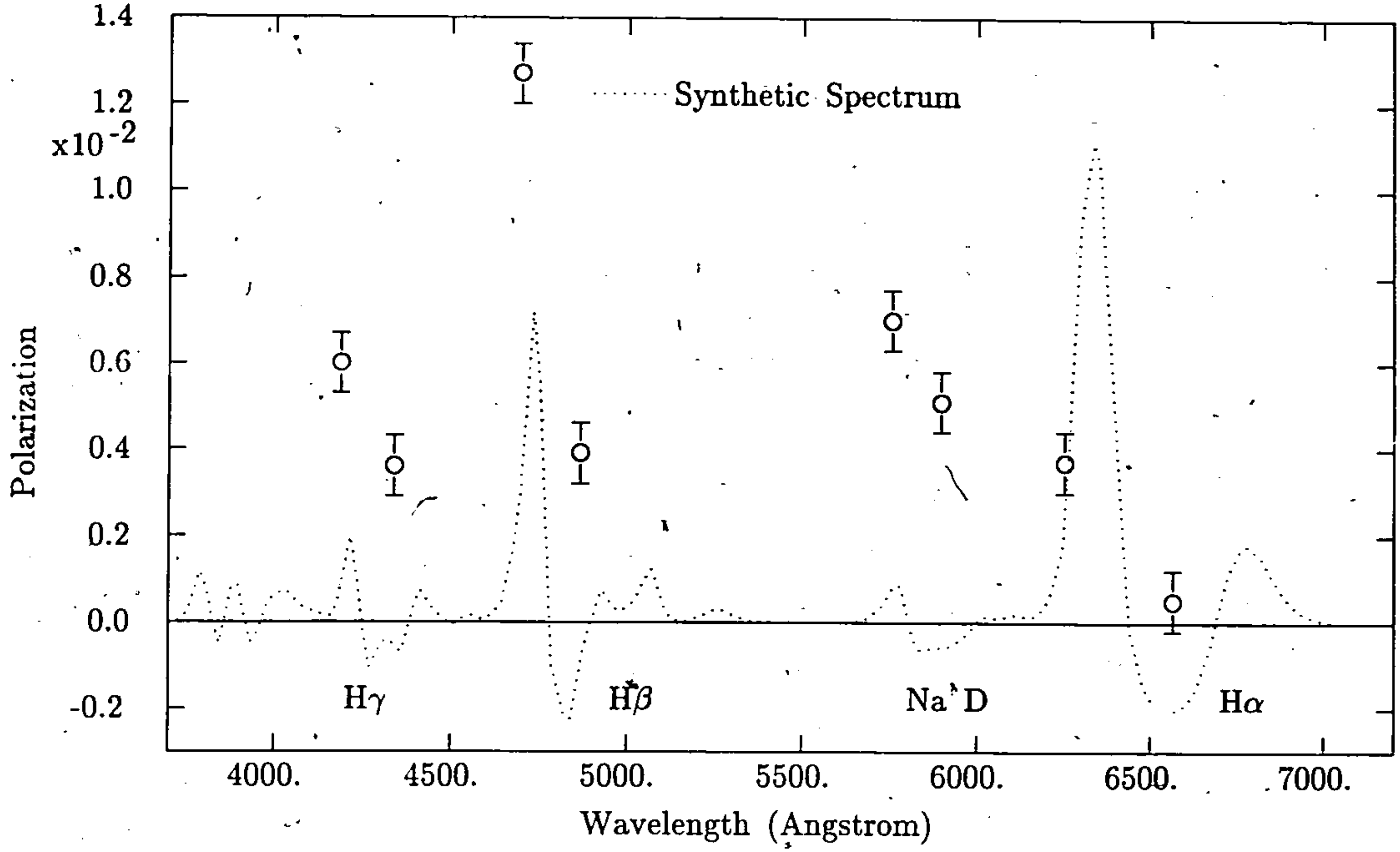

Fig. 5.5b. Polarization data for SN 1987a (Mar. 6-7) and synthetic polarization spectrum for model 5.5.

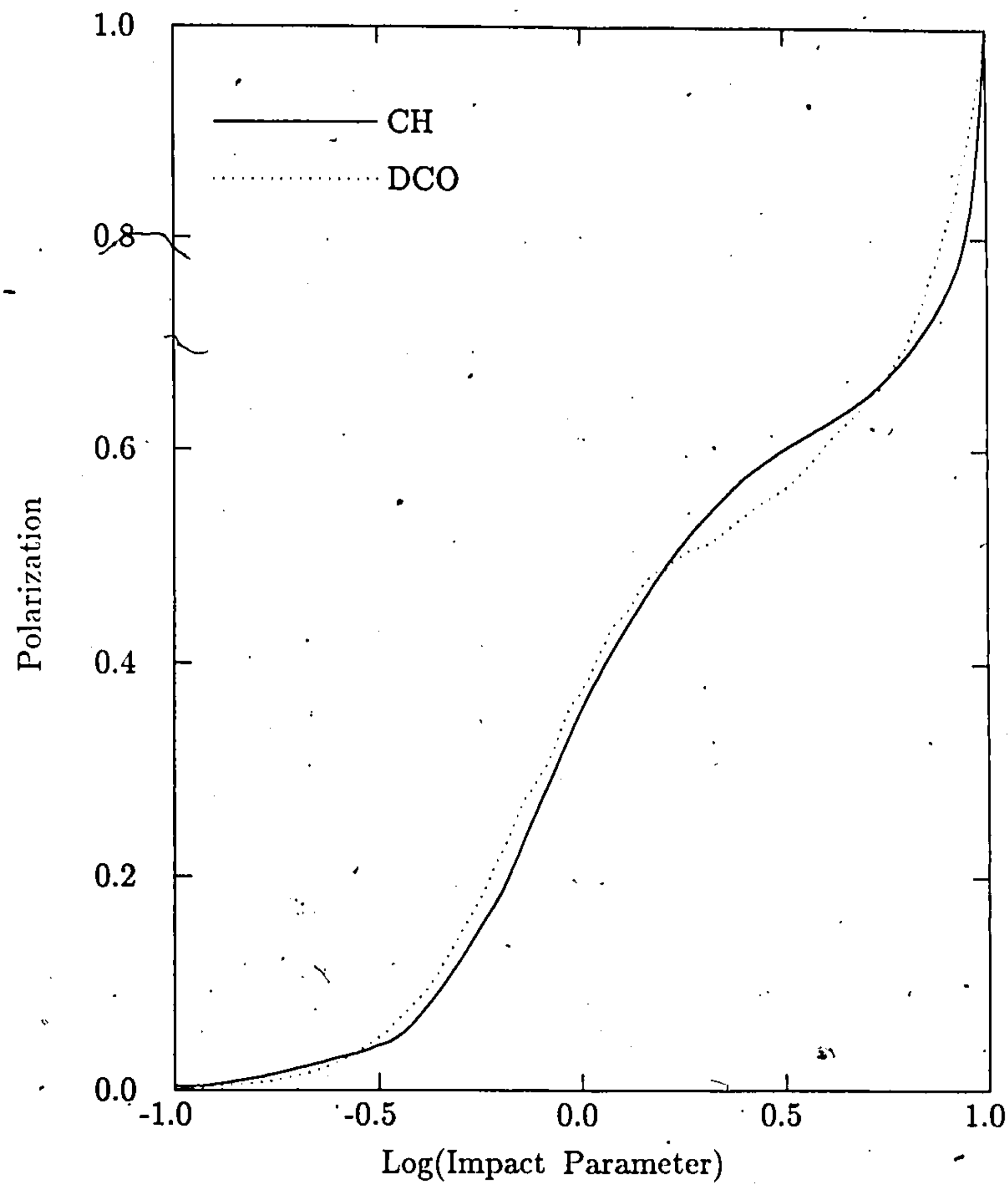

Fig. 5.6. This figure shows the CH (Cassinelli and Hummer, 1971) and DCO (discretized continuous opacity) results for the polarization of specific intensity as a function of the logarithm of the impact parameter. The CH model consisted of a spherical, continuum scattering atmosphere with a central point source of unpolarized flux. The opacity of the CH model is given by $k(r) = r^{-p}$ with p=3; the radial unit of measure was chosen so that k(r=1)=1. The atmosphere has cut-off radius $R = 10$. The DCO model is the same as the CH model, except for numerical reasons the unpolarized flux producing central source had a finite radius of (1/3). The results of the CH and DCO calculations are in good agreement.

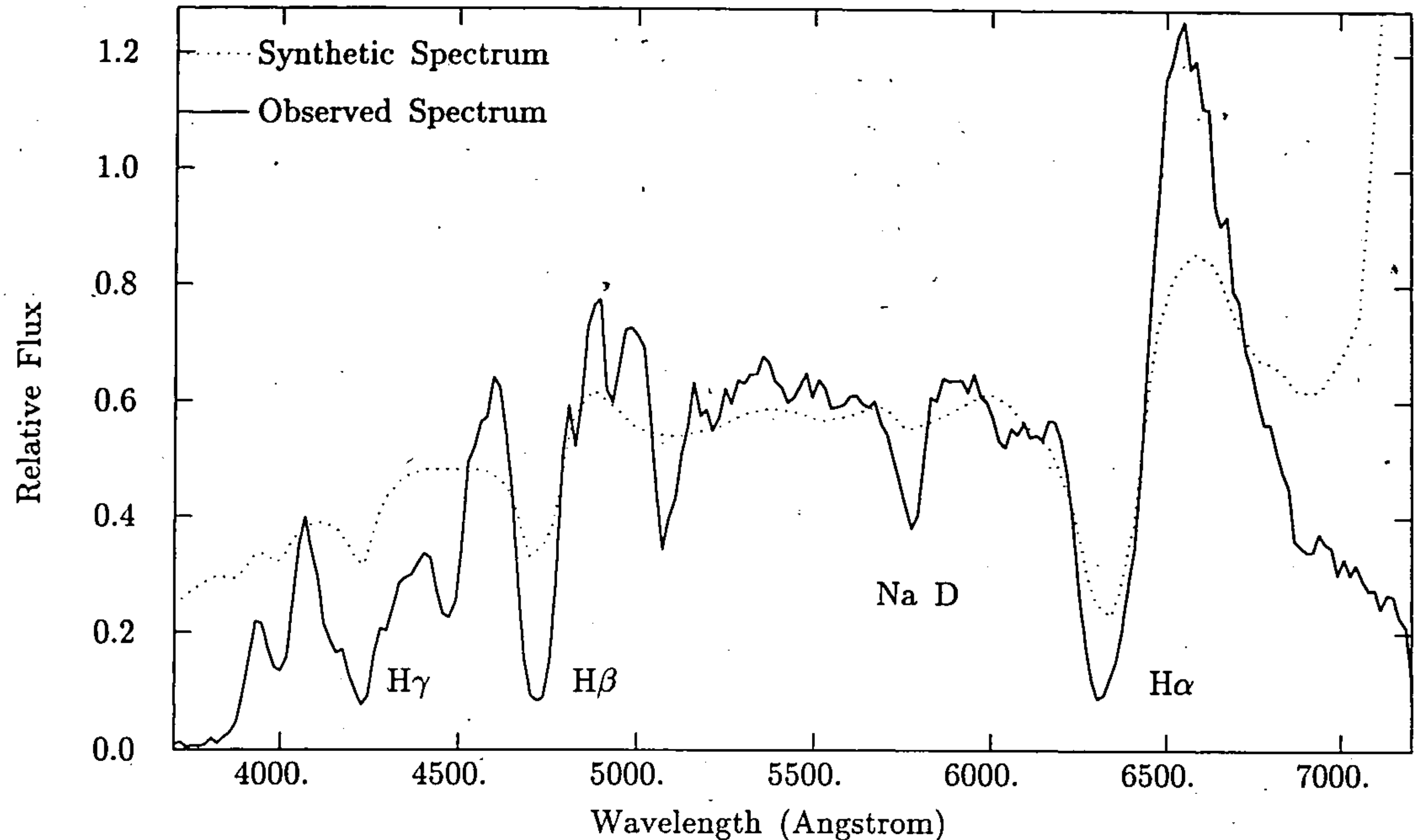

Fig. 5.7a. Observed and synthetic SN 1987a flux spectra (oblate model; θ=90°; ξ_{obl}=.5; discretized continuous opacity ($\Delta\lambda_{ave}$=67.3 Angtsrom, τ_e=7); Mar. 6).

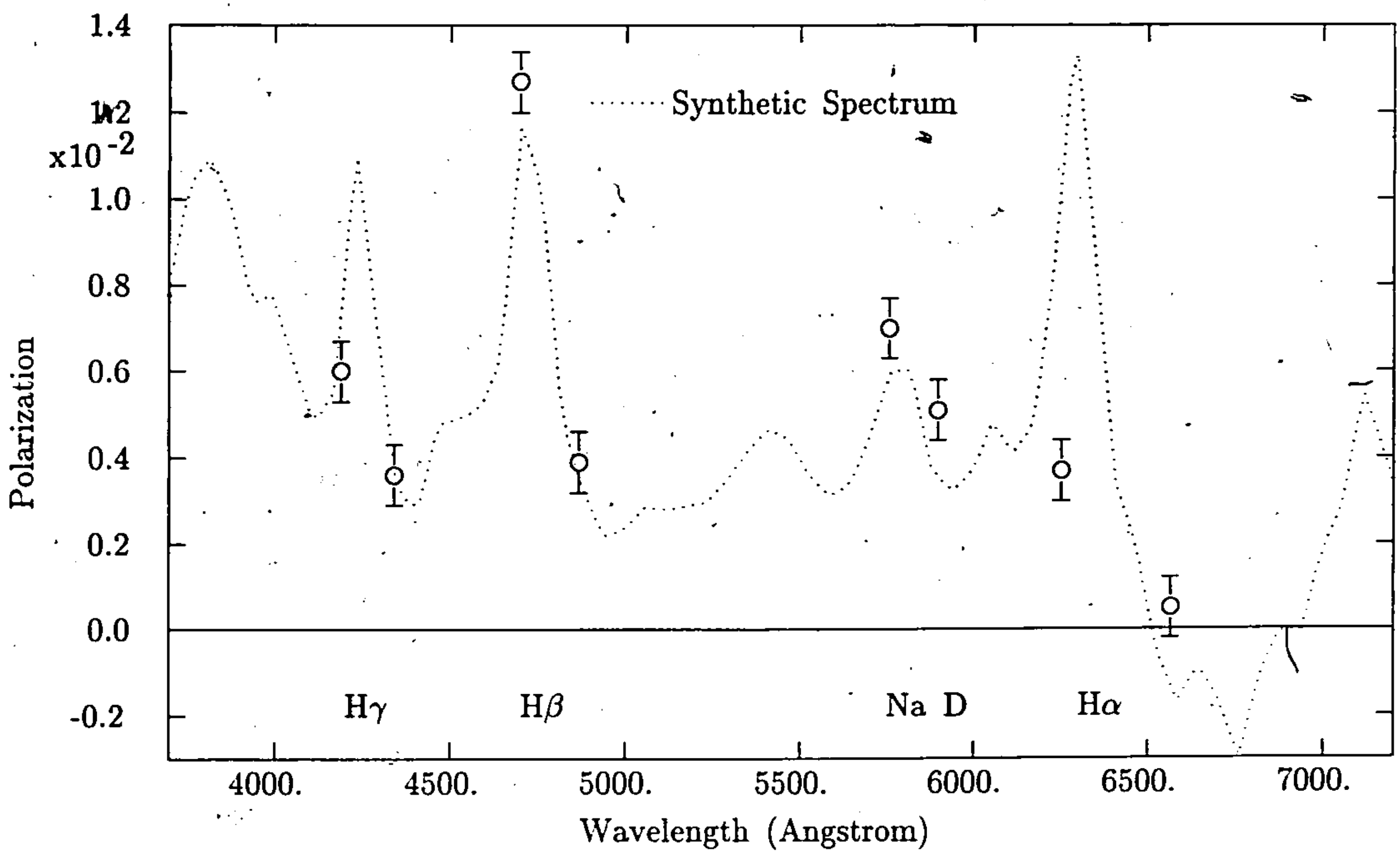

Fig. 5.7b. Polarization data for SN 1987a and synthetic polarization spectrum for model 5.7.

Conclusion

The research reported in this thesis was undertaken to develop a technique for the analysis of spectropolarimetry from supernovae. To do this a modified Sobolev method, here called the Sobolev-H method, was developed for homologously expanding, axisymmetric atmospheres. The Sobolev-H method incorporates Hamilton's phase-matrix for resonance scattering by atomic transitions (1947), and thus allows for the polarizing effect of resonance scattering.

A computer program has been written using the Sobolev-H method that calculates the emergent line flux and polarization profiles. A parameter survey of spherical, and axisymmetric prolate and oblate supernova atmosphere models has been performed using this program. The survey demonstrates that there is considerable polarization structure associated with the P-Cygni lines emergent from the asymmetric models. The emission and absorption polarization features have their position angle of polarization shifted from each other by 90° for both prolate and oblate models.

An analysis of the Mar. 6–7 polarization data for SN 1987a has been performed. Provided the polarization of SN 1987a's flux arises from oblate shape asymmetry, the analysis indicates a 50 % asymmetry ($\xi_{obl} = .5$). A similar asymmetry would be required if SN 1987a were prolate. Since the polarization data indicates that an intrinsic continuum polarization exists, a method here called the discretized continuous opacity or DCO method has been devised in order to calculate synthetic continuum polarization. Calculations with the DCO method show that good qualitative agreement with the observed continuum polarization may be achievable. Improvements in the spectropolarimetry analysis technique and an accurate value for the interstellar polarization in the direction of SN 1987a should lead to more confident conclusions. Only a small fraction of the existing SN 1987a spectropolarimetry data has been analyzed in this thesis. Further analyses of the existing data should give considerable insight into the SN 1987a event.

The improved techniques for spectropolarimetry analysis, developed in response to the challenge of the SN 1987a data, should provide a foundation for the analysis of future supernova spectropolarimetry. Since astronomical observations are always increasing in quantity and quality, it is to be expected that the improved techniques will be necessary.

Appendix 1

Functional Behavior of Some Sobolev Quantities

In section (a) some Sobolev quantities are expressed in the limiting cases of small and large τ. In section (b) the functional behavior of the polarization measure, $\Pi(\tau)$, is examined.

a) Small and Large τ Behavior of Some Sobolev Quantities

Expressions for the Sobolev directional escape probability, and related quantities in the small and large τ limits, can be obtained. The expressions display the behavior in these limits, and can be useful for preventing truncation error in computer calculations.

The quantity $e^{-\tau}$ has the small τ expansion

$$e^{-\tau} = \sum_{k=0}^{\infty} \frac{(-1)^k \tau^k}{k!} = 1 - \tau + \frac{1}{2}\tau^2 - \frac{1}{6}\tau^3 + \frac{1}{24}\tau^4 - \frac{1}{120}\tau^5 + \cdots . \quad (A1.1)$$

The quantity $1 - e^{-\tau}$ has the small τ expansion

$$\begin{aligned} 1 - e^{-\tau} &= \sum_{k=1}^{\infty} \frac{(-1)^{k-1} \tau^k}{k!} = \tau - \frac{1}{2}\tau^2 + \frac{1}{6}\tau^3 - \frac{1}{24}\tau^4 + \frac{1}{120}\tau^5 - \cdots \\ &\approx \tau\left(1 - \frac{1}{2}\tau\left(1 - \frac{1}{3}\tau\left(1 - \frac{1}{4}\tau\left(1 - \frac{1}{5}\tau\right)\right)\right)\right), \end{aligned} \quad (A1.2)$$

where the last expression is an efficient expression for calculations as it has only 4 additions, and 8 multiplications.

The directional escape probability

$$\beta_d = \frac{1 - e^{\tau}}{\tau} \quad (A1.3)$$

has the small τ expansion

$$\begin{aligned} \beta_d &= \sum_{k=0}^{\infty} \frac{(-1)^k \tau^k}{(k+1)!} = 1 - \frac{1}{2}\tau + \frac{1}{6}\tau^2 - \frac{1}{24}\tau^3 + \frac{1}{120}\tau^4 - \cdots \\ &\approx \left(1 - \frac{1}{2}\tau\left(1 - \frac{1}{3}\tau\left(1 - \frac{1}{4}\tau\left(1 - \frac{1}{5}\tau\right)\right)\right)\right), \end{aligned} \quad (A1.4)$$

where the last expression is an efficient expression for calculations as it has only 4 additions, and 7 multiplications. When $\tau \gg 1$

$$\beta_d \approx \frac{1}{\tau}. \tag{A1.5}$$

The quantity $1-\beta_d$ has the small τ expansion

$$\begin{aligned} 1-\beta_d &= \sum_{k=1}^{\infty} \frac{(-1)^{k-1}\tau^k}{(k+1)!} = \frac{1}{2}\tau - \frac{1}{6}\tau^2 + \frac{1}{24}\tau^3 - \frac{1}{120}\tau^4 + \ldots \\ &\approx \frac{1}{2}\tau\left(1-\frac{1}{3}\tau\left(1-\frac{1}{4}\tau\left(1-\frac{1}{5}\tau\right)\right)\right), \end{aligned} \tag{A1.6}$$

where the last expression is an efficient expression for calculations as it has only 3 additions, and 7 multiplications. When $\tau \gg 1$

$$1-\beta_d \approx 1-\frac{1}{\tau}. \tag{A1.7}$$

b) Functional Behavior of the Polarization Measure $\Pi(\tau)$

The polarization measure $\Pi(\tau)$ introduced in Chapter 2 section (d) is given by

$$\Pi = \frac{\beta}{1-(\frac{7}{10})(1-\beta)}(1-e^{-\tau}) = \frac{10}{3}\frac{1}{\tau}\left(\frac{(1-e^{-\tau})^2}{1+\frac{7}{3}(1-e^{-\tau})/\tau}\right), \tag{A1.8}$$

where $\beta = \beta_d$ for this expression. For $\tau < .5$

$$\Pi \approx \tau\left(1-\frac{13}{20}\tau\right), \tag{A1.9}$$

and $\tau \gg 1$

$$\Pi \approx \frac{10}{3}\frac{1}{\tau}\left(1-\frac{7}{3}\frac{1}{\tau}\right). \tag{A1.10}$$

The derivative of $\Pi(\tau)$ is

$$\frac{d\Pi}{d\tau} = 10(1-e^{-\tau})\frac{(-3+e^{-\tau}(6\tau+10)+e^{-2\tau}(-7))}{(3\tau+7(1-e^{-\tau}))^2}. \tag{A1.11}$$

Setting the derivative to zero, the expression

$$\tau = \ln\left(\frac{6\tau+10}{3+7e^{-2\tau}}\right) \tag{A1.12}$$

is obtained. This expression can be solved iteratively for the τ value that gives the maximum of $\Pi(\tau)$. With an initial value of 2, the iteration converges rapidly to give

$$\tau_{Max} = 1.922294, \qquad \text{and} \qquad \Pi(\tau_{Max}) = .6206712.$$

Fig. 2.5 in Chapter 2 section (d) shows a plot of $\Pi(\tau)$ for τ between 0 and 10.

Appendix 2

The Sobolev-H Source Function Coefficients

For a Spherically Symmetric Atmosphere

The Sobolev-H source function coefficients for the homologously moving, axisymmetric atmosphere, given in Chapter 2 section (d), can be easily specialized to the case of a spherically symmetric atmosphere. For a spherically symmetric system any point can be considered to be on a symmetry axis. Therefore in specializing to the spherically symmetric case, the axisymmetric case expressions for the source function coefficients need only be considered for points on the symmetry axis. For on-axis points the d_i integrals (see equations (2.131)) that have integrands that depend linearly on cosines and sines of the azimuthal coordinate ϕ vanish, since spherical symmetry implies that the Stokes parameter specific intensity components are independent of the azimuthal coordinate. The non-zero d_i values are given by

$$d_1 = \frac{1}{2}\int_{-1}^{1} d\mu'\, I_l, \tag{A2.1a}$$

$$d_2 = \frac{1}{2}\int_{-1}^{1} d\mu'\, I_r, \tag{A2.1b}$$

and

$$d_3 = \frac{1}{2}\int_{-1}^{1} d\mu'\, \mu'^2 I_l. \tag{A2.1c}$$

The non-zero D_i are

$$D_1 = \tfrac{1}{2}(1+2E_1)d_1 \quad + \quad \tfrac{1}{2}(1-E_1)d_2 \quad - \quad \tfrac{3}{2}E_1 d_3, \tag{A2.2a}$$

$$D_2 = \tfrac{3}{4}E_1(-2d_1 + d_2 + 3d_3), \tag{A2.2b}$$

and

$$D_5 = \tfrac{1}{2}(1-E_1)d_1 \quad + \quad \tfrac{1}{2}(1+\tfrac{1}{2}E_1)d_2 \quad + \quad \tfrac{3}{4}E_1 d_3. \tag{A2.2c}$$

The non-zero source function coefficients are

$$S_1 = \frac{(1-\epsilon)\beta}{(1-\gamma)\left(1-\gamma(\frac{7}{10})E_1\right)}\left[D_1 + \tfrac{1}{2}\gamma\left[D_2 + \tfrac{1}{3}(1-\tfrac{7}{10}E_1)D_2 - \tfrac{7}{10}E_1(D_1 + D_5)\right]\right]$$

$$+ \quad \frac{\frac{1}{2}G}{1-\gamma}, \tag{A2.3a}$$

$$S_2 = \frac{(1-\epsilon)\beta D_2}{1-\gamma(\frac{7}{10})E_1}, \tag{A2.3b}$$

and

$$S_6 = \frac{(1-\epsilon)\beta}{(1-\gamma)\left(1-\gamma(\frac{7}{10})E_1\right)}\left[D_6 + \tfrac{1}{2}\gamma\left[-D_2 + \tfrac{1}{3}(1-\tfrac{7}{10}E_1)D_2 - \tfrac{7}{10}E_1(D_1+D_6)\right]\right] + \quad \frac{\frac{1}{2}G}{1-\gamma}, \tag{A2.3c}$$

where

$$\gamma \equiv (1-\epsilon)(1-\beta). \tag{A2.4}$$

The expressions for the source function components of the Stokes source function vector are

$$S_l = S_1 + S_2\mu^2 \tag{A2.5a}$$

and

$$S_r = S_6, \tag{A2.5b}$$

where $S_U = 0$ and $S_V = 0$, and $\mu = \cos\theta$. For the spherically symmetric case, θ is interpreted as the angle between the radius vector to the point where the source vector is being evaluated and the vector pointing in the direction of the outgoing specific intensity beam.

A further specialization can be made to a system with the following characteristics. (1) There is a spherical photosphere that emits a constant unpolarized specific intensity. (2) There is only one transition, and thus this is a single velocity surface system. This last characteristic implies that only specific intensity beams emitted by the photosphere are incident on a resonance region. Given these characteristics

$$I_l = I_r = I_c = I_{ph}/2,$$

where I_{ph} is the total specific intensity emitted by the photosphere. The lower μ-integration limit for the d_i integrals is

$$\mu_{ph} = \cos\theta_{ph} = \sqrt{1-(r_{ph}/r)^2}, \tag{A2.6}$$

where r_{ph} is the photospheric radius, and r is the radius of the point where the source function vector is being evaluated. The expressions for the d_i become

$$d_1 = \frac{1}{2}\int_{\mu_{ph}}^{1} d\mu'\, I_c = \frac{1}{2}(1-\mu_{ph})I_c, \tag{A2.7a}$$

$$d_2 = \frac{1}{2}\int_{\mu_{ph}}^{1} d\mu' \, I_c = \frac{1}{2}(1-\mu_{ph})I_c, \tag{A2.7b}$$

and

$$d_3 = \frac{1}{2}\int_{\mu_{ph}}^{1} d\mu' \, \mu'^2 I_c = \frac{1}{6}(1-\mu_{ph}^3)I_c. \tag{A2.7c}$$

The D_i become

$$D_1 = \left[\tfrac{1}{2}(1-\mu_{ph}) - \tfrac{1}{4}\mu_{ph}(1-\mu_{ph}^2)E_1\right] I_c, \tag{A2.8a}$$

$$D_2 = \tfrac{3}{8}\mu_{ph}(1-\mu_{ph}^2)E_1 I_c, \tag{A2.8b}$$

and

$$D_5 = \left[\tfrac{1}{2}(1-\mu_{ph}) + \tfrac{1}{8}\mu_{ph}(1-\mu_{ph}^2)E_1\right] I_c. \tag{A2.8c}$$

Note that

$$D_1 = D_0 - \frac{2}{3}D_2 \qquad \text{and} \qquad D_5 = D_0 + \frac{1}{3}D_2, \tag{A2.9}$$

where $D_0 \equiv \frac{1}{2}(1-\mu_{ph})I_c$. Now

$$\begin{aligned}
&D_1 + \tfrac{1}{2}\gamma\left[D_2 + \tfrac{1}{3}(1-\tfrac{7}{10}E_1)D_2 - \tfrac{7}{10}E_1(D_1+D_5)\right] \\
=&(1-\gamma(\tfrac{7}{10})E_1)D_0 - \tfrac{2}{3}(1-\gamma)D_2 \\
=&\left[\tfrac{1}{2}(1-\mu_{ph})(1-\gamma(\tfrac{7}{10})E_1) - \tfrac{1}{4}\mu_{ph}(1-\mu_{ph}^2)(1-\gamma)E_1\right] I_c.
\end{aligned} \tag{A2.10}$$

Thus the S_i coefficients are given by

$$\begin{aligned}
S_1 = &\frac{(1-\epsilon)\beta}{(1-\gamma)\left(1-\gamma(\frac{7}{10})E_1\right)}\left[\tfrac{1}{2}(1-\mu_{ph})(1-\gamma(\tfrac{7}{10})E_1) - \tfrac{1}{4}\mu_{ph}(1-\mu_{ph}^2)(1-\gamma)E_1\right] I_c \\
&+ \frac{\frac{1}{2}G}{1-\gamma}
\end{aligned} \tag{A2.11a}$$

$$S_2 = \frac{(1-\epsilon)(\frac{3}{8})\beta\mu_{ph}(1-\mu_{ph}^2)E_1 I_c}{1-\gamma(\frac{7}{10})E_1}, \tag{A2.11b}$$

and

$$\begin{aligned}
S_5 = &\frac{(1-\epsilon)\beta}{(1-\gamma)\left(1-\gamma(\frac{7}{10})E_1\right)}\left[\tfrac{1}{2}(1-\mu_{ph})(1-\gamma(\tfrac{7}{10})E_1) + \tfrac{1}{8}\mu_{ph}(1-\mu_{ph}^2)(1-\gamma)E_1\right] \\
&+ \frac{\frac{1}{2}G'}{1-\gamma},
\end{aligned} \tag{A2.11c}$$

where the result $S_5 = S_1 + S_2$ has been used (see equation (2.141)).

For the case of pure two-level resonance scattering $\epsilon \to 0$, $G \to 0$, and $\gamma \to (1-\beta)$. The S_i coefficients become

$$S_1 = \left[\tfrac{1}{2}(1-\mu_{ph}) - \frac{(\frac{1}{4})\beta\mu_{ph}(1-\mu_{ph}^2)E_1}{1-(1-\beta)(\frac{7}{10})E_1}\right] I_c, \tag{A2.12a}$$

$$S_2 = \frac{(\frac{3}{8})\beta\mu_{ph}(1-\mu_{ph}^2)E_1 I_c}{1-(1-\beta)(\frac{7}{10})E_1}, \tag{A2.12b}$$

and

$$S_3 = \left[\tfrac{1}{2}(1-\mu_{ph}) + \frac{(\frac{1}{8})\beta\mu_{ph}(1-\mu_{ph}^2)E_1}{1-(1-\beta)(\frac{7}{10})E_1}\right] I_c. \tag{A2.12c}$$

The components of the Stokes source function vector are

$$S_l = \left[\tfrac{1}{2}(1-\mu_{ph}) - \frac{(\frac{1}{4})\beta\mu_{ph}(1-\mu_{ph}^2)E_1}{1-(1-\beta)(\frac{7}{10})E_1} + \left(\frac{(\frac{3}{8})\beta\mu_{ph}(1-\mu_{ph}^2)E_1}{1-(1-\beta)(\frac{7}{10})E_1}\right)\mu^2\right] I_c, \tag{A2.13a}$$

$$= \left[\tfrac{1}{2}(1-\mu_{ph}) + \left(\frac{\beta\mu_{ph}(1-\mu_{ph}^2)E_1}{1-(1-\beta)(\frac{7}{10})E_1}\right)(\tfrac{1}{4}P_2(\mu) - \tfrac{1}{8})\right] I_c, \tag{A2.13b}$$

and

$$S_r = \left[\tfrac{1}{2}(1-\mu_{ph}) + \frac{(\frac{1}{8})\beta\mu_{ph}(1-\mu_{ph}^2)E_1}{1-(1-\beta)(\frac{7}{10})E_1}\right] I_c, \tag{A2.13c}$$

where $P_2(\mu) = (1/2)(3\mu^2 - 1)$ is the second Legendre polynomial. The total source function is

$$S = \left[\tfrac{1}{2}(1-\mu_{ph}) + \left(\frac{(\frac{1}{8})\beta\mu_{ph}(1-\mu_{ph}^2)E_1}{1-(1-\beta)(\frac{7}{10})E_1}\right) P_2(\mu)\right] I_{ph}, \tag{A2.14}$$

where it should be recalled that $I_c = I_{ph}/2$. The angle-averaged total source function is

$$< S >= \tfrac{1}{2}(1-\mu_{ph})I_{ph} = W(r)I_{ph}, \tag{A2.15}$$

where $W(r)$ is the dilution factor. The expression for the angle-averaged total source function is identical to the expression for total source function obtained using the ordinary Sobolev method (see equation (2.36) in Chapter 2 section (a)). Recall the ordinary Sobolev method is unpolarizing and has complete complete redistribution in scattering angle as well as complete redistribution in frequency.

The net polarization from a spherically symmetric atmosphere is zero. Since only net polarization can be measured for supernovae, the Sobolev-H coefficients and Stokes source function vector components for a homologously moving, spherically symmetric atmosphere may not very useful. However, if a spherically symmetric supernova is partially occulted by something, then these expressions may be of use.

Appendix 3

Some Results Pertaining to Axisymmetric Ellipsoids

Section (a) of this appendix presents some of the expressions used by Shapiro and Sutherland (1982) for integrations of plane-parallel atmosphere solutions (Chandrasekhar 1960, p. 248; Harrington 1969) over axisymmetric ellipsoid surfaces. Presented in section (b) are the expressions for the limits of integration over the solid angle subtended by an axisymmetric ellipsoid at an external point. These expressions are useful for integrating the specific intensity convergent on a point from an ellipsoidal photosphere. Such integrations are used to determine the source function at that point. Presented in section (c) are some expressions for the extrema and projections of axisymmetric ellipsoids in coordinate systems rotated about an axis perpendicular to the symmetry axis. These expressions are useful in integrating over planar velocity surfaces to obtain the emergent flux profiles in the Sobolev method.

a) Plane-parallel Atmosphere Solutions and Ellipsoid Surfaces

The equation of an axisymmetric ellipsoid is

$$r_s = \sqrt{(x/a)^2 + (y/a)^2 + (z/c)^2}, \tag{A3.1}$$

where r_s is a scale parameter introduce for generality, c is the semi-axis aligned with the axis of symmetry, and a is the semi-axis perpendicular to the axis of symmetry. The normal vector to the ellipsoid at any point on its surface is obtained by evaluating and normalizing the gradient of r_s:

$$\hat{n} = \frac{(\sin\theta\cos\phi, \quad \sin\theta\sin\phi, \quad (a/c)^2\cos\theta)}{\sqrt{\sin^2\theta + (a/c)^4\cos^2\theta}}, \tag{A3.2}$$

where

$$x = r\sin\theta\cos\phi, \tag{A3.3a}$$

$$y = r\sin\theta\sin\phi, \tag{A3.3b}$$

and

$$y = r\cos\theta \tag{A3.3b}$$

have been used. Defining

$$e_2 = 1 - (a/c)^2 \tag{A3.4}$$

gives

$$\hat{n} = \frac{(\sin\theta\cos\phi,\quad \sin\theta\sin\phi,\quad (1-e_2)\cos\theta)}{\sqrt{1-e_2(2-e_2)\cos^2\theta}}. \tag{A3.5}$$

Note that

$$\hat{r}\cdot\hat{n} = \frac{1-e_2\cos^2\theta}{\sqrt{1-e_2(2-e_2)\cos^2\theta}}. \tag{A3.6}$$

The distance from the origin to any point on the ellipsoid is

$$\begin{aligned} r &= \sqrt{x^2+y^2+z^2} \\ &= \sqrt{(r_g^2-(z/c)^2)a^2+z^2} \\ &= \sqrt{r_g^2a^2+z^2e_2}. \end{aligned} \tag{A3.7}$$

Using $z = r\cos\theta$, and solving for r gives

$$r(\theta) = \frac{r_g a}{\sqrt{1-e_2\cos^2\theta}}. \tag{A3.8}$$

The differential surface area element of the ellipsoid is

$$\begin{aligned} dA &= \frac{r^2\sin\theta d\theta d\phi}{|\hat{r}\cdot\hat{n}|} \\ &= \frac{r_g^2a^2\sin\theta\sqrt{1-e_2(2-e_2)\cos^2\theta}d\theta d\phi}{(1-e_2\cos^2\theta)^2}. \end{aligned} \tag{A3.9}$$

A distant observer is located in a direction given by

$$\hat{x}' = (\cos\theta_p,\quad 0,\quad \sin\theta_p), \tag{A3.10}$$

where the primed coordinate system is rotated an angle θ_p counterclockwise about the y-axis. Due to ellipsoidal symmetry there is no loss of generality in restricting θ_p to the interval $[0,\pi/2]$. The projection in the y-z' plane of dA is given by

$$\begin{aligned} dA_p &= dA|\hat{n}\cdot\hat{x}'| \\ &= dA\left(\frac{\sin\theta\cos\phi\cos\theta_p+(1-e_2)\cos\theta\sin\theta_p}{\sqrt{1-e_2(2-e_2)\cos^2\theta}}\right) \\ &= \frac{r_g^2a^2\sin\theta(\sin\theta\cos\phi\cos\theta_p+(1-e_2)\cos\theta\sin\theta_p)d\theta d\phi}{(1-e_2\cos^2\theta)^2}. \end{aligned} \tag{A3.11}$$

Only the observer-facing part of the ellipsoid surface can contribute to the integrated flux. The limits of integration can be determined from

$$0 = |\hat{n} \cdot \hat{x}'| = \sin\theta \cos\phi \cos\theta_p + (1 - e_2)\cos\theta \sin\theta_p. \qquad (A3.12)$$

This expression leads to

$$\phi_{max} = \arccos\left[-\frac{(1-e_2)\cos\theta \sin\theta_p}{\sin\theta \cos\theta_p}\right] = \arccos[-(1-e_2)\cot\theta \tan\theta_p] \qquad (A3.13)$$

Numerical integration need only be done over the interval $[0, \phi_{max}]$. The integration over the interval $[0, -\phi_{max}]$ can be done using the azimuthal symmetry of the I_l and I_r fields, and the azimuthal antisymmetry of the U field. The azimuthal symmetries and antisymmetry follow from the axial symmetry of the system. Note that if the argument of arccos of equation (A3.13) is greater than 1, then ϕ_{max} should be set to zero; if the argument is less than -1, then the ϕ_{max} should be set to π. If $\theta_p = \pi/2$, then equation (A3.13) is indeterminant; in this case it should be clear that

$$\phi_{max} = \begin{cases} \pi & \text{for } 0 \geq \theta \leq \frac{\pi}{2}; \\ 0 & \text{for } \frac{\pi}{2} < \theta \leq \pi. \end{cases} \qquad (A3.14)$$

The parallel-plane atmosphere solutions (Chandrasekhar 1960, p. 248; Harrington 1969) for the emergent specific intensity and their polarization are tabulated as functions of

$$\mu = \cos\zeta, \qquad (A3.15)$$

where ζ is the angle between the normal to the plane and the direction of emergence. For the distant observer

$$\mu = \hat{n} \cdot \hat{x}' = \frac{\sin\theta \cos\phi \cos\theta_p + (1-e_2)\cos\theta \sin\theta_p}{\sqrt{1 - e_2(2-e_2)\cos^2\theta}}. \qquad (A3.16)$$

Note that μ is restricted to the interval $[0, 1]$. The Stokes parameters for the solutions are given in a system where the l axis is aligned with the meridian to the normal and the r axis is aligned perpendicular to the meridian (see Chapter 2 section (d) for a discussion of the Stokes parameters). For integration the Stokes parameters have to transformed to a rotated system where the l axis is aligned with the vector

$$\hat{z}' = (-\sin\theta_p, \quad 0, \quad \cos\theta_p). \qquad (A3.17)$$

The parallel-plane solutions have $U = 0$ and $V = 0$, and so a counterclockwise rotation through angle ψ gives the transformations

$$I_l' = I_l \cos^2\psi + I_r \sin^2\psi \tag{A3.18a}$$

$$I_r' = I_l \sin^2\psi + I_r \cos^2\psi \tag{A3.18b}$$

and

$$U' = (I_l - I_r)\sin 2\psi \tag{A3.18c}$$

(Chandrasekhar 1960, p, 34). By symmetry the integrated U' field will be zero. The integrated $Q' = I_l' - I_r'$ field is the only surviving quantity:

$$Q' = (I_l - I_r)(2\cos^2\psi - 1) = (I_l - I_r)\cos 2\psi. \tag{A3.19}$$

A little thought shows that

$$\cos\psi = \hat{x}' \cdot \left(\frac{\hat{x}' \times (\hat{n} \times \hat{x}')}{|\hat{x}' \times (\hat{n} \times \hat{x}')|}\right). \tag{A3.20}$$

Now

$$\hat{n} \times \hat{x}' \propto (\sin\theta \sin\phi \sin\theta_p, \quad (\hat{n} \times \hat{x}')_y, \quad -\sin\theta \sin\phi \cos\theta_p), \tag{A3.21}$$

$$\hat{x}' \times (\hat{n} \times \hat{x}') \propto (-(\hat{n} \times \hat{x}')_y \sin\theta_p, \quad \sin\theta \sin\phi, \quad (\hat{n} \times \hat{x}')_y \cos\theta_p), \tag{A3.22}$$

and

$$|\hat{x}' \times (\hat{n} \times \hat{x}')| \propto \sqrt{(\hat{n} \times \hat{x}')_y^2 + \sin^2\theta \sin^2\phi}. \tag{A3.23}$$

Thus

$$\cos\psi = \frac{(\hat{n} \times \hat{x}')_y}{\sqrt{(\hat{n} \times \hat{x}')_y^2 + \sin^2\theta \sin^2\phi}}, \tag{A3.24}$$

where

$$(\hat{n} \times \hat{x}')_y = (1 - e_2)\cos\theta \cos\theta_p - \sin\theta \cos\phi \sin\theta_p. \tag{A3.25}$$

The integrals for the net flux and the net Q field are

$$F_{obs} = \int_{\substack{projected\\surface}} dA_p \left[\frac{I(\mu)}{f}\right]_{tabulated} f, \tag{A3.26}$$

and

$$Q_{obs} = \int_{\substack{projected\\surface}} dA_p \cos 2\psi \left[\frac{Q(\mu)}{I}\right]_{tabulated} \left[\frac{I(\mu)}{f}\right]_{tabulated} f. \tag{A3.27}$$

Note f is the astrophysical flux and F is the conventional flux: $f = \pi^{-1}F$. The tabulated quantities, as functions of μ, are found in Chandrasekhar (1960), and Harrington (1969); they are also given in Shapiro and Sutherland (1982). The expression for dA_p is given in equation (A3.11), the limits of integration by equation (A3.13), the value of $\cos\psi$ by equation (A3.24), and the value of μ by equation (A3.16). Since the net U field is zero by symmetry, the polarization measured by the distant observer is

$$P = \frac{Q_{obs}}{F_{obs}} \tag{A3.28}$$

(see Chapter 2 section (d)).

It is of some interest to consider two special cases: $\theta_p = 0$ and $\theta_p = \pi/2$. The first case ($\theta_p = 0$) gives the distant observer an equatorial view of the ellipsoidal atmosphere. The θ integration is done over the interval $[0, \pi]$. The relevant quantities are

$$dA_p = \frac{r_g^2 a^2 \sin^2\theta \cos\phi \, d\theta d\phi}{(1 - e_2\cos^2\theta)^2}, \tag{A3.29a}$$

$$\phi_{max} = \frac{\pi}{2}, \tag{A3.29b}$$

$$\mu = \frac{\sin\theta\cos\phi}{\sqrt{1 - e_2(2 - e_2)\cos^2\theta}}, \tag{A3.29c}$$

and

$$\cos\psi = \frac{1}{\sqrt{1 + (1 - e_2)^{-2}\tan^2\theta\sin^2\phi}}. \tag{A3.29d}$$

In the second case ($\theta_p = \pi/2$) the observer has a polar view of the ellipsoidal atmosphere. The θ integration is done over the interval $[0, \pi/2]$. The relevant quantities are

$$dA_p = \frac{r_g^2 a^2 \sin\theta(1 - e_2)\cos\theta \, d\theta d\phi}{(1 - e_2\cos^2\theta)^2}, \tag{A3.30a}$$

$$\phi_{max} = \pi, \tag{A3.30b}$$

$$\mu = \frac{(1 - e_2)\cos\theta}{\sqrt{1 - e_2(2 - e_2)\cos^2\theta}}, \tag{A3.30c}$$

and

$$\cos\psi = -\cos\phi. \tag{A3.30d}$$

Since μ does not depend on ϕ and $\cos 2\psi = \cos 2\phi$ for $\theta_p = \pi/2$, it follows that the integral of equation (A3.27) vanishes, provided f is independent of ϕ. This is not unexpected, since an atmosphere circularly symmetric about the line of sight should produce an unpolarized net flux.

b) Limits for Integration Over the Solid Angle Subtended by an Axisymmetric Ellipsoid

In obtaining the source function for the Sobolev method and the Sobolev-H method, integrations must be done over the solid angle subtended by the photosphere at the point where the source the function is to be evaluated. This point is called the convergence point for this presentation. It is actually more appropriate say that the integration is over the solid angle obtained by the point inversion through the convergence point of the ellipsoid solid angle. This is because the Sobolev formalism is developed using the direction that the photons are going toward, and not the direction they are coming from. The distinction between the two solid angles is important to remember when doing calculations.

The models used in this thesis had axisymmetric ellipsoidal photospheres. The limits of integration for the integrals may be determined numerically; this would be a more generalizable procedure. However, for calculational efficiency analytical expressions for the limits were obtained. These analytical expressions are trivial, but they are rather tedious to derive. Therefore a short non-rigorous presentation is given here for reference. These expressions were implemented in the Sobolev-H computer program listed in Appendix 4.

The equation of an axisymmetric ellipsoid is

$$(x'/a)^2 + (y'/a)^2 + (z'/c)^2 = r_g^2, \tag{A3.31}$$

where r_g is a generalized radius-like parameter introduced for generality. Consider the convergence point $(e,\ 0,\ d)$ in the primed coordinate system. The integration that is to be performed is over the solid angle that is the point inversion through $(e,\ 0,\ d)$ of the solid angle subtended at $(e,\ 0,\ d)$ by an axisymmetric ellipsoidal photosphere. It is convenient to change to a unprimed coordinate system centered on $(e,\ 0,\ d)$. In this unprimed coordinate system, the integration is over the $\mu = \cos\theta$ and ϕ coordinates; θ and ϕ are given their usual spherical coordinate system meanings. The μ-limits of integration are to be obtained as functions of ϕ.

In the unprimed coordinate system the equation of the ellipsoid becomes

$$\left(\frac{x+e}{a}\right)^2 + (y/a)^2 + \left(\frac{z+d}{c}\right)^2 = r_g^2. \tag{A3.32}$$

Consider the vector function of a ray passes through the origin and that is directed away from the ellipsoid:

$$\vec{\sigma} = t\hat{n} = t(\sin\theta\cos\phi,\ \sin\theta\sin\phi,\ \cos\theta)$$

$$
\begin{aligned}
&= t(\sin\theta\gamma,\ \sin\theta\delta,\ \cos\theta)\\
&= t(\sqrt{1-\mu^2}\,\gamma,\ \sqrt{1-\mu^2}\,\delta,\ \mu)\\
&= t(n_1,\ n_2,\ n_3),
\end{aligned}
\tag{A3.33}
$$

where the t parameter gives the magnitude of the vector, $\gamma = \cos\phi$, and $\delta = \sin\phi$. If the vector function components are substituted into equation (A3.32), then the distance from the origin to a point on the ellipsoid can be found by solving for $-t$ for specified μ and ϕ values. Substituting and collecting like terms gives

$$
\begin{aligned}
t^2&\left[(n_1/a)^2 + (n_2/a)^2 + (n_3/c)^2\right]\\
&+t\left[2(n_1e/a^2) + 2(n_3d/c^2)\right]\\
&+\left[(e/a)^2 - r_g^2 + (d/c)^2\right] = 0.
\end{aligned}
\tag{A3.34}
$$

The single-valued solutions to the quadratic equation (A3.34) are for the rays that trace out the edge of the projection of the ellipsoid as seen from the origin. The discriminant for these solutions must equal zero. Thus setting the discriminant to zero gives an equation from which can be obtained an expression for the μ-limit of integration as a function of ϕ. This equation is

$$
\left[(n_1e/a^2) + (n_3d/c^2)\right]^2 - \left[(n_1/a)^2 + (n_2/a)^2 + (n_3/c)^2\right]\left[(e/a)^2 - r_g^2 + (d/c)^2\right] = 0. \tag{A3.35}
$$

Collecting like terms in n_i gives

$$
n_1^2R + n_2^2S + n_3^2T + n_1n_3U = 0, \tag{A3.36}
$$

where

$$
R = \left[(e/a^2)^2 - \frac{1}{a^2}Q\right], \tag{A3.37a}
$$

$$
S = \left[-\frac{1}{a^2}Q\right], \tag{A3.37b}
$$

$$
T = \left[(d/c^2)^2 - \frac{1}{c^2}Q\right], \tag{A3.37c}
$$

$$
U = 2\left[\frac{ed}{a^2c^2}\right], \tag{A3.37d}
$$

and

$$
Q = \left[(e/a)^2 - r_g^2 + (d/c)^2\right]. \tag{A3.38}
$$

Substituting into equation (A3.36) for the n_i from equation (A3.33) gives

$$(1-\mu^2)\gamma^2 P + (1-\mu^2)S + \mu^2 T + \mu\sqrt{1-\mu^2}\,\gamma U = 0, \tag{A3.39}$$

where

$$P = R - S = (e/a^2)^2. \tag{A3.40}$$

This expression is a quartic for μ. Collecting like terms in μ gives

$$\mu^4\left[(T-V)^2 + \gamma^2 U^2\right] + \mu^2\left[2TV - 2V^2 - \gamma^2 U^2\right] + V^2 = 0, \tag{A3.41}$$

where

$$V = \gamma^2 P + S. \tag{A3.42}$$

The solutions for μ are given by

$$\mu = \pm\sqrt{\frac{-B \pm \sqrt{B^2 - 4AC}}{2A}}, \tag{A3.43}$$

where

$$A = \left[(T-V)^2 + \gamma^2 U^2\right], \qquad B = \left[2TV - 2V^2 - \gamma^2 U^2\right], \qquad \text{and} \qquad C = V. \tag{A3.44}$$

Note that $A \geq 0$. From equation (A3.41), it is clear that $B \leq 0$. Note also that $C = V = \gamma^2 P + S$ can be either positive or negative.

Unfortunately there are 4 solutions for the μ-limit as function of ϕ. In deciding which solution applies, it is useful to find the value ϕ for which the discriminant of equation (A3.43) goes to zero. This discriminant is given by

$$\begin{aligned}
Dis &= \left[2TV - 2V^2 - \gamma^2 U^2\right]^2 - 4\left[(T-V)^2 + \gamma^2 U^2\right]V \\
&= \left[4T^2V^2 + 4V^4 - 8TV^3 - 2\gamma^2 U^2(2TV - 2V^2) + \gamma^4 U^4\right] - \left[4T^2V^2 - 8TV^3 + 4V^4 + 4\gamma^2 U^2 V^2\right] \\
&= \gamma^2 U^2\left[\gamma^2 U^2 - 4TV\right] = \gamma^2 U^2\left[-4ST + \gamma^2(U^2 - 4TP)\right] \\
&= \gamma^2 U^2\left[-4ST + \gamma^2\left(4(e/a^2)^2(1/c^2)Q\right)\right] = \gamma^2 U^2\left[-4ST + \gamma^2\left(-4(e/a)^2(1/c^2)S\right)\right] \\
&= \gamma^2 U^2(-4S/c^2)\left[-(e/a)^2 + r_g^2 + \gamma^2(e/a)^2\right] \\
&= \gamma^2 U^2(-4S/c^2)\left[r_g^2 - (e/a)^2(1-\gamma^2)\right].
\end{aligned} \tag{A3.45}$$

Thus the discriminant is zero for values of ϕ given by

$$\phi_{Dis=0} = \pm\frac{\pi}{2}, \tag{A3.46a}$$

and

$$\phi_{Dis=0} = \arccos\left(\pm\sqrt{1-(a/e)^2 r_s^2}\right). \tag{A3.46b}$$

Note that if $e < a$, then $(e/a)^2 < r_s^2$, and thus $(a/e)^2 r_s^2 > 1$. Therefore the equation (A3.46b) has no real value for regions where $e < a$, and the only zero of the discriminant is given by (A3.46a).

The correct limits for μ-integration and ϕ-integration depend on the values of e and d. Due to symmetry, only the quadrant with $x' \geq 0$ and $z' \geq 0$ of the x'-z' plane need be considered. The following 7 cases have been worked out.

Case 1: $\quad e = 0, \quad d \geq c$

In this case the convergence point is on the symmetry axis of the ellipsoid. It is obvious that the upper limit of the μ integration is 1 for all ϕ. Thus

$$\mu_u = 1, \tag{A3.47}$$

where u is for upper limit.

Rather than use equation (A3.43), it is simpler in this case to use to equation (A3.39), since $U = 0$ when $e = 0$. Equation (A3.39) becomes

$$(1-\mu^2)\gamma^2 P + (1-\mu^2)S + \mu^2 T = 0. \tag{A3.48}$$

The solution for μ is then

$$\mu = \pm\sqrt{\frac{\gamma^2 P + S}{\gamma^2 P + S - T}}. \tag{A3.49}$$

Now $P = (e/a^2)^2 = 0$ in this case, and so

$$\mu = \pm\sqrt{\frac{S}{S-T}}. \tag{A3.50}$$

This expression has no dependence on ϕ as one would expect from symmetry. Since the solid angle being cosidered is the point inversion of the solid angle subtended by the ellipsoid, it is clear that the positive solution gives the correct lower limit of the μ integration. Thus

$$\mu_l = \sqrt{\frac{S}{S-T}}. \tag{A3.51}$$

It should be clear that there are μ-limits for all ϕ, and that the ϕ integration is therefore done on the interval

$$[0, \pi]. \tag{A3.52}$$

For axisymmetric systems, the integration over the interval $[-\pi, 0]$ can be done trivially by exploiting symmetry.

Case 2: $\quad e \geq a, \quad d = 0$

In this case $U = (ed/a^2c^2) = 0$, and thus equation (A3.49) applies. It should be obvious from symmetry that

$$\mu_u = \sqrt{\frac{\gamma^2 P + S}{\gamma^2 P + S - T}}, \tag{A3.53}$$

and

$$\mu_l = -\sqrt{\frac{\gamma^2 P + S}{\gamma^2 P + S - T}}. \tag{A3.54}$$

The ϕ integration is done on the interval

$$\left[0, \arccos\left(\sqrt{\frac{-S}{P}}\right)\right]. \tag{A3.55}$$

The negative square root solution for the upper ϕ-limit gives $\phi_u \geq \pi/2$. This solution is excluded, since the integration is over the solid angle subtended by rays directed away from the ellipsoid surface.

Case 3: $\quad (e/a)^2 + (d/b)^2 = r_s^2$

In this case the convergence point is right on ellipsoid surface. Since $e \leq a$ it is immediately clear that the ϕ integration is done on the interval

$$[0, \pi], \tag{A3.56}$$

and that the upper μ-limit is given by

$$\mu_u = 1 \quad \text{for} \quad \phi \in [0, \pi]. \tag{A3.57}$$

In this case $S = 0$, and the discriminant Dis given by equation (A3.45) is always zero. Thus there are only two possible solutions for μ_l and these are given by

$$\mu = \pm\sqrt{\frac{-B}{2A}}. \tag{A3.58}$$

For $S = 0$

$$B = 2\gamma^2 TP - 2\gamma^4 P^2 - \gamma^2 U^2. \tag{A3.59}$$

Thus it follows that there is a transition from the negative to the positive solution for μ_l when $\phi = \pi/2$. Therefore

$$\mu_l = \begin{cases} -\sqrt{\dfrac{-B}{2A}}, & \text{for } 0 \le \phi \le \pi/2\ ; \\ \sqrt{\dfrac{-B}{2A}}, & \text{for } \pi/2 \le \phi \le \pi\ . \end{cases} \tag{A3.60}$$

Note that the smaller μ_l case is for the projection-defining rays with positive x-components.

Case 4: $e \le a, \quad d \ge c$

Since $e \le a$, it is immediately clear that the ϕ integration is done on the interval

$$[0, \pi], \tag{A3.61}$$

that the upper μ-limit is given by

$$\mu_u = 1 \quad \text{for} \quad \phi \in [0, \pi] \tag{A3.62}$$

and that the discriminant $Dis = 0$ only for $\phi_{Dis=0} = \pi/2$.

Since $d \ge c$, it follows that $\mu \ge 0$ for all ϕ. Recall $A \ge 0$ and $B \le 0$ always. It should be clear that the lower μ-limit is given by

$$\mu_l = \begin{cases} \sqrt{\dfrac{-B - \sqrt{B^2 - 4AC}}{2A}}, & \text{for } 0 \le \phi \le \pi/2\ ; \\ \sqrt{\dfrac{-B + \sqrt{B^2 - 4AC}}{2A}}, & \text{for } \pi/2 \le \phi \le \pi. \end{cases} \tag{A3.63}$$

Note that the smaller μ_l case is for the projection-defining rays with positive x-components.

Case 5: $e \leq a, \quad d \leq c$

Since $e \leq a$, it is immediately clear that the ϕ integration is done on the interval

$$[0,\ \pi], \tag{A3.64}$$

that the upper μ-limit is given by

$$\mu_u = 1 \quad \text{for} \quad \phi \in [0,\ \pi] \tag{A3.65}$$

and that the discriminant $Dis = 0$ only for $\phi_{Dis=0} = \pi/2$.

Since $d \leq c$, there is some ϕ interval where $\mu_l \leq 0$. Recalling that $A \geq 0$ and $B \leq 0$, it is clear that the equation (A3.43) for μ goes to zero (for non-zero B) only when $C = V = \gamma^2 P + S = 0$ and the square root of the discriminant has the negative coefficient. Thus the μ solution goes to zero for

$$\phi_{\mu=0} = \arccos\left(\pm\sqrt{\frac{-S}{P}}\right). \tag{A3.66}$$

The negative root $\phi_{\mu=0}$ value is not useful since it is greater than $\pi/2$. The positive root $\phi_{\mu=0}$ value is the transition point from the negative to positive μ_l solution. The $\phi_{Dis=0} = \pi/2$ value is the transition point from the negative to positive coefficient for square root of the discriminant of equation (A3.43). Therefore it should be clear that the lower μ-limit is given by

$$\mu_l = \begin{cases} -\sqrt{\dfrac{-B-\sqrt{B^2-4AC}}{2A}}, & \text{for } 0 \leq \phi \leq \phi_{\mu=0}\ ; \\ \sqrt{\dfrac{-B-\sqrt{B^2-4AC}}{2A}}, & \text{for } \phi_{\mu=0} \leq \phi \leq \pi/2\ ; \\ \sqrt{\dfrac{-B+\sqrt{B^2-4AC}}{2A}}, & \text{for } \pi/2 \leq \phi \leq \pi\ . \end{cases} \tag{A3.67}$$

Case 6: $e \geq a, \quad d \geq c$

Since $e \geq a$ the ϕ integration is now limited to an interval with an upper limit that is less than or equal to $\pi/2$. The upper and lower μ-limits will both be positive since $d \geq c$.

It should be clear that the ϕ integral is done on the interval

$$[0,\ \phi_{Dis=0}], \tag{A3.68}$$

where from equation (A3.46b)

$$\phi_{Dis=0} = \arccos\left(\sqrt{1-(a/e)^2 r_g^2}\right). \tag{A3.69}$$

In this case the upper μ-limit is not 1. Instead

$$\mu_u = \sqrt{\frac{-B+\sqrt{B^2-4AC}}{2A}} \quad \text{for} \quad 0 \le \phi \le \phi_{Dis=0}. \tag{A3.70}$$

The lower μ-limit is given by

$$\mu_l = \sqrt{\frac{-B-\sqrt{B^2-4AC}}{2A}} \quad \text{for} \quad 0 \le \phi \le \phi_{Dis=0}. \tag{A3.71}$$

Case 7: $e \ge a, \quad d \le c$

This case is much the same as Case 6. The ϕ integral is done on the interval

$$[0, \phi_{Dis=0}], \tag{A3.72}$$

where from equation (A3.46b)

$$\phi_{Dis=0} = \arccos\left(\sqrt{1-(a/e)^2 r_g^2}\right). \tag{A3.73}$$

The upper μ-limit is given by

$$\mu_u = \sqrt{\frac{-B+\sqrt{B^2-4AC}}{2A}} \qquad \text{for} \qquad 0 \le \phi \le \phi_{Dis=0}. \tag{A3.74}$$

The lower μ-limit, however, is negative for the smallest ϕ region. The transition ϕ value between the negative and positive regions is again given by

$$\phi_{\mu=0} = \arccos\left(\sqrt{\frac{-S}{P}}\right). \tag{A3.75}$$

Therefore it should be clear that the lower μ-limit is given by

$$\mu_l = \begin{cases} -\sqrt{\dfrac{-B-\sqrt{B^2-4AC}}{2A}}, & \text{for } 0 \le \phi \le \phi_{\mu=0}\ ; \\ \sqrt{\dfrac{-B-\sqrt{B^2-4AC}}{2A}}, & \text{for } \phi_{\mu=0} \le \phi \le \phi_{Dis=0}\ . \end{cases} \tag{A3.76}$$

The 7 cases given above for the μ-limits and ϕ-limits are sufficient to construct the single-line source functions of the Sobolev method and Sobolev-II method for axisymmetric ellipsoidal photospheres.

c) Extrema and Projections of an Axisymmetric Ellipsoid

There are some expressions that are useful in numerically evaluating integrals over planar velocity surfaces in a system with axisymmetric ellipsoidal symmetry. These expressions are trivial, but for reference they are worked here.

The equation for an axisymmetric ellipsoid is

$$(x'/a)^2 + (y'/a)^2 + (z'/c)^2 = r_g^2, \tag{A3.77}$$

where r_g is a generalized radius-like parameter. The planar velocity surfaces will in general be perpendicular to a line in the x'-z' plane. It is therefore convenient to rotate the axes so that the symmetry axis of the ellipsoid is at an oblique angle with respect to the normal to the velocity surfaces. The primed coordinate system will therefore be considered to be rotated by $\pi/2 - \theta$ clockwise about the y-axis from an unprimed coordinate system. This rotation means that the symmetry axis of the ellipsoid, which is along the z' axis, will be a counterclockwise angle θ from the x-axis; the normal to the velocity surfaces is taken as being directed along the x-axis. The primed coordinates are given by

$$x' = x\cos[-(\pi/2-\theta)] + z\sin[-(\pi/2-\theta)] = x\sin\theta - z\cos\theta, \tag{A3.78}$$

$$z' = -x\sin[-(\pi/2-\theta)] + z\cos[-(\pi/2-\theta)] = x\cos\theta + z\sin\theta. \tag{A3.79}$$

For convenience let

$$\alpha = \cos\theta, \qquad \text{and} \qquad \beta = \sin\theta. \tag{A3.80}$$

Thus

$$x' = x\beta - z\alpha, \qquad \text{and} \qquad z' = x\alpha + z\beta. \tag{A3.81}$$

In the unprimed coordinate system the equation of the ellipsoid becomes

$$\left(\frac{x\beta - z\alpha}{a}\right)^2 + (y/a)^2 + \left(\frac{x\alpha + z\beta}{c}\right)^2 = r_g^2. \tag{A3.82}$$

Expanding the squares and collecting like terms gives

$$z^2\left[(\alpha/a)^2+(\beta/c)^2\right]-2zx(\alpha\beta)\left[(1/a^2)-(1/c^2)\right]+x^2\left[(\beta/a)^2+(\alpha/c)^2\right]+(y/a)^2=r_g^2. \quad (A3.83)$$

Let

$$C_1=(\alpha\beta)\left((1/a^2)-(1/c^2)\right), \quad (A3.84a)$$

$$C_2=\left((\alpha/a)^2+(\beta/c)^2\right), \quad (A3.84b)$$

$$C_3=\left((\beta/a)^2+(\alpha/c)^2\right), \quad (A3.84c)$$

and

$$C_4=C_2C_3-C_1^2=1/(ac)^2. \quad (A3.84d)$$

Note that

$$\begin{cases} C_1=0, & \text{for a spherical system;} \\ C_1>0, & \text{for a prolate system;} \\ C_1<0, & \text{for an oblate system.} \end{cases} \quad (A3.85)$$

With these definitions for the C_i equation (A3.83) becomes

$$z^2C_2-2zxC_1+x^2C_3+(y/a)^2=r_g^2. \quad (A3.86)$$

It is useful to have x as a function of y and z. Such an expression is used in deciding whether a point on a velocity surface is in the atmosphere, beneath the photosphere, or outside the atmosphere. The expression is

$$x=\frac{zC_1\pm\sqrt{-z^2C_4+C_3\left(r_g^2-(y/a)^2\right)}}{C_3}. \quad (A3.87)$$

The boundary equations of x-direction projections of ellipsoidal surfaces can be determined by equating the discriminant of equation (A3.87) to zero. These boundary equations are ellipse equations:

$$(y/a)^2+\left(\frac{z}{\sqrt{C_3/C_4}}\right)^2=r_g^2. \quad (A3.88)$$

For a given value of r_g, the extremal values of z and y for the projections are given by the following:

$$z_{ext}=\pm r_g\sqrt{C_3/C_4}, \quad \text{for} \quad x=\pm r_gC_1/\sqrt{C_3C_4} \quad \text{and} \quad y=0; \quad (A3.89)$$

and

$$y_{ext}=\pm r_ga, \quad \text{for} \quad x=0 \quad \text{and} \quad z=0. \quad (A3.90)$$

Having expressions for the projections and the extremal values is useful in setting the limits of integration. The atmosphere cannot be extended to infinity in a numerical calculation, and so a $r_{g_{max}}$ must be set. The velocity surface integrations can then be done over the x direction projected $r_{g_{max}}$-ellipse bounded region while exploiting the elliptical symmetry. Since there is a large discontinuity in the specific intensity emission between the limb and photodisk regions, it improves numerical accuracy to partition the integration into separate limb and photodisk integrations. (For the definitions of limb and photodisk see Chapter 3 section (b).) The photodisk integration is done over the $r_{g_{ph}}$-ellipse bounded region; this region is the projected surface of the photosphere. The limb integration is then done over the elliptical region bounded between the $r_{g_{ph}}$-ellipse and the $r_{g_{max}}$-ellipse.

Only a finite number of velocity surfaces can be integrated over. Therefore a selection of velocity surfaces are chosen at discrete x coordinates with some reasonable increment between the velocity surfaces. The limiting x coordinates can be determined from equation (A3.83) by solving for z and setting the discriminant to zero. z is given by

$$z = \frac{xC_1 \pm \sqrt{-x^2C_4 + C_2\left(r_g^2 - (y/a)^2\right)}}{C_2}. \tag{A3.91}$$

The z direction projections of the ellipsoids are bounded by ellipses given by

$$\left(\frac{x}{\sqrt{C_2/C_4}}\right)^2 + (y/a)^2 = r_g^2. \tag{A3.92}$$

The extremal x values are thus given by

$$x_{ext} = \pm r_g\sqrt{C_2/C_4}, \quad \text{for} \quad y = 0 \quad \text{and} \quad z = \pm r_g C_1/\sqrt{C_2C_4}. \tag{A3.93}$$

Due to occultation by the photosphere the velocity surfaces need not be placed at x coordinates as small as $x_{min} = -r_{g_{max}}\sqrt{C_2/C_4}$ in all cases. What is needed is an expression for the minimum x of the limb region. If the y-z coordinates that give x_{min} lie inside the photodisk's ellipse boundary, then the minimum x limb point must be the point with the smallest x coordinate where the outer atmosphere surface, and the photodisk ellipse boundary intersect; let the coordinates of this intersection point be subscripted by "*occult*" (e.g., x_{occult}). From symmetry it should be clear that the minimum limb point should have $y_{occult} = 0$. From equation (A3.89) it follows that

$$z_{occult} = r_{g_{ph}}\sqrt{C_3/C_4}, \qquad \text{or} \qquad -r_{g_{ph}}\sqrt{C_3/C_4}.$$

Substituting these values for y_{occult} and z_{occult} into equation (A3.87) and setting $r_g = r_{g_{max}}$ gives

$$x = \frac{\pm r_{g_{ph}} C_1/\sqrt{C_4} \pm \sqrt{r_{g_{max}}^2 - r_{g_{ph}}^2}}{\sqrt{C_3}}. \qquad (A3.94)$$

Clearly then the x_{occult} coordinate is given by

$$x_{occult} = \frac{-r_{g_{ph}} |C_1/\sqrt{C_4}| - \sqrt{r_{g_{max}}^2 - r_{g_{ph}}^2}}{\sqrt{C_3}}. \qquad (A3.95)$$

If the y-z coordinates that give x_{min} lie outside the photodisk's ellipse boundary, then the minimum x limb point must be the point with $x = x_{min}$. Thus the prescription for the minimum x coordinate of the limb region is

$$x_{min\ limb} = \begin{cases} \dfrac{-r_{g_{ph}} |C_1/\sqrt{C_4}| - \sqrt{r_{g_{max}}^2 - r_{g_{ph}}^2}}{\sqrt{C_3}}, & |z_{x_{min}}| = |r_{g_{max}} C_1/\sqrt{C_2 C_4}| < r_{g_{ph}} \sqrt{C_3/C_4}; \\ -r_{g_{max}} \sqrt{C_2/C_4}, & |z_{x_{min}}| = |r_{g_{max}} C_1/\sqrt{C_2 C_4}| \geq r_{g_{ph}} \sqrt{C_3/C_4}. \end{cases} \qquad (A3.96)$$

All the above expressions were used in implementing the Sobolev-H computer code that is listed in Appendix 4.

Appendix 4

The Sobolev-H Multi-Line Program

For Axisymmetric Ellipsoidal Atmospheres

```
*123456789*123456789*123456789*123456789*123456789*123456789*123456789*12
*
*
*  The Sobolev-H Multi-line Program for Axisymmetric Ellipsoidal
*  Atmospheres:  The S7 Program
*
*  Written by David J. Jeffery
*  McMaster University
*  1987
*
*  Introduction
*
*     The S7 program is designed to calculate flux and polarization
*  spectra using the Sobolev-H method.  The Sobolev method exploits
*  large velocity gradients to solve the radiative transfer problem
*  in moving atmospheres.  The velocity gradients cause a macroscopic
*  Doppler de-coupling of the atomic transitions in spatially separated
*  parts of such an atmosphere.  It is thus possible to obtain local
*  expressions for source functions at least in the cases of general
*  expansion or general contraction of the atmosphere.  The Sobolev-H
*  method is a modified version of the Sobolev method.  The Sobolev-H
*  method treats the radiation field in terms of the Stokes parameters
*  (Chandrasekhar 1960, p. 24), and includes the polarizing effect
*  of resonance scattering (Hamilton 1947;  Chandrasekhar 1960, p. 50).
*
*     A good reference for the multi-line Sobolev method is Rybicki and
*  Hummer (1978).  For the Sobolev-H method see Jeffery (1988,
*  Chapter 2 section (d)).  Note that hereafter Jeffery (1988) will be
*  referred as J.
*
*     The atmosphere model consists of a scattering atmosphere
*  surrounding a continuum producing photosphere.  The scattering is
*  limited to pure two-level resonance scattering;  a thermal source
*  for line photons can be included.  The atmospheric velocity field
*  is limited to homologous expansion.  This is appropriate for supernova
*  explosions.  The basic atmosphere model was developed from the model
*  of Branch (1980).  However, the atmosphere is allowed to have prolate
*  and oblate asymmetries.  For a description of the model see
*  J (Chapter 4 section (a)).
*
```

```
*      The references made in this program are listed here for convenience:
*
*   Branch, D. 1980, in "Supernova Spectra", ed. R. Meyerott and
*      G.H. Gillespie (New York:  American Institute of Physics), p.39.
*
*   Cassinelli, J. P., and Hummer, D. G. 1971, M.N.R.A.S., 154, 9.
*
*   Chandrasekhar, S. 1960, "Radiative Transfer" (New York:  Dover
*      Publications, Inc.).
*
*   Code, A., Davis, J., Bless, R., and Brown, H. 1976, Ap. J., 203, 417.
*
*   Hamilton, R. 1947, Ap. J., 106, 457.
*
*   Jeffery, D.J. 1988, Ph.D. Thesis, McMaster University, Hamilton
*      Ontario.
*
*   McCall, M. L. 1984, M.N.R.A.S., 210, 829.
*
*   _________. 1985, in 'Supernovae as Distance Indicators', ed. N. Bartel
*      (Berlin: Springer-Verlag), p. 48.
*
*   Rybicki, G.B., and Hummer, D.G. 1978, Ap. J., 219, 654.
*
*   Shapiro, P.R., and Sutherland, P.G. 1982, Ap. J., 262, 902.
*
*
*
*   Running the S7 Program
*
*      The S7 program can be executed interactively by typing RUN S7
*   or can be batchjobbed by submitting the command procedure S7M.COM.
*   The S7M.COM procedure is
*
*           ! S7M.COM;
*           RUN S7.EXE;
*
*   The S7 program is on file S7.FOR.  It reads a model number from
*   a file called S7M.DAT.  S7M.DAT contains a single number that can
*   be between 00 and and 99: e.g., 36.  The program then reads NAMELIST
*   input data from a file with a name that contains the model number:
*   e.g., S736.DAT.  As an example S736.DAT is given below:
*
*            $PAR1
*            IDATA=0,IFREQ=0,ILATE=1,ILOG=0,IPUT=4,ISETYN=1,
*            INORM=1,WNORM=5900.,IRED=1,ERED=.2
*            $END
*
*            $PAR2
*            IANGL=1,ANGL=90.,         10*0.,
```

```
*           IANIS=1,ANIS=5*0.,                            15*0.,
*           IASPH=4,ASPH=.20,.40,.60,.80,
*           IICAS=1,ICAS=2,            10*0,
*           IILIN=1,ILIN=7,            10*0,
*           IPOWE=1,POWE=7.,           10*0.,
*           IPRE=1 ,PRE=.5,            10*0.,
*           IRGMA=1,RGMA=4.,           10*0.,
*           ITAUP=1,TAUP=600.,750,1000.,1500.,2000.,
*           ITEMP=1,TEMP=5500.,       10*0.,
*           ITHER=1,THER=.0,           10*0.,
*           IVELP=1,VELP=.60E+9,        10*0.,
*           IWLIN=1,WLIN=3970.,4101.,4340.,4861.,5889.,5896.,6562.,
*           ZEMAX=1.
*           $END
*
*           $PAR3
*           IIFAM=1
*           IFAM=1,2,
*           ITAUV=1,
*           TAUFAM=600.,2.25,10.,
*           TAUWAV=6562.,5889.9504,4233.159
*           $END
*
*           $PAR4
*           $END
*
* These input parameters are described below.
*
*    Another input are line files (FAM files).  Each FAM file contains a
* set of lines for some atom or ion.  The file has the wavelength of the
* line and some other relevant line data.  These line files are controlled
* by the PAR3 parameters.  More information is given in the parameter
* descriptions below.
*
*    The output from the program consists of a system listing that
* contains the flux and polarization profiles.  This listing also
* gives all the local extrema of these profiles.  The source functions
* can also be outputed.  A simpack plot file called PLOTAPE.DAT is
* also output.  Finally, a file is created containing the flux and
* polarization profiles for the whole atmosphere, and for the limb and
* photodisk regions separately.  This file is called S7//MODEL//.OUT;
* an example file name is S736.OUT.
*
*    The user must be warned that the S7 program is still in a
* developmental stage.  It is thus not very robust.  Certain features
* have never been used and so cannot be guaranteed to work.  Also
* there may be ranges of parameter values that will cause the program
* to bomb.
*
*
```

```
*
*  Input Parameter Descriptions
*
*  PAR1 parameters are mostly program controlling parameters of the
*  yes/no variety.
*
*     IDATA:  This parameter just tells the plot preparing subroutine
*             OUTPUT whether or not to include the continuum polarization
*             data points from Shapiro and Sutherlahd (1982) in the simpack
*             plot file PLOTAPE.DAT:  0 for no inclusion;  1 for inclusion.
*             (default:  IDATA=0)
*
*     IFORM:  This is a null parameter (default:  IFORM=1)
*
*     IFREQ:  This parameter decides whether to calculate the wavelength
*             (IFREQ=0) or the frequency distribution (IFREQ=1) of
*             specific intensity and flux.  In either case the calculated
*             quantity is plotted as a function of wavelength.  Note
*             F(wavelength)*d(wavelength)=F(frequency)*d(frequency) and
*             therefore F(wavelength)=F(frequency)*CLIGHT/WAVELENGTH**2.
*             (default:  IFREQ=0)
*
*     ILATE:  0 for spherical symmetry;  1 for oblate ellipsoid symmetry;
*             2 for prolate ellipsoid symmetry.  Note that spherically
*             symmetric models are much less demanding in computer time.
*             For an asymmetric model the number of operations to perform
*             is roughly the square of the number of operations required by
*             a spherically symmetric model.  (default:  ILATE=1)
*
*     ILOG:   0 for relative flux spectra;  1 for logarithmic flux
*             spectra.  (default:  ILOG=0)
*
*     IPUT:   This parameter decides what information to output:
*             4 gives the spectra in the system listing and in a output
*             file called S7//'MODEL'//.OUT (e.g., S736.OUT) and a
*             simpack plot file named PLOTAPE.DAT;  2 gives the same
*             as 4, but includes the source functions coefficient
*             table in the system listing.  (default:  IPUT=4)
*
*     IISET:  This parameter gives the number of transition lines
*             there are in each group of lines.  The groups of lines are
*             are used in sequential spectra calculations.  This feature
*             is useful in seeing how the spectra vary as line wavelengths,
*             line optical depths, or line E1-coefficients are varied.
*
*     ISETYN:  0 for only one spectra calculation;  1 if a sequence of
*              spectra calculations are to be run (see the PAR2 descriptions
*              below).  (default:  1)
*
*     ITRANS:  This parameter decides whether or not the photosphere is
```

```
*               transparent;  0 for opaque;  1 for transparent.  An
*               artificially transparent photosphere allows flux from the
*               occulted region of the photosphere to contribute to the
*               net flux.  The transparent photosphere is useful for
*               testing energy conservation;  the areas of emission and
*               absorption features of a P-Cygni line should be equal for
*               the transparent photosphere.  (default:  ITRANS=0)
*
*      INORM:  0 for no specified normalization wavelength;  1 for a
*              specified normalization wavelength.  (default:  INORM=0)
*
*      WNORM:  This is normalization wavelength for the flux spectra.
*              It is to be given in Angstroms.
*              (default:  WNORM=5000. Angstrom)
*
*      IFRAG:  0 for ordinary atmosphere projection;  1 for examining
*              the spectra for rectangular sections of the atmosphere
*              projection.  It is sometimes useful in analyzing spectra
*              to see what the various parts of the projected area of the
*              atmosphere are contributing.  Using IFRAG allows one to
*              restrict the output flux from the limb to an area satisfying
*              |Y|<RG(0)*ASEMI*YMAX and |Z|<RG(0)*BSEMI*ZMAX.  YMAX and
*              ZMAX are input parameters specifically for use with IFRAG.
*              RG(0) is the photospheric generalized radius (J, Chapter 4
*              section (a)).  ASEMI and BSEMI are the perpendicular and
*              symmetry semi-axes of the ellipsoidal geometry.
*              (default:  IFRAG=0)
*
*      YMAX and ZMAX:  These parameters are used only in conjunction with
*                      IFRAG.  They are described in the IFRAG description
*                      above.  (default:  YMAX=100 and ZMAX=100;  the
*                      defaults are numerical infinities)
*
*      ERED:  This is the color excess value.  This value determines the
*             reddening to be applied to a flux spectrum according to
*             reddening law given by Code et al. (1976).
*             (default:  ERED=0)
*
*      IRED:  0 for no reddening;  1 for reddening.  (default:  IRED=0)
*
*
*   PAR2 real parameters are, in most cases, real arrays each containing
*   a set of values for a physical variable.  The values for each physical
*   variable are used one at a time (except for line data values) in
*   calculating a sequence of spectra.  Associated with each array
*   parameter is an integer parameter that equals the number of values
*   in the array and also determines the number of spectra in the
*   sequence.  As an example IANGL equals the number of inclination
*   angles there are;  ANGL is an array containing the IANGL
*   inclination angles.  At present the upper limit on the number of
```

```
* values in an array is 11 (except for the line data arrays), but
* this could be easily changed. The exception to the "one at a time"
* rule are the values in the line data arrays.  The lines can all
* be included in one spectrum or can be separated into groups that
* are put in sequential spectrum calculations.  The IISET parameter
* described above gives number of lines in a group.  It should be
* noted that this grouping feature does not apply to lines that are
* input from line files (FAM files), but only to lines input by
* the PAR2 namelist (the FAM file lines are controlled by the
* PAR3 parameters).  The reason for the line grouping feature is
* to be able to study spectra as line variables are altered.
* At present a total of 61 lines can be input.
* WARNING:  The program was designed to run more than one sequence of
* physical values in one job, but this feature has never been tested
* and so probably does not work.  Thus only one physical variable
* can be varied in one job with success expected.
*
*     IANGL and ANGL:  The array ANGL contains the inclination angles.
*                      These are the angles between the line of sight
*                      to the observer and the symmetry axis of the
*                      ellipsoid atmosphere.  ANGL values are restricted
*                      to the range [0, 90] degrees.  (default:  IANGL=1
*                      and ANGL(1)=90. degrees)
*
*     IANIS and ANIS:  The line array ANIS contains the E1-coefficients
*                      (J, Chapter 2 section (d)) for the PAR2 lines.
*                      (default:  IANIS=1 and ANIS(1)=0.)
*
*     IASPH and ASPH:  This is an asymmetry parameter that can vary
*                      between 0 and 1 (J, Chapter 3 section (a),
*                      Chapter 4 section (a)).  (default:  IASPH=1
*                      and ASPH(1)=0.)
*
*     IICAS and ICAS:  1 for a wavelength independent continuum;
*                      2 for a Planck black-body continuum.
*                      (default:  IICAS=1 and ICAS(1)=1)
*
*     IILIN and ILIN:  This array parameter gives a crude ability to
*                      vary the number of lines put into the spectrum:
*                      e. g., if ILIN(1)=3, then the first three PAR2
*                      lines are put in the first spectrum;  if ILIN(2)=7,
*                      then the first 7 lines are put in the second
*                      spectrum;  and so on.  This hopefully will not
*                      conflict with the IISET parameter.
*                      (default:  IILIN=1 and ILIN(1)=1)
*
*     IPOWE and POWE:  This is the power for the optical depth decay
*                      law (J, Chapter 4 section (a)).  (default:
*                      IPOWE=1 and POWE(1)=7.)
*
```

```
*     IPRE and PRE:  This variable controls the numerical precision of
*                    the calculation.  PRE(1)=.5 gives a numerical
*                    uncertainty of about 5% at worst in the spectra;
*                    this is usually acceptable.  The uncertainty goes
*                    roughly as the square of the PRE value;
*                    unfortunately the CPU time required goes roughly
*                    as one over the square of the PRE value.
*                    (default:  IPRE=1 and PRE(1)=.5)
*
*     IRGMA and RGMA:  This variable sets the outer generalized radius
*                      of the atmosphere (J, Chapter 4 section (a)).
*                      (default:  IRGMA=1 and RGMA(1)=3.)
*
*     RGMIN:  This is a single variable, not an array.  It sets the inner
*             generalized radius of the atmosphere (J, Chapter 4 section (a)).
*             Usually the default inner generalized radius of 1 is used.
*             However, to make comparisons between the DCO results
*             (J, Chapter 5 section (b)) and the electron scattering
*             atmosphere results of Cassinelli and Hummer (1971), it is
*             useful to be able to shrink the inner generalized radius.
*             (default:  RGMIN=1.)
*
*     ITAUP and TAUP:  The line array TAUP contains the Sobolev optical
*                      depths (J, Chapter 2 section (a)) for the PAR2 lines.
*                      (default:  ITAUP=1 and TAUP(1)=10.)
*
*     ITEMP and TEMP:  This is the photospheric temperature (J, Chapter 4
*                      section (a)).  These values are not used if the
*                      ICAS value is 1 (default:  ITEMP=1 and
                       TEMP(1)=17000. K)
*
*     ITHER and THER:  This is the thermal coupling parameter (J, Chapter 4
*                      section (a)).  (ITHER=1 and THER(1)=0.)
*
*     ITIM and TIM: This is the time since the ignition of the explosion.
*                   The time can be used to calculate the dimensions of the
*                   atmosphere in absolute units, but no use is made of the
*                   time variable in the current version of the program.
*                   (default:  ITIM=1 and TIM=10.E+5 sec)
*
*     IVELP and VELP:  This is the photospheric velocity (J, Chapter 2
*                      section (c), Chapter 4 section (a)).
*                      (default:  IVELP=1 and VELP(1)=1.E+9 cm/s)
*
*     IWLIN and WLIN:  The line array WLIN contains the line wavelengths
*                      for the PAR2 lines.  (default:  IWLIN=1 and
*                      WLIN(1)=5000. Angstrom)
*
*     ZEMAX:  This is a single variable, not an array.  It is the
*             angle of the wedge of atmosphere projection for which
```

```
*                 spectra is calculated.  ZEMAX is given in units of pi
*                 radians.  For ZEMAX=1 the spectra are calculated for half
*                 the projected atmosphere, but due to the axial symmetry
*                 this is the same as for the whole projection. (In this
*                 case the U Stokes parameter flux is set to zero since it is
*                 zero for the whole projection integration.)  For smaller
*                 ZEMAX the spectra is calculated only for a wedge of the
*                 projection.  The ZEMAX parameter is sometimes useful in
*                 analyzing the polarization spectra.  (default:  ZEMAX=1.)
*
*
*    PAR3 parameters are used for controlling the line information from
*    the line files;  these files are called FAM files for line family.
*    The FAM files are FAM1.DAT (H I lines), FAM2.DAT (Na I lines),
*    FAM3.DAT (Fe II lines), and so on.  Note there is no FAM10.DAT;
*    when 10 is specified for a the FAM number a discretized continuous
*    opacity (DCO) is implemented by the creation of a set of pseudo-lines
*    (see J, Chapter 5 section (b)).  The PAR3 parameters are used almost
*    exclusively in the subroutine FAMILY.
*
*       IIFAM:  0 if no FAM files are to be read.  In this case the
*               PAR2 lines are used in the calculations.  1 if
*               FAM files are to be read and their data used in the
*               calculation.
*
*       IFAM:  This is an array that contains the FAM file numbers:
*              IFAM(1)=1 causes the hydrogen lines to be read;  but
*              IFAM(2)=0 causes no file to be open.  The order of the
*              FAM file numbers in IFAM is unimportant.  Note that
*              an IFAM value of 10 causes the discretized continuous
*              opacity (DCO) to be implemented.
*              (default:  all IFAM values are set to zero)
*
*       ITAUV:  This parameter is the IFAM index of a FAM file
*               number.  Specifying ITAUV and ITAUP>1 (see PAR2)
*               causes the controlling optical depth of the lines in
*               FAM//IFAM(ITAUV)//.DAT to be varied using the values
*               in array TAUP.  (default:  ITAUV=1)
*
*       TAUFAM:  This array contains the controlling optical depths for
*                lines in the FAM files.  For example, the optical depth in
*                TAUFAM(4) is applied to the lines of FAM//IFAM(4)//.DAT
*                Thus the TAUFAM values must be entered in the right order.
*                A controlling optical depth is the Sobolev optical depth
*                of a particular line in a FAM file;  this line has
*                wavelength specified in TAUWAV.  The TAUWAV line is
*                usually chosen because it is a particularly strong line
*                in a spectrum that is being fit.  The other lines in the
*                FAM file have their optical depths fixed by use of their
*                oscillator strengths and the Boltzmann distribution
```

```
*               (see J, Chapter 2 section (c)).  Note if the IFAM value
*               is 10 the pseudo-lines of the discretized continuous opacity
*               are included in the spectrum.  The optical depths of these
*               pseudo-lines are set using the corresponding TAUFAM value
*               (unless ICH=1 and then see below) and the prescription of
*               J (Chapter 5 section (b)).  (default:  all TAUFAM are set
*               to zero)
*
*      TAUWAV:  This array contains the wavelengths of the lines for
*               which controlling optical depths are set.  For example,
*               the wavelength in TAUFAM(4) is for a line in
*               FAM//IFAM(4)//.DAT.  This line is given the photospheric
*               optical depth in TAUFAM(4).
*               (default:  all the TAUWAV are set to zero)
*
*      WAVEL and WAVEH:  Sometimes it is desired that only the
*                        lines in restricted wavelength region be
*                        included in the spectrum.  WAVEL sets the
*                        lower limit on this region, and WAVEH the
*                        upper limit.  (default:  WAVEL=0. and
*                        WAVEH=100000.)
*
*      ICONT:  This integer specifies the number of pseudo-lines to be
*              included in the spectrum if the DCO method is implemented.
*              The logarithms of the pseudo-lines are equally spaced
*              between LOG10(WAVEL) and LOG10(WAVEH).
*              (default:  ICONT=0)
*
*      IBETAP:  This parameter when set to 1 sets all the escape
*               probabilities of the pseudo-lines to 1.  This feature
*               might turn out to be useful in making the DCO method
*               better in reproducing continuum scattering results.
*               (default:  IBETAP=0)
*
*      ICH:  When ICH=1 the continuous opacity of the DCO method is set
*            to 1 at the generalized radius 1.  This setting allows the
*            DCO results to be compared directly to the Cassinelli and
*            Hummer (1971) results for continuum scattering atmospheres;
*            Cassinelli and Hummer set continuous opacity to 1 at radius 1
*            in all their models.  (default:  ICH=0)
*
*
*   PAR4 parameters are used to investigate how the specific intensity
*   and polarization vary as a function of impact parameter.  The impact
*   parameter is the radial coordinate of a cylindrical coordinate system;
*   the cylindrical coordinate system z-axis is along the line-of-sight
*   to the distant observer.  The specific intensity analyzed this way is
*   often called surface brightness.
*
*      ISURF:  0 no surface brightness investigation;  1 spectra calculation
```

```
*               and surface brightness investigation;  2 surface brightness
*               investigation alone.  (default:  ISURF=0)
*
*        IPACT:  This parameter gives the number of impact parameter values
*               for which the surface brightness and polarization are to
*               be calculated; actually there are IPACT+1 values since the
*               0 impact parameter is used also.  The logarithms of the
*               impact parameters are equally spaced between LOG10(.1*RGMIN)
*               and LOG10(.995*RGMAX).  (default:  IPACT=75)
*
*        SURFWA:  This is the wavelength for which the surface brightness is
*                to be calculated.  (default:  SURFWA=6500. Angstrom)
*
*        SURFAN:  This the angle of the cylindrical radius along which the
*                surface brightnesses are calculated.  The angle is
*                measured from the projection of the symmetry axis of
*                atmosphere.  (default:  SURFAN=0 degrees)
*
*123456789*123456789*123456789*123456789*123456789*123456789*123456789*12
*
*  The main program unit does very little:  a few constants are calculated;
*  the S7M.DAT file is read in;  control is transferred to subroutine
*  READIN.  Note if an error on the read occurs the default model is
*  run.  Also note that several model numbers can be read from S7M.DAT,
*  but this feature has never been used or tested.  Note also that after
*  the main program unit, all the subroutines are in alphabetical order.
*
      PROGRAM S7
      COMMON/CONST/CLIGHT,CTA,IFREQ,PI,PITWO,PI2,PLANC1,PLANC2,RADDEG
      PARAMETER (NLAM=125,NLINES=61,NSET=11)
      CHARACTER MODEL*2
      COMMON/SET/CCALL(NLINES),DLAM,
     1 FLUX(0:NLAM,NSET,3),IDATA,IFORM,ILAM(NSET),
     1 IISET,ILATE,ILOG,ITRANS,
     2 MODEL,IPUT,ISET,JSET,JSETS,KSET(NSET),POLAR(0:NLAM,NSET,3),
     3 SET(NSET),WLAM(0:NLAM,NSET)
      DATA BOLTZ,CTA,CLIGHT,PLANCK
     1    /1.380662E-16,1.E+8,2.99792 458E+10,6.62617 66E-27/
*
      PI=ACOS(-1.)
      PITWO=2.*PI
      PI2=PI/2.
      PLANC1=2.*PLANCK*CLIGHT
      PLANC2=PLANCK/BOLTZ
      RADDEG=180./PI
*
      INULL=1
      OPEN(UNIT=1,FILE='S7M.DAT;',STATUS='OLD')
      REWIND1
  110 CONTINUE
```

```
      READ(1,910,END=200,ERR=200) MODEL
  910 FORMAT(A2)
      INULL=0
      CALL READIN
      GO TO 110
*
  200 CONTINUE
      CLOSE(UNIT=2)
      IF(INULL .EQ. 1) THEN
          MODEL='XX'
          CALL READIN
      END IF
*
      END
*
*123456789*123456789*123456789*123456789*123456789*123456789*123456789*12
*
*  ANISOT calculates for each line the coefficients that are needed for the
*  calculation of the direct contributions to the source function, and
*  the coefficients that can be used for calculating the source function
*  components themselves.  ANISOT is called from READIN.  ANISOT must
*  be called whenever the lines or the E1-coefficients (J, Chapter 2
*  section (d)) are changed.
*
      SUBROUTINE ANISOT
      PARAMETER (NLAM=125,NLINES=61,NSET=11)
      COMMON/ANISOT/AN1(NLINES),AN2(NLINES),ANDIR(14,NLINES),
     1 AN17(NLINES),ANS(9,NLINES)
      COMMON/CONST/CLIGHT,CTA,IFREQ,PI,PITWO,PI2,PLANC1,PLANC2,RADDEG
      COMMON/PARAM/ANGLE,ANISO(NLINES),ASEMI,BSEMI,ICASE,
     1             ICOEF,ILINES,POWER,PREC,
     2             RGMAX,RGMIN,TAUPH(NLINES),TEMPH,THERM,
     3             TIME,VELPH,WLINE(NLINES),ZEMAX
*
      DO 410 I=1,ILINES
      AN1(I)=ANISO(I)
      AN2(I)=1.-AN1(I)
*
*  ANISO contains the E1-coefficients (J, Chapter 2 section (d)).  From
*  ANISO the ANDIR's are calculated;  the ANDIR's are the coefficients of
*  the equations for the D_i's (J, equation (2.132)). The ANDIR's are
*  the coefficients needed to construct the direct contributions to the
*  source functions.  They account for the fact that the integration is
*  over only 2*PI solid angle by dividing by 2*PI only instead of by 4*PI.
*  The ANDIR's are used in subroutine GRAL1.
*
      ANDIR(1,I)=.5*(1+2*ANISO(I))/PITWO
      ANDIR(2,I)=.5*(1-  ANISO(I))/PITWO
      ANDIR(3,I)=-1.5*ANISO(I)/PITWO
      ANDIR(4,I)=.75*ANISO(I)*(-2.)/PITWO
```

```
      ANDIR(5,I)=.75*ANISO(I)*(1.)/PITWO
      ANDIR(6,I)=.75*ANISO(I)*(3.)/PITWO
      ANDIR(7,I)=.75*ANISO(I)*(4.)/PITWO
      ANDIR(8,I)=.75*ANISO(I)*(2.)/PITWO
      ANDIR(9,I)=.75*ANISO(I)*(1.)/PITWO
      ANDIR(10,I)=.75*ANISO(I)*(-1.)/PITWO
      ANDIR(11,I)=.75*ANISO(I)*(1.)/PITWO
      ANDIR(12,I)=.5*(1- ANISO(I))/PITWO
      ANDIR(13,I)=.5*(1+.5*ANISO(I))/PITWO
      ANDIR(14,I)=.75*ANISO(I)/PITWO
*
*  AN17 is a coefficient that comes from equation (2.146) of J.
*  This equation calculates the source function components from the
*  direct contributions.  AN17 is used in subroutine SOURC2.
*
      AN17(I)=.7*AN1(I)
*
*  ANS coefficients come from equation (2.139) of J.  They are
*  used for a linear algebra solution for the source function components
*  from the direct contributions.  Since the explicit solutions are
*  given equation (2.146) of J, those coefficients are redundant
*  except for testing purposes.  The ANS values are used in subroutine
*  SOURC2.
*
      ANS(1,I)= AN1(I)    +AN2(I)/2.
      ANS(2,I)= AN1(I)/5. +AN2(I)/6.
      ANS(3,I)=           AN2(I)/2.
      ANS(4,I)=-AN1(I)*.75
      ANS(5,I)=-AN1(I)/20.
      ANS(6,I)= AN1(I)*.75
      ANS(7,I)= AN1(I)/4. +AN2(I)/2.
      ANS(8,I)= AN1(I)*.15+AN2(I)/6.
      ANS(9,I)= AN1(I)*.75+AN2(I)/2.
  410 CONTINUE
*
      RETURN
      END
*
*123456789*123456789*123456789*123456789*123456789*123456789*123456789*12
*
*  BETAFO is a test subroutine for the BETA and BETA1 series expansions.
*  BETAFO is called from subroutine TEST.
*
      SUBROUTINE BETAFO(ITABLE)
*
      ITABLE=ITABLE+1
      PRINT910,ITABLE
  910 FORMAT('1','TEST-TABLE ',I2,':  A COMPARISON OF THE ',
     1 'INTRINSIC AND SERIES VALUES FOR BETA AND BETA1'//
     2 ' ',12X,'TAU',13X,'BETA',13X,12X,'BETA1'//
```

```
     3  ' ',15X,2(6X,'INTRINSIC',9X,'SERIES')/)
  920 FORMAT(' '5E15.7)
      DTAU=10.
*
      DO 410 I=1,6
      TAU=DTAU
      DTAU=.1*DTAU
      DO 420 J=1,10
      BETA=(1.-EXP(-TAU))/TAU
      BETA1=1.-BETA
      BETA1S=(TAU/2.)*(1. - (TAU/3.)*(1. - (TAU/4.)
     1               *(1. - (TAU/5.)*(1. - (TAU/6.) ))))
      BETAS=1.-BETA1S
      PRINT920,TAU,BETA,BETAS,BETA1,BETA1S
      TAU=TAU-DTAU
  420 CONTINUE
      PRINT*,'  '
  410 CONTINUE
*
      RETURN
      END
*
*123456789*123456789*123456789*123456789*123456789*123456789*123456789*12
*
*  BETAF1 produces BETA and BETA1=1-BETA, the homologous expansion
*  single-line escape and scatter probabilities.  These quantities
*  discussed in J (Chapter 2 section (a)).  Note that expansions
*  are used for small TAU's (see J, Appendix 1 section (a)).  BETAF1
*  is called by subroutine SOURC1.
*
      SUBROUTINE BETAF1(JLINE,RGGG,BETA,BETA1)
      PARAMETER (NLAM=125,NLINES=61,NSET=11)
      COMMON/PARAM/ANGLE,ANISO(NLINES),ASEMI,BSEMI,ICASE,
     1             ICOEF,ILINES,POWER,PREC,
     2             RGMAX,RGMIN,TAUPH(NLINES),TEMPH,THERM,
     3             TIME,VELPH,WLINE(NLINES),ZEMAX
*
      TAU=TAUPH(JLINE)*(RGMIN/RGGG)**POWER
      IF(TAU .GT. .1054) THEN
          BETA=(1.-EXP(-TAU))/TAU
          BETA1=1.-BETA
        ELSE
          BETA1=(TAU/2.)*(1. - (TAU/3.)*(1. - (TAU/4.)
     1                   *(1. - (TAU/5.)*(1. - (TAU/6.) ))))
          BETA=1.-BETA1
      END IF
*
      RETURN
      END
*
```

```
*123456789*123456789*123456789*123456789*123456789*123456789*123456789*12
*
*  ETAUF produces EXP(-TAU) and 1.-EXP(-TAU) (see J, Chapter 2 section(a)).
*  These quantities are used to calculate the formal Sobolev solution for
*  emergent specific intensity.  The small TAU expansion are given in
*  J (Appendix 1 section (a)).  ETAUF is called from subroutines SPECT1 and
*  SURFBR.
*
      SUBROUTINE ETAUF(JLINE,RGGG,ETAU,ETAU1)
      PARAMETER (NLAM=125,NLINES=61,NSET=11)
      COMMON/PARAM/ANGLE,ANISO(NLINES),ASEMI,BSEMI,ICASE,
     1               ICOEF,ILINES,POWER,PREC,
     2               RGMAX,RGMIN,TAUPH(NLINES),TEMPH,THERM,
     3               TIME,VELPH,WLINE(NLINES),ZEMAX
*
      TAU=TAUPH(JLINE)*(RGMIN/RGGG)**POWER
      ETAU=EXP(-TAU)
      IF(TAU .GT. .1054) THEN
          ETAU1=1.-ETAU
        ELSE
          ETAU1=TAU*(1.-(TAU/2.)*(1.-(TAU/3.)*(1.-(TAU/4.)*
     1               (1.-(TAU/5.) ))))
      END IF
*
      RETURN
      END
*
*123456789*123456789*123456789*123456789*123456789*123456789*123456789*12
*
*  FAMILY reads in the line data files: i. e.,  the FAM files.  These files
*  usually contain the line wavelengths in Angstroms, weighted oscillator
*  strengths (or logarithms of the weighted oscillator strengths), the
*  statistical weights of the lower levels of the lines, the energies in eV
*  of the lower and upper levels of the lines, and the total angular
*  momenta of the lower and upper levels of the lines.  There are some
*  variation in the quantities in the FAM files and these variations are
*  accounted for in the treatment of input data.  These input data are used
*  to calculate the E1-coefficients (J, Chapter 2 section (d)) and the
*  photospheric Sobolev optical depths for the lines (J, Chapter 2
*  section (c)).  The parameters controlling FAMILY are discussed in
*  Input Parameter Descriptions (see the PAR3 namelist).  FAMILY is called
*  from subroutine READIN.
*
*
      SUBROUTINE FAMILY
      PARAMETER (NFAM=10)
      COMMON/FAM/IIFAM,IFAM(NFAM),TAUFAM(NFAM),TAUWAV(NFAM),
     1 WAVEL,WAVEH,ICONT,IBETAP,ICH
      PARAMETER (NLAM=125,NLINES=61,NSET=11)
      COMMON/CONST/CLIGHT,CTA,IFREQ,PI,PITWO,PI2,PLANC1,PLANC2,RADDEG
```

```
      COMMON/PARAM/ANGLE,ANISO(NLINES),ASEMI,BSEMI,ICASE,
     1             ICOEF,ILINES,POWER,PREC,
     2             RGMAX,RGMIN,TAUPH(NLINES),TEMPH,THERM,
     3             TIME,VELPH,WLINE(NLINES),ZEMAX
      COMMON/PSEUD/IPSEUD(NLINES)
      DIMENSION EMPTY(NLINES)
      CHARACTER FAMFIL(NFAM)*4
      DATA FAMFIL/'FAM1','FAM2','FAM3','FAM4','FAM5','FAM6',
     1 'FAM7','FAM8','FAM9',' '/
      DATA BOLTZ/8.61735E-5/,EMPTY/NLINES*0./
*
      ILINE=1
      DO 410 I=1,NFAM
      ILINEB=ILINE
*
*
      IF(IFAM(I) .GT. 0  .AND.  IFAM(I) .LT. 10) THEN
      IFF=IFAM(I)
      OPEN(UNIT=4,FILE=FAMFIL(IFF)//'.DAT',STATUS='OLD')
      READ(4,*) IA,IB,IC
  100 CONTINUE
      READ(4,*,ERR=100,END=110) WLINE(ILINE),GF,ELOW,EHIG,XJLOW,XJHIG
      IF(WLINE(ILINE) .LT. WAVEL-.1  .OR.
     1   WLINE(ILINE) .GT. WAVEH+.1) GO TO 100
      IF(IA .EQ. 1) THEN
          DELTAJ=XJHIG-XJLOW
          CALL HAMILTON(XJLOW,DELTAJ,ANISO(ILINE))
        ELSE IF(IA .EQ. 2) THEN
          ANISO(ILINE)=XJHIG
      END IF
      IF(IB .EQ. 1) THEN
          GGF=GF
         ELSE IF(IB .EQ. 2) THEN
          GGF=GF
         ELSE IF(IB .EQ. 3) THEN
          GGF=(10.**GF)
         ELSE IF(IB .EQ. 4) THEN
          GGF=GF
      END IF
      IF(IC .EQ. 1) THEN
         TAUPH(ILINE)=WLINE(ILINE)*GGF*EXP(-ELOW/(BOLTZ*TEMPH) )
        ELSE IF(IC .EQ. 2) THEN
         TAUPH(ILINE)=GGF
      END IF
      IF(ABS(TAUWAV(I)-WLINE(ILINE)) .LE.  .01) THEN
         TAUNOR=TAUFAM(I)/TAUPH(ILINE)
      END IF
      ILINE=ILINE+1
      GO TO 100
  110 CONTINUE
```

```
*
      DO 420 J=ILINEB,ILINE-1
      TAUPH(J)=TAUPH(J)*TAUNOR
      IPSEUD(J)=0
  420 CONTINUE
      CLOSE(UNIT=4)
*
*
        ELSE IF(IFAM(I) .EQ. 10  .AND.  ICONT .NE. 0) THEN
*           DELWAV=(WAVEH-WAVEL)/REAL(ICONT-1)
          WAVMUL=10.**(  LOG10(WAVEH/WAVEL)/REAL(ICONT-1)  )
          IF(ICH .EQ. 0) THEN
              TAUE=TAUFAM(I)
            ELSE
              TAUE=1./( (POWER-1.)*RGMIN**(POWER-1.)  )
          END IF
*          TAUPS=(POWER-1.)*TAUE*DELWAV*(CLIGHT/VELPH)
          TAUPS=(POWER-1.)*TAUE*(WAVMUL-1.)*(CLIGHT/VELPH)
          WWW=WAVEL
          DO 425 J=ILINEB,ILINEB+ICONT-1
          WLINE(ILINE)=WWW
          ANISO(ILINE)=1.
*          TAUPH(ILINE)=TAUPS/WWW
          TAUPH(ILINE)=TAUPS
          IPSEUD(ILINE)=IBETAP
          WWW=WWW*WAVMUL
*          WWW=WWW+DELWAV
          ILINE=ILINE+1
  425     CONTINUE
*
*
      END IF
  410 CONTINUE
*
      ILINES=ILINE-1
      CALL SORT(NLINES,ILINES,WLINE,ANISO,TAUPH,EMPTY,IPSEUD)
*
      DO 430 I=1,ILINES
      PRINT*,I,WLINE(I),ANISO(I),TAUPH(I),IPSEUD(I)
  430 CONTINUE
*
      RETURN
      END
*
*123456789*123456789*123456789*123456789*123456789*123456789*123456789*12
*
*  GRAL1 is a Simpson's rule integration routine.  It does a PHI integration
*  over the projected face of an ellipsoid (defined by z-axis=B and
*  x-axis=y-axis=A) as seen from a point (C,D) in the single line case,
*  and the PHI integration from 0 to PI in the multi-line case.  The
```

```
*   integrands are the Stokes parameter components of the radiation field.
*   The radiation emitted by the photosphere is taken as
*   unpolarized.  The integrands are symmetric with regard to PHI=0 due
*   to the axial symmetry of the atmosphere model used (J, Chapter 4
*   section (a)).  GRAL1 is called by subroutine SOURC2.
*
      SUBROUTINE GRAL1(ILINE,A,B,C,D,DIRECT,PHIC)
      PARAMETER (NLAM=125,NLINES=61,NSET=11)
      COMMON/ANISOT/AN1(NLINES),AN2(NLINES),ANDIR(14,NLINES),
     1 AN17(NLINES),ANS(9,NLINES)
      COMMON/CONST/CLIGHT,CTA,IFREQ,PI,PITWO,PI2,PLANC1,PLANC2,RADDEG
      COMMON/GRAL/RGRAL1,RGRAL2
      COMMON/PARAM/ANGLE,ANISO(NLINES),ASEMI,BSEMI,ICASE,
     1              ICOEF,ILINES,POWER,PREC,
     2              RGMAX,RGMIN,TAUPH(NLINES),TEMPH,THERM,
     3              TIME,VELPH,WLINE(NLINES),ZEMAX
      COMMON/SET/CCALL(NLINES),DLAM,
     1 FLUX(0:NLAM,NSET,3),IDATA,IFORM,ILAM(NSET),
     1 IISET,ILATE,ILOG,ITRANS,
     2 MODEL,IPUT,ISET,JSET,JSETS,KSET(NSET),POLAR(0:NLAM,NSET,3),
     3 SET(NSET),WLAM(0:NLAM,NSET)
      DIMENSION DIRECT(5),DIR(8,2),DIR1(8),DIR2(8)
*
      CALL XMU1(A,B,C,D,PHIC)
      IF(PHIC .LE. 0.  .AND. ILINE .EQ. 1) THEN
          DO 405 I=1,5
          DIRECT(I)=0.
  405     CONTINUE
          GO TO 200
      END IF
*
      IF(ILATE .EQ. 0) THEN
           CALL GRAL2(ILINE,C,D,0,1,DIR1)
           DO 406 I=1,8
           DIR(I,1)=PI*DIR1(I)
  406      CONTINUE
           GO TO 190
      END IF
*
      IF(ILINE .EQ. 1  .OR.  PHIC .GE. PI) THEN
          ISEC=1
        ELSE
          ISEC=2
      END IF
      DO 407 ISOLID=1,ISEC
      IF(ISOLID .EQ. 1) THEN
          RPHI=RGRAL1*(PHIC/PITWO)
          PHIA=0.
          PHIB=PHIC
        ELSE
```

```
            RPHI=RGRAL1*(PI-PHIC)/PITWO
            PHIA=PHIC
            PHIB=PI
         END IF
         IPHI=INT(RPHI)
         IF(REAL(IPHI) .LT. RPHI) IPHI=IPHI+1
         IF(MOD(IPHI,2) .NE. 0) IPHI=IPHI+1
         DPHI=(PHIB-PHIA)/REAL(IPHI)
*
         CALL GRAL2(ILINE,C,D,PHIA,ISOLID,DIR1)
         PHI=PHIA+DPHI
         CALL GRAL2(ILINE,C,D,PHI,ISOLID,DIR2)
         DO 410 I=1,8
         DIR(I,ISOLID)=DIR1(I)+4.*DIR2(I)
  410    CONTINUE
*
         DO 420 I=2,IPHI-2,2
         PHI=PHI+DPHI
         CALL GRAL2(ILINE,C,D,PHI,ISOLID,DIR1)
         PHI=PHI+DPHI
         CALL GRAL2(ILINE,C,D,PHI,ISOLID,DIR2)
         DO 430 J=1,8
         DIR(J,ISOLID)=DIR(J,ISOLID)+2.*DIR1(J)+4.*DIR2(J)
  430    CONTINUE
  420    CONTINUE
*
         CALL GRAL2(ILINE,C,D,PHIB,ISOLID,DIR1)
         DPHI3=DPHI/3.
         DO 440 I=1,8
         DIR(I,ISOLID)=DPHI3*(DIR(I,ISOLID)+DIR1(I))
  440    CONTINUE
*
  407    CONTINUE
*
         IF(ISEC .EQ. 2) THEN
            DO 450 I=1,8
            DIR(I,1)=DIR(I,1)+DIR(I,2)
  450       CONTINUE
         END IF
*
  190    CONTINUE
*
         DIRECT(1)=ANDIR(1,ILINE)*DIR(1,1)+ANDIR(2,ILINE)*DIR(2,1)
        1                               +ANDIR(3,ILINE)*DIR(3,1)
         DIRECT(2)=ANDIR(4,ILINE)*DIR(1,1)+ANDIR(5,ILINE)*DIR(2,1)
        1                               +ANDIR(6,ILINE)*DIR(3,1)
         DIRECT(3)=ANDIR(7,ILINE)*DIR(4,1)+ANDIR(8,ILINE)*DIR(5,1)
         DIRECT(4)=ANDIR(9,ILINE)*DIR(6,1)+ANDIR(10,ILINE)*DIR(7,1)
        1                               +ANDIR(11,ILINE)*DIR(8,1)
         DIRECT(5)=ANDIR(12,ILINE)*DIR(1,1)+ANDIR(13,ILINE)*DIR(2,1)
```

```
     1                                       +ANDIR(14,ILINE)*DIR(3,1)
*
  200 CONTINUE
      RETURN
      END
*
*123456789*123456789*123456789*123456789*123456789*123456789*123456789*12
*
*  GRAL2 is a integration routine.  It does a XMU integration
*  over the projected face of an ellipsoid (defined by z-axis=B and
*  x-axis=y-axis=A) as seen from a point (C,D) in the single-line case
*  and the XMU integration from -1 to 1 in the multi-line case.  Note
*  that if
*
*       ICASE=1 and ILINE=1 :  -the integration is analytic.
*                              -the integrands are independant of XMU.
*                              -the total specific intensity is
*                               frequency-independent and is set to 1.
*
*       else:       -the integration is by Simpson's rule.
*                   -the specific intensity is Planckian and exhibits
*                     limb-darkening owing to the Doppler shift.
*
*  GRAL2 is called by GRAL1.
*
      SUBROUTINE GRAL2(ILINE,C,D,PHI,ISOL,GRAND)
      COMMON/GRAL/RGRAL1,RGRAL2
      PARAMETER (NLAM=125,NLINES=61,NSET=11)
      COMMON/PARAM/ANGLE,ANISO(NLINES),ASEMI,BSEMI,ICASE,
     1             ICOEF,ILINES,POWER,PREC,
     2             RGMAX,RGMIN,TAUPH(NLINES),TEMPH,THERM,
     3             TIME,VELPH,WLINE(NLINES),ZEMAX
      DIMENSION GRAND(8),GRAN1(8),GRAN2(8),GRAN3(8)
*
      DO 405 I=1,8
      GRAND(I)=0.
  405 CONTINUE
      IF(ISOL .EQ. 1) THEN
          CALL XMU2(PHI,XMUL,XMUH)
*       PRINT*,'GRAL2 ',C,D,PHI,XMUL,XMUH
          XMUDIF=XMUH-XMUL
          IF(XMUDIF .LE. 0.  .AND.  ILINE .EQ. 1) GO TO 200
      END IF
*
*  If ICASE is 1 and ILINE is 1 then the integration is over
*  a bare unpolarized photosphere and analytic results are available
*  for the GRAND constants which apart from coefficients are
*  the d_i's of J (equation (2.131)).
*
      IF(ICASE .EQ. 1  .AND.  ILINE .EQ. 1) THEN
```

```
          FI2=.5
          GRAND(1)=FI2*(  XMUH-XMUL  )
          GRAND(2)=FI2*(  XMUH-XMUL  )
          GRAND(3)=FI2*(  XMUH**3-XMUL**3  )/3.
          GRAND(4)=FI2*COS(PHI)*(  MAX(0.,  1.-XMUL**2  )**1.5 -
     +                             MAX(0.,  1.-XMUH**2  )**1.5  )/3.
          GRAND(5)=0.
          GRAND(6)=GRAND(3)*COS(2.*PHI)
          GRAND(7)=GRAND(2)*COS(2.*PHI)
          GRAND(8)=0.
          GO TO 200
      END IF
*
      IF(ILINE .EQ. 1) THEN
          ISECA=2
          ISECB=2
        ELSE IF(ISOL .EQ. 1) THEN
          IF(XMUH .GE. 1) THEN
              ISECA=1
              ISECB=2
            ELSE
              ISECA=1
              ISECB=3
          END IF
        ELSE
          ISECA=1
          ISECB=1
          XMUL=1.
      END IF
      DO 407 ISOLID=ISECA,ISECB
      IF(ISOLID .EQ. 1) THEN
          RXMU=RGRAL2*(XMUL-(-1.))/2
          XMULL=-1.
          XMUHH=XMUL
        ELSE IF(ISOLID .EQ. 2) THEN
          RXMU=RGRAL2*(XMUH-XMUL)/2.
          XMULL=XMUL
          XMUHH=XMUH
        ELSE
          RXMU=RGRAL2*(1.-XMUH)/2.
          XMULL=XMUH
          XMUHH=1.
      END IF
      IF(RXMU .EQ. 0.) GO TO 407
      IXMU=INT(RXMU)
      IF(REAL(IXMU) .LT. RXMU) IXMU=IXMU+1
      IF(MOD(IXMU,2) .NE. 0) IXMU=IXMU+1
      DXMU=(XMUHH-XMULL)/REAL(IXMU)
*
      CALL GRAL3(ILINE,C,D,PHI,XMULL,ISOLID,GRAN1)
```

```
      XMU=XMULL+DXMU
      CALL GRAL3(ILINE,C,D,PHI,XMU,ISOLID,GRAN2)
      DO 410 I=1,8
      GRAN3(I)=GRAN1(I)+4.*GRAN2(I)
  410 CONTINUE
*
      DO 420 I=2,IXMU-2,2
      XMU=XMU+DXMU
      CALL GRAL3(ILINE,C,D,PHI,XMU,ISOLID,GRAN1)
      XMU=XMU+DXMU
      CALL GRAL3(ILINE,C,D,PHI,XMU,ISOLID,GRAN2)
      DO 430 J=1,8
      GRAN3(J)=GRAN3(J)+2.*GRAN1(J)+4.*GRAN2(J)
  430 CONTINUE
  420 CONTINUE
*
      CALL GRAL3(ILINE,C,D,PHI,XMUHH,ISOLID,GRAN1)
      DXMU3=DXMU/3.
      DO 440 I=1,8
      GRAN3(I)=DXMU3*(GRAN3(I)+GRAN1(I))
      GRAND(I)=GRAND(I)+GRAN3(I)
  440 CONTINUE
*
  407 CONTINUE
*
      GRAND(4)=GRAND(4)*COS(PHI)
      GRAND(5)=GRAND(5)*SIN(PHI)
      GRAND(6)=GRAND(6)*COS(2.*PHI)
      GRAND(7)=GRAND(7)*COS(2.*PHI)
      GRAND(8)=GRAND(8)*SIN(2.*PHI)
*
  200 CONTINUE
      RETURN
      END
*
*123456789*123456789*123456789*123456789*123456789*123456789*123456789*12
*
*  GRAL3 prepares the integrand values for GRAL1 and GRAL2.  It
*  provides the Stokes parameter specific intensity components that
*  converge on the resonance point for which the source function is
*  being evaluated (see J, equation (2.149)).  The direct and
*  diffuse contributions are calculated, and these are multiplied by
*  the appropriate factors from the the Rayleigh-phase matrix (J,
*  equation (2.131)).  GRAL3 is called from GRAL2.
*
      SUBROUTINE GRAL3(ILINE,C,D,PHI,XMU,ISOLID,GRAN)
      PARAMETER (NLAM=125,NLINES=61,NSET=11)
      COMMON/PARAM/ANGLE,ANISO(NLINES),ASEMI,BSEMI,ICASE,
     1             ICOEF,ILINES,POWER,PREC,
     2             RGMAX,RGMIN,TAUPH(NLINES),TEMPH,THERM,
```

```
     3             TIME,VELPH,WLINE(NLINES),ZEMAX
      COMMON/SOURC/ASQ,BSQ,THETA,ALP,ALPSQ,BET,BETSQ,
     1 CON1,CON2,CON3,CON4,BPRI,GMAXSQ,GMINSQ,
     2 XXLIMB,XXCORE,XXOCUL,XXCUT,QC,XTC
      DIMENSION GRAN(8),SMENTS(3)
*
      XMUSQ=XMU**2
      SINE=SQRT(MAX(0.,  1.-XMUSQ  ))
      XN1=SINE*COS(PHI)
      XN2=SINE*SIN(PHI)
      AAA=   XN1**2/ASQ+XN2**2/ASQ+XMUSQ/BSQ
      BBB=2.*(XN1*C/ASQ      +     XMU*D/BSQ)
      IF(ISOLID .EQ. 2) THEN
          CCC=     C**2/ASQ  -   GMINSQ  +  D**2/BSQ
          XT=ABS(  (-BBB+SQRT(MAX(0.,  BBB**2-4.*AAA*CCC))  )
     1                         /(2.*AAA)  )
        ELSE
          CCC=     C**2/ASQ  -   GMAXSQ  +  D**2/BSQ
          XT=ABS(  (-BBB-SQRT(MAX(0.,  BBB**2-4.*AAA*CCC))  )
     1                         /(2.*AAA)  )
      END IF
*
      EXPTAU=1.
      DLL=0.
      DRR=0.
      DUU=0.
      DO 410 JLINE=ILINE-1,1,-1
      XR=(1-WLINE(JLINE)/WLINE(ILINE) )/QC
      IF(XR .GE. XT) GO TO 200
      DELX=XR*XN1
      DELY=XR*XN2
      DELZ=XR*XMU
      X1=C-DELX
      Y1=-DELY
      Z1=D-DELZ
      XMU1=XMU
      DELR=SQRT(DELX**2+DELY**2)
      RHO1=SQRT(X1**2+Y1**2)
      IF(DELR .EQ. 0.) THEN
          PHI1=PHI
        ELSE IF(RHO1 .NE. 0.) THEN
          ARGUE=MAX(-1.,MIN(1.,(X1*DELX+Y1*DELY)/(DELR*RHO1) ))
          PHI1=ACOS(ARGUE)
        ELSE
          PHI1=0.
      END IF
      CALL SOURC3(JLINE,1,X1,Y1,Z1,XMU1,PHI1,SCOEF,SMENTS)
      RGGG=SQRT(X1**2/ASQ + Y1**2/ASQ + Z1**2/BSQ)
      CALL ETAUF(JLINE,RGGG,ETAU,ETAU1)
      DLL=DLL+SMENTS(1)*ETAU1*EXPTAU
```

```
      DRR=DRR+SMENTS(2)*ETAU1*EXPTAU
      DUU=DUU+SMENTS(3)*ETAU1*EXPTAU
      EXPTAU=EXPTAU*ETAU
  410 CONTINUE
  200 CONTINUE
*
      IF(ISOLID .EQ. 2) THEN
          IF(ICASE .EQ. 1) THEN
              FI2=.5
            ELSE
              CALL PLANCF(WLINE(ILINE),QC*XT,FI2)
          END IF
          DLL=DLL+FI2*EXPTAU
          DRR=DRR+FI2*EXPTAU
      END IF
*
*      PRINT*,'GRAL3 ',XT,DLL,DRR,DUU
      GRAN(1)=DLL
      GRAN(2)=DRR
      GRAN(3)=XMUSQ*DLL
      GRAN(4)=XMU*SINE*DLL
      GRAN(5)=SINE*DUU
      GRAN(6)=XMUSQ*DLL
      GRAN(7)=DRR
      GRAN(8)=XMU*DUU
*
      RETURN
      END
*
*123456789*123456789*123456789*123456789*123456789*123456789*123456789*12
*
*  HAMILTON calculates the E1-coefficient of a line (see J, Table 2.1).
*  HAMILTON is called from FAMILY.
*
      SUBROUTINE HAMILTON(XJLOW,DELTAJ,E1)
*
      IF(ABS(DELTAJ-1.) .LT. .1) THEN
           E1=(2.*XJLOW+5.)*(XJLOW+2.)
     1      /10./(XJLOW+1.)/(2.*XJLOW+1.)
        ELSE IF(ABS(DELTAJ) .LT. .1) THEN
           E1=(2.*XJLOW-1.)*(2.*XJLOW+3.)
     1       /10./XJLOW/(XJLOW+1.)
        ELSE
           E1=(2.*XJLOW-3.)*(XJLOW-1.)
     1        /10./XJLOW/(2.*XJLOW+1.)
      END IF
*
      RETURN
      END
*
```

```
*123456789*123456789*123456789*123456789*123456789*123456789*123456789*12
*
*  LIN3 takes an augmented 3*4 matrix and solves for the coefficients.
*  This routine is used to calculate the source function components from
*  equations (2.139) of J.  Since explicit expressions are given for
*  the source functions this routine is redundant and is used only for
*  testing purposes.  LIN3 is called from SOURC2.
*
      SUBROUTINE LIN3(XMAT,ACC,COEF)
      DIMENSION X(3),XMAT(3,4),COEF(3)
*
      X(1)=XMAT(1,1)*XMAT(2,2)-XMAT(1,2)*XMAT(2,1)
      X(2)=XMAT(1,1)*XMAT(3,4)-XMAT(1,4)*XMAT(3,1)
      X(3)=XMAT(1,1)*XMAT(2,4)-XMAT(1,4)*XMAT(2,1)
      X(4)=XMAT(1,1)*XMAT(3,2)-XMAT(1,2)*XMAT(3,1)
      X(5)=XMAT(1,1)*XMAT(3,3)-XMAT(1,3)*XMAT(3,1)
      X(6)=XMAT(1,1)*XMAT(2,3)-XMAT(1,3)*XMAT(2,1)
*
      COEF(3)=(X(1)*X(2)-X(3)*X(4))/(X(1)*X(5)-X(6)*X(4))
      COEF(2)=(X(3)-X(6)*COEF(3))/X(1)
      COEF(1)=(XMAT(1,4)-XMAT(1,2)*COEF(2)-XMAT(1,3)*COEF(3))/XMAT(1,1)
*
      ACC=ABS(  (COEF(1)*XMAT(3,1)+COEF(2)*XMAT(3,2)+
     +             COEF(3)*XMAT(3,3)-       XMAT(3,4))/XMAT(3,4)  )
*
      RETURN
      END
*
*123456789*123456789*123456789*123456789*123456789*123456789*123456789*12
*
*  OUTPUT gives the system listing of the spectra and, if desired, the
*  source function component table. It also creates a S7//MODEL//.OUT
*  file containing the spectra data.  A plot file called PLOTAPE.DAT is
*  also created.  The IPUT parameter controls the output (see Input
*  Parameter Descriptions).  OUTPUT is admittedly something of a mess
*  and needs some re-coding.  OUTPUT is called from subroutines READIN
*  and SOURC1.
*
      SUBROUTINE OUTPUT(IPRINT)
      COMMON/CONST/CLIGHT,CTA,IFREQ,PI,PITWO,PI2,PLANC1,PLANC2,RADDEG
      PARAMETER (NLAM=125,NLINES=61,NSET=11)
      COMMON/PARAM/ANGLE,ANISO(NLINES),ASEMI,BSEMI,ICASE,
     1              ICOEF,ILINES,POWER,PREC,
     2              RGMAX,RGMIN,TAUPH(NLINES),TEMPH,THERM,
     3              TIME,VELPH,WLINE(NLINES),ZEMAX
      CHARACTER MODEL*2
      COMMON/SET/CCALL(NLINES),DLAM,
     1 FLUX(0:NLAM,NSET,3),IDATA,IFORM,ILAM(NSET),
     1 IISET,ILATE,ILOG,ITRANS,
     2 MODEL,IPUT,ISET,JSET,JSETS,KSET(NSET),POLAR(0:NLAM,NSET,3),
```

```
     3 SET(NSET),WLAM(0:NLAM,NSET)
      PARAMETER (NCOEF=5,ZPREC=.10,NRG=INT(6./ZPREC)+1,
     1 NZETA=INT(4./ZPREC)+2)
      COMMON/SOURCE/DRGLOG,DZETA,IRG,IRG1,IZETA,IZETA1,
     1 RG(0:NRG),RGH,RGL,SOURC(NCOEF,0:NRG,0:NZETA,NLINES),ZETA(0:NZETA)
      DIMENSION THETA(0:NZETA),ZET(0:NZETA)
      PARAMETER (NSTAT=5*NLINES)
      DIMENSION FMAX(NSTAT,2),FMIN(NSTAT,2),PMAX(NSTAT,2),
     1 PMIN(NSTAT,2),WORK(1500)
      DIMENSION CALEXT(NSET),FXMAX(NSET),FXMIN(NSET),
     1 POLMAX(NSET),POLMIN(NSET),IEMPTY(NSET)
      DIMENSION DATX(11,2),DATY(11,2),IDAT(2)
      CHARACTER CHARAC(14)*10,TITLE(3)*50
      DATA CHARAC/'ANGLE','ANISO','ASPH',
     1             'ICASE','ILINES','POWER','PREC',
     2             'RGMAX','TAUPH','TEMPH','THERM','TIME',
     3             'VELPH','WLINE'/
      DATA JTABLE/0/
      DATA IDAT/11,11/,
     1 DATX/0.,.1,.2,.3,.4,.5,.6,.7,.8,.9,1.0,
     2      0.,.1,.2,.3,.4,.5,.6,.7,.8,.9,1.0/,
     3 DATY/0.,-.0016 ,-.0032 ,-.0040 ,-.0065 ,-.0081 ,-.0129 ,-.0177 ,
     4          -.0258 ,-.0452 ,-.117  ,
     3      0.,.00098,.00196,.00277,.00375,.00465,.00554,.00636,
     4          .00701,.0075 ,.0077/
      NAMELIST/PAR/ANGLE,ANISO       ,ASEMI,BSEMI,ICOEF,
     1             ICASE,ILINES,POWER,PREC,
     2             RGMAX,RGMIN,TAUPH       ,TEMPH,THERM,
     3             TIME,VELPH,WLINE        ,ZEMAX
*
      GO TO (110,120,130),IPRINT
*
  110 CONTINUE
      IF(ISET .GT. 0) THEN
          PRINT910,JSET,CHARAC(ISET)
        ELSE
          PRINT920,JSET
      END IF
      PRINT PAR
  910 FORMAT('1','PARAMETER(JSET=',I2,')=',A10/)
  920 FORMAT('1','PARAMETER(JSET=',I2,')'/)
      JCOEF=MIN(ICOEF,8)
      DO 410 I=0,IZETA-1
      THETA(I)=RADDEG*ATAN( (ASEMI/BSEMI)*TAN(ZETA(I)) )
      ZET(I)=RADDEG*ZETA(I)
  410 CONTINUE
      THETA(IZETA)=90.
      ZET(IZETA)=90.
*
      JTABLE=JTABLE+1
```

```
      PRINT930,JTABLE
  930 FORMAT(//' ','TABLE ',I2,'.  THE SOURCE FUNCTION ',
     1 'COEFFICIENTS')
  940 FORMAT(//' ','FOR ILINE=',I2,5X,'ZETA=',F10.7,5X,'THETA=',
     1 F10.7//' ',13X,'RG',8(13X,I2)/)
  950 FORMAT(' ',9E15.7)
*
      DO 420 I=1,ILINES
      DO 430 J=0,IZETA
      PRINT940,I,ZET(J),THETA(J),(L,L=1,JCOEF)
      DO 440 K=0,IRG
      PRINT950,RG(K),(SOURC(L,K,J,I),L=1,JCOEF)
  440 CONTINUE
  430 CONTINUE
  420 CONTINUE
*
      GO TO 200
*
  120 CONTINUE
      IF(IPUT .GE. 3) THEN
          IF(ISET .GT. 0) THEN
              PRINT910,JSET,CHARAC(ISET)
            ELSE
              PRINT920,JSET
          END IF
          PRINT PAR
      END IF
      JTABLE=JTABLE+1
      PRINT960,JTABLE
  960 FORMAT(///' ','TABLE ',I2,'.  THE LOGARITHMIC FLUX SPECTRUM',
     1                               ' AND POLARIZATION SPECTRUM',//
     2 ' ',4X,'I',5X,'WAVELENGTH',6X,'LOG(FLUX)',3X,'POLARIZATION',
     3 1X,'LOG(LIMB FLUX)',5X,'LIMB POLAR',
     4 1X,'LOG(CORE FLUX)',5X,'CORE POLAR'/)
  970 FORMAT(' ',I5,F15.2,6E15.7)
*
      PRINT*,'THIS IS DLAM AND IT IS NOT ZERO ',DLAM
*
      DLAMA1=2.*DLAM
      DLAMA2=DLAMA1*DLAM
      IFMAX=0
      IFMIN=0
      IPMAX=0
      IPMIN=0
      DO 445 I=1,NSTAT
      DO 446 J=1,2
      FMIN(I,J)=0.
      FMAX(I,J)=0.
      PMIN(I,J)=0.
      PMAX(I,J)=0.
```

```
  446 CONTINUE
  445 CONTINUE
      FSUM=0.
      DO 450 I=0,ILAM(JSET)
      PRINT970,I,WLAM(I,JSET),FLUX(I,JSET,3),POLAR(I,JSET,3),
     1 FLUX(I,JSET,2),POLAR(I,JSET,2),FLUX(I,JSET,1),POLAR(I,JSET,1)
      IF(ILOG .EQ. 1) THEN
          FSUM=FSUM+SIMWT(0,I,ILAM(JSET))*10**FLUX(I,JSET,3)
        ELSE
          FSUM=FSUM+SIMWT(0,I,ILAM(JSET))*FLUX(I,JSET,3)
      END IF
      IF(I .GE. 2) THEN
          DEL01=FLUX(I-1,JSET,3)-FLUX(I-2,JSET,3)
          DEL12=FLUX(I,JSET,3)-FLUX(I-1,JSET,3)
          IF(DEL01*DEL12 .LT. 0.) THEN
            A2=(    FLUX(I-2,JSET,3)-2.*FLUX(I-1,JSET,3)+
     1                FLUX(I,JSET,3)  )      /DLAMA2
            A1=(-3.*FLUX(I-2,JSET,3)+4.*FLUX(I-1,JSET,3)-
     1                FLUX(I,JSET,3)  )      /DLAMA1
            IF(A2 .LT. 0.) THEN
                IFMAX=IFMAX+1
                FMAX(IFMAX,1)=-A1/(2.*A2)  +  WLAM(I-2,JSET)
                FMAX(IFMAX,2)=-.25*(A1**2)/A2+FLUX(I-2,JSET,3)
              ELSE
                IFMIN=IFMIN+1
                FMIN(IFMIN,1)=-A1/(2.*A2)  +  WLAM(I-2,JSET)
                FMIN(IFMIN,2)=-.25*(A1**2)/A2+FLUX(I-2,JSET,3)
             END IF
          END IF
          DEL01=POLAR(I-1,JSET,3)-POLAR(I-2,JSET,3)
          DEL12=POLAR(I,JSET,3)-POLAR(I-1,JSET,3)
          IF(DEL01*DEL12 .LT. 0.) THEN
            A2=(    POLAR(I-2,JSET,3)-2.*POLAR(I-1,JSET,3)+
     1                POLAR(I,JSET,3)  )            /DLAMA2
            A1=(-3.*POLAR(I-2,JSET,3)+4.*POLAR(I-1,JSET,3)-
     1                POLAR(I,JSET,3)  )            /DLAMA1
            IF(A2 .LT. 0.) THEN
                IPMAX=IPMAX+1
                PMAX(IPMAX,1)=-A1/(2.*A2)  +  WLAM(I-2,JSET)
                PMAX(IPMAX,2)=-.25*(A1**2)/A2+POLAR(I-2,JSET,3)
              ELSE
                IPMIN=IPMIN+1
                PMIN(IPMIN,1)=-A1/(2.*A2)  +  WLAM(I-2,JSET)
                PMIN(IPMIN,2)=-.25*(A1**2)/A2+POLAR(I-2,JSET,3)
             END IF
          END IF
      END IF
  450 CONTINUE
      PRINT980
  980 FORMAT(///' ','THE STATIONARY POINTS FOR FLUX AND POLARIZATION'//
```

```
     1 ' ',4X,'I',5X,'FLUX MINIMA',14X,5X,'FLUX MAXIMA',14X,
     2            5X,'POLARIZATION MINIMA',6X,5X,'POLARIZATION MAXIMA'//
     3 ' ',5X,2(5X,'WAVELENGTH',4X,'LOG10(FLUX)'),
     4        2(5X,'WAVELENGTH',3X,'POLARIZATION') )
  990 FORMAT(' ',I5,8E15.7)
      FXMIN(JSET)=MIN(  FLUX(0,JSET,3),FLUX(ILAM(JSET),JSET,3)  )
      FXMAX(JSET)=MAX(  FLUX(0,JSET,3),FLUX(ILAM(JSET),JSET,3)  )
      POLMIN(JSET)=MIN(  POLAR(0,JSET,3),POLAR(ILAM(JSET),JSET,3)  )
      POLMAX(JSET)=MAX(  POLAR(0,JSET,3),POLAR(ILAM(JSET),JSET,3)  )
      DO 453 I=1,MAX(IFMIN,IFMAX,IPMIN,IPMAX)
      PRINT990,I,FMIN(I,1),FMIN(I,2),FMAX(I,1),FMAX(I,2),
     1 PMIN(I,1),PMIN(I,2),PMAX(I,1),PMAX(I,2)
      FXMIN(JSET)=MIN(FXMIN(JSET),FMIN(  MIN(I,IFMIN)  ,2))
      FXMAX(JSET)=MAX(FXMAX(JSET),FMAX(  MIN(I,IFMAX)  ,2))
      POLMIN(JSET)=MIN(POLMIN(JSET),PMIN(  MIN(I,IPMIN)  ,2))
      POLMAX(JSET)=MAX(POLMAX(JSET),PMAX(  MIN(I,IPMAX)  ,2))
  453 CONTINUE
*
      PRINT992
  992 FORMAT(///' ','THE McCALL POLARIZATION PEAKS'//
     1 ' ','ILINE',5X,'WAVELENGTH',11X,'PEAK'/)
  993 FORMAT(' 'I5,2E15.7)
      CALEXT(JSET)=0.
      DO 454 I=1,ILINES
      PRINT993,I,WLINE(I),CCALL(I+ (JSET-1)*IISET  )
      IF(ASEMI .LE. BSEMI) THEN
         CALEXT(JSET)=MAX(CALEXT(JSET),
     1                   CCALL(I+ (JSET-1)*IISET  )  )
       ELSE
         CALEXT(JSET)=MIN(CALEXT(JSET),
     1                   CCALL(I+ (JSET-1)*IISET  )  )
      END IF
  454 CONTINUE
*
      PRINT*,' '
      PRINT*,'THE MEAN FLUX IS ',(DLAM/3.)*FSUM
     1 /(  WLAM(ILAM(JSET),JSET)-WLAM(0,JSET)  )
*
      GO TO 200
*
  130 CONTINUE
*       IF(ISET .NE. 7) THEN
         OPEN(UNIT=3,FILE='S7'//MODEL//'.OUT;',STATUS='NEW')
         REWIND3
         WRITE(3,*) IFORM,ILATE,ISET,JSETS
         WRITE(3,996) MODEL
         DO 456 JSET=1,JSETS
         WRITE(3,994) ILAM(JSET),CALEXT(JSET),POLMAX(JSET),
     1    POLMIN(JSET),SET(JSET)
         DO 457 I=0,ILAM(JSET)
```

```
          WRITE(3,995) I,WLAM(I,JSET),FLUX(I,JSET,3),FLUX(I,JSET,2),
     1   FLUX(I,JSET,1),POLAR(I,JSET,3),POLAR(I,JSET,2),POLAR(I,JSET,1)
 457      CONTINUE
 456      CONTINUE
 994      FORMAT(' ',I5,4E16.8)
 995      FORMAT(' ',I5,7E16.8)
 996      FORMAT(A2)
          CLOSE(UNIT=3)
*      END IF
        XMIN=FXMIN(1)
        XMAX=FXMAX(1)
        YMIN=POLMIN(1)
        YMAX=POLMAX(1)
        DO 458 I=2,JSETS
        XMIN=MIN(XMIN,FXMIN(I))
        XMAX=MAX(XMAX,FXMAX(I))
        YMIN=MIN(YMIN,POLMIN(I))
        YMAX=MAX(YMAX,POLMAX(I))
 458    CONTINUE
        XDIFF=.03*(XMAX-XMIN)
        XMIN=XMIN-XDIFF
        XMAX=XMAX+XDIFF
        YDIFF=.03*(YMAX-YMIN)
        YMIN=YMIN-YDIFF
        YMAX=YMAX+YDIFF
*
        CALL SIMSTART(.FALSE.,.FALSE.)
*        IF(JSETS .GT. 4  .AND.  ILOG .EQ. 1) CALL SIMSAME(.TRUE.)
        CALL NEWPEN(3)
        CALL ROTATE(1)
        CALL SIMTRAN(.25,.25)
        CALL SIMSIZE(4.75,7.5)
*
        IF(MODEL(1:1) .NE. '0') THEN
            IM=1
          ELSE
            IM=2
        END IF
*
        IF(ILOG .EQ. 1) THEN
            TITLE(1)='FIG. '//MODEL(IM:2)//
     1       'Ai.  LOGARITHMIC CORE FLUX SPECTRUM'
            TITLE(2)='FIG. '//MODEL(IM:2)//
     1       'Aii.  LOGARITHMIC LIMB FLUX SPECTRUM'
            TITLE(3)='FIG. '//MODEL(IM:2)//
     1       'Aiii.  LOGARITHMIC FLUX SPECTRUM'
          ELSE
            TITLE(1)='FIG. '//MODEL(IM:2)//'Ai.  CORE FLUX SPECTRUM'
            TITLE(2)='FIG. '//MODEL(IM:2)//'Aii.  LIMB FLUX SPECTRUM'
            TITLE(3)='FIG. '//MODEL(IM:2)//'Aiii.  FLUX SPECTRUM'
```

```
      END IF
      CALL SIMANN(.TRUE.)
      XLOW=MIN(WLAM(0,1),WLAM(0,JSETS))
      XHIGH=MAX(WLAM(ILAM(1),1)  ,  WLAM(ILAM(JSETS),JSETS)  )
      CALL SIMXRNG(XLOW,XHIGH)
*      CALL SIMXRNG(WLAM(0,1),WLAM(ILAM(1),1))
      CALL SIMYRNG(XMIN,XMAX)
      DO 459 I=1,3
      CALL SIMKRNG(.TRUE.)
*     CALL SIMPLOT(WLAM(0,1),FLUX(0,1,I),1+NLAM,1+ILAM(1),JSETS,WORK)
      CALL SIMPLOT(WLAM(0,1),FLUX(0,1,I),1+NLAM,1+ILAM(1),1,WORK)
      DO 461 JSET=2,JSETS
      CALL SIMCURV(WLAM(0,JSET),FLUX(0,JSET,I),
     1 1+ILAM(JSET),WORK)
  461 CONTINUE
      CALL SIMXLAB('WAVELENGTH (ANGSTROM)')
      IF(ILOG .EQ. 1) THEN
         CALL SIMYLAB('LOG10(FLUX)')
        ELSE
         CALL SIMYLAB('FLUX')
      END IF
      CALL SIMTITL(TITLE(I))
  459 CONTINUE
*
      TITLE(1)='FIG. '//MODEL(IM:2)//'Bi.  CORE POLARIZATION SPECTRUM'
      TITLE(2)='FIG. '//MODEL(IM:2)//'Bii.  LIMB POLARIZATION SPECTRUM'
      TITLE(3)='FIG. '//MODEL(IM:2)//'Biii.  POLARIZATION SRECTRUM'
*      IF(JSETS .GT. 4) CALL SIMSAME(.TRUE.)
      CALL SIMANN(.TRUE.)
*      CALL SIMXRNG(WLAM(0,1),WLAM(ILAM(1),1))
      CALL SIMXRNG(XLOW,XHIGH)
      CALL SIMYRNG(YMIN,YMAX)
      DO 468 I=1,3
      CALL SIMKRNG(.TRUE.)
*      CALL SIMPLOT(WLAM(0,1),POLAR(0,1,I),1+NLAM,1+ILAM(1),JSETS,WORK)
      CALL SIMPLOT(WLAM(0,1),POLAR(0,1,I),1+NLAM,1+ILAM(1),1,WORK)
      DO 464 JSET=2,JSETS
      CALL SIMCURV(WLAM(0,JSET),POLAR(0,JSET,I),
     1 1+ILAM(JSET),WORK)
  464 CONTINUE
      CALL SIMXLAB('WAVELENGTH (ANGSTROM)')
      CALL SIMYLAB('POLARIZATION')
      CALL SIMTITL(TITLE(I))
  468 CONTINUE
*
      IF(JSETS .LE. 3) GO TO 200
      CALL SORT(NSET,JSETS,SET,POLMAX,POLMIN,CALEXT,IEMPTY)
      IF(ABS(SET(JSETS)-1.) .GE. .1) THEN
         SETL=SET(JSETS)
        ELSE
```

```
            SETL=1.
        END IF
        CALL SIMANN(.TRUE.)
        CALL SIMXRNG(SET(1),SETL)
        CALL SIMYRNG(YMIN,YMAX)
        CALL SIMPLOT(SET,POLMAX,NSET,JSETS,1,WORK)
        CALL SIMDAT(SET,POLMAX,JSETS)
        CALL SIMCURV(SET,POLMIN,JSETS,WORK)
        CALL SIMDAT(SET,POLMIN,JSETS)
        CALL SIMCURV(SET,CALEXT,JSETS,WORK)
        CALL SIMDAT(SET,CALEXT,JSETS)
        IF(IDATA .EQ. 1) THEN
            CALL SIMCURV(DATX(1,1),DATY(1,1),IDAT(1),WORK)
            CALL SIMCURV(DATX(1,2),DATY(1,2),IDAT(2),WORK)
        END IF
        CALL SIMXLAB(CHARAC(ISET))
        CALL SIMYLAB('POLARIZATION')
        TITLE(1)='FIG. '//MODEL(IM:2)//'C.  POLARIZATION EXTREMA'
        CALL SIMTITL(TITLE(1))
        CALL SIMEND
*
    200 CONTINUE
        RETURN
        END
*
*123456789*123456789*123456789*123456789*123456789*123456789*123456789*12
*
*  PLANCF calculates the Planck black-body specific intensity for a
*  given wavelength, and a given Doppler shift parameter
*  DELTA=(velocity/CLIGHT).  PLANCF is called by subroutines GRAL3,
*  SOURC1, SPECT1, and SURFBR.
*
        SUBROUTINE PLANCF(WAVELN,DELTA,FI2)
        COMMON/CONST/CLIGHT,CTA,IFREQ,PI,PITWO,PI2,PLANC1,PLANC2,RADDEG
        PARAMETER (NLAM=125,NLINES=61,NSET=11)
        COMMON/PARAM/ANGLE,ANISO(NLINES),ASEMI,BSEMI,ICASE,
       1             ICOEF,ILINES,POWER,PREC,
       2             RGMAX,RGMIN,TAUPH(NLINES),TEMPH,THERM,
       3             TIME,VELPH,WLINE(NLINES),ZEMAX
*
*        DELTA=0.
        WNU=CLIGHT*CTA/( WAVELN * (1.-DELTA)  )
*        PRINT*,WNU,CLIGHT,CTA,WAVELN,DELTA
*        PRINT*,PLANC1,WNU/CLIGHT,PLANC2,PLANC2*WNU/TEMPH
        FI2=.5*PLANC1*((WNU/CLIGHT)**3)/(EXP(PLANC2*WNU/TEMPH) - 1.)
        IF(IFREQ .NE. 1) FI2=FI2*(WNU**2/CLIGHT)
*
        RETURN
        END
*
```

```
*123456789*123456789*123456789*123456789*123456789*123456789*123456789*12
*
*  PRECIS sets out the gridding for the discretized source function, and
*  decides the number of increments to be used in the GRAL1 and GRAL2
*  integrations. These choices are made according to a prescription
*  (see private Sobolev notes of D.J. Jeffery p. 111), and using the
*  PREC variable.  The PREC variable is just equal to an element of
*  the PRE input array (see Input Parameter Descriptions).  PRECIS is
*  called from subroutine READIN.
*
      SUBROUTINE PRECIS
      COMMON/CONST/CLIGHT,CTA,IFREQ,PI,PITWO,PI2,PLANC1,PLANC2,RADDEG
      COMMON/GRAL/RGRAL1,RGRAL2
      PARAMETER (NLAM=125,NLINES=61,NSET=11)
      COMMON/PARAM/ANGLE,ANISO(NLINES),ASEMI,BSEMI,ICASE,
     1             ICOEF,ILINES,POWER,PREC,
     2             RGMAX,RGMIN,TAUPH(NLINES),TEMPH,THERM,
     3             TIME,VELPH,WLINE(NLINES),ZEMAX
      PARAMETER (NCOEF=5,ZPREC=.10,NRG=INT(6./ZPREC)+1,
     1 NZETA=INT(4./ZPREC)+2)
      COMMON/SOURCE/DRGLOG,DZETA,IRG,IRG1,IZETA,IZETA1,
     1 RG(0:NRG),RGH,RGL,SOURC(NCOEF,0:NRG,0:NZETA,NLINES),ZETA(0:NZETA)
*
      RGRAL1=8./PREC
      RGRAL2=8./PREC
*
      RGFACT=1.+.2*PREC
      IMULT=MIN(NRG,  INT(.6021/LOG10(RGFACT) )+1  )
*
* .6021 is just the logarithm of 4; the ratio of (RGMAX/RGMIN)=4 as it
*  turned out had a sufficiently good discretization and so this
*  discretization will be maintained for all RGMAX and RGMIN cases.
*
      RGMULT=10.**(  LOG10(RGMAX/RGMIN)/IMULT  )
      DRGLOG=LOG10(RGMULT)
*
      ICOUNT=0
      RG(0)=RGMIN
  110 CONTINUE
      ICOUNT=ICOUNT+1
      RG(ICOUNT)=RG(ICOUNT-1)*RGMULT
*      PRINT*,'From PRECIS ',ICOUNT,RG(0),RG(ICOUNT)
      IF(RG(ICOUNT) .LT. RGMAX) GO TO 110
      IF(ICOUNT .GT. 1) THEN
         IRG=ICOUNT
       ELSE
         IRG=2
         RG(1)=.5*(RG(0)+RGMAX)
      END IF
      IRG1=IRG-1
```

```
      RG(IRG)=RGMAX
      RGL=RG(0)/SQRT(RGMULT)
      RGH=RGMAX*SQRT(RGMULT)
*
      RZETA=4./PREC
      IZETA=INT(RZETA)
      IF(REAL(IZETA) .LT. RZETA) IZETA=IZETA+1
      IF(MOD(IZETA,2) .NE. 0) IZETA=IZETA+1
      IZETA1=IZETA-1
      DZETA=PI2/REAL(IZETA)
      ZETA(0)=0.
      DO 410 I=1,IZETA1
      ZETA(I)=ZETA(I-1)+DZETA
  410 CONTINUE
      ZETA(IZETA)=PI2
*
      RETURN
      END
*
*123456789*123456789*123456789*123456789*123456789*123456789*123456789*12
*
*  READIN reads from the S7//MODEL//.DAT input file the parameters for a
*  spectra calculation.  Default parameters are provided.  READIN also
*  calls the routines that generate and output the results.  It handles all
*  the re-assignment of variables for calculating a sequence of spectra
*  using the parameters of PAR2 (see Input Parameter Descriptions).
*  READIN is called by the main program unit S7.
*
      SUBROUTINE READIN
      COMMON/CONST/CLIGHT,CTA,IFREQ,PI,PITWO,PI2,PLANC1,PLANC2,RADDEG
      PARAMETER (NFAM=10)
      COMMON/FAM/IIFAM,IFAM(NFAM),TAUFAM(NFAM),TAUWAV(NFAM),
     1 WAVEL,WAVEH,ICONT,IBETAP,ICH
      COMMON/NORM/INORM,WNORM,IFRAG,YMAX,ZMAX
      PARAMETER (NLAM=125,NLINES=61,NSET=11)
      COMMON/PARAM/ANGLE,ANISO(NLINES),ASEMI,BSEMI,ICASE,
     1             ICOEF,ILINES,POWER,PREC,
     2             RGMAX,RGMIN,TAUPH(NLINES),TEMPH,THERM,
     3             TIME,VELPH,WLINE(NLINES),ZEMAX
      CHARACTER MODEL*2
      COMMON/RED/ERED,IRED
      COMMON/SET/CCALL(NLINES),DLAM,
     1 FLUX(0:NLAM,NSET,3),IDATA,IFORM,ILAM(NSET),
     1 IISET,ILATE,ILOG,ITRANS,
     2 MODEL,IPUT,ISET,JSET,JSETS,KSET(NSET),POLAR(0:NLAM,NSET,3),
     3 SET(NSET),WLAM(0:NLAM,NSET)
      COMMON/SURF/ISURF,IPACT,SURFWA,SURFAN
      DIMENSION ANGL(NSET),ANIS(NLINES),ASPH(NSET),ICAS(NSET),
     1 ILIN(NSET),POWE(NSET),PRE(NSET),RGMA(NSET),TAUP(NLINES),
     2 TEMP(NSET),THER(NSET),TIM(NSET),VELP(NSET),WLIN(NLINES)
```

```
      NAMELIST/PAR1/IDATA,IFORM,IFREQ,ILATE,ILOG,IPUT,IISET,
     1 ISETYN,ITRANS,   INORM,WNORM,IFRAG,YMAX,ZMAX,ERED,IRED
      DATA ICOEF/5/,IDATA/0/,IFORM/1/,IFREQ/0/,
     1-ILATE/1/,ILOG/1/,
     1 IPUT/4/,IISET/1/,ISETYN/1/,
     1      ITRANS/0/
      DATA INORM/0/,WNORM/5000./,IFRAG/0/,YMAX/100./,ZMAX/100/,
     1 ERED/0./,IRED/0/
      NAMELIST/PAR2/IANGL,ANGL,IANIS,ANIS,IASPH,ASPH,
     1                IICAS,ICAS,IILIN,ILIN,IPOWE,POWE,
     2                IPRE ,PRE ,IRGMA,RGMA,RGMIN,ITAUP,TAUP,
     3                ITEMP,TEMP,ITHER,THER,ITIM ,TIM , -
     4                IVELP,VELP,IWLIN,WLIN,ZEMAX
      DATA
     1 IANGL/1/,ANGL
     +        / 90.,     10*0./,
     2 IANIS/1/,ANIS
     +        /NLINES*0./,
     3 IASPH/1/,ASPH
     +        / 0.,.1,.2,.3,.4,.5,.6,.7,.8,.9,.999/,
     4 IICAS/1/ICAS
     +        /1 ,       10*0 /,
     5 IILIN/1/ILIN
     +        /1 ,       10*0 /,
     6 IPOWE/1/,POWE
     +        / 7.,      10*0./,
     7 IPRE/1/,PRE
     +        / .5,.5,.25,.125,     7*0. /,
     8 IRGMA/1/,RGMA
     +        / 3.,      10*0./,
     +          RGMIN/1./,
     9 ITAUP/1/,TAUP
     +        /NLINES*10./,
     A ITEMP/1/,TEMP
     +        /17000.,   10*0./,
     B ITHER/1/,THER
     +        / 0.,      10*0./,
     C ITIM/1/,TIM
     +       / 10.E+5,   10*0./,
     D IVELP/1/,VELP
     +        /1.E+9,    10*0./,
     E IWLIN/1/,WLIN
     +        /NLINES*5000./,
     + ZEMAX/1./
      NAMELIST/PAR3/IIFAM,IFAM,ITAUV,TAUFAM,TAUWAV,
     1 WAVEL,WAVEH,ICONT,IBETAP,ICH
      DATA IISET/50/,IIFAM/0/,
     1 IFAM/NFAM*0/,ITAUV/1/,TAUFAM/NFAM*0./,TAUWAV/NFAM*0./,
     2 WAVEL/0./,WAVEH/100000./,ICONT/0/,IBETAP/0/,ICH/0/
      NAMELIST/PAR4/ISURF,IPACT,SURFWA,SURFAN
```

```
      DATA ISURF/0/,IPACT/75/,SURFWA/6500./SURFAN/0./
*
      IF(MODEL .NE. 'XX') THEN
          OPEN(UNIT=2,FILE='S7'//MODEL//'.DAT;',STATUS='OLD')
          REWIND2
          READ(2,PAR1)
          READ(2,PAR2)
          READ(2,PAR3)
          READ(2,PAR4)
          CLOSE(UNIT=2)
      END IF
      PRINT910,'MODEL S7'//MODEL
  910 FORMAT('1',A10/)
      PRINT PAR1
      PRINT*,' '
      PRINT PAR2
      PRINT*,' '
      PRINT PAR3
      PRINT*,' '
      PRINT PAR4
*
      ISET=0
      JSET=1
      JSETS=1
      ANGLE=ANGL(1)
      ASEMI=1.
      IF(ILATE .EQ. 0) THEN
          BSEMI=ASEMI
        ELSE IF(ILATE .EQ. 1) THEN
          BSEMI=ASEMI*(1.-ASPH(1))
        ELSE
          BSEMI=ASEMI/(1.-ASPH(1))
      END IF
      ICASE=ICAS(1)
      ILINES=ILIN(1)
      POWER=POWE(1)
      PREC=PRE(1)
      RGMAX=RGMA(1)
      TEMPH=TEMP(1)
      THERM=THER(1)
      TIME=TIM(1)
      VELPH=VELP(1)
      ZEMAX=ZEMAX*PI
      IF(IIFAN .EQ. 0) THEN
          DO 400 I=1,ILINES
          ANISO(I)=ANIS(I)
          TAUPH(I)=TAUP(I)
          WLINE(I)=WLIN(I)
  400     CONTINUE
        ELSE
```

```
          CALL FAMILY
      END IF
      CALL ANISOT
      CALL PRECIS
*      CALL TEST(1)
*      CALL TEST(2)
      CALL SOURC1
*      CALL TEST(3)
      IF(ISURF .GT. 0) OPEN(UNIT=5,
     1 FILE='S7'//MODEL//'B.OUT',STATUS='UNKNOWN')
      IF(ISURF .EQ. 0) THEN
          CALL SPECT1
          CALL OUTPUT(2)
        ELSE IF(ISURF .EQ. 1) THEN
          CALL SPECT1
          CALL OUTPUT(2)
          CALL SURFBR
        ELSE IF(ISURF .EQ. 2) THEN
          CALL SURFBR
      END IF
      IF(ISETYN .EQ. 0  .AND.  MOD(IPUT,2) .EQ. 0) THEN
          CALL OUTPUT(3)
          GO TO 200
      END IF
*
      IF(IANGL .GT. 1) THEN
          ISET=1
          JSETS=IANGL
          SET(1)=ANGLE
          DO 410 JSET=2,JSETS
          ANGLE=ANGL(JSET)
          SET(JSET)=ANGLE
          IF(ICASE .EQ. 2) CALL SOURC1
          CALL SPECT1
          CALL OUTPUT(2)
  410     CONTINUE
          IF(MOD(IPUT,2) .EQ. 0) CALL OUTPUT(3)
          ANGLE=ANGL(1)
      END IF
*
      IF(IANIS .GT. 1) THEN
          ISET=2
          JSETS=IANIS
          SET(1)=ANIS(1)
          DO 420 JSET=2,JSETS
          SET(JSET)=ANIS(1+ (JSET-1)*IISET  )
          DO 422 I=1,ILINES
          ANISO(I)=ANIS(I+ (JSET-1)*IISET  )
  422     CONTINUE
          CALL ANISOT
```

```
            CALL SOURC1
            CALL SPECT1
            CALL OUTPUT(2)
  420       CONTINUE
            IF(MOD(IPUT,2) .EQ. 0) CALL OUTPUT(3)
            DO 424 I=ILINES
            ANISO(I)=ANIS(I)
  424       CONTINUE
        END IF
*
        IF(IASPH .GT. 1) THEN
            IF(ILATE .EQ. 0) THEN
                ITATEM=0
                ILATE=1
              ELSE
                ILATEM=1
            END IF
            ISET=3
            JSETS=IASPH
            SET(1)=ASPH(1)
            DO 430 JSET=2,JSETS
            SET(JSET)=ASPH(JSET)
            IF(ILATE .EQ. 1) THEN
                BSEMI=ASEMI*(1.-ASPH(JSET))
              ELSE
                BSEMI=ASEMI/(1.-ASPH(JSET))
            END IF
            CALL SOURC1
            CALL SPECT1
            CALL OUTPUT(2)
  430       CONTINUE
            IF(MOD(IPUT,2) .EQ. 0) CALL OUTPUT(3)
            IF(ILATEM .EQ. 0) ILATE=0
            IF(ILATE .EQ. 0) THEN
                BSEMI=ASEMI
              ELSE IF(ILATE .EQ. 1) THEN
                BSEMI=ASEMI*(1.-ASPH(1))
              ELSE
                BSEMI=ASEMI/(1.-ASPH(1))
            END IF
        END IF
*
        IF(IILIN .GT. 1) THEN
            ISET=5
            JSETS=IILIN
            SET(1)=REAL(ILIN(1))
            DO 450 JSET=2,JSETS
            SET(JSET)=REAL(ILIN(1))
            ILINES=ILIN(JSET)
            CALL ANISOT
```

```
            CALL SOURC1
*            CALL TEST(3)
            CALL SPECT1
            CALL OUTPUT(2)
  450       CONTINUE
            IF(MOD(IPUT,2) .EQ. 0) CALL OUTPUT(3)
            ILINES=ILIN(1)
        END IF
*
        IF(IPOWE .GT. 1) THEN
            ISET=6
            JSETS=IPOWE
            SET(1)=POWER
            DO 460 JSET=2,JSETS
            POWER=POWE(JSET)
            SET(JSET)=POWER
            CALL SOURC1
*            CALL TEST(3)
            CALL SPECT1
            CALL OUTPUT(2)
  460       CONTINUE
            IF(MOD(IPUT,2) .EQ. 0) CALL OUTPUT(3)
            POWER=POWE(1)
        END IF
*
        IF(IPRE .GT. 1) THEN
            ISET=7
            JSETS=IPRE
            SET(1)=PREC
            DO 470 JSET=2,JSETS
            PREC=PRE(JSET)
            SET(JSET)=PREC
            CALL PRECIS
            CALL SOURC1
*            CALL TEST(3)
            CALL SPECT1
            CALL OUTPUT(2)
  470       CONTINUE
            IF(MOD(IPUT,2) .EQ. 0) CALL OUTPUT(3)
            PREC=PRE(1)
        END IF
*
        IF(IRGMA .GT. 1) THEN
            ISET=8
            JSETS=IRGMA
            SET(1)=RGMAX
            DO 480 JSET=2,JSETS
            RGMAX=RGMA(JSET)
            SET(JSET)=RGMAX
            CALL PRECIS
```

```
                CALL SOURC1
*                CALL TEST(3)
                IF(ISURF .EQ. 0) THEN
                    CALL SPECT1
                    CALL OUTPUT(2)
                  ELSE IF(ISURF .EQ. 1) THEN
                    CALL SPECT1
                    CALL OUTPUT(2)
                    CALL SURFBR
                  ELSE IF(ISURF .EQ. 2) THEN
                    CALL SURFBR
                END IF
  480           CONTINUE
                IF(MOD(IPUT,2) .EQ. 0) CALL OUTPUT(3)
                RGMAX=RGMA(1)
            END IF
*
            IF(ITAUP .GT. 1) THEN
                ISET=9
                JSETS=ITAUP
                SET(1)=TAUP(1)
                DO 490 JSET=2,JSETS
                IF(IIFAM .EQ. 0) THEN
                    SET(JSET)=TAUP(1+ (JSET-1)*IISET  )
                    DO 492 I=1,ILINES
                    TAUPH(I)=TAUP(I+ (JSET-1)*IISET  )
  492               CONTINUE
                  ELSE
                    SET(JSET)=TAUP(JSET)
                    TAUFAM(ITAUV)=TAUP(JSET)
                    CALL FAMILY
                END IF
                CALL SOURC1
*                CALL TEST(3)
                CALL SPECT1
                CALL OUTPUT(2)
  490           CONTINUE
                IF(MOD(IPUT,2) .EQ. 0) CALL OUTPUT(3)
                IF(IIFAM .EQ. 0) THEN
                     DO 494 I=1,ILINES
                     TAUPH(I)=TAUP(I)
  494                CONTINUE
                  ELSE
                     TAUFAM(ITAUV)=TAUP(1)
                     CALL FAMILY
                 END IF
            END IF
*
            IF(ITEMP .GT. 1) THEN
                ISET=10
```

```
              JSETS=ITEMP
              SET(1)=TEMPH
              DO 500 JSET=2,JSETS
              TEMPH=TEMP(JSET)
              SET(JSET)=TEMPH
              CALL SOURC1
*              CALL TEST(3)
              CALL SPECT1
              CALL OUTPUT(2)
  500         CONTINUE
              IF(MOD(IPUT,2) .EQ. 0) CALL OUTPUT(3)
              TEMPH=TEMP(1)
          END IF
*
          IF(IWLIN .GT. 1) THEN
              ISET=14
              JSETS=IWLIN
              IF(ILINES .EQ. 1) THEN
                  SET(1)=WLIN(1+ (JSET-1)*IISET  )
                ELSE
                  SET(1)=WLIN(2+ (JSET-1)*IISET  )
     1                  -WLIN(1+ (JSET-1)*IISET  )
              END IF
              DO 540 JSET=2,JSETS
              IF(ILINES .EQ. 1) THEN
                  SET(JSET)=WLIN(1+ (JSET-1)*IISET  )
                ELSE
                  SET(JSET)=WLIN(2+ (JSET-1)*IISET  )
     1                     -WLIN(1+ (JSET-1)*IISET  )
              END IF
              DO 542 I=1,ILINES
              WLINE(I)=WLIN(I+ (JSET-1)*IISET  )
  542         CONTINUE
              CALL SOURC1
*              CALL TEST(3)
              CALL SPECT1
              CALL OUTPUT(2)
  540         CONTINUE
              IF(MOD(IPUT,2) .EQ. 0) CALL OUTPUT(3)
              DO 544 I=1,ILINES
              WLINE(I)=WLIN(I+ (JSET-1)*IISET  )
  544         CONTINUE
          END IF
*
  200 CONTINUE
      CLOSE(UNIT=5)
      RETURN
      END
*
*123456789*123456789*123456789*123456789*123456789*123456789*123456789*12
```

```
*
*  REDDEN calculates a reddening factor for a given wavelength and a given
*  color excess (i.e., WAVELN and EXTRED).  The reddening law table comes
*  from Code et al. (1976).  A simple binary search is done to find the
*  right wavelength interval of the table for the given WAVELN.  A linear
*  interpolation is then done to find absorption magnitude.  Then the
*  reddening factor is calculated.  REDDEN is called from SPECT1.
*
      FUNCTION REDDEN(WAVELN,EXTRED)
      PARAMETER (NWAVE=48)
      DIMENSION AE(NWAVE),WAVE(NWAVE)
      DATA WAVE/1100.,1200.,1300.,1400.,1500.,
     1          1600.,1700.,1800.,1900.,2000.,
     1          2100.,2160.,2200.,2300.,2400.,2500.,
*
     2          2600.,2700.,2800.,2900.,3000.,
     2          3300.,3500.,3700.,3900.,4100.,
     2          4300.,4500.,4700.,4900.,5100.,5300.,
*
     3          5500.,5700.,5900.,6100.,6300.,
     3          6500.,6700.,6900.,7100.,7300.,
     3          7500.,7700.,7900.,8100.,8300.,8500./,
*
     1      AE/11.70,10.20, 9.19, 8.54, 8.29,
     1           8.03, 7.85, 7.90, 8.38, 9.05,
     1           9.90,10.10, 9.85, 8.75, 7.92, 7.30,
*
     2           6.82, 6.41, 6.10, 5.85, 5.65,
     2           5.16, 4.92, 4.70, 4.51, 4.35,
     2           4.14, 3.94, 3.76, 3.57, 3.40, 3.24,
*
     3           3.09, 2.95, 2.80, 2.65, 2.50,
     3           2.36, 2.25, 2.15, 2.05, 1.96,
     3           1.87, 1.76, 1.69, 1.62, 1.55, 1.49/
*
      DATA INNN/33/
*
      IF(WAVELN .LE. WAVE(1)) THEN
          INN=1
          GO TO 200
        ELSE IF(WAVELN .GE. WAVE(NWAVE)) THEN
          INN=NWAVE-1
          GO TO 200
      END IF
*
      IBOT=1
      INN=INNN
      ITOP=NWAVE
  110 CONTINUE
      INNOLD=INN
```

```
      IF(WAVELN .LT. WAVE(INN)) THEN
          ITOP=INN
          INN=(IBOT+ITOP)/2
        ELSE
          IBOT=INN
          INN=(IBOT+ITOP)/2
      END IF
      IF(INN .NE. INNOLD) GO TO 110
*
 200 CONTINUE
      AWAVE=(  (AE(INN+1)-AE(INN))/
     1 (WAVE(INN+1)-WAVE(INN))          )*
     2 (WAVELN-WAVE(INN))   +    AE(INN)
*
      REDDEN=10**(-AWAVE*EXTRED/2.5)
*
      RETURN
      END
*
*123456789*123456789*123456789*123456789*123456789*123456789*123456789*12
*
*  SIMWT calculates the Simpson's rule weight for a given term in the
*  Simpson's rule sum.  SIMWT is called by SPECT1.
*
      FUNCTION SIMWT(IZERO,I,ILAST)
*
      IF(I .EQ. IZERO) THEN
          SIMWT=1.
        ELSE IF(I .LT. ILAST-1) THEN
          SIMWT=2.+2.*REAL(  MOD(I-IZERO,2)  )
        ELSE IF(I .EQ. ILAST-1) THEN
          IF(MOD(ILAST-IZERO,2) .EQ. 0) THEN
              SIMWT=4.
            ELSE
              SIMWT=2.5
          END IF
        ELSE
          IF(MOD(ILAST-IZERO,2) .EQ. 0) THEN
             SIMWT=1.
            ELSE
             SIMWT=1.5
          END IF
      END IF
*
      RETURN
      END
*
*123456789*123456789*123456789*123456789*123456789*123456789*123456789*12
*
*  SORT does a bubble sort on the items in the array GROUP; the items
```

```
*  are ordered from smallest to largest.  The items in GROUP1, GROUP2,
*  GROUP3, and IGROUP4 with the same index as an item in GROUP form a
*  record along with the GROUP item.  Thus the GROUP1, GROUP2, GROUP3,
*  and IGROUP4 items are sorted along with the GROUP items in order to
*  maintain the records.  SORT is called by FAMILY and OUTPUT.
*
      SUBROUTINE SORT(NGROUP,IGROUP,GROUP,GROUP1,GROUP2,GROUP3,IGROUP4)
      DIMENSION GROUP(NGROUP),GROUP1(NGROUP),GROUP2(NGROUP),
     1 GROUP3(NGROUP),IGROUP4(NGROUP)
*
      DO 410 I=IGROUP,2,-1
      DO 420 J=1,I-1
      IF(GROUP(J) .GT. GROUP(J+1)) THEN
          TEMP=GROUP(J+1)
          GROUP(J+1)=GROUP(J)
          GROUP(J)=TEMP
          TEMP=GROUP1(J+1)
          GROUP1(J+1)=GROUP1(J)
          GROUP1(J)=TEMP
          TEMP=GROUP2(J+1)
          GROUP2(J+1)=GROUP2(J)
          GROUP2(J)=TEMP
          TEMP=GROUP3(J+1)
          GROUP3(J+1)=GROUP3(J)
          GROUP3(J)=TEMP
          ITEMP=IGROUP4(J+1)
          IGROUP4(J+1)=IGROUP4(J)
          IGROUP4(J)=ITEMP
      END IF
  420 CONTINUE
  410 CONTINUE
*
      RETURN
      END
*
*123456789*123456789*123456789*123456789*123456789*123456789*123456789*12
*
*  SOURCO tests the interpolation routine SOURC3 by using it to recreate
*  the table of source function coefficients.  This table can be output
*  by subroutine OUTPUT.  SOURCO is called from subroutine TEST..
*
      SUBROUTINE SOURCO(ITABLE)
      COMMON/CONST/CLIGHT,CTA,IFREQ,PI,PITWO,PI2,PLANC1,PLANC2,RADDEG
      PARAMETER (NLAM=125,NLINES=61,NSET=11)
      COMMON/PARAM/ANGLE,ANISO(NLINES),ASEMI,BSEMI,ICASE,
     1             ICOEF,ILINES,POWER,PREC,
     2             RGMAX,RGMIN,TAUPH(NLINES),TEMPH,THERM,
     3             TIME,VELPH,WLINE(NLINES),ZEMAX
      PARAMETER (NCOEF=5,ZPREC=.10,NRG=INT(6./ZPREC)+1,
     1 NZETA=INT(4./ZPREC)+2)
```

```
      COMMON/SOURCE/DRGLOG,DZETA,IRG,IRG1,IZETA,IZETA1,
     1 RG(0:NRG),RGH,RGL,SOURC(NCOEF,0:NRG,0:NZETA,NLINES),ZETA(0:NZETA)
      DIMENSION RGG(0:2*NRG),SCOEF(NCOEF),SMENTS(3),ZET(0:4)
      DATA IZET/4/,ZET/ 0.0,22.5,45.0,67.5,90.0/
*
      ITABLE=ITABLE+1
      PRINT910,ITABLE
  910 FORMAT('1','TEST-TABLE ',I2,'.  THE SOURCE FUNCTION ',
     1 'COEFFICIENTS FROM THE INTERPOLATION TABLE')
  920 FORMAT(/' ',I5,5X,'IZETA=',F10.7//
     2 ' ',13X,'RG',8(13X,I2)/)
  930 FORMAT(' ',9(E15.7))
*
      RGG(0)=RG(0)
      DO 410 I=2,2*IRG,2
      RGG(I)=RG(I/2)
      RGG(I-1)=.5*(RGG(I-2)+RGG(I))
  410 CONTINUE
*
      JCOEF=MIN(ICOEF,8)
      DO 420 I=0,IZET
      PRINT920,I,ZET(I),(J,J=1,JCOEF)
      IF(ZET(I) .NE. 90.) THEN
          ZE=ZET(I)/RADDEG
          COSPRI=BSEMI*COS(ZE)
          SINPRI=ASEMI*SIN(ZE)
        ELSE
          COSPRI=0.
          SINPRI=ASEMI
      END IF
      DO 430 J=0,2*IRG
      ZZ=RGG(J)*COSPRI
      XX=RGG(J)*SINPRI
      CALL SOURC3(0.,XX,0.,ZZ,SCOEF,SMENTS)
      PRINT930,RGG(J),(SCOEF(K),K=1,JCOEF)
  430 CONTINUE
  420 CONTINUE
*
      RETURN
      END
*
*123456789*123456789*123456789*123456789*123456789*123456789*123456789*12
*
*  SOURC1 constructs the table of source function coefficients (see J,
*  equation (2.146)) using SOURC2 as an auxiliary subroutine.  Some
*  expressions taken from Appendix 3 section (c) of J are used to
*  obtain the XXCORE value. SOURC1 is called from READIN.
*
      SUBROUTINE SOURC1
      COMMON/CONST/CLIGHT,CTA,IFREQ,PI,PITWO,PI2,PLANC1,PLANC2,RADDEG
```

```
      PARAMETER (NLAM=125,NLINES=61,NSET=11)
      COMMON/PARAM/ANGLE,ANISO(NLINES),ASEMI,BSEMI,ICASE,
     1            ICOEF,ILINES,POWER,PREC,
     2            RGMAX,RGMIN,TAUPH(NLINES),TEMPH,THERM,
     3            TIME,VELPH,WLINE(NLINES),ZEMAX
      COMMON/PSEUD/IPSEUD(NLINES)
      CHARACTER MODEL*2
      COMMON/SET/CCALL(NLINES),DLAM,
     1 FLUX(0:NLAM,NSET,3),IDATA,IFORM,ILAM(NSET),
     1 IISET,ILATE,ILOG,ITRANS,
     2 MODEL,IPUT,ISET,JSET,JSETS,KSET(NSET),POLAR(0:NLAM,NSET,3),
     3 SET(NSET),WLAM(0:NLAM,NSET)
      PARAMETER (NCOEF=5,ZPREC=.10,NRG=INT(6./ZPREC)+1,
     1 NZETA=INT(4./ZPREC)+2)
      COMMON/SOURCE/DRGLOG,DZETA,IRG,IRG1,IZETA,IZETA1,
     1 RG(0:NRG),RGH,RGL,SOURC(NCOEF,0:NRG,0:NZETA,NLINES),ZETA(0:NZETA)
      COMMON/SOURC/ASQ,BSQ,THETA,ALP,ALPSQ,BET,BETSQ,
     1 CON1,CON2,CON3,CON4,BPRI,GMAXSQ,GMINSQ,
     2 XXLIMB,XXCORE,XXOCUL,XXCUT,QC,XTC
      DIMENSION DIRECT(NCOEF),SOUR(NCOEF)
      DIMENSION COS1(0:NZETA),SIN1(0:NZETA)
*
      ASQ=ASEMI**2
      BSQ=BSEMI**2
      THETA=ANGLE/RADDEG
      ALP=COS(THETA)
      ALPSQ=ALP**2
      BET=SIN(THETA)
      BETSQ=BET**2
*
      CON1=(1./ASQ-1./BSQ)*ALP*BET
      CON2=ALPSQ/ASQ+BETSQ/BSQ
      CON3=BETSQ/ASQ+ALPSQ/BSQ
      CON4=1./(ASQ*BSQ)
*
      IF(ANGLE .EQ. 0.  .OR.  ANGLE .EQ. 180) THEN
          BPRI=ASEMI
        ELSE IF(ANGLE .EQ. 90.) THEN
          BPRI=BSEMI
        ELSE
          BPRI=ASEMI*BSEMI*SQRT(CON3)
      END IF
      GMAXSQ=RGMAX**2
      GMINSQ=RG(0)**2
*
      XXLIMB=RGMAX*SQRT(CON2/CON4)
      XXCORE=RG(0)*SQRT(CON2/CON4)
      XXOCUL=-(  ABS(CON1*RG(0))/SQRT(CON4)  +
     1           SQRT(GMAXSQ-GMINSQ)          )
     2       /(  SQRT(CON3)  )
```

```
*
      IF((   (RGMAX/RG(0))*ABS(CON1)/SQRT(CON2*CON3) .LT. 1.)
     1           .AND.  ITRANS .EQ. 0)  THEN
          XXCUT=XXOCUL
        ELSE
          XXCUT=-XXLIMB
      END IF
      QC=(VELPH/XXCORE)/CLIGHT
      XTC=TIME*VELPH/XXCORE
      A=RG(0)*ASEMI
      B=RG(0)*BSEMI
*      PRINT*,'From SOURC1 ',A,B,QC,XXCORE,XXCUT,XXLIMB,XXOCUL
*
      SIN1(0)=0.
      COS1(0)=BSEMI
      IF(ILATE .EQ. 0) THEN
          IZETAL=0
        ELSE
          IZETAL=IZETA
          DO 410 I=1,IZETA1
          SIN1(I)=ASEMI*SIN(ZETA(I))
          COS1(I)=BSEMI*COS(ZETA(I))
  410     CONTINUE
          SIN1(IZETA)=ASEMI
          COS1(IZETA)=0.
      END IF
*
      DO 415 ILINE=1,ILINES
*
      DO 420 I=0,IRG
*
      IF(THERM .EQ. 0.) THEN
          EPSIL1=1.
          G1=0.
          G2=0.
        ELSE
          EPSIL1=1.-THERM
          IF(ICASE .LT. 2) THEN
              G1=.5
              G2=.5
            ELSE
              CALL PLANCF(WLINE(ILINE),0.,G1)
              G1=G1*THERM
              G2=G1
          END IF
      END IF
*
      IF(IPSEUD(ILINE) .EQ. 0) CALL BETAF1(ILINE,RG(I),BETA,BETA1)
*
      DO 430 J=0,IZETAL
```

```
      C=RG(I)*SIN1(J)
      D=RG(I)*COS1(J)
*
      CALL SOURC2(A,B,C,D,BETA,BETA1,EPSIL1,G1,G2,ILINE,
     + ACC125,DIRECT,SOUR)
*
      DO 440 K=1,ICOEF
      SOURC(K,I,J,ILINE)=SOUR(K)
  440 CONTINUE
*
  430 CONTINUE
  420 CONTINUE
  415 CONTINUE
*
      IF(IPUT .LE. 2) CALL OUTPUT(1)
      RETURN
      END
*
*123456789*123456789*123456789*123456789*123456789*123456789*123456789*12
*
*  SOURC2 constructs the source function coefficients using the GRALI
*  routines to obtain the direct coefficients.  The explicit expressions
*  for the source function coefficients come from equation (2.146) of J.
*  SOURC2 is called from SOURC1.
*
      SUBROUTINE SOURC2(A,B,C,D,BETA,BETA1,EPSIL1,G1,G2,ILINE,
     + ACC125,DIRECT,SOUR)
      PARAMETER (NLAM=125,NLINES=61,NSET=11)
      COMMON/ANISOT/AN1(NLINES),AN2(NLINES),ANDIR(14,NLINES),
     1 AN17(NLINES),ANS(9,NLINES)
      COMMON/PSEUD/IPSEUD(NLINES)
      DIMENSION DIRECT(5),SOUR(5)
      DIMENSION SA(3),SAMAT(3,4)
*
      CALL GRAL1(ILINE,A,B,C,D,DIRECT,PHIC)
      IF(PHIC .LE. 0) THEN
          DO 410 I=1,ICOEF
          DIRECT(I)=0.
          SOUR(I)=0.
  410     CONTINUE
          GO TO 200
      END IF
*
      IF(IPSEUD(ILINE) .EQ. 0) THEN
      COEF1=EPSIL1*BETA/(1.-EPSIL1*BETA1*AN17(ILINE))
      COEF2=1./(1-EPSIL1*BETA1)
      COEF3=COEF2*COEF1
      COEF4=EPSIL1*BETA1
*
      REST=DIRECT(2)*(1-AN17(ILINE))/3.
```

```
     1          -AN17(ILINE)*(  DIRECT(1)+DIRECT(5)  )
      SOUR(1)=COEF3*(DIRECT(1) + .5*COEF4*(DIRECT(2)+REST )) +COEF2*G1
      SOUR(2)=COEF1*DIRECT(2)
      SOUR(3)=COEF1*DIRECT(3)
      SOUR(4)=COEF1*DIRECT(4)
      SOUR(5)=COEF3*(DIRECT(5) + .5*COEF4*(-DIRECT(2)+REST ))+COEF2*G2
*
      ELSE
*
      SOUR(1)=EPSIL1*DIRECT(1)+G1
      SOUR(2)=EPSIL1*DIRECT(2)
      SOUR(3)=EPSIL1*DIRECT(3)
      SOUR(4)=EPSIL1*DIRECT(4)
      SOUR(5)=EPSIL1*DIRECT(5)+G2
      END IF
*
* The following program particle was used for testing the explicit
* expressions for the source function coefficients.
*
      IF(1 .NE. 2) GO TO 200
      SAMAT(1,1)=EPSIL1*BETA1*ANS(1,ILINE)-1.
      SAMAT(1,2)=EPSIL1*BETA1*ANS(2,ILINE)
      SAMAT(1,3)=EPSIL1*BETA1*ANS(3,ILINE)
      SAMAT(1,4)=-EPSIL1*BETA*DIRECT(1)-G1
*
      SAMAT(2,1)=EPSIL1*BETA1*ANS(4,ILINE)
      SAMAT(2,2)=EPSIL1*BETA1*ANS(5,ILINE)-1.
      SAMAT(2,3)=EPSIL1*BETA1*ANS(6,ILINE)
      SAMAT(2,4)=-EPSIL1*BETA*DIRECT(2)
*
      SAMAT(3,1)=EPSIL1*BETA1*ANS(7,ILINE)
      SAMAT(3,2)=EPSIL1*BETA1*ANS(8,ILINE)
      SAMAT(3,3)=EPSIL1*BETA1*ANS(9,ILINE)-1.
      SAMAT(3,4)=-EPSIL1*BETA*DIRECT(5)-G2
*
      CALL LIN3(SAMAT,ACC125,SA)
      IF(SOUR(1) .NE. 0.) THEN
          CHECK1=ABS( (SA(1)-SOUR(1))/SOUR(1) )
          IF(CHECK1 .GT. 1.E-3) THEN
               PRINT*,' CHECK1 IS TOO LARGE ',CHECK1
          END IF
      END IF
      IF(SOUR(2) .NE. 0.) THEN
          CHECK2=ABS( (SA(2)-SOUR(2))/SOUR(2) )
          IF(CHECK2 .GT. 1.E-3  .AND.
     1      ABS(SOUR(2)/SOUR(1)) .GT. 1.E-3) THEN
               PRINT*,' CHECK2 IS TOO LARGE ',CHECK2
          END IF
      END IF
      IF(SOUR(5) .NE. 0.) THEN
```

```
            CHECK5=ABS( (SA(3)-SOUR(5))/SOUR(5) )
            IF(CHECK5 .GT. 1.E-3) THEN
                 PRINT*,' CHECK5 IS TOO LARGE ',CHECK5
            END IF
        END IF
*
  200 CONTINUE
        RETURN
        END
*
*123456789*123456789*123456789*123456789*123456789*123456789*123456789*12
*
*  SOURC3 evaluates the source function coefficients from the table
*  constructed by SOURC1, and calculates the source function Stokes
*  parameter fields.  The coefficients are determined by quadratic
*  interpolation from the 2-dimensional table.  SOURC3 is called from
*  GRAL3, SOURCO, SPECT1, and SURFBR.
*
        SUBROUTINE SOURC3(ILINE,IWHERE,X,Y,Z,XMU,PHI,SCOEF,SMENTS)
        COMMON/CONST/CLIGHT,CTA,IFREQ,PI,PITWO,PI2,PLANC1,PLANC2,RADDEG
        PARAMETER (NLAM=125,NLINES=61,NSET=11)
        COMMON/PARAM/ANGLE,ANISO(NLINES),ASEMI,BSEMI,ICASE,
       1             ICOEF,ILINES,POWER,PREC,
       2             RGMAX,RGMIN,TAUPH(NLINES),TEMPH,THERM,
       3             TIME,VELPH,WLINE(NLINES),ZEMAX
        COMMON/SET/CCALL(NLINES),DLAM,
       1 FLUX(0:NLAM,NSET,3),IDATA,IFORM,ILAM(NSET),
       1 IISET,ILATE,ILOG,ITRANS,
       2 MODEL,IPUT,ISET,JSET,JSETS,KSET(NSET),POLAR(0:NLAM,NSET,3),
       3 SET(NSET),WLAM(0:NLAM,NSET)
        PARAMETER (NCOEF=5,ZPREC=.10,NRG=INT(6./ZPREC)+1,
       1 NZETA=INT(4./ZPREC)+2)
        COMMON/SOURCE/DRGLOG,DZETA,IRG,IRG1,IZETA,IZETA1,
       1 RG(0:NRG),RGH,RGL,SOURC(NCOEF,0:NRG,0:NZETA,NLINES),ZETA(0:NZETA)
        COMMON/SOURC/ASQ,BSQ,THETA,ALP,ALPSQ,BET,BETSQ,
       1 CON1,CON2,CON3,CON4,BPRI,GMAXSQ,GMINSQ,
       2 XXLIMB,XXCORE,XXOCUL,XXCUT,QC,XTC
        DIMENSION SMENTS(3),SCOEF(NCOEF),SZETA(0:2)
*
        IF(ILATE .NE. 0) GO TO 150
*
        RXYZ=SQRT(X**2+Y**2+Z**2)
        IF(IWHERE .EQ. 1) THEN
            THETAZ=ACOS(MIN(1.,MAX(-1.,XMU) ) )
            THETAR=ACOS(MIN(1.,MAX(-1.,Z/RXYZ) ) )
            XMUP=COS(THETAZ+THETAR)
          ELSE
            DOTPRO=X*SQRT(MAX(0.,  1.-XMU**2))+Z*XMU
            XMUP=DOTPRO/RXYZ
        END IF
```

```
*
      XYGSQ=(X**2+Y**2)/ASQ
      ZG=ABS(Z)/BSEMI
      RGGG=SQRT(XYGSQ+ZG**2)
      RGLOG=LOG10(RGGG/RGMIN)
*
      IF(RGGG .LT. RGL  .OR.  RGGG .GT. RGH) THEN
          DO 401 I=1,ICOEF
          SCOEF(I)=0.
 401      CONTINUE
          DO 402 I=1,3
          SMENTS(I)=0.
 402      CONTINUE
          GO TO 200
      END IF
*
      JRG1=MAX(1,MIN(IRG1,  INT(RGLOG/DRGLOG)  ))
      JRG0=JRG1-1
      JRG2=JRG1+1
      DELR=RGGG-RG(JRG0)
      DELRSQ=DELR**2
      DEL1=RG(JRG1)-RG(JRG0)
      DEL1SQ=DEL1**2
      DEL2=RG(JRG2)-RG(JRG0)
      DEL2SQ=DEL2**2
      DELA=DEL1*DEL2
      DELB=DELA*(DEL1-DEL2)
      DELC=-(DEL1+DEL2)/DELA
*
      DO 403 I=1,ICOEF
      IF(I .EQ. 3  .OR.  I  .EQ. 4) GO TO 403
*

      SZETA(0)=SOURC(I,JRG0,0,ILINE)
      SZETA(1)=SOURC(I,JRG1,0,ILINE)
      SZETA(2)=SOURC(I,JRG2,0,ILINE)
*
      A1=SZETA(0)*DELC  -
     1  (SZETA(1)*DEL2SQ-SZETA(2)*DEL1SQ)/DELB
      A2=SZETA(0)/DELA  +
     1  (SZETA(1)*DEL2  -SZETA(2)*DEL1  )/DELB
      SCOEF(I)=A2*DELRSQ + A1*DELR + SZETA(0)
*
 403  CONTINUE
*
      SMENTS(1)=SCOEF(1) + SCOEF(2)*XMUP**2
      SMENTS(2)=SCOEF(5)
      SMENTS(3)=0.
      GO TO 200
*
```

```
****    Above the spherically symmetric Stokes source fields are
*      evaluated.
*
****    Below the the full axisymmetric Stokes source fields are
*      evaluated.
*
  150 CONTINUE
*
      IF(IWHERE .EQ. 1) THEN
          COS1=COS(PHI)
          COS2=COS(2.*PHI)
          SIN1=SIN(PHI)
          SIN2=SIN(2.*PHI)
        ELSE
          RXY=SQRT(X**2+Y**2)
          IF(RXY .NE. 0.) THEN
              COS1=X/RXY
              COS2=2.*COS1**2-1.
              SIN1=-Y/RXY
              SIN2=2.*SIN1*COS1
            ELSE
              COS1=0.
              COS2=0.
              SIN1=0.
              SIN2=0.
          END IF
      END IF
*
      XMUP=XMU
      IF(Z .LT. 0.) XMUP=-XMUP
      XMUPSQ=XMUP**2
      XMUP1=SQRT(MAX(0.,  1.-XMUPSQ  ))
*
      XYGSQ=(X**2+Y**2)/ASQ
      ZG=ABS(Z)/BSEMI
      RGGG=SQRT(XYGSQ+ZG**2)
      RGLOG=LOG10(RGGG/RGMIN)
*
      IF(RGGG .LT. RGL  .OR.  RGGG .GT. RGH) THEN
          DO 410 I=1,ICOEF
          SCOEF(I)=0.
  410     CONTINUE
          DO 420 I=1,3
          SMENTS(I)=0.
  420     CONTINUE
          GO TO 200
      END IF
*
      JRG1=MAX(1,MIN(IRG1,  INT(RGLOG/DRGLOG)  ))
      JRG0=JRG1-1
```

```
      JRG2=JRG1+1
      DELR=RGGG-RG(JRGO)
      DELRSQ=DELR**2
      DEL1=RG(JRG1)-RG(JRGO)
      DEL1SQ=DEL1**2
      DEL2=RG(JRG2)-RG(JRGO)
      DEL2SQ=DEL2**2
      DELA=DEL1*DEL2
      DELB=DELA*(DEL1-DEL2)
      DELC=-(DEL1+DEL2)/DELA
*
      IF(Z .NE. 0.) THEN
          ZETAGG=ATAN(SQRT(XYGSQ)/ZG)
          JZETA1=MAX(1,MIN(IZETA1,  INT(ZETAGG/DZETA)  ))
        ELSE
          ZETAGG=PI2
          JZETA1=IZETA1
      END IF
      JZETAO=JZETA1-1
      JZETA2=JZETA1+1
      DIFZ=ZETAGG-ZETA(JZETAO)
      DIFZSQ=DIFZ**2
      DIF1=ZETA(JZETA1)-ZETA(JZETAO)
      DIF1SQ=DIF1**2
      DIF2=ZETA(JZETA2)-ZETA(JZETAO)
      DIF2SQ=DIF2**2
      DIFA=DIF1*DIF2
      DIFB=DIFA*(DIF1-DIF2)
      DIFC=-(DIF1+DIF2)/DIFA
*
*
*
      DO 430 I=1,ICOEF
*
      DO 440 J=0,2
      A1=SOURC(I,JRGO+J,JZETAO,ILINE)*DIFC -
     1  (SOURC(I,JRGO+J,JZETA1,ILINE)*DIF2SQ -
     2   SOURC(I,JRGO+J,JZETA2,ILINE)*DIF1SQ)/DIFB
      A2=SOURC(I,JRGO+J,JZETAO,ILINE)/DIFA +
     1  (SOURC(I,JRGO+J,JZETA1,ILINE)*DIF2 -
     2   SOURC(I,JRGO+J,JZETA2,ILINE)*DIF1)/DIFB
      SZETA(J)=A2*DIFZSQ+A1*DIFZ+SOURC(I,JRGO+J,JZETAO,ILINE)
  440 CONTINUE
*
      A1=SZETA(0)*DELC  -
     1  (SZETA(1)*DEL2SQ-SZETA(2)*DEL1SQ)/DELB
      A2=SZETA(0)/DELA  +
     1  (SZETA(1)*DEL2  -SZETA(2)*DEL1  )/DELB
      SCOEF(I)=A2*DELRSQ + A1*DELR + SZETA(0)
*
```

```
 430 CONTINUE
*
     SMENTS(1)=SCOEF(1) + SCOEF(2)*XMUPSQ +
    1        SCOEF(3)*XMUP*XMUP1*COS1 +
    2        SCOEF(4)*XMUPSQ*COS2
     SMENTS(2)=SCOEF(5) - SCOEF(4)*COS2
     SMENTS(3)=SCOEF(3)*XMUP1*SIN1+2.*SCOEF(4)*XMUP*SIN2
*     PRINT*,SCOEF(1),SCOEF(2),SCOEF(3),SCOEF(4),SCOEF(5)
*     PRINT*,SMENTS(1),SMENTS(2),SMENTS(3)
*
 200 CONTINUE
     RETURN
     END
*
*123456789*123456789*123456789*123456789*123456789*123456789*123456789*12
*
*  SPECT1 calculates the flux and polarization spectra.  The expression
*  used to find the formal Sobolev solution for the emergent specific
*  intensity is given by equation (2.150) of J.  The specific intensity
*  is integrated over the projection of atmosphere using Simpson's rule.
*  SPECT1 also normalizes and reddens the flux spectra if these operations
*  are specified by the INORM and IRED parameters of PAR1.  McCall's
*  prescription (1984, 1985) for the net polarization is evaluated for the
*  purpose of comparison to the Sobolev-H polarizations.  Some expressions
*  for the extrema and projections of the atmosphere and photosphere are
*  taken from Appendix 3 section (c) of J.  SPECT1 is called from READIN.
*
     SUBROUTINE SPECT1
     COMMON/CONST/CLIGHT,CTA,IFREQ,PI,PITWO,PI2,PLANC1,PLANC2,RADDEG
     COMMON/NORM/INORM,WNORM,IFRAG,YMAX,ZMAX
     PARAMETER (NLAM=125,NLINES=61,NSET=11)
     COMMON/PARAM/ANGLE,ANISO(NLINES),ASEMI,BSEMI,ICASE,
    1             ICOEF,ILINES,POWER,PREC,
    2             RGMAX,RGMIN,TAUPH(NLINES),TEMPH,THERM,
    3             TIME,VELPH,WLINE(NLINES),ZEMAX
     CHARACTER MODEL*2
     COMMON/RED/ERED,IRED
     COMMON/SET/CCALL(NLINES),DLAM,
    1 FLUX(0:NLAM,NSET,3),IDATA,IFORM,ILAM(NSET),
    1 IISET,ILATE,ILOG,ITRANS,
    2 MODEL,IPUT,ISET,JSET,JSETS,KSET(NSET),POLAR(0:NLAM,NSET,3),
    3 SET(NSET),WLAM(0:NLAM,NSET)
     PARAMETER (NCOEF=5,ZPREC=.10,NRG=INT(6./ZPREC)+1,
    1 NZETA=INT(4./ZPREC)+2)
     COMMON/SOURCE/DRGLOG,DZETA,IRG,IRG1,IZETA,IZETA1,
    1 RG(0:NRG),RGH,RGL,SOURC(NCOEF,0:NRG,0:NZETA,NLINES),ZETA(0:NZETA)
     COMMON/SOURC/ASQ,BSQ,THETA,ALP,ALPSQ,BET,BETSQ,
    1 CON1,CON2,CON3,CON4,BPRI,GMAXSQ,GMINSQ,
    2 XXLIMB,XXCORE,XXOCUL,XXCUT,QC,XTC
     PARAMETER (NGG=INT(12./ZPREC)+4,NZE=INT(4./ZPREC)+2)
```

```
      DIMENSION GG(0:NGG),SMENTS(3),SCOEF(NCOEF),
     1 YY(0:NGG,0:NZE),ZZ(0:NGG,0:NZE)
      DATA SMENTS/3*0./
      XSURF(Y,Z,GSQ)=(  CON1*Z +
     + SQRT(MAX(0.,  -CON4*Z**2+CON3*(GSQ-Y**2/ASQ)  ))  )/CON3
      XSURFN(Y,Z,GSQ)=(  CON1*Z -
     + SQRT(MAX(0.,  -CON4*Z**2+CON3*(GSQ-Y**2/ASQ)  ))  )/CON3
*
      IF(ISET .EQ. 1  .AND.  JSET .GT. 1  .AND.  ICASE .NE. 2) THEN
          THETA=ANGLE/RADDEG
          ALP=COS(THETA)
          ALPSQ=ALP**2
          BET=SIN(THETA)
          BETSQ=BET**2
*
          CON1=(1./ASQ-1./BSQ)*ALP*BET
          CON2=ALPSQ/ASQ+BETSQ/BSQ
          CON3=BETSQ/ASQ+ALPSQ/BSQ
          CON4=1./(ASQ*BSQ)
*
          IF(ANGLE .EQ. 0.  .OR.  ANGLE .EQ. 180) THEN
              BPRI=ASEMI
            ELSE IF(ANGLE .EQ. 90.) THEN
              BPRI=BSEMI
            ELSE
              BPRI=ASEMI*BSEMI*SQRT(CON3)
          END IF
          GMAXSQ=RGMAX**2
          GMINSQ=RG(0)**2
*
          XXLIMB=RGMAX*SQRT(CON2/CON4)
          XXCORE=RG(0)*SQRT(CON2/CON4)
          XXOCUL=-(  ABS(CON1*RG(0))/SQRT(CON4)  +
     1               SQRT(GMAXSQ-GMINSQ)           )
     2           /(  SQRT(CON3)  )
*
          IF((   (RGMAX/RG(0))*ABS(CON1)/SQRT(CON2*CON3) .LT. 1.)
     1          .AND.  ITRANS .EQ. 0)  THEN
              XXCUT=XXOCUL
            ELSE
              XXCUT=-XXLIMB
          END IF
*
          XQC=(VELPH/XXCORE)/CLIGHT
          XTC=TIME*VELPH/XXCORE
      END IF
*
      IF(IFRAG .NE. 0) THEN
          YMAXX=RG(0)*ASEMI*YMAX
          ZMAXX=RG(0)*BPRI*ZMAX
```

```
      END IF
*
*      BLAM=WLINE(1)/(1.+QC*XXLIMB)
*      TLAM=WLINE(ILINES)/(1.+QC*XXCUT)
      BLAM=WLINE(1)*(1.-QC*XXLIMB)
      TLAM=WLINE(ILINES)*(1.-QC*XXCUT)
      PRINT*,BLAM,TLAM,XXCORE,XXCORE*QC*CLIGHT
*      TLAM=WLINE(ILINES)/(1.-QC*XXLIMB)
*      IF(PREC .GT. .1) THEN
*          XINCR=49.
*        ELSE
*          XINCR=59.
*      END IF
*      DLAM=WLINE(1)*(  (VELPH/CLIGHT)/(1.+VELPH/CLIGHT)  )*SQRT(PREC/9.)
      DLAM=WLINE(1)*(  (VELPH/CLIGHT)/(1.+VELPH/CLIGHT)  )*(PREC/3.)
      IF(PREC .LE. .125) THEN
          XINCR=124.
          DLAM=(TLAM-BLAM)/XINCR
        ELSE IF(PREC .LE. .25) THEN
          XINCR=99.
          DLAM=(TLAM-BLAM)/XINCR
        ELSE IF(PREC .LE. .5) THEN
          XINCR=74.
          DLAM=(TLAM-BLAM)/XINCR
      END IF
*      XINCR=99
*      DLAMMN=(TLAM-BLAM)/XINCR
*      DLAM=MAX(DLAM,DLAMMN)
      IBLAM=INT((WLINE(1)-BLAM)/DLAM)
      ITLAM=INT((TLAM-WLINE(1))/DLAM)+1
      ILAM(JSET)=IBLAM+ITLAM+1
      WLAM(IBLAM+1,JSET)=WLINE(1)
      DO 410 I=IBLAM,0,-1
      WLAM(I,JSET)=WLAM(I+1,JSET)-DLAM
  410 CONTINUE
      DO 420 I=IBLAM+2,ILAM(JSET)
      WLAM(I,JSET)=WLAM(I-1,JSET)+DLAM
  420 CONTINUE
*
      IF(PLATE .EQ. 0) THEN
           IF(ABS(ZEMAX-PI) .LT. .0001) THEN
               DZE3=PI
             ELSE
               DZE3=ZEMAX
           END IF
           IZEL=0
           SLICE=1.
        ELSE
          IF( (ANGLE .EQ. 90.  .OR.  ANGLE .EQ. 0.)  .AND.
     1         ABS(ZEMAX-PI) .LT. .0001            )THEN
```

```
                  SLICE=2.
                ELSE
                  SLICE=1.
              END IF
              ZESLICE=ZEMAX/SLICE
              DZE=(ZEMAX/4.)*PREC
              IZE=INT(ZESLICE/DZE)
              IF(REAL(IZE) .LT. ZESLICE/DZE) IZE=IZE+1
              IF(MOD(IZE,2) .NE. 0) IZE=IZE+1
              IZEL=IZE
              DZE=ZESLICE/REAL(IZE)
              DZE3=DZE/3.
          END IF
*
*          DGCORE=(RG(0)/4.)*PREC
          DGCOR=.2*PREC
*      .2 seems to work pretty well;  no other justification has been thought of.
          IGCORE=INT(RG(0)/DGCOR)
          IF(REAL(IGCORE) .LT. RG(0)/DGCOR) IGCORE=IGCORE+1
          IF(MOD(IGCORE,2) .NE. 0) IGCORE=IGCORE+1
          DGCORE=RG(0)/REAL(IGCORE)
          IGLIMB=MIN(NGG-2-IGCORE, INT(  (RGMAX-RG(0))/DGCOR  )  )
          IF(REAL(IGLIMB) .LT. (RGMAX-RG(0))/DGCOR) IGLIMB=IGLIMB+1
          IF(MOD(IGLIMB,2) .NE. 0) IGLIMB=IGLIMB+1
          DGLIMB=(RGMAX-RG(0))/REAL(IGLIMB)
          IGTOT=IGCORE+IGLIMB
*
          GG(0)=0.
          DO 430 I=1,IGTOT
          IF(I .LT. IGCORE) THEN
              GG(I)=GG(I-1)+DGCORE
            ELSE IF(I .EQ. IGCORE) THEN
              GG(I)=RG(0)
            ELSE IF(I .LT. IGTOT) THEN
              GG(I)=GG(I-1)+DGLIMB
            ELSE
              GG(I)=RGMAX
          END IF
*          PRINT*,I,GG(I)
      430 CONTINUE
*
          ZE=0.
          DO 440 I=0,IZEL
          YYCOEF=ASEMI*SIN(ZE)
          ZZCOEF=BPRI*COS(ZE)
          IF(I .LT. IZE) THEN
              ZE=ZE+DZE
            ELSE
              ZE=ZESLICE
          END IF
```

```
      DO 450 J=0,IGTOT
      YY(J,I)=YYCOEF*GG(J)
      ZZ(J,I)=ZZCOEF*GG(J)
*      PRINT*,' ',I,J,GG(J),ZZCOEF,YY(J,I),ZZ(J,I)
  450 CONTINUE
  440 CONTINUE
*
      DO 460 I=0,IGTOT
      GG(I)=GG(I)+ASEMI*BPRI*SIMWT(0,I,IGTOT)/3.
  460 CONTINUE
      GG(IGCORE)=GG(IGCORE)/2.
*
      IF(INORM .NE. 0) THEN
         IF(WNORM .LT. WLAM(0,JSET)  .OR.
     1      WNORM .GT. WLAM(ILAM(JSET),JSET)   ) THEN
             WNORM=.5*(WLAM(0,JSET)+WLAM(ILAM(JSET),JSET)  )
         END IF
      END IF
      MLINE=1
*
      DO 470 I=0,ILAM(JSET)
*      XX=(WLINE(ILINE)/WLAM(I,JSET) - 1.)/QC
*      DXX=DLAM*(WLINE(ILINE)/WLAM(I,JSET)**2)/QC
*     DDXX=0.*DXX
      FCONT=0.
      FLZE=0.
      FRZE=0.
      UZE=0.
      FLZEC=0.
      FLZEL=0.
      FRZEC=0.
      FRZEL=0.
      UZEC=0.
      UZEL=0.
      DO 480 J=0,IZEL
*      DO 480 J=0,0
      WEZE=SIMWT(0,J,IZE)
      FCONTGG=0.
      FLGG=0.
      FRGG=0.
      UGG=0.
*
      DO 490 K=0,IGCORE
*      DO 490 K=0,-1
      XXC=XSURF(YY(K,J),ZZ(K,J),GMINSQ)
      XXCN=XSURFN(YY(K,J),ZZ(K,J),GMINSQ)
      XXS=XSURF(YY(K,J),ZZ(K,J),GMAXSQ)
      XXSN=XSURFN(YY(K,J),ZZ(K,J),GMAXSQ)
      IF(ICASE .EQ. 1) THEN
         FI2=.5
```

```
          ELSE
            CALL PLANCF(WLAM(I,JSET),-QC*XXC,FI2)
*           The -QC*XXC is right here, I think, because the distant observer
*           sees a blueshifted part of the spectrum (i.e., from a redder part
*           of the continuum than WLAM, but blueshifted to WLAM).  This is
*           explanation is just turned around if XXC<0.
          END IF
*
          FLG=0.
          FRG=0.
          UG=0.
          EXPTAU=1.
          EXPPHO=1.
          DO 492 ILINE=ILINES,1,-1
*          XX=(WLINE(ILINE)/WLAM(I,JSET) - 1.)/QC
          XX=(1.-WLAM(I,JSET)/WLINE(ILINE))/QC
          IF(XX .LT. XXC  .AND.  ITRANS .EQ. 0) GO TO 200
          IF(XX .LT. XXSN) GO TO 200
          IF( (XX .LT. XXS  .AND.  XX .GT. XXC)
     1 .OR.  (XX .LT. XXCN  .AND.  XX .GT. XXSN) ) THEN
              XPR=XX*BET-ZZ(K,J)*ALP
              ZPR=XX*ALP+ZZ(K,J)*BET
              RGGG=SQRT((XPR/ASEMI)**2+YY(K,J)**2/ASQ+(ZPR/BSEMI)**2)
              CALL ETAUF(ILINE,RGGG,ETAU,ETAU1)
              CALL SOURC3(ILINE,2,XPR,YY(K,J),ZPR,ALP,0,SCOEF,SMENTS)
              FLG=FLG+SMENTS(1)*ETAU1*EXPTAU
              FRG=FRG+SMENTS(2)*ETAU1*EXPTAU
              UG=UG+SMENTS(3)*ETAU1*EXPTAU
              EXPTAU=EXPTAU*ETAU
              IF(XX .GT. XXC ) EXPPHO=EXPTAU
          END IF
  492 CONTINUE
  200 CONTINUE
          FLG=FLG+FI2*EXPPHO
          FRG=FRG+FI2*EXPPHO
*
          FLGG=FLGG+GG(K)*FLG
          FRGG=FRGG+GG(K)*FRG
          UGG =UGG +GG(K)*UG
          FCONTGG=FCONTGG+GG(K)*2.*FI2
*
  490 CONTINUE
*
          FLGGL=0.
          FRGGL=0.
          UGGL=0.
*
          DO 500 K=IGCORE,IGTOT
          IF(IFRAG .NE. 0) THEN
               IF(ABS(YY(K,J)) .GE. YMAXX) GO TO 500
```

```
            IF(ABS(ZZ(K,J)) .GE. ZMAXX) GO TO 500
         END IF
         XXS=XSURF(YY(K,J),ZZ(K,J),GMAXSQ)
         XXSN=XSURFN(YY(K,J),ZZ(K,J),GMAXSQ)
         FLG=0.
         FRG=0.
         UG=0.
         EXPTAU=1.
         DO 494 ILINE=ILINES,1,-1
*         XX=(WLINE(ILINE)/WLAM(I,JSET) - 1.)/QC
         XX=(1.-WLAM(I,JSET)/WLINE(ILINE))/QC
         IF(XX .LT. XXS  .AND.  XX .GT. XXSN) THEN
             XPR=XX*BET-ZZ(K,J)*ALP
             ZPR=XX*ALP+ZZ(K,J)*BET
             RGGG=SQRT((XPR/ASEMI)**2+YY(K,J)**2/ASQ+(ZPR/BSEMI)**2)
             CALL ETAUF(ILINE,RGGG,ETAU,ETAU1)
             CALL SOURC3(ILINE,2,XPR,YY(K,J),ZPR,ALP,0,SCOEF,SMENTS)
             FLG=FLG+SMENTS(1)*ETAU1*EXPTAU
             FRG=FRG+SMENTS(2)*ETAU1*EXPTAU
             UG=UG+SMENTS(3)*ETAU1*EXPTAU
             EXPTAU=EXPTAU*ETAU
           ELSE IF(XX .LE. XXSN) THEN
             GO TO 210
         END IF
     494 CONTINUE
     210 CONTINUE
         FLGGL=FLGGL+GG(K)*FLG
         FRGGL=FRGGL+GG(K)*FRG
         UGGL =UGGL +GG(K)*UG
     500 CONTINUE
*
         FCONT=FCONT+WEZE*DGCORE*FCONTGG
         FLZE=FLZE+WEZE*(DGCORE*FLGG+DGLIMB*FLGGL)
         FRZE=FRZE+WEZE*(DGCORE*FRGG+DGLIMB*FRGGL)
         UZE=UZE+WEZE*(DGCORE*UGG+DGLIMB*UGGL)
         FLZEC=FLZEC+WEZE*DGCORE*FLGG
         FLZEL=FLZEL+WEZE*DGLIMB*FLGGL
         FRZEC=FRZEC+WEZE*DGCORE*FRGG
         FRZEL=FRZEL+WEZE*DGLIMB*FRGGL
         UZEC= UZEC +WEZE*DGCQRE*UGG
         UZEL= UZEL +WEZE*DGLIMB*UGGL
     480 CONTINUE
         FCONT=DZE3*FCONT
         FLZE=DZE3*FLZE
         FRZE=DZE3*FRZE
         UZE=DZE3*UZE
         FLZEC=DZE3*FLZEC
         FRZEC=DZE3*FRZEC
         FLZEL=DZE3*FLZEL
         FRZEL=DZE3*FRZEL
```

```
      FTOT=FLZE+FRZE
      FTOT1=FLZEC+FRZEC
      FTOT2=FLZEL+FRZEL
      IF(INORM .EQ. 0) THEN
          IF(I .EQ. 0) THEN
              FNORM=FTOT
              JNORM=0
          END IF
        ELSE
          IF(ABS(WNORM-WLAM(I,JSET)) .LE. .51*DLAM) THEN
               FNORM=FCONT
               JNORM=I
          END IF
      END IF
      FLUX(I,JSET,3)=FTOT
      FLUX(I,JSET,1)=FTOT1
      IF(ICASE .EQ. 1) THEN
          IF(I .EQ. 0) FCORE=FCONT
          FLUX(I,JSET,2)=FTOT2+FCORE
        ELSE
          FLUX(I,JSET,2)=FTOT2+FCONT
      END IF
      POLAR(I,JSET,3)=(FLZE-FRZE)/FTOT
      POLAR(I,JSET,2)=(FLZEL-FRZEL)/FTOT
      POLAR(I,JSET,1)=(FLZEC-FRZEC)/FTOT
      IF(ABS(ZEMAX-PI) .GT. .0001) THEN
          POLAR(I,JSET,3)=SQRT(POLAR(I,JSET,3)**2+(UZE/FTOT)**2)
          POLAR(I,JSET,2)=SQRT(POLAR(I,JSET,2)**2+(UZEL/FTOT)**2)
          POLAR(I,JSET,1)=SQRT(POLAR(I,JSET,1)**2+(UZEC/FTOT)**2)
        ELSE IF(ILATE .EQ. 0) THEN
          POLAR(I,JSET,3)=0.
          POLAR(I,JSET,2)=0.
          POLAR(I,JSET,1)=0.
      END IF
      IF(ABS(WLAM(I,JSET)-WLINE(MLINE)) .LT. .51*DLAM) THEN
          CCALL(MLINE+ (JSET-1)*IISET  )=(FTOT2/FTOT)*
     1     (  (BPRI-ASEMI)/(BPRI+ASEMI)  )*
     2     ((POWER+1)/(POWER+3))*
     3     (3.*ANISO(MLINE))/(4.-ANISO(MLINE))
           MLINE=MIN(MLINE+1,ILINES)
      END IF
*
  470 CONTINUE
*
      IF(ILOG .EQ. 0  .AND.  IRED .NE. 0) THEN
           FNORM=FNORM*REDDEN(WLAM(JNORM,JSET),ERED)
      END IF
*
      DO 505 I=0,ILAM(JSET)
      IF(IRED .NE. 0) THEN
```

```
            REDDER=REDDEN(WLAM(I,JSET),ERED)
          ELSE
            REDDER=1.
        END IF
        DO 506 J=1,3
        IF(ILOG .EQ. 0) THEN
            FLUX(I,JSET,J)=
     1        FLUX(I,JSET,J)*REDDER/FNORM
          ELSE
            FLUX(I,JSET,J)=LOG10(2.*SLICE*
     1        FLUX(I,JSET,J)*REDDER    )
        END IF
  506 CONTINUE
  505 CONTINUE
*
  910 FORMAT(///' ',4X,'I',11X,'WAVELENGTH'/' ',I5,E20.7)
  920 FORMAT(/' ',3(12X,'SMENTS ',I1)/' ',3E20.7)
  930 FORMAT(/' ',5(13X, 'SCOEF ',I1)/' ',5E20.7)
  940 FORMAT(/' ',16X,'FLZE',16X,'FRZE',17X,'UZE'/' ',3E20.7)
  950 FORMAT(/' ',15X,'FLZEC',15X,'FRZEC',16X,'POLC',
     1               15X,'FLZEL',15X,'FRZEL',16X,'POLL'/
     2 ' ',6E20.7)
*
        RETURN
        END
*
*123456789*123456789*123456789*123456789*123456789*123456789*123456789*12
*
*  SURFBR calculates the surface brightness and polarization of the
*  atmosphere at a specified wavelength.  The expression used to find
*  the formal Sobolev solution for the emergent specific intensity is
*  given by equation (2.150) of J.  The PAR4 parameters control the
*  operation of this subroutine.  Some expressions for the extrema and
*  projections of the atmosphere and photosphere are taken from
*  Appendix 3 section (c) of J.  SURFBR is called from READIN.
*
*
        SUBROUTINE SURFBR
        COMMON/CONST/CLIGHT,CTA,IFREQ,PI,PITWO,PI2,PLANC1,PLANC2,RADDEG
        COMMON/NORM/INORM,WNORM,IFRAG,YMAX,ZMAX
        PARAMETER (NLAM=125,NLINES=61,NSET=11)
        COMMON/PARAM/ANGLE,ANISO(NLINES),ASEMI,BSEMI,ICASE,
     1               ICOEF,ILINES,POWER,PREC,
     2               RGMAX,RGMIN,TAUPH(NLINES),TEMPH,THERM,
     3               TIME,VELPH,WLINE(NLINES),ZEMAX
        CHARACTER MODEL*2
        COMMON/RED/ERED,IRED
        COMMON/SET/CCALL(NLINES),DLAM,
     1 FLUX(0:NLAM,NSET,3),IDATA,IFORM,ILAM(NSET),
     1 IISET,ILATE,ILOG,ITRANS,
```

```
     2 MODEL,IPUT,ISET,JSET,JSETS,KSET(NSET),POLAR(0:NLAM,NSET,3),
     3 SET(NSET),WLAM(0:NLAM,NSET)
      PARAMETER (NCOEF=5,ZPREC=.10,NRG=INT(6./ZPREC)+1,
     1 NZETA=INT(4./ZPREC)+2)
      COMMON/SOURCE/DRGLOG,DZETA,IRG,IRG1,IZETA,IZETA1,
     1 RG(0:NRG),RGH,RGL,SOURC(NCOEF,0:NRG,0:NZETA,NLINES),ZETA(0:NZETA)
      COMMON/SOURC/ASQ,BSQ,THETA,ALP,ALPSQ,BET,BETSQ,
     1 CON1,CON2,CON3,CON4,BPRI,GMAXSQ,GMINSQ,
     2 XXLIMB,XXCORE,XXOCUL,XXCUT,QC,XTC
      COMMON/SURF/ISURF,IPACT,SURFWA,SURFAN
      DIMENSION SMENTS(3),SCOEF(NCOEF)
      DATA SMENTS/3*0./
      XSURF(Y,Z,GSQ)=(  CON1*Z +
     + SQRT(MAX(0.,  -CON4*Z**2+CON3*(GSQ-Y**2/ASQ)  ))  )/CON3
      XSURFN(Y,Z,GSQ)=(  CON1*Z -
     + SQRT(MAX(0.,  -CON4*Z**2+CON3*(GSQ-Y**2/ASQ)  ))  )/CON3
*
      IF(ISET .EQ. 1  .AND.  JSET .GT. 1  .AND.  ICASE .NE. 2) THEN
          THETA=ANGLE/RADDEG
          ALP=COS(THETA)
          ALPSQ=ALP**2
          BET=SIN(THETA)
          BETSQ=BET**2
*
          CON1=(1./ASQ-1./BSQ)*ALP*BET
          CON2=ALPSQ/ASQ+BETSQ/BSQ
          CON3=BETSQ/ASQ+ALPSQ/BSQ
          CON4=1./(ASQ*BSQ)
*
          IF(ANGLE .EQ. 0.  .OR.  ANGLE .EQ. 180) THEN
              BPRI=ASEMI
            ELSE IF(ANGLE .EQ. 90.) THEN
              BPRI=BSEMI
            ELSE
              BPRI=ASEMI*BSEMI*SQRT(CON3)
          END IF
          GMAXSQ=RGMAX**2
          GMINSQ=RG(0)**2
*
          XXLIMB=RGMAX*SQRT(CON2/CON4)
          XXCORE=RG(0)*SQRT(CON2/CON4)
          XXOCUL=-(  ABS(CON1*RG(0))/SQRT(CON4)  +
     1                SQRT(GMAXSQ-GMINSQ)          )
     2            /(  SQRT(CON3)  )
*
          IF((   (RGMAX/RG(0))*ABS(CON1)/SQRT(CON2*CON3) .LT. 1.)
     1           .AND.  ITRANS .EQ. 0)  THEN
              XXCUT=XXOCUL
            ELSE
              XXCUT=-XXLIMB
```

```
            END IF
*
            QC=(VELPH/XXCORE)/CLIGHT
            XTC=TIME*VELPH/XXCORE
        END IF
*
        GGST=.1*RG(0)
        GGMULT=10.**(  LOG10(.995*RGMAX/GGST)/REAL(IPACT-1)  )
        GG=0.
        SURFRA=SURFAN/RADDEG
        WRITE(5,*) JSET,IPACT,SURFWA,SURFAN
        DO 410 I=0,IPACT
        ZE=(BPRI/ASEMI)*TAN(SURFRA)
        YY=ASEMI*SIN(ZE)*GG
        ZZ=BPRI*COS(ZE)*GG
        PACT=SQRT(YY**2+ZZ**2)
*
        XXS=XSURF(YY,ZZ,GMAXSQ)
        XXSN=XSURFN(YY,ZZ,GMAXSQ)
*
        FLG=0.
        FRG=0.
        UG=0.
        EXPTAU=1.

        IF(GG .LE. RG(0)) THEN
*
        XXC=XSURF(YY,ZZ,GMINSQ)
        XXCN=XSURFN(YY,ZZ,GMINSQ)
        EXPPHO=1.
        DO 492 ILINE=ILINES,1,-1
        XX=(1.-SURFWA/WLINE(ILINE))/QC
        IF(XX .LT. XXC  .AND.  ITRANS .EQ. 0) GO TO 200
        IF(XX .LT. XXSN) GO TO 200
        IF( (XX .LT. XXS  .AND.  XX .GT. XXC)
       1 .OR.  (XX .LT. XXCN  .AND.  XX .GT. XXSN) ) THEN
            XPR=XX*BET-ZZ*ALP
            ZPR=XX*ALP+ZZ*BET
            RGGG=SQRT((XPR/ASEMI)**2+YY**2/ASQ+(ZPR/BSEMI)**2)
            CALL ETAUF(ILINE,RGGG,ETAU,ETAU1)
            CALL SOURC3(ILINE,2,XPR,YY,ZPR,ALP,0,SCOEF,SMENTS)
            FLG=FLG+SMENTS(1)*ETAU1*EXPTAU
            FRG=FRG+SMENTS(2)*ETAU1*EXPTAU
            UG=UG+SMENTS(3)*ETAU1*EXPTAU
            EXPTAU=EXPTAU*ETAU
            IF(XX .GT. XXC ) EXPPHO=EXPTAU
        END IF
    492 CONTINUE
    200 CONTINUE
        IF(ICASE .EQ. 1) THEN
```

```
            FI2=.5
          ELSE
            CALL PLANCF(SURFWA,-QC*XXC,FI2)
*           The -QC*XXC is right here, I think, because the distant observer
*           sees a blueshifted part of the spectrum (i.e., from a redder part
*           of the continuum than SURFWA, but blueshifted to SURFWA).  This
*           is explanation is just turned around if XXC<0.
        END IF
        FLG=FLG+FI2*EXPPHO
        FRG=FRG+FI2*EXPPHO
*
        ELSE
*
        DO 430 ILINE=ILINES,1,-1
        XX=(1.-SURFWA/WLINE(ILINE))/QC
        IF(XX .GT. XXS) GO TO 430
        IF(XX .LT. XXSN) GO TO 210
            XPR=XX*BET-ZZ*ALP
            ZPR=XX*ALP+ZZ*BET
            RGGG=SQRT((XPR/ASEMI)**2+YY**2/ASQ+(ZPR/BSEMI)**2)
            CALL ETAUF(ILINE,RGGG,ETAU,ETAU1)
            CALL SOURC3(ILINE,2,XPR,YY,ZPR,ALP,0,SCOEF,SMENTS)
            FLG=FLG+SMENTS(1)*ETAU1*EXPTAU
            FRG=FRG+SMENTS(2)*ETAU1*EXPTAU
            UG=UG+SMENTS(3)*ETAU1*EXPTAU
            EXPTAU=EXPTAU*ETAU
  430   CONTINUE
  210   CONTINUE
*
        END IF
*
        FLUXX=FLG+FRG
        QG=FLG-FRG
        IF(FLUXX .NE. 0.) THEN
            POL=SQRT(QG**2+UG**2)/FLUXX
          ELSE
            POL=-1.
        END IF
        IF(QG .NE. 0) THEN
            CHI=ATAN(UG/QG)
          ELSE
            CHI=0.
        END IF
        POL1=QG*COS(CHI)+UG*SIN(CHI)
        POL2=QG*COS(CHI+PI)+UG*SIN(CHI+PI)
        CHI=RADDEG*.5*CHI
        IF(POL1 .LT. POL2) CHI=CHI+90.
        WRITE(5,*) I,PACT,FLUXX,POL,CHI,QG,UG
*
        IF(I .EQ. 0) THEN
```

```
            GG=GGST
*         ELSE IF(I .EQ. IPACT-1) THEN
*             GG=RGMAX
          ELSE
              GG=GG*GGMULT
          END IF
  410 CONTINUE
*
      RETURN
      END
*
*123456789*123456789*123456789*123456789*123456789*123456789*123456789*12
*
*  TEST calls a number of subroutines that test various working subroutines
*  of the S7 program.  The test subroutines are identified by their
*  0-suffixes.  These test subroutines were only used in the early
*  development of the S7 program and it is no longer certain that they
*  will perform properly.  However, they could be revived if needed.  TEST
*  is called from READIN.
*
      SUBROUTINE TEST(ITEST)
      PARAMETER (NLAM=125,NLINES=61,NSET=11)
      COMMON/PARAM/ANGLE,ANISO(NLINES),ASEMI,BSEMI,ICASE,
     1             ICOEF,ILINES,POWER,PREC,
     2             RGMAX,RGMIN,TAUPH(NLINES),TEMPH,THERM,
     3             TIME,VELPH,WLINE(NLINES),ZEMAX
      DATA ITABLE/0/
*
      GO TO (110,120,130,140,150),ITEST
*
  110 CONTINUE
      CALL BETAFO(ITABLE)
      GO TO 200
*
  120 CONTINUE
      GO TO 200
*
  130 CONTINUE
      CALL SOURCO(ITABLE)
      GO TO 200
*
  140 CONTINUE
      CALL XMUO(ITABLE,20,1)
      GO TO 200
*
  150 CONTINUE
      CALL XMUOA
*
  200 CONTINUE
      RETURN
```

```
      END
*
*123456789*123456789*123456789*123456789*123456789*123456789*123456789*12
*
*  XMUO, and XMUOA are testing routines for the XMU1, XMU2, and XMU3
*  subroutines.  They are both called from subroutine TEST.
*
      SUBROUTINE XMUO(ITABLE,JPOINT,IOUT)
      PARAMETER (ICASS=9,IPOINT=50,ISPHRD=3)
      PARAMETER (IWORK=MAX(4*(IPOINT+1),800) )
      COMMON/CONST/CLIGHT,CTA,IFREQ,PI,PITWO,PI2,PLANC1,PLANC2,RADDEG
      DIMENSION A(ISPHRD),B(ISPHRD),CC(ICASS),
     1 DD(ICASS),FX(0:IPOINT,2*ICASS),WORK(IWORK),X(0:IPOINT)
      DATA IDONE/0/
      DATA A/0.5,1.0,4.0/,
     1     B/4.0,1.0,0.5/
      DATA CC/0.0,1.5,0.5,0.5,0.5,1.5,1.5,0.0,1.0/,
     1     DD/1.5,0.0,0.0,1.5,0.0,1.5,0.5,1.0,0.0/
*
      IF(IDONE .EQ. 0) PRINT905
      IDONE=1
  905 FORMAT('1','TEST RESULTS FOR THE XMU-ROUTINES')
      KPOINT=MIN(JPOINT,IPOINT)
      DD(3)=SQRT(1.-CC(3)**2)
      DD(5)=.5*(  1.+SQRT(1.-CC(5)**2)  )
      DPHI=PI/REAL(KPOINT)
      X(0)=0.
      DO 405 I=1,KPOINT-1
      X(I)=X(I-1)+DPHI
  405 CONTINUE
      X(KPOINT)=PI
*
      DO 410 I=1,ISPHRD
      DO 420 J=1,ICASS
*
      ITABLE=ITABLE+1
      C=CC(J)*A(I)
      D=DD(J)*B(I)
      CALL XMU1(A(I),B(I),C,D,PHIC)
      PRINT910,ITABLE,A(I),B(I),C,D,PHIC
  910 FORMAT(///' ','TEST-TABLE ',I2,':  XMUL(PHI) AND XMUH(PHI)'//
     1 ' ',11X,5X,'A=',F5.2,5X,'B=',F5.2,/
     2 ' ',11X,5X,'C=',F5.2,5X,'D=',F5.2,/
     3 ' ',11X,2X,'PHIC=',E14.7)
      PRINT920
  920 FORMAT(///' ',9X,'I',12X,'PHI',11X,'XMUL',11X,'XMUH'/)
  930 FORMAT(' ',I10,3E15.7)
*
      IPHIC=-1
      DO 430 K=0,KPOINT
```

```
      IF(X(K) .LE. PHIC) THEN
        CALL XMU2(X(K),FX(K,J),FX(K,J+ICASS))
        PRINT930,K,X(K),FX(K,J),FX(K,J+ICASS)
       ELSE IF(IPHIC .LT. 0) THEN
        CALL XMU2(PHIC,FX1,FX2)
        PRINT930,K,PHIC,FX1,FX2
        IPHIC=1
        FX(K,J)=FX1
        FX(K,J+ICASS)=FX2
       ELSE
        FX(K,J)=FX1
        FX(K,J+ICASS)=FX2
      END IF
  430 CONTINUE
*
  420 CONTINUE
      IF(IOUT .GT. 1) THEN
*         CALL SIMSTART(.TRUE.,.FALSE.)
        CALL SIMANN(.TRUE.)
        CALL SIMXRNG(0.,PI)
        CALL SIMYRNG(-1.05,1.05)
        CALL SIMSAME(.TRUE.)
        CALL SIMINT(1)
        CALL SIMPLOT(X(0),FX(0,1),KPOINT+1,KPOINT+1,2*KPOINT,WORK)
        CALL SIMXLAB('PHI')
        CALL SIMYLAB('XMU')
        CALL SIMTITL('FIGURE  :  XMU BOUNDS')
      END IF
*
  410 CONTINUE
*
      RETURN
      END
*
*
*
*
      SUBROUTINE XMUOA
      COMMON/XMU/ICAS,PHIZ,XMUCON,AA4,AA2,AA0,BB4,BB2,BB0,DIS4,DIS2,
     1 PMU,QMU,SMU
      DATA A,B,C,D/.5,4.0,.75,6.0/
*
  110 CONTINUE
      CALL XMU1(A,B,C,D,PHIC)
      CALL XMU2(PHIC,XMUL,XMUH)
      CALL XMU3(PHIC,CON1,CON2)
      GAMMA=COS(PHIC)
      GAMSQ=GAMMA**2
      GAMQU=GAMSQ**2
      DIS=(DIS4*GAMSQ+DIS2)*GAMSQ
```

```
      PRINT*,D,PHIC,XMUL,XMUH
      PRINT*,D,GAMMA,CON1,CON2
      PRINT*,D,GAMSQ,DIS2,DIS4,DIS
      PRINT*,'GIVE A NEW D (D<0 STOPS THE EXECUTION).'
      READ*,D
      IF(D .GE. 0) GO TO 110
*
      RETURN
      END
*
*123456789*123456789*123456789*123456789*123456789*123456789*123456789*12
*
* XMU1, XMU2, and XMU3 find xmu limits of integration for integrating
* over the projected face of an axisymmetric ellipsoid with x-y semiaxes
* A and z semiaxis B, as seen from the point (x=C,z=D). XMU1 determines
* the case and some constant values for a given point (C,D).  XMU2
* evaluates the xmu limits for for each PHI value, and XMU3 is an
* auxiliary to XMU2.  The expressions used for the integration limits
* are derived in Appendix 3 section (b) of J.  XMU1 is called called
* from GRAL1, XMU0, and XMU0A.  XMU2 is called in GRAL2, XMU0, and XMU0A.
* XMU3 is called from XMU0A, and XMU2.
*
*
      SUBROUTINE XMU1(A,B,C,D,PHIC)
      COMMON/CONST/CLIGHT,CTA,IFREQ,PI,PITWO,PI2,PLANC1,PLANC2,RADDEG
      COMMON/XMU/ICAS,PHIZ,XMUCON,AA4,AA2,AA0,BB4,BB2,BB0,DIS4,DIS2,
     1 PMU,QMU,SMU
*
      ASQ=A**2
      BSQ=B**2
      CASQ=(C/A)**2
      PMU=(C/ASQ)**2
      SMU=(1.-CASQ-(D/B)**2)/ASQ
      TMU=(1.-CASQ)/BSQ
      UMU=2.*C*D/(ASQ*BSQ)
      QMU=SMU-TMU
*
      AA4=PMU**2
      AA2=UMU**2+2*PMU*QMU
      AA0=QMU**2
      BB4=-2.*AA4
      BB2=2.*PMU*(TMU-2.*SMU)-UMU**2
      BB0=-2.*SMU*QMU
      DISCON=-4.*SMU*(UMU/B)**2
      DIS4=DISCON*CASQ
      DIS2=DISCON*(1.-CASQ)
*
      IF(C .LE. 0.) THEN
         ICAS=1
         PHIC=PI
```

```
          XMUCON=SQRT(MAX(0.,  SMU/QMU  ))
        ELSE IF(D .LE. 0.) THEN
          ICAS=2
          PHIC=ACOS(SQRT(MAX(0.,  -SMU/PMU  )))
        ELSE IF(SMU .GE. 0.) THEN
          ICAS=3
          PHIC=PI
        ELSE IF(C .LE. A  .AND.  D .GE. B) THEN
          ICAS=4
          PHIC=PI
        ELSE IF(C .LE. A) THEN
          ICAS=5
          PHIC=PI
          PHIZ=ACOS(SQRT(MAX(0.,  -SMU/PMU  )))
        ELSE IF(D .GE. B) THEN
          ICAS=6
          PHIC=ACOS(SQRT(MAX(0.,  1.-1./CASQ  )))
        ELSE
          ICAS=7
          PHIC=ACOS(SQRT(MAX(0.,  1.-1./CASQ  )))
          PHIZ=ACOS(SQRT(MAX(0.,  -SMU/PMU  )))
      END IF
*
      RETURN
      END
*
*
*
*
      SUBROUTINE XMU2(PHI,XMUL,XMUH)
      COMMON/CONST/CLIGHT,CTA,IFREQ,PI,PITWO,PI2,PLANC1,PLANC2,RADDEG
      COMMON/XMU/ICAS,PHIZ,XMUCON,AA4,AA2,AA0,BB4,BB2,BB0,DIS4,DIS2,
     1 PMU,QMU,SMU
*
      GO TO (110,120,130,140,150,160,170),ICAS
*
  110 CONTINUE
      XMUH=1.
      XMUL=XMUCON
      GO TO 200
  120 CONTINUE
      IF(PHI .LT. PI2) THEN
          CON1=(COS(PHI)**2)*PMU
          XMUH=SQRT(MAX(0.,  (CON1+SMU)/(CON1+QMU)  ))
        ELSE
          XMUH=1.
      END IF
      XMUL=-XMUH
      GO TO 200
  130 CONTINUE
```

```
      XMUH=1.
      CALL XMU3(PHI,CON1,CON2)
      XMUL=SQRT(MAX(0.,  CON1  ))
      IF(PHI .LT. PI2) XMUL=-XMUL
      GO TO 200
  140 CONTINUE
      XMUH=1.
      CALL XMU3(PHI,CON1,CON2)
      IF(PHI .LT. PI2) THEN
          XMUL=SQRT(MAX(0.,  CON1-CON2  ))
        ELSE
          XMUL=SQRT(MAX(0.,  CON1+CON2  ))
      END IF
      GO TO 200
  150 CONTINUE
      XMUH=1.
      CALL XMU3(PHI,CON1,CON2)
      IF(PHI .LT. PI2) THEN
          XMUL=SQRT(MAX(0.,  CON1-CON2  ))
          IF(PHI .LT. PHIZ) XMUL=-XMUL
        ELSE
          XMUL=SQRT(MAX(0.,  CON1+CON2  ))
      END IF
      GO TO 200
  160 CONTINUE
      CALL XMU3(PHI,CON1,CON2)
      XMUH=SQRT(MAX(0.,  CON1+CON2  ))
      XMUL=SQRT(MAX(0.,  CON1-CON2  ))
      GO TO 200
  170 CONTINUE
      CALL XMU3(PHI,CON1,CON2)
      XMUH=SQRT(MAX(0.,  CON1+CON2  ))
      XMUL=SQRT(MAX(0.,  CON1-CON2  ))
      IF(PHI .LT. PHIZ) XMUL=-XMUL
*
  200 CONTINUE
      XMUH=MIN(1.,MAX(-1.,  XMUH  ))
      XMUL=MIN(1.,MAX(-1.,  XMUL  ))
      RETURN
      END
*
*
*
*
      SUBROUTINE XMU3(PHI,CON1,CON2)
      COMMON/XMU/ICAS,PHIZ,XMUCON,AA4,AA2,AA0,BB4,BB2,BB0,DIS4,DIS2,
     1 PMU,QMU,SMU
*
      GAMSQ=COS(PHI)**2
      AA=(AA4*GAMSQ+AA2)*GAMSQ+AA0
```

```
      BB=(BB4*GAMSQ+BB2)*GAMSQ+BB0
      DIS=(DIS4*GAMSQ+DIS2)*GAMSQ
      CON1=-BB/(2.*AA)
      CON2=SQRT(MAX(0.,  DIS  ))/(2.*AA)
*
      RETURN
      END
```

REFERENCES

Allen, C. W. 1976, *Astrophysical Quantities* (London: The Athlone Press).

Ambwani, K. 1986, M.Sc. Thesis, McMaster University, Hamilton Ontario.

Ambwani, K., and Sutherland, P. G. 1988, *Ap. J.*, in press.

Arnett, W. D. 1979, *Ap. J. (Letters)*, **230**, L37.

_______. 1980, *Ap. J.*, **237**, 541.

Arnett, W. D., and Falk, S. W. 1976, *Ap. J.*, **210**, 733.

Axelrod, T. S. 1980a, Ph.D. Thesis, University of California, Santa Cruz.

Axelrod, T. S. 1980b, in *Proceedings of the Texas Workshop on Type I Supernovae*, ed. J. C. Wheeler (Austin: University of Texas), p. 80.

Baade, W. 1926, *Astr. Nachr.*, **228**, 359.

Bahcall, J. N., Piran, T., Press, W. H., and Spergel, D. N. 1987, *Nature*, **327**, 682.

Ballagh, R. J., and Cooper, J. 1977, *Ap. J.*, **213**, 479.

Barbon, R. 1980, in *Proceedings of the Texas Workshop on Type I Supernovae*, ed. J. C. Wheeler (Austin: University of Texas), p. 16.

Barbon, R., Ciatti, F., and Rosino, L. 1973, *Astron. Astrophys.*, **25**, 241.

Barbon, R., Ciatti, F., and Rosino, L. 1979, *Astron. Astrophys.*, **72**, 287.

Barrett, P. 1987, *IAU Circ.*, No. 4337.

Bartunov, O. S., and Mozgovoi, A. L. 1987, *Astrophysics*, **26**, 136.

Beckwith, S., and Natta, A. 1987, *Astron. Astrophys.*, **181**, 57.

Benvenuti, P., Sanz Fernandez de Cordoba, L., Wamsteker, W., Macchetto, F., Palumbo, G. C., and Panagia, N. 1982, ESA SP-1046.

Biermann, P., and Tinsley B. M. 1974, *Publ. Astron. Soc. Pac.*, **86**, 791.

Bionta, R. M., Blewitt, G., Bratton, C. B., Casper, C., Ciocio, A., Claus, R., Cortez B., Crouch, M., Dye, S. T., Errede, S., Foster, G. W., Gajewsik, W., Ganezer, K. S., Goldhaber, M., Haines, T. J., Jones, T. W., Kielczewska, D., Kropp, W. R., Learned, J. G., LoSecco, J. M., Matthews, J., Millar, R., Mudan, M. S., Park, H. S., Price, L. R., Reines, F., Schultz, J., Seidel, S., Shumard, E., Sinclair, D., Sobel, H. W., Stone, J. L., Sulak, L. R., Svoboda, R., Thornton, G., van der Velde, J. C., and Wuest, C. 1987, *Phys. Rev. Letters*, **58**, 1494.

Bisnovatyi-Kogan, G. S., and Blinnikov, S. I. 1980, in *Supernova Remnants and Their X-ray Emission*, ed. J. Danziger and P. Gorenstein (Dordrecht: D. Reidel Publishing Company), p. 125.

Blanco, V. M., Gregory, B., Hamuy, M., Heathcote, S. R., Phillips, M. M., Suntzeff, N. B., Terndrup, D. M., Walker, A. R., Williams, R. E., Pastoriza, M. G., Storchi-Bergmann, T., and Matthews, J. M. 1987, *Ap. J.*, **320**, 589.

Bodenheimer, P., and Woosley, S. E. 1983, *Ap. J.*, **269**, 281.

Bouchet, R., Stanga, R., Le Bertre, T., Epchtein, N., Hamann, W. R., Lorenzetti, D. 1987, *Astron. Astrophys.*, **177**, L9.

Branch, D. 1980, in *Supernova Spectra*, ed. R. Meyerott and G. H. Gillespie (New York: American Institute of Physics), p. 39.

_______. 1982, in *Supernovae: A Survey of Current Research*, ed. M. J. Rees and R. J. Stoneham (Dordrecht: D. Reidel Publishing Company), p. 267.

_______. 1986, *Ap. J. (Letters)*, **300**, L51.

_______. 1987a, *Ap. J. (Letters)*, **316**, L81.

_______. 1987b, *Ap. J. (Letters)*, **320**, L23.

Branch, D., Falk, S. W., McCall, M. L., Rybski, P., Uomoto, A., and Wills, B. J. 1981, *Ap. J.*, **244**, 780.

Branch, D., Buta, R., Falk, S. W., McCall, M. L., Sutherland, P. G., Uomoto, A., Wheeler, J. C., and Wills, B. J. 1982, *Ap. J. (Letters)*, **252**, L61.

Branch, D., Lacy, C H., McCall, M. L., Sutherland, P. G., Uomoto, A., Wheeler, J. C., and Wills, B. J. 1983, *Ap. J.*, **270**, 123.

Branch, D., Doggett, J. B., Nomoto, K., and Thielemann, F.-K. 1985, *Ap. J.*, **294**, 619.

Brown, J. C., and McLean, I. S. 1977, *Astron. Astophys.*, **57**, 141.

Burrows, A., and Lattimer, J. M. 1987, *Ap. J. (Letters)*, **318**, L63.

Cadonau, R., Sandage, A., and Tammann, G. A. 1985, in *Supernovae as Distance Indicators*, ed. N. Bartel (Berlin: Springer-Verlag), p. 48.

Cassinelli, J. P., and Hummer, D. G. 1971, *M.N.R.A.S.*, **154**, 9.

Castor, J. I. 1970, *M.N.R.A.S.*, **149**, 111.

Castor, J. K., and Lamers, H.J.G.L.M. 1979, *Ap. J. Suppl.*, **39**, 481.

Chandrasekhar, S. 1960, *Radiative Transfer* (New York: Dover Publications, Inc.).

Chevalier, R. A. 1976, *Ap. J.*, **207**, 872.

_______. 1984, *Ann. NY Acad. Sci.*, **422**, 215.

Chevalier, R. A., and Klein, R. I. 1978, *Ap. J.*, **219**, 994.

Clark, D. H., and Stephenson, F. R. 1982, in *Supernovae: A Survey of Current Research*, ed. M. J. Rees and R. J. Stoneham (Dordrecht: D. Reidel Publishing Company), p. 355.

Clark, D. H., and Tuohy, I. R. 1980, in *Supernova Remnants and Their X-ray Emission*, ed. J. Danziger and P. Gorenstein (Dordrecht: D. Reidel Publishing Company), p. 153.

Code, A. D. 1950, *Ap. J.*, **112**, 22.

Code, A., Davis, J., Bless, R., and Brown, H. 1976, *Ap. J.*, **203**, 417.

Colgate, S. A. 1982, in *Supernovae; A Survey of Current Research*, ed. M. J. Rees and R. J. Stoneham (Dordrecht: D. Reidel Publishing Company), p. 319.

Colgate, S. A., and McKee, C. 1969, *Ap. J.*, **157**, 623.

Colgate, S. A., Petschek, A. G., and Kriese, J. T. 1980, *Ap. J. (Letters)*, **237**, L81.

Cooper, J., Ballagh, R. J., Burnett, K., and Hummer, D. G. 1982., *Ap. J.*, **260**, 299.

Cropper, M., Bailey, J., McCowage, J., Cannon, R. D., Couch, W. J., Walsh, J. R., Straede, J. 0., and Freeman F. 1987, submitted to *M.N.R.A.S.*

Danziger, I. J., Fosbury, R. A. E., Alloin, D., Cristiani, S., Dachs, J., Gouiffes, C., Jarvis, B., and Sahu, K. C. 1987, *Astron. Astrophys.*, **177**, L13.

de Jong, T., Chu, S-I., and Dalgarno, A. 1975, *Ap. J.*, **199**, 69.

Doggett, J. B., and Branch, D. 1985, *Astron. J.*, **90**, 2303.

Dwek, E., A'Hearn, M. F., Becklin, E. E., Brown, R. H., Capps, R. W., Dinerstein, H. L., Gatley, I., Morrison, D., Telesco, C. M., Togunaka, A. T., Werner, M. W., Wynn-Williams, C. G. 1983, *Ap. J.*, **274**, 168.

Elias, J. H., Frogel, J. A., Hackwell, J. A., and Persson, S. E. 1981, *Ap. J. (Letters)*, **251**, L13.

Evans, R. 1986, in *Highlights in Astronomy*, Vol. 7, ed. J.-P. Swings (Dordrecht: D. Reidel Publishing Company), p. 579.

Falk, S. W., and Arnett, W. D. 1973, *Ap. J. (Letters)*, **180**, L65.

Falk, S. W., and Arnett, W. D. 1977, *Ap. J. Suppl.*, **33**, 515.

Fransson, C. 1984, *Physica Scripta*, T7, 50.

Feldt, A. N. 1980, Ph.D. Thesis, University of Oklahoma, Norman Oklahoma.

Grassberg, E. K., Imshennik, V. S., and Nadëzhin, D. K. 1971, *Astrophys. Space Sci.*, **10**, 28.

Gilmozzi, R., Cassatella, A., Clavel, J., Fransson, C., Gonzalez, R., Gry, C., Panagia, N., Talavera, A., and Wamsteker, W. 1987, *Nature*, **328**, 318.

Glen, W. T. G. 1985, Ph.D. Thesis, McMaster University, Hamilton Ontario.

Gunn, J. E., and Ostriker, J. P. 1969, *Nature*, **221**, 454.

Haman, W.-R. 1981, *Aston. Astrophys.*, **93**, 353.

Hamilton, D. R. 1940, *Phys. Rev.*, **58**, 122.

_______. 1947, *Ap. J.*, **106**, 457.

Harkness, R. 1985, in *Supernovae as Distance Indicators*, ed. N. Bartel (Berlin: Springer-Verlag), p. 183.

_______. 1986, in *Radiation Hydrodynamics in Stars and Compact Objects*, ed. D. Mihalas and K.-H. A. Winkler (Berlin: Springer-Verlag), p. 166.

Harkness, R. P., *et al.* 1987, Ap. J., in press.

Harrington, J. P. 1969, *Ap. J. (Letters)*, **3**, 165.

Hempe, K. 1985, in *Supernovae as Distance Indicators*, ed. N. Bartel (Berlin: Springer-Verlag), p. 192.

Hillebrandt, W. 1982, in *Supernovae: A Survey of Current Research*, ed. M. J. Rees and R. J. Stoneham (Dordrecht: D. Reidel Publishing Company), p. 123.

Hirata, K., Kajita, T., Koshiba, M., Nakahata, M., Oyama, Y., Sato, N., Suzuki, A., Takita, M., Totsuka, Y., Kifune, T., Suda, T., Takahashi, K., Tanimori, T., Miyano, K., Yamada, M., Beier, E. W., Feldscher, L. R., Kim, S. B., Mann, A. K., Newcomer, F. M., Van Berg, R., Zhang, W., and Cortez, B. G. 1987, *Phys. Rev. Letters*, **58**, 1490.

Hummer, D. G. 1962, *M.N.R.A.S.*, **125**, 21.

_______. 1969, *M.N.R.A.S.*, **145**, 95.

Hummer, D. G., and Rybicki, G. B. 1985, *Ap. J.*, **293**, 258.

Iben, I. Jr., and Renzini, A. 1983, *Ann. Rev. Asron. Astrophys.*, **21**, 271.

Imshennik, V. S., and Nadëzhin, D. K. 1964, *Astron. Zh.*, **41**, 829.

Jeffery, D. J. 1983, M.Sc. Thesis, McMaster University, Hamilton Ontario.

———. 1987, *Nature*, **329**, 419.

Jeffery, D. J., and Sutherland, P. G. 1985, *Ap. Sp. Sci.*, **109**, 277.

Kare, J. T., Pennypacker, C. R., Muller, R. A., Mast, T. S., Crawford, F. S., and Burns, M. S. 1982, in *Supernovae: A Survey of Current Research*, ed. M. J. Rees and R. J. Stoneham (Dordrecht: D. Reidel Publishing Company), p. 325.

Karovska, M., Nisenson, P., Noyes, R., and Papaliolios, C. 1987, *IAU Circ.*, No. 4382.

Karp, A. H., Lasher, G., Chan, K. L., and Salpeter, E. E. 1977, *Ap. J.*, **214**, 161.

Kirshner, R. P., and Kwan, J. 1974, *Ap. J.*, **193**, 27.

Kowal, C. T. 1968, *Astron. J.*, **73**, 1021.

Laney, C. D., and Stobie, R. G. 1986, *M.N.R.A.S.*, **222**, 449.

Lasker, B. M. 1980, *Ap. J.*, **237**, 765.

LeBlanc, J. M., and Wilson, J. R. 1970, *Ap. J.*, **161**, 541.

Livio, M., Buchler, J. R., and Colgate, S. A. 1980, *Ap. J. (Letters)*, **238**, L139.

Lombardi, G. G., and Kelleher, D. E. 1983, in *Spectral line Shapes II*, ed. K. Burnett (Berlin: De Gruyter), p. 835.

Lombardi, G. G., and Kelleher, D. E. 1985, *Ap. J.*, **288**, 820.

Lucy, L. B. 1971, *Ap. J.*, **163**, 95.

Magalhaes, A. M., and Velloso, E. W. 1987, *IAU Circ.*, No. 4361.

Markert, T. H., Canizares, C. R., Clark G. W., and Winkler, P. F. 1981, *Bull. AAS*, **12**, 799.

Martin, P. G. 1974, *Ap. J.*, **187**, 461.

Matcher, S. J., Meikle, P. S., and Morgan, B. L. 1987, *IAU Circ.*, No. 4391.

Maza, J., van den Bergh, S. 1976, *Ap. J.*, **204**, 519.

McCall, M. L. 1984, *M.N.R.A.S.*, **210**, 829.

———. 1985, in *Supernovae as Distance Indicators*, ed. N. Bartel (Berlin: Springer-Verlag), p. 48.

McCall, M. L., Reid, N., Bessell, M. S., and Wickramasinghe, D. T. 1984, *M.N.R.A.S.*, **210**, 839.

McKenna, S. J. 1985, *Astrophysics and Space Science*, **108**, 31.

Méndez, M., Clocchiatti, A., Benvenuto, O. G., Feinstein, C., and Marraco, H. G. 1987, submitted to *Ap. J.*.

Meyerott, R. E. 1978, *Ap. J.*, **221**, 975.

Mihalas, D. 1978, *Stellar Atmospheres* (San Francisco: W. H. Freeman and Company).

Mihalas, D., Kunasz, P., B., and Hummer, D. G. 1975, *Ap. J.*, 202, 465.

Müller, E., and Hillebrandt, W. 1981, *Astron. Astrophys.*, **103**, 358.

Müller, E., and Arnett, W. D. 1982, *Ap. J. (Letters)*, **261**, L109.

Natta, A., and Beckwith, S. 1986, *Astron. Astrophys.*, **158**, 310.

Nisenson, P., Papaliolios, C., Karovska, M., and Noyes, R. 1987, *Ap. J. (Letters)*, **320**, L15.

Nomoto, K. 1980a, in *Type I Supernovae*, ed. J. C. Wheeler (Austin: Univ. Texas), p. 164.

_______. 1980b, *Space Sci. Rev.*, **27**, 563.

_______. 1981, in *Fundamental Problems in the Theory of Stellar Evolution*, ed. D. Sugimoto, D. Q. Lamb and D. N. Schramm (Dordrecht: Reidel), p. 295.

Nomoto, K., Sugimoto, D., and Neo, S. 1976, *Astrophysics and Space Science*, **39**, L37.

Nomoto, K., Thielemann, F.-K., and Yokoi, K. 1984, *Ap. J.*, **268**, 644.

Oemler, A., and Tinsley, B. M. 1979, *Astron. J.*, **84**, 985.

Olson, G. L. 1982, *Ap. J.*, **255**, 267.

Panagia, N. 1985, in *Supernovae as Distance Indicators*, ed. N. Bartel (Berlin: Springer-Verlag), p. 14.

Pankey, T. Jr. 1962, Ph.D. Thesis, Howard University, Washington, DC.

Pengelly, R. M., and Seaton, M. J. 1964, *M.N.R.A.S.*, **127**, 165.

Pennypacker, C., Burns, S., Crawford, F., Friedman, P., Muller, J., Perlutter, S., Smith, C., Treffers, R., Williamson, A., Junkkarinen, V., Filippenko, A. V., McCarthy, P. J., and Rosino, L. 1986, *IAU Circ.*, No. 4219.

Phillips, M. M. 1979, *Ap. J. Suppl.*, **39**, 377.

Piel, J. *et al.* , ed. 1986, *Scientific American*, **Vol. 255 No. 2** (August), 65.

Pskovskii, Y. P. 1977, *Sov. Astron.*, **21**, 675.

Rybicki, G. B. 1970, in *Spectrum Formation in Stars with Steady-State Extended Atmospheres*, ed. H. Groh and P. Wellmann, NBS Spec. Publ. No. 332 (Washington: U.S. Government Printing Office), p. 87.

_______. 1984, in *Methods in Radiative Transfer*, ed. W. Kalkofen (Cambridge: Cambridge University Press), p. 1.

Rybicki, G. B., and Hummer, D. G. 1978, *Ap. J.*, **219**, 654.

Schwarz, H. E. 1987, preprint.

Schwarz, H. E., and Mundt, R. 1987, *Astron. Astrophys.*, 177, L4.

Serkowski, K. 1970, *Ap. J.*, 160, 1083.

Serkowski, K., Mathewson, D. S., and Ford, V. L. 1975, *Ap. J.*, 196, 261.

Shakhovskoi, N. M. 1976, *Soviet Astr.-AJ (Letters)*, 2, 107.

Shakhovskoi, N. M., and Efimov, Yu. S. 1973, *Soviet Astr.-AJ*, 16, 7.

Shapiro, P. R., and Sutherland, P. G. 1982, *Ap. J.*, 263, 902.

Shapiro, S. L., and Teukolsky, S. A. 1983, *Black Holes, White Dwarfs, and Neutron Stars: The Physics of Compact Objects* (New York: John Wiley & Sons, Inc.).

Shelton, I. 1987, *IAU Circ.*, No. 4316.

Sobolev, V. V. 1947, *Moving Envelopes of Stars* (Leningrad: Leningrad State University [in Russian]); English transl. S. Gaposchkin (Cambridge: Harvard University press, 1960).

Striganov, A. R., and Sventitskii, N. S. 1968, *Tables of Spectral Lines of Neutral and Ionized Atoms* (New York: IFI/Plenum Data Corporation).

Sutherland, P. G., and Wheeler, J. C. 1984, *Ap. J.*, 280, 282.

Symbalisty, E. M. D. 1984, *Ap. J.*, 285, 729.

_______. 1985, in *Numerical Astrophysics*, ed. J. M. Centrella, J. M. LeBlanc and R. L. Bowers (Boston: Jones and Bartlett Publishers, Inc.), p. 453.

Tammann, G. A. 1978, *Mem. Soc. Astron. Italiana*, 49, 315.

_______. 1982, in *Supernovae: A Survey of Current Research*, ed. M. J. Rees and R. J. Stoneham (Dordrecht: D. Reidel Publishing Company), p. 371.

Trimble, V. L. 1982, in *Supernovae: A Survey of Current Research*, ed. M. J. Rees and R. J. Stoneham (Dordrecht: D. Reidel Publishing Company), p. xv.

Tuohy, J. R., Clark, D. H., and Burton, A. P. 1980, *Space Sci. Rev.*, 27, L65.

Wagoner, R., V. 1981, *Ap. J. (Letters)*, 250, L65.

Walsh, J. R., Bailey, J. A., and Ogura, K. 1987, *IAU Circ.*, No. 4328.

Weaver, T. A., and Woosley, S. E. 1980, *Ann. NY Acad. Sci.*, 336, 335.

Wesselink, A. J. 1949, *B.A.N.*, 10, 91.

Wheeler, J. C. 1978, *Ap. J.*, 225, 212.

Wheeler, J. C., and Levreault, R. 1985, *Ap. J. (Letters)*, 294, L17.

Wheeler, J. C., Harkness, R. P., Barker, E. S., Cochran, A. L., and Wills, D. 1987, *Ap. J. (Letters)*, 313, L69.

Whelan, J. C., and Iben, I. Jr. 1973, *Ap. J.*, **186**, 1007.

Wilson, J. R., 1985, in *Numerical Astrophysics*, ed. J. M. Centrella, J. M. LeBlanc and R. L. Bowers (Boston: Jones and Bartlett Publishers, Inc.), p. 422.

Wolstencroft, R. D., and Kemp, J. C. 1972, *Nature*, **238**, 452.

Woosley, S. E. 1987, submitted to *Ap. J.*.

Woosley, S. E., Axelrod, T. S., Weaver, T. A. 1984, in *Stellar Nucleosynthesis*, ed. C. Chiosi and A. Renzini (Dordrecht: Reidel) p. 263.

Woosley, S. E., Taam, R. E., and Weaver, T. A. 1986, *Ap. J.*, **301**, 601.

Woosley, S. E., and Weaver, T. A. 1986, *Ann. Rev. Astron. and Ap.*, **24**, 205.